JOINT EUROPEAN TORUS

JET

JET JOINT UNDERTAKING

PROGRESS REPORT 1985

EUR 10616 EN
EUR-JET-PR3

JET JOINT UNDERTAKING

PROGRESS REPORT 1985

MARCH 1986

This document is intended for information only
and should not be used as a technical reference.

EUR 10616 EN (EUR-JET-PR3) March 1986.
Editorial work on this report was carried out by B.E. Keen
The preparation for publication was undertaken by
the Documentation Service Units, Culham Laboratory.

Printed in England

Contents

Foreword

This is the third JET Progress Report which covers the second full year of JET's operation. These Progress Reports were introduced in 1983 to provide a more detailed account of JET's scientific and technical progress than that contained in the JET Annual Reports. The first two Reports (in 1983 and 1984) described the main activities and advances made on JET during the relevant periods, and concentrated on the scientific and technical involvement of the relevant JET Departments.

These previous Progress Reports provided good reference documents of JET developments and results during the early operation period, before these advances were published in the conventional literature. Now, JET results receive world-wide dissemination at international Conferences and meetings and in various scientific journals, at an earlier stage. Therefore, there is now less need for such a detailed record of all JET events, as the machine now operates almost in a routine manner. In addition, the staff effort required for preparation and compilation of the text was considerable and in many cases produced a duplication of material already published. Consequently, it was decided to change the format of the 1985 Progress Report, so that it provided an overview summary of the scientific and technical advances during the year, supplemented by appendices of detailed contributions (in preprint form) of the more important JET articles produced during that year. This Report represents an experiment in this respect, and comments from recipients would be welcomed.

The document is still aimed not only at specialists and experts engaged in nuclear fusion and plasma physics, but also at a more general scientific community. To assist in meeting these general aims, the Report contains a brief summary of the background to the Project, describes the basic objectives of JET and the principal design aspects of the machine. In addition, since the Project Team structure was changed during 1985, these changes are detailed, as it is within this structure that the activities and responsibilities for machine operation are carried out and the scientific programme is executed.

1985 was marred by the sudden and untimely death, on 30 June, of Dr Hans-Otto Wüster, the then Director of the Project. We shall always be indebted to him for his leadership and contributions to the formation and success of the Project. Many tributes to his memory came from all over the world. Fusion in Europe and the world has lost a great man, but, above all, everyone within the JET Project has lost a great friend.

As the new Director, it will be a difficult task to follow such a leader as Dr Wüster, but with the dedication, enthusiasm and skill of all Project staff, I am sure that this obstacle will be surmounted and we will continue to meet with confidence the tremendous challenges offered by the Project. Other changes in the Project included that of Dr R J Bickerton, formerly an Associate Director and Head of Scientific Department, who was appointed Deputy Director and Head of Heating and Theory Department. Also Dr M Keilhacker joined JET from IPP Garching, F.R.G., as an Associate Director and Head of the Experimental Department.

During 1985, the machine again provided excellent technical performance. The Project entered Phase IIA of its programme devoted to additional heating studies to observe the effects of large power ion cyclotron resonance heating (ICRH) on the plasma temperature and confinement properties. Two RF antenna had been installed during the shutdown at the end of 1984, and these were used during operations in the first half of 1985. From July, a four month shutdown was scheduled to allow installation of additional components including a third RF antenna. Final preparations were also completed for the first neutral injection system. Operations were continued until the end of the year.

In 1985, there was 1446 tokamak pulses with plasma current exceeding 1 MA. This represented a consistent increase over 69 in 1983 and 472 in 1984. Throughout 1985, many plasma pulses were produced with the maximum rated toroidal magnetic field value of 3.45 T. A plasma current of 5 MA was reached and maintained for 1 s. At present, machine operations at high currents are restricted to plasma elongation ratios of 1.4 to avoid the possibility of damage to the machine, if control of the vertical stability was lost. The design of new vessel supports is nearly complete and when installed, this restriction should be removed. Other modifications are planned to enable the current to be maintained at 5 MA for longer time periods, with the possibility of cautiously raising the current to higher levels.

During 1985, RF additional heating used reached a record input power of 6 MW, with 15 MJ of energy coupled to the plasma. A degradation of confinement time with increasing power was observed, similar to that seen on smaller tokamaks, but experience there has shown that this degradation can be reduced or avoided by operating in a mode limited with a magnetic separatrix. This so called X-point operation has been demonstrated on JET with plasma currents up to 1.5 MA, but not yet with additional heating, so that

the beneficial effects of this mode have still to be demonstrated on JET.

Plasma impurities remained high in 1985, as previously, and although they do not lead to a significant radiated power loss from the plasma core, they dilute the number of ions available for useful fusion reactions. A combination of multiple pellet refuelling and powerful additional heating, which will be tested in 1987, are likely contenders to improve this situation.

The scientific results so far achieved on JET are encouraging. In terms of the plasma parameters — density, temperature and confinement — JET has already reached the stage where each of these parameters is within a factor of two of three of those needed for fusion reactor. At the end of 1985, the first neutral injection system for additional heating was installed and this will further improve the additional heating power introduced into the plasma.

The successful construction of the device and the most encouraging results obtained so far are a tribute to the dedication and skill of all who work on the Project. They also reflect the continuous co-operation and assistance received from the Associated Laboratories and from the Commission of the European Communities. They support the confidence and guidance given to the Project management by the JET Council, JET Executive Committee and JET Scientific Council.

With such devotion from all sides, the Project faces, with confidence, the many problems and challenges that are likely to be encountered in the future.

Dr P H Rebut
April 1986

Introduction, Background and Report Summary

Introduction

Following the formal start of the Operation Phase of the JET Project in June 1983, it was decided to produce an annual JET Progress Report which should provide a more detailed account of JET's scientific activities than that which was provided in the JET Annual Report. The first two JET Progress Reports (EUR-JET-PR1) and (EUR-JET-PR2) described activities and advances up to the end of 1983 and 1984, respectively, and concentrated mainly on the scientific and technical activities of the relevant Departments in JET.

Although it was desirable to have this detailed record of JET's achievements and advances in all its aspects, the staff effort involved in preparation and compilation of the text was considerable and the information was already outdated by the time of publication. Consequently, for the 1985 version, it was decided that, in order to speed up the production process and to minimise the staff effort involved, a Progress Report would be produced which provided an overall summary of the scientific and technical advances achieved during the year, followed by appendices of detailed contributions (in preprint form) of the most important JET technical articles produced during that year. As an experiment, this is the first Progress Report produced in this form.

For completeness, this section contains a brief summary of the background to the Project. It describes the basic objectives of JET and the principal design aspects of the machine. In addition, since the Project Team structure was changed during 1985, these changes are detailed, as it is within this structure that the activities and responsibilities for machine operation are carried out and the scientific programme is executed.

Background

Objectives of JET

The Joint European Torus (JET) is the largest single project of the nuclear fusion research programme of the European Atomic Energy Community (EURATOM). The project was designed with the essential objective of obtaining and studying plasma in conditions and with dimensions approaching those needed in a fusion reactor. The studies are aimed at:

a) Investigating plasma processes and scaling laws, as plasma dimensions and parameters approach those necessary for a fusion reactor;

b) Examining and controlling plasma-wall interactions and impurity influxes in near-reactor conditions;

c) Demonstrating effective heating techniques, capable of approaching reactor temperatures in JET, in the presence of the prevailing loss processes (particularly, RF and Neutral Beam Heating processes);

d) Studying alpha-particle production, confinement and subsequent plasma interaction and heating produced as a result of fusion between deuterium and tritium.

Two of the key technological issues in the subsequent development of a fusion reactor are likely to be faced for the first time in JET. These are the use of tritium and the application of remote maintenance and repair techniques. The physics basis of the post-JET programme will be greatly strengthened if other fusion experiments currently in progress are successful. The way should then be clear to concentrate on the engineering and technical problems involved in progressing from an advanced experimental device like JET to a prototype power reactor.

Basic JET Design

To meet these overall aims, the basic JET apparatus was designed as a large tokamak device with overall dimensions of about 15m in diameter and 12m in height. A diagram of the apparatus is shown in Fig. 1 and its principal parameters are given in Table I. At the heart of the machine, there is a toroidal vacuum vessel of major radius 2.96m having a D-shaped cross-section 2.5m wide by 4.2m high. During operation of the machine, a small quantity of gas (hydrogen, deuterium or tritium) is introduced into the vacuum chamber and is heated by passing a large current (up to 3.8MA during the initial phase, and up to 4.8MA during the full design phase) through the gas. This current is produced by transformer action using the massive eight-limbed magnetic circuit, which dominates the apparatus (see Fig. 1). A set of coils around the centre limb of the magnetic circuit forms the primary winding of the transformer with the plasma

acting as the single turn secondary. Additional heating of the plasma is provided by propagating and dissipating high power radio frequency waves in the plasma and by injecting beams of energetic neutral atoms into the system.

The plasma is confined away from the walls of the vacuum vessel by a complex system of magnetic fields, in which the main component, the toroidal field, is provided by 32 D-shaped coils surrounding the vacuum vessel. This field, coupled with that produced by the current flowing through the plasma, forms the basic magnetic field for the tokamak confinement system, which provides a full design field at the centre of 3.45T. The poloidal coils, positioned around the outside of the vacuum vessel, shape and position the plasma in operation.

Initial experiments have been undertaken using hydrogen and deuterium plasmas, but in the later stages of the operation, it is planned to operate with deuterium-tritium plasmas, so that fusion reactions can occur to produce significant α-particle heating in the plasma.

TABLE I
Principal JET Parameters

Parameter	*Value*
Plasma minor radius (horizontally), a	1.25m
Plasma minor radius (vertically), b	2.10m
Plasma major radius, R_o	2.96m
Plasma aspect ratio, R_o/a	2.37
Plasma elongation ratio, e=b/a	1.68
Flat top pulse length	10s
Toroidal magnetic field (plasma centre)	3.45T
Plasma current, circular plasma	3.2MA
D shaped plasma	4.8MA
Volt-seconds available	34Vs
Toroidal field peak power	380MW
Poloidal field peak power	300MW
Additional heating power (in plasma)	25MW
Weight of vacuum vessel	108t
Weight of toroidal field coils	384t
Weight of iron core	2800t

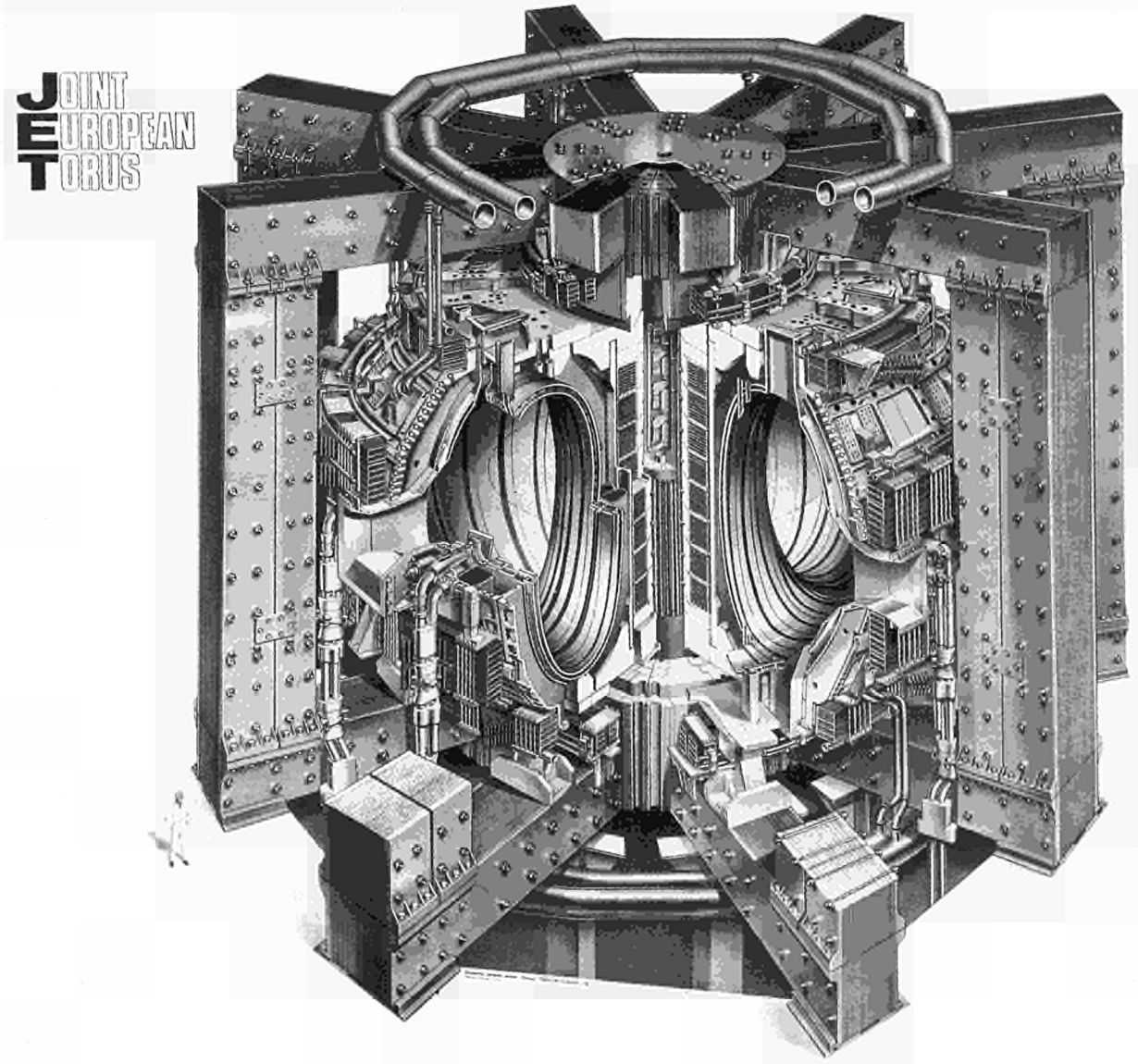

Fig. 1: Diagram of the JET Tokamak

In order to reach conditions close to those relevant to a fusion reactor, a plasma density of $\sim 10^{20} m^{-3}$ at a temperature of 10keV would be needed. Even with a current of 4.8MA in JET, this would be inadequate to provide the temperature required using ohmic heating alone. Consequently, additional heating is required and two main systems are gradually being added to JET over the years, as follows:

- Injection into the plasma of highly energetic neutral atoms (Neutral Injection Heating)
- Coupling of high power electromagnetic radiation to the plasma (Radio Frequency (RF) heating).

The total power into the plasma will increase in discrete steps up to ~25MW.

Project Team Structure

Up to mid-1985, machine operation and execution of the scientific programme had been undertaken within a Team Structure divided between three Departments, as follows:

(i) Operation and Development Department;
(ii) Scientific Department;
(iii) Administration Department.

This structure has been described in detail in previous JET Annual and Progress Reports (See EUR-JET-AR7 and EUR-JET-PR2).

However, following the sad death of Dr H-O Wüster in mid-1985 and the appointment of the new Director, Dr P H Rebut, a rationalization of the Project Structure was undertaken. The structure adopted, for management purposes was divided into four Departments (See Table II):

(i) Machine and Development Department;
(ii) Experimental Department;
(iii) Heating and Theory Department;
(iv) Administration Department.

The main duties of the Administration Department have been described in previous JET Annual Reports. This Report concentrates on progress made in the scientific and technical Departments during 1985. To aid this description, the functions of these Departments are described below.

Machine and Development Department

The Machine and Development Department is responsible for the performance capacity of the machine as well as equipment for the active phase, together with enhancements directly related to it (excluding heating) and the integration of any new elements on to the machine. In addition, the Department is responsible for machine services. The Department contains three Divisions:

(1) Magnet and Power Supplies Division, which is responsible for the design, installation,

TABLE II
Project Team Structure

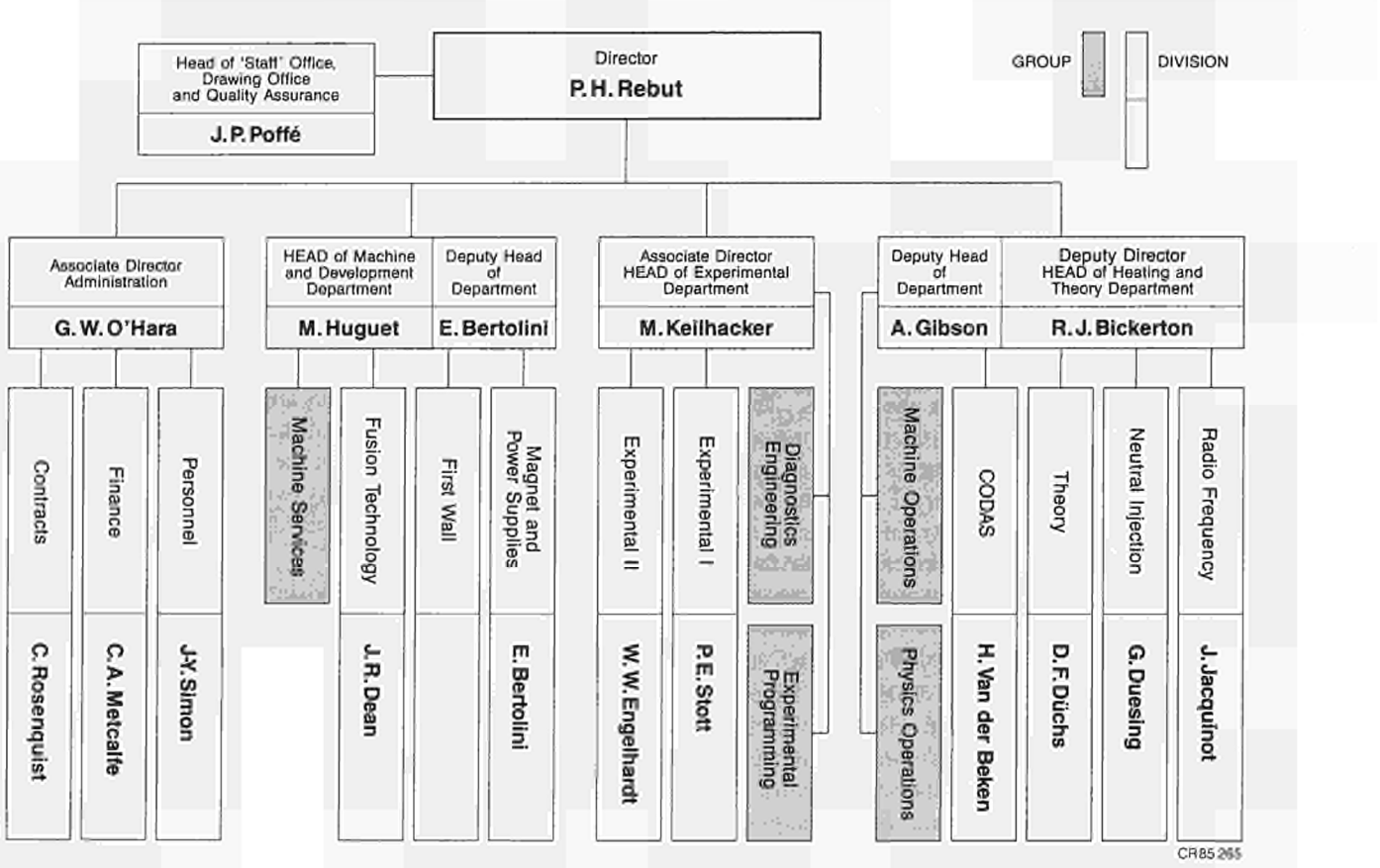

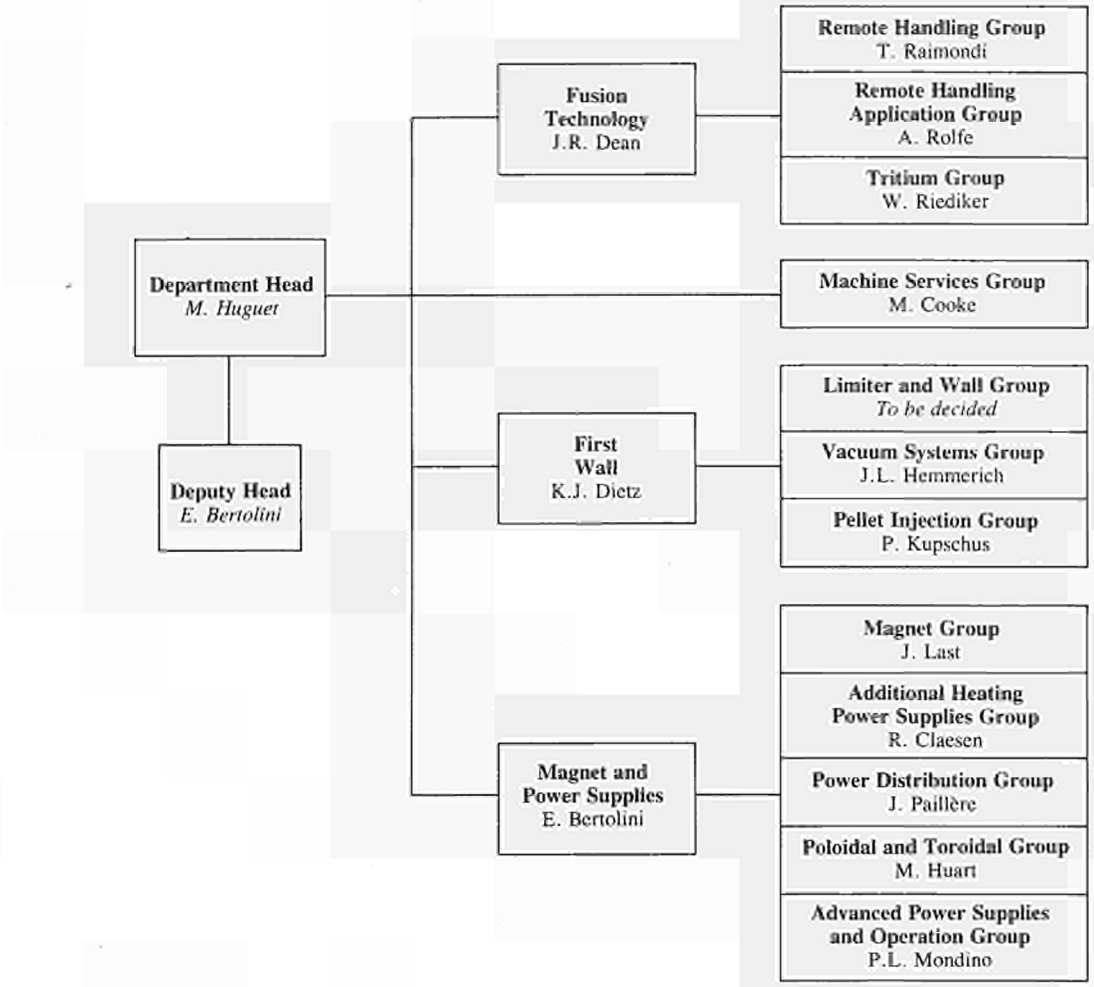

Fig. 2: Machine and Development Department, Group Structure (December, 1985)

operation, maintenance and modification of all power supply equipment needed by the Project. In addition, the Department is responsible for maintenance and operation of the coil systems, structural components and machine instrumentation;

(2) First Wall Division, which is responsible for the vital area of plasma wall interactions. Its main tasks include the provision and maintenance inside the vacuum vessel of conditions leading to high quality plasma discharges. The Division develops, designs, procures and installs first wall systems and components, such as limiters, wall protections and internal pumping devices. The area of responsibility encompasses the vacuum vessel as a whole together with its associated systems, such as pumping, bake-out and gas introduction;

(3) Fusion Technology Division, which is responsible for the design and development of remote handling methods and tools to cope with the requirements of the JET device, and for maintenance, inspection and repairs. Tasks also include the design and construction of facilities for handling of tritium.

The structure of the Machine and Development Department to Group Leader level is shown in Fig. 2 and the list of staff within the Department is shown in Fig. 3.

Experimental Department

The main functions of the Department relate to the measurement and validation of plasma parameters. The main tasks are (i) to conceive and define a set of coherent measurements; (ii) to be responsible for the construction of necessary diagnostics; (iii) to be responsible for the operation of the diagnostics and the quality of measurements and the definition of the plasma parameters; and (iv) to play a major role in the interpretation of data.

The Department contains two Groups (on Diagnostics Engineering and Experimental Programming) and two Divisions:

(1) Experimental Division 1 (ED1), which is responsible for specification, procurement and operation of approximately half the JET diagnostic systems. ED1 undertakes electrical measurements, electron temperature measurements, surface and limiter physics and neutron diagnostics;

(2) Experimental Division 2 (ED2), which is responsible for specification, procurement and

MACHINE AND DEVELOPMENT DEPARTMENT

Head of Department: M. Huguet
Deputy Head of Department: E. Bertolini

D. Carre	Mrs. I. Hyde	Mrs. M. Rydalm
Mrs. A. Cranstone	L. Nickesson	M. Walravens

FUSION TECHNOLOGY
Head: J.R. Dean

S.J. Booth	P.D. Jones	W. Riediker
R. Cusack	A. Konstantellos	J. Schreibmaier
Mrs. M. Daish	A. Nowak	L. Sonnerup
L. Galbiati	M. Pescatore	A. Tesini
A. Galetsas	P. Presle	M. Tschudin
E. Gebler	T. Raimondi	M. Wykes
Mrs. M.E. Jones	J. Removille	

FIRST WALL
Head: K.J. Dietz

W.P. Bailey	K. Grabenstätter	G. McCarthy
B. Bignaux	L. Grobusch	J. Orchard
A. Boschi	J. Hemmerich	R.L. Shaw
H. Buttgereit	D. Holland	K. Sonnenberg
G. Celentano	G. Israel	R. Thomas
W. Daser	H. Jensen	E. Usselmann
C. Froger	P. Kupschus	T. Winkel

MAGNET AND POWER SUPPLIES
Head: E. Bertolini

Mrs. C. Allen	A. Keymer	K. Selin
T. Bonicelli	J.R. Last	S. Shaw
O. Buc	V. Marchese	A. Skinstad
D. Cacaut	G. Marcon	S. Turley
J. Carwardine	L. Mears	J. van Veen
C. Christodoulopoulos	A. Moissonnier	N. Walker
R. Claesen	P. Mondino	Mrs. L.T. Wall
J. Dobbing	G. Murphy	C.R. Wilson
P. Doidge	Mrs. J. Nolan	G.C. Wilson
B.T. Eriksson	P. Noll	M.E. Young
H. Fielding	J. Paillère	L. Zannelli
J. Goff	I. Piacentini	J. Zwart
D. Halliwell	C. Raymond	
M. Huart	A. Santagiustina	

Fig. 3: Project Team Staff in the Machine and Development Department (December, 1985)

operation of the other half of the JET diagnostic systems. ED2 undertakes all spectroscopic diagnostics, bolometry, interferometry, the soft X-ray array and neutral particle analysis.

The structure of the Experimental Department to Group Leader level is shown in Fig. 4 and the list of staff in the Department is shown in Fig. 5.

Heating and Theory Department

Heating and Theory Department is responsible for heating the plasma, the theory of tokamak physics, the organisation of experimental data, and the day to day operation of the machine. The main functions of the Department are (i) following the theory of tokamak physics; (ii) heating of the plasma and analysis of its effects; (iii) centralising the interpretation of experimental results and investigating their coherence; (iv) organising data acquisition and computers; and (v) preparing and co-ordinating operation of the machine across the different Departments.

The Department is composed of two groups (Machine Operations Group and Physics Operation Group) specifically charged with operating JET, and four Divisions:

(1) Control and Data Acquisition System Division (CODAS), which is responsible for the implementation, upgrading and operation of computer-based control and data acquisition systems for JET;

(2) Neutral Beam Heating Division, which is responsible for the construction, installation, commissioning and operation of the neutral injection system, including development towards full power operation of the device. The Division also participates in studies of the physics of neutral beam heating;

(3) Radio Frequency Heating Division, which is responsible for the design, construction, commissioning and operating the RF heating

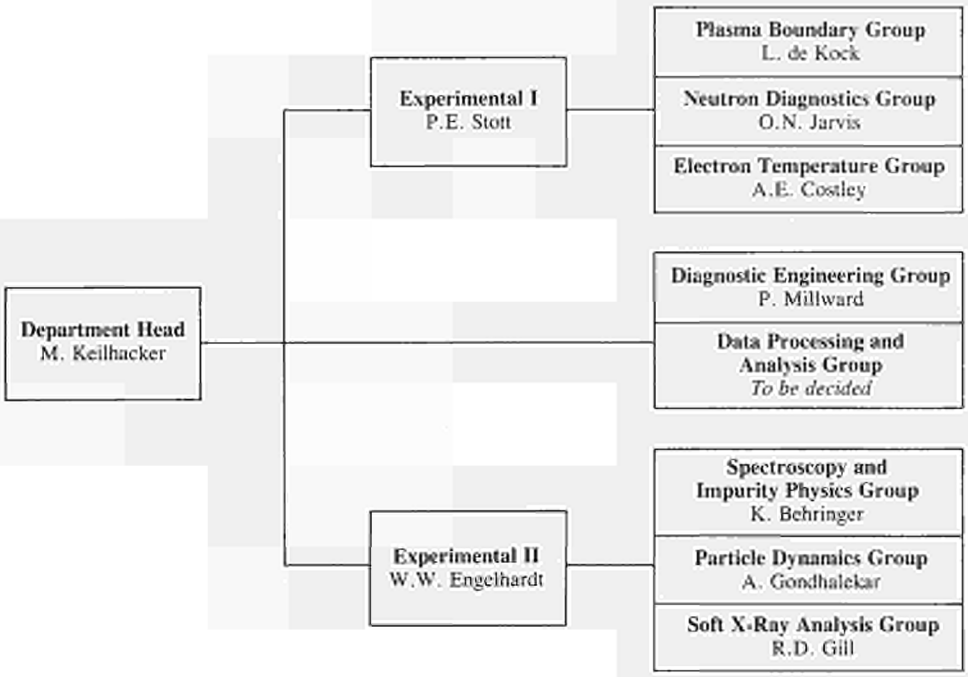

Fig. 4: Experimental Department, Group Structure (December 1985)

EXPERIMENTAL DEPARTMENT

Head of Department: M. Keilhacker

A. Ainsworth	C.J. Hancock	P.J. Roberts
M. Barnes	R.C. Lobel	A. Tiscornia
C. Caldwell-Nichols	P. Millward	C.H. Wilson
N. Foden	B. Oliver	
J. Gowman	J. Reid	

EXPERIMENTAL I

Head: P.E. Stott

Mrs. S-J Ashwood	P.J. Harbour	P. Roach
D. Bartlett	M. Hone	G. Sadler
C. Best	I. Hurdle	Miss K. Slavin
B.W. Brown	O. Jarvis	A. Stevens
D. Campbell	L. de Kock	Miss D. Strange
J. Coad	J. Källne	D. Summers
A. Costley	G. Neill	P. van Belle
J. Fessey	C. Nicholson	J. Vince
S. Gregoli	P. Nielsen	D. Wilson
C. Gowers	R. Prentice	

EXPERIMENTAL II

Head: W.W. Engelhardt

K. Behringer	J. Holm	Mrs. W. Prill
G. Braithwaite	Mrs E. Källne	B.K. Scheidt
J.L. Bonnerue	L. Lamb	F. Sieweke
A.D. Cheetham	G. Magyar	Mrs. C. Simmons
S. Corti	J.L. Martin	M. Stamp
Miss G.B. Denne	P. Morgan	A.R. Talbot
A. Edwards	E. Oord	E. van der Goot
Mrs. A. Flowers	J. O'Rourke	M. von Hellermann
R. Gill	A. Ravestein	B. Viaccoz
A. Gondhalekar	J. Ryan	

Fig. 5: Project Team Staff in the Experimental Department (December, 1985)

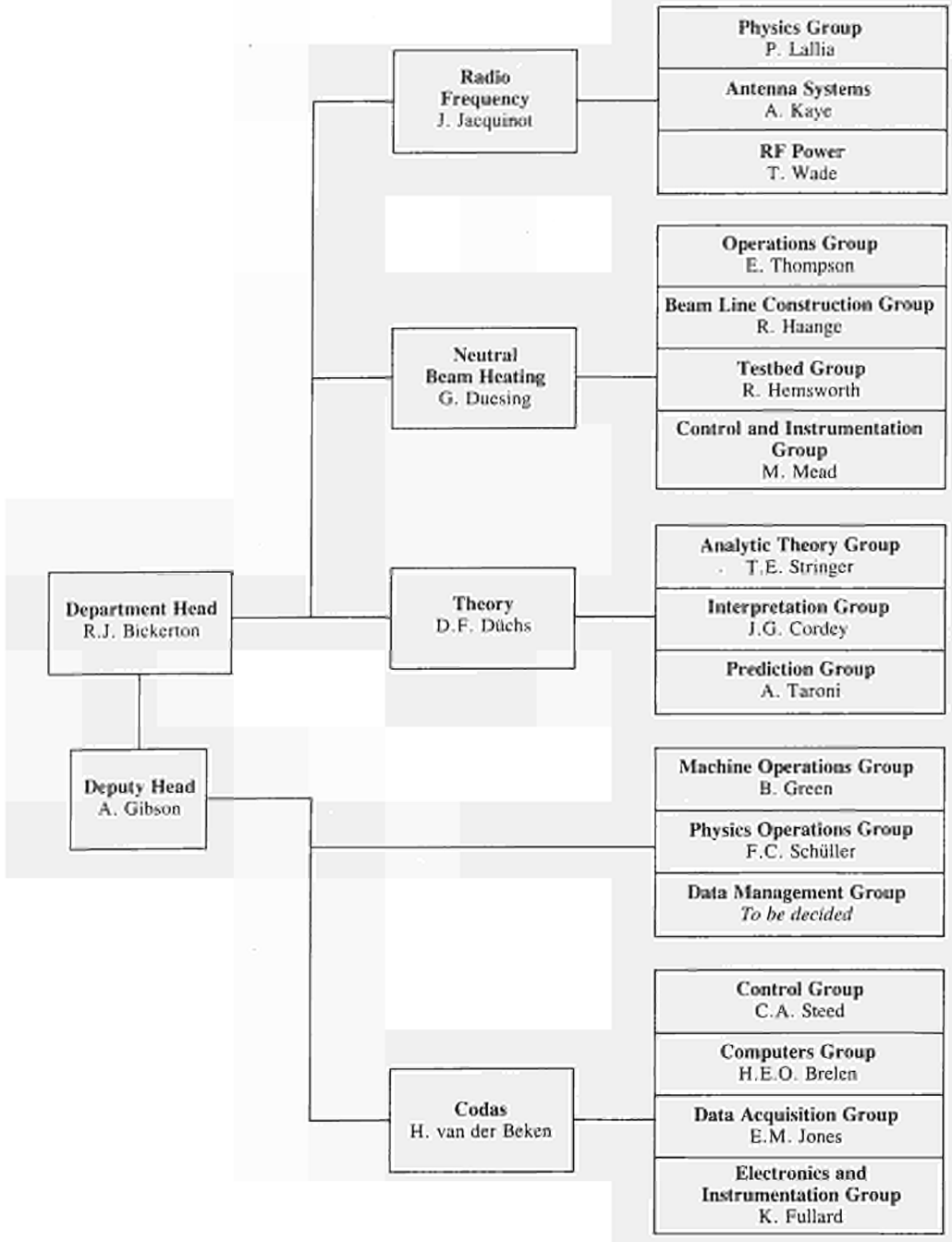

Fig. 6: Heating and Theory Department, Group Structure (December, 1985)

system during the different stages of its development to full power. The Division also participates in studies of the physics of RF heating;

(4) Theory Division, which is responsible for prediction by computer simulation of JET performance, interpretation of JET data and the application of analytic plasma theory to gain an understanding of JET physics.

The structure of the Heating and Theory Department to Group Leader level is shown in Fig. 6, and the list of staff in the Department is shown in Fig. 7.

In addition , all Divisions are involved in:

- Execution of the experimental programme;
- Interpretation of results in collaboration with other appropriate Divisions and Departments;
- Making proposals for future experiments.

Report Summary

Section 1 of this Report provides a brief introduction and some background information relevant to the Report.

HEATING AND THEORY DEPARTMENT

Head of Department: R.J. Bickerton
Deputy Head of Department: A. Gibson

K. Adams
P. Chuilon
A. Conway
D. Cook
S. Cooper
T. Dale
E. Daly
K. Fenton
B. Green
B. Glossop
N. Green
A. Hancock
M. Hughes
H. Key
P. Lomas
M. Malacarne
D. Pratt
Miss A. Reichenau
R. Rigley
Mrs. J. Roberts
Mrs. M.E. Rowe
P. Rutter
F.C. Schüller
W. Smith
A. Tanga
P. Thomas
Miss J.L. Thompson

RADIO FREQUENCY

Head: J. Jacquinot

R.J. Anderson
J. Arbez
S.C. Booth
G. Bosia
M. Brandon
H. Brinkschulte
Mrs. L. Brookes
M. Bures
G. Cottrell
D.T. Edwards
A. Franklin
E. Hanley
R. Horn
G. Jessop
A. Kaye
P. Lallia
C. Maradan
P. Murray
J. Plancoulaine
Mrs. L. Rowe
F. Sand
M. Schmid
A.G. Sibley
T. Wade
C. Walker

NEUTRAL BEAM HEATING

Head: G. Duesing

H. Altmann
A. Browne
C. Brookes
A. Burt
C.D. Challis
D. Cooper
Mrs. D. Cranmer
J.F. Davies
G. Deschamps
A. Dines
D. Ewers
H. Falter
J. Gallacher
Mrs S. Gerring
A. Goede
R. Haange
R. Hemsworth
F. Hurd
J. Jensen
A. Jones
T.T.C. Jones
E. Küssel
D. Kausch
F. Long
J. Lundqvist
D. Martin
P. Massmann
C. Mayaux
M.J. Mead
W. Obert
S. Papastergiou
D. Raisbeck
R. Roberts
D. Stork
E. Thompson
Miss D. Vernall
M. Watson

THEORY

Head: D.F. Düchs

M. Brusati
J. Christiansen
W. Core
J.G. Cordey
Mrs. S. Costar
J.J. Davis
A. Galway
N.A. Gottardi
T. Hellsten
Mrs. S. Hutchinson
B. Keegan
E. Lazzaro
Miss M. Nave
Mrs. M.G. Pacco
R.T. Ross
R. Simonini
E. Springmann
T.E. Stringer
Mrs. P. Stubberfield
A. Taroni
M. Watkins
J. Wesson

CODAS

Head: H. van der Beken

Mrs. A.M. Bellido
M.J. Botman
H.E.O. Brelen
W.J. Brewerton
M.L. Browne
T. Budd
P. Card
Mrs. L.M. Dines
S.E. Dorling
K. Fullard
R.F. Herzog
E.M. Jones
Miss J. Kedward
G.E. Kinahan
J.G. Krom
Miss E. Mathiä
D.S. Nassi
J.P. Nijman
C.G. Pollard
G.D. Rhoden
J.J. Saffert
C.A. Steed
B.A. Wallander
J.E. van Montfoort
I.D. Young

Fig. 7: Project Team Staff in the Heating and Theory Department (December, 1985)

Section 2 sets out an overview of progress on JET during 1984 and, with a survey of scientific and technical achievements during 1984, sets these advances in their general context. This summary is specifically cross-referenced to reports and articles prepared and presented by JET staff during 1985. The more important of these articles, which are of general interest, are reproduced as appendices to this Report.

In Section 3, certain developments are considered which might enable additional improvements/ modifications of the machine to further improve its overall performance. These improvements are considered to overcome certain limitations encountered generally on Tokmaks, particularly concerned with density limits, with plasma MHD behaviour, with impurities and with plasma transport. Some attention has been devoted to methods of surmounting these limitations and these are detailed in this section.

In the Appendices, selected articles prepared by JET authors are reproduced in detail, and provide more details of the activities and achievements made on JET during 1985. In addition, a full list is included of all Articles, Reports and Conference papers published in 1985.

Technical Achievements during 1985

Torus Systems

Vacuum and First Wall

During 1985, many new elements were added to the vacuum system. The second neutral injection box together with its high vacuum rotary valve and a third RF antenna were connected to the main vacuum, and a large number of new diagnostics were also installed. However, the most important developments took place in the area of the first wall. In 1985, the machine was operated for the first time with low-Z (graphite) wall protections at the inboard wall. This was the first step of a long term programme aimed at having only low-Z materials facing the plasma.

Plasma operation in these new conditions was successful, and from a technical viewpoint, the behaviour of the graphite tiles was also satisfactory. When the vessel was opened in July 1985 after six months of plasma operation, very little damage was seen except for some minor, but expected, signs of erosion. This contrasted with the very serious damage observed in 1984 on the Inconel protection plates, even though during this operating period, the energy deposited on the graphite tiles by run-away electrons had been comparable to that during the 1984 campaign.

During the Summer shutdown period, additional graphite protection was installed to further reduce the contamination of the plasma by metal impurities. The inboard protection was extended by eight discrete poloidal rings covering the octant joints (see Fig.8). The limiters were fitted with additional tiling to cover better their Inconel support plate at the back, since there was some evidence of plasma flowing behind the graphite tiles. At the same time, graphite tiles were also fitted at the outboard wall in the vicinity of the Octant No. 5 horizontal port, to protect the vessel wall against tangential neutral beams, originating from Octant No. 8 (see Fig.9)

When operation was resumed early in 1985, the surface of the four discrete graphite limiters had been carefully cleaned. This resulted in metal free plasma discharges during the first 4-6 weeks of operation. However, the metallic contamination already observed in 1984 returned gradually. It was not clear whether this contamination originated from sputtering during glow discharge or plasma discharges, or from metals evaporated from the walls during vertical instibilities. Nevertheless, the good results obtained in January 1985 were a clear encouragement to pursue further the policy

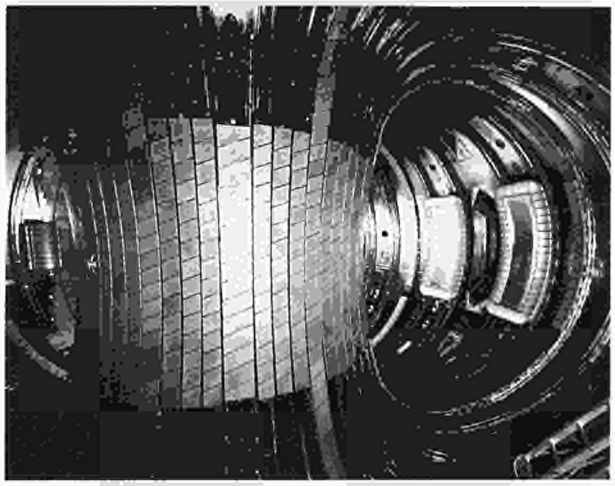

Fig. 8: Graphite protections covering the Octant Joints

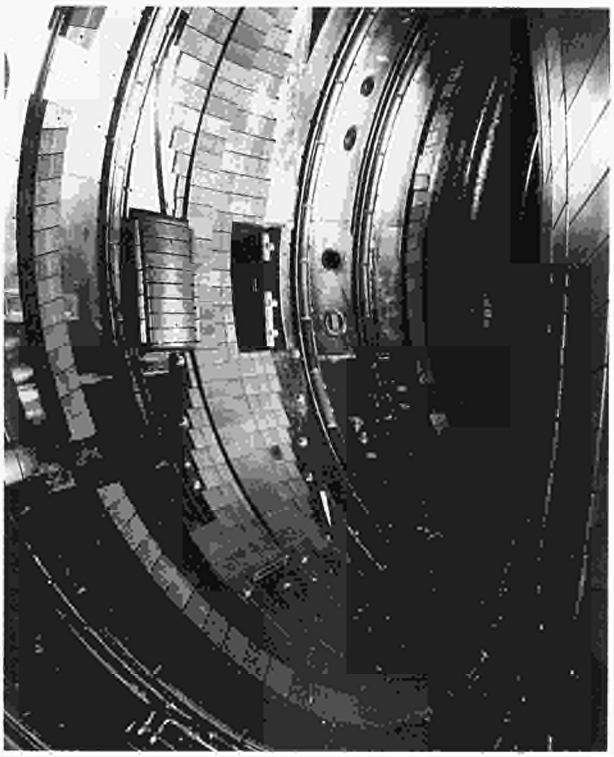

Fig. 9: Neutral Beam protection tiles at Octant No. 5

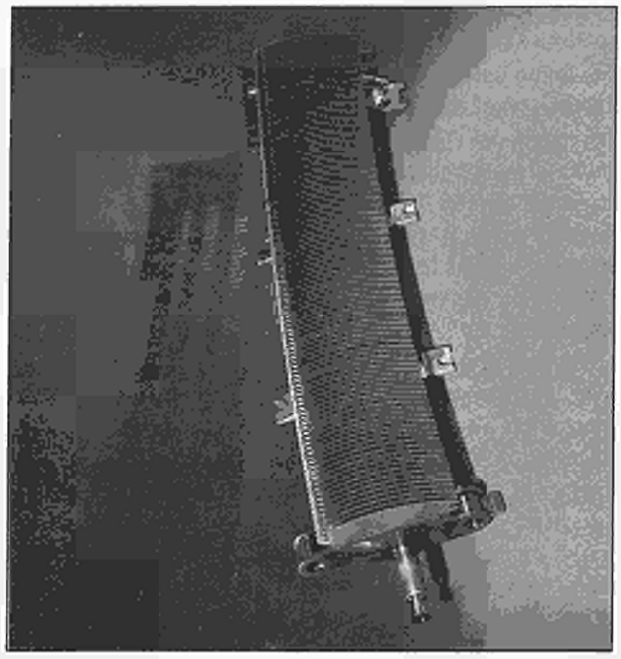

Fig. 10: Prototype sector of the belt limiter cooling structure

of covering the walls with low-Z materials. As a result of this low Z policy, it was decided in July 1985 to remove from the machine the nickel-clad limiters since they represented a potential source of metallic contamination.

Discussions on tile materials for the future belt limiters resulted in the selection of graphite and beryllium, as the most likely options. Beryllium was considered as superior to graphite from the viewpoint of plasma operation, due to its very low-Z and its oxygen getter properties. However, the toxicity of the beryllium dust could complicate future in-vessel maintenance. It was decided to proceed with the procurement of both beryllium and graphite tiles for the belt limiter (and RF antennae), and postpone until the second half of 1986 the choice of the material which would be used first.

The procurement of beryllium and graphite tiles for the belt limiter was initiated. The manufacture of the cooling structure of the belt limiter, made good progress with the completion and testing of a prototype sector (Fig.10).

Containment of Forces During Vertical Instabilities

When operations resumed in January 1985, the vacuum vessel was fitted with additional supports designed to contain the large forces acting on the vessel during vertical instabilities. Tests showed that the vessel displacements during instabilities were effectively reduced and damped by the supports. However, these supports are only a temporary measure and are not capable of restraining safely the vessel at plasma currents in excess of 5MA, with highly elongated cross sections.

The design of a new generation of supports was conducted in 1985. These supports will link the main vertical parts of the vessel to the magnetic limbs (Fig.11). The interference between the new supports and diagnostics will necessitate design modifications of some diagnostics.

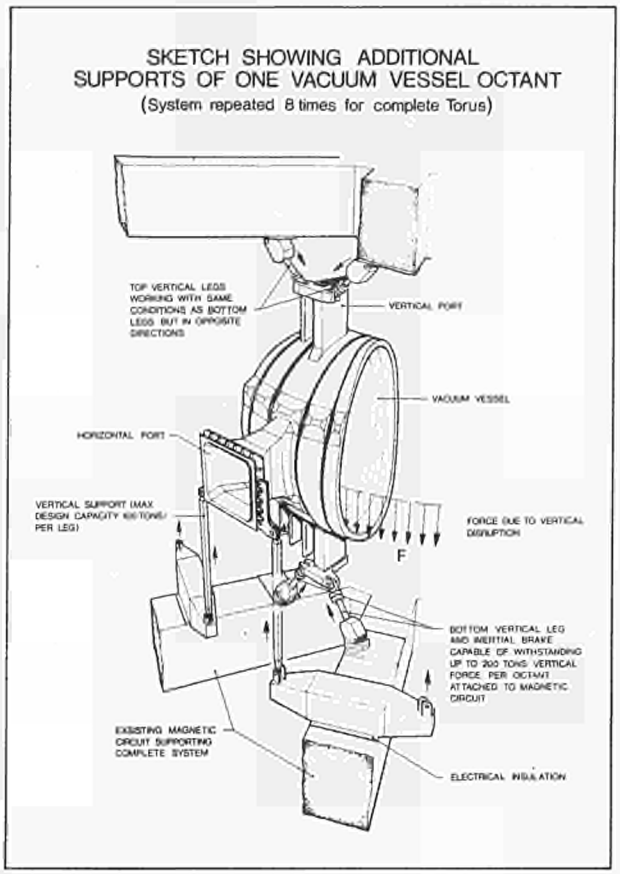

Fig. 11: Final design of the vacuum vessel supports

Power Supply and Magnet Systems

The main activities on the Power Supply and Magnet Systems during 1985, have been in the following areas: completion and progress in the installation of new equipment, studies and implementation of new projects, maintenance of operation equipment and in JET Operation.

Installation and Commissioning

The 400kV/33kV substation has been extended with addition of a third 33kV busbar supplied by a new 300MVA transformer and a set of 33kV breakers: the three independent 33kV busbar systems are now operational.

The planned targets for the Neutral Injection Power Supplies have been achieved:

- All the equipment required to supply the first eight Neutral Injectors (Box 1)at 80kV, 60A, 20s have been installed, and tested on a dummy load up to the full design performance; these include the accelerating grid, the gradient grid, the suppression grid, the arc, the filament, the NI magnet and the snubber power supplies, the SF6 transmission lines, the active snubbers and the SF6 tower. As a consequence, the NI Box 2 is now available for JET operation and eight

injectors have been simultaneously operated up to 60kV on the calorimeter plate and will be injected into the plasma in early 1986;

- For NI Box 2 (eight injectors), all the accelerating grid power supplies have been commissioned, while the auxiliary power supplies are under installation, for the transmission lines, the snubbers and the tower.

All the AC/DC power supplies (including auxiliaries) for the RF generators have been installed and fully commissioned: eight RF antennae can now be supplied. Three antennae have been installed in JET and up to 6MW have been coupled to the plasma.

Magnet Systems

During 1985, the toroidal field magnet was used routinely at the full design value (3.45T) of the current and of the energy dissipated per pulse. For the first time, the primary coils of the poloidal system were connected in series. This reduced the rate of use of the plasma current during the initial phase of the discharge and made it possible to utilize the full flux swing capability of the machine. Experiments in early 1985 showed that operation at full premagnetisation was still unsuccessful. The cause of the problem was identified as strong fields escaping from the saturated iron core. Experimental studies and computer field mapping suggested a number of possible remedies which will be evaluated in 1986.

For the first time in 1985, the poloidal system included the shaping circuit, to control independently the elongation of the plasma cross-section. This new circuit, which includes a part of the poloidal coils Nos. 2 and 3, was used successfully and became a permanent feature of the plasma control system.

New Projects

It has been decided to filter the voltage ripple of all JET magnet power supplies. The toroidal field filter has been installed and is now operational. However, further studies on the poloidal amplifiers are necessary to assess the optimum filter design in the various operational configurations in which account will be taken of the speed of response required for plasma control.

Orders have been placed for a new set of amplifiers (PVFA 5/6) similar in design to the existing plasma shape (PVFA 1/2) and plasma radial position control (PVFA 3/4) amplifiers. These will be used in modifying the JET magnetic configuration under consideration.

Modified design of the poloidal power supply system which makes full use of the flux swing have been defined: plasma currents up to 7MA with a flat top of several seconds and lower currents with longer flat tops, should be achievable. Contracts for the ohmic heating circuit thyristor-make switches and for the new commutating resistors have been placed. Increasing the vertical field amplifier voltage will be achieved either by a set of booster amplifiers or by additional resistors in the ohmic heating (OH) circuit. These modifications will allow the use of a relatively high loop voltage during the first 50-300ms of the current fast rise and afterwards reduce it to limit the plasma current derivative during the remaining part of the fast rise.

During the latter half of 1985, further modifications to the magnetic configuration have been considered, to reduce stray magnetic fields at breakdown and to achieve magnetic limiter configurations (X-points) at plasma currents up to 4MA. A number of circuits have been prepared and the final choice will be made in early 1986.

Work on conversion of the Neutral Injection Power Supplies to 160kV is underway. Preliminary tests were performed and final implementation of the scheme has been performed on the Testbed, where satisfactory control has already been achieved up to 140kV.

During 1985, a decision was taken to reduce the number of planned RF antennae from ten to eight, as the same total power delivered to the plasma could be maintained by replacing the existing 1.5MW RF generator tubes with a newly developed 2.0MW tube. As a consequence, some design modifications on the existing RF AC/DC power supplies have been required. These modifications will affect the HV diode stacks, the thyristor controller and the output filters.

In order to correlate the performance of the power supplies with the behaviour of the 400kV grid, a computerised model has been set up. The predictions of the model, in a variety of JET operating conditions, has shown good agreement with experimental results. Thus, the model has been used to predict the reactive power compensation needs for JET, at its ultimate performance. Since the overall reactive power requirements are much above the maximum level presently allowed (375MVAR), preliminary negotiations have started with the Central Electricity Generating Board (CEGB), aimed at a permissible voltage drop above the present 1.5%. To minimise the size of compensation equipment ultimately needed.

Preliminary consideration has also been given to possible needs for active power compensation in the event of frequent instantaneous fall of full additional heating power (due to plasma disruptions).

Maintenance and Services

The maintenance organisation for the power distribution systems and for the magnet power supplies has been operational at the three planned levels: weekly, quarterly and yearly maintenance leading to an effective improvement in reliability of equipment.

A major task during 1985 was the preparation for and, during the summer shutdown,the implementation of the cabling work in the Basement. This work involved up to thirty electricians for a period of about three months, leading to the installation and/or re-routing of about 50km of cables.

Operation

Improvement in the operation of the power supplies has involved written procedures, level 2 software, and alarm handling. CISS has been revised aimed at a biunivocity between CISS action and alarms. Towards the end of the

year, the fast transient recorders became operational and were shown to be essential for the analysis of power supply faults. In addition, a power supply acquisition and elaboration programme is also available to assess the performance and status of the power supplies, after each pulse.

Neutral Beam Heating System

During 1985, the main emphasis has been placed on completion of the first injector system which consists of 8 beam sources, an integrated beamline system for the eight beams, and ancillary systems of which the most important one is the cryocondensation vacuum pump. The system is designed for 10s pulse lengths and, in its present configuration, for operation with 80keV hydrogen or deuterium beams.

Major progress has also been made in component procurement, assembly and installation for the second injector. This system is ready for commissioning the beam source power supplies and control with pretested sources installed at Octant No. 4, as soon as the power supplies become available.

Beam Sources

The beam sources for the first injector were all modified in two major aspects [1]:

- The plasma source species mix was improved (in close co-opertion with EURATOM-UKAEA Association, Culham Laboratory, UK). By superimposing a long range filter field to the original multipole magnetic field, the $H^+:H_2^+:H_3^+$ ratio in the extracted beams was increased from 64%:28%:8% to 84%:12%:4%;
- The 262 beamlets from a beam source are steered towards a focus in order to counteract the beamlet divergence. The steering is produced by an offset of the apertures in the deceleration grid of the extraction system. The required offset values were experimentally determined at EURATOM-UKAEA Association, Culham Laboratory, in co-operation with JET, and the offset design values were corrected. the apertures of the existing deceleration grids were all re-drilled to about 50% of the original offset.

In the JET Neutral Injection (NI) Testbed, beam sources were operated at 80kV and, 60A for, 15s with hydrogen beams. By optical measurements the species mix of 80kV 41A deuterium beams were determined [2] as $D^+:D_2^+:D_3^+$ = 82%:11%:7%.

Eight pre-tested beam sources were mounted into the injector vacuum box at the Tokamak (Fig.12) and the final system of beam sources, power supplies, control and data acquisition were commissioned. The beam sources were operated simultaneously at 80kV and, 37A each for, 0.5s. The pulse length at this stage was limited by the capability of a provisional beam dump.

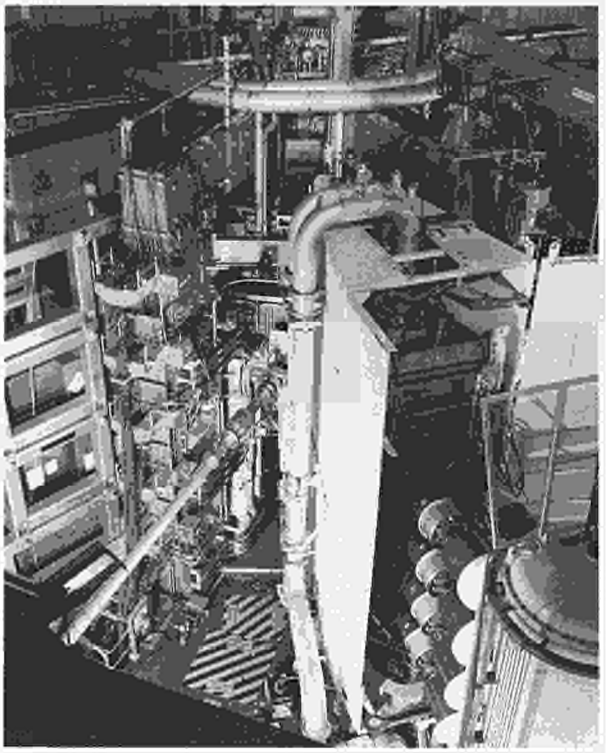

Fig. 12: First neutral injector installed at the Tokamak, showing the eight beam sources and the magnetic shielding around the injector box, and in the foreground the HV transmission tower for the beam source supplies

Beamline System

The central part (Fig.13) of the beamline system for the eight beams consists of a support and water supply (a $1800 m^3 h^{-1}$) column onto which the deflection magnets, full-energy ion dumps, fractional-energy ion dumps and a calorimeter are mounted. The deflection magnets have water-cooled inner liners, and several fractional-energy ion dumps are mounted inside the magnets. The calorimeter, which is capable of catching the eight non-neutralised long-pulse beams, is a two-gate system hinged in the midplane. When it is closed, its back panels act as beam scrapers.

This Central Column consists of four identical quadrants (Fig.14), which each handle the beams from two sources. During 1985, assembly of the Central Column [3] was completed on site, and it was transferred into the NI Testbed (Fig.15).

Testing of one quadrant [2] was performed using ~2000 hydrogen and deuterium beam pulses of various energies (40 - 80kV) and pulse lengths ($\leq$10s). Temperatures were measured and power density levels determined from the initial temperature rise and the equilibrium temperatures of thermocouples mounted 3mm below the surface of the high heat transfer components. Cooling water calorimetry was undertaken using thermocouples in the water outlets and turbine flowmeters of clamp-on ultrasonic flowmeters.

Beam properties were determined from horizontal beam profiles on the Testbed beam dump, 12m from source, and it was found that (a) during beam-on time, the

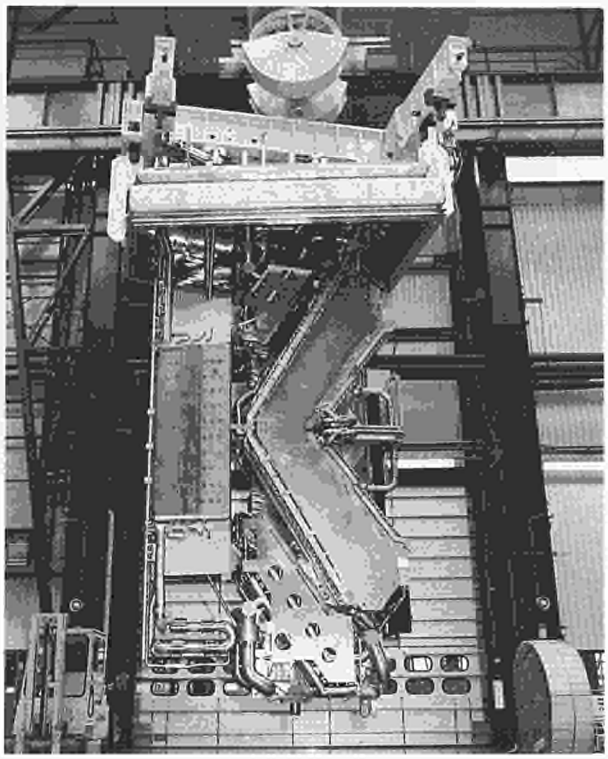

Fig. 13: Central Column of the beamline system attached to the lid of the injector box, showing the deflection magnet at the right, the full-energy ion beam dumps in the middle at the top and bottom, and the rear of the calorimeter at the left

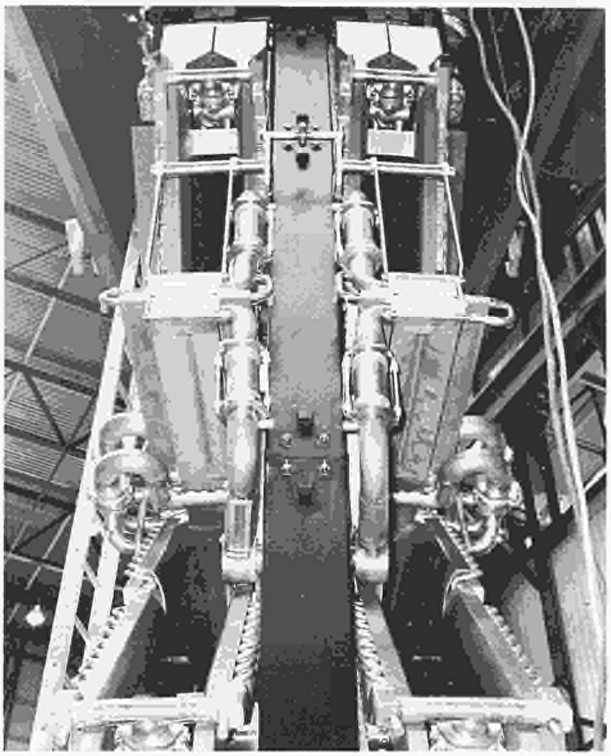

Fig. 14: Beam entrance side of the Central Column, showing the deflection magnet apertures for the four pairs of beams, and at mid height dumps for fractional-energy ions after a 270° deflection

beam moves by 0.1^0, (b) the full beam (ion plus neutrals) showed a constant deflection of 10 – 20mm with respect to the neutral beam which was less than that expected due to the Earths magnetic field, (c) the beamlet divergence deduced from either type of beam was 0.7^0. A discrepancy was found in the absolute values of the power densities derived from the initial temperature rise of the thermocouples during the first few 100ms (peak power density $5.2 kWcm^{-2}$), which is not yet fully understood.

With the beamline system in operation, the power distribution of the extracted ion beam power was determined. For neutraliser line densities of 2.0 (and 1.2) $x10^{16}cm^{-2}$, the results are shown in Table III.

The neutraliser is approximately 130mm x 180mm in cross section and 1.8m in length. Gas is introduced into the source at a point halfway along the neutraliser length.

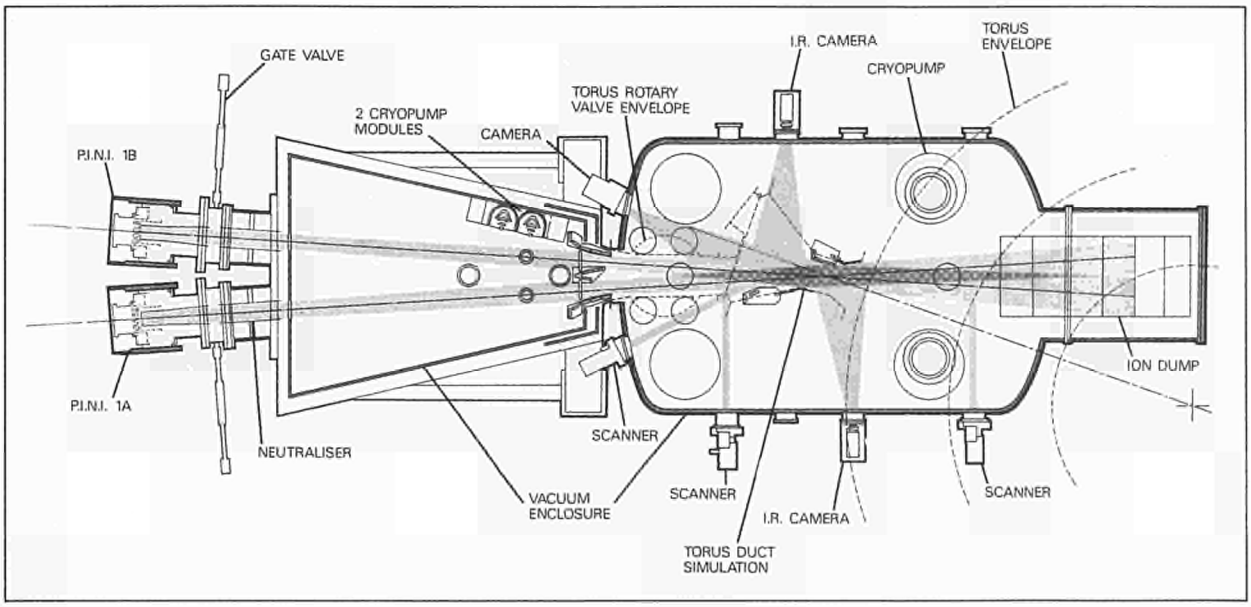

Fig. 15: Schematic of the Neutral Injection Testbed, part of which (at the left) is a standard injector vacuum box

TABLE III
Distribution of Extracted Beam Power

Hydrogen Beam 80kV, 4.8MW	*Deuterium Beam 80kV, 3.2MW*	
12 (10) %	11 (9) %	Lost in source and neutraliser
65 (70) %	37 (45) %	To beam dumps and scrapers
20 (17) %	47 (45) %	Would go to the plasma (minus re-ionisation losses in the Torus duct)

The neutraliser efficiency was determined as a relative measurement of the power onto the Testbed beam dump with and without beam deflection, and was counter-checked by other measurements. The results were found to be independent of the pulse length between 1s and 10s. The efficiency was calculated from the known species mix, published neutralisation cross-sections and the line density determined from neutraliser pressure profile measurements (without beam). Re-ionisation losses were taken into account as determined from the power accountability.

Unexpectedly, agreement between the calculated and measured neutralisation efficiencies was only achieved by taking half the measured line density for the efficiency calculation (Fig.16). Hence, it was concluded that the neutraliser line density during beam-on time was only half the value measured in the absence of beam. The observation has been explained [4] as due to heating of the neutraliser gas by the beam. Fig.17 shows the measured pressure increase in the neutraliser during a beam pulse as corresponding to a gas temperature increase (the gas being in the transition regime between molecular and viscous flow).

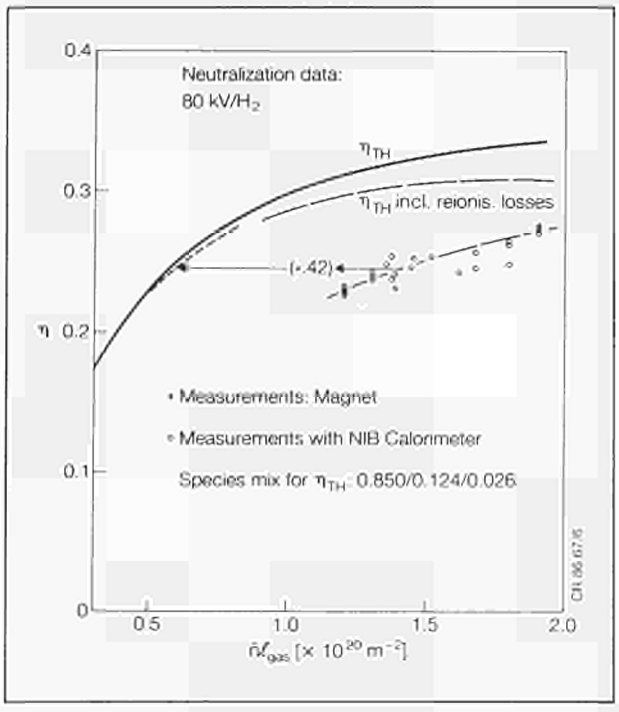

Fig. 16: Calculated and measured neutralisation efficiencies versus the line density measured in the absence of the beam. The discrepancy can be explained by beam heating of the neutraliser gas

Beam profiles on the full-energy ion dump have been determined from ~70 thermocouples. In the non-bend plane, a double-hump profile along the dump surface is expected for the V-shaped dump and from a diverging beam. For 40kV H^+ and 80kV D^+ beams, this has been confirmed by the measurements. However, at higher energies and current densities, discrepancies develop, and at 90kV H^+ (Fig.18), the profile is considerably wider than calculated and peaked in the apex of the dump. A similar profile change has been observed in the beam bending plane. No quantitative explanation is yet available for what may be due to space charge effects in the deflection magnet.

In summary, beams from individual sources in different positions have been run through the Central Column of the beamline system at:

80kV, 60A, 6s in hydrogen,
80kV, 42A, 10s in deuterium.

The unexpected beam profiles on the main ion dump have limited the pulse length of hydrogen beams to the given value, and 80kV operation is considered marginal. It appears that operation of deuterium beams at the given parameters has not reached any operational limits of the injector system.

Cryopump System

The liquid helium (LHe) refrigerator and distribution system [5] (Fig.19) was successfully commissioned, produced 300W at 3.8K in its internal calorimeter and has now completed ~6000 hours of running time. Other cryosystem plant (eg. purifiers), He recovery, LHe storage, and LN_2 storage and supply all now operate routinely. The control of the complete plant is initiated and monitored by its programmable controller, which also updates CODAS and the central control mimic displays with relevant status data.

During 1985, the most important function of the cryoplant was to supply routinely the cryopump (Fig.20) of Octant No. 8 neutral injector through the 80m long cryoliquid transfer lines, in which state the system runs mostly unattended. It is controlled by LHe and LN_2 level sensors in the cryopump. When external faults occur, such as insufficient vacuum or cooling water flow in the injector, it switches off, and restarts automatically when such (intermittent) faults have disappeared. When CODAS (through which temporarily the cryoliquid level

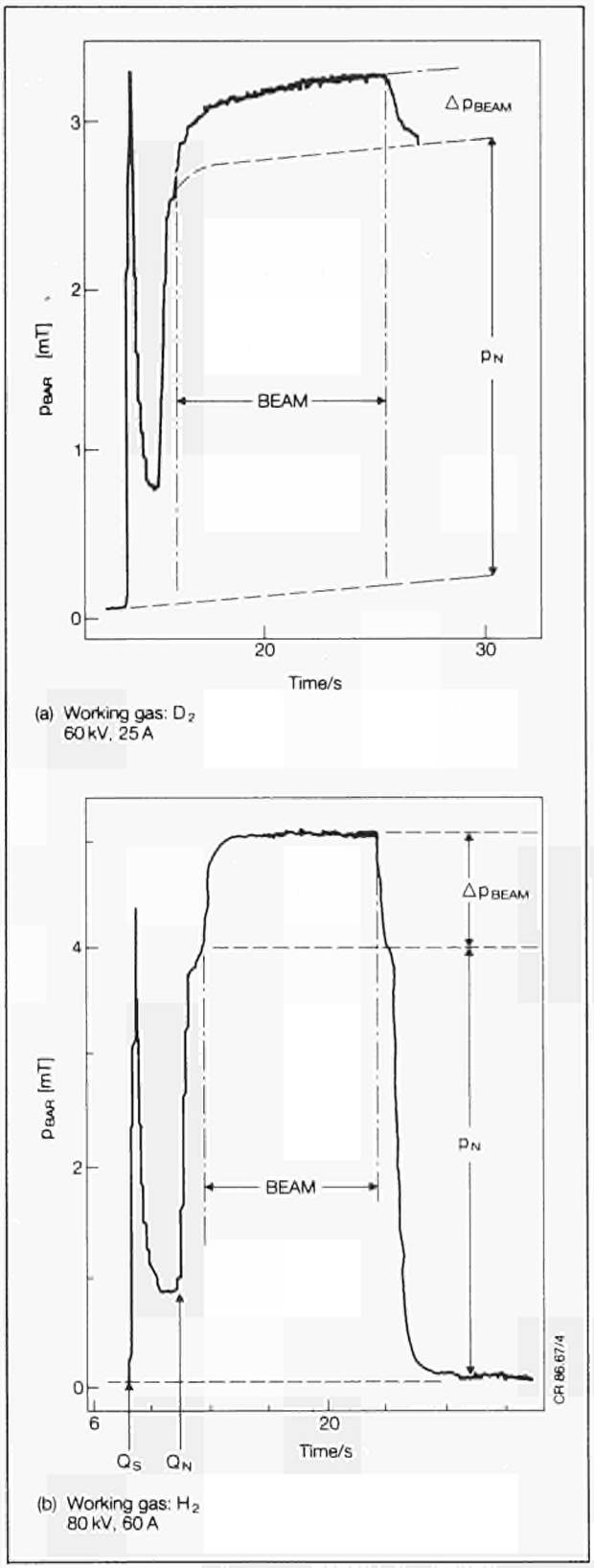

Fig. 17: Pressure at half length of the neutraliser. The pressure increase during the beam pulse is consistent with increased gas temperature

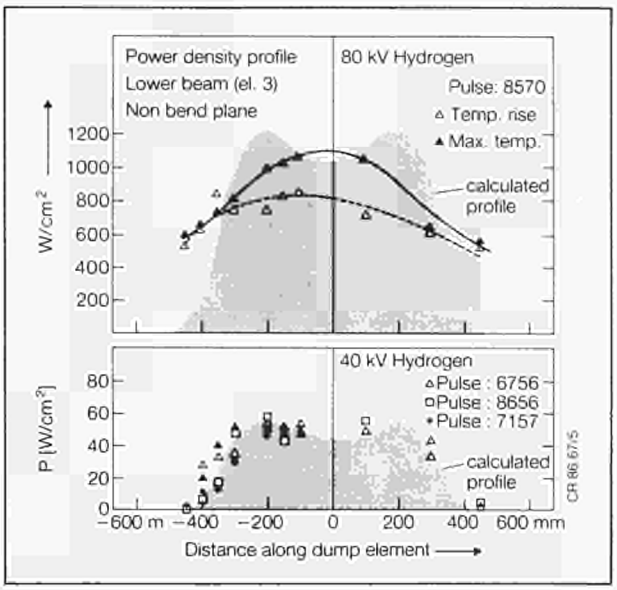

Fig. 18: Power density profile on the full-energy ion dump for 80kV and 40kV hydrogen beams. The shading gives the calculated profiles

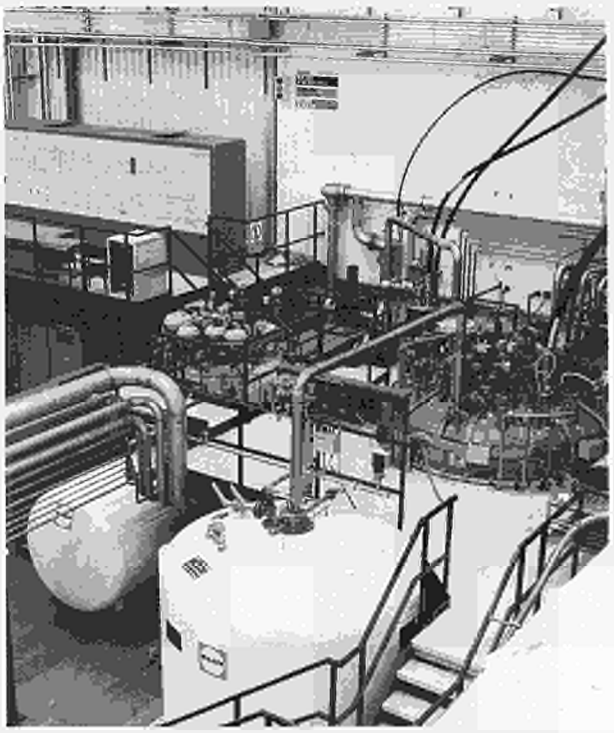

Fig. 19: Cryosupply plant showing the refrigerator cold box in the centre, the LHe distribution box on the right and the back-up subcooler system at the rear

signals are transferred to the cryoplant) fails, the system switches over to a back-up control.

The main operational parameters are as follows. The pump is cooled down and filled with LN_2 in about 2 hours. Then, it is normally left to radiative pre-cool for 15 hours, by which time the LHe panels have reached 160K. Further cool-down and filling from the LHe supply takes another 6 hours. This cool-down procedure requires less than 1000l of LHe.

Warming the pump up from operational conditions to above freezing of injector cooling water takes about 15 hours, in the case of a forced regeneration and a warm-up enhanced by the presence of ~10mbar contact gas in the injector box.

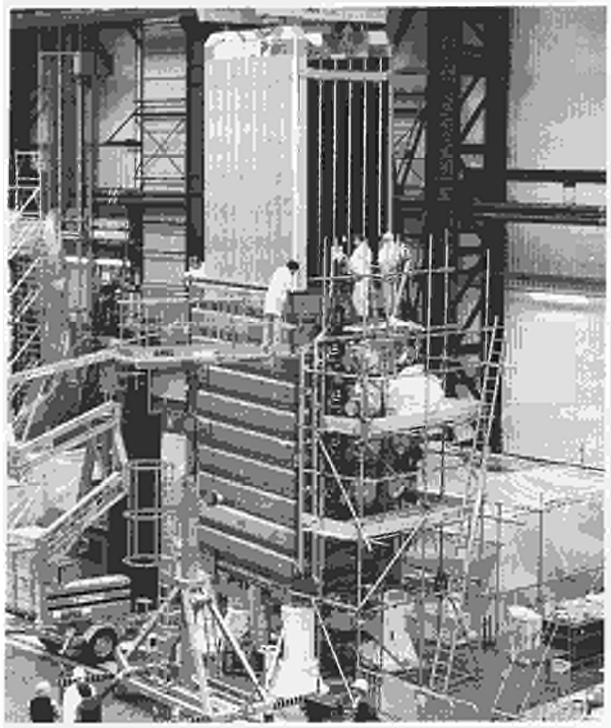

Fig. 20: Installation of the cyropump into the injector vacuum box

Pump regeneration is required when the quantity of condensed H_2 approaches the explosive mixture limit, in case of the occurence of a major air leak and a sudden evaporation of the condensate. The pump has been regenerated several times without problems.

Additional activity has been devoted to the cryosystem for the future Tritium Recycling System (TRS). A cryopump system was laid out and a test rig for TRS cyrocomponents was designed, built and commissioned. A tritium cryogenic transfer pump with an induction heater was designed, built and successfully tested in this rig. The rig was then handed over to the JET Tritium Group.

Injector System Tests

During the 1985 Summer Shutdown, the injector at Octant No. 8 was completed by the installation of the Central Column (improved by extension tiles to the full-energy ion dumps), and the re-installation of the neutralisers (now with Inconel hoses) and the beam sources (with additional electrostatic shields and filament stem protection caps).

The injector was then commissioned, including all associated subsystems, in a mode where the neutral beams were intercepted by the calorimeter. The beam sources were simultaneously operated in hydrogen at 60kV for pulse lengths up to 10s. No significant disturbance of the injector by the Tokamak stray fields was observed. The system was ready for injection into the Torus.

References

[1] "JET Neutral Injection System – Status Report" G Duesing, Report JET-SC22/7 (January 1985);

[2] "Operational Test of the JET Neutral Injection System in the JET Testbed" H D Falter, R S Hemsworth, G H Deschamps, A P H Goede, T T C Jones, P Massmann, M J Mead, A Stäbler, 11th Symposium on Fusion Engineering, Austin, Texas, USA (November 1985), to be published;

[3] "JET Neutral Injection Beamline System, Manufacture and Assembly" R Haange, H Altmann, S Papastergiou, R B Tivey, M J Watson, 11th Symposium on Fusion Engineering, Austin, Texas, USA (November 1985), to be published;

[4] "Gas Heating Effects in the Neutralisers of Neutral Beam Injection Lines" J Pamela, Report EUR-CEA-FC 1279, CEN Fontenay-aux-Roses (September 1985)

[5] "The JET Cryogenic Supply System" R L Roberts, A Jones, P Kupschus, E Kussel, C Mayaux, M J Mead, W Obert, F Spath, C A Steed, B A Wallender, Cryogenic Engineering Conference, Boston, USA (August 1985), to be published.

RF Heating System

1985 was as an exceptional year for the JET ICRF heating programme. The main subsystems, which had been under construction since early 1983, were assembled together for the first time; integrated within the JET apparatus and auxiliaries; and operated on the plasma. The first operation on JET was a crucial step, since it had not been possible to simulate the plasma loading. The system had been conceived on the basis of theoretical estimates of the antenna-plasma coupling and could only be tested on the plasma itself. Progress was made in the following areas:

(i) Installation in the torus of two antennae and transmission lines early in 1985, followed by a third antenna in mid-year;

(ii) Installation and commissioning on dummy loads of three RF generator units of 3MW output each;

(iii) Conditioning of the antennae with RF power and the start of operation on the plasma, in March;

(iv) Achievement of the specified net power coupled to the plasma (half generator power) was obtained about one month after each unit was brought into service;

(v) The net power and energy coupled to the plasma reached 6MW and 15MJ by December. These combined values constituted the highest performance ever achieved with additional heating on Tokamaks;

(vi) Since May, the availability and reliability of the equipment was satisfactory and the experimental physics programme was carried out.

The status of the construction of the ICRF power plant at the end of the year, was that three units of 3MW each had

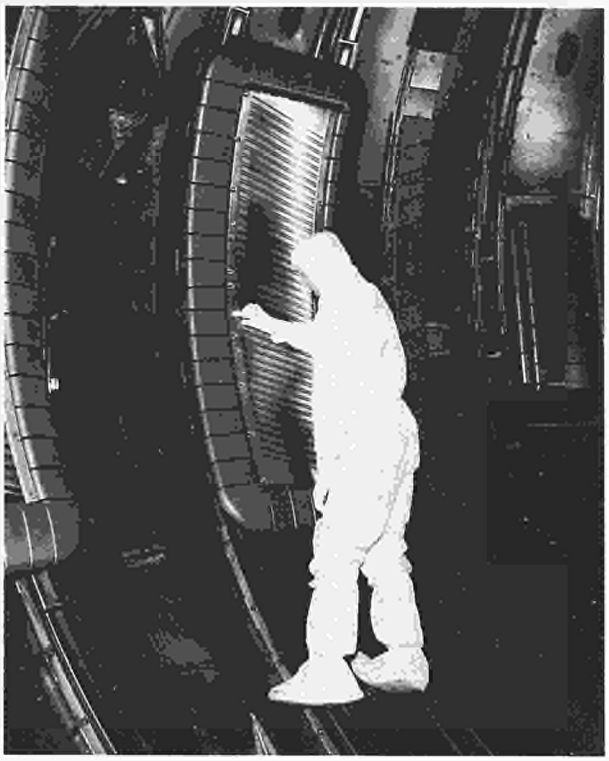

Fig. 21: Two of the three prototype (A_0) installed in the vacuum vessel. The three antennae coupled 6MW of power by the end of 1985 and are expected to be used during the whole of 1986

Fig. 22: Photograph of the vacuum transmission line of the A_1 antenna and its interface with the antenna. 1.5MW of net forward power should be transmitted through this reduced section

been connected to the machine. A total of eight units should be installed by the end of 1986 and connected to a new water cooled version of the antennae.

Fig.21 shows a photograph of two of the three antennae installed in one side of the JET vacuum vessel. The antennae screens are made of overlapped nickel bars with a T shaped cross-section. The entire structures are protected by frames of carbon tiles, which can act as plasma limiters.

Other technical achievements have been made in the preparation for the second phase of the ICRF programme, which is planned to start in 1987 with eight ICRF units each upgraded from 3 to 4MW. The upgrade will be achieved by using larger tetrodes (2MW each) in the final amplifier and new output circuits. Long pulse operation (20s) will require water cooling of the screen and forced air cooling of the vacuum transmission lines. Many components of the new antenna array have been received and testing has started with RF power on the Testbed (moved to the JET site from its previous location at EURATOM-CEA Association, Fontenay-aux-Roses, France). Important initial results have been obtained: the expected improved performance of the new double conical vacuum feed-through (no voltage breakdown above 60kV) has been obtained and voltage stand-off problems in the pressurized transmission lines have been identified. The slow development of long and tenuous whiskers in some tin plated parts of the lines gave rise to progressive deterioration of the voltage performance. Removal of the tin and some modification of the insulators led to stand-off voltages in excess of 50kV.

Elements of the vacuum transmission line of the new antenna system are illustrated in Fig.22, which shows the interface between the coaxial element and an antenna. This interface, as well as the antenna itself, can be installed remotely with a telemanipulator.

1985 was a challenging year. 1986 will be devoted mainly to operation on the plasma and intensive testing of the components necessary for the next phase. 1987 should be another challenging period involving the integration and operation of eight RF units within JET.

Control and Data Acquisition System (CODAS)

The Control and Data Acquisition System (CODAS) Division is responsible for the design, procurement, implementation, upgrade and operation of the computer-based control and data acquisition system of JET. This system, based on a network of NORSK DATA mini-computers, allows centralised control and monitoring. The various components of JET have been logically grouped in subsystems, such as Vacuum, Toroidal Field, Poloidal Field, etc. Each subsystem is controlled and monitored by one computer and the various computer actions are co-ordinated by supervisory software running

on the machine console computer. This supervisory function includes the countdown sequences for each plasma discharge. A description of CODAS [1], and a recent review of its status [2] have been given previously.

The allocation and configuration of all CODAS computers is given in Table IV, while Table V provides other quantitative data.

The main achievements during 1985 are summarised, as follows:

- Introduction of the RF subsystem in the operation of JET;
- Procurement, installation and commissioning of the Neutral Beam Injector subsystem at Octant No. 8 and preparatory work for the Octant No. 4 subsystem;
- Preliminary work on the Remote Handling subsystem for the master-slave tests of the articulated boom;
- Upgrade and commissioning of the Plasma Fault Protection System (PFPS) to include interlocks with Neutral Beam injectors in case of low plasma current and density and improved user interface;
- Extension of the soft termination network facilities;
- Provision of new supervisory software to standardise the countdown sequence and provide easier subsystem operation in stand alone mode for commissioning periods;
- Upgrade of operating system to release J of SINTRAN to benefit from its improved efficiency;

TABLE IV
CODAS Computer Configuration at the end of 1985

Subsystem	*Usage*	*Model*	*Memory (MByte)*	*Disks (MByte)*
AH*	NI Additional Heating	ND100	2.0	1×75
AS	Assembly Database	Compact	0.75	1×45
CA*	Message Switcher A	ND100	0.5	1×75
CB	Message Switcher B	ND100	0.5	1×75
CP	Cable Database	ND530	5.0	1×75 1×288
DA*	On-line diagnostic	ND520	3.0	2×75
DB*	On-line diagnostic	ND520	3.0	1×75 1×288
DC*	On-line diagnostic	ND520	3.0	2×75
DD*	On-line diagnostic	ND520	3.0	2×75
DE*	Off-line diagnostic	ND520	3.0	2×75
DF*	On-line diagnostic	ND520	3.0	2×75
DG	Diagnostic Commissioning	ND520	5.0	2×75
EC*	Experiment Console	ND570	5.0	1×75 1×288
EL	Electronic	ND100	1.0	1×75
GS*	General Services	ND100	1.5	1×75
HL*	Harwell Link	ND100	1.5	1×75 1×108
MC*	Machine Console	ND100	1.5	1×75
PF*	Poloidal Field	ND100	2.0	1×75
RB*	Radio Frequency Test Bed	ND100	1.5	1×75
RF*	Radio Frequency	ND100	1.5	1×75
RH	Remote Handling	ND100	1.5	1×75
SA*	Storage & Analysis	ND560	3.0	1×75 1×288
SB	Standby-System/Backup	ND100	1.5	2×75 2×10 1×288
SD	Built-in, Pool, Computer dB	Compact	0.75	1×45
SS*	Safety & Access	ND100	1.5	1×75
TB*	NI Test Bed	ND530	3.0	2×75
TF*	Toroidal Field	ND100	1.5	1×75
TR	Tritium	ND100	1.5	1×75 1×28
TS	Test	ND100	1.5	1×75
VC*	Vaccum	ND100	2.0	1×75
YB	Integration	ND530	3.0	2×75
YC	CODAS Commissioning/NIB-C	ND100	1.5	1×75
YD	Sc Dpt Development	ND570	5.0	1×75 1×28
YE	CODAS Development	ND520	5.0	2×75

*indicates on-line computers.

TABLE V
Quantitative Information on CODAS Installation at end of 1985

CODAS Interface Cubicle	113
CAMAC Crates	187
CAMAC Modules	2,953
Eurocard Modules (Signal Conditioning)	5,739
Computer Terminal	151
CAMAC Serial Loop (Fibre Optic)	22
On-line Computers	20
Off line and Commissioning Computers	14
Size of JPF	6.6MB
Number of diagnostics on-line with CODAS	15
Number of diagnostics under commissioning with CODAS	8

- Substantial improvements were made on the following packages:
  (i) Alarm handling;
  (ii) Waveform generation and selection;
  (iii) Flywheel generator converter, static units, circuit breakers support software;
  (iv) Gas introduction
  (v) Cryo-system and Helium plant monitoring and control;
  (vi) Access control.
- Continuous development of automated procedures to relieve the operation team from tedious tasks and to implement sequences which have been tried and tested by the operation team.
- Study of data throughput improvements and, as a first phase, installation and Commissioning of a Hyperchannel link between Harwell and JET;
- Complete revision and recommissioning of all existing CISS PLC's and addition of PLC's for Neutral Beam, Neutral Beam Testbed, RF and a second supervisor;
- Design, commissioning and installation of a serial link between the CISS PLCs and CODAS computers to improve fault condition diagnostics;
- Design, manufacture, installation and commissioning of 15 CODAS interface cubicles;
- Installation of 800 additional transient recorder channels to investigate transient and fault conditions;
- Development of a coherent set of user friendly hardware test programs;
- Re-configuration of the physics terminal room to match operation requirements;
- Release to users of the cable management data base which contained 800,000 records by the end of 1985;

TABLE VI
Review of CODAS Electronics Stock Holding
(Installed, Pre-procurement and Spares)

		End 85	*End 84*
1.	CAMAC system modules	705	629
2.	CAMAC digital I/O modules	662	581
3.	Timing system (CAMAC & Eurocard)	910	698
4.	CAMAC analogue I/O modules	803	629
5.	CAMAC display modules	265	255
6.	CAMAC Auxiliary controllers	110	75
7.	CAMAC powered crates	187	187
8.	U-port-adaptor	140	119
9.	CISS modules	753	619
10.	CCTV	582	440
11.	Cubicle frames	223	123
12.	Console devices (not CAMAC)	344	313
13.	Power supply modules	1,350	884
14.	Intercom, Public Address, Computer terminal network	397	202
15.	Pool	818	705
16.	Analogue I/O in Eurocard	1,816	1,674
17.	Digital I/O in Eurocard	3,923	3,257
18.	Eurocard sub-racks	744	705
		14,732	12,171
	Increase	2,561	21%

TABLE VII
Status of JET Diagnostic Systems

Diagnostic System	Diagnostic	Purpose	Association	Status Dec. 1985	Date of Operation in JET
KB1	Bolometer Scan	Time and space resolved total radiated power	IPP Garching	Operational	Mid 1983 partly Early 1984 fully
KC1	Magnetic Diagnostics	Plasma current, loop volts, plasma position, shape of flux surfaces	JET	(1) Operational (2) Enhanacement	Mid 1983 Late 1985
KE1	Single Point Thomson Scattering	T_e and n_e at one point several times	Risø	Operational	Mid 1984
KE3	Lidar Thomson Scattering	T_e and n_e profiles	JET and Stuttgart University	Construction	Early 1987
KG1	Multichannel Far Infrared Interferometer and Polarimeter	(1) $\int n_e ds$ on 7 vertical chord and 3 horizontal chords (2) $\int n_e B_\phi ds$ on 6 vertical channels	CEA Fontenay-aux-Roses	(1) Operational (2) Under construction	Mid 1984 partly Early 1985 fully Early 1987
KG2	Single Channel Microwave	$\int n_e(r) ds$ on 1 vertical and 3 horizontal chords in low density plasmas ($< 10^{20} m^{-3}$)	JET and FOM Rijnhuizen JET	2mm Operational Extension to 1mm	Mid 1983 Not proceeding
KG3	Microwave Reflectometer	n_e profiles and flucutations	JET	(1) Prototype system operating (2) Multichannel system being designed	Mid 1983 Mid 1987
KH1	Hard X-ray Monitors	Runaway electrons and disruptions	JET	Operational	Mid 1983
KH2	X-ray Pulse Height Spectrometer	Plasma purity monitor and T_e on axis	JET	Installed	Early 1986
KJ1	Soft X-ray Diode Arrays	MHD instabilities and location of rational surfaces	IPP Garching	Operational	End 1985
KK1	Electron Cyclotron Emission Spatial Scan	T_e (r,t) with scan time of a few milliseconds	NPL, Culham Lab. and JET	Operational	Late 1985
KK2	Electron Cyclotron Emission Fast System	T_e (r,t) on microsecond time scale	FOM, Rijnhuizen	Operational	Early 1985
KL1	Limiter Surface Temperature	(i) Monitor of hot spots on limiter and RF antennae (ii) Temperature of wall and limiter surface	JET and KFA Jülich	Operational Development	Mid 1984 1986
KM1	2.4MeV Neutron Spectrometer	Neutron spectra in D-D discharges, ion temperatures and energy distributions	UKAEA Harwell	Construction proceeding	1986
KM3	2.4MeV Time-of-Flight Neutron Spectrometer		NEBESD, Studsvik	Commissioning	1986
KM4	2.4MeV Spherical Ionisation Chamber		KFA Jülich	Commissioning	1986
KM2	14MeV Neutron Spectrometer	Neutron spectra in D-T discharges, ion temperatures and energy distributions	UKAEA Harwell	Design completed	
KM5	14MeV Neutron Spectrometer		NEBESD, Gothenberg	Decision on construction under review	
KN1	Time Resolved Neutron Yield Monitor	Time resolved neutron flux	UKAEA Harwell	Operational	Mid 1983
KN2	Neutron Activation	Absolute fluxes of neutrons	UKAEA Harwell	Installation	1986
KN3	Neutron Yield Profile Measuring System	Space and time resolved profile of neutron flux	UKAEA Harwell	Construction proceeding	1986
KN4	Delayed Neutron Activation	Absolute fluxes of neutrons	Mol	Awaiting delivery	1986
KP1	Fusion Product Detectors	Charged particle produced by fusion reactions	JET	Prototype operational Upgrade	1985 1986
KR1	Neutral Particle Analyser Array	Profiles of ion temperature	ENEA Frascati	Operational	Mid 1984 partly End 1985 fully
KS1	Active Phase Spectroscopy	Impurity behaviour in active conditions	IPP Garching	Under construction	Mid 1986
KS2	Spatial Scan X-ray Crystal Spectroscopy	Space and time resolved impurity density profiles	IPP Garching	Under construction	Early 1986
KS3	H-alpha and Visible Light Monitors	Ionisation rate, Z_{eff}, Impurity fluxes	JET	Operational Poloidal Scan	Early 1983 Early 1986
KS4	Active Beam Diagnostics (using heating beam)	Fully ionized light impurity concentration $T_i(r)$ rotation velocities	JET	Provisional system Under construction	Early 1986 Early 1987
KT1	VUV Spectroscopy Spatial Scan	Time and space resolved impuritiy densities	CEA Fontenay-aux-Roses	Operational	Mid 1985
KT2	VUV Broadband Spectroscopy	Impurity survey	UKAEA Culham Lab.	Operational	Early 1984
KT3	Visible Spectroscopy	Impurity fluxes from wall and limiters	JET	Operational	Mid 1983
KT4	Grazing Incidence Spectroscopy	Impurity survey	UKAEA Culham Lab.	Under construction	Early 1986
KX1	High Resolution X-ray Crystal Spectroscopy	Ion temperature by line broadening	ENEA Frascati	Installed	Early 1986
KY1	Surface Analysis Station	Plasma wall and limiter interations including release of hydrogen isotope recylcing	IPP Garching	Commissioning	Mid 1986
KY2	Surface Probe Fast Transfer System		UKAEA Culham Lab.	Commissioning	Mid 1986
KY3	Plasma Boundary Probe	Vertical probe drives for electrical and surface collecting probes	JET UKAEA Culham Lab. IPP Garching	Both units installed	Mid 1984-86
KZ1	Pellet Injector Diagnostic	Particle transport, fueling	IPP Garching	Partly installed	Early 1986

- Work started on the IBM to investigate response time problems, install a JET compatible version of PLOT-10 to improve software compatibility and to allow connection of Westward terminals through a 7171 interface unit.

One of the activities of 1985 which should be emphasised was the participation in the overall improvement of reliability and machine-safety; some aspects have been previously presented [3], [4]. The overall availability of CODAS during operation time was close to 95%, showing a high level of reliability of the considerable amount of hardware. The breakdown of electronics modules is shown in Table VI, which compares the end of 1984 and 1985 figures.

References

[1] CODAS: The JET Control and Data Acquisition System, H van der Beken, CH Best, K Fullard, RF Herzog, EM Jones, CA Steed – To be published in Fusion Technology;

[2] Status of the JET Control and Data Acquisition System, CODAS, EM Jones – 2nd International Workshop on Accelerator Control Systems, (Los Alamos, October 1985) JET Preprint, JET-P(85)21;

[3] Safety aspects of the operation of the JET computer system – H van der Beken, RF Herzog – SAFECOMP 1985;

[4] Interfacing between database and equipment: The JET equipment drivers – RF Herzog, H van der Beken – EUROCON 84, (Brighton UK, 1984).

Diagnostic Systems

The status of JET's diagnostic systems at the end of 1985 is summarised in Table VII and their general layout in the machine is shown in Fig.23. Almost all of the diagnostic systems started during the Construction Phase are now operating and the few still under construction are those which were started later. Further details of the main systems are given below:

Magnetic Measurements

The magnetic diagnostics have been described in previous JET Annual and Progress Reports and have continued to work routinely and reliably during the year. Software has now been implemented to carry out an automatic self-consistency check on the data after each discharge to check for errors and to validate the data. This is working well. The data acquisition system was extended during the year to give additional channels and longer time windows for fluctuation studies.

The diagmagnetic loops have been commissioned and now provides measurements of the plasma energy content consistent with other measurements. This should become a routine measurement during 1986.

Electron Cyclotron Emission Measurements

Radiation emitted from the JET plasma at low harmonics of the electron cyclotron frequency is received by an array of ten antennae which view the plasma along different chords in the poloidal plane. The radiation is transmitted via the Basement to the Diagnostic Hall, where it is analysed by three types of instrument. A mixture of Michelson and Fabry-Perot interferometers are used to measure the spatial profile of electron temperature. Each instrument is connected to one of the antennae and can be scanned in a time of 10ms to measure the temperature profile along that particular plasma chord. By combining results from several chords a two dimensional map of the temperature can be constructed. During 1985, this system has been carefully re-calibrated to within an absolute accuracy of $\sim 10\%$.

The Fabry-Perot interferometers can also be operated in a fixed frequency mode to measure fluctuations in temperature on a much faster time scale at a selected point in the plasma. Temperature fluctuations are also measured using the Multichannel ECE Polychromator which can measure the temperature at twelve pre-selected points along a single chord, with a similar time resolution to that of the Fabry-Perot. These instruments have been used to study the development and collapse of the internal disruption at the plasma centre – the so-called 'sawtooth' oscillations. During the current rise phase in JET and for discharges with a relatively high value of the safety factor q, these discharges are similar in character to those seen in smaller tokamaks. The main feature is that the sawtooth collapse seems to be triggered by a growing precursor oscillation. However, at lower values of q and during the current plateau, the precursor disappears and the sawtooth collapse occurs spontaneously without warning.

The ECE Polychromator has also been used extensively to observe the outwards propagation of the heat pulse following the sawtooth collapse to determine the local value of thermal diffusivity.

Thomson Scattering

The Thomson Scattering diagnostic has worked routinely throughout the year.There is generally good agreement between the Thomson Scattering and ECE diagnostics, but careful analysis of the data has shown that the agreement is not as good as would be expected statisically. This disagreement has only become apparent because of the extremely high accuracy of the absolute calibration of the ECE systems in JET. It has now been established that there is a systematic problem of chromatic abberation in the Thomson Scattering optics and this is being rectified.

Construction has started on the new LIDAR Thomson Scattering System which will use an extremely short pulsed laser to measure the spatial profile of electron temperature by time-of-flight technique. Contracts have now been placed for most of the items of equipment and it is planned to install this new system during the shutdown at the end of 1986.

Microwave Measurements

The microwave interferometer has continued in routine

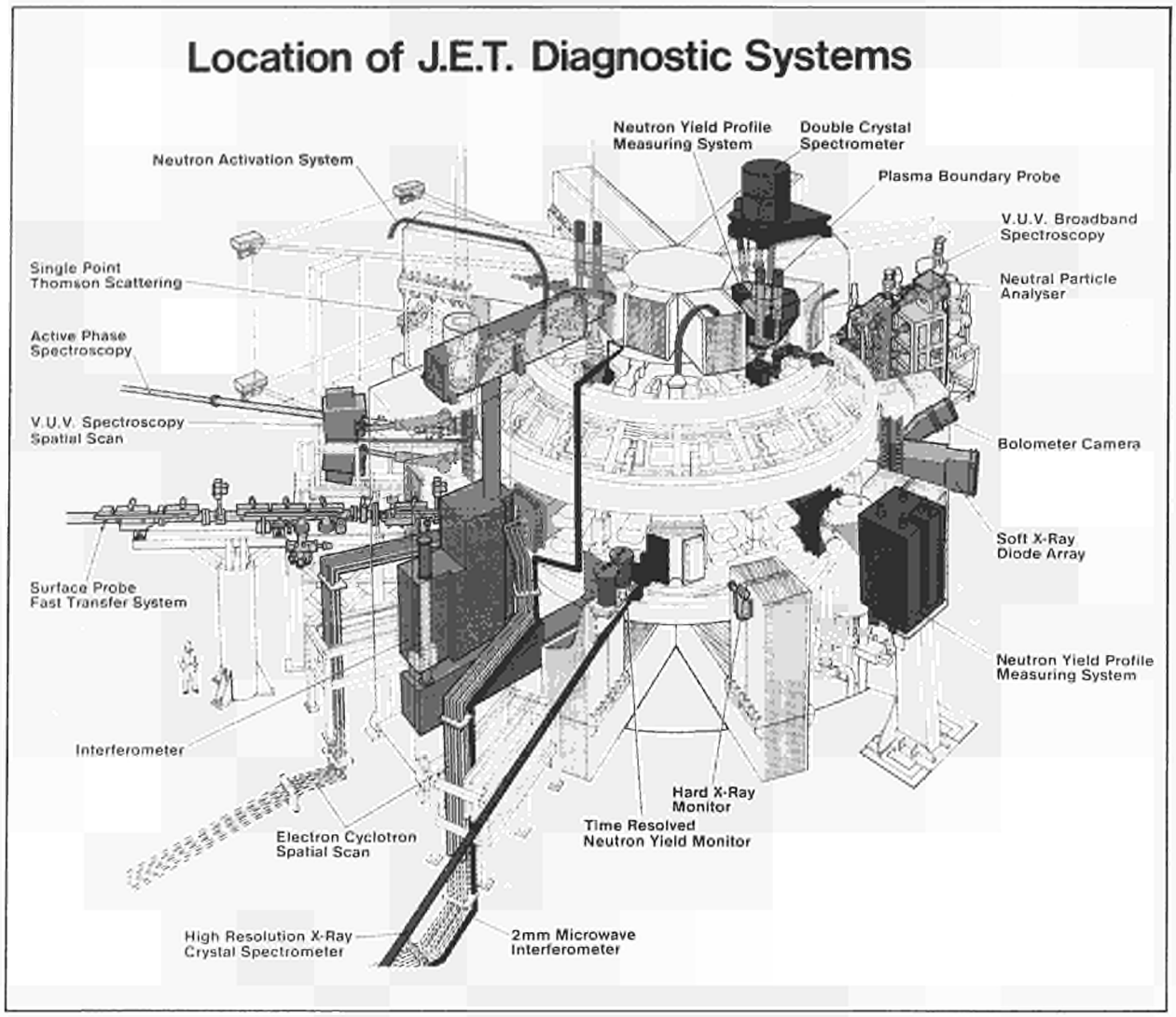

Fig. 23: General layout of diagnostics in the machine

operation for measurements of the line-of-sight density and plasma control purposes. A new microwave reflectometer system has been designed and construction started. The system will have twelve discrete wavelength channels and will be optimised to provide density profile data near the edge of the plasma where data from the FIR interferometer is sparse. The reflectometer can also be used to monitor localised density fluctuations.

Neutron Flux Measurements

Measurements of the total neutron yield using ^{235}U and ^{238}U fission chambers have continued to be made routinely. For discharges in deuterium this now gives a direct measurement of the fusion yield from which the ion temperature can be deduced. The detectors have been absolutely calibrated by means of a neutron source inside the JET vacuum vessel during a shutdown.

Construction has continued on the Neutron Yield Profile Diagnostic and the Neutron Activation System and both systems are now scheduled for installation during 1986.

Neutron Spectrometry

First measurements of neutron spectra in JET have been obtained using a ^{3}He ionisation chamber in the roof laboratory. The penetration in the roof acts as a collimator. Results are in good agreement with other measurements of the ion temperature and when taken simultaneously with the total neutron yield, permit a determination of the deuteron density in the core of the JET plasma. Typical values are $n_d/n_e \sim 0.5$.

The Time-of-Flight Neutron Spectrometer also located in the roof laboratory, has been installed and partly commissioned. Full operation is planned for 1986. Construction on the 2.4 MeV spectrometer collimator and shield for inside the Torus Hall has continued. Installation is planned for mid-1986.

Fusion Products

First measurements of charged fusion products in JET have been obtained with a prototype detector mounted inside the vacuum vessel. These data have given interesting results on the confinement of energetic

particles and have helped to further the design of more sophisticated diagnostics.

Plasma Boundary Probes
Measurements of the plasma temperature, density and heat flux in the region outside the limiter have been made with electrical direct reading probes introduced into the edge of the plasma by a vertical probe drive. These data are important in developing models of the plasma boundary layer.

Limiter Diagnostics
Measurements of the plasma limiter interactions using infra-red cameras have continued, and similar measurements have been extended to the R.F. antennae. The threshold temperature of these cameras is ~ 700°C and when the limiter surface temperature exceeds this value, it is possible to estimate the power flux to the limiter surface. A new more sensitive type of camera is being developed to extend the range to lower temperatures.

Plasma Wall Interactions
Construction and installation of the systems to expose surface collecting probes to the plasma and retrieve the samples for surface analysis has continued with the system scheduled for operation in mid 1986.

Samples have also been exposed on the walls of the vacuum vessel for longer periods and removed for analysis at scheduled maintenance periods. These together with samples taken from the limiters provide valuable data for understanding the migration of impurities from the walls onto the limiter and the processes by which these impurities enter the plasma.

Hard X-Ray Monitors
A measure of the Bremmstrahlung intensity (total power) is monitored with a set of simple detectors mounted on the vertical limbs of the transformer and the walls of the Torus Hall. This provides information on interaction of runaway electrons with walls and limiters in the torus.

H_α Monitors
Absolute values of the H_α light emitted from the plasma at nine points around the Torus is measured. The collected light is transmitted via optical fibres to the Diagnostic Wing where it is analysed by means of filters or spectrometers and detected by photomultipliers.

The system has been in operation since June 1983. It provides measurements of the particle confinement time and gives information on the effective ion charge (Z_{eff}) of the plasma. The system will be supplemented by a poloidal scan of the light emission to yield spatial profiles of the ionisation rate and of Z_{eff}.

Visible Spectroscopy
Some of the optical fibres of the H_α monitors are equipped with visible spectrometers lent to JET under a Task Agreement with EURATOM UKAEA Association, Culham Laboratory, U.K.. In addition, a spectrometer closely coupled to the Torus is installed for limiter observation. In this way, a consistent picture is obtained about the influx of impurities from various sources such as walls, limiters and antennae.

Active Beam Diagnostics
Particles in the neutral beams used for heating can undergo charge exchange reactions with plasma ions, resulting in the emission of radiation due to recombination. Analysis of the radiation, which is emitted over the complete visible spectrum, allows measurements to be made of the impurity concentrations of helium, carbon and oxygen as well as ion temperatures, flow velocities during neutral injection and helium minority temperatures during RF heating. The source of radiation is defined by the intersection of the viewing lines and the trajectory of the neutral beam, thus enabling local measurements to be made. One or more of the neutral beams will be modulated to improve the signal to noise ratio.

A provisional system has been installed which utilises some of the H_α monitors. Light is transmitted from two optical viewing heads along optical fibres to the Diagnostic Hall for analysis. The final system, capable of carrying out a complete radial scan, is under construction and will become operational after the shutdown at the end of 1986. Consideration is being given to the deployment of a low power diagnostic neutral beam for these measurements.

Vacuum Ultraviolet Spectrometry
Vacuum ultraviolet spectrometry covers the spectral range between 1 and 200nm allowing the study of light emission from impurities exposed to temperatures below 1keV. A single channel broadband spectrometer covering the wavelength range 12 to 170nm has a microchannel plate detector and is being used for time-resolved line identification and impurity monitoring studies. This spectrometer has been operational since May 1984. Most of the information on impurity concentrations in JET is based on the results of this instrument. It will be complemented by a grazing-incidence spectrometer covering the wavelength range between 1 and 30nm, which also has survey capability using the same detector. It is aimed particularly at the resonance lines of light impurities.

A spectrometer system supplied by EURATOM CEA Association Fontenay-aux-Roses, France and successfully operated on TFR, is being used to obtain spatial impurity ion profiles. The spectral scan is obtained by viewing the plasma through a rotating mirror with a gold plated face and used in near grazing incidence. A spatial scan takes 3ms to complete and is repeatable every 20ms. The three mirrors, scanning different portions of the plasma cross-section, are synchronised to rotate together and can be stopped to obtain continuous time resolution at fixed chords. The two horizontal channels of the system are operational and provided first results in 1985.

X-Ray Spectroscopy
During additional heating the portion of the plasma, whose temperature can be measured by vacuum ultra-

violet spectroscopy, is shifted to the outer regions. Shorter wavelength instruments are needed to view the highly stripped impurities in the centre of the discharge. Work is in progress at EURATOM-IPP Association, Garching, F.R.G., on a spatial scanning X-ray crystal spectrometer which will operate at shorter wavelengths (0.1-2.4nm). It is scheduled for installation early in 1986. This instrument will use two crystals which must be rotated and translated synchronously to carry out a wavelength scan. To obtain a spatial scan with this spectrometer system, it will be necessary to locate it close to the torus. This means that it cannot be used for deuterium-tritium plasmas with high radiation fluxes.

An active phase spectroscopy system is being designed, which will allow impurity spectroscopy measurements to be continued under active conditions.This will also be based upon a two crystal spectrometer, though the crystals will now be located outside the Torus Hall and will view the plasma through a vacuum pipe passing though a small hole in the shielding wall. The two crystals and the detector will be separated by a neutron shielding labyrinth allowing the detector to be located in a region of a low neutron flux. This system is schedule to be operational in 1986.

High Resolution Spectroscopy

High Resolution Spectroscopy also provides a valuable method of determining plasma ion temperatures by measuring the spectral width of selected impurity lines. A group at EURATOM-ENEN Association, Frascati, Italy has built a high resolution crystal spectrometer for JET which will have both the crystal and the detector placed outside the Torus Hall behind the neutron shielding wall. The system has been installed and will be operational early in 1986.

Soft X-Ray Pulse Height Analysis;

The measurements of the soft X-ray spectrum using a cooled Si(Li) detector is used to obtain estimates of Z_{eff}, the electron temperature T_e, and to measure deviations from a Maxwellian distribution of the electrons. A first provisional system was operational in August 1984. The full system has now been installed and will become operational early in 1986.

Soft X-Ray Diode Arrays

The Soft X-Ray Diode Array is used mainly for investigating MHD and other plasma fluctuations and to locate the magnetic surfaces with rational values of the safety factor q. It can also be used to measure the radial radiation profile, with a coarse spectral resolution, by applying a filter technique. The system built by EURATOM-IPP Association, Garching F.R.G. consists of two X-ray imaging cameras, which view the same toroidal cross-section of JET in orthogonal directions (one mounted on a vertical port and one on a horizontal port).

The provisional system installed in 1983 has now been replaced by the full system. It has already delivered extremely important results on the stability of the plasma core during RF heating. The high time resolution of the detectors allows the development of the periodic sawtooth instability to be followed in detail.

The most serious restriction on this diagnostic arises from the sensitivity of the detectors to neutron and gamma radiation. Massive shielding will be required to allow the system to operate in deuterium plasmas with high power heating. However, this system will not be able to operate in deuterium-tritium plasmas, because of radiation induced signals and detector damage. The search will continue for detectors which are less sensitive to radiation and, therefore, which might be used in the future to extend the range of operation of this system.

Bolometry

The bolometers allows time and space resolved measurements of the total plasma radiation losses. This diagnostic uses multichannel arrays of bolometers to view the JET plasma in orthogonal directions through vertical and horizontal ports. The system was built by EURATOM-IPP Association, Garching, F.R.G..

Total radiation losses and spatially resolved radiation profiles have been obtained and used as input for the evaluation of the energy balance. The total radiation losses vary typically between 40 and 80% of the input power depending on vessel conditions and density. This holds for both ohmic and radio frequency heating. At higher densities, the profiles are generally hollow. They are, however, difficult to assess as the proximity of the antennae leads to a local enhancement of radiation, which perturbs the symmetry of the profiles.

Interferometry

Density is one of the fundamental parameters of the plasma and its measurement has to be made reliably for every pulse. The main system used is a multichannel far-infrared interferometer built by EURATOM-CEA Association, Fontenay-aux-Roses, France. It uses a deuterium cyanide laser with the beams transmitted through crystal quartz windows in the vacuum vessel wall. The optical components for the interferometer are mounted on a single large C-frame which is mechanically decoupled from the JET machine to minimise vibrations.

The interferometer is fully operational including the compensating interferometer for correcting movements of the mirrors mounted inside the torus. Due to carbonisation, these mirrors lose reflectivity and a change of wavelength for the compensating interferometer must be considered.

Polarimetry

The interferometer can also be used to measure Faraday rotation caused by the poloidal field, if the rotation of the polarisation direction is recorded. In this way it is possible to obtain information on the current density profile. These measurements should make it possible to determine the central current density within ±10% accuracy. A contract with EURATOM-CEA Association, Fontenay-aux-Roses, France has been agreed to

carry out the necessary modifications on the existing interferometer.

Reflectometry
In the reflectometer, the microwave beam is reflected from a critical density layer within the plasma. A prototype system has been tested and developed using one of the ECE waveguides. It has been given some useful data on density profiles and a more comprehensive system is now being designed.

Neutral Particle Analysis
The Neutral Particle Analysis System, constructed for JET at the EURATOM-ENEA Association, Frascati, Italy, consists of an array of five separate analysers arranged to view different chords in a vertical section of JET, and is now operational. It provides routine measurements of the ion temperature and of the ratio of hydrogen to deuterium in the plasma as well as ion temperature profiles of the central plasma. Due to its toroidal scanning capability, it should be possible to study the slowing down of the injected neutral beam particles.

Diagnostic Pellet Launcher
The hydrogen/deuterium pellet injector, developed by EURATOM-IPP Association, Garching, F.R.G., is nearly complete, including the work on the JET interface. Preparations are underway for installation of the equipment early in 1986. The planned pellet injector from US DoE, Oak Ridge National Laboratory (ORNL), U.S.A. would intrude on the space presently used by the diagnostic pellet launcher. Therefore it is intended to install both injectors on the same neutral injector box which will be used as a common cryopump.

The pellet injector is of the pneumatic type. The pellet is accelerated over a path of up to 80cm by application of room temperature pressurised hydrogen or helium gas behind the solid hydrogen or deuterium pellet. Cylindrical pellets with diameters of 2.6mm, 3.6mm and 4.6mm will be obtained at velocities between 1200m/s and 1500m/s. The pellets contain sufficient atoms to produce a 10 to 100% increase in the particle content of JET at the plasma densities and volumes expected during 1986.

The pellet injector will expand the scope of studies of particle transport, confinement and recycling of the host species and also impurities (using neon doped hydrogen/deuterium pellets). It will also facilitate the tailoring of the plasma density profile to optimise heating and also provide empirical data to arrive at a specification of a pellet refuelling device for JET.

Remote Handling

Progress has been made in specifying, acquiring and commissioning major items of remote handling equipment. This equipment comprises special tools to suit the features and to provide access to JET components; end-effectors to lift and attach large components; large, high-precision transporters to carry the equipment to all parts of the JET machine; and control systems for all this equipment.

During 1985, considerable effort was devoted to analysis of tasks inside and outside the vessel to provide the basis for specifications of equipment and to supply material for data bases which will be used to direct operations.

The introduction of tritium into the plasma, which will require that all work on the JET machine is performed by remote control from outside the Torus Hall, is now predicted for mid-1991. Until this time, increasing background radiation, the generation of slightly activated dust and the use of beryllium will necessitate special equipment and methods for gaining access and carrying out hands-on work safely inside the torus.

Transporters
The articulated boom, which is the principal in-vessel transporter, was commissioned early in 1985. In June, it was used successfully to remove a number of nickel limiters and to fit A_0 type RF antennae. These operations are shown in Figs. 24 and 25. A three-axis extension to the boom, to provide pan, tilt and roll motions of the end effectors was also procured and commissioned. Successful working of the complete chain of machines for in-vessel maintenance was demonstrated. These comprised the boom, extension, servomanipulator and some of the special tools which the servomanipulator will handle, as shown in Fig.26. An additional joint, which can be added to the boom to extend its reach to cover the whole torus

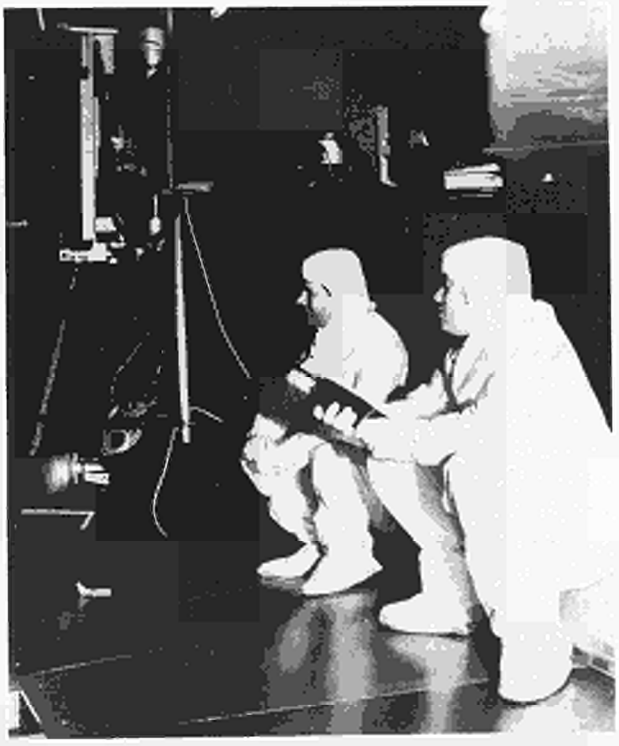

Fig. 24: Articulated boom in use for hands-on removal of limiters

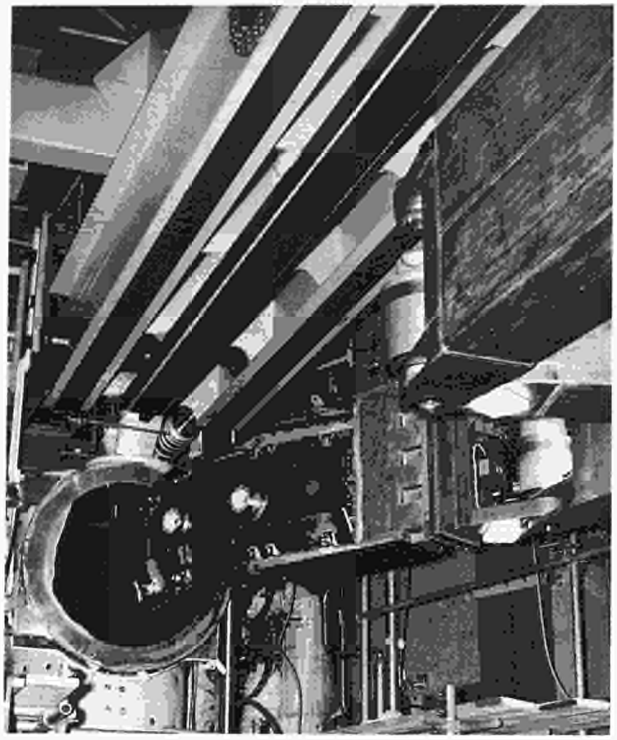

Fig. 25: Articulated boom in use for fitting A_0 type antennae

Fig. 27: Support Vehicle

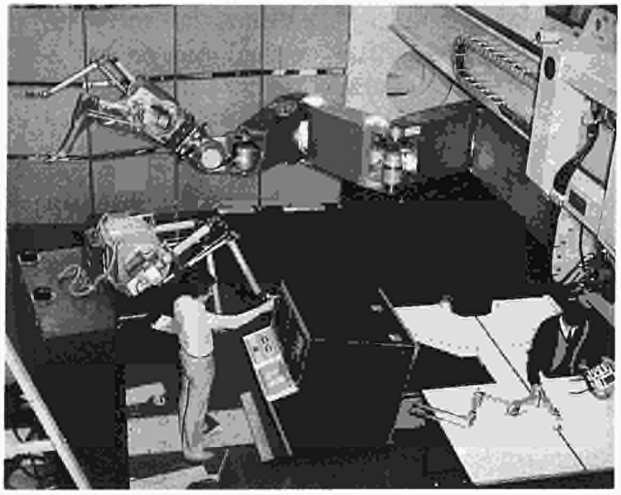

Fig. 26: Chain of machines for in-vessel remote maintenance

from a single port, was designed and ordered. The load capacity with this "boom addition" will be 350kg (compared with the 1 tonne capacity without it when the boom can reach only half of the torus from one port).

A concept and feasibility study was made of a vertical telescopic arm with a telescopic horizontal boom to be carried on the main crane crab and used to carry manipulators, end effectors and tools to locations on the machine outside the torus. Work on this transporter is continuing.

A turret truck to lift manipulators, end effectors and components for attachment to the boom was procured during 1985 and used in June. A roving support vehicles was delivered late in 1985, as shown in Fig.27. This is driven from batteries, is radio-controlled and carries a simple manipulator and TV cameras.

Servomanipulators and End Effectors

The relationship of articulated boom, end effectors, manipulators and tools is shown in Fig.28. The old Mascot servomanipulator used during recent years for feasibility tests has been reduced in size and refurbished to a high standard. It was mounted on the boom and inserted into the torus during the Summer Shutdown (see Fig.29). Two new models are under construction for delivery in September 1986, which will have microprocessor control and serial links providing computer-aided operation modes such as teach-and-repeat.

A specially designed gripper, mounted on the boom, was used to install the A_0 RF antennae, in June, and a special tool for connecting the A_0 antennae to their transmission lines was also manufactured and used. Grippers for the belt limiters and for the shield and housing of the new A_1 type antennae, to be fitted in the vessel at the end of 1986, were designed and a call for tender was issued.

Tools

Considerable effort was devoted to defining and designing special tools, which will initially be used in hands-on operation for defined shutdown tasks and later will be capable of fully remote deployment and operation. Examples of such tasks are the installation of the belt limiters and RF antennae and replacement of all vacuum vessel windows at the end of 1986. As part of this strategy, a detailed specification was written for a power pack to act as a source and strike the arc of a welding head

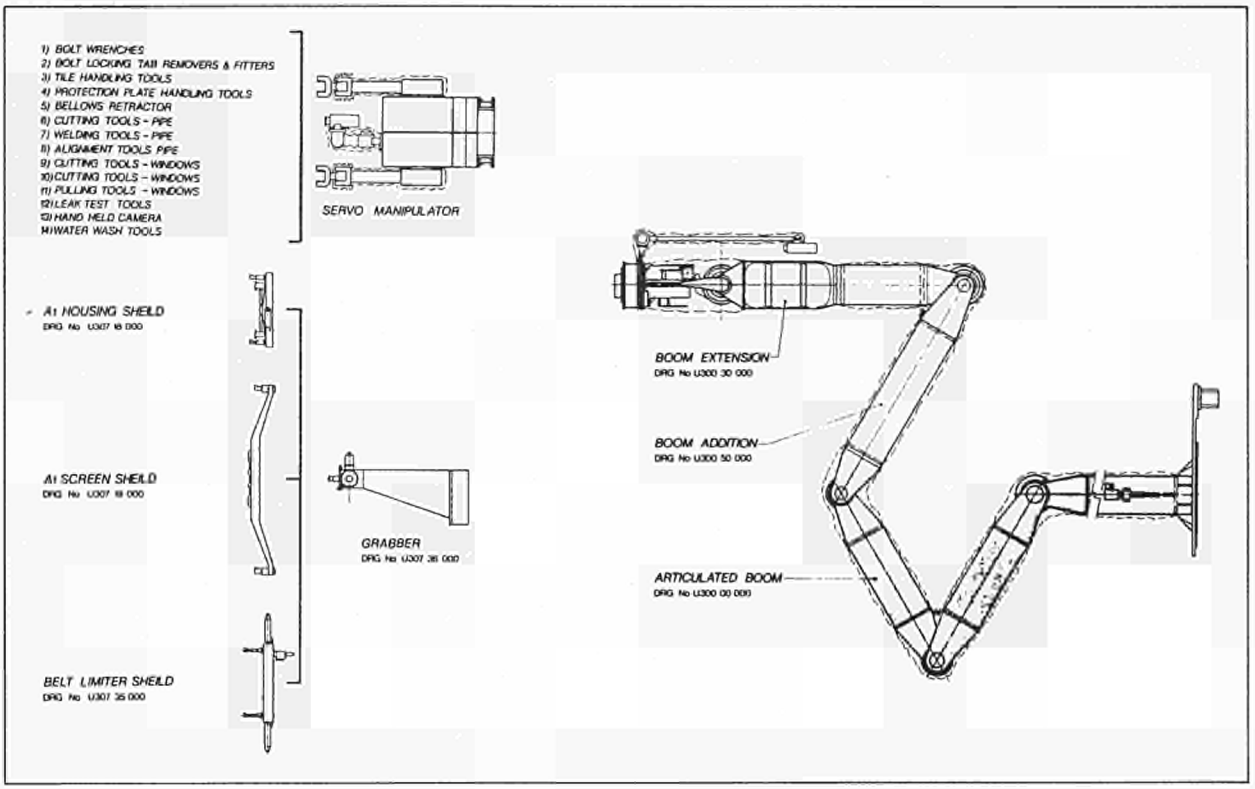

Fig. 28: Articulated Boom and End Effectors

connected by 100m of cable. Two units will be procured during 1986.

Experimental versions of the self-propelled lip-welding and cutting machines were used in the June and December Shutdowns to cut and re-weld the horizontal port flanges connecting the neutral injector boxes to the vacuum vessel. The welding machine has been developed so that it can now follow round flange corners with a radius of 60mm. Parts have been ordered to construct three prototypes. The cutting machine is being developed, similarly.

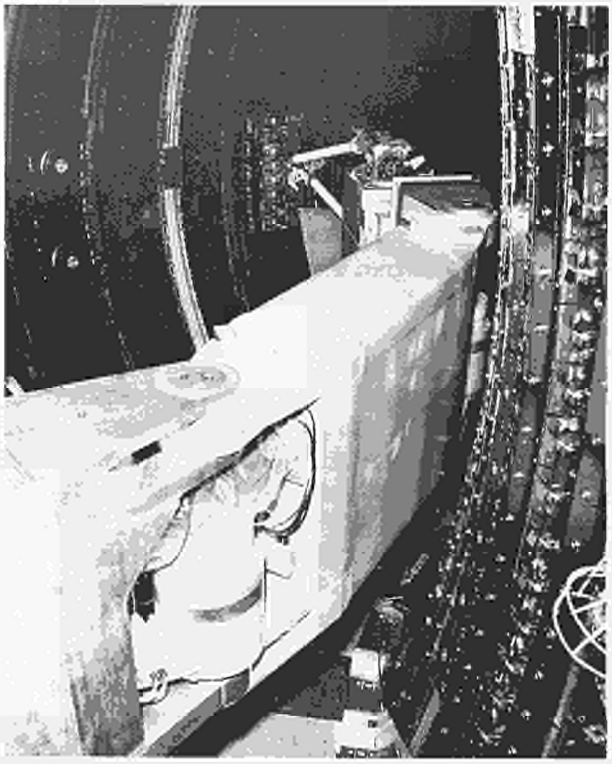

Fig. 29: Mascot servomanipulator on articulated boom inside torus

Television

TV cameras and motorised arms to position them in the working area of the manipulator have been specified and ordered. The arms will be carried on the last segment of the boom extension. In February, the in-vessel inspection system was used to scan the inside of the vessel. The pictures were acceptable and showed detail down to 2mm. However, the inside of the vessel was dark because of the graphite tiles and carbonisation. This has been overcome by a device which allows the illumination integration of a number of successive flashes.

Remote Handling Controls

The control system will link real-time local control units (LCUs) with general purpose workstations for all equipment except the servomanipulators, which have their own dedicated workstations. A conceptual design of a general-purpose workstation has been finalised and is shown in Fig.30. Construction has started of a prototype, which will be used at the end of 1986. The LCU to operate the boom and its end effectors and manipulators will be a combination of direct camera views and a computer-generated perspective graphical display. The application of graphical display is being developed by JET and by personnel assigned to JET from KFK, Karlsrhue, FRG.

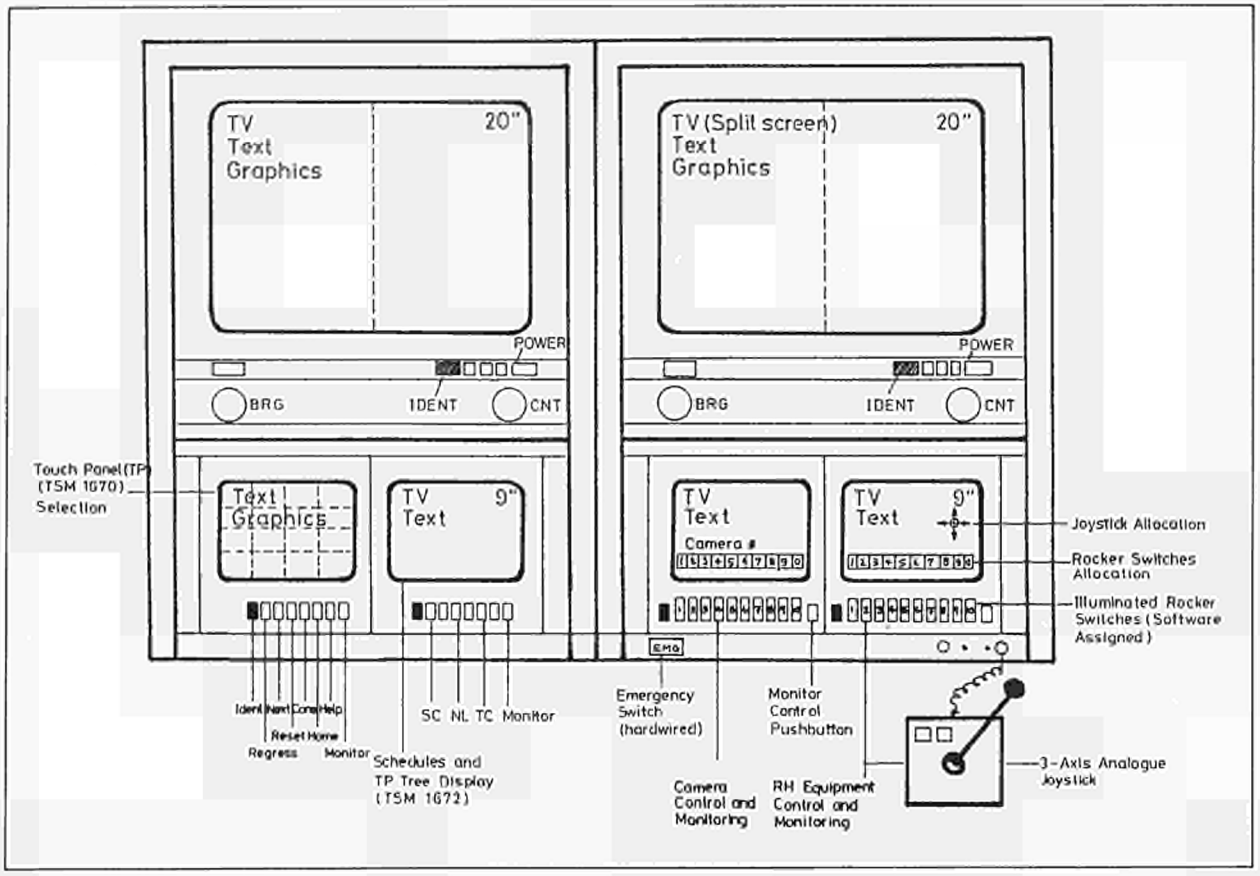

Fig. 30: General Purpose Remote Handling Work-Station

The two special servomanipulator workstations will each control the manipulator arms; four independent cameras on articulated arms carried by the boom extension and the manipulator body; the boom extension; the end effectors; and all the remote handling tools. A concept design of this workstation, taking into account the technical and ergonomic requirements and based on a range of remote handling tasks, is being developed by EURATOM-CEA Association, Saclay, France, under an Article 14 Contract.

One programmable controller will control the remote welding power sources and the machines carrying the welding heads and a second one will control the remote cutters. The articulated boom has been used so far with a manual push-button controller, but control by a 1/5 scale master, with corresponding joints linked by closed servo loops, has also been developed. These controls can be seen in Fig.26.

Active and Toxic Component Handling

During 1985, a design was completed and an order placed for delivery in July 1986 of a "torus access cabin" (TAC) through which workers can enter the torus in airline suits, while it is contaminated with beryillium dust or lightly activated dust. The cabin, shown in Fig.31, will seal onto a vacuum vessel port and will contain showers, changing facilities and all the necessary services and monitoring systems. It will have a work room through which components can pass and be decontaminated.

Tritium Handling

During 1985, design work and studies have been undertaken mainly in the areas of system design, design, manufacture and performance testing of prototype components, materials behaviour over wide temperature ranges, safety, tritium supply and waste disposal. A detailed cost evaluation has also been made.

System Design

The conceptual design of various process subsystems, such as cyrogenic gas handling and purification, storage, gas-chromatography and the tritium make-up and disposal system, has been developed to a level which allows the start of mechanical design.

The design philosophy has been adopted of containing any primary process equipment holding significant tritium inventories of unacceptable release potential, in leak tight secondary containment vessels operating under full vacuum but pressure designed to withstand any failure of primary equipment, such as the warming of cyrogenic fluids. Primary equipment will be rigorously leak tested with helium at 200°C. All flange and weld joints will be accessible to allow testing and repairs. When in service the equipment and containment vessels will be bakeable at 200°C under vacuum to remove the bulk contamination, otherwise released during repair work. Gases removed from the vacuum vessels will be processed in a small clean-up system.

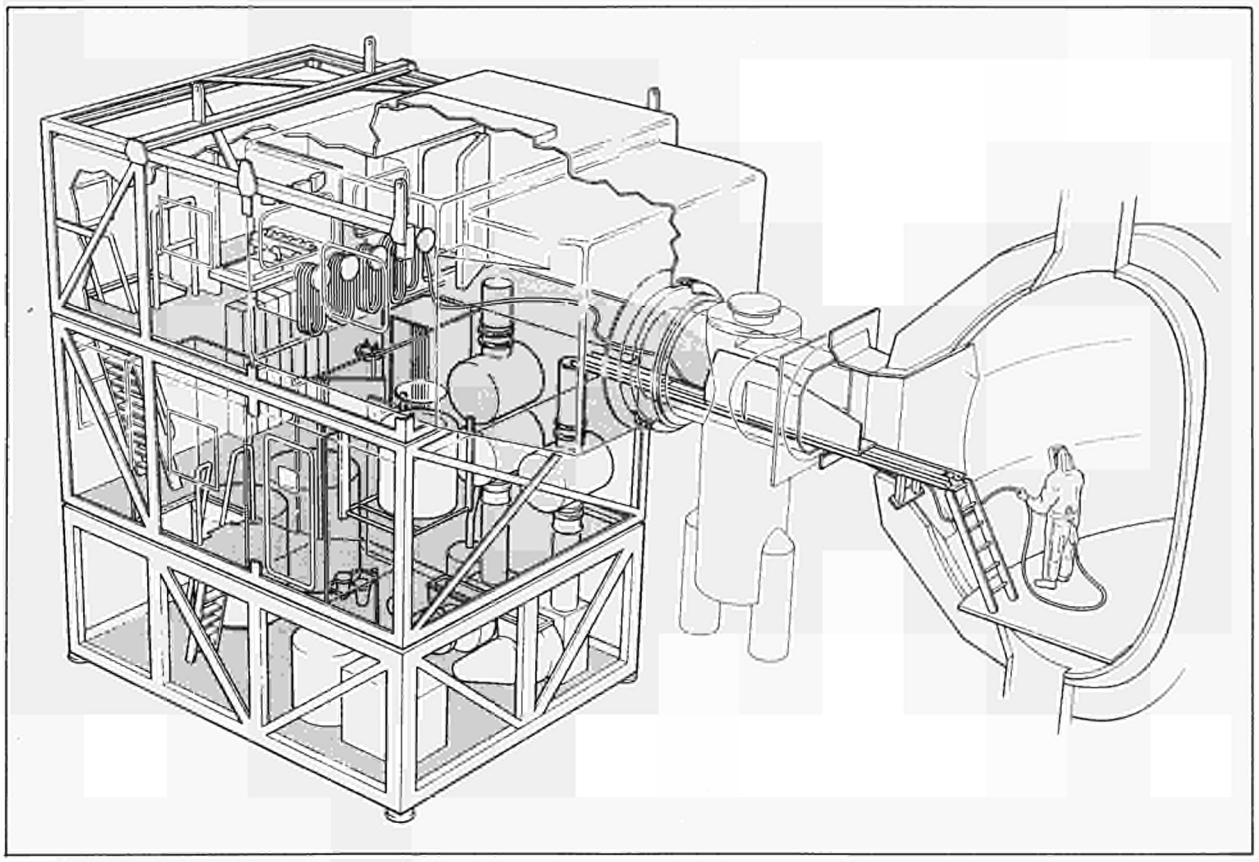

Fig. 31: Torus Access Cabin

Cost Evaluation

A cost evaluation was based on detailed flow diagrams, a preliminary mechanical layout, estimated costs of the cryogenic primary components and the costs of orthodox equipment. The total of 15-20 MECU (1985 values) is expected to be made up in the major proportions of vessel and box structures 27%, process instrumentation 24%, vacuum system and link to the torus 12%, process valves 12%, civil engineering 6% and radiological protection and transport equipment 4%.

Component Design and Testing

A number of prototype process components have been designed and are being tested. First results confirm the feasibility of the engineering approach, particularly in the use of cryogenic techniques for the hold-up, transfer and purification of the gases from the torus and neutral injectors. Further testing will provide data from which to work out more precisely the optimum control and operating parameters.

Material Technology Studies and Tests

Handling hydrogen isotopes, including tritium, at process temperatures ranging from 4K to 752K and at pressures of full vacuum to 6bar, limit the choice of materials to stainless steels of series 304 or 316 and to nickel alloys such as Inconel. Particular attention has been paid to welding these materials, since the ductility of welded materials may be reduced drastically at cryogenic temperatures unless materials and welding procedures are chosen with care.

A study contract has been placed with a private organisation, well experienced in cryogenics and material technology, to develop weld procedures and test procedures covering the typical range required for the JET tritium plant, with tube and plate thickness of 3-10mm. Results from initial tests have successfully identified materials and procedures that will allow manufacture of components with mechanical properties well above the minimum requirements specified by applicable engineering codes.

Safety Studies

A preliminary estimate of chronic tritium releases during normal D-T operation has included permeation through the torus walls into the Torus Hall and into the bake-out loop, losses from the bake-out loop and releases from the tritium recycling system and other regions where tritium will be present.

Of the estimated released of about 1000Ci year, about half has been attributed to maintenance when the torus is opened and while replacing faulty tritium plant components. About 20 maintenance events per year were assumed for the tritium plant. It is expected that baking and glow discharge cleaning will reduce tritium levels in the torus.

It has been decided to equip the torus with an internal cladding shield, which will eliminate atomic driven flux

thorough the torus walls leaving the much smaller contribution from pressure-driven permeation. A pessimistic calculation for clean, non-oxidised surfaces with walls at 300°C and the ports at 200°C gives 5600Ci/year into the bake-out loop and 24Ci/year into the Torus Hall.
A risk-based design criterion has been established, in conjunction with the UKAEA's Safety and Reliability Directorate. This provides that the product of the maximum release of HTO and the annual frequency of the release should not exceed 10. This criterion will be satisfied comfortably in respect of seismic damage by a plant whose failsafe system isolates the various tritium-bearing loops.

Tritium Supply and Waste Management

In a tritium make-up and disposal system, flasks up to 15ℓ in volume will be connected to or removed from the plant through a double-lidded lock system which maintains leak tightness and exposes only non-contaminated surfaces. The transport container will dock onto one of three vacuum boxes containing externally operable levers to move the flasks and clamp them onto the process line flanges. For ease of handling, all waste containers, eg. disposable waste pumps, adsorbers, and dryer beds, will have the same external dimensions.

Approximately 3 x 10^5Ci of tritiated wastes in about 70 containers will need disposal in the 2½ years of D-T operation. The total tritium supply is expected to be about 5 x 10^5Ci to provide the initial fill (tritium plant inventory) and replacement of burn-up and extracted waste.

Scientific Achievements during 1985

Plasma Optimization

Considerable attention has been devoted to optimization of conditions in ohmic heating plasmas, in which studies have been undertaken on the four phases: start-up, current rise, flat-top and termination. An understanding of the dynamic processes associated with transitions from each phase to the next is essential if these conditions are to be optimized. The specific characteristics of the various transitions are summarized in Table VIII.

Start-Up Phase

In the breakdown phase, application of a toroidal electric field (E_T) causes free electrons to be accelerated along the toroidal magnetic field B_T, and if the ratio of E_T and the gas pressure p exceeds a certain threshold, then the electrons gain sufficient kinetic energy to ionise the filling gas. In certain conditions, this leads to an avalanche process resulting in the formation of a fully ionised gas. However, the formation of the avalanche can be prevented by loss mechanisms. In stray magnetic fields B_{stray}, particles follow the resultant total field, and can be lost at the torus wall. The probability of a successful breakdown is increased with decreasing B_{stray}/B_T and increasing E_T/p as shown in Fig.32.

Stray fields increase non-linearly with the premagnetisation current as the iron transformer becomes progressively more "leaky". Consequently, increasingly larger electric fields must be applied if the levels of premagnetisation needed to produce higher flat-top plasma currents of longer duration are to be obtained. At the full design value of 20MA-turns for the premagnetisation, the electric field required is so high, that when an avalanche occurs and develops into a plasma, the toroidal current I_p increases too rapidly. This results in the production of extreme skin currents and introduces positional control problems. Reliable breakdown has been obtained only up to 12MA-turns. Hardware changes will be necessary to make use of the full 20MA-turns. Voltage reduction switches will be introduced, which will lower the electric field immediately after breakdown has occurred (e.g. within 50ms from the start). Without these switches, it will not be possible to obtain voltage reduction prior to 400ms after breakdown. The stray fields can be reduced at high premagnetisation by manipulating the current distribution to the coil PF1. However, the distribution has been homogeneous but it is hoped to provide extra busbars to improve this facility.

TABLE VIII
Start-Up Phases in JET Pulse Operation

TRANSITION		
FROM	*TO*	*PROCESS AND PROBLEMS*
Premagnetisation	Fast Rise	Breakdown and ionisation in the presence of stray fields.
Fast Rise	Slow Rise	Current rise too rapid leading to skin currents and instabilities.
Slow Rise	Flat Top	Skin effects must be counteracted by simultaneous ramping of fields and plasma shape; build up of density; increased risk of disruption.
Flat Top	Decay	Density Decay not always sufficiently fast; "marfes"; disruptions; negative skin current effects.

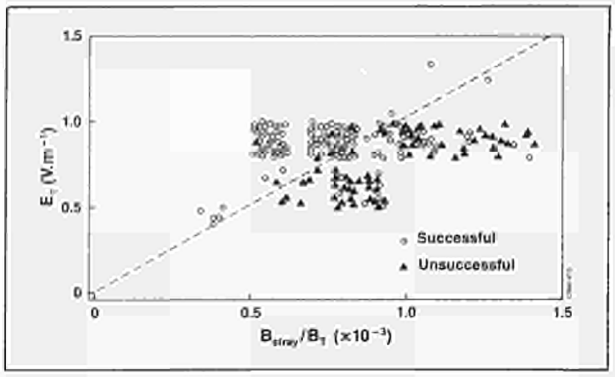

Fig. 32: Successful and unsuccessful breakdown in the plane of toroidal electric field E_T versus ratio of stray magnetic field to toroidal field (B_{stray}/B_T)

Current Rise Phase

Once ionisation is complete, the plasma temperature begins to rise with current. As a consequence, the conductivity increases and the magnetic fields penetrate the plasma more slowly. A current skin starts to form on the outside, which is highly unstable and the current is redistributed in a series of internal rearrangements of the plasma.

Complications then arise, since plasmas with hollow current distributions resulting from the skin effect, are prone to tearing mode instabilities. These instabilities result in the inward redistribution of the current, producing an anomalously fast skin relaxation time. Observations have shown an increase in the skin effect and relaxation time, due to off-axis heating, with increasing ramp rate. However, above a certain threshold, anomalously short relaxation times are produced with a strong increase in magnetic activity. The threshold between classical and anomalous current penetration in JET lies at about 1MAs^{-1} with constant aperture and B_T.

This means that, with the full design value of 5MA plasma current, at least 5s of pulse time are needed to avoid instabilities during current ramp-up. At faster ramp rates, the instabilities resulting from the anomalous penetration cause an increase in the level of impurities. However, this effect, can be kept to acceptable levels if metal impurities are avoided.

Flat-Top Phase

An effect produced by the faster ramp rate is that the plasma locks itself in a state of continuous instability, even during the subsequent flat-top period. This leads to an increased chance of a disruption occurring at very low density levels, both in the early part of the flat-top and the start of additional heating.

Two ways of increasing the critical ramp rate of 1MAs^{-1} have been studied with some success:

(a) ramping the toroidal field together with the current enhances the classical penetration;

(b) expanding the plasma aperture in conjunction with the current so that the average current density remains constant.

Using these methods, the critical ramp-rate has been increased to 2MAs^{-1} and further studies of skin current relaxation will be carried out.

Plasma Position and Current Control (PPCC)

During 1985, two previously prepared developments of the plasma control system have been used on a routine basis. These are the feedback control systems of the plasma current and of the plasma vertical diameter (ie. shape control). In addition, the stabilisation system of the vertical plasma position has been improved. The shape feedback control system, investigations on the instability of the vertical position and the performance of the stabilising system have been described previously [1] (see Appendix IV).

The plasma current feedback control has a relatively long response time of ~0.5s for small changes of the preprogrammed reference current. The control error is usually smaller than 5% and can be further reduced by an appropriate choice of the preprogrammed control voltage of the poloidal flywheel generator. To avoid excessive currents in the ohmic heating (OH) coils in the event of disruptive plasma behaviour, the feedback and preprogrammed voltages are automatically set to zero, if a plasma fault is detected by the Plasma Fault Protection System (PFPS). This plasma current control system had already been tested and used in 1984.

In 1985, protection was enhanced by the inclusion of a plasma current error monitor which creates a soft termination of the pulse, whenever the current error exceeds a preset limit. This facility prevents futile attempts of the current feedback system to maintain or raise the current in cases where disruptive or faltering plasma behaviour is not discovered by the plasma fault protection system.

In early 1985, the poloidal field configuration was altered: the vertical field coil was separated from the OH-coil and supplied solely from the poloidal vertical field amplifier (PVFA). The plasma current feedback controller was not re-adjusted for the new load characteristics of the poloidal flywheel generator convertor. This created an increased current overshoot at the transition from slow rise to flat-top conditions. Nevertheless, a satisfactory current control was achieved by minor modifications of the preprogrammed reference current waveforms.

In the new shape control system, the same control principle is used as in the radial position control: the flux difference between the limiter and two symmetric and continuously adjustable reference positions in the upper and lower halves of the vessel is measured and controls the current in a pair of shaping coils by means of a proportional controller and the poloidal shaping field amplifier (PSFA). The control error is about ±10% due to the absence of integral feedback but this error is acceptable. In this way, in conjunction with the radial position control, satisfactory control was obtained of the vertical plasma diameter and of the elongation ratio (b/a)

of the plasma cross-section. This system includes an automatic limitation of the shaping current/plasma current ratio, defined by a reprogrammable waveform. Without this limitation, the stabilisation limit for the vertical position control might be exceeded in abnormal conditions, such as very strong peaking of the current profile, incompatible choice of reference functions for the vertical and radial plasma diameters, or failure of the shape feedback control.

In cases, where the turns ratio of the shaping coil are chosen incorrectly, the magnetic interaction between the shaping and radial position control systems can become critical and lead to oscillation of both systems. This was demonstrated in an experiment where coil P3 was used solely as the shaping coil. In principle, it is possible to decouple the systems electronically, but it was preferred to restrict the choice of turn ratios in the shaping coils P2/P3.

With the shape control system, it was possible to produce plasmas with an elongation ration b/a <1.8 and also plasmas with an internal magnetic separatrix which has two "X-points" close to the vessel walls at top and bottom.

The current, radial position and shape feedback control system and their interactions have been studied on the basis of simplified models of the plasma and of the poloidal field systems and compared with experimental tests where step perturbations where applied as reference functions. The agreement with experimental results was reasonable, but an improvement of the model is possible, when a better knowledge of some system parameters becomes available.

In the stablisation system for the vertical plasma position, an improvement was obtained by doubling the voltage range of the poloidal radial field amplifier (use of two units in series) and by reducing its small amplitude voltage step response time from about 3.5ms to 2ms. This made it possible to stabilize the vertical position of plasmas with an elongation ratio exceeding b/a = 1.8.

The effects of disabling the stabilisation under different plasma conditions (size, elongation ratio, q-value, current) were investigated, mainly in order to establish safe operation limits, to safeguard against excessive vertical forces and stresses at the vessel resulting from a stabilisation failure. Details have been described previously [1]. The main conclusion is that, at present, the elongation ratio b/a must be limited by maintaining the inequality:

$$I_p^2 \, (b/a - 1.2) < 5 \; (MA)^2$$

Additional vertical vessel supports are being designed to permit safe operation with large currents ($I_p \approx 5$MA or more) and full size ($2a \approx 2.45$m, $2b \approx 4.0$m).

Reference

[1] P Noll et al, 11th Symposium on Fusion Engineering, (Austin, Texas, USA. 1985) (to be published) and JET Report JET-P(85)26.

Impurities and Radiation Losses

During 1985, the impurity content of the plasma was monitored routinely by the VUV survey spectrometer (KT2) and analysed by essentially the same methods as described previously (EUR-JET-PR2). First results of the measured emission shells of O VI and Ni XVII, from the VUV spatial scan spectrometer (KTI), support the estimates of impurity transport used in the analysis code. Results on the consequences of several 1985 carbonisations, and the impurity behaviour during ICRF heating are reported below.

As previously, visible spectroscopy was used for indentifying impurity sources and measuring impurity influxes from different locations. The analysis methods of visible line intensities were improved considerably in 1985, both in the field of atomic physics (i.e. excitation rate coefficients), as well as in the area of excitation-ionisation models. The importance of metastable levels was assessed for the first time theoretically and experimentally, and reliable oxygen and carbon influxes from the limiters were obtained [1]. Observation of the chromium coated screen of the 2D antenna in late 1985 proved unambiguously that chromium fluxes were entering the plasma from the antenna during RF. This observation is demonstrated in Fig.33 which shows the carbon and chromium visible line intensities, measured in front of the 2D antenna during Pulse No. 6051.

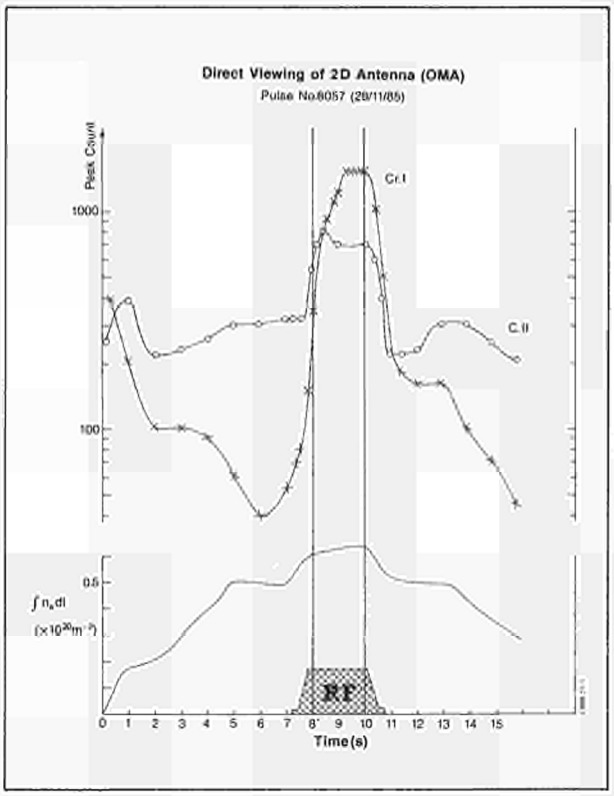

Fig. 33: H_α, C II and Cr I visible line intensities measured in front of the 2D RF antenna during Pulse No. 6051. The RF power to the antenna and line density are also shown

For 1985 operation, the carbon limiters had been fitted with new carbon tiles, which did not have any metal coating or molybdenum contamination on their surfaces. In addition, the inner wall was protected by carbon plates within ± 1m of the horizontal midplane, in order to avoid damage and metal splashes during disruptions. The vessel was washed with pure water, and a very light carbonisation (2% CH_4, 6 hours) was carried out prior to first plasma operation. A number of further carbonisations were undertaken during 1985 operation, with the aim of suppressing metal impurities during ICRF heating.

The overall impurity behaviour during 1985 ohmically heated (OH) discharges was similar to that of previous operational periods [2]. In particular, metal impurities were reduced at higher average electron densities (n_e). Oxygen and carbon were weak functions of n_e, although low electron densities tend to favour high concentrations of carbon, while oxygen dominates at higher densities. These results are in accord with the trends of impurity fluxes from the limiters. The ratio of nickel to chromium changed in favour of nickel, which means that nickel originated from the Ni antennae screens rather than the inconel vessel walls. Molybdenum had disappeared and chlorine played a minor role for radiation and Z_{eff}, although it had no tendency to decrease further.

During the first week of operation with new carbon tiles, metal concentrations in the plasma were very low and the radiation power was only 40% of the ohmic power (P_Ω). Later on, the graphite became coated by metals leading to higher metal concentrations in the plasma, particularly at low electron densities. This behaviour is illustrated in Fig.34a showing the recorded brightness of the NI XXV line as a function of pulse number for selected pulses ($n_e = 2 \times 10^{19} m^{-3}$) from the two periods. O V and C IV intensities are also shown in Fig.34 for comparison.

When the limiters were metal coated, a light carbonisation (12% CH_4, 6 hours) led to an immediate reduction of metal impurities by a factor of five and a reduction of radiation power from about 70%P_Ω to 50%P_Ω. Both levels recovered after about 20 plasma pulses, as shown by the Ni XXV intensity behaviour in Fig.34b. Oxygen had a tendency to decrease in the long term, while carbon remained unchanged or increased slightly. These observations are in good agreement with the results of the 1984 carbonisations [2]. After a very heavy carbonisation (17% CH_4, 48 hours), the metals reduced by a factor of 100, and the recovery period was extended to some 200 plasma pulses. Typical impurity concentrations for a carbonised vessel were 3%n_e of C, 1%n_e of O, 0.05%n_e of Cl and 0.01%n_e of metals resulting in $Z_{eff} \approx 3$ [3].

During RF heating, increased influxes of hydrogen and impurities were observed [4] leading to an increase in n_e[5]. Flatter radial n_e profiles and higher edge densities were measured during injected RF power [5]. Due to this, and possibly to enhanced particle transport, the hydrogen particle confinement (measured from H_α), reduced by a factor of two [6]. Light impurity concentration did not change significantly during RF

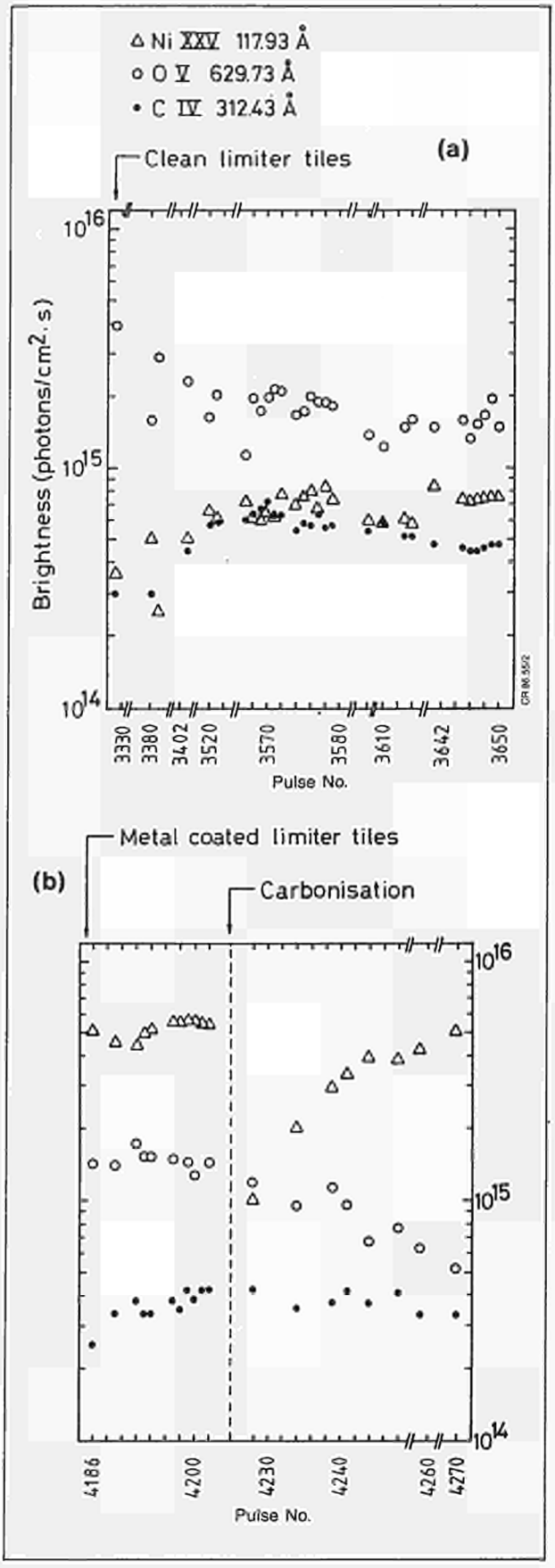

Fig. 34: Intensities of some VUV impurity lines for selected plasma pulses ($\bar{n}_e = 2 \times 10^{19} m^{-3}$):
a) Clean limiter tiles;
b) Metal coated limiter tiles, including light carbonisation.

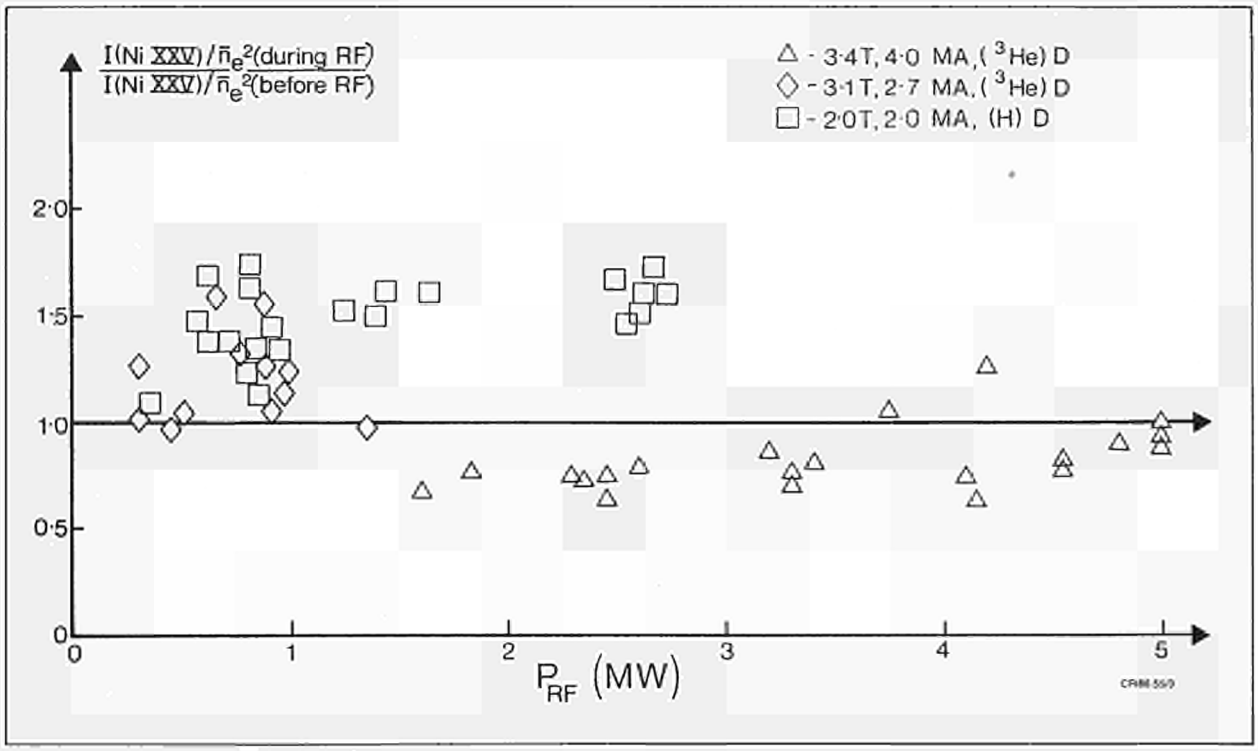

Fig. 35: Variation of Ni XXV intensity/$\bar{n}_e^2$ ($\propto$ nickel concentration) with RF power for three campaigns after carbonisation.

heating. Systematic studies of metal behaviour (after carbonisation) showed that the metal concentration was essentially constant during ^{3}He minority heating (B_T = 3.4T), while it increased to some extent during H minority heating (B_T = 2.0T) [3]. The respective results are summarised in Fig.35 which shows normalized Ni XXV line intensities as a function of RF power for three ICRH campaigns. Nomalization of the intensities through division by n_e^2 provides a good measure of the nickel concentrations in the plasma. The basic metal levels during these pulses were very low due to carbonisation (0.01%n_e). If no carbonisation was carried out for a longer time period, the absolute increase of metal concentrations appeared to be similar but started from a higher basic level.

Due to higher n_e values and flatter n_e profiles, the radiated power increased during RF in such a way that about 50% of the total input power was radiated [3]. Z_{eff} remained virtually constant during RF heating. Within the experimental error bars no significant differences were detected as far as antennae configurations were concerned. During preliminary X-point studies in JET, the total radiated power approached 100%P_{in} and about 30% of this radiation was localised in the vicinity of the X-points.

The general impurity situation in 1985 was similar to that at the end of 1984. It did not deteriorate significantly during RF heating, but the usual decrease of impurity concentrations and Z with higher electron densities (at constant plasma current) was not observed, either. The main problem at present is still the high fraction of carbon and oxygen in the plasma, causing an appreciable dilution of the deuterons ($n_D \approx 70\% n_e$).

References

[1] K H Behringer, B Denne, M R Stamp, H P Summers. 27th Annual Meeting Division of Plasma Physics (APS) (San Diego, USA, November 1985);

[2] K Behringer, P G Carolan, B Denne, G Decker, W Engelhardt, M J Forrest, R Gill, N Gottardi, N C Hawkes, E Kallne, H Krause, G Magyar, M Mansfield, F Mast, P Morgan, N J Peacock, M F Stamp, H P Summers. JET Report JET-P(85)08.

[3] B Denne, K H Behringer, W Engelhardt, R D Gill, N C Hawkes, E Kallne, H Krause, G Magyar, M Mansfield, K F Mast, C De Michelis, P D Morgan, D Pasini, N J Peacock, H P Summers. 12th European Conference on Controlled Fusion and Plasma Physics (Budapest, 1985). Europhysics Conference Abstracts *9F* (Part 1), p.379 and JET Report JET-P(85)10 p.45.

[4] M F Stamp, K H Behringer, M J Forrest, P D Morgan, H P Summers. 12th European Conference on Controlled Fusion and Plasma Physics (Budapest,1985). Europhysics Abstracts *9F* (Part 2), p.539 and JET Report JET-P(85)10, p.93;

[5] P Lomas, M Malacarne, H W Piekaar, F C Schuller, A Tanga, P Thomas. 27th Annual Meeting Division of Plasma Physics (APS) (San Diego, USA, November 1985);

[6] P D Morgan, S Corti, J Ehrenberg, M J Forrest, A Gondhalekar, C W Gowers, G Magyar, J J O'Rourke, M F Stamp, D D R Summers, A Tanga, M L Watkins. 12th European Conference

on Controlled Fusion and Plasma Physics (Budapest, 1985). Europhysics Conference Abstracts 9F (Part 2) p.535 and JET Report JET-P(85)10, p.41.

Plasma Boundary Phenomena

The study of plasma boundary phenomena aims at understanding the mechanisms of release of impurities from the wall and limiters and their subsequent penetration into the plasma. Recycling of hydrogen/deuterium and wall pumping are also studied with the main aims of control of the plasma density, and to estimate the inventory of hydrogen isotopes for future D-T operation.

During 1985, understanding has substantially broadened of the behaviour of impurities both of metals (originating from the wall) and of carbon (originating from the limiters, protection tiles and carbonisation). This has been accomplished by relating the analysis of data from Langmiur probes, surface analysis of exposed material, and H_α and impurity spectroscopy. One limiter and two RF antennae have been observed by an automated video system. Digitisation of the video pictures has provided a better understanding of the visual information, which consists partly of radiation of thermal origin and partly of line radiation of an unknown combination of molecular hydrogen and hydrocarbon lines. The two sources of radiation can be satisfactorily separated as they have a completely different temporal evolution. The footprint of the plasma on the limiter has been modelled successfully to include the details of the shape. In order to obtain a complete fit, it was necessary to postulate toroidal rotation of the plasma. It has not been possible to measure routinely the power loading on the limiter due to the presence of the RF antennae which took a substantial fraction of the power flowing in the boundary, causing the limiter surface temperature to drop below the detection threshold.

As mentioned previously, considerable carbonisation of the torus has been undertaken during 1985, with the intention of reducing the ratio P_{rad}/P_{in} and extending the power that the RF system could couple to the plasma without disruption. The thickness of the carbon deposit has been measured (Fig. 36) and a clear relation established between the thickness and the amount deposited, calculated from the throughput of CO/CO_2 during glow discharge and the duration and percentage of methane [1, 2]. The immediate effects of carbonisation were to cover the surfaces of the limiters from which the metal impurities originated. This reduced P_{rad}/P_{in}, until this covering layer had been eroded. Long term effects were only obtained when the limiter was heated to high temperatures so that metals on the limiter could either diffuse into

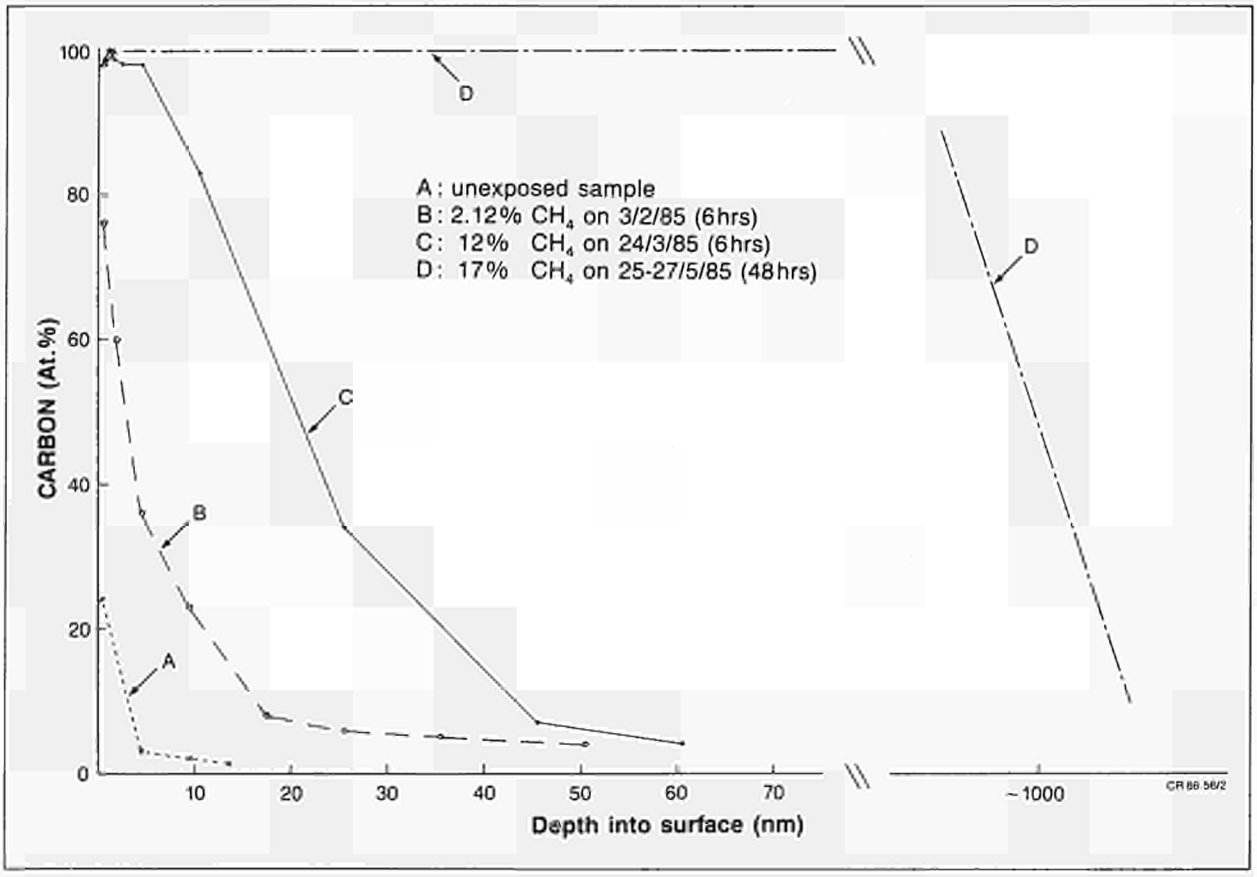

Fig. 36: The amount of carbon found on Inconel samples exposed to carbonisation in the JET vessel in 1985. The analysis method was Auger Spectroscopy, except for the main depth of the coating of 25-27 May 1985, which was measured by Rutherford Backscattering

the bulk material or were evaporated, both processes caused the cleaning of the surface. Other possible effects such as covering the walls with a thick ($\sim 1\mu m$) layer of carbon, (causing a decrease in the metal impurity content) seemed to be less important, as plasma-wall interaction was generally much smaller than plasma-limiter interaction. It has been shown by means of depth profiling that a substantial amount of the carbon diffused into the bulk of the Inconel 600 and even more into the nickel (see Fig.36).

Consequent surface analyses over several experimental periods of well chosen samples of limiters, protective tiles and of small samples of different materials attached to the first wall of JET has led to new understanding of migration of metals and carbon.

The surface coverage found on the limiters can be described by a global model assuming uniform coverage (by GDC or disruptions, for example) and erosion and redeposition processes during normal plasma discharges. The measured distribution, shows a clear relation to the shape of the footprint measured by the CCD limiter viewing camera and therefore it its assumed that the majority of the erosion and deposition takes place during the flat top of the discharge.

From a simple model, it is found that the distribution of impurities on the 1983 limiter was determined by net erosion, while on the 1984 limiter, deposition was dominant. This can be explained in terms of the experimental conditions in the respective periods. On the limiter removed in 1985, the shadow of the RF antennae could be seen separating an area of erosion from one of redeposition (Fig.37). Therefore, this limiter distribution cannot be analysed in the same way, due to the shadowing effects of the RF antennae. Surprisingly, on all limiters analysed, approximately the same surface coverage of impurities on the central part is found, indicating that an equilibrium state exists which establishes itself relatively quickly. On the edges of the limiter, a very large deuterium inventory ($>10^{22}m^{-2}$) was measured, which is attributed to code/position of carbon and deuterium. Similar inventories have been found on samples attached to walls.

Depth profiling of the wall samples, including carbon with two ^{13}C markers at a depth of 28nm and 440nm,

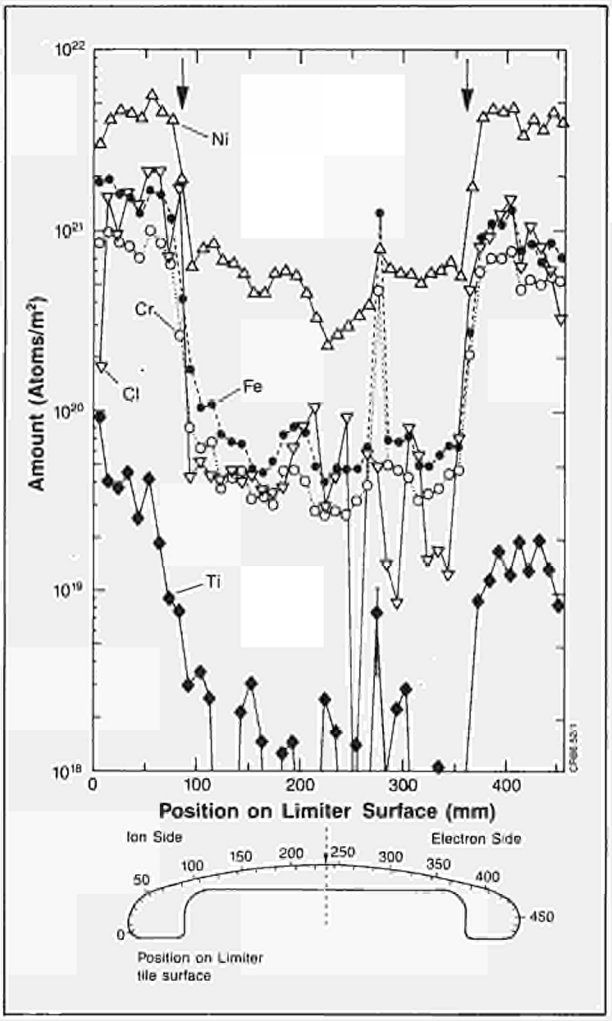

Fig. 37: Concentration of the elements Ni, Cr, Fe, Cl and Ti found at points on the surface of Tile 4 of the limiter in Octant No. 4 in January-June 1985, measured by Proton Induced X-Ray Emission (PIXE). The arrows mark the edges of the region shadowed by the RF antennae

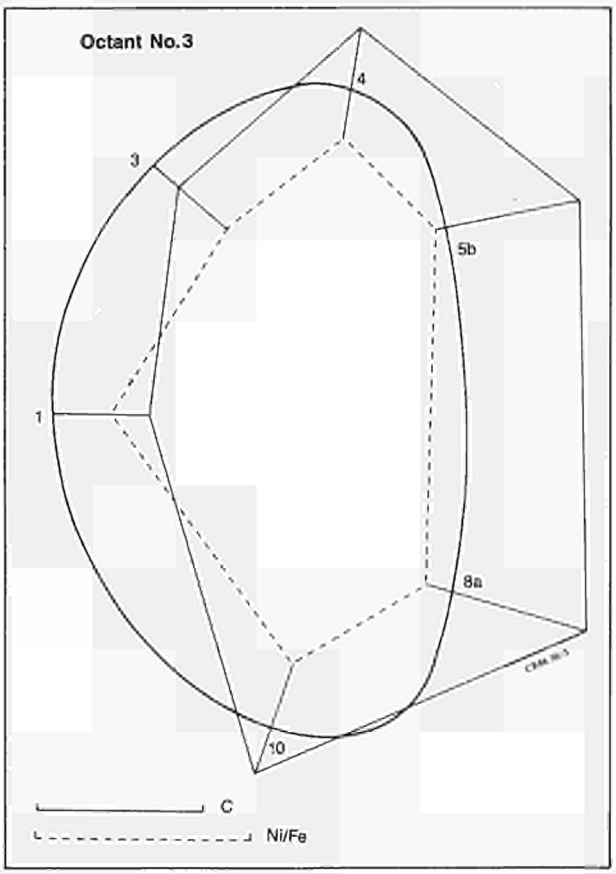

Fig. 38: Diagrammatic representation of the amount of deposition/erosion at six poloidal positions in Octant No. 3, as measured by C^{13} tracer experiments combined with Secondary Ion Mass Spectroscopy (SIMS). The amount of deposition is plotted normal to the vessel wall at each point, distances into the vessel being net deposition, whilst distances out from the vessel represent net erosion/sputtering (carbon and Ni/Fe are on different scales). At point 1, the carbon deposition is $4 \times 10^{18}/cm^2$, whilst Ni/Fe is $2.3 \times 10^{17}/cm^2$

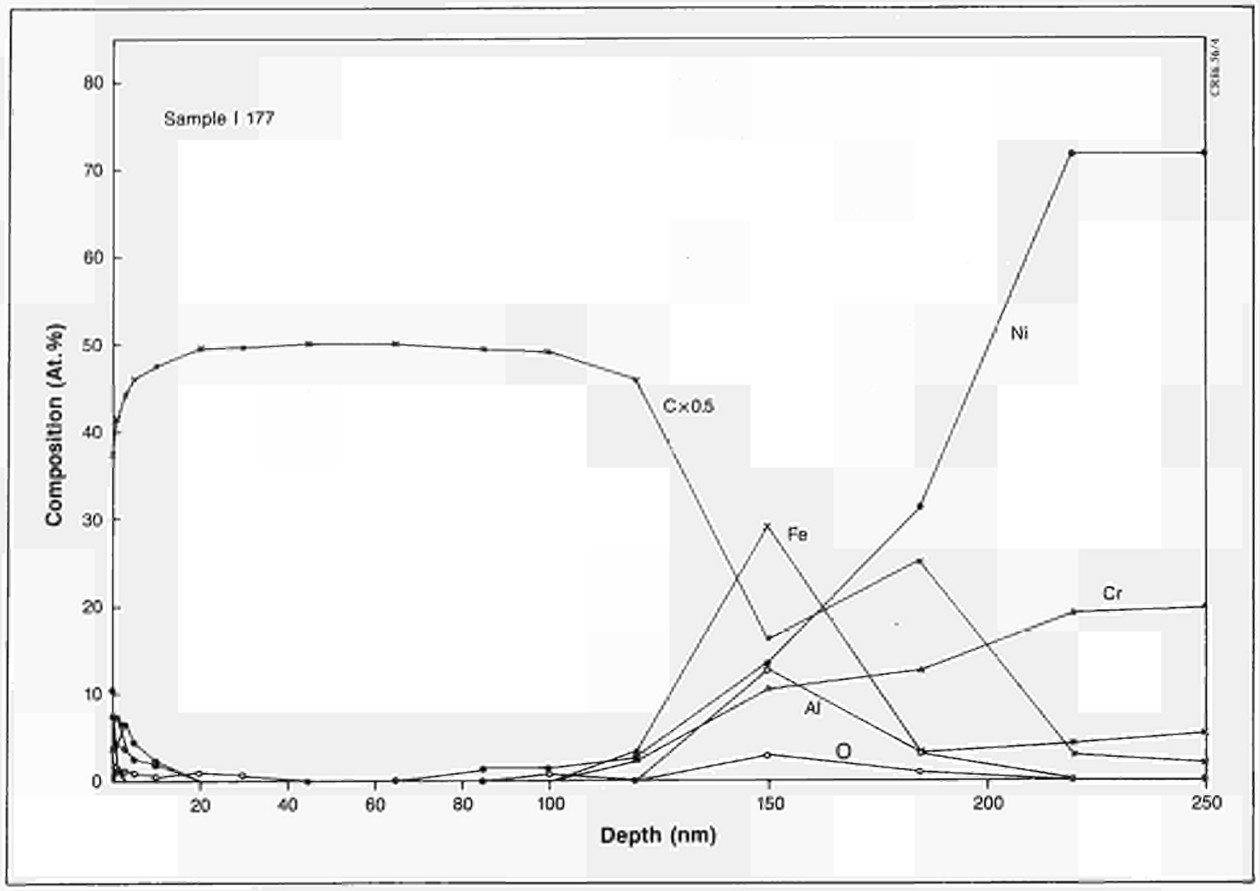

Fig. 39: Depth profile through the surface film on long-term sample I177 obtained by Auger Spectroscopy

have shown that in some areas material is eroded (Fig.38). The outboard wall near he limiters shows a net deposition of carbon ofthese samples (largely from carbonisation). The coverage on the outboard wall shows an "archeological" profile reflecting the major events of the six-month programme, indicating that in this region the wall is protected by the limiter from erosion during tokamak discharges (Fig.39).

Evidence from an incident, in which stainless steel was evaporated, shows the effect of a single disruption. Stainless steel was initially distributed around the torus from the source near the top of Octant No. 5 (according to a r^{-2} law). Direct uniform coverage of some limiters occurred and these were subsequently cleaned by the erosion/redeposition process within a week of operation. Coverage of wall samples still containing the constituents of stainless steel did not seem to effect the plasma purity. However, after removal the limiter placed closest to the source proved to have a higher iron (Fe) content than normal for Inconel.

Measurements using the Langmuir pulse array in the plasma boundary have continued. Results have been obtained over a range of plasma conditions with plasma current from 1.1-3.1MA. Effort has continued to improve the quality of Langmuir probe measurements. Fitting procedures to the current/voltage (I-V) characteristics have been improved and a particular anomaly has been removed from the measured section temperature (T_e) profiles by taking only voltages below the floating potential into account. In addition to the measurements made with the probe drive at the top of the vessel,

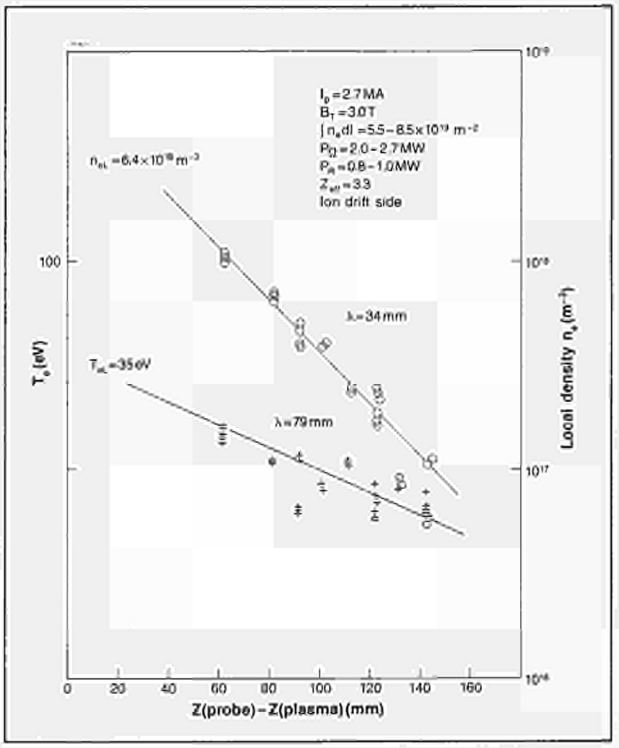

Fig. 40: The profile of the saturation ion current and temperature behind the plasma edge, obtained from Langmuir probe measurements

Langmuir probes have been imbedded in the shielding tiles of RF antennae. Both sets of probes have been used to make measurements during RF heating of the plasma.

In the ohmically heated part of the discharge the profiles and absolute values of density, n_e, temperature, T_e etc, are well understood but during application of RF power measurements on both instruments have shown very rapid variation of parameters, suggesting a direct RF power effect on the measurements. This aspect is still under study. A typical data set for an ohmically heated discharge is shown in Fig.40.

For one consistent set of measurements a model of the scrape-off layer has been used to calculate the impurity influxes from the limiters. The result is shown in Table IX and is compared with the spectroscopically measured fluxes. Using the measured impurity fluxes one can also use a simple analytical edge transport model to obtain the central impurity concentration. For the same typical set using measured edge parameters, good agreement is obtained with the spectroscopic measurements (Table X).

References

[1] J P Coad, 'Analysis of Samples Exposed to Carbonisation in the JET Vessel', JET-IR(85)03.

[2] J P Coad, G M McCracken, S K Erents, J Ehrenberg, L de Kock, P C Stangeby, T Tagle, 'Impurity Fluxes in the Boundary Layer of JET', 12th European Conf. on Controlled Fusion and Plasma Physics, Budapest, Hungary (September 1985). JET-P(85)10.

TABLE IX
Plasma and Edge Parameters from JET Ohmic Discharges September 1984 – June 1985

Discharge Series and Date	I_{plasma}	B_T	$\int n_e dl$	I_S (ion)		T_e (ion)		N_e (ion)		P_d		H_α(LIM) TOTAL D	Langmuir Probe	Z_{eff}	q_s	P_Ω	P_R (Bolometer)	$\delta = \frac{Pd}{I_S \cdot T_e}$	L_c+	$D_\perp$
				I_{SL}	λ_I	T_{eL}	λ_{Te}	*N_{eL}	λ_{Ne}	P_{dL}	λ_{Pd}									
	MA	T	m^{-2} ($\times 10^{20}$)	Am^{-2} ($\times 10^4$)	mm	eV	mm	m^{-3} ($\times 10^{18}$)	mm	MWm^{-2}	mm	Flux to Limiter $10^{21}s^{-1}$	Flux to Limiters $10^{21}s^{-1}$			MW	MW		m	m^2s^{-1}
2978-2982 24.9.84	2.8	(2.5) −3.4	0.7	0.8	40	−30	−100	1.9	50	3	30	4.4-8.2	1.6	5.5-5	3.8 +4.8	2.6	1.6	12.5	27-34	0.55
3044-3052 27.9.84	3.7	3.4	0.9	0.9	53	−25	−160	2.3	63	2		12-14	2.4	4.5-5.5	4.6	3.2	1.3 −2.1		33	0.75
3752-3754 14.2.85	1.1	3.4	0.3	0.6	80	−17	−300	1.9	92	1		18-21	2.4	4.5	−10	0.6 −1.5	0.3 −1.2		77	0.60
3756-3784 15.2.85	2.8-3.1	3.4	0.7	2.0	30	−100	46	3.2	44	5-10	−30	3.9-9.3	3.7	(2.5) −4	5.2 +5.5	2.2	0.9	5 (max)	37-39	0.62
5460-5461 11.6.85	2.7	3.0	(.45) −.65	1.1 −1.6	30	50	60	2.4	40	3-5	27	1.6-1.8	2.0	5.7	5.5 +6.2	2.8 −2.1	1.1	9 (max)	39-44	0.33
5450-5465 (Before RF) 11.6.85	2.7	3.0	(.45) −.65	0.9 −1.0	33	50	55	1.7	47	2.5	28	1.5-2.3	1.6	5.5	5.5 +6.2	2.8 +2.1	1.1	5	39-44	0.46
5395-5421 (Before RF) 7.6.85	2.1	2.0	0.65	0.4	54	−10	−300	1.6	59	0.4		3.1-3.9	1.1	2.7	5.5	1.4	0.8		39	0.34
5366-5382 (Before RF) 6.6.85	2.7	3.0	(.55) −.85	3.0	27	35	79	6.4	34	10		1.7-2.4	4.1	3.3	6-6.5	2.7-2	1.0-0.8		42-45	0.19

* In view of extrapolations and scatter in I_S and T_e, error in N_{eL} must be considered to be ±100%.

\+ Taken as ½ distance along field line between probe and limiter, because of bi-directional flow of plasma to sink.
Power calculated assuming δ = 10

TABLE X
Impurity to Hydrogen Fluxes Measured Spectroscopically

	Ratio of Impurity to Hydrogen Flux at the Limiter (ϕ_I/ϕ_H)	*Ion Energy at Limiter (eV) (for Charge +4)*	*Sputter Yield Ions/Atom*
Carbon	0.08	700	0.35
Oxygen	0.01	700	1.0
Metals	0.02	700	0.2

Instabilities and Disruptive Phenomena

Disruptions

The upper density in JET is limited by disruptions. This density limit is consistent with a model in which radiation losses lead to a strongly magneto-hydrodynamic (MHD) unstable configuration. In JET the operating regime has a density limit given approximately by $n\ (m^{-3}) < 1.2 \times 10^{20}\ B_T(T)/R_o(m)q_c$, where n is the mean electron density, and $q_c = 2AB_T/\mu_o I R_o$, A being the plasma area and I the plasma current. For a given value of plasma current, the highest electron density is achieved on the current fall. Fig.41 shows a plot of such disruption in the normalised density-current (Hugill) diagram.

Prior to density limit disruption, the total radiation power from the plasma increases, reaching a value ~ 100% of the input power at the time of disruption. This radiation comes mainly from the edge of the plasma. The dependence of the radiation on the parameter $n R_o q_c/B_T$ is consistent with theoretical expectations.

The disruptive behaviour is understandable in terms of a model in which the plasma column becomes unstable to contraction, when the power radiated at the edge approaches 100% of the input power. The growth rate of the instability is of order $1/\tau_E$, where τ_E is the energy confinement time. This contraction (after a time ~ 1s), produces a fast disruption. The complete sequence of events, including the MHD instability, has been reproduced in numerical simulations. Figs.42 and 43 show experimental results illustrating the contraction of the radiating layer and the electron temperature profiles during the period involved in the disruption.

The current quench which follows the rapid temperature fall depends upon the ability of the position control circuitry to ramp down the vertical field. If the power amplifier saturates, control is lost and a fast current quench ensues. the timescale is typically 25ms. If the position is controlled, the current quench timescale is typically 10 times longer.

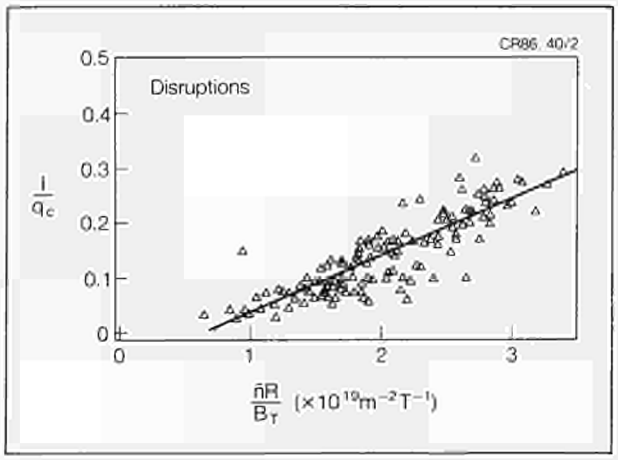

Fig. 41: Disruptions on plot of normalized current (q/q_c) versus normalized density ($\bar{n}R/B_T$)

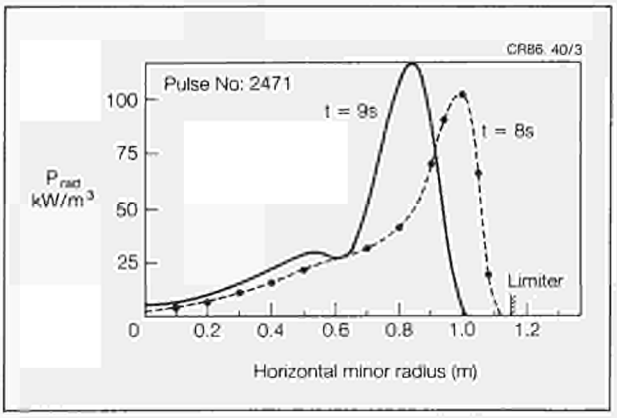

Fig. 42: Plot of radiated power (P_{rad}) versus horizontal minor radius before and during a disruption.

Sawtooth Oscillations

Detailed studies of sawtooth activity in JET have revealed significant differences from previously reported observations, and discrepancies with conventional models of sawtooth behaviour. Compound sawteeth, which display an intermediate collapse during the ramp phase, are observed in most discharges. In contrast to observations on smaller tokamaks, the main collapse usually has no precursor activity, but is often followed by successor oscillations. The collapse time is typically 100μs. This is much shorter than the time predicted by the Kadomtsev reconnection model. A selection of types of sawtooth behaviour is shown in Fig.44, where results for four different values of current are given.

The soft X-ray diagnostic has been extended to provide 100 viewing channels. The signals are used to obtain a tomographic reconstruction of the sawtooth behaviour and, in particular, to give a detailed picture of the emission during the collapse. A set of two-dimensional graphs in the poloidal plane is shown in Fig.45.

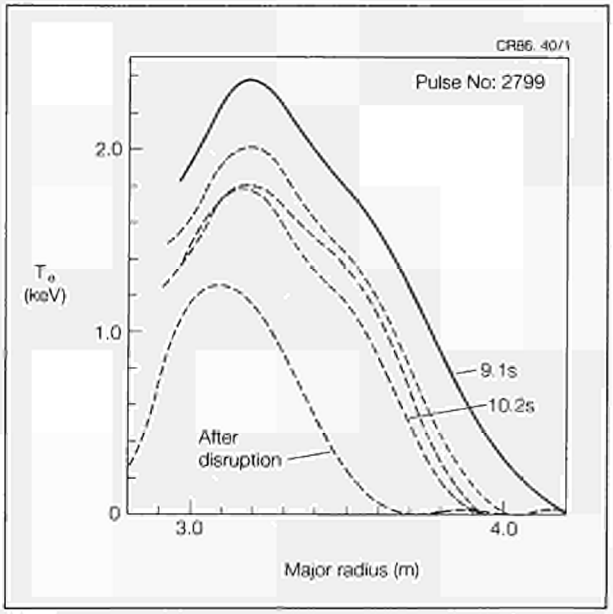

Fig. 43: Plot of electron temperature (T_e) profile illustrating the narrowing of the profile during a disruption

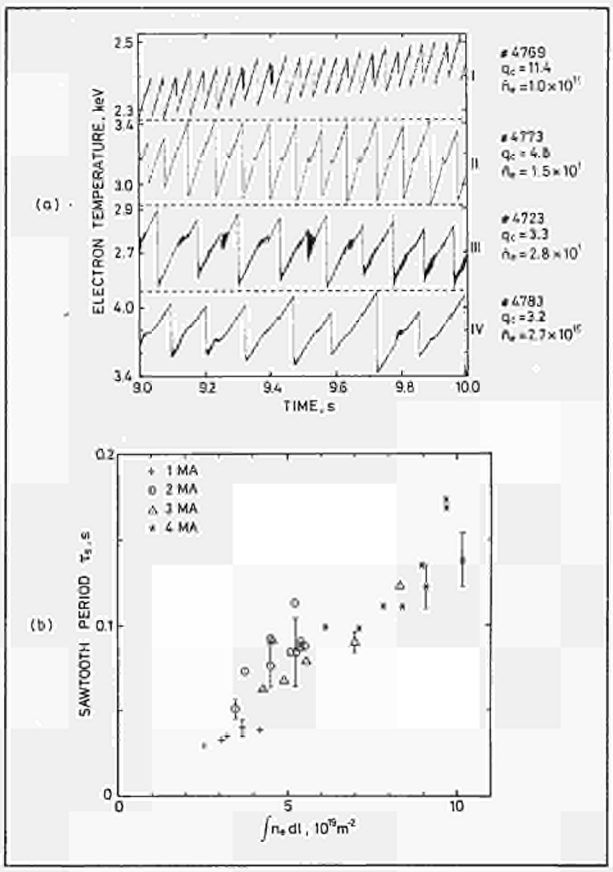

Fig. 44: (a) Plot of types of sawtooth behaviour for four different values of current;
(b) Sawtooth period (τ_s) versus density

Using the clues given by the experimental data the theory of sawteeth has been re-examined. A calculation of the change in q during the ramp phase indicates a change of $\sim 10^{-2}$. It has been shown that is $|1 - q_o| \sim 10^{-2}$ in the central region, the plasma can be unstable to an *ideal* m = 1 mode. This leads to a non-linear quasi-interchange in which the magnetic field is carried with the fluid in a convective motion. This results in the replacement of the hot core by a plasma bubble formed of cooler plasma from an outer region around the q = 1 surface, as shown in Fig.46.

Magnetic Activity

Using pick up coils and saddle loops studies of the MHD activity in JET have identified modes with toroidal mode numbers n = 1 and 2. The observed poloidal variation in phase and amplitude is in qualitative agreement with the theoretical predictions of tearing modes in non-circular toroidal geometry. The n = 2 mode is in some cases triggered at a critical level of the amplitude of the n = 1 mode. Discharges with $q_\psi > 2.3$ can be free from MHD activity. Disruptions are associated with large m = 2, n = 1 perturbations which grow rapidly but involve little n = 2 activity.

The magnetic activity associated with the sawtooth instability has been investigated revealing a fast n = 1, and $2 < m < 5$ magnetic signal at the plasma surface at the time of the sawtooth collapse (Fig.47). Close analysis has shown a growing signal, on a timescale $\sim 100\mu s$, immediately before the collapse. The level of broadband

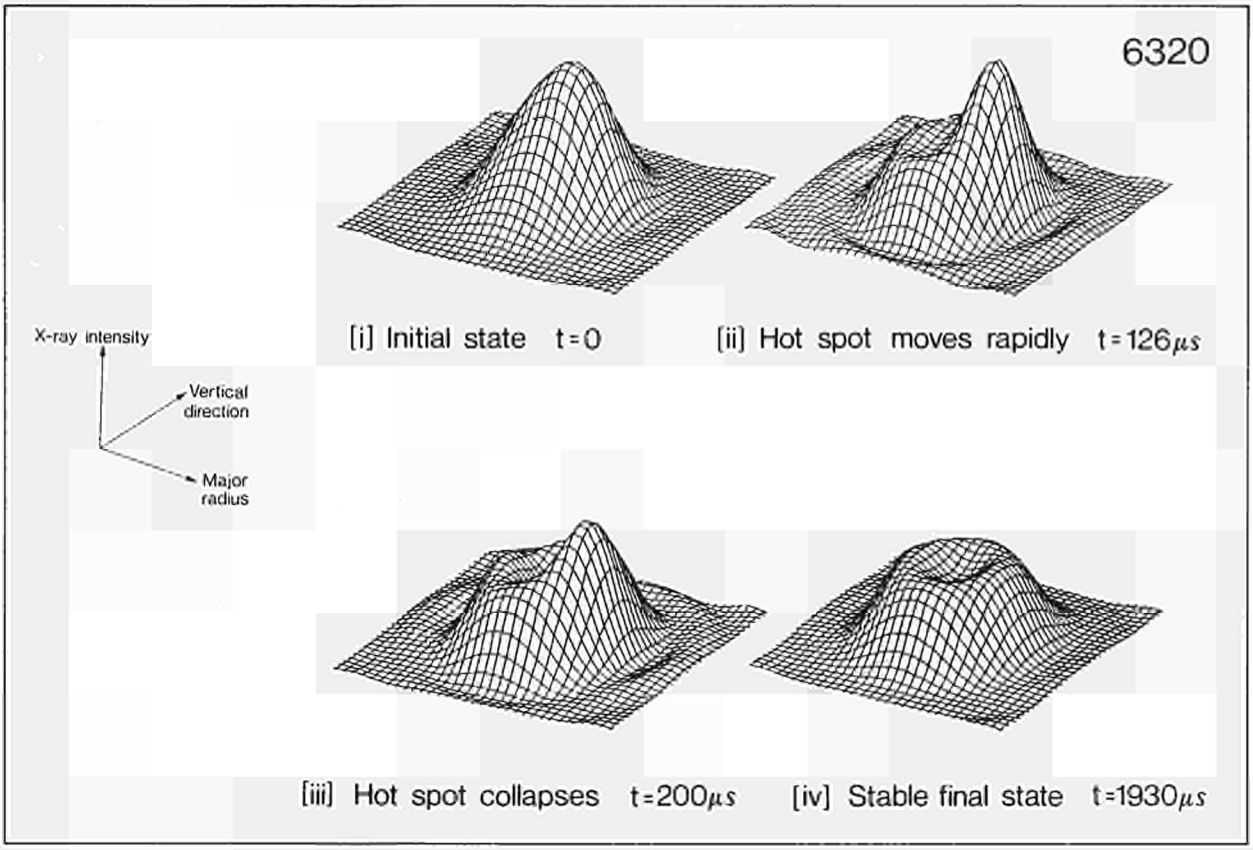

Fig. 45: X-Ray emission during a sawtooth crash (Pulse No: 6320)

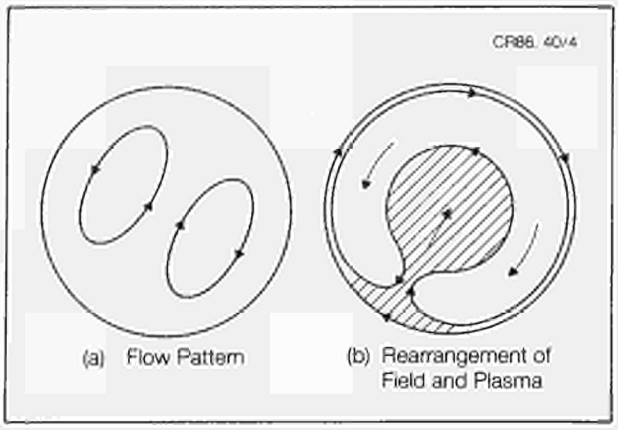

Fig. 46: Illustrating rearrangement of field and plasma

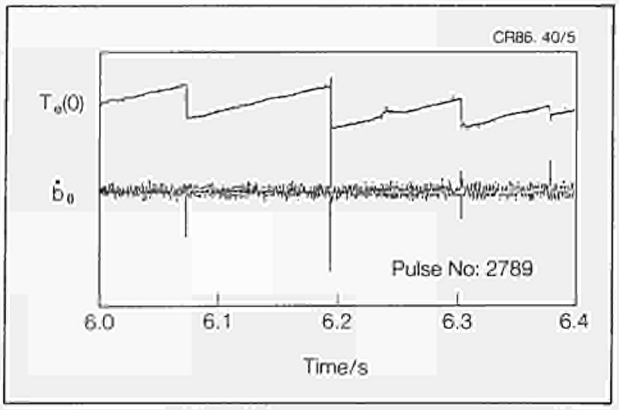

Fig. 47: Magnetic signal at the surface during sawtooth oscillations

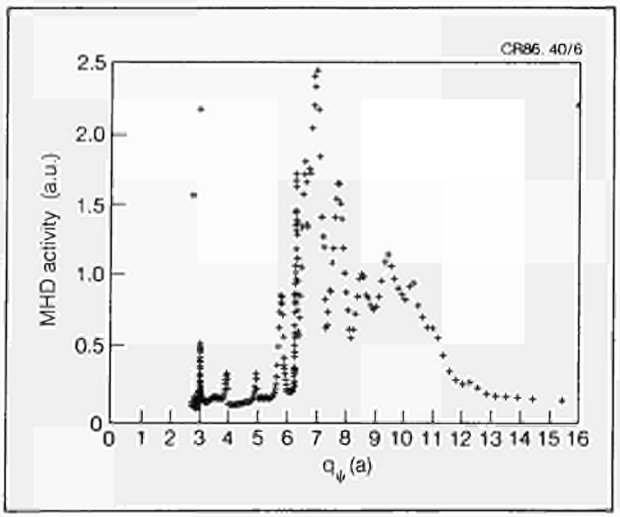

Fig. 48: MHD Activity as a function of $q_\psi(a)$

magnetic fluctuations has also been measured. The observed activity in the range 10 -60kHz shows a $f^{-2\pm0.5}$ frequency dependence with a typical level of a few 10^{-8} $TkHz^{-1/2}$ at 10kHz.

Current Rise

An analysis of the time trajectories in the (q_o, q_a) plane has been started, where q_o and q_a are the values of the safety factor at the centre and edge of the | o aC plasma. This enables an interpretation of the observed behaviour in terms of MHD stability of the plasma. The dependence of this behaviour on the type of current rise is being investigated. Fig.48 gives a graph of the magnetic activity as a function of q_ψ (a) showing clearly bursts of activity around integral values of $q_\psi(a)$.

RF Heating

RF heating operations in JET started in February 1985 with two prototype antennae installed into the torus, each being connected to a 3MW peak powerRF generator. The two antennae located in diametrically opposed octants had a different inner conductor configuration for assessing the effect of exciting shorter wavelengths in the toroidal direction. Initial operations were mostly devoted to test the RF system, to check its power capability with plasma, to measure the coupling resistance of the antennae and to compare the relative merits of the two types of excitation, monopole or quadrupole.

The results have been previously reported [1,2]. Operations resumed in November 1985 after the summer shutdown, and the major change to the RF system was the installation of a third antenna in Octant No.2 close to the existing one.

The major conclusions of this year's operation can be summarized as follows:

(i) In most of the experiments, the wave frequency was adjusted to provide a minority ion resonance layer close to the centre of the discharge. An increase in sawtoothing activity of the plasma was observed, leading to a 2.5keV modulation of the peak electron temperature, reflecting the peaking of the power deposition profile. Fig.49 shows a typical increase in the sawtooth amplitude and period,in response to 5.5MW "on axis" ICRF pulse (where the central electron temperature was measured by the ECE diagnostic). ^{3}He was used as the minority species. The volume averaged electron temperature was increased by a much smaller factor.

Fig.50 shows the evolution of the peak and volume averaged electron temperature versus the ratio of input power to the average density during a scan in plasma current from 2 to 4MA. The magnetic field was 3.4T and the ICRF frequency was 33MHz ensuring on axis heating in this (^{3}He)D plasma. The sensitivity of the electron temperature to the plasma current value was not large, as ohmic points at low density and 2MA are close to RF points at high density and 4MA. A linear fit gives:

$$<n>\Delta<T_e>/\Delta P_{tot} \approx 0.5\times10^{19}keVm^{-3}MW^{-1}$$

(ii) A modulation of the central ion temperature was also observed, but contrary to the electron case, the minimum value at the sawtooth relaxation was significantly above the value without RF. On

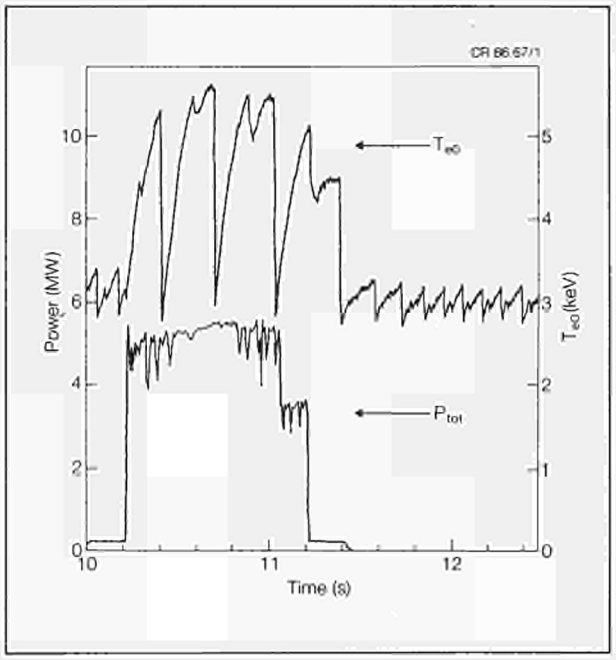

Fig. 49: Peak electron temperature measured by ECE during a 5.5MW ICRF pulse. (Pulse No: 6315: B_T=2.9T; D plasma ^{3}He minority; f=28MHz; I_p=3.5MA; $<n_e>$=2.3 $10^{19}m^{-3}$; $P_\Omega \approx 2.0MW$)

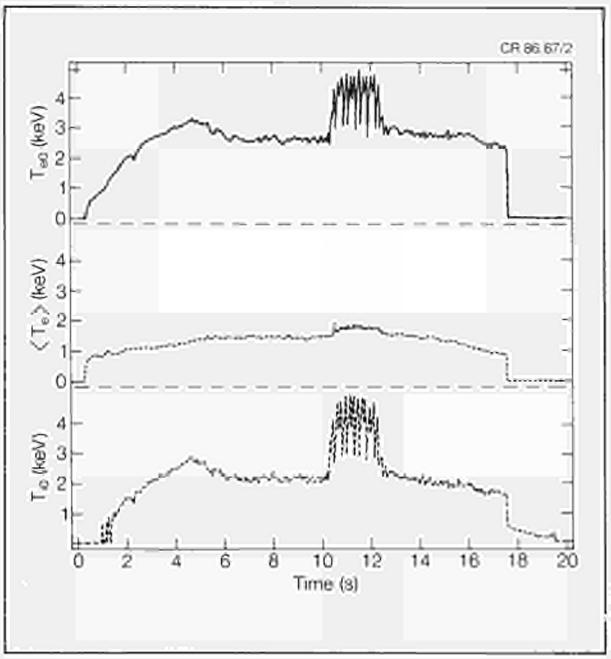

Fig. 51: Time evolution of the peak T_{e0} and volume averaged $<T_e>$ electron temperatures and of the peak ion temperature T_{io}. The 6MW ICRF pulse is applied between t=10.2 and 12.2s (Pulse No. 6322)

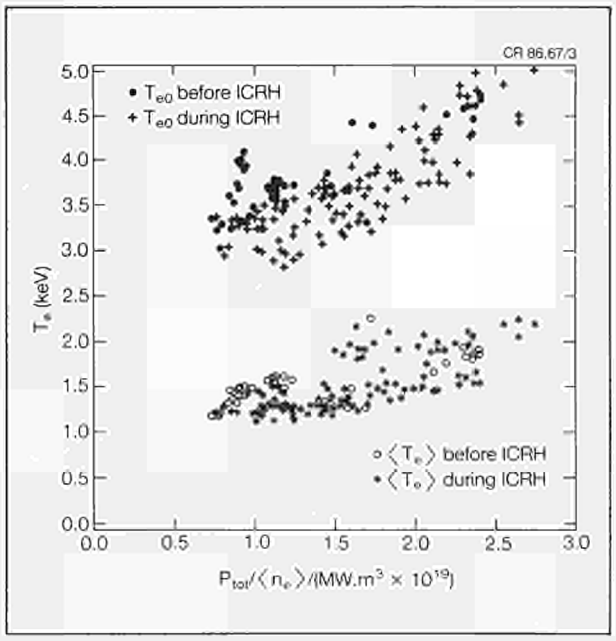

Fig. 50: T_{eo} and $<T_e>$ (measured by ECE) versus $P_{tot}/<n_e>$, where $P_{tot}=P_r+P_{rf}$. (B_T=3.4T; D plasma ^{3}He minority; f=33MHZ; I_p=2−3 and 4MA)

average, the central ion temperature was increased by up to 1.5 − 2keV, bringing ion and electrons to close peak temperatures. This is illustrated in Fig.51 which shows the response of a 3.5MA JET discharge to a 6MW 2s RF square pulse;

(iii) As a consequence of the small increase in the volume average electron temperature, the global energy confinement time decreased despite a significant increase in electron density by up to 30%. The degradation seemed to follow a similar trend to previous ICRF heated Tokamaks, showing a saturation for the highest RF power yet achieved;

(iv) Impurity influx during RF heating has not proved to be a problem in JET. The relative importance of the power radiated by impurities in the power balance and the effective ion charge of the plasma, Z_{eff}, were not significantly increased above ohmic levels. Z_{eff} was nevertheless higher than in ohmic plasmas with the same electron and current densities;

(v) The expected difference in coupling resistance between the various types of antennae excitation was observed. However, the heating efficiency in terms of plasma energy increase per unit of input RF power was similar, at about 0.2 − 0.3MJ/MW. The quadrupole system was shown not to induce sawteeth as large as the monopole/dipole configuration;

(vi) A preliminary comparison between the heating efficiency of ^{3}He and H minority species did not show any significant difference but tended to a larger impurity influx with the latter species.

References

[1] J. Jacquinot et al, Plasma Physics and Controlled Fusion, (1985) 27, No.12A, 1379-1390

[2] J. Jacquinot et al, 12th European Conf. on Controlled Fusion and Plasma Physics (Budapest, Hungary, September 2-6 1985), Plasma Physics and Controlled Fusion, (1986) 28, No.1A, 1-16

Energy Confinement

An extensive series of experiments were carried out on JET during 1985 to characterise the energy confinement properties during ohmic heating (OH). Experiments with ion cyclotron resonance heating (ICRH) were started and by the end of the year, the ICRH power coupled to the plasma exceeded the ohmic input power by a factor of two. A preliminary assessment of the effect of this additional heating on confinement has been obtained.

In the ohmic heating studies, the toroidal field, B_T, the toroidal current, I_p, density and size and shape of the plasma were all varied. The energy confinement time τ_E was found to increase almost linearly with density at low densities and then to saturate at higher densities ($n \sim 2.5 \times 10^{19}\ m^{-3}$). This can be seem clearly in Fig.52, where a few representative density scans are shown in a plot of τ_E versus nqR^2a (neo-Alcator scaling). The saturation in the confinement time at high densities is typical of tokamak behaviour and has been seen in many smaller experiments. The reason for this saturation is not fully clear. The power lost by radiation increases as the critical density is approached, but this is probably due to a change in plasma edge conditions associated with the poor penetration of neutrals at high densities rather than an increase in the accumulation of impurities.

Fig.52 shows that the neo-Alcator scaling $\tau_E \propto nqR^2a$ provides a reasonable description of the JET data set and the best fit line is close to that of the TFTR/PLT data set [1]. A slightly improved fit to the data can be obtained by using regression analysis, which gives the global energy confinement time, τ_E(s), as:

$$\tau_E = 0.013\ B_T^{0.5}\ q^{0.3}\ n^{0.4}\ K^{0.2}\ R^{1.2}\ \epsilon^{1.7}\ A^{0.5}$$

where q is the cylindrical safety factor, K the elongation, R(m) the major radius, $\epsilon = R/a$ the inverse aspect ratio, B(T) is the toroidal field, n(m^{-3}) is the mean density and A is the atomic mass. (The JET data set includes both D and H plasmas).

The local transport properties of these discharges have been analysed by both interpretative and predictive computer codes. The dominant energy loss processes change with minor radius (a), and three distinct regions have been clearly identified; (i) an inner region in which the main energy transport is by field line mixing following sawtooth collapse; (ii) a central region in which electron and ion thermal transport are dominant; and (iii) an edge region in which impurity radiation and other atomic processes dominate.

In the second region, it is found that the main loss route is via electrons. The ion thermal conductivity is between 1 and 5 times neo-classical values, with the higher values occurring at lower densities. The electron thermal conductivity, χ_e, in this region decreases with increasing density, with a coefficient $\chi_e = 1\text{-}2 \times 10^{19}/n(m^2/s)$. So far, no clear dependence on toroidal magnetic field or plasma current has been observed.

An independent measurement of the electron thermal conductivity has been obtained by following the relaxation of the electron temperature profile after the sawtooth collapse using the 12-channel ECE grating polychrometer. Preliminary analysis of the data from this instrument gave a χ_e(HP) $\propto \sqrt{I/n}$ in ohmic discharges and no change was observed during ion cyclotron resonance heating. The parametric dependence is similar to that obtained from transport studies, but numerically χ_e(HP) is a factor 2-5 greater. This discrepancy may be a consequence of the simple diffusion model used in the analysis of the heat pulse propagation. Simulating the evolution of the heat pulse with a full transport code, including sources and sinks, appears to give a smaller discrepancy between the measured and simulated pulse propagation speeds.

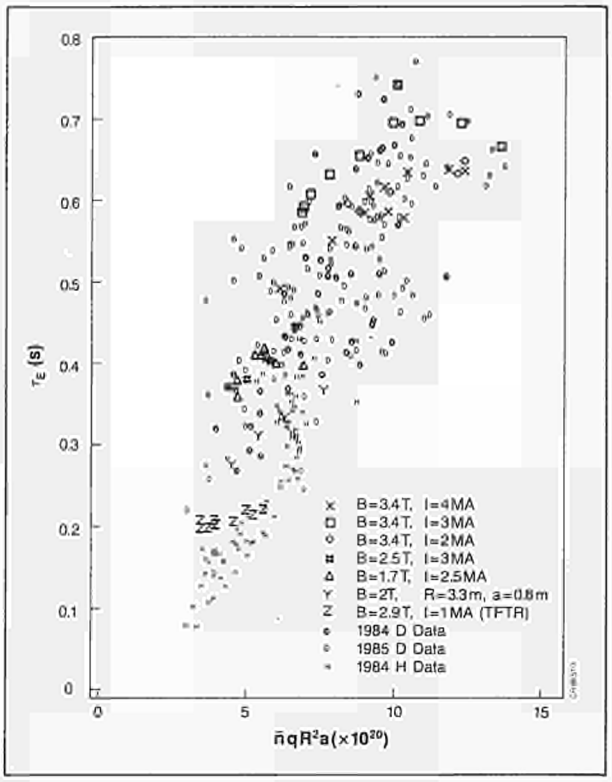

Fig. 52: Plot of global energy confinement time (τ_E) versus $\bar{n}qR^2a$ (new-Alcator scaling).

A preliminary investigation has been undertaken of current and temperature profiles under different conditions in JET. It has been found that both the current and electron temperature profiles appear to be a function only of the safety factor, when the plasma is in steady-state with the current fully diffused. Several different explanations for the invariance of these profiles (profile consistency) have been proposed [2,3].

The addition of ion cyclotron resonance heating (ICRH) shows the classic L-mode behaviour observed in smaller tokamaks, with the confinement time reducing with increasing input power. In Fig. 53, both the total kinetic energy, W, and energy confinement time, τ_E, are shown plotted versus input power, P, for several different conditions of current and toroidal magnetic field. Under all conditions, it is found that the total kinetic energy, W, increases approximately linearly with

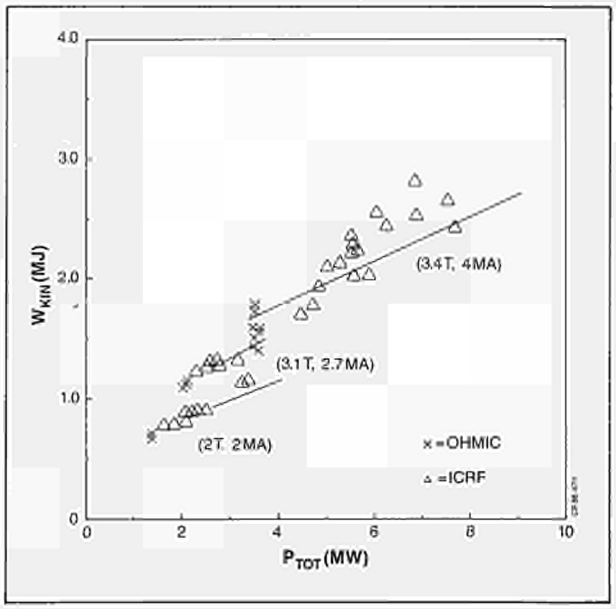

Fig. 53: Plot of total kinetic energy of plasma (W_{KIN}) versus total input power (P_{tot})

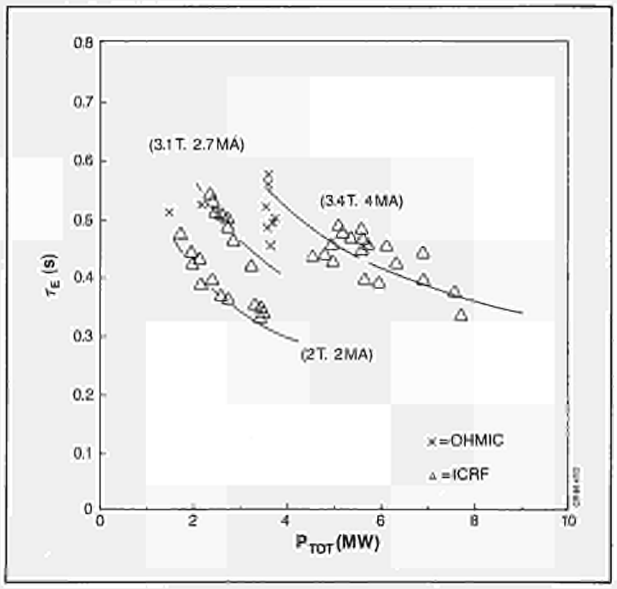

Fig. 54: Global energy confinement time (τ_E) versus total input power (P_{tot})

the additional heating power, and hence, the data in Figs.53 and 54 has been fitted to the forms:

$$W = P_\Omega \tau_\Omega + (P - P_\Omega) \tau_{aux}$$

and

$$\tau_E = (P_\Omega/P)\tau_\Omega + (1-P_\Omega/P)\tau_{aux}$$

where P is the total input power, P_Ω the ohmic input power, τ_Ω is the ohmic heating confinement time, and τ_{aux} is the auxiliary heating confinement time. In smaller experiments, τ_{aux} has been found to be a strong function of toroidal current, I_p. This strong current dependence has not yet been seen in JET, but this may be due to the fact that the range of power used at low currents has been limited.

References

[1] M Murakami. 12th European Conference on Controlled Fusion and Plasma Physics, (Budapest, 1985). To be published in Plasma Physics and Controlled Fusion.

[2] P H Rebut and M Brusati. 12th European Conference on Controlled Fusion and Plasma Physics, (Budapest, 1985). To be published in Plasma Physics and Controlled Fusion, and JET Report JET-P(85)18.

[3] H P Furth, A H Glasser, W Park, P Rutherford, H Selberg, and R B White. 12th European Conference on Controlled Fusion and Plasma Physics (Budapest, 1985). Europhysics Abstracts, *9F* (Part 2), p. 358.

Theory

Theoretical work at JET concentrates on the prediction of JET performance by computer simulation, the interpretation of JET data, and the application of analytic plasma theory to gain an understanding of plasma behaviour in JET. In addition, theoreticians assist in the execution of the JET programme and in making proposals for future experiments, in collaboration with the Experimental Divisions, the Physics Operations Group, and the Machine Development Department.

Interpretation plays a key role in the assessment of plasma performance, and hence in optimisation studies and programme planning. Prediction work continuously checks the measured behaviour against the different computational models, and provides a basis for long term programme planning. A major role of analytic theory is to compare the observed behaviour against that expected from existing analysis, and to modify the latter when there is divergence. However, effort within JET on analytic theory has been limited, in the expectation that theorists within the Associations would provide support, by extended visits and by work done under Article 14 Contracts. Valuable assistance has been provided over the past year.

A central task has been to provide a quantitative model of tokamak plasmas, with particular attention to JET behaviour. The ultimate objective is to include in this model all the important effects observed in JET and other tokamaks. Although it is preferable to understand each effect theoretically, in some cases it may be necessary to rely on an empirical description.

Activities during 1985 can be sub-divided under the following headings:

(a) Data Banks (and computing hardware);
(b) Data Management Software;
(c) Code Libraries (Interpretation and Prediction);
(d) Data Interpretation;
(e) Modelling of JET Plasmas;
(f) Comparisons of Model Results and Measurements;

(g) Predictive Computations;
(h) Analytic Plasma Theory.

These activities are described in further detail in Appendix I, which summarizes the work of Theory Division in JET.

Summary of JET Results

During the year, there has been steady progress in improving the plasma operating conditions. Discharges with the full design value of the toroidal field, B_T = 3.4T, with plasma currents up to 4MA for flat top times as long as 10s, and with elongations up to b/a ~ 1.65 have become routine. The maximum design value of plasma current was reached in a discharge with I_p = 5MA, b/a = 1.4 and safety factors q_{cyl} ~2.25 and q_ψ ~3.25.

Impurities

Prior to 1985 operation, the inner wall of the vacuum vessel on the small major radius side of the plasma was covered with carbon tiles to a height of ±1m above and below the mid-plane. Four carbon limiters (0.8 x 0.4m) were symmetrically located around the outer major radius of the plasma. In addition, four nickel limiters of similar dimensions remained in the torus but were always retracted behind the carbon limiters. Two ICRH antennae were located in similar positions, but at slightly larger major radii. The antennae had nickel screens and were surrounded by protective tiles, which also acted as limiters. The torus vacuum vessel was routinely carbonised by glow discharge cleaning in deuterium, with the addition of hydrogenated methane.

The main impurities observed and their typical ranges of concentrations (as percentages of the electron density) were: Carbon 2 − 4%; Oxygen 1 − 2%; Chlorine 0.05 − 0.15%; and metals (Ni, Fe, Cr) 0.001 − 0.3%. Carbon was the main light impurity, which entered the plasma both from the walls and the limiter, as did the oxygen. Nickel was the main metallic impurity and the main route into the plasma appeared to be via the carbon limiters, which when analysed by surface techniques after their removal from the torus were found to be heavily contaminated with metals. The nickel and chromium usually appeared to be in approximately the ratio expected for inconel indicating that the vessel walls were the original source. However, recent spectroscopic evidence clearly showed that nickel was released from the antennae screens during ICRH.

The typical range of Z_{eff} was between 3 and 8 and appeared to increase nearly linearly with the ratio of mean current density to mean electron density. Thus, Z_{eff} was not significantly changed by carbonisation or by ICRH at the power levels used. A serious effect of impurities in JET is the substantial depletion of hydrogenic ions. Values of n_d/n_e ~ 0.5 have been measured by comparing the total neutron yield with the ion temperature measured by a neutron spectrometer.

The ratio of total radiated power to total ohmic input was in the range 40-60%. Similar values, were found with ICRH, and P_{RAD}/P_{OH} did not appear to change significantly over the range of coupled powers.

ICRF Heating

First results were obtained with ICRF additional heating at coupled powers up to 5MW, using H and ^{3}He minority species in D plasmas. The main emphasis was to commissioning the RF heating systems with plasma and to compare with the coupling efficiencies of different antenna configurations. Initial heating studies showed that the power deposition was well localised close to the resonant surface. The maximum RF power coupled to the plasma was about 5MW for a 2s pulse corresponding to a ratio of P_{RF}/P_{OH} of ~ 2.5. The maximum stored plasma energy was ~3MJ with central electron and ion temperatures of ~5keV and ~4keV, respectively. The global energy confinement time with ICRH was in the range 0.35 to 0.45s compared to a value with ohmic heating alone of ~0.55s, for the same plasma conditions. There were clear indications that the confinement degraded with increasing additional heating, but the range of JET data obtained did not allow a clear determination between L mode scaling with $\tau_E = 0.34(I_p/P_t)^{1/2}B_T^{1/2}$ whereby the confinement would continuously decrease as the inverse square root of the total power $P_t = P_{OH} + P_{RF}$, or a saturated mode $\tau_E = ((0.3/P_t)+0.1)I_p^{1/2}B_T^{1/4}$, where the confinement would saturate with increasing power.

Instabilities

In common with most other tokamaks, sawtooth oscillations of the temperature and density in the core of the discharge are observed in JET. The sawteeth are strongly influenced by RF heating when the resonance zone is inside the q=1 surface. In particular, the amplitude of the sawteeth is increased so that for P_{RF} ~3MW, ΔT_e ~ 1.5keV with a peak value of $T_e(0)$ of about 4keV.

In relatively high q, low current (I_p<2MA), low density (n_e<2x10^{19}m^{-3}) discharges and during the current rise phase (typically the first 5s) of low q, high current discharges, small amplitude sawteeth ($\Delta T_e/T_e$ ~ 2%) are usually seen. Their characteristics are similar to sawteeth studied extensively in other tokamaks.

However, in low q, high current (I_p<2MA) discharges, the characteristics of the sawteeth change markedly during the current 'flat-top' equilibrium phase. The electron temperature profiles become broader and, in ohmic discharges, there is little temperature peaking on axis before the sawtooth collapse. Typical characteristics of these so called 'compound' sawteeth are that the temperature and density rise linearly but reach much higher values before the sawtooth collapses ($\Delta T_e/T_e$ ~ 10-15% and $\Delta n_e/n_e$ ~ 5%, in ohmic plasmas). During this linear rise phase, there can be one or more partial collapses, which affect only the outer zone of the plasma core and do not penetrate to the axis.

With the addition of ICRF heating, the basic characteristics of the compound sawteeth remain unchanged, but their amplitudes increase substantially, so that $\Delta\ddot{a}T_e/T_e \sim 30\%$ for $P_F \sim 3MW$. Under these conditions the temperature profile peaks on axis before the collapse. The period of the sawteeth also appears to be extended by the RF heating with indications that the period depends on the mode of the launching antenna.

Energy Confinement Scaling

The study of the scaling of the global energy confinement time τ_E with plasma parameters in ohmically heated discharges has been extended over a wide range of plasma parameters in a systematic way. In particular, the full range of plasma dimensions and elongations permitted by the JET vacuum vessel has been explored. This has included full-bore discharges with elongations up to 1.65 and circular discharges limited on the outer limiters ($R_o = 2.5m$, $a = 0.8m$), closely simulating TFTR discharges.

The study of energy confinement scaling in ohmically heated plasmas has shown a dependence of the confinement time τ_E on plasma density and safety factor which is weaker in JET than in smaller tokamaks, and there is clear evidence of saturation in the density dependence at higher densities. A strong dependence of energy confinement time on plasma dimensions was seen with $\tau_E \sim R^{1.7} a^{1.3}$. The best value of global energy confinement time in an ohmically heated discharge was $\sim 0.8s$. Deuterium plasmas were used throughout the period.

The best value of the Lawson product $n_i T_i \tau_E$ was $\sim 6 \times 10^{19} m^{-3} keVs$ where the effect of ion depletion ($\sim 50\%$) has been included in the central deuteron ion density.

Magnetic Separatrix Experiments

The goal of increasing the quality of confinement in tokamaks has lead to a renewed interest in the "divertor" and "magnetic limiter" configurations in which the plasma boundary is defined by a magnetic separatrix, detached from the material limiter and the vacuum vessel.

The formation of a magnetic separatrix has been shown to be possible in JET. In a preliminary experiment, the separatrix configuration has been established and maintained for several seconds in discharges with plasma currents of 1.5 and 2.0MA. The toroidal field was 2.6T and the line average density was $\sim 1.0 \times 10^{19} m^{-3}$. The presence of two null points in the poloidal field some 10-15cm inside the vacuum vessel and the plasma well detached from the limiter and inner vessel wall was demonstrated. This is confirmed by the absence of the H_∞ emission from these surfaces at the time of separatrix formation. The area of intersection of the plasma at the separatrix points with the vacuum vessel wall was observed on an infra-red camera, and the change in field line connection length was observed with a Langmuir probe. There was insufficient time in these preliminary experiments for an extensive exploration of the plasma properties of this configuration, but preliminary data suggest that impurity concentrations and energy confinement were comparable to discharges with a limiter.

Developments and Future Plans

Analysis of the results so far obtained on JET, in some respects indicate performance exceeding expectations (e.g. plasma temperatures and confinement during ohmic heating). However, the results also show that further improvements/modifications of the machine may be necessary in addition to those already planned as part of the JET development programme, so that ultimate machine performance may be brought into the region where significant α-heating is evident. The limitations encountered on many Tokamaks are mainly concerned with density limits and control, with plasma MHD behaviour, with impurities and with plasma transport. In particular, confinement degradation with additional heating calls for modes of operation where the plasma current density and the electron temperature are decoupled.

The design concept of JET allows a high degree of flexibility for modifications and improvements, without affecting the basic structure of the machine. Thus, limited additional resources and time should be required to introduce them. However, implementation of such enhancements may require some re-appraisal of the original development plan shown in previous Annual and Progress Reports.

The following sections describe various developments which are being considered for JET to overcome these limitations, and these are summarised in Table XI.

Separatrix Experiments

Both in JET and in other Tokamaks with additional heating, a degradation of confinement time, τ_E, with increasing total power (P_{tot}) has been observed ($\tau_E \propto P_{tot}^{-1/2}$). Subsequently, a good confinement regime with additionally heated plasma has been observed in a number of tokamaks with magnetic limiters or divertors. In this so called H-mode of operation, the confinement time is typically 2-3 times greater than the degraded case.

A space effective divertor-like magnetic field configuration is that in which a magnetic separatrix (or X-point) is located inside the vessel wall, removing the effective outer flux surface away from the limiter. The configuration of poloidal field coils on JET allows the formation of a separatrix with two stagnation (or X) points, at the top and bottom of the vessel, or a single null situation. Experiments with ohmic heating only have been carried out to demonstrate this mode of operation

TABLE XI
Experimental Phenomena, Limitations and Possible Remedies

	Phenomenon	*Limitations*	*Possible Remedies*
(a)	Disruptions	i) Density Limits ii) High Forces and Heat Fluxes on the Vessel	i) Additional Heating ii) Pellet Injection iii) Pumping Panels iv) Strengthen Vessel
(b)	Sawtooth Oscillations	i) Electron (T_e) and Ion (T_i) Temperature Limitations ii) τ_E Limitations	i) Feedback Stabilization ii) Profile Control (LCRH and ICRF) and Current Drive
(c)	Impurities	i) Large P_{rad} (lowers τ_E) ii) Reduced n_i iii) Reduced Density Limit	i) Low-Z (C or Be) walls and Limiters ii) Pellet Injection
(d)	Confinement Degradation (Additional Heating)	i) Reduces τ_E ($\propto P_{tot}^{-1/2}$)	i) Magnetic Limiter (Separatrix) coupled with Dump Plates (Pumping Panels)
(e)	β Limits	i) $\beta(\max)\% = gI_p/B_T(T)a(m)$	i) Increase Current ($I_p \approx 7MA$)

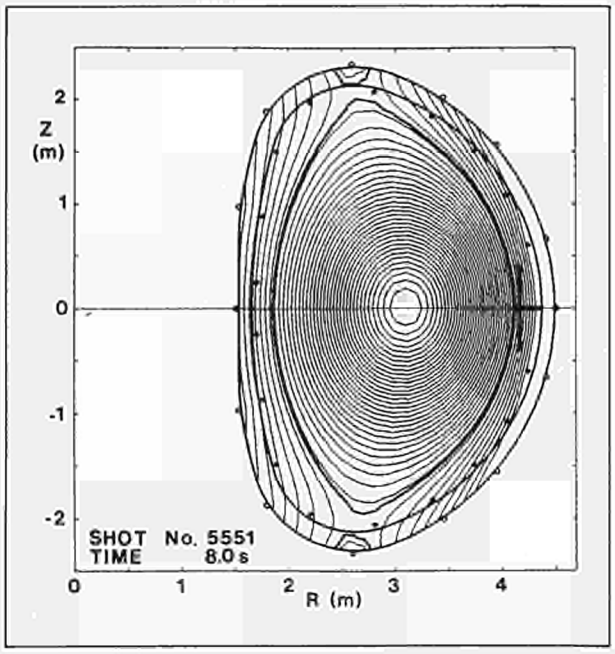

Fig. 55: Poloidal flux contours with plasma current ~1.5MA, poloidal beta ~0.26, internal inductance ~1.29, and plasma elongation ~1.75

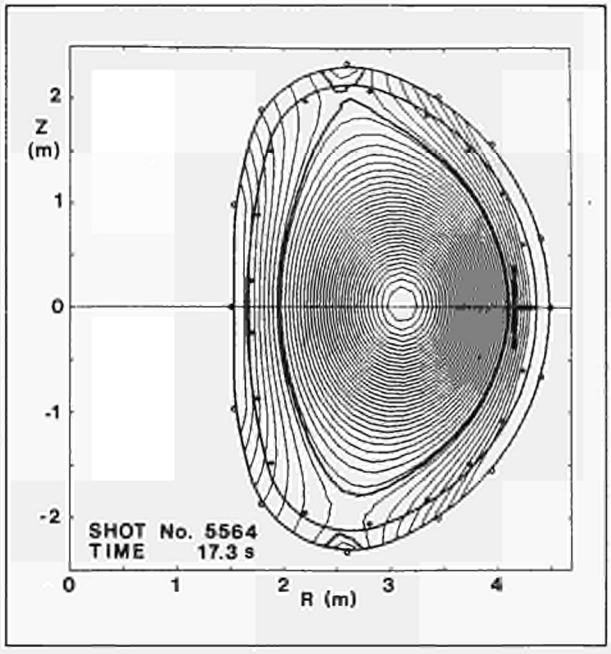

Fig. 56: Poloidal flux contours with plasma current 2.0MA, poloidal beta ~0.09, internal inductance ~1.4 and plasma elongation ~1.8

and to study a number of technical questions relating to the up-down stability and heat loads on the vessel.

The separatrix configuration has been maintained for several seconds in JET discharges with plasma currents of 1.5MA and 2.0MA. The value of the toroidal field was 2.6T, and the line average density was about $10^{19}m^{-3}$. A plot of the poloidal flux contours at 1.5MA is shown in Fig.55.

The separatrix configuration for discharges at 2.0MA plasma current was obtained during the final five seconds of a 20s tokamak discharge. The poloidal flux plot is shown in Fig.56, for this case. The presence of the two null points located approximately 10-15cm inside the vessel is apparent. The plasma was well detached from both the limiter and the inner vessel. This was also confirmed by the absence of H_α emission from these surfaces. Measurements of radiated power were obtained from a multi-channel array bolometer camera. The signals along the viewing lines pointing to the regions of the X-point were up to ten times larger than the average. The generalised Abel inversion of the radial profile (excluding the channels affected by the enhanced radiation around the X-points) showed that, for the 1.5MA discharges, most of the radiated power came from the outer regions of the plasma. The total radiated power could be described as the sum of the power which is radiated by the whole volume of the plasma (= 0.45MW) and the power which is radiated in the regions of the X points (= 0.25MW). The total ohmic input power was 1.78MW.

A preliminary analysis of the spectral lines of the impurities showed that the nickel content of the discharge was very low and well below 0.1%, whilst the concentration of oxygen and carbon was about 1%. Further details have been reported [1].

During 1986, experiments will be extended to 2-2.5MA with limited additional heating power, in order to obtain a more direct comparison of performance between limiter and magnetic separatrix configurations in JET. Further, the potential for modifications will be examined to permit future use of the configuration at currents greater than 4MA, with full additional heating.

Control of Sawteeth Oscillations

In common with most other tomamaks, sawtooth oscillations of temperature and density are observed in the discharge core, where $q < 1$, although there are some important differences in JET. Sawteeth are strongly influenced by RF heating (see Fig.57) when the resonance heating zone is inside the $q \approx 1$ surface. In particular, the amplitude of the sawteeth is increased so that for $P_{RF} \sim 3MW$, $\Delta T_e \sim 1.5keV$ with the peak value of $T_e(0)$ reaching about 4keV. In typical discharges, the change in the plasma kinetic energy associated with the sawteeth inside the $q = 1$ surface can be relatively large (≈ 20 - 40%), although the corresponding change in the total plasma kinetic energy is smaller ($\sim$ 12 - 24%). Whilst sawteeth have a relatively small effect on the global energy confinement time τ_E, they could have a larger effect on the fusion yield which is more strongly weighted to the core of the discharge.

The principal aim of controlling sawteeth is to avoid the periodic loss of confinement from the plasma core associated with the sawtooth collapse. There may also be some gains in stability against the m = 2 mode by

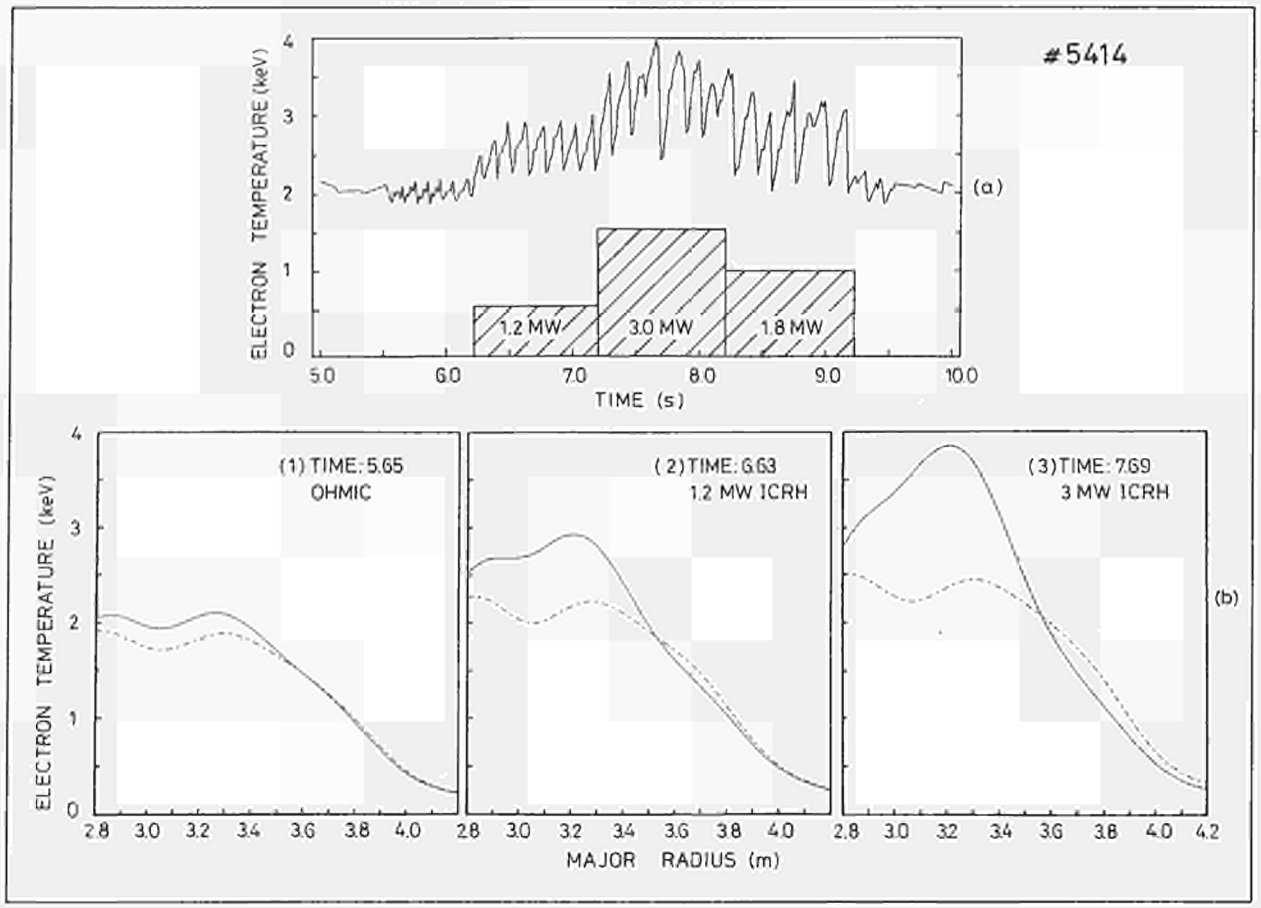

Fig. 57: Electron Temperature (T_e) as a function of time, showing the effect of RF power input on the sawtooth oscillations. The effect on maximum and minimum temperature as a function of radius is shown at times t=5.65s, 6.63s and 7.69s. (Pulse No: 544)

allowing more peaked profiles of current density. The main objective is to freeze the temperature and density profiles close to or exceeding the most peaked profiles which would normally be reached just before the collapse. There would be little point in suppressing sawteeth if the resulting profiles were close to the flat profiles characteristic of those after the collapse.

A number of schemes have been proposed to stabilise sawteeth and some have been tested experimentally in other devices. The possibility of controlling sawteeth by feedback methods has been considered, whereby heating or current drive would be localised within the island generated by the non-linear growth of the m = 1 resistive mode. In principle, feedback stabilisation might be possible but it would be expected to be difficult due to the proximity of ideal instability. This results in an unfavourable scaling of the required current drive or localised heating with plasma conductivity, and for high temperature plasmas control appears to be impossible unless the conditions for ideal stability are also satisfied. Shaping of the plasma cross-section (ie. triangularity) does not appear to be sufficiently effective, but introducing high energy weakly trapped particles inside the $q < 1$ surfaces might provide sufficient ideal stability by localising pressure in regions of favourable curvature, but this has not been tested experimentally.

A difficulty of considering feedback as a technique for stabilising sawteeth in JET is the apparent absence of any precursor to the sawtooth collapse. The collapse is seen to take place spontaneously without any associated precursor activity and, therefore, it is difficult to see how a conventional feedback technique could be applied. A few sawteeth without precursors have been examined for evidence of locked modes using the X-ray diode camera diagnostics and no indication of any locked modes has been found. It is difficult to state categorically that locked modes do not exist, but present evidence strongly suggests that there are no locked modes in JET. However, further detailed measurements are in progress to confirm this.

Growing modes, with m = 1, n = 1 localised around the annulus where $q \sim 1$, are seen in JET at the partial collapse of sawteeth, but the resulting disturbance is usually confined to an annular region and does not propagate to the plasma centre. Since it seems that with compound sawteeth, the partial collapse heralded by a precursor may postpone the full collapse, it is worth considering if the sawtooth period could be extended by inducing additional partial collapses.

There is a need to continue studies of sawteeth to obtain a better understanding of the mechanisms involved, so that firmer proposals for control can be made. The effects

of RF and NB heating require detailed study, particularly to understand the effects on sawteeth amplitude and period with a view to possibly increasing the sawtooth period by controlled localised power deposition. Only a modest extension of the sawtooth period would exceed the global energy confinement time. These possibilities need more detailed evaluation before firm proposals on control methods can be made.

Profile Control

Investigations of the possibility of controlling the plasma current profile in JET started in the second half of 1985. Analysis work at JET was supported by work carried out under Task Agreements and Article 14 Contracts with several Associations (EUR-CEA, EUR-IPP, EUR-FOM, EUR-UKAEA, EUR-ERM/KMS). The approach adopted was to address the question at two levels; the possibility of profile control with existing equipment (NBI, ICRF); and, alternatively, the possibility offered by the procurement of new systems such as those at Lower Hybrid and Electron Cyclotron frequencies.

Experimental results obtained on other Tokamaks as well as with JET during the rise of the plasma current suggested that profile control would allow the JET plasma to be operated in new regimes characterized by:

- The suppression of the large internal instabilities ("sawteeth"), resulting in high central temperatures. This possibility has been demonstrated in quasi-stationary conditions with several Tokamaks using Lower Hybrid waves. It has also been demonstrated on JET (Fig.58) during the initial transient phase when a broad current profile is maintained due to the slow inward diffusion caused by the skin effect;
- Improved or maintained energy confinement properties; in particular, at low or moderate densities.

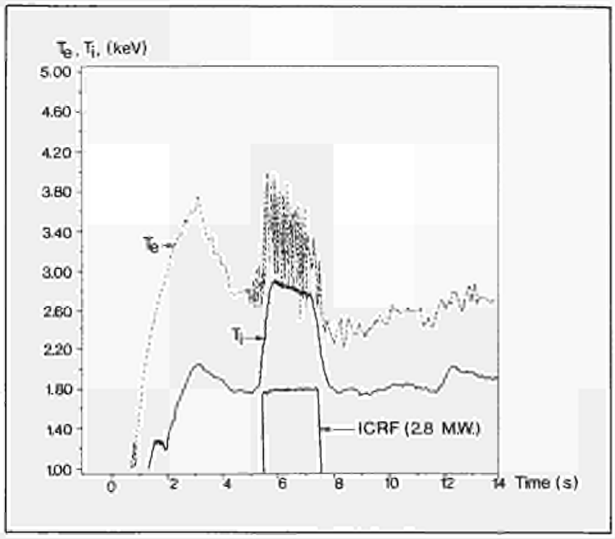

Fig. 58: Evolution of the electron and ion temperatures (T_e and T_i respectively) during a typical JET discharge ($I_p = 2MA$, $B_T = 2.6T$). The largest value of T_e is always observed at the end of the current ramp up (~3s), before internal instabilities start. These instabilities can be clearly seen at times between 5 and 8s, when a high sampling rate of measurements is used. These instabilities prevent the attainment of high values of electron temperature when additional heating is used

These favourable properties are related to the fundamental aspect that non-inductive current drive allows decoupling of the plasma current density (J) from the electron temperature (T_e), which, in inductive current drive are strictly related by the Ohm's law, $J \propto T_e^{3/2}$. Other favourable effects can be expected from profile control (see Table XII). These concern the stabilisation of other instabilities (m = 2) occurring in the outer region, which limit the plasma density. Current drive also helps to decrease the Volt-second consumption, allowing extension of the plasma duration at full performance.

Preliminary analysis shows that the most efficient and proven method to achieve desired profile control would

TABLE XII
Motivations for Non-Inductive Current Drive and Suprathermal Electron Production

	Motivations	*Means*	*Expected Effects*
(a)	Remove the $J \propto T_e^{3/2}$ relation	Current drive in the temperature gradient	Improved confinement
(b)	Suppress sawteeth oscillations	Maintain $q > 1$	– Higher $T_e(0)$, $T_i(0)$ – Improved Q (Fusion output)
(c)	Stabilize sawteeth or m = 2 instabilities	Suprathermal electrons in $q = \approx 1$ or $q = \approx 2$ regions	Higher $T_e(0)$ and higher $n_e(0)$
(d)	Decrease the Volt-second consumption	Current drive	Longer pulses at high current

be to combine the use of Neutral Beam Injection (NBI) and ICRF to drive a reverse current in the inner part of the plasma and to use Lower Hybrid waves driving a forward current, localized in the outer part of the plasma. It is estimated that the stabilisation of internal instabilities would require control of 30% of the Tokamak current (at 5MA). This strategy requires the procurement of a 10MW Lower Hybrid system working at high frequency (~4GHz) with a high degree of flexibility in the choice of the wave radiation patterns.

Multi-Pellet Injection for Fuelling/Re-Fuelling

In recent years, the injection of solid hydrogen or deuterium pellets into tokamak discharges have led to a number of interesting features which may well prove advantageous on the route towards ignited fusion plasmas. Among these features are: peaked density profiles with peak values higher than otherwise attainable, and with longer decay times; some have shown increased energy confinement times; and some featured impurity flushing of the plasma centre effective even beyond dilution. The pellet ablation models now provide a sufficiently reliable guide for extrapolation and have shown that the effects of hot ions from additional heating on ablation can only be minor.

Although results are not fully understood, JET decided to employ this method for fuelling/re-fuelling with a central or deep particle deposition (beyond the recycling layer but also beyond or close to certain q-surfaces of MHD importance) so that a further method would be available to provide density control, which was not connected to recycling and additional heating features. Ablation code calculations suggest that the lifetime of a pellet in an homogemeous plasma is roughly proportional to $d^{1.7}$ and T_e^{-2}, where d is the pellet diameter, and that it is only very weakly dependent on electron density. These calculations further reveal that for the various phases of plasma build-up during a pulse, 2.5 – 6mm pellets, suitably fired when required, are of interest (the latter size leads to an immediate increase in density of $\sim 6.7 \times 10^{19} m^{-3}$). For the expected high plasma temperatures, pellet velocities are required as high as conceivable (ie. > $10 kms^{-1}$, to obtain sufficient penetration if central deposition turns out to be important). Requirements on the repetition frequency must be guided by results of particle confinement times and reheating requirements (to heat ~4mm pellet to ~5keV requires about 7MJ) and are about $1 s^{-1}$.

Since present pneumatic gun technology fulfils all these requirements except high velocity features (<$1.6 kms^{-1}$ at present), JET decided on a stepwise strategy to achieve a full range pellet injection capability:

(a) To undertake joint collaboration with the USDoE (starting in 1987), to investigate pellet injection physics on JET. USDoE (Oak Ridge National Laboratory) should provide a triple-barrel repetitive launcher (2.6, 4, and 6mm diameter pellets with velocities around $1.5 kms^{-1}$ and repetition frequencies of several s^{-1}). JET should provide various interfaces, of which the largest would be the vacuum interface to the torus providing the necessary differential pumping and for which JET would employ another neutral injector box (NIB) and cryopump system. This choice is compatible with later extension to high pellet velocity and allows considerable savings in manpower and time for design and procurement since these components are already designed with regard to tritium and remote handling compatibility and experience in manufacture exists. The Agreement is now being finalised. However, work has started at JET on long lead items (ie. pellet injector box and cryosystem have been ordered);

(b) To set up a development programme designed to develop gun technology enabling a reliable high-speed gun of similar performance, available in 1989.

By the end of 1985, a Pellet Injection Group was established in the newly formed First Wall Division to cover these two tasks.

In the development programme, it was accepted that within the time constraints, the only option with a reasonable likelihood of success was to extend the pneumatic acceleration principle, which presently yields the highest velocities limited by the finite sound velocity of the hydrogen propellent in connection with the pressure drop along the barrel of the adiabatically expanding gas. To extend the operational range of the gun towards higher speeds, the sound velocity must be increased by heating the gas to about 10,000K, and during acceleration the pressure at the barrel entrance must be raised to compensate the adiabatic pressure decrease; the ideal is a constant pressure acting on the pellet of limited mechanical strength. A further technical requirement governs the cryogenic problems of pellet generation when high-temperature, high-enthalpy flow of propellent is employed. These problems are being considered in the following way:

- Since June 1984, the Riso National Laboratory has investigated the arc heater concept to provide adequate propellant flow conditions. A test stand for the acceleration of 3.2mm diameter deuterium pellets was brought into operation and with the arc chamber fuelled with precondensed propellant hydrogen and operated from a preliminary power supply (~500J), velocities in excess of $1.9 kms^{-1}$ with peak accelerations of $8.10^6 ms^{-2}$ have been achieved. Simultaneously, a larger power supply (~20kJ) to allow $10 kms^{-1}$ speeds and an impedance matching transformer were built by JET and will shortly be delivered to Riso;
- From early 1985, EURATOM-CEA Association (CENG) Grenoble, France, has worked to solve

problems of cryogenics and initial acceleration limits. The construction of a test-stand has been completed and 6mm diameter pellets have been successfully formed. The method makes use of only a small fraction of the extruded ice which presents a problem in gas handling logistics, especially if later use of tritium is anticipated. A newly built 100bar Fast Valve has been commissioned to increase the initial acceleration, and a 300 bar Valve is under design;

- The Ernst-Mach-Institut of the Fraunhofer-Gesellschaft, Freiburg, FRG, has started an Article 14 Contract to investigate a piston-driven pneumatic amplifier to programme the pressure during acceleration. If successful, this device could be used to achieve velocities of $3kms^{-1}$ with cold pneumatics, or deliver suitably programmed gas flow to an arc heated gas gun. This contract is intended to expand the piston drive principle into the regime of adiabatic heating, which is an alternative to the arc heater scheme and is actually successfully employed in the two-stage guns.

Density Control and Separatrix Dump Plates

In this area, there are two main new developments. The first one concerns the provision of particle exhaust at the end of a discharge. During high density discharges, when full additionally heating is used, these must be terminated in a controlled way, and during discharges with pellet injections, it must be possible to control the edge density. Pumping panels, pump limiter systems and ergodic limiters will be assessed, but the major development effort will be concentrated on pump limiters and pumping panels.

A further activity is related to the provision of dump plates for separatrix operation, which, ultimately, should allow separatrix operation of JET at full additional heating. Depending on the ratio of radiated to conducted power, this may require installation of cooled dumps, so that the cooling down time after discharges will not become the determining factor for the pulse rate.

Pumping Panels

It has been frequently observed that the JET walls pump almost as efficiently as a pump limiter system. In particular, pumping efficiencies (ie. particle removal rate over the total particle flux in the scrape off layer) up to 7% have been observed when the plasma is moved to touch the inboard wall. It is proposed to employ this effect for pumping, although it is currently not understood. Even though a systematic evaluation of existing data has not been completed, it seems that hydrogen trapping in graphite or transient pumping of the metal or graphite walls cannot account for this effect, and detailed investigations will be necessary. In particular, it is crucial to find out whether saturation effects will reduce the pumping efficiency for higher plasma densities and wall fluxes, during full performance of JET.

Apart from more systematic studies at JET, it is envisaged that recently developed high flux plasma simulation sources (10^{17} – 10^{18} particles/cm^2s) will be used to simulate and study wall pumping for different low Z materials, such as graphite with different porosity, carbonised Inconel and porous beryllium.

Pumping panels could be positioned preferentially in the vicinity of the belt limiter because of the presence of a high recycling flux. In any case, such plates will be required in this area to avoid high Z contamination of the plasma caused by sputtering of the vessel wall.

Pump Limiter

To meet the requirements on pump limiters, it is proposed to proceed in two steps. The first step will be installation of a prototype at the earliest possible opportunity (1988), to corroborate the physics underlying the design of the pump limiters and to obtain data on the pumping efficiency with JET boundary conditions. The prototype will be a radiation cooled limiter, with sufficient pumping speed to observe effects on the plasma density, but which will not allow continuous operation (only 1-2s) during a discharge because of temperature and stress limitations of the non-actively cooled leading edge. The prototype will also be employed to select and develop internal pumping panels (volume or sublimation getter) for the final pump limiter at JET. Detailed model calculations for the JET plasma edge with the belt limiter present, and Monte Carlo calculations to optimize the limiter geometry will be necessary. A rough estimate for the prototype gives pumping efficiencies between 1 and 5% and time constants for the density decay of 6 – 30s. The prototype should be available in mid-1988.

In parallel, with the development of the prototype the design for an actively cooled pump limiter system will start. This system should have about 4 times the prototype efficiency (5-20% and 1.5 – 6s density decay times) and should withstand continuous operation during a JET discharge. This requires development of an actively cooled leading edge with can sustain stationary heat loads of about $3kW/cm^2$. For this purpose, a programme for developing and testing beryllium plated copper swirl tubes and other high heat flux components (eg. neutralizer plate) has started. The actively cooled pump limiter should be ready for installation in 1989. For both stages – prototype and actively cooled system – the belt limiter will function as the main limiter, taking most of the power load and protecting the leading edge of the pump limiter against damage from runaway electrons.

Dump Plates for Separatrix Operation

Different concepts have been assessed for protecting the top and bottom of the vessel against the head load during separatrix operation. At the beginning of 1986, 40 graphite tiled bellows protection rings will be installed in JET. The distance between adjacent protection rings will

be sufficiently small at the top and bottom section to protect the uncovered rigid sector against the particle flux which impinges on the tiles at an angle smaller than $\sim 2^0$. However, the rigid sectors, will not be protected against radiative power from the separatrix. Although there are several uncertainties in calculating the operational limits, it appears that the radiation onto the rigid sectors is the limiting factor if more than about 40% of the power is radiated. Below 40%, the thermal stresses in the graphite tiles and the strength of the inconel support plate limit the power or the pulse length. Safe limits are achieved if the surface temperature of the graphite tiles stays below 200°C, the support plate temperature is less than 700°C and if the temperature increase of the rigid sector walls is less than 50°C. This in turn would limit the total power for single null operation to 5-9MW during a 10s pulse, depending on the ratio of radiated and conducted power.

This could be improved by covering the rigid sectors with additional graphite tiles, avoiding radiation problems and increasing the total surface, but it would not provide a long term solution. Since the tiles are only cooled by radiation, long cool down times would be required (1h). Also, it would not be compatible with beryllium, since it is highly unlikely that a beryllium coating of the graphite tiles would survive surface temperature much higher than the melting point of beryllium.

A long term solution can only be obtained with water cooled protection tiles. A design using pressure contacts for heat transfer from the tiles to water cooled support plates would provide a sufficient cooling rate (ie. ≈ 10 min cool-down times) and it would be compatible with beryllium and graphite tiles. For single null operation and a 10s pulse, a total power of about 30MW could be safely loaded onto such a wall protection.

Appendix I

Work of Theory Division

(Division Head: Dr. D.F. Düchs)

Theory Division is responsible for the prediction of JET performance by computer simulation, the interpretation of JET data, and the application of analytic plasma theory to gain an understanding of plasma behaviour in JET.In addition, the Division assists in the execution of the programme and in making proposals for future experiments, in collaboration with the Experimental Divisions, the Physics Operations Group, and the Machine Development Department.

Theory Division interacts with experiment much more strongly than in most plasma physics Theory Divisions. Interpretation plays a key role in the assessment of plasma performance, and hence in optimisation studies and programme planning. Prediction work continuously checks the measured behaviour against the different computational models, and provides a basis for long term programme planning. A major role of analytic theory is to compare the observed behaviour against that expected from existing analysis, and to modify the latter where they diverge. The effort allocated within JET to analytic theory was limited, in the expectation that theorists within the Associations would provide support, by extended visits and by work done under Article 14 Contracts. Valuable assistance has been provided in this and the other areas over the past year.

The central task of the Division is to provide a quantitative model of tokamak plasmas, with particular attention to JET behaviour. The ultimate objective is to include in this model all the important effects observed in JET and other tokamaks. Although it is preferable to understand each effect theoretically, in some cases it may be necessary to rely on an empirical description.

The Division's 1985 activities can be sub-divided under the following headings:

1. Data Banks (and computing hardware);
2. Data Management Software;
3. Code Libraries (Interpretation and Prediction);
4. Data Interpretation;
5. Modelling of JET Plasmas;
6. Comparisons of Model Results and Measurements;
7. Predictive Computations;
8. Analytic Plasma Theory;

The Division is divided into three groups; Interpretation Group; Prediction Group; and Analytic Theory Group. There is much overlap between these different roles, requiring extensive collaboration between the groups. The close interaction between theory and experimental groups, has been most beneficial.

A considerable amount of theoretical work has also been carried out through contracts, as follows:

Article 14 Contracts with Associations:

Impurity diffusion package	IPP Garching, FRG.
MHD stability	UKAEA, Culham Laboratory, UK.
1½-D transport code with free boundary	ENEA, Bologna, Italy.
Electron cyclotron emission	CNR Milan, Italy.
Non-thermal ECE spectra	FOM Jutphaas, Netherlands.
Plasma boundary identification	CEA FAR, France.
Global wave ICRF heating	CRPP Lausane, Switzerland. CEA, FAR, France.
Ion velocity distribution during ICRH	Chalmers, Göteborg, Sweden.

Other Contracts:

Autoionisation	AERE Harwell/Queens University, Belfast, UK.
Charge exchange	AERE Harwell, UK.
Atomic physics and plasma transport	Oxford University, UK.

The Division has hosted the following visitors during the year:

As Associated Staff members: Dr. D. Anderson (Chalmers University, Sweden); Dr. L-G. Eriksson (Chalmers University, Sweden); Dr. W. Feneberg (IPP, Garching, FRG); Dr. D. Lortz (IPP, Garching, FRG); Dr. K. Thomsen (Riso Laboratory, Denmark); Dr. H. Wilhelmsson (Chalmers University, Sweden).

As "Visiting Scientists": Dr. S. Ejima (GA Technologies, USA); Dr. A. Fukuyama (Okayama University, Japan); Dr. K. Itoh (JAERI, Japan); Dr. S-I.Itoh (Hiroshima University, Japan); Dr L Sugiyama

(MIT, USA); Prof. R. Zelazny (Institute of Nuclear Studies, Poland).

Under other arrangements (Fellowships, etc.) the Division benefited from work by Mr. P. Ashman, Dr. H. Hamnén, Ms. L. Lauro-Taroni, Ms. M. Lorentz-Gottardi, Ms. D. Sealey, Dr. F. Tibone and Mr. D. Ward.

The Divisions' progress is described under the following subject headings:

1. Data Banks (and computing hardware)

The raw data from each pulse is transmitted to the UKAEAs' Harwell Laboratory IBM 3085 within a few minutes of completion of the pulse, and stored on the JET Pulse File (JPF), created by the Experimental Divisions and CODAS. This data is then processed and evaluated by the Experimental Divisions and the Interpretation Group.

The Processing of Data and its Assembly into Data Banks
(M. Brusati, J.P. Christiansen, J.G. Cordey, A. Galway, N. Gottardi, B. Keegan, E. Lazzaro, R.T. Ross, K. Thomsen)

One of the major responsibilities of the Interpretation Group during 1985 was the processing of data and its assembly into processed pulse file (PPF) data base. The first part of this operation is performed during machine operation, when the data from a given shot is processed and the data written into the PPF data base about 20 minutes after the completion of the shot. A sample set of graphical traces are then produced and these are used for guiding the experimental programme, and also used initially to check the consistency of the data from different diagnostics. Further checks are then performed, both computationally and visually, to establish the validity of the data.

During 1985, improvements were made to the calibration of several diagnostics and this involved fairly extensive reprocessing of the data taken during the January-June period of operation.

IBM Computing Support
(J. Davis, J. Roberts)

The use of the Harwell IBM and CRAY computers continues to increase. Currently there are 200 IBM users from JET and the hardware available on the JET site has been expanded to accommodate this increased usage. The system comprises 32 colour graphics terminals and 46 non-graphics terminals controlled by 5 cluster controllers. Four Versatec printer-plotters are available for printed and graphical output. In addition, there is an IBM5285 microcomputer with floppy disc unit which facilitates the transfer of programs between the local NORD system, the IBM mainframe computer, and an IBM3270-PC/GX. Future planned developments include the installation of further Versatec printer-plotters, and an additional cluster controller with associated terminals.

2. Data Management Software

Data Storage and Management
(R.T. Ross, A. Galway, B. Keegan)

The extent of processing of JET data continues to grow both in the amount of data analysed for each plasma shot, and in the depth of the analysis. The present state of the processing chain is summarised in Fig.A1. For each fully analysed shot some 1.5 MBytes of data are written into the processed pulse file (PPF) data base system. Currently some 2 GBytes of analysed data from 2400 plasma shots are stored in the PPF system, compared with some 13 GBytes of raw JPF data. The processing of this data has become increasingly more automated, with the necessary data controls being built into the system. A representative subset of the analysed data from the PPF system is released to the organisations in the form of a survey data bank. Several other high level data banks, such as the global TRANSPORT bank are also derived from the PPF data base and stored under the statistical analysis system SAS. A new high level data bank DIAGNOST, which contains sample data from both the PPF and JPF data banks, has been set up in order to monitor the consistency of the data between different diagnostics and to monitor the performance of a diagnostic over an operational period. Recently improvements have been made in the interface between the PPF system and these high level data banks. There have also been several improvements made to the SAS application programs which provide the major statistical

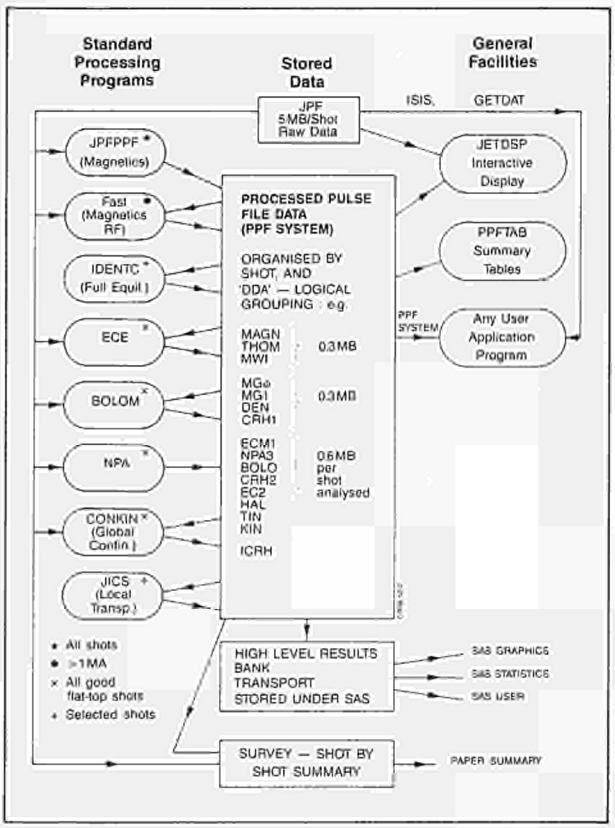

Fig. A1: JET Data - Processing, Storage and Access on the IBM3084Q and CRAY 1A Computers;

followed by typical discharges in the parameter plane (q(O), q(a)), where the boundaries of various MHD instability regions are drawn, is a convenient description of the characteristic pattern of evolution which gives insight into the processes accompanying current penetration (Fig.A2). The qualitative picture obtained shows that current evolution occurs in an angular region in the (q(O), q(a)) space, associated with the early MHD instabilities, often showing peaks of MHD activity at rational values of q(a) (Fig.A3). The flat top phase is reached at $q(O) < 1$ and the decay phase is largely within the region where tearing modes are possible and is independent of the initial phase. Most JET shots seem to avoid the ideal MHD stable region. Density and current rate determine the initial current penetration process. Disruptions in the rise phase seem to affect discharges located entirely in the kink region, while decay disruptions are possibly of the tearing type. Further analysis of the current penetration provided by the ECE temperature measurements, compared with the results from the poloidal flux diffusion equation, shows that the resistivity is anomalous during the current ramp up and is neoclassical at the end of the MHD dominated stage.

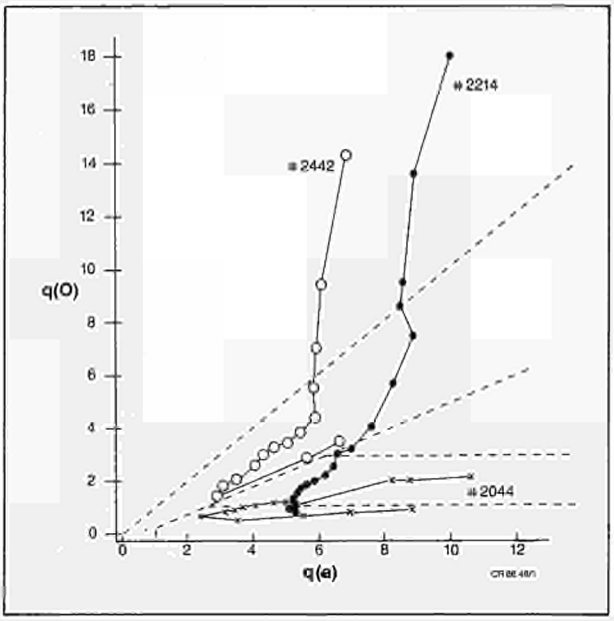

Fig. A2: Specification of different MHD stability regions;

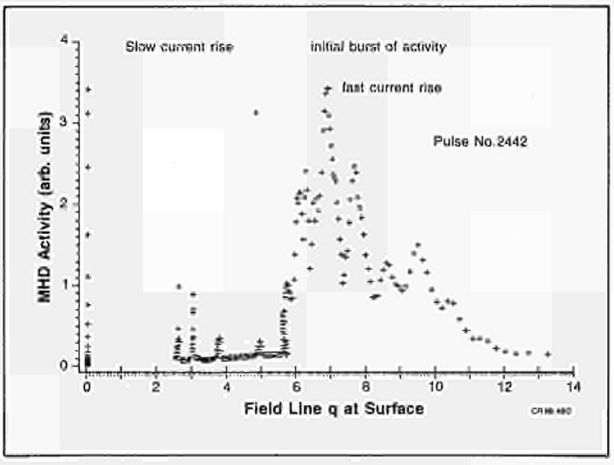

Fig. A3: MHD activity as a function of q(a);

Design and Diagnosis of Magnetic Separatrix Experiments

(E. Lazzaro, E. Springmann, A. Tanga)

The analysis of the multipolar field produced by the poloidal field coils of JET has allowed the identification of a regime of operation in which the plasma boundary is a magnetic separatrix, with one or two stagnation points within the vacuum vessel. The operating conditions for an experimental test of the configuration were studied. Successful discharges with plasma current of 1.5-2 MA were produced with a separatrix (Fig.A4) for several seconds during the flat top with toroidal field of 2.6T, line average density of $1 \times 10^{19} m^{-3}$, and plasma elongation of 1.7-1.8. The measured nickel concentration was well below 0.1% of the electron density, while carbon and oxygen were the dominant impurities. The power radiated at the X-points was 30% of the ohmic input while the total radiated power was 60%, so that the heat load to the protection plates was reduced. The configuration was diagnosed by the JET equilibrium identification code IDENTC modified for accurate determination of the separatrix. Operation in this configuration, with currents up to 4 MA, would require modifications of the poloidal field system. The magnetic equilibrium code has been modified and extended to allow the analysis of new poloidal field coil configurations. A new mesh has been created and preliminary tests of accuracy have been made. Extensive studies of divertor configurations and plasma shaping have been carried out and continue. In cooperation with the Machine Development Department and the Operation Group, designs of separatrix configurations have been devised, both for the current experimental campaign and

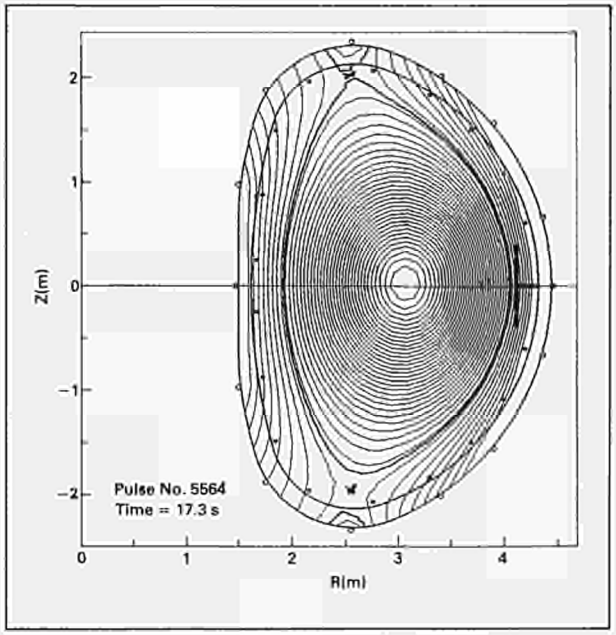

Fig. A4: Poloidal flux contours showing formation of separatrices (Pulse No: 5538, $I_p = 1.5MA$, $B_T = 2.6T$);

analysis tool for this type of data. In order to make the JET data increasingly easier to access, the IBM interactive graphical display programs and the general access package GETDAT have been upgraded in collaboration with the Experimental Divisions.

The Group continues to provide support for IBM computing at JET, and has played an ever increasing role in the planning of major upgrades to both the available hardware and the locally produced software.

JET data bases and related software
(A. Galway, B. Hodge, E. Springmann, M.G. Pacco)
Considerable effort has been devoted to the implementation of data bases in the NOMAD2 system installed at JET at the beginning of 1985. A Survey Data Base (SDB) has been designed and implemented. This data base should provide a quick overview of all shots. It contains basic information on every JET discharge in which a plasma has been produced and is available on hardcopy to all Associations. The SDB is accessable to all JET users. A user interface based on menus has been developed. It allows the user to select pulses which satisfy some criteria, and/or within a pulse number range, which contain some specified traces. Driven by menus, the user can produce several plots and displays and obtain the corresponding hard copies.

A Detailed Physics Data Base (DPDB) has been designed and its scheme has been implemented. A full set of FORTRAN subroutines to write data into the DPDB, and to read data from it, has been written, which have the same parameter list as the corresponding PPF routines and their use requires only a re-link of the FORTRAN programs. Menus for enquiries on the contents of DPDB have been written. Until now, data has only been tested in the DPDB.

3. Code Libraries

The JET Interpretation Code Library is a collection of systematically written and maintained codes, available for data interpretation. This library has been expanded and further documented. A similar collection of predictive codes, the JET Predictive Code Library, was set up during 1985.

Magnetic Calculations for Boundary Probe Diagnostics and RF
(E Lazzaro)
Special additions to the magnetic identification code IDENTB have been made to calculate the connection lengths of field lines in the plasma scrape off region. Online calculations of the rational q surfaces, has also been produced for use in RF experiments, and correlation with sawteeth and MHD activity.

Magnetic Field Calculation for Breakdown Condition Studies
(E. Lazzaro, R.T. Ross)
A special version of the magnetic code has been prepared for magnetostatic calculations which allow the analysis of the poloidal field at start up and compares the results with measurements.

An Interactive Program to trace Hugill Trajectories
(M.F.F. Nave)
HUGILL is an easily used interactive program which plots the evolution of JET pulses in a Hugill diagram (i.e. in the plane $1/q_{cyl}$, $M = \bar{n}R/B_T$). This is available to all JET IBM users.

Intershot Analysis on the Nord ED Computer
(J.P. Christiansen, S. Cooper)
The analysis program FAST [1] has been fully integrated as a "real-time" program with the control service program on the Nord EC computer.

Improvements to Analysis Methods
(J.P. Christiansen)
During 1985 the two analysis programs FAST and CONKIN [2] have been expanded to regularly process data from i) the diamagnetic loop, ii) the multi-channel FIR-interferometer, iii) the new gas introduction system. The improvements to the analysis methods include:

a) Determination of the X-points in separatrix plasmas;
b) Better separation of l_i and β;
c) Flux surface geometry derived from plasma boundary, l_i, β and axial ellipticity;
d) Use of this geometry in interpretation of chord measurements and global confinement analysis;
e) Derivation of impurity influx (not measured) from Z_{eff} and plasma composition.

Reprocessing of 1985 Data
(J.P. Christiansen, J.G. Cordey)
The improvements to analysis methods and the extended processing capability of the analysis programs FAST and CONKIN have been employed in reprocessing most of the 1985 JET data. This has led to a consolidation of the JET databank of PPF files and eliminated inconsistencies between results from 1984 and from 1985.

4. Data Interpretation

Results of the Analysis of Current and Temperature Build Up in JET
(E. Lazzaro, D. Campbell, J.P. Christiansen, W. Morris*, M.F.F. Nave, F.C. Schüller, P. Thomas, J.A. Wesson)
(* EURATOM-UKAEA Association, Culham Laboratory, UK)

Observations on the formation of the tokamak temperature and current profiles have been compared with MHD stability criteria. The diagnostic tools available at JET, (the equilibrium identification codes IDENTC, FAST and the ECE measurements of electron temperature profiles T_e), allow a detailed analysis of the evolution of the discharge to a state of ohmic consistency, in which the temperature and current profiles are related through neoclassical resistivity. An analysis of the path

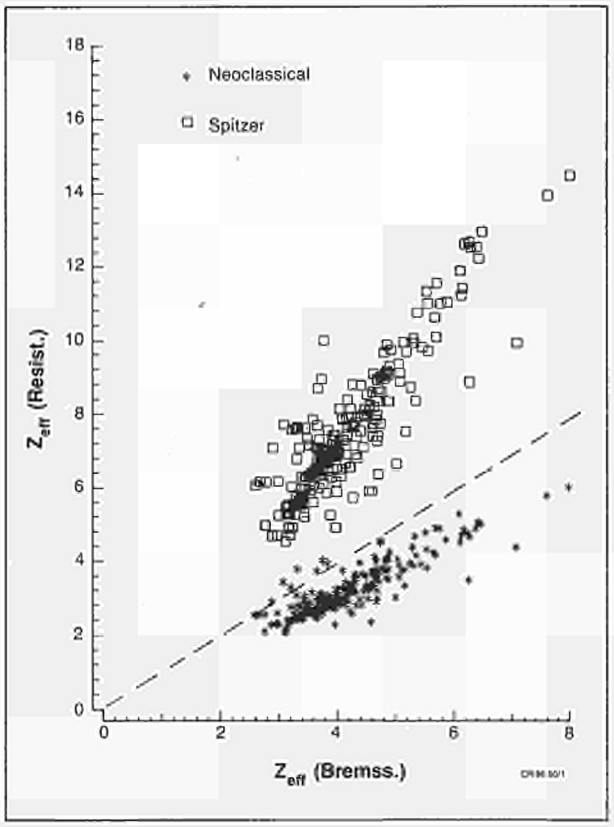

Fig. A5: Effective ion charge (Z_{eff}) obtained from resitivity measurements (Spitzer and neoclassical values) versus that obtained from visible Bremsstrahlung intensity;

for a future upgrading of the tokamak. A new arrangement of coils allowing more flexible shape control has also been considered.

Resistivity Studies

(J.P. Christiansen, J.G. Cordey, E. Lazzaro, D. Campbell, S. Ejima*)

(* GA Technologies Inc., California , USA)

Studies have been made of resistivity and various estimates of Z_{eff}. The analysis [3] shows the resistivity in JET to be close to the neoclassical value. This is shown in Fig.A5 where the effective plasma charge obtained from the plasma resistivity using the Spitzer and neoclassical formulae is compared with that obtained from visible Bremsstrahlung.

Power Absorption with ICRH

(J P Christiansen, J G Cordey, S Ejima, K Thomsen)

The power absorbed by the plasma ion cyclotron resonance heating has been checked independently by examining the time behaviour of the plasma energy content during the switch-on and switch-off phases. Exponential curves have been fitted to the plasma energy as is shown in Fig.A6. For this case, the fit shows that ~75% of the total power coupled into the Torus from transmission line measurements is actually absorbed by the plasma. The relaxation time of this added energy is between 0.2s and 0.25s which is significantly less than

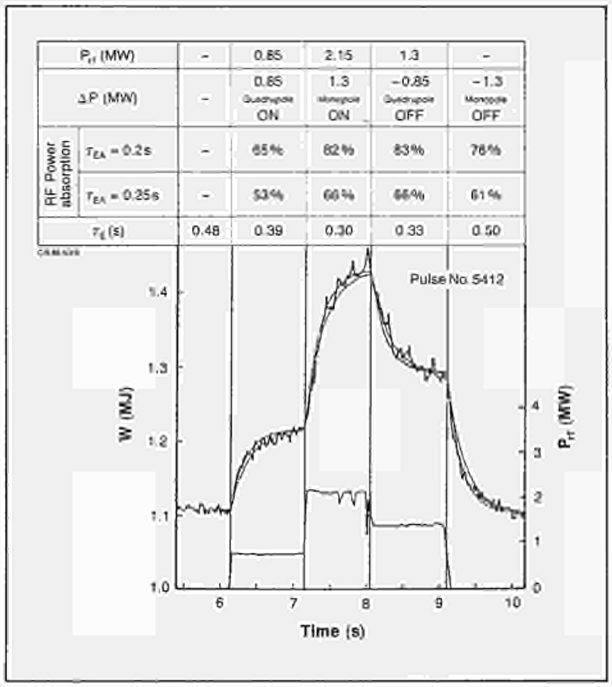

P_{rf} (MW)	–	0.85	2.15	1.3	–
ΔP (MW)	–	0.85 Quadrupole ON	1.3 Monopole ON	−0.85 Quadrupole OFF	−1.3 Monopole OFF
RF Power absorption τ_{EA} = 0.2s	–	65%	82%	83%	76%
RF Power absorption τ_{EA} = 0.25s	–	53%	66%	66%	61%
τ_E (s)	0.48	0.39	0.30	0.33	0.50

Fig. A6: Time behaviour of plasma during switch-on and switch-off phases of RF power;

the ohmic energy confinement time (~0.6s) but is close to the confinement time when the ICRH input power dominates over the ohmic input power.

Analysis of RF Transmission Line Measurements

(K. Thomsen, M. Bures, F. Sand, P. Lallia)

During 1985, a code was developed and installed on the IBM to provide the global confinement program CONKIN with the total coupled RF-power (Fig A7). In addition, this program RFCALC calculates for each RF-antenna the generator power, coupling resistances,

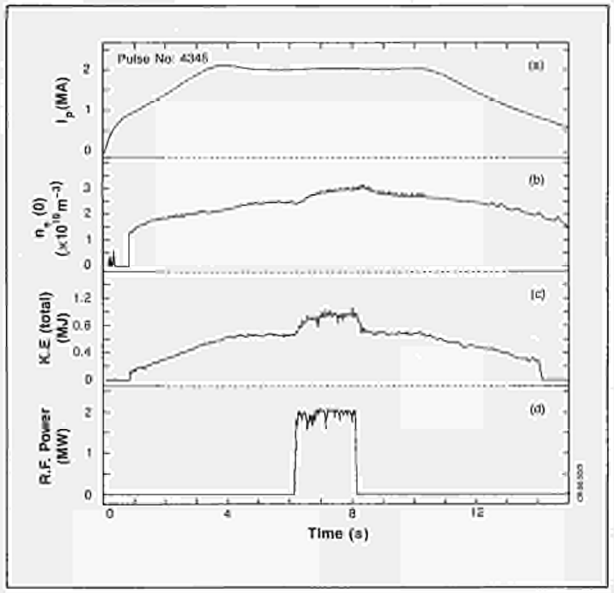

Fig. A7: Pulse No. 4345: ICRH heated discharge: (a) plasma current; (b) axial electron density; (c) total kinetic energy and (d) total coupled RF-power versus time;

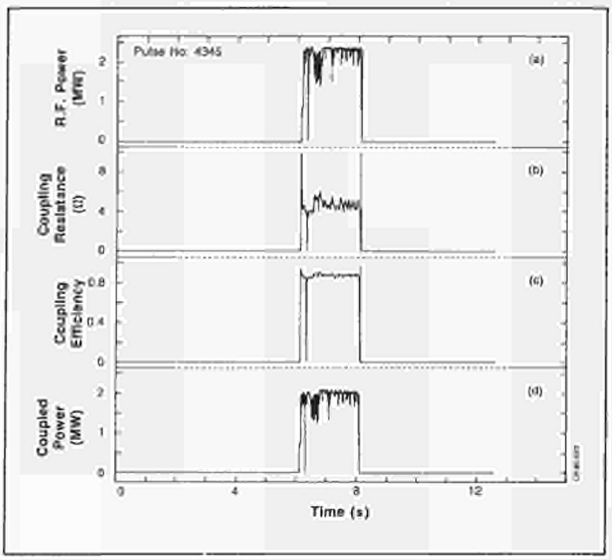

Fig. A8: Pulse No. 4345: Characteristics of antenna 2B: (a) generator power; (b) average coupling resistance; (c) coupling efficiency and (d) coupled power versus time;

coupling efficiency, voltage standing wave ratios and coupled RF-power from transmission line measurements. All these quantities are stored in the JET data banks of PPF files. Fig.A8 shows a few of these parameters versus time for Pulse No. 4345. A catalogue has been created which contains information such as: antenna configuration, frequency, RF-pulse start time, RF-pulse length, maximum RF-power, average RF-power and average coupling resistance. All 1985 shots with ICRH have been analysed with the program and the catalogue has been completed.

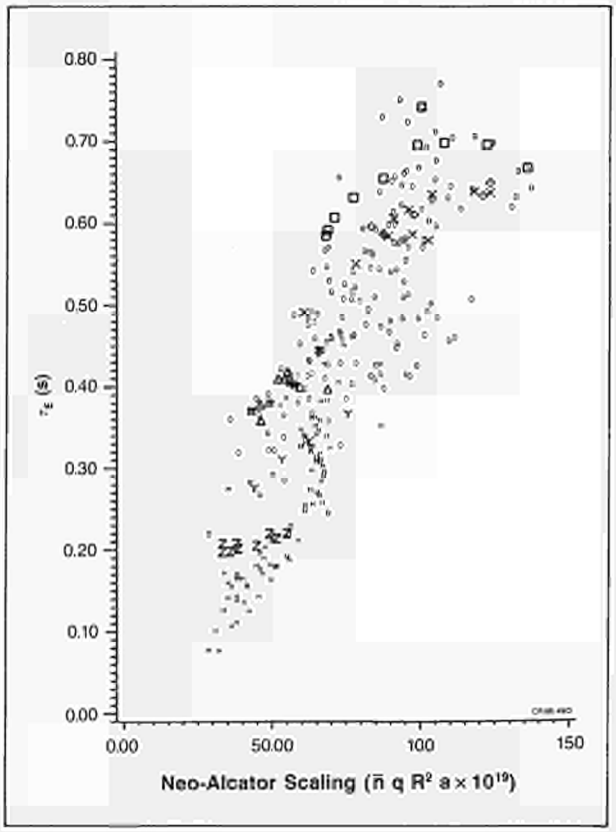

Fig. A9: The energy containment time τ_E (from ohmic heating data) versus the neo-Alcator scaling law (nqR^2a);

Global Energy Transport Studies With Ohmic and Ion Cyclotron Resonance

(J.G. Cordey, J.P. Christiansen, S. Ejima*, B. Keegan, K. Thomsen)

(* GA Technologies Inc., California, USA)

JET has now been operated with both ohmic and ion cyclotron resonance heating (ICRH) over a wide range of plasma conditions. The toroidal magnetic field B_T, current I_p, density n, elongation K, the ICRH power P, the major radius R and minor radius a have all been varied, and the energy confinement characteristics have been examined as a function of these parameters.

With ohmic heating the energy confinement time τ_{OH} increases roughly linearly with density at low densities, but then saturates at high densities ($\bar{n} > 3 \times 10^{19} m^{-3}$) attaining a peak value of $\tau_{OH} = 0.8s$ at the highest toroidal field (B = 3.4T). This saturation can be seen in Fig.A9 where τ_{OH} is shown versus the simple neo-Alcator scaling law nqR^2a for the complete JET ohmic data set 1983-85.

A regression analysis has been completed to obtain the dependence of τ_{OH} on the plasma parameters. It is found that τ_{OH} scales as $(nBA)^{½}q^{1/3}K^{0.2}$ where A is the atomic mass (JET has been operated with both hydrogen and deuterium plasmas). The data set has been combined with that of Doublet III to obtain the scaling of τ_{OH} with dimensions. It is found that τ_{OH} increases roughly cubically with dimensions and has a stronger dependence on R than a.

The ohmic heating constraint relations on the input power P, the electron temperature and effective charge Z_{eff} have also been determined as a function of the plasma parameters n,B,q and K.

The addition of ion cyclotron resonance heating means that the power dependence of the energy confinement time τ_E may be determined. By writing τ_E in terms of n,B,I,K,R,a and P/P_Ω, where P is the ohmic heating power, an expression for τ_E may be derived which satisfies both the ohmic and additionally heated data sets. Several different functional forms have been examined, the form which gives the best fit to both data sets is:

$$\tau_E = \frac{P_\Omega}{P}\,\tau_{OH} + \left(1 - \frac{P_\Omega}{P}\right)\tau_{aux}$$

where τ_{OH} and τ_{aux} are functions of n,B,I, etc. Typically τ_{aux} is found to be approximately one third of τ_{OH} and to be only weakly dependent on I. The fit is shown in Fig.A10.

Local Transport Analysis

(M. Brusati, A. Galway)

The interpretation code JICS has been used to analyse the power balance and the local confinement properties for JET plasmas for a variety of conditions. It is found that

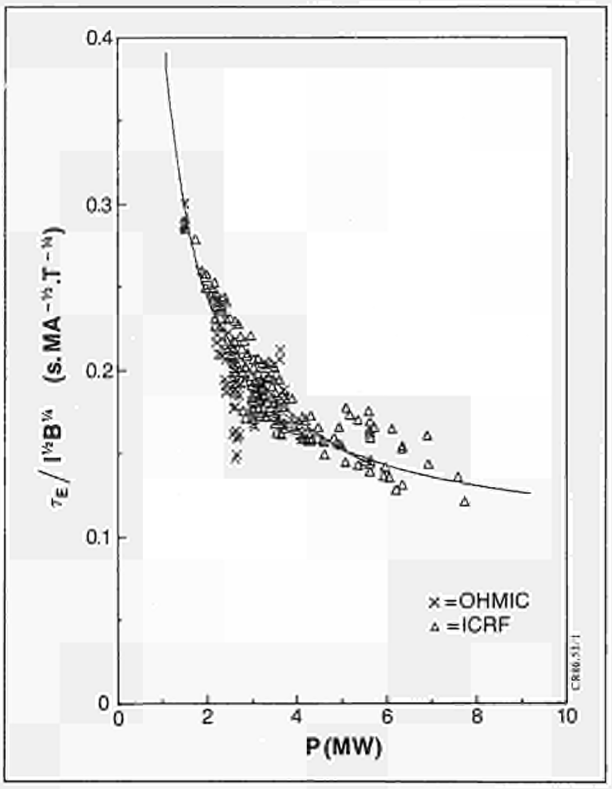

Fig. A10: The energy containment time, τ_E, from all auxiliary heating data, showing best fit $\tau_E(s) = [0.29/P(MW) + 0.095]I^{1/2}(MA)^{1/2} B^{1/4}(T)^{1/4}$;

the balance of power in JET follows the conventional tokamak pattern, with most of the input power being lost through the electron channel; conduction is the main loss mechanism in the bulk plasma while radiation losses dominate at the plasma edge ($q > 2$) and play a major role in the observed saturation of energy confinement time with density. Ion losses account for up to 30%-40% of the total at the highest densities. These are due mainly to thermal conduction which is systematically higher than that estimated from neoclassical theory. The departure from neoclassical values decreases at higher electron densities.

The confinement time is nearly constant across the plasma minor radius and shows a clear deterioration at the radiation dominated plasma edge (up to 30% at $\bar{n} = 3.5 \times 10^{19}$ m^{-3}).

Electron Temperature Profile Consistency and Field Line Topology

(M. Brusati, A. Galway, B. Keegan, P.H. Rebut)

Studies have been undertaken to assess the existence of electron temperature profiles consistent with a basic set of non-dimensional combinations of plasma parameters. This idea follows a model for the plasma evolution where a phase transition takes place when the electron temperature profile reaches a critical gradient in the region where island overlap can occur ($q > 1$). In this case an equilibrium can be established among laminar flux surfaces, magnetic islands and ergodic domains, which maintains locally a critical electron temperature during changes in heating rate.

A preliminary scaling of the electron temperature gradient, obtained using most of 1985 data, shows a favourable dependence on plasma current, toroidal field and machine size.

Generalised Abel Inversion

(N. Gottardi)

A study of the asymmetries of the plasma radiation detected by the bolometers has been carried out for many plasma parameters using the projection method for inverting integrated measurements. Sometimes a marked difference between the shape of the magnetic flux surfaces, as calculated by the equilibrium code IDENTB, and the isoemissivity lines is observed. This difference depends on B_T, n_e, I and K and hampers a precise determination of the radiation profiles using the projection method.

Other methods of inversion based on polygonal pixels (the solution being obtained from (a) a least squares fit to an overdetermined linear system of equations and (b) a Monte-Carlo technique) have been tested but, due to the small number of useful channels, did not give an appreciable improvement. An examination of the electron density profiles obtained by means of the projection method, showed that there was good agreement between the shape of the magnetic flux surfaces and the isodensity surfaces. An example of the evolution of the density profile in JET with ICR heating is shown in Fig.A11.

Disruption Behaviour

(M.F.F. Nave, J.A. Wesson)

The analysis of disruptions has been extended to include time dependent trajectories in the Hugill diagram. This has allowed a better understanding of the pre-disruption behaviour and of the consequences of wall carbonisation. In particular, it is found that carbonisation delays disruptions so that they occur at lower currents during the current decay. This allows the achievement of slightly higher densities during the flat top, but does not allow an increase in density beyond the previous limit observed

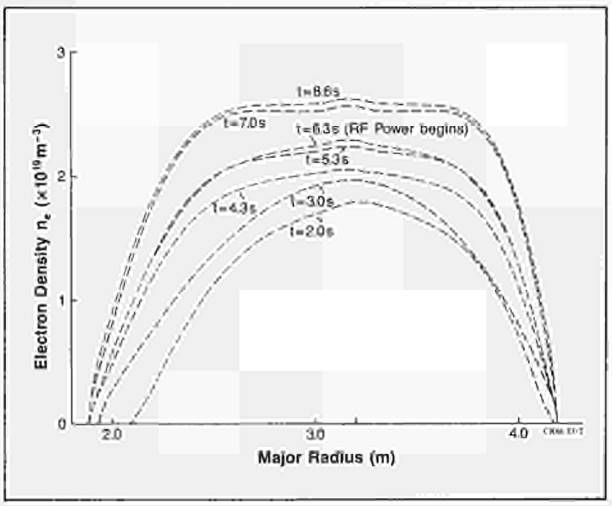

Fig. A11: Evolution of electron density profile (with RF heating).

during current decay. A straight line is the best fit for disruptions on the tail of the current decay, determined from pulses before carbonisation. The carbonisation pulses have peak current Murakami parameters which approach the limiting values for disruptions. The pulses decay with trajectories parallel to the limiting line.

Sawtooth Heat Pulse Propagation and Anomalous Transport
(T.E. Stringer)
Analysis has continued of the heat pulse, which propagates outwards in JET after a saw tooth crash. This now uses the temperature variation at fixed points as measured by the ECE grating spectrometer. The temperature variation in space and time is consistent with a diffusive process. However, the required thermal diffusivity in ohmic plasmas is several times that deduced from steady state energy balance. When RF heating is applied the propagation velocity of the heat pulse is almost unchanged, although the steady state energy confinement time is reduced by up to a factor two. This apparent discrepancy in diffusivity could be reconciled if the heat flux included a convective, as well as a diffusive component. The theory of anomalous transport processes is being studied to find an explanation for such a heat flux.

Derivation of the Diffusion Coefficient from the Sawtooth Density Variation
(A. Hubbard*, D. Ward*, T.E. Stringer)
* Imperial College of Science and Technology, University of London, UK

The flattening of the density profile inside the q = 1 radius during a sawtooth crash gives rise to a density perturbation. This perturbation propagates outwards, similarly to the sawtooth heat pulse. Its propagation in JET has been measured using the fixed frequency microwave reflectometer.The delay between the crash and the arrival of the perturbation maximum at distant points is compared with numerical simulation, to deduce the particle diffusion coefficient. The value obtained (0.4-0.6 m^2/s) is consistent with that derived from the steady state density profile.

Sawtooth Variation in Neutron Yield
(T.E. Stringer)
If the ion temperature change during a sawtooth collapse is similar to that observed for the electrons (i.e., flattening inside the mixing radius) the decrease in neutron yield from inside the inversion radius is partly cancelled by an increase from outside the radius. The sawtooth variation in neutron yield measured in JET is larger than predicted for such a temperature change. Among the possible explanations being studied is a preferential loss of tail ions during the collapse.

5. Modelling of JET Plasmas

The improvement of existing transport codes, and their extension to include effects such as pellet fuelling, is a continuous activity in the Prediction Group. Development of more exact codes to compute the distribution of ICRF heating in space, and between different species, has continued within the Analytic Theory Group.

Transport codes and related packages
(A. van Maanen-Abels, D. Muir, E. Springmann, P.M. Stubberfield, A. Taroni, F. Tibone, M.L. Watkins)
Work in this field has concentrated on the updating and improvement of the 1½-D transport codes GETTO and ICARUS. The transport code GETTO has now been developed to allow simulation of the evolution of a free boundary plasma, including plasma compression. Computation of the magnetic configuration outside the plasma, and in particular, of the magnetic field at the pick-up coils on the vacuum vessel of JET has also been implemented into this code. This allows comparisons of computed and measured magnetic fields when real JET discharges are simulated.

The ICARUS code has been linked to a new version of the pellet injection code. The link between ICARUS and the non-coronal impurity transport code NONCOR (previously called IMPUDI) has been completed and extended to the plasma boundary region.

The RF auxiliary heating package used in both transport codes has been updated on the basis of results obtained in JET. It is intended as a reference stand-alone package, to be used both for predictive and interpretative codes such as JICS. This has already been done during 1985 for the multiple pencil beam package for the simulation of neutral beam injection, originally developed for ICARUS. It will be used in GETTO and the interpretation codes as well. A reference stand-alone package has also been made available for pellet injection.

The stand-alone impurity transport code BITC, which can treat full neo-classical transport in addition to anomalous transport, has been speeded up considerably. This has been achieved by switching off the solution of the diffusion equations for those ions which have negligible density.

Boundary plasma code
(R. Simonini, A. Taroni)
The 2-D version of the code for solving the fluid equations in the plasma boundary region with a toroidal limiter has been completed. This code has been linked to a Monte Carlo code (NIMBUS) for the simulation of neutral particles.

The Evolution of the Resonant Ion Distribution During RF Heating
(W.G.F. Core, H. Hamnén, T. Hellsten)
Ion cyclotron heating produces a high energy tail on the velocity distribution of the heated species. This enhances the fusion yield when the heated species undergoes fusion reactions. Information on the cyclotron absorption can be obtained by measuring the yield or energy spectra of the fusion products. The velocity distribution of the heated

species is also needed to calculate the energy transferred to the various background plasma species.

A Fokker-Planck code has been developed to describe the evolution of this velocity distribution function. It is based on the code, BACCHUS, supplied by the CRPP Lausanne group [K. Appert, S. Succi and J. Vaclavik]. It has been changed from an electron to an ion code (BAFIC: Bounce Averaged Fokker-Planck Ion Cyclotron code) and extended to include the effects of trapped particles. A source function corresponding to neutral beam injection has also been added.

Fundamental minority/second harmonic, and RF/beam-plasma hybrid systems have been considered. For these scenarios, the calculations indicate that trapped particle effects are not very important in the calculation of fusion yield and bulk plasma heating rates. Second harmonic heating leads to important modifications of the plasma dielectric properties through the change in the distribution function. Combined neutral beam and second harmonic heating further enhances these modifications, which for practical power levels cannot be represented by a linear treatment.

With the same code, minority ion current drive by ICRF heating at the fundamental ICR frequency has also been studied for a deuterium-majority plasma. Toroidicity effects have been included, but not the possibility of currents in the electron species. It has been shown that toroidicity normally enhances the minority ion current drive efficiency. For low power levels and narrow velocity space resonance widths, the efficiency would typically reach 0.15 A/W. However, for practical power levels and resonance widths, much lower efficiences are expected. Processes preventing the distribution function from reaching a steady state (e.g. sawtooth activity), could further reduce the efficiency.

To avoid lengthy computations a semi-analytical model for determining the velocity distribution during RF and neutral beam heating is being developed under an Article 14 contract with Chalmers University of Technology, Göteborg [D. Andersson, L. Eriksson, L. Lisak and L. Pekkani]. A model has been developed which treats fundamental as well as second harmonic heating in the presence of neutral beams, including the effect of finite Larmor radius. This semi-analytic model gives good agreement with the BAFIC code for macroscopic quantities, such as fusion yield and power transfer.

Analysis of ICRF Waves in JET Plasmas
(S.I. Itoh*, K. Itoh+ and A. Fukuyama#)
* Hiroshima University, Japan, + Kyoto University, Japan, # Okayama University, Japan.

The power deposition and structure of the wave field are investigated for H minority heating in a D-plasma, using 1-D and 2-D wave propagation codes. The wave field is found to be strongly localised in front of the antenna and propagates radially inwards. For low temperatures, direct heating of the H species dominates. As the temperature or density increases, electron Landau and transit time damping become more important.

6. Comparison of Model Results with Measurements

Simulation of Ohmic Discharges in JET
(P.M. Stubberfield, R. Simonini, E. Springmann, A. Taroni, F. Tibone, M.L.Watkins)
The prediction codes GETTO and ICARUS have been used extensively to simulate JET ohmic discharges. Particular attention has been devoted to studying the consistency of experimental results with widely accepted transport models, both theoretical and empirical.

It was first pointed out that the observed values of the central temperature difference $T_e(O)$-$T_i(O)$ in 1985 discharges were not consistent with the moderate ion thermal transport usually assumed (one to five times neo-classical). More generally, transport models that fitted well the 1984 JET discharges appeared not to work for high density 1985 discharges. After recalibration of the ECE electron temperature measurements, the transport picture given in 1984 for ohmic discharges was found to apply to all ohmic discharges in JET. Neoclassical resistivity has been found to provide better agreement with experimental observations, than Spitzer resistivity.

Electron energy transport remains difficult to assess uniquely. However, it has been confirmed that, and better understood why, a coefficient χ related to profile consistency, such as the so called Coppi-Mazzucato-Gruber coefficient, can be used to simulate discharges in JET as well as in smaller devices, without explicit dependence on the dimensions. A detailed study of the distribution of background neutrals in JET ohmic discharges has been performed, taking into account the poloidal asymmetry due to limiters, the effects of non circular plasma cross-section, and toroidicity. It has been shown that the poloidal asymmetry can be strong (a factor of 5) even well inside the plasma ($r \approx 50$cm).

ICRH discharges
(P.M. Stubberfield, A. Taroni, F. Tibone, M.L. Watkins)
Existing transport models and energy deposition profiles for electrons and ions have been tested against experimental observations in JET with ICRH auxiliary heating. Results obtained show that the following simplified RF power deposition model can be used to produce "reasonable" results:

- the additional power is uniformly deposited within a rectangular portion (the same for electrons and ions) of the poloidal plasma section;
- the absorption region is bounded by major radii corresponding to the position of the ion-ion hybrid and the ion cyclotron resonance for the minority species, and by a height Z determined by ray tracing calculations ($Z \sim 1.5$m);
- direct heating of the electrons by mode conversion using the Budden formulae, and minority ion heating by ion cyclotron damping are estimated;
- heating of the background plasma ions and of the electrons is then estimated using a steady-state

solution to the Fokker-Planck equation for the minority species distribution function.

Confinement degradation during RF heating has been simulated through an enhancement of the ohmic electron thermal diffusivity by a power-dependent factor, along the lines suggested by the principle of profile consistency.

Simulation of deuterium plasmas at various plasma currents, densities and toroidal fields, with either hydrogen or helium minority concentrations, and RF power levels up to 5MW indicates the following plausible scenario:

- a significant fraction of the RF power is absorbed near the plasma centre;
- electron transport near the plasma centre is moderate;
- electron energy transport degradation (scaling roughly as P_{in}/P_{Ω}) is required to reproduce experimental results if most of the coupled RF power is absorbed in the plasma centre.

However, a scenario in which less power ($\sim$ 50% P_{rf}) is absorbed and transport is not degraded cannot be excluded at present.

The interaction of transport, sawtooth activity, and RF absorption has been studied within the frame work of the sawtooth model developed at JET in 1984. It was shown that sawtooth activity can indeed help in separating the heating and transport properties of the plasma.

7. Predictive Computations

New regimes of plasma operations

(P.M. Stubberfield, M.L. Watkins)

Transport code predictions for tritium operation in JET at the full planned power have been made with the aim of allowing conclusions to be drawn regarding the choice of limiter material and the effect of dissimilar materials also being present.

Results can be summarised as follows:

- Systems consisting entirely of low-Z material lead to high edge temperatures, high power flows to the limiter, high limiter erosion and low impurity radiation for both low and high plasma density;
- Low-Z impurity levels remain tolerably low (despite the large limiter fluxes and the assumed transport model which peaks impurities on axis), because redeposition on the limiter and modest transverse transport into the bulk plasma occurs. This model is appropriate for present ohmic discharges in JET;
- Systems including mixed-Z materials are shown to be much more sensitive to changes in, for example, the plasma density. At low density, the edge temperature, the power flow to the limiter and the limiter erosion are all high and the impurity radiation is low, similar to the corresponding all low-Z cases. However, at high density the edge temperature, the power flow to the limiter and the limiter erosion are all low and the impurity radiation is high;
- There is little to choose between beryllium or carbon as the limiter material for JET. This result is independent of the effective wall material, the plasma density and the heating model.

The effects of pellet injection on JET performance was also studied. The range of pellet speeds and sizes necessary for present and future JET plasmas has been determined. Pellets up to 6mm diameter and speeds at least up to $10 kms^{-1}$ have been found necessary to penetrate to the q = 1 region in a plasma with central electron temperature and density of 10keV and $10^{20} m^{-3}$, respectively.

The change in performance resulting from pellet injection into ohmic, auxiliary heated (neutral beam and RF) and deuterium/tritium plasmas have been examined. The results can be summarised as follows. Pellet injection can be beneficial in building-up the plasma density from low levels, with peaked density profiles leading to reduced edge particle fluxes, including impurity fluxes. However, pellet injection can also lead to higher edge radiation and a thermal collapse of the plasma. Additional heating helps to avoid this by facilitating the re-heat of the plasma following pellet injection. When all the additional heating power is needed to maintain the plasma close to ignition, it is necessary to rely on the alpha power available *after* pellet injection to re-heat the plasma. In general, this is insufficient, and a re-heat to ignition is only possible if the energy confinement improves after pellet injection.

8. Analytic Plasma Theory

Sawtooth Behaviour

(J.A. Wesson, M.F. Nave, J. Hastie*, P. Kirby*)

* EURATOM-UKAEA Association, Culham Laboratory, UK

The sawtooth behaviour observed in JET appears to be inconsistent with previously accepted models. In particular, the absence of precursors and the rapidity of the collapse were not understood. In response, to this a theoretical model has been developed which predicts behaviour consistent with the observations.

The first step was to recalculate the stability of the ideal m = 1 kink mode, allowing for the expected form of the q-profile. It was found that the mode was unstable, whereas previously it had been predicted to be stable. The nature of the eigenfunction gives a different type of behaviour from that previously assumed and corresponds to a convective cell motion in the plasma. The non-linear consequence is the formation of a cold plasma bubble at the centre of the plasma. (Such a bubble has subsequently been found experimentally in the soft X-ray tomography studies.) An explanation of the catastrophe nature of the collapse is proposed in terms of an off-axis minimum in q falling through resistive diffusion until $q_{min} = 1$. This is calculated to give a rapid onset of the instability described above.

Sawtooth Control
(J.A. Wesson, H. Hamnén)
A study has been made of the methods and consequences of control of the m = 1 internal instability. In particular, the further instabilities resulting from feedback stabilisation have been investigated and the methods and feasibility of producing stable current profiles with ICRH and neutral beam current drive have been studied.

Theory of Disruptions
(J.A. Wesson, M.F. Turner*)
* EURATOM-UKAEA Association, Culham Laboratory, UK

The disruption density limit in JET has been explained in terms of the instability to contraction of a surface radiating layer. This phenomenon has been studied in detail and numerical simulations have been carried out including transport, radiation and the non-linear behaviour of the MHD instabilities. The results are entirely consistent with the observed behaviour.

Constraints on JET Operations
(J.A. Wesson, M.F. Nave)
The MHD limits on β, the disruption limits on density and the observed energy losses constrain the achievable parameters on JET. The effect of these constraints on the α-particle power of a D-T plasma has been calculated for a number of models.

Plasma Flows in Tokamaks
(R. Zelazny*)
* Institute of Nuclear Studies, Poland

The MHD equilibrium equations have been analysed, including stationary poloidal and toroidal flows. Such flows may be driven by additional heating. Parameter space may be divided into two regions where the equilibrium equation is elliptic, separated by a hyperbolic sonic barrier. Equilibria in the different regions are being studied in more detail.

Impurity Transport in Rotating Plasma
(W. Feneberg*)
* EURATOM-IPP Association, Garching, FRG

The steady-state fluid equations are solved for the density and velocity variation over flux surfaces in a large-aspect-ratio tokamak. The toroidal and poloidal velocities are treated as free parameters, as opposed to some earlier treatments where they are assumed to be related by the neoclassical condition. Over certain ranges of toroidal and poloidal rotation a strong outward neoclassical impurity flux is found.

Scaling Law Systematics
(D.F. Düchs, L. Taroni)
Following the theoretical work of Pfirsch and Düchs [4], a code is being implemented to identify and discard the inner relations from statistical material. In addition, experimental errors are taken into account to give the uncertainty on the exponents in the scaling laws. A procedure to find the maximum allowed number of variables to be discussed is under study.

References

[1] JET Progress Report, 1984. (EUR-JET-PR1) EUR-10223-En (1985);
[2] Calculations Used for Interpretation of JET Data, J. P. Christiansen. (To be published);
[3] Resistivity and Field Diffusion in JET, J. P. Christiansen, D. J . Campbell, J. G. Cordey, S. Ejima, E. Lazzaro, 12th European Conference on Controlled Fusion and Plasma Physics, (Budapest, Hungary) Vol I, p 327 (1985);
[4] D. Pfirsch, D. F. Düchs, Scaling Law Systematics, JET-R(85)01.

Appendix II

JET Task Agreements 1985

Title	*Associations (JET Responsible Officer)*	*Duration of Agreement*	*Present Status*
RF HEATING DIVISION			
ICRF CURRENT DRIVE EFFECTS – Asymmetric heating of minority species ions, Absorption of fast magnetosonic waves by TTMP of suprathermal electrons, ICRF enhancement of beam driven currents	EUR-UKAEA CULHAM LABORATORY (CUL/TA6) (J Jacquinot)	Started November 1984	a method has been chosen a code is being developed
RF ANTENNA DEVELOPMENT, TESTING, COMMISSIONING AND OPERATION	EUC-CEA FAR (FAR/TA2) (J Jacquinot)	Sept 1984–Aug 1986	a contract for additional Testbed equipment is placed. The Testbed has been moved from FAR to JET
ICRH HEATING – The operation of ECRH antennae, The evaluation of the heating performance and the comparison to theoretical expectations, The theory of RF current drive.	EUR-CEA (FAR/TA3/GREN/TA1) (J Jacquinot)	Sept 1984–Sept 1986	Since January 1985, FAR staff have been participating actively in analysis of results already obtained.
ICRH HEATING – Coupling calculations of ICRH antennae, Calculations of the power deposition profile by the method of ray tracing, Experiments with a complete ICRH system on the Textor Tokamak	EUR-ERM/KMS (J Jacquinot)	1 Feb 1985–30 Sept 1986	Agreement just established (ERM2)
EXPERIMENTAL DIVISION 1			
PHYSICS OF SHAPED CROSS-SECTIONS	CULHAM CUL/TA4 (P E Stott)	Started March 1983	Work continuing, and task agreement has been extended.
EDGE PLASMAS & PLASMA SURFACE INTERACTIONS	CULHAM CUL/TA2 (P E Stott)	June 1983–May 1986	Work proceeding
PLASMA WALL INTERACTIONS	GARCHING IPP/TS2 (P E Stott)	January 1984–December 1986	Work proceeding
MHD ACTIVITY, DISRUPTIONS AND RF WAVEFIELDS, EDGE PLASMAS UNDER INTENSE RF FIELDS	LAUSANNE CRPP/TA1 (P E Stott)	March 1984–March 1986	Work proceeding
NEUTRON PRODUCTION, RELATED PHYSICS AND ASSOCIATED DIAGNOSTICS	SWEDEN SERC/TA1 (P E Stott)	January 1984–December 1986	Work proceeding
PLASMA SURFACE INTERACTIONS	SWEDEN SERC/TA2 (P E Stott)	July 1984–June 1987	Work proceeding

EXPERIMENTAL DIVISION 2			
BULK IMPURITY PHYSICS AND IMPURITY RELATED DIAGNOSTICS	EUR-IPP FRG (W W Engelhardt)	Started February 1983	Work proceeding
IMPURITY ANALYSIS	EUR-UKAEA CULHAM LABORATORY (W W Engelhardt)	Started February 1983	Work proceeding
SPECTROSCOPIC MEASUREMENTS: INTERPRETATION AND IMPURITY	EUR-CEA FAR (W W Engelhardt)	Started July 1984	Work proceeding
PHYSICS OF ION AND ELECTRON ENERGY TRANSPORT AND RELATED DIAGNOSTICS	EUR-ENEA CREF (W W Engelhardt)	Started October 1983	Work proceeding
PHYSICS OF NEUTRAL BEAM HEATING OPTIMISATION	EUR-UKAEA CULHAM LABORATORY (W W Engelhardt)	Started July 1983	Work proceeding

Appendix III

Articles, Reports and Conference Papers Published, 1985

1. Manufacture of beam sources and neutralisers for JET neutral injection.
   Altmann H.
   Fusion Technology 13th Symposium, Varese, 24-28 September 1984, Oxford, Pergamon, 1984.
   Vol. 1, pp. 579-585.
2. Textbook finite element methods applied to linear wave propagation problems involving conversion and absorption.
   Appert K, Hellsten T, Vaclavik J, Villard L.
   Ecole Polytechnique Federale de Lausanne, September 1985.
   Report LRP 268/85.
   Presented at the 3rd European Workshop on Problems in the Numerical Modeling of Plasmas, Varenna, September 1985.
3. Overmoded millimetre waveguide transmission system for the JET ECE diagnostic.
   Baker E A M, Daly D J, Dellis A, Bartlett D V, Campbell D J, Costley A E, de Kock L C J M, Fessey J.
   Electron Cyclotron Emission and Electron Cyclotron Resonance Heating, 4th Int. Workshop, Rome, 28-30 March 1984.
   Rome, Editor dall'ENEA, 1984.
   pp. 11-14.
4. Absolute calibration of the JET ECE system.
   Baker E A M, Bartlett D V, Campbell D J, Costley A E, Hubbard A E, Moss D G.
   Electron Cyclotron Emission and Electron Cyclotron Resonance Heating, 4th Int. Workshop, Rome, 28-30 March 1984.
   Rome, Editor dall'ENEA, 1984.
   pp. 23-26.
5. An interpretation code for ECE measurements on JET.
   Bartlett D V.
   Electron Cyclotron Emission and Electron Cyclotron Resonance Heating, 4th Int. Workshop, Rome, 28-30 March 1984.
   Rome, Editor dall'ENEA, 1984.
   pp. 27-33.
6. Measurement and interpretation of electron cyclotron emission on JET.,
   Bartlett D V, Baker E A M, Campbell D J, Costley A E.
   Review of Scientific Instruments.
   Vol. 56, No. 5, pt. 2, May 1985.
   (Procs, 5th Topical Conference on High Temperature Plasma Diagnostics, Tahoe City, California, 16-20 September 1984).
   p. 940.
7. The neutral injector auxiliary power supply system in JET: design, manufacture and tests.
   Basile G L, Ciscato D, Dobbing J A, Mondino P L.
   Fusion Technology 13th Symposium, Varese, 24-28 September 1984, Oxford, Pergamon, 1984.
   Vol. 2, pp. 835-842.
8. RF tests on JET first stage antenna system.
   Arbez J, Beaumont B, Brugnetti R, Franklin A, Hanley E, Jacquinot J, Kaye A, Plancoulaine J, Speziale A, Walker C.
   Fusion Technology 13th Symposium, Varese, 24-28 September 1984, Oxford, Pergamon, 1984.
   Vol. 1, pp. 599-604.
9. Impurity studies and transport code modelling of JET plasmas.
   Behringer K H, Bonnerue J, Bulliard A, Carolan P G, Decker G, Denne B, Duchs D F, Ehrenberg J, Engelhardt W W, Forrest M J, Gill R, Gondhalekar A, Hawkes N C, Kallne E, Krause H, Magyar G, Martin J L, Mast F, McCracken G M, Morgan P, Muir D, O'Rourke J, Peacock N J, Ravestein A, Stamp M F, Stubberfield P M, Taroni A, van Maanen-Abels A, Watkins M L.
   Plasma Physics and controlled nuclear Fusion Research, 10th Int. Conference, London, 12-19 September 1984, Vienna, IAEA, 1985.
   Vol. 1, pp. 291-300.
10. Measurement of impurity influxes in JET by visible and VUV spectropscopy.
    Behringer K H, Denne B, Forrest M J, Stamp M F, Summers H P.
    American Physical Society, Bulletin, October 1985, (27th Annual Meeting of the Division of Plasma Physics, San Deigo, 4-8 November 1985).
    Vol. 30, No. 9, pp. 1414.
11. Impurity and radiation studies during the JET ohmic heating phase.

Behringer K H, Denne B, Engelhardt W W, Gill R, Gottardi N, Kallne E, Magyar Mansfield M, Morgan P, Stamp M F, Summers H P, Carolan P G, Forrest M J, Hawkes N C, Peacock N J, Decker G, Krause H, Mast F.
Joint European Torus, JET, 1984, report JET-P(85)08.

12. Tokamak Experiments: by R J Bickerton and B E Keen.
JET Report, JÉT-P(85)24

13. Physics performance of the Joint European Torus.
Bickerton R J.
Plasma Physics and Controlled Fusion, December 1984.
Vol. 26, No. 12a, pp. 1355-1365 and JET Report JET-P(84)02.

14. Latest Results from JET.
Bickerton R J, Alladio F, Bartlett D V, Behringer K, Behrisch R, Bertolini E, Best C, Bonicelli T, Bracco G, Brusati M, Campbell D J, Carolan P G, Christiansen J, Chuilon P, Coad J P, Cordey J G, Corti S, Costley A E, Crisanti, de Michelis C, Denne B, Dietz K J, Duchs D F, Dupperrex P A, Edwards A, Ejima S, Engelhardt W W, Ehrenberg J, Erents S K, Ericksson B T, Forrest M J, Gadeberg M, Gibson A, Gill R, Gondhalekar A, Goodhall D, Gottardi N, Gowers C, Green B J, Grosso G, Hawkes N C, Hemmerich J, Hendricks F, Huart M, Huguet M, Jacquinot J, Jarvis O N, Jones E M, Kallne E, Kallne J C, Kellman A, Kissel S, de Kock L, Krause H, Kukral H, Lallia P, Last J, Lazzaro E, Lomas P, McCracken G, Magyar G, Malacarne M, Mansfield M, Marchese V, Martinelli P, Mast F K, Mondino P L, Morgan P D, Morris A W, Murphy G, Nave MF F, Nielsen P, Niestadt R M, Noll P, O'Rourke J, Pasini D, Peacock N J, Piekaar M W, Pochelon A, Prentice R, Rebut P H, Robinson D C, Ross R, Sadler G, Santaguistina A, Schuller F C, Segre S, Stamp M F, Stangeby P, Steed C A, Stott P E, Stringer T E, Summers D, Summers H P, Tagle J A, Tanga A, Taroni A, Thomas P R, Thomsen K, Tonetti G, Tubbing B J D, Turner M, Valisa M, van Belle P, van der Beken H, Watkins M L, Wesson J A, Zanza V.
JET Report, JET-P(85)15.

15. Integrated control and data acquisition of experimental facilities.
Bombi F.
Computing in Accelerator Design and Operation Europhysics Conference held in Berlin, 20-23 September 1983. Edited by Busse W, and Zelazny R, Springer-Verlag, 1984.
pp. 311-315.

16. The central interlock and safety system of JET.
Bombi F, Nijman J, Van Montfoort J.
Fusion Technology 13th Symposium, Varese, 24-28 September 1984, Oxford, Pergamon, 1984.
Vol. 2, pp. 1133-1139.

17. The gas introduction system of JET.
Boschi A, Dietz K J, Rebut P H.
Fusion Technology 13th Symposium, Varese, 24-18 September 1984, Oxford, Pergamon, 1984.
Vol.1, pp. 247-254.

18. Transport analysis of JET discharges.
Brusati M, Cordey J G.
Controlled Fusion and Plasma Physics, 12th European Conference, Budapest, 2-6 September 1985. Contributed papers, 3 volumes. European Physical Society, 1985.
Vol. 1, pp. 247-254.

19. Plasma-antenna coupling and the related scrape-off layer studies on JET.
Bures M, Evrard M P, Jacquinot J, Lallia P, Sand F.
Controlled Fusion and Plasma Physics 12th European Conference, Budapest, 21-6September 1985. Contributed papers, 3 volumes. European Physical Society, 1985.
Vol. 2, pp. 148-151.

20. Analysis of sawtooth instabilities in JET.
Bartlett D V, Best C, Brusati M, Campbell D J, Christiansen J P, Coda S, Cordey J G, Costley A E, Cottrell G A, de Kock L, Dupperex P A, Edwards A, Fessey J A, Gambier D J, Gill R D, Gondhalekar A, Gowers C W, Hugill J, Hubbard A, Jacquinot J, Jarvis O H, Kissel S E, Lallia P P, Lazzaro E, Morgan P D, Niestadt R M, O'Rourke J, Oyevaar Th, Piekaar H W, Pochelon A, Prentice R, Ross R T, Sadler G, Stamp M F, Stinger T E, Summers D, Tonetti G, Tubbing B J D, Valisa M, van Belle P, Wesson J A.
Controlled Fusion and Plasma Physics, 12th European Conference, Budapest, 2-6September 1985. Contributed papers, 3 volumes. European Physical Society, 1985.
Vol. 1, pp. 130-133.

21. Observation of Zeeman splitting of spectral lines from the JET plasmas.
Carolan P G, Peacock N J, Forrest M J, Trotman D L.
Joint European Torus, JET, 1985, report JET-P(85)05.

22. Charge exchange recombination spectroscopy of ASDEX.
Carolan P G, Duval B P, Field A R, Fielding S J, Hawkes N C, Peacock N J, Behringer K H, Fussman G, Janeschitz G, Soldner F.
Controlled Fusion and Plasma Physics, 12th European Conference, Budapest, 2-6September 19851. Contributed papers, 3 volumes. European Physical Society, 1985.
Vol. 1, pp. 267-270.

23. Resistivity and field diffusion in JET.
Christiansen J P, Campbell D J, Cordey J G, Ejima S, Lazzaro E.
Controlled Fusion and Plasma Physics, 12th European Conference, Budapest, 2-6 September 1985. Contributed papers, 2 volumes. European

Physical Society, 1985.
Vol. 1, pp. 327-330.

24. Commissioning and early operation of the power supply and protection system for the extraction grid of the JET neutral injectors.
Claesen R, Dobbing J A, Hartline R, Egerszegi L, Hrabal D, Mondino P L, Tournesac B.
Fusion Technology 13th Symposium, Varese, 24-28 September 1984, Oxford, Pergamon, 1984.
Vol. 2, pp. 571-834.

25. Impurity fluxes in the boundary layer of JET.
Coad J P, de Kock L, Tagle T, McCracken G M, Erents S K.
Controlled Fusion and Plasma Physics, 12th European Conference, Budapest, 2-6 September 1985. Contributed papers, 3 volumes. European Physical Society, 1985.
Vol. 2, pp. 571-574.

26. Erosion and redeposition of wall and limiter material in JET.
Coad J P, de Kock L, McCracken G M.
Controlled Fusion and Plasma Physics, 12th European Conference, Budapest, 2-6 September 1985. Contributed papers, 3 volumes. European Physical Society, 1985.
Vol. 2, pp. 575-578.

27. Impurity sources in JET.
Coad P, de Kock L, Stott P E, Erents S K, McCracken G, Ehrenberg E, Behrisch R.
American Physical Society, Bulletin, October 1985 (27th annual Meeting of the Division of Plasma Physics, San Diego, 4-8 November 1985).
Vol. 30, No. 9, p. 1525.

28. Particle and energy confinement in ohmically heated JET plasmas.
Cordey J G, D V Bartlett, Bickerton R J, Bracco G, Brusati M, Campbell D J, Christiansen J P, Corti S, Costley A E, de Kock L, Fessey J, Gadeberg M,Gibson A, Gill R D, Gottardi N, Gondhalekar A, Gower C W, Hubbard A, Hugenholtz C A, Jarvis O N, Krause H, Lazzaro E, Lomas P J, Mast F K, Morgan P D, Nielsen P, Noll P, Pick M, Prentice R, Ross R T, Sadler G, Schuller F, Stamp M F, Summers D, Tanga A, Thomas P R, Tonetti G, van Belle P, Zanza V.
Plasma Physics and Controlled Nuclear Fusion Research, 10th Int. Conference, London, 12-19 September 1984, Vienna, IAEA, 1985
Vol. 1, pp.167-177.

29. Present status of JET.
Cordey J G.
Journal of Nuclear Materials, August 1985, (Procs. 1sr Int. Conference on Fusion Reactor Materials, Tokyo, Japan, 3-6 December 1984).
Vol. 133/134, pp. 14-17 and Joint European Torus, JET, 1985 report JET-P(85)06

30. Unification of Ohmic and Additionally Heated Energy Confinement Scaling Laws
Cordey J G. JET Report, JET-P(85)28.

31. Global energy confinement studies in ohmically heated JET plasmas.
Cordey J G, Bartlett D V, Bickerton R J, Brusati M, Campbell D J, Christiansen J P, Corti S, Costley A E, Edwards A, Ejima S, Fessey J, Gadeberg M, Gibson A, Gill R D, Gottardi N, Gondhalekar A, Gowers C W, Hendriks F, Jarvies O N, Kallne E, Kallne J, Kissel S, de Kock L, Krause H, Lazzaro E, Lomas P J, Mast F K, Morgan P D, Nielsen P, Prentice R, Ross R T,O'Rourke J, Sadler G, Schuller F, Stamp M F, Stott P E, Summers D R, Tanga A, Thomas P R, Tonetti G, Watkins M L.
Controlled Fusion and Plasma Physics, 12th European Conference, Budapest, 2-6 September 1985. Contributed papers, 3 volumes. European Physical Society, 1985.
Vol. 1, pp. 26-29

32. A Solution of the ICRF Fokker-Planck Equation.
Core W G.
JET Report, JET-P(85)30

33. Analysis of neutral particles in JET.
Corti S, Bracco G, Brusati M, Gondhalekar A, Cordey J G, Grosso G, Hendriks F, Segre S, Zanza V.
Controlled Fusion and Plasma Physics, 12th European Conference, Budapest, 2-6 September 1985. Contributed Papers, 3 volumes. European Physical Society 1985.
Vol. 1, pp. 219-222.

34. First measurements of ECE from JET.
Costley A E, Baker E A M, Bartlett D V, Campbell D J, Kiff M G, Neill G F.
Electron Cyclotron Emission and Electron Cyclotron Resonance Heating, 4th Int. Workshop Rome, 28-30 March 1984, Rome Editor dall'ENEA, 1984.
pp. 1-10

35. Measurements of electron cyclotron emission on JET.
Costley A E, Baker E A M, Bartlett D V, Campbell D J, Kissel S E, Piekaar H W, Niestadt R M, Tubbing B J D.
American Physical Society, Bulletin, vol. 30, no. 9, October 1985 (27th Annual Meeting of the Division of Plasma Physics, San Diego, 4-8 November 1985.
pp. 1414.

36. Electron temperature measurements on JET.
Costley A E, Baker E A M, Brusati M, Bartlett D V, Campbell D J, Decker G, Gadeberg M, Gill R D, Kallne E, Kissel S, Nielsen P, Pasini D, Prentice R.
Controlled Fusion and Plasma Physics, 12th European Conference, Budapest, 2-6 September 1985. Contributed papers, 3 volumes. European Physical Society 1985.
Vol. 1, pp. 227-230.

37. Measurements of Ion Cyclotron Emission from Ohmic and ICRF Disharges in JET. Cottrell G A.
JET Report JET-P(85)13.

38. Determination of experimental tokamak plasma profiles using maximum-entropy analysis.
Cottrell G A, Fairbanks E S, Stockdale R E.
Review of Scientific Instruments, vol. 56, no. 5, pt. 2, May 1985, (Procs. 5th Topical Conference on High Temperature Plasma Diagnostics, Tahoe City, California, 16-20 September 1984)
pp. 984-986.

39. Impurity behaviour during RF heating in JET.
Denne B, Behringer K, Mansfield M, Morgan P D, Stamp M F, Summers H P, Hawkes N C, Peacock N J.
American Physical Society, Bulletin, vol. 30, no. 9, October 1985 (27th Annual Meeting of the Division of Plasma Physics, San Diego, 4-8 November 1985.
p. 1585.

40. Spectroscopic measurements of the impurity content of JET plasmas with ohmicand RF heating.
Denne B, Behringer K H, Engelhardt W, Gill R D, Kallne E, Magyar G, Mansfield M, Morgan P D, Summers H P, Hawkes N C, Peacock N J, Krause H, Mast K F, De Michelis C, Pasini D,
Controlled Fusion and Plasma Physics, 12th European Conference, Budapest, 2-6 September 1985. Contributed papers, 3 volumes. European Physical Society 1985.
Vol. 1, pp. 379-383.

41. Fabrication and characterization of graphite 5890 PT limiters used in TFR and JET tokamaks.
Deschamps P, Dietz K, Yvars M.
Fusion Technology 13th Symposium, Varese, 24-28 September 1984, Oxford, Pergamon, 1984.
Vol. 2, pp. 1243-1246.

42. Start-up and initial operation of JET.
Dietz K J, Bartlett D, Baumel G, Behringer K, Bertolini E, Best C, Bickerton R J, Bombi F, Boschi A, Browne M L, Brusati M, Bulliard A, Campbell D, Carolan P G, Clausing R, Christiansen J, Chuilon P, Cordey J G, Costley A, de Kock L, Duchs D F, Duesing G, Emery R K F, Engelhardt W W, Eriksson T, Forrest M J, Froger C, Fullard K, Gibson A, Gill R, Gondhalekar A, Gowers C,Green B J, Hemmerich J, Huart M, Hugenholtz C A, Huguet M, Jarvis O N, Jensen B E, Krause H, Kupschus P, Last J, Lazzaro E, McCracken G M, Magyar G, Mast F K, Mead M, Mondino P L, Morgan P, Morris A W, Nickesson L, Niedermeyer H, Noll P, Paillere J, Peacock N J, Pick M, Raymond C, Rebut P H, Ross R, Sadler G, Schmidt V, Schuller F C, Sonnenberg K, Stamp M F, Steed C A, Stella A, Stott P E, Summers D, Tanga A, Thomas P R, Usselmann E, van Belle P, van der Beken H, van Montfoort J E, Waelbroeck F, Wesson J A, Winkel T, Winter J, Zwart.
Journal of Nuclear Materials, vol. 128 and 129 December 1984, (Proc. 6th Int. Conference on Plasma Surface Interactions in Controlled Fusion Devices, Nagoya, Japan, 14-18 May 1984).
pp. 10-18.

43. Impurity control in JET.
Dietz K J, Sonnenberg K.
American Physical Society, Bulletin, vol. 30, no. 9, October 1985 (27th Annual Meeting of the Division of Plasma Physics, San Diego, 4-8 November 1985).
p. 1585.

44. Wall Protection in JET.
K J Dietz et al.
JET Report, JET-P(85)16.

45. JET neutral beam injection system, construction and component tests.
Duesing G.
Fusion Technology 13th Symposium, Varese, 24-28 September 1984, Oxford, Pergamon, 1984.
Vol. 1, pp. 59-75.

46. Construction, operation and enhancement of JET.
Dietz K J, Duesing G.
Journal of Vacuum Science and Technology A: Vacuum, Surface and films, vol.3, no. 3, pt. 2 May/June 1985, (Proc. 31st National Symposium American Vacuum Society, Reno, 4-7 December 1984).
pp. 1151-1156.

47. Relation of magnetic activity with confinement in JET and TCA tokamaks.
Duperrex P A, Keller R, Pochelon A, Sawley M L.
Laser Aided Plasma Diagnotics 2nd Int. Symposium, Culham Laboratory, 10-12 September 1985, Culham, Culham Laboratory 1985.
pp. 53-58.

48. Magnetic activity during internal disruptions in JET discharges.
Duperrex P A, Keller R, Malacarne M, Pochelon A.
Controlled Fusion and Plasma Physics, 12th European Conference, Budapest, 2-6 September 1985. Contributed papers, 3 volumes. European Physical Society 1985.
Vol. 1, pp 126-129.

49. Technical aspects of the joint JET-ISX-B beryllium limiter experiment.
Edmonds P H, Dietz K J, Goodall D H J.
Oak Ridge National Laboratory 1984, 19p, Report CONF 841219-19.

50. Technical aspects of the joint JET-TSX-B beryllium limiter experiment.
Edwards P H, Dietz K J, Goodhall D H J.
Journal of Vacuum Science and Technology A: Vacuum, Surfaces and Films, vol. 3, no. 3, pt. 2 May/June 1985 (Proc. 31st National Symposium American Vacuum Society, Reno, 4-7 December 1984).
pp. 1100-1104.

51. Energy confinement scaling of ohmic and ICRF heated JET plasmas.
Ejima S, Bures M, Christiansen J P, Cordey J G,

Jacquinot J, Lallia P P, Thomsen K.
American Physical Society, Bulletin, vol. 30, no. 9, October 1985 (27th Annual Meeting of the Division of Plasma Physics, San Diego, 4-8 November 1985).
pp. 1525.

52. Parameters of the JET edge plasma during OH, RF and open boundary experiments from Langmiur/heat flux probes.
Erents S K, McCracken G, Stangeby P, Tagle J A, de Kock L.
American Physical Society, Bulletin, vol. 30, no. 9, October 1985 (27th Annual Meeting of the Division of Plasma Physics, San Diego, 4-8 November 1985).
p. 1525.

53. Operation and control of the JET poloidal field power supply system.
Eriksson T, Corbyn D B, Huart M, Marchese V, Mondino P L, Raymond C.
Fusion Technology 13th Symposium, Varese, 14-18 September 1984, Oxford, Pergamon, 1984.
Vol. 2, pp. 843-850.

54. The JET neutral beam test bed facility and first results.
Falter H D, Cowern N E B, Deschamps G H, Hemsworth R S, Jones T T C, Massmann P, Mead M J, Stork D.
Fusion Technology 13th Symposium, Varese, 24-28 September 1984, Oxford, Pergamon, 1984.
pp. 571-578.

55. JET plasma electron density measurements from 2mm wave interferometry.
Fessey J A, Gowers C W, Hugenholtz C A J, Slavin K.
Joint European Torus, JET, July 1985, report JET-P(85)04.

56. Studies of the edge plasma in JET by visible spectroscopy during ICRF heating.
Forrest M J, Carolan P G, Hawkes N C, Peacock N J, Cottrell G, Lallia P.
American Physical Society, Bulletin, vol. 30, no. 9, October 1985 (27th Annual Meeting of the Division of Plasma Physics, San Diego, 4-8 November 1985).
p. 1415.

57. Recycling, isotopic exchange and density behaviour in JET discharges.
Forrest M J, Morgan P D, Corti S, Gondhalekar A, Gowers C W, Magyar G, O'Rourke J J, Stamp M F, Summers D D R, Tanga A, Watkins M L, Ehrenberg J.
Controlled Fusion ad Plasma Physics, 12th European Conference, Budapest, 2-6September 1985. Contributed papers, 3 volumes. European Physical Society 1985.
Vol. 2, pp. 535-538.

58. Impurity sources and impurity influxes in the JET tokamak.
Forrest M J, Stamp M F, Behringer K H, Morgan P D, Summers H P.
Controlled Fusion and Plasma Physics, 12th European Conference, Budapest, 2-6 September 1985. Contributed papers, 3 volumes. European Physical Society 1985.
Vol. 2, pp. 539-542.

59. Minimum required beta in a tokamak reactor.
Freidberg J P, Wesson J A.
Nuclear Fusion, vol. 25, no. 7, July 1985.
pp. 759-769.

60. Electron power deposition profile during ICRF heating on JET.
Gambier D J, Bartlett D V, Bures M, Campbell D J, Cottrell G A, Jacquinot J,Kissel S, Lallia P, Niestadt R, Sand F, Thomsen K, Tubbing B J D.
Controlled Fusion and Plasma Physics 12th European Conference, Budapest, 2-6 September 1985. Contributed papers, 3 volumes. European Physical Society 1985.
Vol. 2, pp. 152-155.

61. Resistively heated plasmas in JET: characteristics and implications.
Gibson A.
Int. Conference on Plasma Physics, Lausanne, 27 June - 3 July 1984. Invitedpapers, 2 volumes, 1984, Brussels, EEC.
pp. 13-38.

62. Obituary - Dr H O Wüster.
Gibson A.
Plasma Physics and Controlled Fusion, vol. 27, no. 8, August 1985.
pp. I-II.

63. Sawtooth oscillations in JET.
Gill R D, Campbell D J, Bartlett D V, Best C, Coda S, Costley A E, Edwards A, Gowers C W, Hubbard A, Kissel S E, Morgan P, Ross R, Stringer T E, Wesson J A.
Institute of Physics Plasma Physics Group 12th Annual Conference on Plasma Physics, Glasgow, 26-28 June 1985.

64. Real-time plasma fault protection system for JET.
Gondhalekar A, Lomas P, Noll P, Reed K, Schuller F.
Fusion Technology 13th Symposium, Varese, 24-28 September 1984, Oxford, Pergamon, 1984.
Vol. 2, pp. 1661-1665.

65. Density build-up in JET.
Gondhalekar A, Cheetham A, Corti S, Morgan P, O'Rourke J, Schuller F C, Watkins M.
American Physical Society, Bulletin, vol. 30, no. 9, October 1985, (27th Annual Meeting of the Division of Plasma Physics, San Diego, 4-8 November 1985.
p. 1525.1

66. Limits in evaluating energy loss profiles from bolometric measurements at JET.
Gottardi N, Krause H, Mast F.
Controlled Fusion and Plasma Physics, 12th European Conference, Budapest, 2-6 September

1985. Contributed papers, 3 volumes. European Physical Society 1985.
Vol. 1, pp. 30-33.

67. The scientific programme of the Joint European Torus, JET.
Green B J.
Physikalische Blatter, vol. 40, no. 3, 1984.
pp. 70-72 (In German).

68. Controlled nuclear fusion. Inexhaustible energy from plasma.
Green B J.
Umschau, vol.84, no. 25/26, 1984.
pp. 770-773 (In German).

69. Developments in neutral injection heating.
Green T S, Coupland J R, Hammond D P, Holmes A J T, Martin A R, Hemsworth R S, Thompson E.
Plasma Physics and Controlled Nuclear Fusion Research, 10th Int. Conference, London, 12-19 September 1984, Vienna, IAEA, 1985.
Vol. 3, pp. 319-327.

70. Components for the neutral injection beam lines.
Haange R.
Preprints of papers presented to The Institution of Mechanical Engineers seminar on The Mechanical Engineering aspects of JET, London, November 1984.
Joint European Torus, JET, 1984, report JET-P(84)12.

71. Effect of particle trapping in ICRF-beam heated tokamak plasmas.
Hellsten T, Core W, Hamnen H, Appert K, Succi S.
Controlled Fusion and Plasma Physics 12th European Conference, Budapest, 2-6 September 1985. Contributed papers, 3 volumes. European Physical Society 1985.
Vol. 2, pp. 124-127.

72. Commissioning of the JET flywheel-generator-convertor systems.
Huart M.
Fusion Technology 13th Symposium, Varese, 24-28 September 1984, Oxford, Pergamon 1984.
Vol. 2, pp. 851-858.

73. JET flywheel generators.
Huart M.
Preprint of papers presented to The Institution of Mechanical Engineers seminar on The Mechanical Engineering aspects of JET, London, November 1984.
Joint European Torus, JET 1984, report JET-P(84)12.

74. A Simple Fixed Frequency Reflectometer for Plasma Density Profile Measurements on JET.
Hubbard A E, Costley A E, Gowers C W.
JET Report, JET-P(85)32.

75. Assembly, commissioning and first operation of JET.
Huguet M.
Joint European Torus, JET, 1984, report JET-P(84)03.

76. Present status of commissioning and operation of JET.
Huguet M and others.
Fusion Technology 13th Symposium, Varese, 24-28 September 1984, Oxford, Pergamon, 1984.
Vol. 1, pp. 91-103.

77. JET Contributions to the 11th Symposium on Fusion Engineering (Austin, Texas, USA, November 1875).
Huguet M, Bertolini E, Noll P et al.
JET Report, JET-P(85)26.

78. Fusion power and the JET project: A general presentation.
Huguet M.
Preprint of papers presented to The Institution of Mechanical Engineers seminar on The Mechanical Engineering aspects of JET, London, November 1984, Joint European Torus, JET, 1984, report JET-P(84)12.

79. JET Contributions to the 13th Symposium on Fusion Technology (SOFT).
Part 1 - Invited papers.
Huguet M, Duesing G, Hemmcrich H, van der Beken H, and Mondino P L.

80. Impurity accumulation in ISX-B during counter-injection - are alternative hypotheses valid?
Isler R C, Morgan P D, Peacock N J.
Nuclear Fusion, vol. 25, no. 3, March 1985.
pp. 386-392.

81. Heating and Current Drive Scenarios with ICRF
Jacquinot J.
JET Report JET-P(85)112.

82. Preliminary RF heating results from JET.
Jacquinot J.
Institute of Physics Plasma Physics Group 12th Annual Conference on Plasma Physics, Glasgow, 26-28 June 1985.

83. ICRF studes on JET.
Jacquinot J, Anderson R J, Arbez J, Bartlett D, Beaumont B, K Behringer, Bertolini E, Bhatnagar V P, Bonicelli T, Bosia G F, Brinkschulte H W, Browne M L, Brusati M, Bures M, Campbell D, Christiansen J P, Christodoulopoulos C O A, Chuilon P, Claesen R, Coad J P, Cordey J G, Corti S, Costley A, Cottrell G, Denne B, Dietz K, Ejima S, Erents S K, Eriksson B T, Evrard M, Fullard K, Gambier D, Gill R D, Gottardi N, Breen B, Grosso G, Hawkes N C, Hellsten T, Hemmerich J L, Huguet M, Jarvis O N, Jones E, Kaye A S, Kimura H, de Kock J, de Kock L, Krause H, Lallia P P, Last J, Lazzaro E, Lomas P J,Magyar G, Mansfield M, Marchese B, Mast F K, McCracken G M, Mondino P, Morgan P, Niedstadt R M, O'Rourke J, Piekaar H, Plancoulaine J, Rebut P H, Rhoden G, Sadler G, Sand F, Santaquistina A, Schmic M S, Schüller F, Segre S, Sibley A, Stamp M F, Steed C A, Summers D, Tanga A, Tagle J A, Thomas P R, Thmosen K, Tubbing B J D, Valisa

M, van der Beken H, Watkins M, Wade T J, Walker C I.
JET Report, JET-P(85)20.

84. Preliminary ICRF results from JET.
Jacquinot J, Anderson R, Arbez J Bartlett D, Beaumont B, Behringer K, Bertolini E, Abosia G, Brinkschulte H, Bures M, Campbell D, Christiansen K, Christodoulopoulos C, Claesen R, Cordey J, Corti S, Costley A, Cottrell G, Denne B, Evrard M, Gambier D, Green B, Grosso G, Huguet M, Jarvis O N, Kaye A, Kimura H, Krause H, Lallia P P, Lomas P, Magyar G Mansfield M, Mast K, Mondino P L, Morgan P Plancoulaine J, O'Rourke J, Rebut P H, Sadler G, Sand F, Schmid M, Segre S, Sibley A, Stamp M, Summers D, Thomsen K, Tanga A, Valise M, Wade T, Walker C.
Plasma Physics and Controlled Fusion, vol. 27, no. 12A, December 1985 (12th Annual Conference, Plasma Physics Group of the Institute of Physics, 26-28 June 1985, University of Glasgow: Invited papers. Edited by R J Bickerton).
pp. 1379-1390 and JET Report JET-P(85)09.

85. Nuclear Data Involved in Present-Day Fusion Reactors.
Jarvis O N.
JET Report, JET-P(85)22.

86. Ion temperature and density measurements in JET using neutron diagnostics.
Jarvis O N, Gordi G, Hone M, Kallen J, Merlo V, Sadler G, van Belle P.
Controlled Fusion and Plasma Physics, 12th European Conference, Budapest, 2-6 September 1985. Contributed papers, 3 volumes. European Physical Society 1985.
Vol. 1, pp. 223-226.

87. Status of the JET Control and Data Acquisition System (CODAS).
Jones E M.
JET Report, JET-P(85)21.

88. Control, data acquisition and analysis for the JET neutral injection testbed.
Jones T T C, Brenan P R, Rodgers M E, Stork D, Young I D.
Fusion Technology 13th Symposium, Varese, 24-28 September 1984, Oxford, Pergamon, 1984.
Vol. 2, pp. 1125-1132.

89. High resolution X-ray spectroscopy diagnostics of high temperature plasmas.
Kallne E, Kallne J, Marmar E S, Rice J E.
Massachusetts Institute of Technology, Plasma Fusion Centre, February 1985.
Report PFC/JA-85-10.

90. Study of diagram lines and satellites in plasma atomic X-ray spectroscopy.
Kallne E, Kallne J, Marmar E S, Rice J E.
American Physical Society, Bulletin, vol. 30, no. 6, June 1985 (Minutes of 5th APS Topical Conference on Atomic Processes in High Temperature Plasmas, Pacific Grove, California, 25-28 February 1985).
p. 1115.

91. Plasma atomic X-ray spectroscopy of tokamaks.
Kallne E, Kallne J, Marmar E S, Rice J E.
Nuclear Instruments and Methods in Physics Research, section B: Beam Interactions with Material and Atoms, vol. B9, no. 4, July 1985 (Procs. Int.Conf. on the Physics of Highly Ionised Atoms, Oxford, England, 2-5 July 1984).
pp. 698-703.

92. Neutron time-of-flight spectrometer for diagnostics for D-T fusion plasma.
Kallne J, Elevant T.
Joint European Torus, JET, 1985, report JET-P(85)03.

93. The JET ICRF antennae systems: description and testbed results.
Kaye A, Arbez J, Beaumont B, Franklin A, Hanley E, Jacquinot J, Panissie H, Plancoulaine J, Walker C.
Fusion Technology 13th Symposium, Varese, 24-28 September 1984, Oxford, Pergamon, 1984.
Vol. 1, pp. 669-674.

94. Breakdown conditions in JET.
Kellman A, Lazzaro E, Noll P, Schüller F C, Thomas P.
American Physical Society, Bulletin, vol. 30, no. 9, October 1985 (27th Annual Meeting of the Division of Plasma Physics, San Diego, 4-8 November 1985).
p. 1524.

95. Status and Prospects of RF Waves in Tokamaks.
Lallia P.
JET Report, JET-P(85)29.

96. The toroidal and poloidal coil systems of JET.
Last J R.
Preprints of papers presented to The Institution of Mechanical Engineers seminar on the Mechanical Engineering aspects of JET, London, November 1984.
Joint European Torus, JET, 1984, report JET-P(84)12.

97. Magnetic separatrix formation in JET.
Lazzaro E, Campbell D, Cordey J G, Denne B, Gibson A, Gottardi N, Kellman A,Last J, Noll P, Schuller F, Summers D, Tanga A, Tagle T, Taroni A, Thomas P.
American Physical Society, Bulletin, vol. 30, no. 9, October 1985 (27th Annual Meeting of the Division of Plasma Physics, San Diego, 4-8 November 1985.
p. 1585.

98. Identification of magnetic helical perturbation in a tokamak.
Lazzaro E, Alladio F, Crisanti F,
Controlled Fusion and Plasma Physics, 12th European Conference, Budapest, 2-6 September 1985. Contributed papers, 3 volumes. European Physical Society, 1985.
Vol. 1, pp. 319-322.

99. Neutral Injection heating in fusion devices: Beam production and heating mechanism.
Lomas P.
Europhysics News. European Physical Society, Bulletin, vol. 16, no. 4, April 1985.
pp. 5-8.

100. Current ramp rate variations in JET.
Lomas P, Malacarne M, Piekaar H W, Schuller R C, Tanga A, Thomas P.
American Physical Society, Bulletin, vol. 30, no. 9, October 1985 (27th Annual Meeting of the Division of Plasma Physics, San Diego, 4-8 November 1985.
p. 1524.

101. Precision measurement of the 1s lamb shift in hydrogen-like argon on the Alcator C tokamak.
Marmar E S, Rice J E, Kallne E, Kallne J, LaVilla R,
American Physical Society, Bulletin, vol. 30, no. 6, June 1985 (Minutes of 5th APS Topical Conference on Atomic Processes in High Temperature Plasmas, Pacific Grove, California, 25-28 February 1985).
p. 1117.

102. Precision measurement of the 1s lamb shift in hydrogen-like argon.
Marmar E S, Rice J E, Kallne E, Kallne J and others.
Massachusetts Institute of Technology, Plasma Fusion Centre, October 1985, 12p, report PFC/JA-85-33.

103. Bolometric diagnostics in JET.
Mast K F, Krause H, Behringer K, Bulliard A, Magyar G,
Review of Scientific Instruments, vol. 56, no. 5, pt. 2, May 1985 (Procs. 5th Topical Conference on Plasma Physics, Glasgow, 26-28 June 1985. Glasgow Institute of Physics, 1985, paper 1.

104. The Interpretation of Plasma Edge Conditions in Tokamaks.
McCracken G M, Stangeby P.
JET Report, JET-P(85)27.

105. The JET power supplies: a review after one year of operation.
Mondino P L.
Fusion Technology 13th Symposium, Varese, Oxford, Pergamon, 1984.
Vol. 1, pp. 119-131 and Joint European Torus, JET, 1984.

106. Spectroscopic measurements of the Joint European Torus using optical fibres to relay visible radiation.
Morgan P D, Behringer K H, Stamp M F, Carolan P G, Forrest M J, Peacock N J.
Review of Scientific Instruments, vol. 56, no. 5, pt. 2, May 1985 (Procs. 5th Topical Conference on High Temperature Plasma Diagnostics, Tahoe City, California, 16-20 September 1984).
pp. 862-864.

107. The JET plasma position and current control system.
Noll P, Browne M, Huart M, Piacentini I, Santaguistina A, Watkins J R.
Fusion Technology 13th Symposium, Varese, 24-28 September 1984, Oxford, Pergamon, 1984.
Vol. 1, pp. 503-509 and Joint European Torus, JET, 1984, report JET-P(84)08.

108. The JET cryopump system -and its cryolines for neutral injection.
Obert W, Duesing G, Kussel E, Kupschus P, Mayaux C, Rebut P H, Santos H.
Fusion Technology 13th Symposium, Varese, 24-28 September 1984, Oxford, Pergamon, 1984.
Vol. 1, pp. 311-318.

109. Poloidally asymmetric edge phenomena in JET.
O'Rourke J, Campbell D, Denne B, Gondhalekar A, Gottardi N, Krause H, MagyarG, Malacarne M, Mast F, Morgan P, Nave M F, Schüller F C, Stamp M F, Summers D.
Controlled Fusion and Plasma Physics, 12th European Conference, Budapest, 2-6 September 1985. Contributed papers, 3 volumes. European Physical Society 1985.
Vol. 1, pp. 155-158.

110. Impurity fluxes and concentrations in the ISX-B beryllium limiter experiment.
Peacock N J, Kallne E, Morgan P D, Lomas P J, Isler R C and others.
Nuclear Fusion, vol. 25, no. 11, November 1985.
pp. 1635-1655.

111. Scaling law systematics.
Pfirsch D, Duchs D F,
Joint European Torus, JET, 1985, report JET-R(85)01.

112. Limiter viewing on JET.
Pick M A, Summers D.
Journal of Nuclear Materials, vol. 128 and 129 December 1984 (Proc. 6th Int.Conference on Plasma Surface Interactions in Controlled Fusion Devices, Nagoya, 14-18 May 1984).
pp. 440-444.

113. The role of metal-hydrogen systems in fusion research.
Pick M A.
Journal of the Less-Common Metals, 103, 1984, papers presented at the Int. Symposium on the Properties and Applications of Metal Hydrides IV, Eilat, 9-13 April 1984.
pp. 5-17.

114. A model for atomic hydrogen-metal interactions application to recycling, recombination and permeation.
Pick M A, Sonnenberg K.
Journal of Nuclear Materials, vol. 131, no. 2+3, April 1985.
pp. 208-220.

115. Electron thermal conductivity coefficients derived from the electron temperature relaxation after an internal disruption.
Piekaar H W, Goedheer W, Niestadt R M, Stringer T, Tubbing B J D.

American Physical Society, Bulletin, vol. 30, no. 9, October 1985 (27th Annual Meeting of the Division of Plasma Physics, San Diego, 4-8 November 1985.
p. 1525.

116. First results from Thomson scattering on JET.
Prentice R, Nielsen P, Gadeberg M.
Review of Scientific Instruments, vol. 56, no. 5, pt. 2, May 1985 (Procs. 5th Topical Conference on Hight Temperature Plasma Diagnostics, Tahoe City, California, 16-20 September 1984).
p. 1070.

117. Report on the 3rd European Tokamak Programme Workshop.
Rager J P, Gibson A, Engelmann F, Wegrowe J G.
Plasma Physics and Controlled Fusion, vol. 27, no. 7, July 1985.
pp. 801-825.

118. First experiments in JET.
Rebut P H, Bartlett D V, Baumel G, Behringer K, Behrisch R, Bertolini E, Best C, Bickerton R J, Bombi F, Bonnerue J L, Boschi A, Bracco G, Browne M L, Brusati M, Bulliard A, Campbell D J, Carolan P G, Christiansen J, Chuilon P, Cordey J G, Corti S, Costley A E, Decker G, de Kock L, Dietz K J, Duchs D F, Duesing G, Emery R K Fk, Engelhardt W W, Eriksson T, Fessey J, Forrest M J, Froger C, Fullard K, Gadeberg M, Gibson A, Gill R, Gondhalekar A, Gowers C, Green B J, Grosso G, Hawkes N C, Hemmerich J, Huart M, Hubbard A, Hugenholtz C A, Huguet M, Jarvis O H, Jensen B E, Jones E M, Kallne G E, Kallne J C, Krause H, Kupschus P, Last J R, Lazzaro E, Lomas P, McCracken G M, Magyar G, Mast F K, Mead M, Mondino P L, Morgan P, Morris A W, Nickesson L, Niedermeyer H, Nielsen P, Noll P, Paillere J, Peacock N J, Pick M, Poffe J P, Prentice R, Raymond C, Robinson D C, Ross R, Sadler G, Saffert J, Schmidt V, Schuller F C, Sonnenberg K, Stamp M F, Steed C A, Stella A, StottP E, Summers D, Tanga A, Thomas P R, Tonetti G, Usselmann E, von Belle P, van der Beken H, von Mondtfoort J E, Watkins M L, Wesson J A, Winkel T, Zanza V, Zwart J.
Culham Laboratory Plasma Physics and Controlled Nuclear Fusion Research, 10th Int. Conference, London, 12-19 September 1984, Vienna, IAEA, 1985.
Vol. 1, pp. 11-27.

119. Thermal instability and disruptions in a tokamak.
Rebut P H, Hugon M.
Plasma Physics and Controlled Nuclear Fusion Research, 10th Int. Conference, London, 12-19 September 1984, Vienna, IAEA, 1985.
Vol. 2, pp. 197-211.

120. First JET results and it prospects.
Rebut P H.
Twenty Years of Plasma Physics Workshop, International Centre for Theorectical Physics, Trieste, September 1984. Edited by B McNamara Philadelphia, World Scientific, 1985.
pp. 3-14 and Euratom Joint European Torus, JET, 1984, report JET-P(84)11.

121. The Joint European Torus: installation, first results and prospects.
Rebut P H, Bickerton R J, Keen B E.
Nuclear Fusion, vol. 25, no. 9, September 1985.
pp. 1011-1022.

122. Low-Z material for limiters and wall surfaces in JET: Beryllium and carbon.
Rebut P H, Hugon M, Booth S J, Dean J R, Dietz K J, Sonnenberg K, Watkins M L, Joint European Torus, JET, 1985, report JET-R(85)03.

123. Magnetic topology, disruptions and electron heat transport.
Rebut P H, Brusati M,
Joint European Torus, JET, 1985, Report JET-P(85)18, (Invited paper at the 12th European Conference on Controlled Fusion and Plasma Physics, Budapest, 2-6 September 1985).

124. Observations of recombination dominated population of upper levels in helium-like argon in the Alcator C tokamak.
Rice J E, Marmar E S, Kallne E, Kallne J.
American Physical Society, Bulletin, vol 30, no. 6, June 1985 (Minutes of 5th APS Topical Conference on Atomic Processes in High Temperature Plasmas, Pacific Grove, California, 25-28 February 1985).
p. 1116.

125. High resolution X-ray observation of argon, molybdenum and sulphur from the Alcator C tokamak.
Rice J E, Marmar E S, Petrasso R, Kallne E, Kallne J, Cowan R.
IEEE Int. Conference on Plasma Science, St. Louis, 14-16 May 1984. Abstracts, New York, IEEE, 1984.
p. 43.

126. Observation of charge transfer between intrinsic neutral hydrogen and Ar (sup 17+) in the Alcator C tokamak.
Rice J E, Marmar E S, Fiore C L, Kallne E, Kallne J.
American Physical Society, bulletin, vol. 30, no. 9, October 1985 (27th Annual Meeting of the Division of Plasma Physics, San Diego, 4-8 November 1985.
p. 1413.

127. Observation of charge-transfer between intrinsic neutral hydrogen and Ar(sup +16) from neutral hydrogen in the ground and excited states in a tokamak plasma.
Rice J E, Marmar E S, Terry J L, Kallne E, Kallne J.
Physical Review Letters, vol. 56, no. 1, 6 January 1986.
pp. 50-53.

128. The JET Cryogenic Supply System.
Roberts R L et al.
JET Report, JET-P(85)14.

129. Modulation of the turbulence level and of the energy flux by sawtooth relaxations in tokamaks.
Rogister A, Hasselberg G, Kaleck A, Boileau A, van Andel H W H, von Hellermann M.
Laser Aided Plasma Diagnostics 2nd Int. Symposium, Culham Laboratory, 10-12 September 1985, Culham, Culham Laboratory, 1985.
pp. 7-12.

130. MHD Activitiy on JET.
Robinson D C, Haynes P, Morris A W.
JET Report JET-P(85)11.

131. Charged particle fusion product measurements in JET.
Sadler G, Jarvis O N, van Belle P, Gowman J, Hone M, Kallne J, Merlo V.
American Physical Society, Bulletin, vol. 30, no. 9, October 1985 (27th Annual Meeting of the Division of Plasma Physics, San Diego, 4-8 November 1985.
p. 1585.

132. Fokker-Planck calculations for JET ICRF heating scenarios.
Scharer J, Jacquinot J, Lallia P, Sand F.
Nuclear Fusion, vol. 25, no. 4, April 1985.
pp. 435-444.

133. Fokker-Planck calculations for JET ICRF heating scenarios.
Scharer J, Jacquinot J, Lallia P, Sand F.
Controlled Fusion and Plasma Physics 12th European Conference, Budapest, 2-6 September 1985k. Contributed papers, 3 volumes. European Physical Society 1985.
Vol. 2, pp. 144-147.

134. Fokker-Planck calculations for JET ICRF heating scenarios.
Scharer J E, Jacquinot J, Lallia P.
American Physical Society, Bulletin, vol. 30, no. 9, October 1985 (27th Annual Meeting of the Division of Plasma Physics, San Diego, 4-8 November 1985.
p. 1589.

135. Experimental observation of disruptions in JET.
Schüller F C, Alladio F, Campbell D, Crisanti F, Kast F K, de Kock L, Krause H, Lomas P, Malacarne M, Nave M F F, Niestadt R, Tonneti G, Tubbing B, Wesson J.
Controlled Fusion and Plasma Physics, 12th European Conference, Budapest, 2-6 September 1985. Contributed papers, 3 volumes. European Physical Society 1985.
Vol. 1, pp. 151-154.

136. Plasma evolution and skin-effects in JET.
Schüller F C, Thomas P R, Kellman A, Lazzaro E, Lomas P, Piekaar H W, Tanga A.
Controlled Fusion and Plasma Physics, 12th European Conference, Budapest, 2-6 September 1985. Contributed papers, 3 volumes. European Physical Society 1985.
Vol. 1, pp. 287-290.

137. Mechanical Design Assessments of Structural Components and Auxiliaries of JET.
Sonnerup L.
JET Report, JET-P(85)19.

138. Tables of excited quantum shell populations of hydrogen-like and lithium-like impurity ions in fusion plasmas, I. The bundled n picture.
Spence J, Summers H P.
Joint European Torus, JET, 1985, report JET-R(85)02.

139. MESHJET. A mesh generation package for finite element MHD equilibrium codesat JET.
Springmann E, Taroni A.
Joint European Torus, JET, 1984, report JET-R(84)01.

140. Recent results from the JET tokamak.
Stott P E.
American Physical Society, Bulletin, vol. 30, no. 9, October 1985 (27th Annual Meeting of the Division of Plasma Physics, San Diego, 4-8 November 1985.
Vol. 1, pp. 86-89.

141. A theory of marfes.
Stringer T E.
Controlled Fusion and Plasma Physics, 12th European Conference, Budapest, 2-6 September 1985. Contributed papers, 3 volumes. European Physical Society 1985.
Vol. 1, pp. 86-89.

142. Anomolous Transport in Tokamak Confinement.
Stringer T.
JET Report, JET-P(85)17.

143. Computational models for wave-particle interactions.
Succi S, Appert K, Core W, Hamnen H, Hellsten T, Vaclavik J.
Ecole Polytechnique Federale de Lausanne, September 1985, 45p, report LRP 269/85.
Presented at the 3rd European Workshop on Problems in the Numerical Modelingof Plasmas, Varenna, September 1985.

144. Infrared measurements on carbon limiters in JET.
Summers D, Lowry C, Mast F, Morgan P, Stangeby P C.
Institute of Physics Plasma Physics Group 12th Annual Conference on Plasma Physics, Glasgow, 26-28 June 1985.

145. Density, temperature and power measurements in the JET edge plasma using heat flux/Langmuir probes.
Tagle J A, de Kock L, Erents S K, McCracken G M.
Controlled Fusion and Plasma Physics, 12th European Conference, Budapest, 2-6 September 1985. Contributed papers, 3 volumes. European Physical Society 1985.
Vol. 2, pp. 579-582.

146. Global particle balance and recycling in first JET discharges.
Tanga A, Gowers C W, Hugenholtz C A, Morgan P, Schüller F C.
Joint European Torus, JET, 1984, report JET-P(84)09.

147. Start-up of the Ohmic Phase.
Tanga A and Thomas P R.
JET Report, JET-P(85)23.

148. The formation of a magnetic separatrix in JET.
Tanga A, Campbell D J, Denne B, Gibson A, Gottardi N, Kellman A, Lazzaro E, Mast K F, Noll P, Schuller F C, Summers D, Tagle A J, Thomas P R, Valisa M, McCracken G, Stangeby P.
Controlled Fusion and Plasma Physics, 12th European Conference, held in Budapest, 2-6 September 1985. Contributed papers, 3 volumes. European Physical Society 1985.
Vol. 1, pp. 22-25.

149. Transport calculations for JET discharges with ICRH.
Taroni A, Abels van-Maanen A E P M, Core W, Duchs D F, Hellsten T, Muir D G, Stubberfield P M, Tibone F, Watkins M L.
Controlled Fusion and Plasma Physics, 12th European Conference, Budapest, 2-6 September 1985. Contributed papers, 3 volumes. European Physical Society 1985.
Vol. 1, pp. 22-25.

150. ICRF heating experiments in TFR using a low-field-side antenna.
TFR Group, Sand F.
Nuclear Fusion, vol. 25, no. 12, December 1985. pp. 1719-1732.

151. MHD behaviour and discharge optimization in JET.
Thomas P R, Wesson J A, Alladio F, Bartlett D, Behringer K, Bickerton R J, Brusati M, Campbell D J, Christiansen J P, Cordey J G, Costley A E, CrisantiF, de Kock L, Dietz K J, Dupperrex P A, Engelhardt W W, Gibson A, Gill R D, Gottardi N, Gowers C W, Green B J, Hemmerich J L, Hugenholtz C A, Huguet M, Keller R, Krause H, Last J, Lazzaro E, Mast F K, Morgan P, Morris A W, Niedermeyer H, Noll P, Pick M, Pochelon A, Rebut P H, Robinson D C, Ross R T, Sadler G, Schuller F C, Stringer T E, Summers D, Tanga A, Tonetti G, van Belle P.
Plasma Physics and Controlled Nuclear Fusion Research, 10th Int. Conference,London, 12-19 September 1984, Vienna, IAEA, 1985.
Vol. 1, pp. 353-361.

152. Volt-seconds consumption of JET discharges.
Thomas P R, Christiansen J P, Ejima S,
Controlled Fusion and Plasma Physics, 12th European Conference, Budapest, 2-6 September 1985. Contributed papers, 3 volumes. European Physical Society 1985.
Vol. 1, pp. 283-286.

153. A twelve-channel grating polychromator for measurement of electron temperature in JET.
Tubbing B J D, Barbian E, Campbell D J, Hugenholtz C A J, Niestadt R M, Oyevaar Th, Piekaar H W.
Controlled Fusion and Plasma Physics, 12th European Conference, Budapest, 2-6 September 1985. Contributed papers, 3 volumes. European Physical Society 1985.
Vol. 1, p. 215-218.

154. Vacuum system and wall conditioning in JET.
Usselmann E, Dietz K J, Hemmerich H, Schüller F C, Tanga A.
Fusion Technology 13th Symposium, Varese, 24-28 September 1984, Oxford, Pergamon, 1984.
Vol. 1, pp. 105-117.

155. Fluctuation measurements on Textor using C02 laser scattering.
van Andel H W H, Boileau A, von Hellermann M.
Laser Aided Plasma Diagnostics 2nd Int. Symposium, Culham Laboratory, 10-12 September 1985, Culham, Culham Laboratory 1985.
pp. 1-6.

157. JET ICRF power plant.
Wade T, Anderson R, Bosia G, Schmid M.
Fusion Technology 13th Symposium, Varese, 24-28 September 1984, Oxford Pergamon, 1984.
Vol. 1, pp. 727-732.

158. The vacuum vessel.
Walravens M J.
Preprint of papers presented to The Institution of Mechanical Engineers seminar on The Mechanical Engineering aspects of JET, London, November 1984. Joint European Torus, JET, 1984, report JET-P(84)12.

159. Welding and Brazing of JET Machine Components.
Walravens M (Ed.).
JET Report, JET-R(85)04.

160. Sawtooth Oscillations.
Wesson J.
JET Report, JET-P(85)25.

161. Density limit disruptions in JET.
Wesson J, Gowers C, Mast F, Nave F, Watkins M, Turner M F, Hahn W.
Controlled Fusion and Plasma Physics, 12th European Conference, Budapest, 2-6 September 1985. Contributed papers, 3 volumes. European Physical Society 1985.
Vol. 1, pp. 147-150.

162. Tokamak disruptions.
Wesson J A, Sykes A, Turner M F.
Plasma Physics and Controlled Nuclear Fusion Research, 10th Int. Conference, London, 12-19 September 1984, Volume 2, Vienna, IAEA, 1985.
pp. 28-31.

163. JET magnet coil instrumentation.
Zwart J W, Keane D V, Thomsen F.
Fusion Technology 13th Symposium, Varese,

24-28 September 1984, Oxford, Pergamon 1984. Vol. 2, pp. 1119-1124.

164. JET Joint Undertaking Progress Report 1984. Edited and compiled by Keen B E, Kupschus P. Euratom, JET Joint Undertaking, September 1985. 161p. EUR 10223EN, EUR-JET-PR2.

165. Annual Report 1984. Edited by Kind P J D, O'Hara G W. Euratom, JET´ Joint Undertaking, Abingdon, August 1985 82p EUR 10222EN, EUR-JET-AR7.

166. JET contributions to 12th European Conference on Controlled Fusion and Plasma Physics, Budapest, 2-6 September 1985. Many JET Authors. Joint European Torus, JET, 1985, Report JET-P(85)10.

167. JET Poster Contributions at 27th American Physical Society (APS) Meeting (San Diego, USA, November 1985). Many JET authors. JET Report, JET-P(85)31.

Appendix IV

Low-Z Material for Limiters and Wall Surfaces in Jet: Beryllium and Carbon

P.H. Rebut, M. Hugon, S.J. Booth, J.R. Dean,
K.J. Dietz, K. Sonnenberg and M.L. Watkins

Jet Joint Undertaking
(Abingdon, Oxon OX14 3EA, U.K.)

ABSTRACT

It is proposed to use in JET a single low-Z material for the belt limiters and the walls to reduce impurity radiation losses to the lowest level. The only practical materials are graphite and beryllium. Their relative merits are compared in this paper. Graphite has better thermomechanical properties than beryllium, but simulation experiments on beryllium carried out at Sandia National Laboratory and in ISX-B have proved these properties sufficient for the belt limiters. Recent measurements indicate that beryllium retains 2-3 times less hydrogen than graphite. The ISX-B experiments have shown that beryllium has an excellent gettering action also. The main drawback of beryllium is the toxicity of its dust, but the control of beryllium dust is well within standard industrial techniques. It is concluded that beryllium offers the best prospects as a material for the JET belt limiters and walls.

I INTRODUCTION

The study of plasma-wall interactions is one of the four main aims of the JET experiment as outlined in Ref. /1/. To reach the near-reactor conditions aimed at in JET and hence to justify the eventual use of tritium, it will be necessary to solve the plasma-wall problem to the extent that both the radiation and the dilution effects in the plasma core are sufficiently small.

1. Belt limiters

In the next phases of the project additional heating will be applied progressively to increase the power input into the torus from the present ohmic level of 2-3MW up to ~40MW. To take this increase in power the present discrete, uncooled, carbon limiters will be replaced by two continuous, radiation-cooled, "belt" limiters mounted above and below the mid-plane on the large major radius part of the vacuum vessel (see Fig. 1). The RF antennae will be mounted between these limiters. The design is such that the main plasma-wall interaction takes place on the edges of specially shaped tiles on the belt limiters with a similar arrangement for the antennae protection.

2. Cool plasma mantle or high temperature edge

There are two extreme scenarios for the operation of JET:

- impurities of medium-Z are present in the outer regions in sufficient quantity so that a large fraction of the power input is radiated by the "cool plasma mantle". This mode is probably inescapable if the limiter is made of middle-Z material, (e.g. nickel), or if the Inconel walls are exposed to the plasma. The "cool plasma mantle" mode has the advantage of reducing the power load on the limiters and of being self-regulating.
- the alternative mode of operation is one in which the major part of the power input is deposited on the limiters with only a small fraction radiated. To achieve this, the impurities must have a very low Z ($Z < 8$). This could be obtained, if the plasma only interacts with a very low-Z material (limiters, walls, antennae,....). In this case, it would still be possible to operate in the "cool plasma mantle" mode by controlled injection of elements, such as argon, into the plasma. Clearly, this low-Z solution gives maximum flexibility in permitting a study of both operational modes.

3. Consequences of radiative losses

To reach ignition conditions, radiative power losses due to impurities must be only a limited fraction (<50%) of α-particle heating. When the impurities are fully ionised, bremsstrahlung losses impose an upper limit on Z_{eff} (typically Z_{eff} <6 for Te ≈15keV), which defines a maximum impurity concentration in the plasma centre.

Although the global power balance in a tokamak is fundamental, radiative losses at the edge may play a critical role in plasma stability and confinement.

Disruptions impose a major limitation on tokamak performance: they impose limits on plasma parameters such as the maximum electron density and the lowest q-values attainable and, as a consequence, on the product $n\tau$; they limit machine performance by the forces induced on the vacuum vessel and coils, and by thermal stresses on limiters and walls. With increases in plasma current and, probably, in β, disruptions occur faster, since the plasma requires a more important readjustment of the vertical field to stay in equilibrium. As the densities reached with additional heating may exceed the density limit with ohmic heating, termination of the discharge may well induce further disruptions, once additional heating is stopped. Experimentally, it has been found that disruptions are sensitive to plasma edge conditions (impurities, radiation, wall carbonisation on JET). In a theoretical model /2/, it is predicted that disruptions due to the high density limit could be suppressed by strongly decreasing external losses (radiation and recycling).

Assuming that disruptions could be controlled, thermal collapse might occur, if the losses in the outer plasma region exceed the total input power. The power balance permits the derivation of an upper density limit in the edge, which depends on the nature of the impurities and on the total input power /3/.

"H-mode" properties are interesting to improve the energy confinement time. "H-mode" is due to the emergence of a zone close to the separatrix in the outermost plasma layer, where the confinement is good (classical?). This allows a strong temperature gradient at the edge and higher plasma performance. Under these conditions, impurity accumulation is currently observed: e.g. iron in ASDEX, nickel, chromium and titanium in PBX. When their concentration becomes too large, most of the plasma energy is lost by radiation or charge exchange. This eventually returns the plasma to the "L-mode".

This discussion clearly indicates the necessity of limiting the radiative losses right to the outermost plasma zone. Only impurities with very low atomic number could be tolerated at relatively large concentrations at the plasma edge. The main advantages of having only impurities of very low atomic number Z can be summarised as follows:

- ions are fully stripped and therefore line radiation loss is suppressed at temperatures of a few keV; this is true for $Z \lesssim 10$ at T=3keV;
- the tolerable concentration can be relatively large, since the critical impurity concentration for inhibiting ignition is proportional to Z^{-1} (see Fig. 2);
- for a stationary state, if the ion confinement is close to classical, the impurity density may strongly peak in the plasma centre. The maximum magnitude decreases, as Z decreases.

4. Importance of having a single material for the limiters and the walls

In a tokamak, the main sources of impurities are the limiters and the wall. Their magnitude is generally enhanced by additional heating.

Deposition of wall materials on the limiters and the inverse process are observed in all tokamaks. In JET, the graphite limiters have been covered by the constituents of the wall (in particular nickel) with an average layer of up to 50 monolayers; in ISX-B, the beryllium limiter has been covered with chromium, evaporated on the walls for a prior gettering experiment; in TFR, molybdenum has been deposited on the walls when molybdenum limiters were used and in ISX-B beryllium has covered a part of the wall after the melting of the beryllium limiter. This indicates that is is practically impossible to segregate limiter and wall materials. When different materials are used, it is difficult to know the composition of the materials in contact with the plasma and the effect of the mixture (e.g. carbides, when graphite is used).

5. Present low-Z experiments

In JET, recent experiments have been carried out with four discrete graphite limiters (total area $1.3m^2$) and power input in the range 1-3MW. In order to suppress high-Z impurities and to observe the effect of disoharges with low radiation at the edge, the walls have been carbonised by glow discharge cleaning in mixtures of methane and hydrogen. After carbonisation, the main features of the discharges are:

- the nickel content is strongly reduced. Typically, for a relatively high density pulse ($\bar{n}_e = 3 \times 10^{19} m^{-3}$), the measured impurity concentrations relative to the central electron density are 2.5%, 1% and 0.015% for carbon, oxygen and nickel, respectively. These concentrations give $Z_{eff} = 2.4$ and $n_D/n_e = 0.77$;

- the power radiated by impurities is about 50% of the ohmic power input;
- the release of hydrogen from limiters and wall makes density control difficult during the current pulse.

The trend of using a single low-Z material in JET has been followed in TEXTOR, where heavy wall carbonisation has allowed the injection of 1MW RF heating without disruption, whereas previously it had been limited to 100kW.

6. Ideal limiter and wall requirements

Ideally, the limiter and wall material should have the following properties:

- very low atomic number;
- negligible porosity;
- high melting point;
- large thermal conductivity;
- good resistance against thermal shock;
- low erosion through sputtering or chemical effects;
- low hydrogen retention and low chemical affinity with hydrogen;
- strong affinity to oxygen (gettering action).

7. Summary

These considerations all tend to the conclusion that using a single low-Z material for limiters and walls provides a solution to reduce impurity radiation losses to an acceptable level. The only materials which meet a sufficient number of the above criteria are beryllium and carbon. In this paper, the relative merits of the two materials are discussed. Section II sets out transport code predictions, and thermomechanical and physical properties are compared in Section III. To clarify these points, a beryllium limiter experiment has been undertaken in ISX-B at ORNL, USA; the results of this experiment are reported in Section IV. Due to the toxicity of beryllium, precautions required when entering the JET vacuum vessel containing beryllium are discussed in Section V.

II THE EFFECT OF LOW-Z LIMITER AND WALL MATERIAL ON THE APPROACH TO IGNITION

1. Introduction

Transport code predictions for tritium operation in JET at the full planned power are presented with the aim of allowing conclusions to be drawn regarding the choice of limiter material and the effect of dissimilar materials also being present.

Several impurity contaminants are likely to be present in JET (e.g. nickel deposits from the wall and radiofrequency antennae onto beryllium or carbon limiters, intrinsic oxygen, injected neon). Two ideal situations are considered, classified as "all low-Z" (the limiter and wall are of the same low-Z material, either beryllium or carbon) or "mixed-Z" (the limiter is of low-Z material, the wall is nickel and is assumed not to contaminate the limiter). The oxygen level is assumed to be sufficiently low that gettering is not needed. 100% recycling of the hydrogen isotopes is assumed. Only physical sputtering of impurities is taken into account.

Earlier calculations comparing the use of heryllium and carbon (and nickel) as limiter materials /5, 6/ used a variety of plausible transport models, since no single model existed then to describe tokamak plasmas in all detail.

The results of ohmic operation in JET have allowed some of the uncertainties in these models to be removed, allowing the identification of the most appropriate transport model then used (Section II.2). The results of these calculations are reviewed in Section II.3.

These calculations have also been updated, taking account of the results of JET operation to date (Sections II.4 and II.5).

2. Model assumptions for the most relevant cases in Refs./5,6/

The form of the ICARUS transport model used can be found in /5,6/.

The most important features for the present study are: ALCATOR/INTOR anomalous electron thermal losses ($\chi_e=5\times10^{19}/n_e$); anomalous diffuaive ($D=\frac{1}{4}\chi_e$) and inward convective ($V=2rD/a^2$) particle fluxes; neoclassical values for the ion thermal losses and the electrical resistivity (including trapped particle corrections); transport in the scrape-off layer is characterised by the parallel confinement time, $\tau_{\parallel}=L/V$ (where L is the effective connection length taken to be πRq and V is the effective ion flow speed); impurities are produced at the limiter by sputtering by charged particles, and at the wall by charged particles and charge-exchanged neutrals (self sputtering is included); coronal radiation losses are assumed.

This model is applied to a circular cross-section torus with the same volume as the JET configuration (limiter radius, $a_L=1.62$m; wall radius, $a_W=1.72$m; major radiua R=2.96m).

The heating sources correspond to those for the full planned power of JET (Phase IV operation with a toroidal field of 3.45T) and comprise the sum of:

a. ohmic heating with a current of 4.8MA from time, t=0s;
b. injection of neutral deuterium at a power level of 10MW at an energy of 160keV (a total power of 17.25MW including the fractional energy components) from time, t=0s;
c. a uniform ion heating profile of about 0.1MWm^{-3} to represent some form of radiofrequency heating at an effective level of 15MW within the limiter radius from time, t=1s; and
d. alpha particle heating by plasma-plasma and beam-plasma interactions assuming a 50:50 mixture of deuterium and tritium.

A mean deuterium/tritium starting density of $4.4\times10^{19}\text{m}^{-3}$ is assumed.

3. Results of the most relevant cases in Refs. /5,6/

The results of simulations presented in /5,6/ for all low-Z and mixed-Z cases are summarised in Table I at a time of 3a, when the central ion temperature has, in most cases, reached its maximum value.

In terms of plasma performance for these high density cases (central deuterium/tritium densities $\sim10^{20}\text{m}^{-3}$), there is little to choose between beryllium and carbon as the limiter material for either the all low-Z or the mixed-Z cases. The central temperatures are quite high (9-10keV) and a modest alpha power results (3-6MW).

The main difference arises between the all low-Z and the mixed-Z cases in the level of limiter erosion and radiated power. With all low-Z cases, the edge temperature, the power flux to the limiter and the limiter erosion are all high, and the radiated power is low. With mixed-Z cases, the edge temperature, the power flux to the limiter and the limiter erosion are all low, and the radiated power is high.

4. Updated model assumptions

A result of ohmic operation in JET has been the refinement of the basic transport model, the most important changes being an anomalous electron thermal diffusivity that is one-half of the ALCATOR/INTOR value ($\chi_e=2.5\times10^{19}/n_e$) during the ohmic phase of operation; during additional heating the value of the ohmic diffusivity is increased by a factor of two and held independent of density; twice the neoclassical ion thermal losses; and a particle diffusion coefficient, $D=0.5\text{m}^2\text{s}^{-1}$.

The model is applied to a full aperture, D-shaped JET plasma (limiter radius, $a_L=4.21$m, wall radius, $a_W=4.32$m, major radius, R=2.96m in the horizontal mid-plane; ellipticity=1.6; triangularity=0.25).

The heating sources are as indicated in Section II.2, except:

a. ohmic heating with 3.8MA starts at time, t=0s;
b. the injection of neutral deuterium from time, t=1s at a power level of 10MW at an energy of 160keV (a total power of 15MW with the present best estimates of the fractional energy components) is modelled more accurately by a multiple pencil beam description which takes full account of the neutral beam injection and tokamak plasma geometries;
c. the radiofrequency heating starts at time, t=2s.

A lower mean deuterium/tritium starting density of $2.2\times10^{19}\text{m}^{-3}$ is assumed, consistent with the density limit observed so far in ohmic operation.

5. Results of updated calculations

The results of the more recent calculations are summarised in Table II at a time of 3s. Most differences with the previous calculations may be attributed to the assumed lower ohmic starting density.

In terms of plasma performance for these low density cases (central deuterium/tritium densities $\sim 6 \times 10^{19} m^{-3}$ at 3s), there is still little to choose between beryllium and carbon as limiter material. The central temperatures (10-13keV) are a little higher than those obtained previously, but the alpha power is lower ($\sim$2MW) as a result of the lower density. The limiter erosion and the low-Z concentrations are higher.

The main difference from the earlier calculations arises with the mixed-Z cases, in which, at low plasma density, insufficient nickel accumulates in the low density edge region to radiate more than 50% of the input power. The edge temperature, the power flux to the limiter and the limiter erosion are therefore high, similar to the corresponding all low-Z cases.

6. Conclusions

With the models examined (which assume a negligible oxygen level, 100% recycling of hydrogen isotopes and only physical sputtering of impurities) these calculations indicate there is little to choose between beryllium or carbon as the limiter material for JET. This result is independent of the effective wall material, the plasma density and the heating model.

Systems comprising all low-Z material lead to high edge temperatures, high power flows to the limiter, high limiter erosion and low impurity radiation for both low and high plasma density.

Low-Z impurity levels remain tolerably low (despite the large limiter fluxes and the assumed transport model which peaks impurities on axis) because redeposition on the limiter and modest transverse transport into the bulk plasma occurs. This model is appropriate for present ohmic discharges in JET.

Systems comprising mixed-Z materials are shown to be much more sensitive to changes in, for example, the plasma density. At low density, the edge temperature, the power flow to the limiter and the limiter erosion are all high and the impurity radiation is low, similar to the corresponding all low-Z cases. At high density, however, the edge temperature, the power flow to the limiter and the limiter erosion are all low and the impurity radiation is high.

III COMPARISON OF BERYLLIUM AND GRAPHITE PROPERTIES

1. Physical properties

Table III compares some of the physical properties of beryllium and graphite.

Properties favouring beryllium as a limiter material are its low Z value and its negligible porosity. However, its relatively low melting point makes it more vulnerable to disruptions (see Section 2c).

Graphite has the advantage of not melting but sublimating and exhibits a larger heat of sublimation. Its main disadvantage is its relatively large porosity, which could generate a serious outgassing problem if a complete coverage of the inner wall with graphite is envisaged.

2. Thermal and mechanical resistance

a. During normal plasma pulses

To compare the effects of thermal stresses on different materials, $\sigma_B/E.\alpha.\Delta Ts$ is usually quoted as a figure of merit. For short temperature pulses, $\Delta T_s \propto (c.k)^{-\frac{1}{2}}$, the figure of merit is about 5 times larger for graphite than for beryllium (see Table III). However, this factor of 5 is likely to be an overestimate, since it does not take into account the large ductility of beryllium (particularly at high temperature).

To test the thermomechanical properties of beryllium for suitability as the JET belt limiters, thermal fatigue experiments have been undertaken:

- in the ISX-B tokamak at Oak Ridge, where a beryllium limiter was subjected to short high power heat pulses (2500 W/cm^2 for 0.3s) (see Section IV.2);

- in an electron beam facility at Sandia National Laboratory, where beryllium samples were exposed to heat loads similar to those that would be experienced in JET (300 - 450W/cm^2 for 10s). A first set of samples has survived 10000 cycles of 300W/cm^2 without structural damage. Microcrack formation was observed after about 3000 cycles. These cracks widened in the course of the experiment and additional microcracks appeared. The range of crack growth did not exceed 5mm and is in good agreement with the range of plastic deformation obtained from elastic-plastic finite element calculation. Thermal fatigue tests at higher heat loads (450 W/cm^2 for 10 s) are being performed, but from the elastic-plastic calculations no dramatic change in crack formation is expected.

Apart from thermal stresses, the heat load may also be limited by excessive temperatures at the limiter surface. This would result in very large evaporation of the limiter surface material and in intolerable concentrations of this material in the plasma. Surface temperatures of the JET belt limiters have been calculated for an average heat load of 300W/cm^2 and different peak loads. They are compared in Table IV for beryllium and carbon materials. The values shown in Table IV are steady state temperatures after about 10 pulses with a duration of 10s and at a repetition rate of 20mn.

In the case of beryllium, a conservative upper limit for the heat load on the limiter can be defined by the surface temperature at which the evaporation rate is about a factor of 10 lower than the sputtering rate* (see Fig. 3): it is about 440 W/cm^2. Assuming that the scrape-off layer thickness varies by less than a factor of 4, it is possible to shape the belt limiter so that the local peak loads are about 60% higher than the average load.

---

*As the sputtering rate has been calculated for the maximum energy of the particles impinging on the limiter (E=900eV), it is a lower limit. For lower energies (300<E<900eV), the particle flux would be larger for the same power flux and the sputtering yield would also be higher.
Taking for the peak loads 440W/cm^2, the average power flux on the belt limiter is 275W/cm^2, which corresponds to a total load of about 40MW. Surface melting is expected at heat loads of 600W/cm^2 for 10 s. The margin between 440 and 600W/cm^2 may be considered as a safety factor of 1.4 for the beryllium belt limiter.

b. Damage by runaway electrons

In this case, the temperature increase is not determined by the thermal conductivity, but by the specific heat. The figure of merit then becomes $\sigma_B.c/E.\alpha$. The value for graphite is about 5 times higher than for beryllium, but this comparison does not take into account the high ductility of beryllium.

So far, damage by runaway electrons has been observed for graphite only /7/. It shows a laminar fracture about 1 mm deep. Similar damage is expected for beryllium, since the heat effected zone (determined by the density of the material) should be the same for both materials.

It should be noted that, in contrast to Inconel in JET, beryllium is not expected to melt under runaway electron impacts. The temperature increase resulting from volumetric energy deposition should be only about 500°C in beryllium due to its low density.

c. Damage by disruptions

Only theoretical calculations are available. For example, disruptions depositing an energy density of 1000J/cm^2 over a period of 5ms are expected to evaporate a 100µm thick layer and to melt an additional layer of about 100µm thickness for beryllium. Evaporation to a depth of only 50µm is expected for graphite

due to its higher heat of sublimation. Since it is not clear whether the melted layer of beryllium will be stable against eddy current forces /8/ or internal pressure, erosion could be 2 to 4 times higher for beryllium than for graphite.

3. Sputtering

For graphite, sputtering depends strongly on temperature: it is enhanced by chemical effects around 550°C and by radiation damage at higher temperatures /9/. By contrast, for beryllium, the sputtering exhibits only a weak temperature dependence /10/. At the temperatures indicated in Table IV, yields on sputtering by hydrogen and deuterium are lower for beryllium than for graphite.

4. H - recycling

a. Retention and release of injected (≥50eV) hydrogen

During plasma build-up, a fraction of the hydrogen impinging on the belt limiter is trapped in a thin surface layer. When the limiter is heated up by the plasma pulse, part of the trapped hydrogen is thermally released. The amount of hydrogen trapped and released during the pulse depends on the limiter material, on its temperature when implantation occurs and on the energy of the impinging hydrogen.

Most of the experimental studies for hydrogen retention in materials as a function of temperature have been made using the following procedure: after hydrogen implantation at 20°C, the hydrogen content is measured for different temperatures of the material. The data obtained for beryllium and graphite are shown in Fig. 4 (full symbols). A comparison is only possible for implantation at 1500eV. At room temperature, the amount of trapped hydrogen is larger by nearly a factor of 2 in graphite than in beryllium. However, the release of hydrogen upon heating is quite different for both materials. Beryllium exhibits two release stages at 200 and 480°C, whereas for graphite hydrogen is released in a single stage at about 700°C/11/. These measurements indicate that after heating above 300°C hydrogen retention is larger by more than one order of magnitude in graphite than in beryllium.

However, the above results do not reflect the reality. In JET, while hydrogen implantation occurs, the temperature of the belt limiter will be about 300°C and will further increase after additional heating is applied (see Table IV). Recent measurements for hydrogen retention in beryllium as a function of the implantation temperature /12/ are compared with the data for graphite in Fig. 4 (open symbols). In the case of implantation at 1500eV, beryllium retains less (factor 2-3) hydrogen than graphite above 200°C. This reflects the fact that hydrogen is thermally released from beryllium at a lower temperature than from graphite. As the hydrogen retention curves for beryllium seem to present the same type of behaviour as a function of implantation temperature for different energies, the factor of 2-3 is assumed to be valid for lower energies also.

Hydrogen release by the belt limiter in the case of graphite has been estimated in two different ways: (i) from isotope exchange experiments in JET (e.g. Pulse No. 2751); (ii) by a simple calculation which assumes an electron temperature of 100eV in front of the limiter and a maximum value of 300eV for the sheath potential. Both estimations indicate that an increase in average density of 2 to $8\times10^{19}m^{-3}$ is expected during the discharge as soon as the limiter temperature exceeds 800°C (see Table IV). This might make density control difficult in JET.

b. No reliable data are available for diffusion, solubility and surface recombination of hydrogen for beryllium and graphite.

5. Reaction with oxygen

Carbon combines with oxygen to give volatile oxides (carbon dioxide and carbon monoxide). In contrast, beryllium forms a non volatile, thermally extremely stable oxide. This property allows the use of beryllium as an oxygen getter, as shown in the experiments performed in UNITOR and ISX-B (see Section IV).

6. Conclusions

Although the thermomechanical properties of beryllium are not as good as those of graphite, simulation experiments have proved them sufficient for JET application. However, compared to graphite, beryllium has a lower Z value, has a negligible porosity, retains less hydrogen at high temperatures, has a lower yield on sputtering by hydrogen and can be used as a getter.

IV RESULTS OF THE ISX-B BERYLLIUM LIMITER EXPERIMENT

Before using beryllium as a limiter material in JET, it was decided to study the behaviour of smaller tokamaks equipped with beryllium limiters. A preliminary experiment was carried out in a small tokamak, UNITOR, in Dusseldorf. After the first encouraging results, a more comprehensive set of tests was carried out in ISX-B in Oak Ridge. A brief summary of the ISX-B experimental results /13/ is given in this section.

1. Experiment specifications

The objectives of the experiment were to study in a beam heated machine the behaviour of plasmas in the presence of a beryllium limiter and to investigate the mechanical suitability of this material under high heat loads and high particle fluences.

The experiment was specified for a deuterium fluence of about 10^{22} ions/cm^2 to the limiter. This corresponded to 3000 beam-heated discharges. The limiter was designed to experience a surface temperature rise of 600°C per discharge. The resulting power flux was 2.5kW/cm^2 during a plasma pulse of 0.3s.

To simulate JET conditions, the base temperature of the limiter was kept between 200°C and 300°C at all times. The beryllium limiter was inertially cooled during discharges and had an actively cooled baseplate to remove heat between discharges.

The beryllium limiter was installed at the top of the machine, acting as a rail limiter.

Up to the introduction of beryllium, ISX-B operated with titanium carbide coated graphite limiters, the walls of the vessel being stainless steel, sometimes gettered by titanium and for a short period by chromium. The reference discharges for the assessment of the beryllium limiter were made with the TiC limiter and without gettering. A set of standard parameters was established with plasma major radius 94cm, minor radius 24cm, elongation ≤1.2, toroidal field 1.4 T, plasma current 120kA, average electron density $4.5\times10^{19}m^{-3}$, electron temperature ~700-800eV and injected power 0.8MW. The operational envelope was surveyed by scans of plasma density and current; at the same time, spectroscopic measurements were carried out to assess the impurity behaviour.

2. Limiter performance and heat loads for the different conditions of operation

The beryllium limiter was mainly studied under three conditions:

a. ungettered discharges

During the first three weeks of operation, about 800 shots were performed with ohmic heating only. Power fluxes to the limiter of 400-900W/cm^2 caused surface temperature rises of 100-200°C, and no damage to the limiter was observed.

For the remainder of the experiment, in addition to the ohmic heating, the plasma was heated by neutral injection. With power loads on the limiter up to the design load of 2.5 kW/cm^2, daily still photography of the limiter did not reveal any damage either.

During the first phase of the experiment, the plasma behaviour was dominated by the wall. Due to the high power losses by radiation from impurities coming from the wall, the specified temperature rise of 600°C for the limiter surface could not be achieved with the parameters chosen for the load test (power flux of 2.5kW/cm^2; plasma current of 120kA).

A current scan up to 165kA revealed that the power deposited onto the limiter increased with the plasma current. With current exceeding 140kA, power fluxes of 4-5kW/cm^2 were measured and the limiter surface showed signs of melting. Some cracks were observed on the limiter surface and a few chips spalled off the centre tiles (see Fig. 5-a). Reducing the power flux to the design load again caused no further limiter melting.

b. discharges with limiter surface melting

In order to reduce the effects of the wall on the plasma, it was decided to raise the power load on the beryllium limiter to melt its surface and to cover the walls with beryllium.

In the course of a prolonged series of high power discharges at a fixed plasma current (150kA), the power flux to the limiter was increased from 2.2kW/cm^2 to values exceeding 4kW/cm^2. The limiter surface melted and evaporation of beryllium caused strong gettering of the vacuum vessel. Fig. 5-b shows the damage done to the limiter surface by melting after 500 such discharges. During the shots where melting occurred, plasma operation was possible but not very reproducible.

c. gettered discharges

The power flux was then reduced to the design load again (2.5kW/cm^2). Because of the roughness of the limiter surface, the power flux was high enough at solidified droplets and protrusions to melt the surface locally. This resulted in beryllium evaporation, which gettered the walls sufficiently. Even with the limiter surface damaged, the discharges were good and reproducible. About 2000 shots were performed under these conditions (fluence test). There was no further gross melting and the surface topology was mainly preserved throughout the fluence test. Towards the end of the test, the features became somewhat finer due to evaporation and probably surface cracking (see Fig. 5-c).

Half of the limiter tiles were tesselated (as shown in Fig. 5-a) to reduce surface stress. Post-mortem analysis of the limiter tiles revealed that the tesselations had been quite successful in reducing surface stresses. While the non tesselated tiles show (as expected) surface cracks up to several millimeters deep, the tesselated ones show considerably less cracking. The total weight loss of the limiter, mostly in form of molten droplets, was 2g compared to a total weight of 3kg.

3. Impurities

a. ungettered discharges

For ohmic discharges as well as for low current beam discharges, the main impurity source was the wall and not the limiter. The beryllium content in the plasma was negligible (0.07% at the centre corresponding to a density of 4x10^{16}m^{-3}). The impurity content was dominated by oxygen, carbon and nitrogen with concentrations of about 1% each. The total Z_{eff} from hydrogen and light impurities was 2.4. The contribution from metals was only a few tenths; the titanium and chromium content of the plasma appeared to be 4 times smaller than that observed during operation with the TiC limiter.

b. discharges with limiter surface melting

For discharges with limiter surface melting, the radiated power dropped from 300kW to 150kW at constant plasma current (150kA) and density. The beryllium line intensities increased by factors of 15 to 300. The beryllium content in the plasma could reach values of about 5%. At the same time, radiation from light impurities decreased, indicating that beryllium was very effective in gettering the walls. The central radiation of C and O fell by factors of 2 to 4. Radiation from peripheral ions decreased by a factor of about 10. Fig. 6 illustrates for Be IV and O VI radiation the differences between ungettered and gettered discharges.

c. gettered discharges

Throughout the fluence test and during the post-fluence test, the beryllium influx was comparable (only a factor of 2 lower) to that observed for the discharges with limiter surface melting. The beryllium content in the discharge was about 2%. Because of its low atomic number (Z=4), beryllium does not contribute significantly to the plasma radiation. This is demonstrated very clearly in Fig. 7 which shows the total radiation together with the Be I and O VI radiation. Although the beryllium influx at the limiter increases drastically during the discharge, the total radiation seems to be dominated by the oxygen radiation, even though the oxygen content in the plasma is less than 0.5%.

Table V gives a comparison between the intensities of a few impurity lines for different conditions of operation of ISX-B. Note in particular that during the post-fluence test the oxygen radiation was considerably reduced compared to its level when TiC limiters were used.

4. Plasma behaviour

a. density limit

In ohmic discharges, the plasma performance in the presence of the beryllium limiter was much the same as with the TiC-coated graphite limiters. This is shown in the Hugill diagram (open and full squares in Fig. 8). The density limit was 6x10^{19}m^{-3} for a plasma current of 170kA.

Scans obtained with additional heating (neutral beam injection) before properly gettering the walls are shown in Fig. 8 (full circles and open triangles). In particular, the density scan for a 116kA plasma current indicates that the plasma performance was comparable to previous data obtained with TiC limiters. The density limit was 9x10^{19}m^{-3}.

When the limiter surface melted during the shot, the discharges were not very reproducible and it was difficult to make a full density scan (crosses in Fig. 8). The highest electron density investigated was 9x10^{19}m^{-3} for a 150kA plasma current.

With well gettered walls and a plasma current of 116kA, a maximum electron density of 1.3x10^{20}m^{-3} was achieved before disruption (open circles in Fig. 8).

In ISX-B, beryllium gettering made it possible to reach density limits about 50% larger than titanium gettering and about 20% lower than chromium gettering. It should be emphasized here that the measurements were performed under different experimental conditions for the three investigated getter materials: evaporators were used to getter the walls either with titanium or chromium; during the chromium experiment, pump limiters with a gas flow rate of about 20 torr.l.s^{-1} were also operational; beryllium gettering was done by merely melting the limiter. Thus it cannot be concluded that there is a significant difference in the density limit obtained with the three materials investigated.

b. Confinement

In the case of pure ohmic heating, the energy confinement time was 15ms for an electron density of 6x10^{19}m^{-3} and a plasma current of 170kA. This value is comparable to the previous measurements made with TiC limiters.

Typical values of the energy confinement time τ_E measured with neutral beam heating in beryllium gettered discharges are plotted in Fig. 9 against the mean plasma density n_e.

The majority of the τ_E values measured under these conditions are independent of n_e and in good agreement with the empirical scaling found in ISX-B for gettered discharges: $\tau_E = \tau_E^{ISX}$.

However, a small number of these measurements exhibit a density dependence and are observed to approach the empirical scaling found in ungettered discharges and in gettered discharges with controlled neon puffing (the so-called Z-mode). This improvement in confinement is attributed by the ISX-B team to an outward radial shift of 1-2 cm in the plasma position /14/.
After careful analysis of the data for the beryllium gettered discharges, it can be concluded that beryllium gettering is similar

in its effects on confinement compared to titanium and chromium gettering.

5. Conclusion

As far as we can conclude from the results of ISX-B experiments, beryllium is a prime candidate as a limiter and getter material for JET:

- its contribution to the plasma radiation is negligible, even at high concentrations, due to its very low Z value.
- it is an excellent getter material; its gettering efficiency is similar to that of titanium and chromium, when considering the plasma performance.
- the limiter has successfully withstood the specified fluence and load tests. In addition, thousands of reproducible plasma shots could be performed with the limiter, the surface of which was very rough after intentional melting.

V JET MAINTENANCE WITH BERYLLIUM

1. Introduction

Beryllium is one of the industrial materials (such as asbestos and sandblast debris) for which precautions must be taken against inhalation when they are present as airborne dust. This section explains how the JET vessel can be entered safely to carry out hands-on maintenance when there is a possibility that fine beryllium dust or lightly activated dust has been produced by plasma action. When tritium is also used, all maintenance within the Torus Hall will be executed remotely.

2. Inside the vacuum vessel

It is of paramount importance to the operation of JET that the surfaces forming the vacuum envelope remain absolutely clean, to a level at which molecular quantities are significant. Stringent precautions prevent contamination by people and tools when the vessel is opened. The vessel is entered through an access cabin with a changing room, entering air is filtered, and finally the walls are washed with high pressure demineralised water. It is intended that in future the flow of air into the torus will be minimised by supplying breathing air to the 3 to 6 operators by using air blouses with airlines as shown in Fig. 10, which are light, comfortable and easy to work in.

By the time beryllium is introduced the present access cabin will have been replaced by one illustrated in Fig. 11, which is sealed onto the pumping chamber, contains a personnel access lock and showers and provides the services, air, light, power and communications. The cabin will ensure cleanliness of the vessel and prevent migration of dust in either direction.

In the event that beryllium or active dust contamination is high enough to require precautions, the vessel will be washed with demineralised water, as at present, and wet vacuum cleaned. It might also be vented with steam before it is opened, to produce condensation which will damp down any dust, but the windows cannot at present tolerate water.

Air blouses are readily available and widely used for cleanliness in the pharmaceutical and electronics industries and as protection against airborne dust in others. A probably acceptable average level of airborne beryllium during an 8 hour shift would be about 2 mg/m^3. During entry and throughout the operations the air in the torus and in the various areas of the access cabin will be monitored by drawing known samples through filters and analysing the residue in an atomic absorption spectrometer. Results could be obtained every 30 minutes from any monitor. A static filter and mouthpiece are built into each blouse, for short-term safety in emergencies. Operators will carry monitors inside their blouses, close to their emergency filters. Protection from contact and inhalation of lightly activated dust or of beryllium dust is the same except for the monitoring methods. Radioactivity can be detected immediately.

Surface contamination will also be monitored in the torus and in the various areas of the access cabin. This is not important in the torus since the operators will in any case be completely covered. Beryllium firmly attached to the surface represents no hazard, although it could be removed by dilute nitric acid. Operators will wash down their outer garments in the access cabin and post them out to be cleaned and re-used or discarded.

If conditions should ever require them full suits, as Fig. 12, could be used.

There is no intention to clean up the inside of the torus in order to declare it an area for working with no protection, or to provide ventilation at 20 changes per hour, as required for direct breathing. The greater throughflow might carry dust and would require larger filters which in turn need to be disposed of.

3. Using the articulated boom

An existing overhead rail and travelling hoist can be passed in pieces through the entry cabin and erected inside the torus to carry and position heavy components.

If monitoring shows contamination levels to be sufficiently low, the articulated boom could be used instead, through the port opposite to the entry cabin. Contamination of the boom itself should be insignificant; it will not touch the walls and it is designed so that it can be washed as it is withdrawn. As an extra guarantee against any risk of spreading contamination beyond the boom support rail area, a local PVC enclosure can be set up.

4. Peripheral equipment connected to the torus

Experiments with beryllium in the UNITOR tokamak at the University of Dusseldorf and in the ISX-B at Oak Ridge show that transfer of beryllium into the vacuum circuit will be trivial and probably negligible. Monitored temporary enclosures, tents and bags were used successfully in both cases and can be used similarly on JET components if the vacuum circuit is breached at a point other than an entry point.

The neutral injection boxes and some of the diagnostics are identified as areas where these techniques must be carefully planned and proved in advance.

5. In the Torus Hall

With any possible contamination confined to the torus, or at worst to the access cabin or temporary enclosures, work on components having no connection with beryllium can continue in the Torus Hall with no precautions other than routine air monitoring.

6. Contaminated material

Materials which may have been contaminated will be washed in the lined operating box of the access cabin, then bagged and disposed of. The cabin can be sealed off and used for this and preparatory work while in the Assembly Hall. Large, new or decontaminated components will be passed directly through a roof hatch. If contaminated they could be passed through using bagging techniques.

7. Extra time and personnel needed for maintenance of the vacuum vessel with beryllium

The intended sequences of operations in sending personnel safely into the vacuum vessel are listed in Appendix I. The entry into and the exit out of the torus requires about 35 hours, when it is contaminated by beryllium dust, and around 22 hours, when it is not contaminated. This represents an extra time of 13 hours. To this figure must be added the two days of continuous washing of the vessel to remove beryllium dust before entry, which brings the total extra time to 61 hours. Taking into account the lack of experience at the beginning, one working week extra would be needed for the shutdown in order to have access safely into the torus containing beryllium dust.

One or two supplementary men are needed to look after the operations. An increase of 20% of the teams which enter the torus should be envisaged, to take into account the time lost in changes and showers.

VI CONCLUSIONS

The relative merits of beryllium and graphite as material for the JET limiters and wall have been discussed in length in this report. They can be summarised as follows:

- As beryllium has a lower Z-value than carbon, the total radiation losses are between 2 and 3 times smaller with beryllium than with carbon at the same concentration of impurity ions. However, in both cases, these losses remain low compared to conduction losses in the centre. Nevertheless, in the recent JET experiments with graphite limiters and carbonised walls, it has been observed that a large fraction of the radiated power at the edge is due to carbon and oxygen.

- Beryllium has a negligible porosity and a lower yield on sputtering by hydrogen compared to graphite. At the actual temperatures of the JET belt limiters, the hydrogen retention is 2-3 times lower in beryllium than in graphite. After heating at 800°C, the graphite tiles of the belt limiter could release between 2 and 8×10^{19} hydrogen atoms $/m^3$ on average. This might make density control difficult.

- The thermomechanical properties of beryllium do not appear as good as those of graphite; in particular, surface melting of the beryllium limiter could occur in the case of a severe heat overloading. However, the series of tests carried out at Sandia National Laboratory and in ISX-B have shown that these properties are suitable for JET. In ISX-B, even after melting the limiter surface by intentional heat overloading, its structural integrity was preserved and thousands of reproducible discharges could be performed. For a total input power of 40MW in JET, the beryllium belt limiter will be designed with a safety factor of 1.4 with respect to melting, taking for local peak loads an upper limit imposed by the evaporation rate.

- On best knowledge beryllium is the only low-Z element which can be used as a structural material for limiters and which also acts as an excellent getter. Beryllium is then the best candidate to reduce radiated power losses in the centre as well as at the edge of the plasma, if used as a material for the limiters and wall.

- The main drawback of beryllium is the toxicity of its dust. However, the control of beryllium dust is well within standard industrial techniques. This should be even simpler in JET, because it is a closed system conceived to operate with tritium.

It should be possible to use graphite limiters covered by a thin beryllium layer, but the behaviour of such limiters is still not known (e.g.beryllium carbide formation, melting of beryllium on the graphite surface, which would be heated above the melting point of beryllium). Thus beryllium appears to offer the best prospects as a material for the JET limiters and wall. If gettering is not needed and if the density can be easily controlled, the use of graphite limiters could also be a good solution.

Acknowledgements: The authors are very grateful to Drs R Bickerton, W Engelhardt and P Stott for stimulating discussions and useful criticisms. They also thank Dr B E Keen for a careful reading of the typescipt.

REFERENCES

/1/ The JET Project - Design Proposal - Report of the Commission of the European Communities, EUR 5516e (EUR-JET-R5) (1976)

/2/ Rebut PH and Hugon M, in Plasma Physics and Cont. Nuc.Fusion Res. (Proc. 10th Int. Conf., London, 1984) 2, IAEA, Vienna (1985) 197

/3/ Rebut PH and Green BJ, in Plasma Physics and Cont. Nuc. Fusion Res. (Proc. 6th Int. Conf., Berchtesgaden, 1976) 2, IAEA, Vienna (1977) 3

/4/ Vernickel H and Bohdansky J, Nuclear Fusion 18 (1978) 1467

/5/ Watkins ML and Abels-van Maanen AEPM, Proc. 11th Eur. Conf. on Cont. Fusion and Plasma Physics, Aachen, 1983, 2, EPS (1983) 303

/6/ Watkins ML et al, J. Nucl. Mater. 121 (1984) 429

/7/ Sevier DL et al, J. Nucl. Mater. 103, 104 (1981) 187

/8/ Wolfer WG et al, J. Nuol. Mater. 111, 112 (1982) 560

/9/ Roth J et al, J. Nucl. Mater. 111, 112 (1982) 775

/10/ Bohdansky J et al, Report on Sputtering Measurements of Beryllium, IPP-JET No 31 (1985)

/11/ Doyle BL et al, J. Nucl. Mater. 103, 104 (1981) 513

/12/ Möller W et al, Retention and Release of Deuterium Implanted into Beryllium, IPP-JET No 26 (1985)

/13/ JET Beryllium Limiter Test on ISX-B, Reports of January to December 1984

/14/ Wootton AJ, Bush CE, Edmonds PH, Lazarus EA, Ma CH, Murakami M and Neilson GH(1985), to be published

SYMBOL KEY TO TABLES I AND II

$\hat{T}_i$	Central ion temperature
$\hat{n}_{DT}$	Central deuterium/tritium density
$\hat{Z}_{eff}$	Central effective ionic charge
$\hat{f}_{low}$	Central ratio of low Z impurity and electron densities
$\hat{f}_{med}$	Central ratio of medium Z impurity and electron densities
$\bar{\tau}_E$	Global energy confinement time
$\bar{n}_e$	Volume averaged electron density
$n_{e(lim)}$	Electron density at limiter tip
$T_{i(lim)}$	Ion temperature at limiter tip
$T_{e(lim)}$	Electron temperature at limiter tip
P_{in}	Net input power from radiofrequency heating (15MW), neutral beam injection heating (17.25MW, Table II; 15MW, Table IV) and ohmic heating - Prompt charge exchange losses from the neutral beam
P_α	Alpha Power
P_{rad}	Radiated Power
P_{lim}	Parallel Transport Power to the limiter
P_{wall}	Perpendicular Transport Power to wall
P_{neut}	Charge-exchange and Ionisation Power
$\dot{W}$	Rate of increase of plasma energy
S_{low}	Rate of erosion of low Z material
S_{med}	Rate of erosion of medium Z material

TABLE I

Limiter/Wall	Be/Be	C/C	Be/Ni	C/Ni
$\hat{T}_i$ (keV)	9.8*	9.8	8.7	8.5
$\hat{n}_{DT}$ ($\times 10^{19} m^{-3}$)	10.8	10.9	10.2	10.2
$\hat{f}_{low} / \hat{f}_{med}$ (%)	.5/0	.5/0	.3/.1	.3/.1
$\hat{Z}_{eff}$	1.1	1.1	1.7	1.7
$n_{e(lim)}$ ($\times 10^{19} m^{-3}$)	1.5	1.3	0.72	0.66
$T_{i(lim)}$ (eV)	181	206	39	40
$T_{e(lim)}$ (eV)	229	246	21	20
$\bar{n}_e$ ($\times 10^{20} m^{-3}$)	0.59	0.57	0.51	0.50
$\bar{\tau}_E$ (s)	1.1	1.0	0.6	0.6
P_{in} (MW)	26.6	26.5	29.6	29.7
P_α (MW)	5.6	5.5	3.4	3.2
P_{rad} (MW)	1.1	1.3	32.9	32.8
P_{lim} (MW)	19.5	18.9	0.6	0.5
P_{wall} (MW)	2.3	2.6	.6	.7
P_{neut} (MW)	3.5	5.3	.4	.3
$\dot{W}$ (MW)	5.8	3.9	- 1.5	- 1.4
S_{low}/S_{med} ($\times 10^{22}$ particles/s)	.6/0	.4/0	.02/.1	.04/.1

*$\hat{T}_i$ still increasing at time, t=3s.

TABLE II

Limiter/Wall	Be/Be	C/C	Be/Ni	C/Ni
$\hat{T}_i$ (keV)	12.8	11.3	10.9	9.9
$\hat{n}_{DT}$ ($\times 10^{19} m^{-3}$)	6.0	5.8	6.0	5.8
$\hat{f}_{low} / \hat{f}_{med}$ (%)	3.7/0.0	3.1/0.0	3.5/.09	2.7/.1
$\hat{Z}_{eff}$	1.4	1.9	2.0	2.4
$n_{e(lim)}$ ($\times 10^{19} m^{-3}$)	.68	.84	.68	.82
$T_{i(lim)}$ (eV)	107	132	128	133
$T_{e(lim)}$ (eV)	202	170	172	148
$\bar{n}_e$ ($\times 10^{20} m^{-3}$)	·42	·43	·44	·44
$\bar{\tau}_E$ (s)	.71	.56	.51	.44
P_{in} (MW)	25.4	26.2	26.7	27.1
P_α (MW)	2.5	1.8	1.7	1.4
P_{rad} (MW)	.7	.9	10.1	10.1
P_{lim} (MW)	19.0	20.2	13.5	14.4
P_{wall} (MW)	2.6	2.2	.2	.2
P_{neut} (MW)	1.1	1.1	.2	.3
$\dot{W}$ (MW)	4.5	3.6	4.4	3.5
S_{low}/S_{med} ($\times 10^{22}$ particles/s)	1.4/0.0	1.1/0.0	.8/.09	.7/.08

*$\hat{T}_i$ still increasing at time, t=3s.

TABLE III

	Be	graphite
Z	4	6
density (g/cm^3)	1.85	1.6-1.85
porosity	≈ 0	18% - 28%
electrical resistivity ($\mu\Omega.cm$)	0.03	11.4
heat of evaporation (J/mol)	3.10^5	7.10^5
melting point	1277°C	-
boiling/sublimation point	2770°C	4450°C
k, thermal conductivity ($W.m^{-1}.K^{-1}$)	120	70
c, specific heat ($J.kg^{-1}.K^{-1}$)	2700	1500
α, thermal expansion coefficient ($^oC^{-1}$)	$13x10^{-6}$	$5x10^{-6}$
E, elastic modulus x 10^{-5} ($N.mm^{-2}$)	3-1	0.13
σ_B, ultimate tensile strength ($N.mm^{-2}$)	300-100	50
ductility (% elongation)	4-50	

TABLE IV

	Be			C		
Peak load (W/cm^2)	300	400	500	300	400	500
T_S(°C) at the end of each pulse	740	920	1120	1050	1310	1610
T_S(°C) at the start of each pulse	280	280	280	280	280	280

TABLE V

Ion	λ(Å)	TiC limiter	Beryllium Limiter		
			116kA no melting	155kA melting	116kA post fluence
Be I (L)	2348	–	17	430	357
Be II (L)	3131	–	300	4800	4288
Be IV	76	–	0.4	29	15.2
Cr XIII	328	1.5	0.35	0.70	~0.25
Ti XI (L)	386	7.0	2.35	~0.06	0.7
Ti XII	461	6.0	1.4	1.00	~0.4
Fe XVI	361	2.0	0.9	0.75	0.18
O VI	1032	450	300	30	8.5

CR 85.43

Absolute intensities of typical impurity lines. (L) denotes observation of the limiter.

APPENDIX I: DETAILED PROCEDURE FOR INTERVENING IN THE VACUUM VESSEL THROUGH OCTANT NO. 1

Intervention into the vaouum vessel includes three distinct phases: entry, work inside and exit. The successive operations for the three phases are listed below with their durations, when beryllium dust is present (column A) and absent (oolumn B). The durations are given in hours.

Entry into the vaouum vessel	A	B
1. Vent the vessel to atmosphere. Possibly add steam to condense and damp down dust.		
2. Carry the access oabin (Fig. 11) into the Torus Hall by crane, with prepared equipment in the operating box.	1	1
3. Wheel access cabin into position so that the seal on the cabin mates with a flange on the pumping chamber door. Jacks controlled by a man on a platform adjust the cabin height.	½	½
4. Inflate pneumatic seal between cabin and flange and fit extensible PVC sleeve around it (Fig. 13).	½	0
5. Connect services to cabin, ie water (some at 80 bar for washing vessel), electricity, compressed air, television, intercom, and breathing air for air lines.	½	½
6. Switch on ventilation plant in cabin to produce about 5 mbar depression in operating box. Air is drawn through the change room and personnel lock and discharges back onto the torus hall through HEPA filters.	½	½
7. Connect operating box to pumping chamber by a flexible pipe containing a HEPA filter, to balance pressures. Check balance by flow meter.		
8. Operators don protective clothing (plastic suits and air blouses with airlines) in the interspace between showers in the personnel air lock. Minimum of 3 operators.	½	½
9. Open pumping chamber door, either on hinges or remove by hoist on operating box ceiling.	1	1
10. Health physioist in full suit checks radiation level at and near the torus entry by radiation detectors, air dust samples and swabs.	2	1
11. Additionally, if beryllium present, health physicists take air samples and swabs which are taken away for analysis.		
12. Fit seal face protector on door flange and tape it to the face of the operating box. Fit a protecting tube inside the pumping chamber passage (to prevent things falling into the pumps) and lay staging along the bottom of the tube with a ladder extending down into the vessel.	1	1
13. Plug in services leading below staging into the vessel.	½	½
14. Health physicist enters vessel and monitors conditions.	2	1
Times are for each measurement: the operation will be repeated as deemed neoessary.		
15. Operators enter vessel and clean up contamination as and if necessary by:		
a. Dry vacuum cleaners with HEPA filters	4	0
b. Protecting windows and washing with high-pressure water followed by wet vacuum cleaning.	48	0

Work inside the torus	A	B
16. Progressively extend lighting, TV cameras, microphones and other services.		
17. Proceed with work in vessel. Wearing air suits will not restrict the period over which a man can work without a break. Other factors would impose the limit. These suits, with fresh air cool or warm, are found to be very comfortable.		
Care must be taken as pookets which may contain beryllium dust are exposed when components are removed: they can be washed as they are exposed. Cutting and welding could release beryllium bonded to surfaces: debris must be drawn off by vacuum cleaners into filters.		
18. Contaminated components and materials will be passed into the operating box where they can be washed, bagged if necessary, and posted via the waste drum.		
Some bench work may be done in the operating box.		
Exit from the vacuum vessel		
19. When work is finished, progressively dismantle equipment and carry it back into the operating box, cleaning up the vessel and water washing in the same way as at present.	8	8
20. Re-install the pumping chamber door and wipe down all the surfaces as far as the pneumatic seal (Fig. 13).	6	4
21. Remove the pressure balance pipe, with filter.	½	½
22. Pump down the vacuum vessel and test the door for leaks. Re-fit until satisfactory.		
23. Withdraw cabin until PVC sleeve is extended.	2	0
24. Crimp weld and out the sleeve (Fig. 13, broken lines).		
25. Fit a closure lid over the PVC bag stub on the cabin. The stub remains in position until the next intervention.	½	0
26. At convenient times while the services are connected, personnel may leave the operating box through the personnel air lock which contains 2 showers. They doff their suits between the 2 showers and post them out for deoontamination and re-use or disposal.	½	½
27. Take away the cabin which can be connected to services elsewhere so that further work and cleaning up can continue.	1	1
28. Remove the PVC bag stub from the pumping chamber (Fig. 13, broken line), using vacuum cleaners with HEPA filters, washing down, air monitoring and taking swabs, all under health physics supervision. Access to the Torus Hall must he restricted.	2	0
29. Normal operating conditions are restored.		
- Total times assuming single monitoring operation at item 14 and excluding washing at item 15b:	34½	21½
- Washing at item 15b:	48	0

If it is necessary to have access also in the torus through Octant No. 5, 6 extra hours (3 for item 2 and 3 for item 27) should be needed to carry the intervention module in two sections over the neutral beam injector.

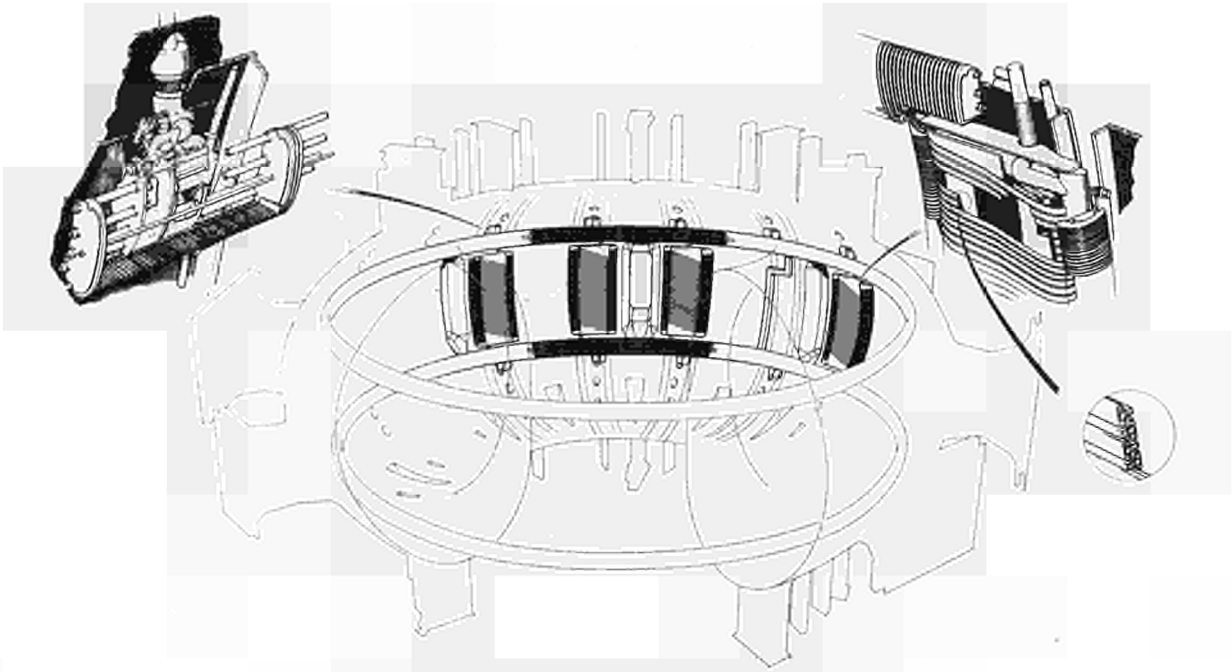

Fig. 1 Antenna and Toroidal Limiter.

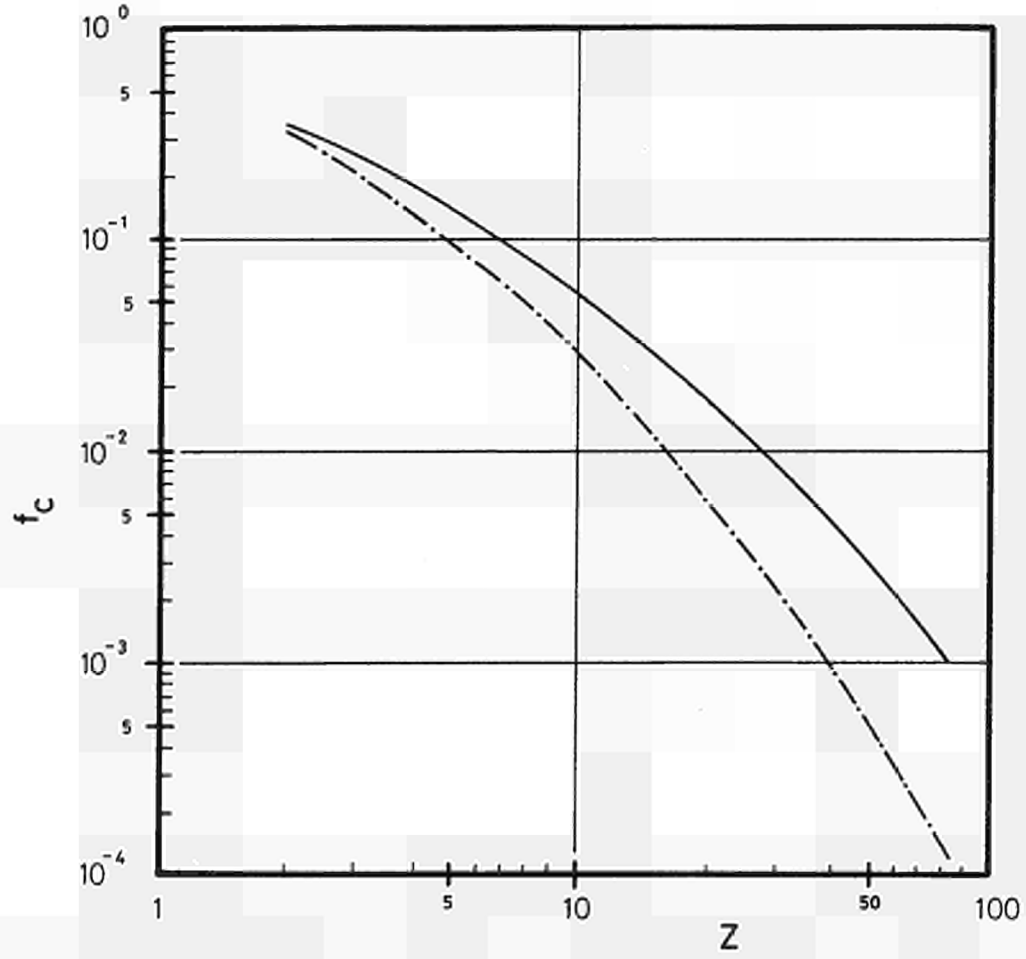

Fig. 2 Critical impurity concentration f_c as a function of atomic number Z for two electron temperatures (———: T = 35 keV; —·—·—·—: T = 12 keV). For Z < 6, radiation loss was considered to be bremsstrahlung only (see Ref./4/).

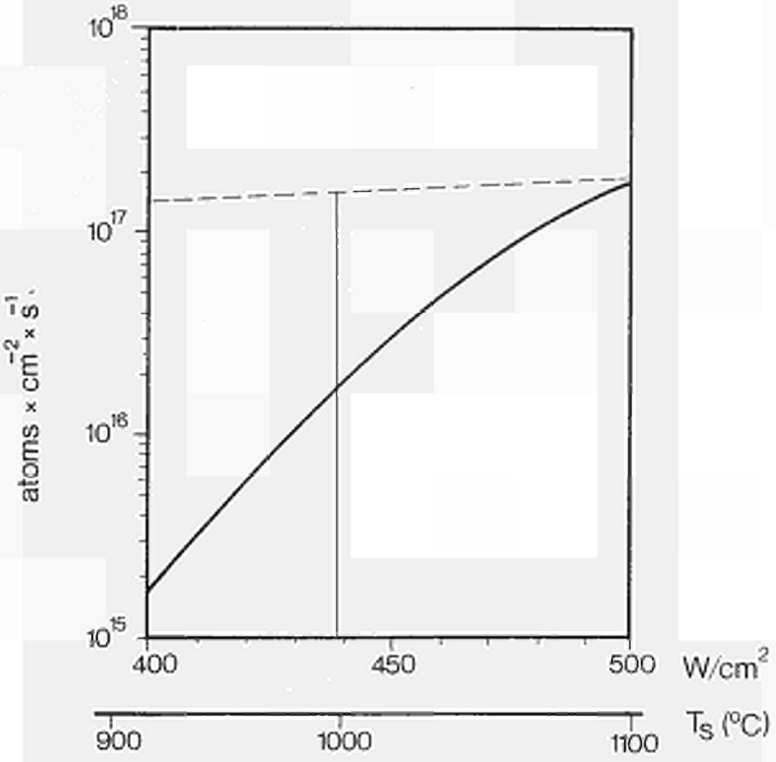

Fig. 3 Evaporation rate (full line) and sputtering rate (dotted line) of beryllium as a function of temperature.

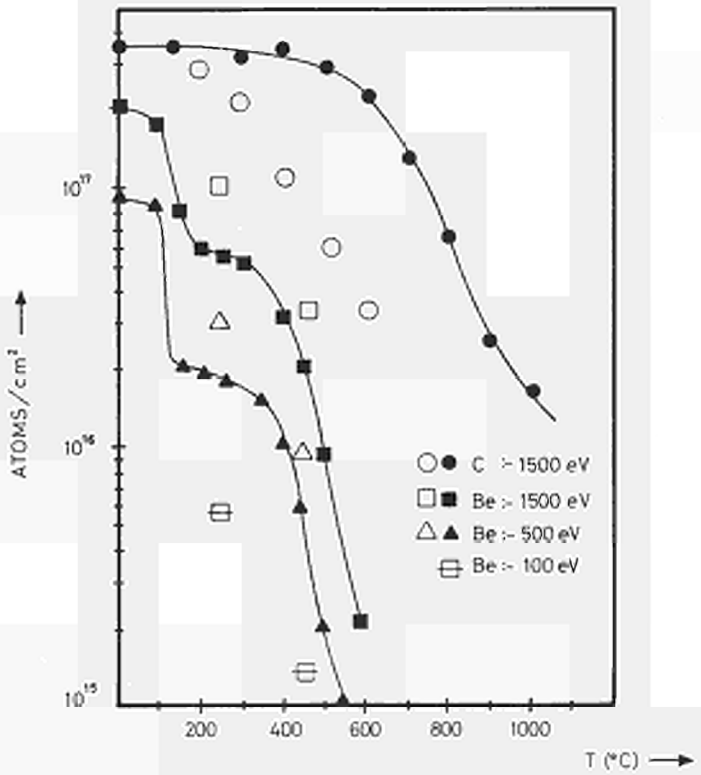

Fig. 4 Hydrogen retention as a function of temperature. The full symbols are the data obtained for implantation at room temperature and a subsequent heating to the temperatures indicated on the graph. The open symbols correspond to the results obtained for implantation at the temperatures indicated on the graph.

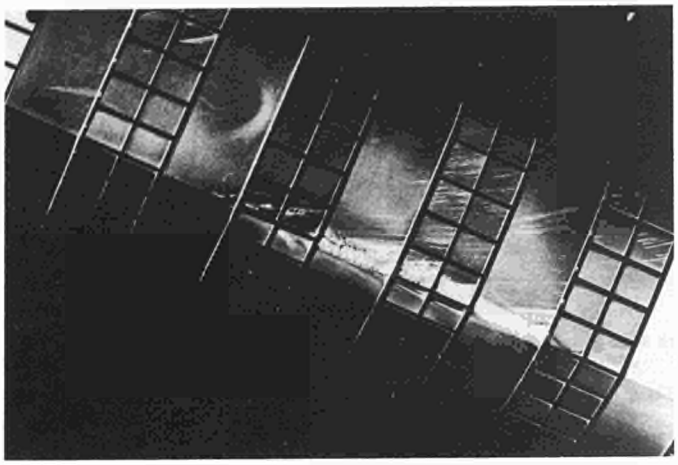

a)

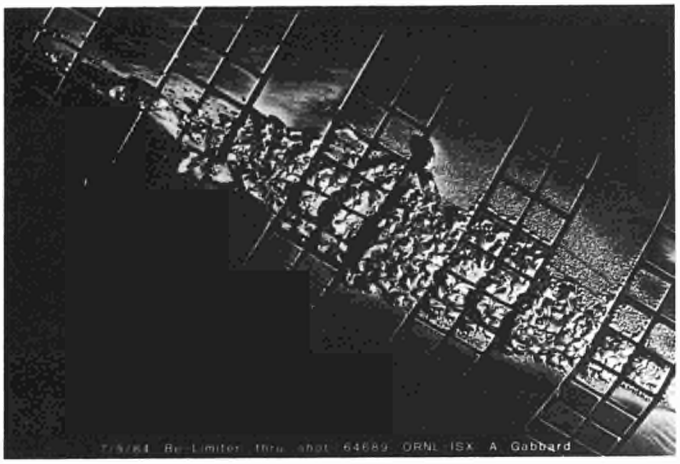

b)

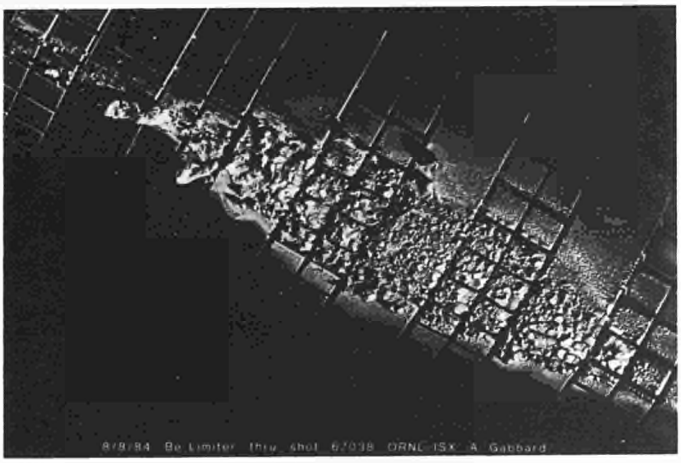

c)

Fig. 5 Surface structure of beryllium limiter after:
(a) a few shots with power fluxes exceeding 4 kW/cm^2
(b) melting
(c) the fluence test.

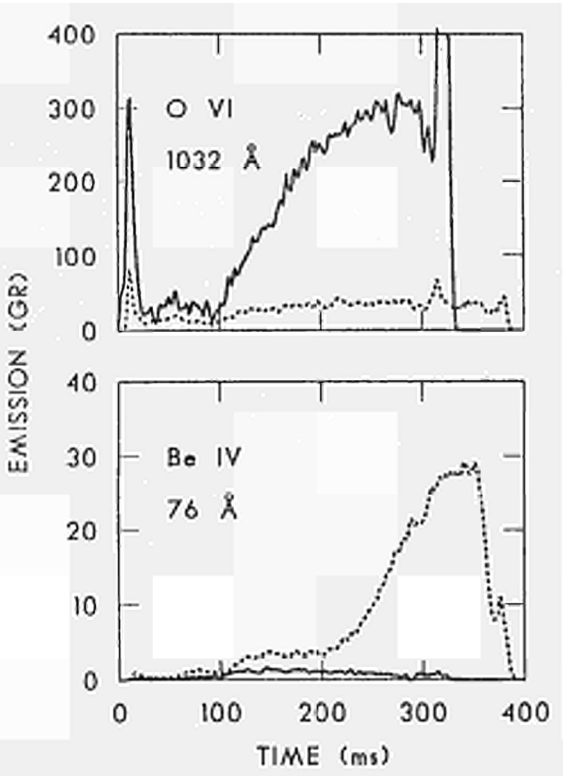

Fig. 6 Temporal behaviour of beryllium and oxygen radiation for ungettered discharges at 116kA (solid curve) and gettered discharges at 150kA (dashed curve). The injected beam power is 0.85MW.

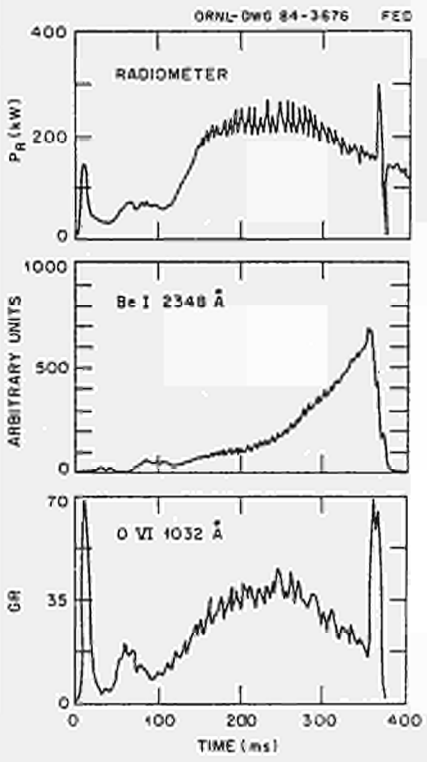

Fig. 7 Temporal behaviour of total radiation, Be I radiation at the limiter, and Ovi radiation. The plasma current is 116kA and the beam heating power is 0.85MW.

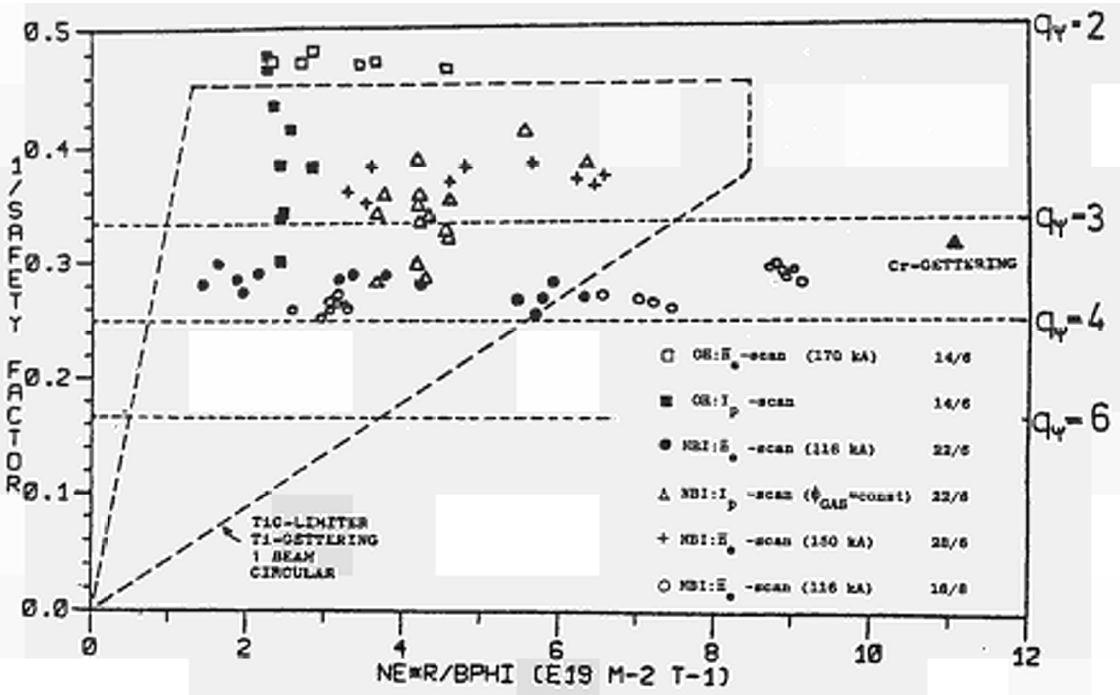

Fig. 8 Hugill Diagram with beryllium in ISX-B (see text).

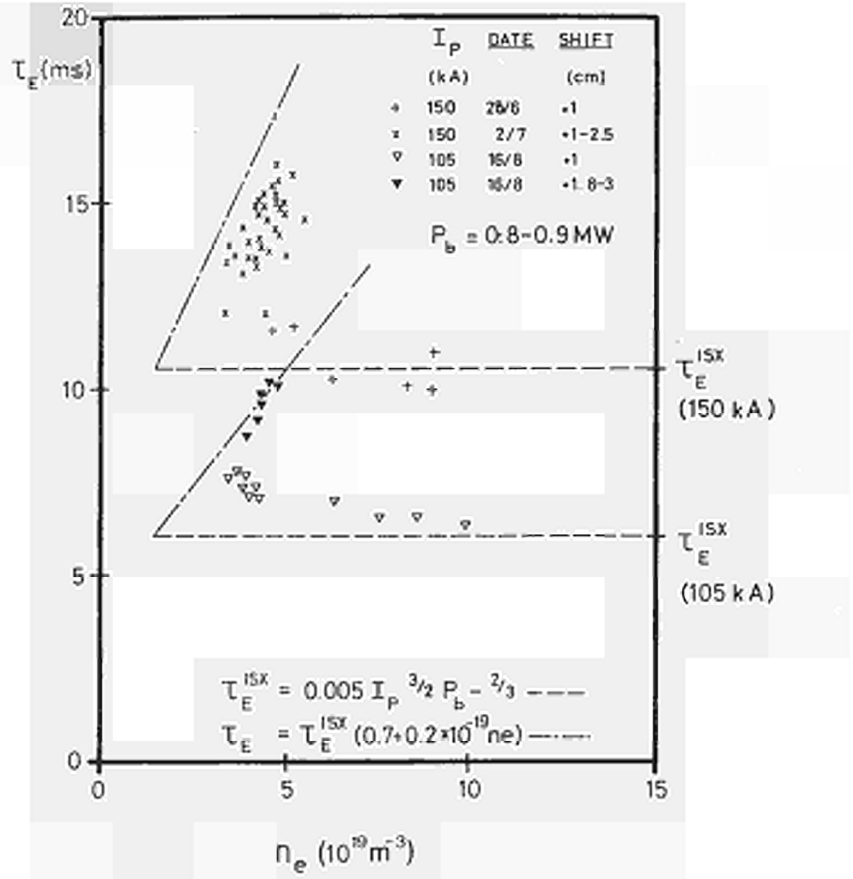

Fig. 9 Density scans of energy confinement time for the beryllium experiment in ISX-B.

Fig. 10 Typical air-blouse. Can use airline in place of filter/power unit shown.

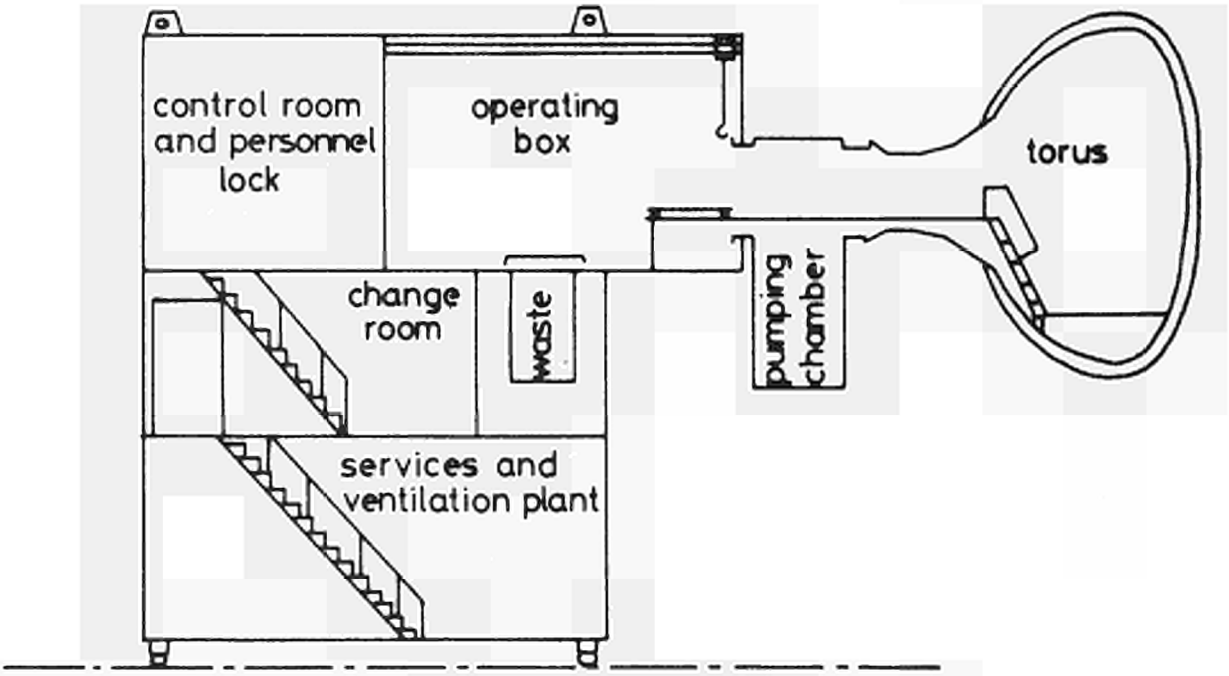

Fig. 11 Torus access cabin.

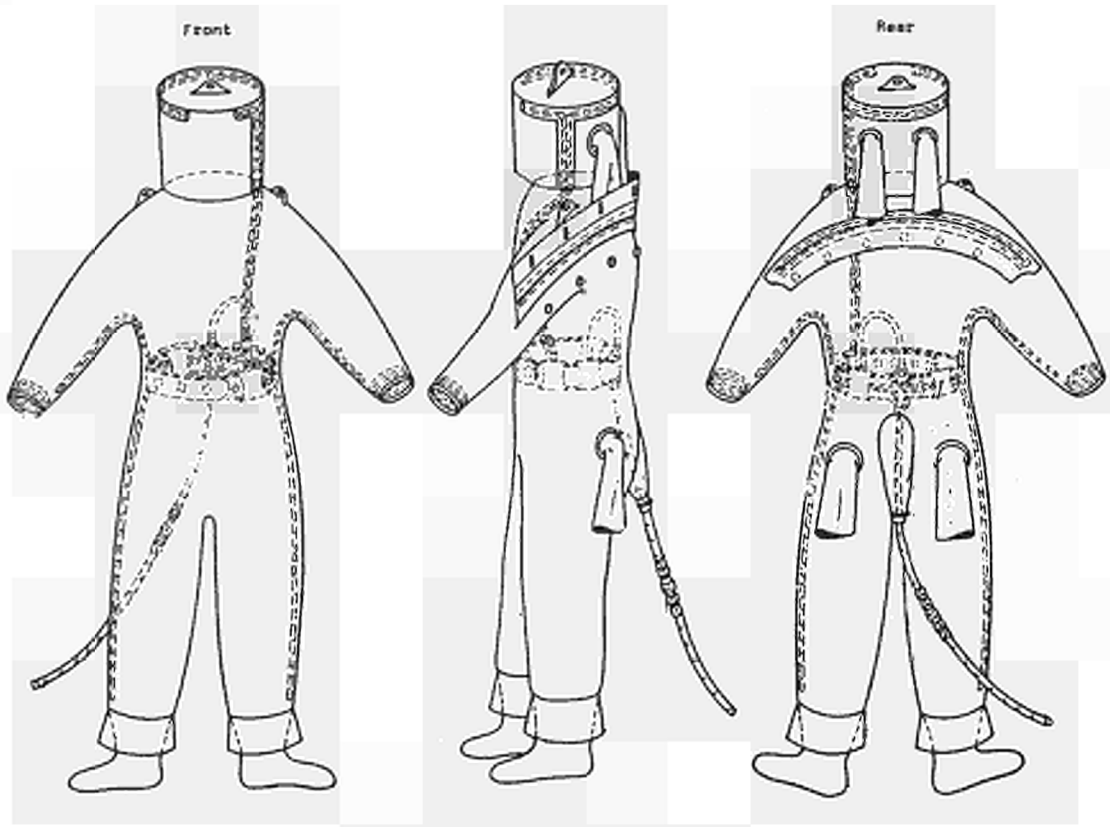

Fig. 12 Typical full air suit.

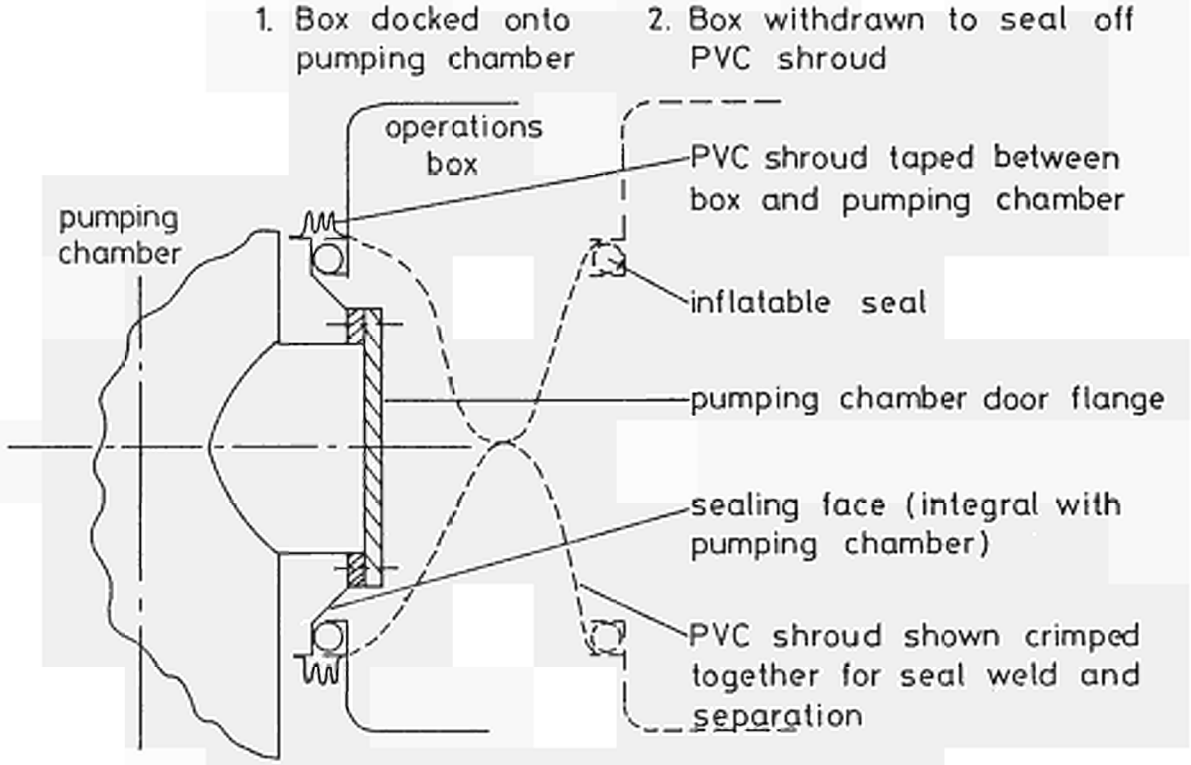

Fig. 13 Access cabin docked onto pumping chamber.

Impurity and Radiation Studies During the JET Ohmic Heating Phase

K.H. Behringer, P.G. Carolan*, B. Denne,
G. Decker†, W. Engelhardt, M.J. Forrest*, R. Gill, N. Gottardi,
N.C. Hawkes*, E. Källne, H. Krause†, G. Magyar, M. Mansfield,
F. Mast†, P. Morgan, N.J. Peacock*, M.F.Stamp, H.P. Summers

JET Joint Undertaking
(Abingdon, Oxon OX14 3EA, U.K.)

+ EURATOM-IPP Association, IPP-Garching, Federal Republic of Germany.

* EURATOM-UKAEA Association, Culham Laboratory, Abingdon, Oxon OX14 3DB, UK.

ABSTRACT

During the Ohmic Heating Phase of JET operation(June 1983 - September 1984), impurities in the plasma have been studied by visible and VUV spectroscopy, and from bolometer and soft X-ray signals. The measurements provide information on impurity influxes and impurity densities in the plasma. Plasma dimensions and parameters were a=1.1 m, b=1.3-1.5 m, R=3 m, $I_p \leq 3.7$ MA, $\bar{n}_e \leq 3.3 \cdot 10^{19}$ m^{-3}.

Oxygen, carbon, wall material (Ni,Cr,Fe), molybdenum and chlorine have been identified as the main impurities in the plasma. The metal impurities came mainly from the carbon limiter surfaces, where they had been deposited during operation and cleaning procedures. The metal densities increased with plasma current and decreased with electron density, while light impurities depended more on the state of the vacuum vessel and size and elongation of the plasma. There is a consistent anti-correlation of light impurities and metals.

There were two main campaigns to clean the plasma: a period of 12000 PDC pulses and repetitive carbonisation of the vessel walls. In the first case, some reduction of oxygen and chlorine was noted and the molybdenum fraction in the plasma decreased. However, at densities of 2.10^{19} m^{-3}, the radiated power was still about 80% of the ohmic input power and Z_{eff} was about 4.5. Carbonisation reduced the metal content by about a factor five, and oxygen and chlorine decreased gradually. Thus the radiated power was as low as 40% P_Ω. High electron densities ($\tilde{>} 3.10^{19}$ m^{-3}) led to higher radiated power (80% P_Ω, hollow radiation profiles), but reduced Z_{eff} to values below three. The impurity levels of high density pulses after carbonisation were as low as 2.5% C, 1% O, 0.05% Cl and 0.015% metals, resulting in $Z_{eff} \tilde{<} 2.6$ and a fraction of deuterons of about 75%.

1. INTRODUCTION

One of the main objectives of the large JET tokamak (plasma dimensions a=1.1 m, b=1.3-1.5 m, major radius R=3 m) is to study impurity behaviour and plasma-wall interaction in a machine of near reactor size and with plasma parameters aiming for core ignition. Radiation losses caused by impurities were of particular concern for the JET start-up phase, since the volume is large ($\tilde{>}$ 100 m^3) and the ohmic power density is therefore small compared to other tokamaks. This was an important argument for operating with carbon limiters. Although radiation levels have been high, often quite close to 100% of the input power, the aims in performance for ohmically heated plasmas have essentially been achieved or even exceeded. At toroidal fields of 3.4 T, the maximum plasma currents were 3.7 MA. A flat-top length of 6 s and overall pulse duration of more than 15 s were standard parameters the end of the 1984 operation period. Peak electron densities of 5.10^{19} m^{-3} and temperatures of 3-4 keV were obtained. The energy confinement time approached 0.8 s in deuterium plasmas. A comprehensive description of machine operation and detailed results concerning plasma performance will be published elsewhere. The present paper concentrates on the study of impurities in JET plasmas, the control of which is of major importance in the JET programme. In particular, the effects of several cleaning methods are discussed, which have been studied during the Ohmic Heating Phase (June 1983 - September 1984).

Diagnostic capabilities for impurity studies improved steadily during the first 15 months of JET operation. Therefore, impurity behaviour and impurity levels were much better known at the end of that period than at the beginning. In particular, spectroscopic observations had been restricted to the visible and UV range of the spectrum until the end of May 1984, when the first VUV spectrometer was installed. Visible spectroscopy enabled identifications of the main impurity elements in the JET plasma and, to some extent, their relative concentrations. Conclusions on absolute levels had to be drawn from bolometry and Z_{eff} measurements. Once VUV spectra were available, this knowledge improved considerably, particularly on heavy impurities. In the following, the present status of relevant diagnostics will be described and a few examples of individual measurements will be given. Subsequently, present methods of analysing visible and VUV spectra will be discussed, demonstrating the accuracy and limitations of present knowledge of impurities. Finally, results will be presented, dealing mainly with the cleaning methods applied in JET. These were glow discharge cleaning (GDC), pulse-discharge-cleaning (PDC) and carbonisation of the vacuum vessel, ie the deposition of a carbon layer on walls and limiters by means of a glow-discharge in methane. After each opening, the torus was baked to 300°C for 48 hours. Prior to the initial operation in 1983 and the first operation in 1984 a high pressure water rinse was carried out using a detergent. During the major part of the plasma experiments the vessel walls were kept at 250°C.

The sequence of operation phases, referred to in this paper, is shown in Table 1, together with the respective time periods and some information on the plasma pulses obtained.

TABLE 1 : JET operation periods during the Ohmic Heating Phase

Operation Phase	Date	Vessel Conditioning	No. of Pulses	$I_{p,max}$ (MA)
Start-up	June 25 - July 22, 1983	water rinse, GDC	26	0.6
	October 10 - December 16, 1983	GDC	181	3
Parameter Studies	March 19 - May 11, 1984	water rinse, GDC	124	3.2
Pre-PDC	June 18 - June 29, 1984	GDC	32	3
PDC	July 2nd - July 13, 1984	12000 PDC pulses	41	3
Pre-Carbonisation	July 16 - August 4, 1984	-	124	3.4
Carbonisation	August 26 - September 29, 1984	light/heavy carbonisation	186	3.7

2. DIAGNOSTICS FOR IMPURITY STUDIES

The main diagnostics referred to in the following sections are indicated in Fig.1, showing their position on the torus and their lines-of-sight with respect to the vacuum vessel and the limiters. During this phase the four carbon limiters were used to define the plasma boundary, while the nickel limiters were withdrawn from plasma contact. All these diagnostics have been described in the JET Progress Report 1983 /1/. Detailed presentations of the H_α diagnostic and the bolometer array are available in /2/ and /3/. Therefore, only brief outlines will be given here.

2.1 Bolometer Diagnostic

A 14 channel vertical bolometer array and a 20 channel horizontal bolometer array are used for measuring the integral radiation losses and the local radiated power from the plasma, P_{rad}. Abel-inversion of the raw data, using all available channels, was carried out originally by assuming constant emissivity on nested, elliptical surfaces, the elongation $\varepsilon = b/a$ of which was taken from magnetic measurements. Subsequently, the calculated shape of the magnetic flux surfaces was fed into the inversion program and the results were obtained as a function of flux co-ordinate Φ or as a function of R in the horizontal mid-plane of the torus. In either case, the measured line-of-sight integrals were transformed to a common co-ordinate system in order to check the assumption of constant emissivity on flux surfaces. Eight single bolometers, one on top of each octant, provide information on the toroidal symmetry of the radiative power losses.

As an example, Fig.2 shows the bolometer raw data and the inverted radiation profile as a function of horizontal viewing angle for Pulse No. 3049. The radiation of this high density plasma after carbonisation is dominated by light impurities. It is concentrated in a narrow shell at the plasma boundary and the power losses from the plasma centre are very small, ie less than 10 kW/m^3, while the input power density is about 70 kW/m^3. In this example, the global radiation amounts to about 70% of the ohmic input P_Ω.

2.2 Visible Spectroscopy

Visible spectroscopy utilises light from the JET tokamak relayed by optical fibres to detectors outside the biological shield, where personnel access is unrestricted. Eleven telescopes collect plasma light along selected chords of diameter $\tilde{\sim}$ 12 cm, terminated on the upper torus walls (vertical chords), or on carbon or nickel limiters (horizontal chords). By means of fibres and photomultipliers most of the channels monitor the H_α line emission, one channel observes the continuum radiation at 523.5 nm. These signals have been used routinely for deriving the hydrogen fluxes at walls and limiters, and for measuring the effective ion charge of the plasma Z_{eff}. Three fibres are connected to 0.6 m and 1 m grating spectrometers, one of which is equipped with an optical multi-channel analyser (OMA). In this way, the temporal and spectral evolution of various spectral lines can be followed. OMA recordings have shown that the wavelength range of 523.5 ± 0.5 nm, used for the continuum measurement, is free of line emission. However, the spectral range of these instruments is restricted to wavelengths above 350 nm by the cut-off in the fibre transmission. All channels were calibrated from lens to detector by means of a standard tungsten ribbon lamp.

In order to extend the wavelength coverage down to about 200 nm, a close-coupled torus spectrometer is set up on Octant No. 5 viewing the carbon limiter in Octant No. 8. This 1 m instrument is used in photographic and in monochromator mode. Spectral scans are easily obtained by rotation of the grating during the long JET pulses. Thus, spectral line widths can be measured and impurity ion temperatures can be derived.

Part of a photographic spectrum recorded by the torus spectrometer is shown in Fig.3. The respective carbon limiter and the adjacent outer wall are imaged on the entrance slit, such that the horizontal co-ordinate represents the different locations while the vertical co-ordinate corresponds to the usual wavelength scale. In the wavelength range shown, lines of low ion stages of carbon and oxygen have been identified. Neutral lines of metals (Cr I, Fe I, Mo I) appear just at the limiter surfaces (short lines) demonstrating the existence of metal influxes from the carbon tiles.

2.3 VUV Spectroscopy

The JET VUV survey spectrometer is a Schoeffel McPherson Model 251 grazing-incidence instrument covering the wavelength range from about 10 nm up to 170 nm by means of two interchangeable gratings. The instrument is similar to that developed by R J Fonck et al /4/ and tested on the PDX tokamak. Spectral resolution is only moderate (0.2 - 0.3 nm) leading to some problems in the identification of spectral lines. For a first sensitivity calibration of the spectrometer, Fonck's results /4/ served as a guideline. The relative system response curve was modified slightly according to the observed relative intensities of hydrogen and oxygen lines. The absolute calibration is based on the H_α-L_β branching ratio. Usually, the VUV instrument was used in survey mode, ie recording about 70 complete spectra during a plasma discharge. These were taken in 16 ms intervals during the break-down phase of the pulse and at 600 ms intervals subsequently.

After the JET operation, the VUV survey spectrometer was installed on the ASDEX tokamak in collaboration with Euratom IPP Association, Garching, FRG. The purpose of this experiment was to study charge exchange excited lines during neutral beam injection. The intensity ratios of these lines are well established theoretically allowing a relative sensitivity calibration of the instrument /5/. A preliminary analysis of the respective results essentially confirms Fonck's calibration curve.

Fig.4 shows an example of the JET VUV spectrum between 10 and 100 nm during the flat-top phase of Pulse No. 2892. This is a high density plasma after carbonisation, and the VUV radiation is dominated by the lines of light impurities, ie oxygen and carbon. Lines of chlorine are also prominent, while there is hardly any evidence of metals from the vessel walls. These walls consist of Inconel 600, ie 72% nickel, 16% chromium and 8% iron. The time dependences of the impurity lines O VI, 103.2 nm, and Ni XXV, 11.8 nm, are shown in Fig.5 together with the plasma current, I_p, and the average electron density, $\bar{n}_e$, for the same plasma pulse. The metal line intensity decreases when $\bar{n}_e$ is high. Signals from light impurities and metals are inversely correlated, a behaviour which has been observed regularly in JET.

2.4 Soft X-Ray and Pulse-Height Analysis Systems

The single channel soft X-ray system consists of four detectors behind a single pinhole. These silicon diodes are equipped with beryllium filters of different thicknesses in order to distinguish high and low energy radiation. Foil thicknesses of 0, 2, 12.7 and 50 μm have been used, the latter resulting in an energy cut-off at about 1300 eV. The main aim of this diagnostic was to look for MHD effects, particularly sawtooth activity (during the more recent JET pulses with electron temperatures in the several keV range only inverted sawteeth could be observed). Additionally, the diode signals yielded estimates of the high energy radiation losses of the plasma and of the X-ray continuum enhancement factors.

The single channel pulse-height-analysis system consists of a beryllium window, a variable aperture and a mercury-iodide detector. This detector does not require cooling but its energy resolution is somewhat poorer than that of the usual Si-Li diodes, ie about 500 eV. As an example, Fig.6 shows the recorded X-ray spectrum for JET Pulse No. 3058. The continuum slope yields an electron temperature of 3.2 keV in this case, in agreement with that from electron cyclotron emission (ECE) measurements. The K_α lines of nickel and chromium are clearly visible. The nickel line has been used for deriving the nickel content in the centre of the plasma and the respective results will be discussed together with the data from VUV spectroscopy.

3. INTERPRETATION OF VISIBLE SPECTROSCOPY

The effective ion charge of the plasma, Z_{eff} averaged over the chord length, is determined from the visible continuum at 523.5 nm. In the analysis, T_e profiles are taken from the ECE diagnostic. For n_e, typical, essentially parabolic profiles are being used as indicated by a fixed frequency reflectometer. Z_{eff} is given by the ratio of the measured radiance to that calculated for a pure hydrogen plasma, taking into account the appropriate Gaunt factors. Due to the n_e^2 dependence of continuum emission, the main contribution originates from the centre region of the plasma. Therefore, the results essentially represent Z_{eff} on axis. The Maxwellian averaged Gaunt factors involved are calculated in a hydrogenic approximation as a function of temperature and ion charge, and are in agreement with Karzas and Latter /6/. Z_{eff} values referred to in this paper are always derived from visible Bremsstrahlung.

JET spectra in the visible and UV wavelength range contain lines of neutral atoms, low ionisation stages of different impurity ions and forbidden ground state transitions of nickel and chromium. An example of the latter is the $^2P_{3/2}$ - $^2P_{1/2}$ transition in Ni XII at 423.1 nm. At proton densities above 10^{18} m^{-3} statistical population of these levels may be assumed /7/ and the line emission coefficients reflect directly the Ni XII ground state population. This line has been used routinely as a monitor of nickel edge density. For quantitative analyses, emission shells and ionisation balance have been calculated by the impurity transport code described in Section 4. The other lines have been regarded mainly as an indication of local influx at the observed plasma surface position.

3.1 Flux Measurements

The neutral particles are ionised in a narrow shell at the plasma periphery. Under usual conditions of negligible recombination, the ionisation rate per unit surface area, integrated over the shell width, equals the neutral influx density. The ionisation process is accompanied by the emission of spectral lines and, in the most important case of corona population equilibrium, the numbers of ionisation events and emitted photons are closely correlated. Therefore, the local flux density Γ_o may be derived from the line-of-sight intensities of the neutral line emission, I_o. The flux Γ_o is given by the relation

$$\Gamma_o = 4\pi \frac{S_o}{\vec{X}_o \cdot \vec{B}_o} I_o \qquad (1)$$

where, respectively, $\bar{S}_o$ and $\bar{X}_o$ are the average values of ionisation rate coefficients and excitation rate coefficients to the particular upper level, and B_o is the branching ratio for the observed spectral line. Since S and X have roughly the same temperature dependence for the lines in question, T_e need not be known with high accuracy for flux measurements.

The above equation, or a somewhat more sophisticated version /8/, is commonly used for deriving the hydrogen influx from H_α measurements, a method which is used here as well. Wall and limiter fluxes are measured separately by vertical and horizontal chords of the H_α diagnostic. Neutral lines of several metals (Cr I, Ni I, Mo I) have been analysed in terms of limiter and wall fluxes, and have been used to evaluate the relative densities of these elements in the plasma. In the cases of chromium and molybdenum, there is a complication with the existence of metastable ^5S and ^5D ground states. A significant population may accumulate in these levels, or the sputtered atoms may already enter the plasma in these excited states.

The importance of these metastable levels has been assessed experimentally, assuming that the excitation of allowed transitions within systems of the same multiplicity is much more likely than inter-system excitation. This assumption is particularly well justified in this case where electron energies are much higher than the level energy differences, ΔE. The comparatively low intensities of lines in the quintet system (eg ^5D-$^5F^o$) are considered as an indication that the metastable atoms represent only a small fraction of the ground state number density. These levels are probably underpopulated in the plasma because of the short lifetime of the atom before ionisation.

Within certain limitations, ion lines of low ionisation stages can still be used for flux measurements. However, the higher the ionisation stage, the more the local information is lost and is being replaced by a spatial average, since the ions spread along the magnetic field lines. Furthermore, the lines no longer reflect the neutral influx, but a flux diminished by the losses in all lower ionisation stages including the observed one. In the case of once or twice ionised ions the latter fraction is small for the JET edge plasma conditions. Its value follows from detailed transport calculations.

The electron excitation rates of strong ion lines in the visible are often difficult to calculate, since the respective upper levels do not combine with the ground state. As discussed for metal atoms, the levels may not even be populated by an excitation from the ground state, but rather from a metastable level of the same multiplicity. Examples of the latter case are the 3s - 3p $^2D^o$ transitions in OII, which are stronger than the 3s - 3p $^4D^o$ transitions, and are probably not a result of inter-system excitation. In order to obtain the influxes of light impurities presented in this paper, the populations of the metastable states have been estimated from the measured visible or VUV lines. Then, ground states and metastable state have been added. Electron excitation rates for non-dipole and intersystem excitation have been calculated from a van Regemorter type formula /9/, using f-values of corresponding allowed lines and Mewe's prescription /10/ for the Gaunt factors. In some cases, the validity of this procedure is supported by detailed calculations (eg Mann /11/ for C II). Ionisation rates are taken from Lotz /12/. The electron temperature at the plasma boundary is obtained by an interpolation of ECE and Langmuir-probe measurements. Depending on electron density, $T_e(a)$ is in the range 50-100 eV. Several lines of different ionisation stages have been analysed and found to agree within about a factor of two. Nevertheless, it is clear that the flux measurements based on visible lines have considerable error bars due to atomic physics and plasma physics problems.

4. ANALYSIS OF VUV SPECTRA

In order to interpret the measured spectral line intensities in terms of impurity concentrations, line excitation rates and ionisation balance must be calculated from atomic physics models using measured plasma parameters for the respective discharges. Impurity transport modifies the ionisation equilibrium particularly at the plasma edge, ie the region of steep gradients, and is responsible for the radial profile shape of the total ion densities. In the present analysis, a numerical code /13/ is used to describe the impurity behaviour. It solves, in cylindrical co-ordinates, the coupled set of time-dependent continuity equations for the individual ionisation stages of a particular element, taking into account ionisation, recombination and diffusion processes. The code calculates the radial distributions of ground state densities, as well as emission shells and line-of-sight integrals of selected lines to be compared with the respective experimental results. It also gives local and global radiation losses caused by line emission. The code has been set up to compute the time dependence of the above quantities after impurity injection or for varying plasma parameters. However, at present, only the stationary solution is being used for impurity analysis during the stationary conditions of current and density flat-top. The results presented were obtained between 4.4 s and 6.8 s in the pulse.

For the interpretation of JET spectra, the T_e profiles from ECE diagnostics have been used in the code. Electron density profiles have been taken from fixed-frequency reflectometer measurements, except for the last few pulses of the 1984 operation period, when profiles from the multi-channel DCN interferometer became available. The conditions at the plasma boundary have been estimated from an interpolation of ECE and Langmuir probe measurements. Fall-off lengths of density and temperature in the scrape-off layer have been modelled as to fit the probe data. An example of the calculated ground state distributions of nickel for Pulse No. 2984 at 5 s, is given in Fig.7.

4.1 Rate Coefficients and Radiation Data

The ionisation rate coefficients are calculated as proposed by Lotz /12/. For the Na-like ions, where inner-shell ionisation is known to be important, correction factors to the Lotz formula have been calculated for the relevant temperature range and are implemented in the code. Inner shell ionisation enhances the total rate coefficients by a factor of two for Na-like chlorine, and by a factor of three for Na-like nickel ions. Radiative recombination is treated in the usual way by applying the hydrogen formula and introducing effective quantum numbers. For dielectronic recombination, the Burgess prescription /14/ has been used but taking into account modifications by Merts et al /15/. A density dependence of the latter rate coefficient has been adopted following Post et al. /16/. For calculating individual resonance line radiation of systems of one and two electrons in the outermost shell, a survey of the existing theories has been carried out /17/ and interpolation routines have been established, if necessary, for the present requirements. In order to calculate the total power emitted by line radiation, two effective resonance lines have been defined for each ionisation stage as to account for $\Delta n=0$ and $\Delta n\neq 0$ transitions. For this purpose processed data sets were used, based on f-values from Wiese et al /18,19/ for light impurities and for chlorine, and from Fuhr et al /20/ for nickel. An attempt has been made to fill in gaps by interpolation along the isoelectronic sequence. Line radiation is calculated according to a van Regemorter type formula /9/, the Gaunt factors being taken from Mewe /10/. In the case of non-dipole lines, the f-values of the allowed lines are used and the Gaunt factors are taken again from Mewe's prescription. The resonance line data for allowed transitions are also used for calculating the dielectronic recombination rate coefficients. Systematic improvement of the atomic rate data base is in progress.

4.2 Transport Coefficients

The fluxes of all elements and ionisation stages Γ_k are described by the sum of an anomalous spreading term and a convective term

$$\Gamma_k = - D \frac{\partial n_k}{\partial r} + V_D n_k \qquad (2)$$

The anomolous diffusion coefficient D and the drift velocity V_D are probably a function of plasma parameters, but are assumed to be constant in the present analysis. In Eq. (2), n_k is the number density of a particular species.

Due to an accidental impurity injection described in Section 6 of this paper, evidence exists that the spreading coefficient D in

JET is similar to that in other tokamaks, ie about 0.6 m²/s. However, the magnitude of the corresponding drift velocity V_D, determining the radial profile shape of impurity densities, is not known, though a rough estimate is possible by analysing different ionisation stages of heavy impurities. In /21/ the drift velocity was assumed to be given by

$$V_D = -2\ D\ r/a^2 \qquad (3)$$

resulting in moderately peaked radial profiles similar to those measured for electron densities. In the transport code, used for interpreting the JET VUV spectra, this same expression has been adopted.

The problems associated with the uncertainties of the transport model are of a different nature for the light and for the heavy impurities. At the present electron temperatures in JET, metal lines are observed in the VUV spectrum, emitted from the inner half radius of the plasma, where corona ionisation equilibrium is expected to hold. Therefore, information on the metal content should be quite reliable from the transport view point. Light impurities radiate only at the plasma edge, where both the electron density and temperature are poorly known. Then, the transport model must be used in order to calculate the concentrations in the plasma interior. Due to these problems, the light impurity results at the plasma centre have large error bars.

4.3 Consistency of Analysis

The most important spectral lines, which have been used more or less routinely for analysis, are shown in Table 2.

Table 2: Most important impurity lines used in analysis of the JET VUV spectrum.

C III	97.70 nm	+	C III	45.96 nm
C IV	31.24 nm			
O IV	55.43 nm	+	O IV	62.51 nm
O V	62.97 nm	+	O V	76.03 nm
O VI	103.19 nm			
Cl VI	67.14 nm	+	Cl VI	73.03 nm
Cl VII	80.07 nm			
Cl XIV	23.77 nm	(+	Cl XIV	28.63 nm)
Cl XV	38.40 nm		(blended with CIV)	
Ni XII	432.12 nm		(visible spectrum)	
Ni XVIII	29.20 nm			
Ni XXV	11.80 nm		(≈ 30% correction due to Ni XXII and Ni XXIV lines)	
Ni XXVI	16.54 nm			
Cr XXII	22.30 nm			
Fe XVI	33.54 nm			
Mo XXXII	12.78 nm			

By means of the impurity transport code, the respective impurity densities in the centre of the plasma are calculated from line-of-sight integrals of these line intensities. The second transition, listed for light impurity ions, is used for measuring the metastable state population, which is found to be particularly important in the case of O V. The results obtained from different ionisation stages of the same element agree within about a factor of two, ie the expected error limits of calibration and excitation models. In the case of nickel, where ionisation stages are observed radiating within the inner half radius and right at the boundary, the radial profile assumed in the code is confirmed within the same uncertainty margin.

In all cases checked, calculations of the total radiation losses based on measured impurity densities are consistent with the bolometer results, ie the total radiated power. This is not surprising, since the strongest lines contributing to the bolometer signals are observed in the region of the present VUV instrument and the impurity densities are derived from these particular lines. It is more difficult to compare measured and calculated radiation profiles. Examples of the code calculations are shown in Fig.8, together with the Abel-inverted bolometer data. The local emission due to line radiation is shown as computed for 1% of oxygen and 3% of carbon, and for the parameters of the respective discharge. According to the calculations, carbon is mainly responsible for the radiative power losses in this particular case. The spatial resolution of the bolometer (15 cm in the respective midplanes) is obviously not sufficient to resolve the individual shells. Taking into account spatial averaging, the height of the measured profile is in reasonable agreement with the calculations. Its position is displaced by about 5 cm, a value which is certainly within the error limits of the measurement.

The values of Z_{eff} derived from the measured impurity concentrations usually agree with those derived from visible Bremsstrahlungto within one, but can differ by up to 1.5. Under normal conditions, this discrepancy cannot be explained by the uncertainties of the metal concentrations, as they contribute little to Z_{eff}. It must be attributed to light impurity results, which are less reliable too, since they are only obtained for the plasma edge. Insufficient knowledge of the plasma edge parameters may easily change the light impurity results by a factor of two, while their ratio is expected to be more accurate. Therefore a method of proceeding is to scale these numbers as to explain the measured Z_{eff}. However, for the period reported, poor knowledge of density profiles and the usual uncertainties of intensity calibration and temperature measurements lead to about 30% error bars for Z_{eff} from Bremsstrahlung. This means that the accuracy of the spectroscopic results cannot be substantially improved by such a scaling. Therefore, the light impurity densities are presented as derived from the code analysis.

5. RESULTS

5.1 Important Impurities and Trends

Due to the presence of carbon limiters, carbon has always been an important impurity in JET. The carbon concentration in the plasma was 2-3% n_e, consistently throughout the whole operation period. The limiters are a main source of carbon influx, but the vessel walls are found to be almost equally important, in particular, when the plasma elongation is high and the boundary approaches top and bottom of the vacuum vessel. The carbon influx is a steep function of electron density, just as the hydrogen flux, but is almost insensitive to the plasma current I_p. This means that the respective production mechanisms hardly depend on temperature but on the number of recycling hydrogen ions.

The oxygen level in JET has been much more variable and reflects the cleanliness of the vacuum vessel. Judging from the respective influxes, the torus walls are equally effective oxygen sources as the limiter surfaces. Just as in the case of carbon, the oxygen production is not correlated with plasma current, but with electron density. However, since impurity shielding improves with n_e, the concentrations of both carbon and oxygen are weak functions of density for a particular experimental campaign. The lowest levels of oxygen were achieved at the end of the 1983 start-up period, after extensive glow discharge cleaning, and in September 1984, after repetitive carbonisation.

Strong lines of chlorine were observed in the visible spectra during the first JET plasma pulses, but their significance was only realised when VUV spectra became available, and the chlorine resonance lines could be analysed. According to these results, several per cent of chlorine must have contaminated the first JET plasmas. Chlorine was probably introduced into the torus by the washing procedure using a detergent. The chlorine level has decreased significantly in the course of operation and as a consequence of cleaning procedures. However, it is still an important impurity. In cases of strong plasma-wall interaction, eg high elongation or density limit studies, the chlorine

fraction in the plasma is appreciable, and the VUV spectra may even be dominated by Cl lines.

Significant amounts of wall material, nickel, chromium and iron were found in the plasma particularly at low electron densities before carbonisation. The carbon limiters have been identified as the main source of these metal impurities. As confirmed by a post-mortem limiter surface analysis, these have been coated by wall material either during glow-discharge cleaning or normal tokamak operation. Arcing and disruptions may play a significant role, too, melting and evaporating large amounts of metal. Molybdenum was found both in the plasma and on the limiter surfaces. It was deposited on the graphite tiles by accident during manufacturing. However, it has always represented a minor fraction of the metals and has even become less important during the operation period. Metal fluxes and metal densities increase with plasma current and decrease with electron density. Furthermore, an inverse relationship was found to exist between metals and low-Z impurities, as has been observed before in other tokamaks /22/. This behaviour can be explained by the sensitivity of metal sputtering rates to the plasma edge temperature.

The trends of light and heavy impurities, described above, lead to the usual steep decrease of Z_{eff} with n_e for a given experimental campaign, as long as metals play an important role. For light impurity dominated plasmas, Z_{eff} tends to be a rather weak function of n_e. In the first case, the radiative power losses, P_{rad}, are reasonably constant, since the increase of n_e is compensated by a decrease of metal number densities. However, the radiation depends strongly on plasma current. At high densities, metal impurities become insignificant. P_{rad} increases, usually up to 100% of P_Ω at the density limit, due to light impurity radiation.

5.2 Impurity Behaviour during the Start-Up Phase

In the November-December 1983 operation period, after extensive GDC, long quiet plasma pulses were obtained. The electron temperature approached 2 keV in the centre and sawtooth activity was observed regularly on the soft X-ray diodes. The impurity behaviour had become fairly consistent, allowing trends and parameter dependencies to be studied, but only by visible spectroscopy. For the metal impurities, the following analysis was carried out: the relative concentrations of Ni, Cr and Mo were inferred from the respective influxes at the limiter, for which ratios of 7:1:1 were measured. The intensity of the Ni XII line was used to derive the nickel concentration in the plasma. In this way, a total metal content of 0.2% n_e was derived for I_p=2 MA, $\bar{n}_e$=1.8·10^{19} m^{-3} and ε=1.2. This value is in good agreement with the radiated power from the plasma centre and with the absolute signals of the soft X-ray diodes. The metal production rate at the limiter surface was measured to be 2% of the respective hydrogen flux Φ_H ($\tilde{=}5.10^{21}s^{-1}$), a value which is just sufficient to explain the metal content of the plasma, and which is easily interpreted in terms of hydrogen and low-Z impurity ion sputtering, even if the carbon is only partly covered by metals (for rate coefficients see eg. /23/).

During the Spring 1984 shutdown, a post-mortem surface analysis of carbon limiter tiles was carried out. It confirmed that they were indeed covered by wall material with an average layer thickness of about 10^{21} metal atoms/m^2. Considering that the measured sputtering rate was close to 10^{20} atoms/m^{2}s, the metals must have been eroded and redeposited many times during JET operation.

An assessment of light impurities in the plasma was more difficult. Carbon and oxygen influxes from the limiters were measured to amount to 10% Φ_H and 3% Φ_H respectively. The high yield of carbon may just be explained by a combination of hydrogen, impurity ion and self-sputtering. The mechanism responsible for the oxygen release is not known. From these fluxes concentrations of 2% C and 0.5% O were estimated, in reasonable agreement with a transport code analysis of C III and O IV. The resulting Z_{eff} of 3.2 compares favourably with 3.5 from Bremsstrahlung. The chlorine fraction in the plasma could not be measured but, according to the visible chlorine lines, it was probably quite small. 70% of P_Ω was radiated in these early JET plasmas, metals being mainly responsible for P_{rad}.

During the subsequent operation period in Spring 1984, cleaning procedures were the same as before and the impurity situation was not expected to change substantially. VUV spectroscopy was only available for the last few days, but the usual signals in the visible, ie O IV, C III and Ni XII, were recorded routinely. Judging from these results, the metals remained approximately constant for comparable pulses. The carbon wall influx from top and bottom of the vessel increased for vertically elongated plasmas generated during this period. The situation with respect to oxygen deteriorated somewhat during the Spring operation period probably due to this enhanced plasma - wall interaction. However, these observations could not explain the high values of Z_{eff} found particularly at the beginning of March 1984. A summary of Z_{eff} data for several experimental campaigns is shown in Fig.9, including some of the 1983 results. The measured Z_{eff} values did show the usual decreasing tendency with n_e, and were decreasing gradually in the course of operation, but never quite reached the low results of 1983. A high fraction of radiated power (80-100% P_Ω) and flat radiation profiles confirmed that the plasmas were metal-dominated as they had been in December 1983. For an unknown reason, pulses with lower toroidal field and lower q radiated a larger fraction of the input power, usually close to 100% P_Ω.

When the first VUV spectra were available, it was realised that chlorine was an important impurity in JET, which was probably introduced by the detergent used for washing. Since the torus had been washed again before the March operation, a possible explanation for the high values of Z_{eff} may be a high chlorine contamination (up to 1.5% n_e would have been required), which reduced gradually in the course of operation. However, there are no measurements to prove this hypothesis.

A detailed analysis of VUV spectra is available for Pulse No. 2050, which is comparable to the 1983 plasmas as well as to the later reference discharges to be discussed in the next paragraph. It had the following parameters: I_p=2.3 MA, $\bar{n}_e$=1.6·10^{19} m^{-3}, B_T=2.6 T, ε=1.4. The respective results for the metals are very close to the values obtained for the 1983 plasmas (values in parenthesis), ie a total metal content of about 0.2% (0.2%) and a ratio of Ni:Cr:Mo: of 8:1:0.5 (7:1:1). Iron was determined to be about 4% of the total metal content. The straightforward results for oxygen and carbon were 1.6% and 2% respectively. This means that the carbon level is in very good agreement with the 1983 result (2%), while the oxygen may have been somewhat underestimated (0.5%), though it has probably increased by a factor of two in the March-May operation. The chlorine fraction of pulse # 2050 was found to be 0.16%. The respective values of impurity concentrations are marked on the left-hand side of Fig.10 as starting points for trends throughout the remaining operation time.

5.3 PDC Period

For the assessment of PDC effectiveness glow discharge cleaning, which had been used routinely before, was abandoned in order not to confuse the PDC results. A total of 12000 PDC discharges was carried out, mostly in Taylor mode ($p\tilde{=}10^{-5}$mb H_2, I_p=30-40 kA, B_T=0.15 T, $t\tilde{=}0.1$ s), some in high power mode (I_p=400 kA, t=0.6 s). In order to study the plasma response, the parameters of a reference discharge were defined (I_p=2 MA, b/a=1.4, B_T=2.5 T, $\bar{n}_e$=2.10^{19} m^{-3}), which was then repeated throughout the following operation periods and allowed an easy comparison of the plasmas achieved. The development of impurities will be described referring to the data in Fig.10. However, it must be kept in mind that only a few examples are being discussed, which are considered to be representative. Even comparing pulses with the same gross parameters, the scatter in the results amounts to 20% or more.

The reference discharges before PDC showed an increase in oxygen and a respective reduction in metal impurities as compared to the May situation. The Cl level increased distinctively too. After about 4000 PDC pulses oxygen, carbon and nickel were virtually

unchanged while the chlorine showed a reduction of about a factor of two After 12000 pulses there is some effect on the oxygen, accompanied by an increase in metal concentration. Carbon and chlorine remained constant. These differences, which are all not dramatic, are essentially in agreement with the respective influxes of oxygen, chlorine and nickel. There was a change in the ratio of Ni:Cr:Mo, ie more chromium and less molybdenum were found after PDC, but again, the differences are only minor. The total radiated power hardly changed during the PDC period and was about 80% of P_Ω. At the end of the PDC assessment, Z_{eff} was still of the order of 5 for the parameters of the reference discharges. All together, 12000 PDC pulses seem not to be sufficient to have a large impact on the impurity situation in JET. For the Pre PDC pulses, we estimate the following impurity influxes from the CII, CIII, OII, OIV and CrI signals:

$$\Phi_C/\Phi_H \tilde{\approx} 0.20 \qquad \Phi_{wall}/\Phi_{Limiter} \tilde{\approx} 1$$
$$\Phi_O/\Phi_H \tilde{\approx} 0.15 \qquad \Phi_{wall}/\Phi_{Limiter} \tilde{\approx} 1$$
$$\Phi_{Metal}/\Phi_H \tilde{\approx} 0.02 \qquad \Phi_{wall}/\Phi_{Limiter} \tilde{\approx} 0.1$$

The limiter fluxes of carbon and metals are similar to the 1983 operation. However, it was realised at that stage that the carbon wall production is similar to that on the limiters. For oxygen, influxes were higher than 1983 and the walls seemed to play an important role.

5.4 Reference Discharges after Carbonisation

After a period of high density and deuterium operation, which will be commented on in the next paragraph, light and heavy carbonisation of the vacuum vessel were carried out in order to remove oxygen and chlorine, and to assess the influence of an all carbon wall on plasma behaviour and metal contamination. Less than one monolayer of carbon was deposited on the vessel walls and removed again before tokamak operation (light carbonisation). The impurity situation was then much the same as after PDC (see Fig.10), except that the chlorine seems to have recovered again after the break in operation.

During heavy carbonisation /24/, about 50 monolayers of carbon were deposited on walls and limiters. This procedure made a definite impact on plasma performance. Z_{eff} dropped, at least initially, the radiated power reduced to about 50% P_Ω at moderate densities, and consequently, the carbon limiters heated up to as much as 1500°C.

From the spectroscopy viewpoint the main differences were a strong reduction in metals and an increase in carbon. The bolometer profiles became hollow and the centre radiation was very low. Metals considerably increased after a weekend of glow discharge cleaning, and even after ageing of the carbon layer for two days. Oxygen and, in particular, chlorine seemed to decline gradually during the last weeks of operation, but not as a consequence of specific actions taken. The conclusions drawn from the VUV spectra are again confirmed well by the respective impurity influxes and Ni XII signals. The higher carbon level is due to an increased influx from the carbon limiters. The observed reduction of metal influxes from the limiters confirms the present idea, that metal depositions on the carbon limiters had been responsible for the metal problem.

When the limiters reached a high temperature at the end of the flat-top period of some of the pulses, a sudden increase in metal influx was observed, which is attributed to metal evaporation. It seems that due to this process the limiters were better conditioned throughout the remaining operation period, and metal influxes and densities never returned to such high values as previously. It should be noted that during these limiter temperature excursions the carbon influx, as derived from C II signals, followed the electron density in the usual way. There was no indication of the existence of chemical sputtering /25/ expected to occur around carbon surface temperatures of 900 K. On the other hand, the high carbon yield measured (10% Φ_H), could be indicative of a - temperature independent - chemical release mechanism.

Although carbonisation had the favourable effect of reducing metals and lowering the radiated power in the plasma centre, there was a problem of a high concentration of carbon in the plasma leading to a dilution of the working gas. Furthermore, disregarding the pulses immediately after fresh carbonisation, the values of Z_{eff} were again up in the range 4-5.

5.5 High Density Discharges

During the Pre-carbonisation period, toroidal field and plasma current were increased at moderate plasma elongation (ε=1.2). Then, average electron densities of about 3.10^{19} m^{-3} were achieved in both hydrogen and deuterium at $I_p \tilde{>} 3$ MA, B_T=3.4 T. Later on, similarly high densities were achieved at lower toroidal fields and lower currents, but at an elongation of 1.4. The consequences of carbonisation on high density plasmas were studied for different plasma currents (2.8-3.5 MA), elongations (1.2-1.4) and toroidal fields (2.6-3.4 T). Nevertheless, these discharges behaved quite similarly in many respects, though there was some scatter in the individual results.

At high electron densities and a significant level of light impurities, edge radiation cools the plasma boundary and reduces the production of metal impurities. Therefore, the metal concentration of such discharges was very low throughout, even before carbonisation. If the density is pushed even further the plasma may eventually detach completely from the limiter and shrink, as is demonstrated by the bolometer profiles of Fig. 11 for the later phase of Pulse No. 2471. Before carbonisation, the level of oxygen and carbon could have been as high as 4%, but there may be some problems in analysing the VUV signals because of poloidal asymmetries. After carbonisation, oxygen was reduced and the carbon stayed at about 2.5%, very similar to Fig.10, but the analysis is not consistent in all details with that of the reference pulses. A consistent result was that the chlorine showed a tendency to reduce and reached the very low level of 0.05% at the end of September operation. For high density pulses after carbonisation, typical impurity concentrations are 1% O, 2.5% C, 0.05% Cl and 0.015% metals, resulting in a Z_{eff} value of about 2.6.

During the Pre-carbonisation and carbonisation periods, no significant change in impurity levels was observed when changing the working gas from hydrogen to deuterium.

5.6 Radiation and Z_{eff}

The reference pulses after light carbonisation still radiated about 90% P_Ω. It was only after heavy carbonisation that the radiation levels for moderate densities ($\tilde{>} 2.10^{19}$ m^{-3}) reduced to 50% and even 40% after repetitive carbon deposition. Judging by the spectroscopic results, this reduction is due to lower concentrations of oxygen and chlorine. The metals do play a role but, when they recovered significantly after removing the carbon layer, the increase in radiated power was only moderate, ie from 40% to 60% P_Ω.

For higher electron densities, the fraction of radiated power increased both before and after carbonisation. In the latter case, however, it increased from a much lower level. This behaviour is demonstrated in Fig.12. Going from low to high densities, the radiation in the plasma centre dropped from about 10 kW/m³ to almost zero, while the edge radiation increased. JET high density discharges are obviously light impurity dominated and, after carbonisation, oxygen and carbon contribute about equal amounts to the total radiation.

Fig.13 shows the measured values of Z_{eff} before and after carbonisation as a function of electron density over current density, a presentation, which accounts for the increase of Z_{eff} with current. Generally, the pulses with carbon have somewhat lower Z_{eff} values, the reason being again a reduction in oxygen and chlorine. The diagram also shows that higher electron densities have been achieved at a given current density. The lowest Z_{eff} values of Fig.13 are between two and three.

5.7 PHA Results

Nickel impurity concentrations have been deduced from the line emission spectra at 7.8 keV. The nickel line emission intensity is generally found to increase steadily in the beginning of the

pulse and to stay constant or to decrease during the flat top and the decay of the pulse, just as observed by VUV spectroscopy. The nickel concentrations have been evaluated during a 4 s flat top of the pulse, using theoretical excitation rates for the four main lines in the Ni^{26+} spectrum and using the electron temperatures as obtained from the high energy tail. Corona ionisation equilibrium is assumed to predict the total nickel impurity concentration in the centre of the plasma. X-ray enhancement factors calculated from the intensity of the continuum at 15 keV are in general agreement with those values obtained from the X-ray diode signals measured at 2 keV. However, the enhancement factors have a tendency to be lower than these predicted from the Z_{eff} measurements using the visible continuum particularly at high electron densities.

The nickel concentrations after carbonisation deduced from the X-ray spectra are shown in Fig.14 as a function of line average density $\bar{n}_e$. The trend of a decreasing nickel concentration with increasing $\bar{n}_e$ is in agreement with data obtained from the VUV spectroscopy. The respective results are also shown in Fig.14. The different methods give consistent values within the 30-40% error bars although the values deduced from the pulse height spectra have a tendency to be lower than those deduced from the VUV spectra by about 50%.

6. ADDITIONAL OBSERVATIONS

6.1 Measurement of Diffusion Coefficient

During the flat-top of Pulse No. 2542 a sudden increase and subsequent decay was observed in the spectral line intensities of iron. Apparently, a piece of iron fell into the plasma, which was sufficiently small that it did not perturb the plasma parameters. The decay of the respective lines can therefore be used for measuring the impurity particle transport in the plasma. As shown in Fig.15, the different ionisation stages yield the same time constant, ie 390 ms. Within the framework of a purely diffusive transport model the resulting spreading coefficient is 0.6 m^2/s, a value close to those found in other tokamaks.

6.2 Measurement of Ion Temperature

Lines of different impurity species and ionisation stages, located in the visible or UV spectrum, have been scanned during the pulse in order to obtain values of Doppler broadening, ie ion temperatures. Examples are the $1s2s^3S$-$1s2p^3P^0$ transition in C V, which, in second order, have a full half-width of about 0.14 nm. When corrections are made the instrument width, the following typical ion temperatures result:

O II	$\approx$	30 eV	C III	$\approx$	35 eV
O III	$\approx$	37 eV	C V	$\approx$	190 eV
O IV	$\approx$	60 eV			
O V	$\approx$	60 eV	Cr XIX	$\approx$	1300 eV

These values are upper limits because of Zeeman splitting, which has not been taken into account. In the case of O II, O III and C III the ionisation times may actually be too short for the impurity ions to be in equilibrium with the protons/deuterons. Assuming that the ion temperature is equal to the electron temperature, O IV, O V and C V are just found where they are expected from the code calculations, ie at a temperature corresponding to half the ionisation energy. This is another important corroboration of the present analysis assumptions. Cr XIX should appear at $T_e \approx 800$ eV. In this case, the measurement is probably high due to a neighbouring carbon line. The spatial scan spectrometers have to be awaited, in order to determine the pertinent radial locations of the shells.

6.3 Poloidal Asymmetries of Radiation

At high electron densities, poloidal asymmetries of the plasma radiation are frequently observed. An example is given in Fig.16, showing the 20 channels of the horizontal Bolometer camera as a function of time for Pulse No. 2471. The phenomenon, which has been observed before in other Tokamaks (e.g /26,27/) is first indicated by a local increase of radiation in the horizontal midplane near the inner wall. At the same time, the intensities of low ionisation stages of C, O and Cl, viewed along a horizontal chord, increase steeply. The radiating layer then grows in poloidal direction and eventually forms a radiation mantle all around the plasma. Judging from the individual bolometers around the torus, the effect is toroidally symmetrical. These asymmetries are precursors of a high density disruption which, in the above case, occurs at t=9.2 s.

7. SUMMARY

In spite of its low heating power density, JET had no problems in overcoming the radiation barrier after an initial period of baking and glow discharge cleaning. In fact, light impurities appeared to be well controlled by these methods during the start-up phase in 1983. Significant amounts of metal impurities led to high radiation power losses for fully developed plasmas, ie 70% P_Ω. Wall material (Ni, Cr, Fe) deposited on the carbon limiter was mainly responsible for the metal contamination of the plasma. A comparatively small amount of molybdenum was detected both in the plasma and on the limiter surface, which is due to the manufacturing process of the carbon tiles. Chlorine was a very important impurity in the early JET discharges and was reduced subsequently by cleaning procedures. It was probably introduced by washing the torus. At the end of 1983, Z_{eff} was about 2.5 for $\bar{n}_e = 2.6 \cdot 10^{19} m^{-3}$.

During the subsequent operation period in Spring 1984, cleaning procedures were the same as before and the impurity situation was not expected to change substantially. However, Z_{eff} and radiated power were considerably higher than 1983. The reason for this behaviour is not clear, since the essential impurities, ie C, O, Ni, were virtually unchanged. Chlorine was not monitored and only received attention when the first VUV spectrometer was installed at the end of May 1984 and strong Cl lines were observed in the VUV spectrum. The torus had been washed again before the 1984 operation; therefore, a high fraction of chlorine may well be responsible for the early 1984 results. The plasmas became cleaner gradually in the course of operation, although the oxygen level was increasing due to enhanced plasma-wall interaction.

The period of PDC assessment was expected to reduce light impurities and possibly metals due to lower light impurity sputtering rates. However, the PDC campaign made little impact on the plasma impurities. Oxygen and chlorine concentration were somewhat lower after PDC, but the metals had increased instead and there were only minor improvements in Z_{eff} and P_{rad}.

High density operation at higher toroidal fields and plasma currents resulted in a much reduced metal content, but led to oxygen dominated plasmas with strong edge cooling. Poloidal asymmetries were observed in the radiation and sometimes a radiation mantle formed and led to a shrinking of the plasma radius.

By means of heavy carbonisation, the metals could be reduced even at lower electron densities and without high edge radiation. In the process of depositing and removing carbon, both oxygen and chlorine levels reduced, leading to quite clean plasmas with radiation levels between 40% P_Ω at moderate densities and 80% P_Ω close to the density limit. A drawback of carbonisation is the high percentage of carbon present in the plasma. At Z_{eff} values around 3, about 40% of the plasma electrons originate from impurities.

Generally, it was observed that light impurity concentrations hardly depended on plasma current or electron density. Metals increased with current and decreased with n_e. An inverse relationship was found to exist between metals and low-Z impurities. These trends, as well as the behaviour of Z_{eff} and P_{rad}, are much in line with findings on other limiter tokamaks.

Typical impurity levels at the end of the 1984 operation were 1% O, 2.5% C, 0.05% Cl and 0.015% metals resulting in a Z_{eff} value of 2.6. According to the code calculations, oxygen and carbon are responsible for the measured radiation losses and contribute about equal amounts. By means of longer operation and repetitive carbonisation the oxygen level can be further reduced.

This will probably allow higher electron densities, even if the carbon fraction remains in the range of a few percent. For the Ohmic Heating operation phase, the present impurity levels did not cause any serious problems. However, they would raise the $\langle n_e \tau_E \rangle$ requirements for ignition by a factor of two due to enhanced Bremsstrahlung and dilution of the deuterium/tritium plasma.

ACKNOWLEDGEMENT

The work reported in this paper has been made possible by the efforts of JET Project and Associate Staff involved in construction, operation, measurement and theory. The authors are particularly grateful to the members of the two Experimental Divisions and Theory Division's Interpretation Group for making freely available the results of their own work and for much valuable discussion.

29TH MAY 1985

REFERENCES:

/1/ JET Joint Undertaking, Progress Report 1983 EUR 9472 EN

/2/ P D Morgan, K H Behringer, P G Carolan, M J Forrest, N J Peacock, M F Stamp, Rev. Sci.Instrum., in print (1985)

/3/ K F Mast, H Krause, Rev. Sci. Instrum., in print (1985)

/4/ R J Fonck, A T Ramsey, R V Yelle, Appl. Opt. 21, 2115(1982)

/5/ R C Isler, R A Langley, Appl. Opt. 24, 254(1985)

/6/ W J Karzas, R Latter, Astrophys. J. Suppl. No.55, 6, 167(1961)

/7/ H Gordon, H P Summers, J A Tully, The Calculation of Spectrum Line Emission from Plasmas I, Culham Laboratory Report, CLM-R229 1982

/8/ L C Johnson and E Hinnov, J. Quant.Spectrosc. Radiat. Transfer 13, 333-358(1973)

/9/ H Van Regemorter, Astrophys. J. 136, 906 (1962)

/10/ R Mewe, Astron. Astrophys. 20, 215 (1972)

/11/ J B Mann, quoted in Los Alamos Scientific Laboratory Report, LA-6691-MS (1977)

/12/ W Lotz, Lab. Reports IPP 1/62 (1967) and IPP 1/76 (1968), Garching, Germany

/13/ K Lackner, K Behringer, W Engelhardt, R Wunderlich, Z. Naturforsch. 37a, 931-938 (1982)

/14/ A Burgess, Astrophys. J. 141, 1588 (1968)

/15/ A L Merts, R D Cowan, N H Magee, Los Alamos Scientific Laboratory Report LA-6220-Ms (1976)

/16/ D E Post, R V Jensen, C B Tarter W H Grasberger, W A Lokke, Atomic Data and Nuclear Data Tables 20, 397 (1977)

/17/ H Gordon, H P Summers, The Calculation of Spectral Line Emission from Plasmas II, in print, Culham Laboratory Report 1985 (in print)

/18/ W L Wiese, M W Smith, B M Glennon, National Bureau of Standards Report NSRDS-NBS4 (1966)

/19/ W L Wiese, M W Smith, B M Miles, National Bureau of Standards Report NSRDS-NBS 22 (1969)

/20/ J R Fuhr, G A Martin, W L Wiese, S M Younger, J Phys. Chem. Ref. Data 10, 305 (1981)

/21/ K Behringer, W Engelhardt, G Fussmann, ASDEX-Team, Proc. IAEA Techn. Comm. Meeting on Divertors and Impurity Control Garching 1981, 42.

/22/ E Hinnov, S Suckewer, K Bol, R J Hawryluk, J Hosea, E Meservey, Plasma Phys. 20, 723-734 (1978)

/23/ E Hechtl, J Bohdansky, J Roth, J. Nucl. Mat. 103 No. 1-3, 333(1982)

/24/ F Waelbroeck, TEXTOR Team, J. Nucl. Mat. 121 378(1984) and private communications

/25/ J Roth, Sputtering by Particle Bombardment II, Topics in Applied Physics Vol. 52, p.91, Springer Verlag, Berlin, New York, Tokyo, 1983

/26/ B Lipschultz, B La Bombard, E S Marmar, M M Pickrell, J L Terry, R Watterson, S M Wolfe, Nucl. Fusion 24, 977 (1984)

/27/ H Niedermeyer, ASDEX-Team, IPP Report III/90, 1983

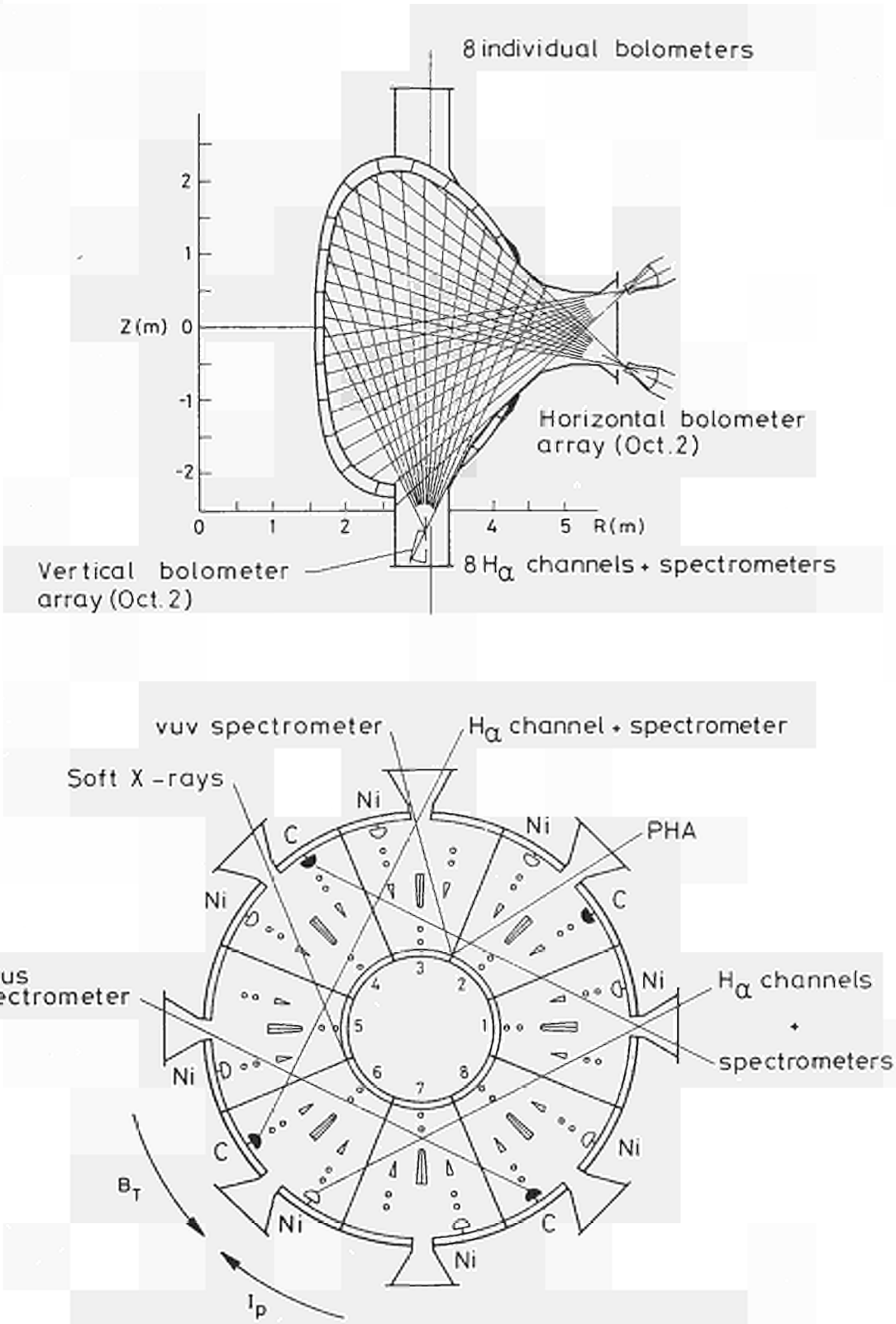

Fig. 1 Location and sightlines of diagnostics for impurity studies.

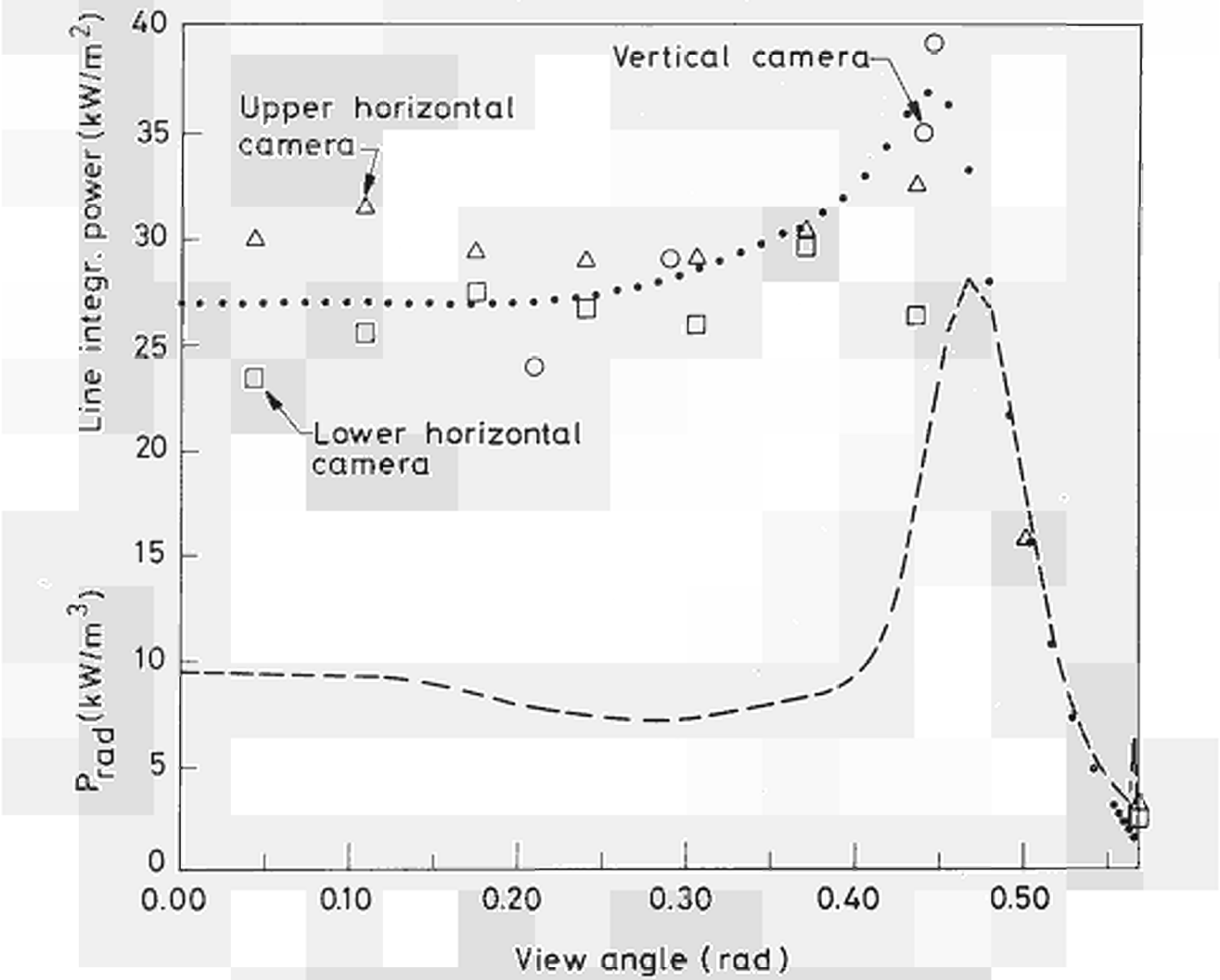

Fig. 2 Bolometer raw data and inverted profile versus horizontal viewing angle for a high density plasma after carbonisation.

JET UV SPECTRUM

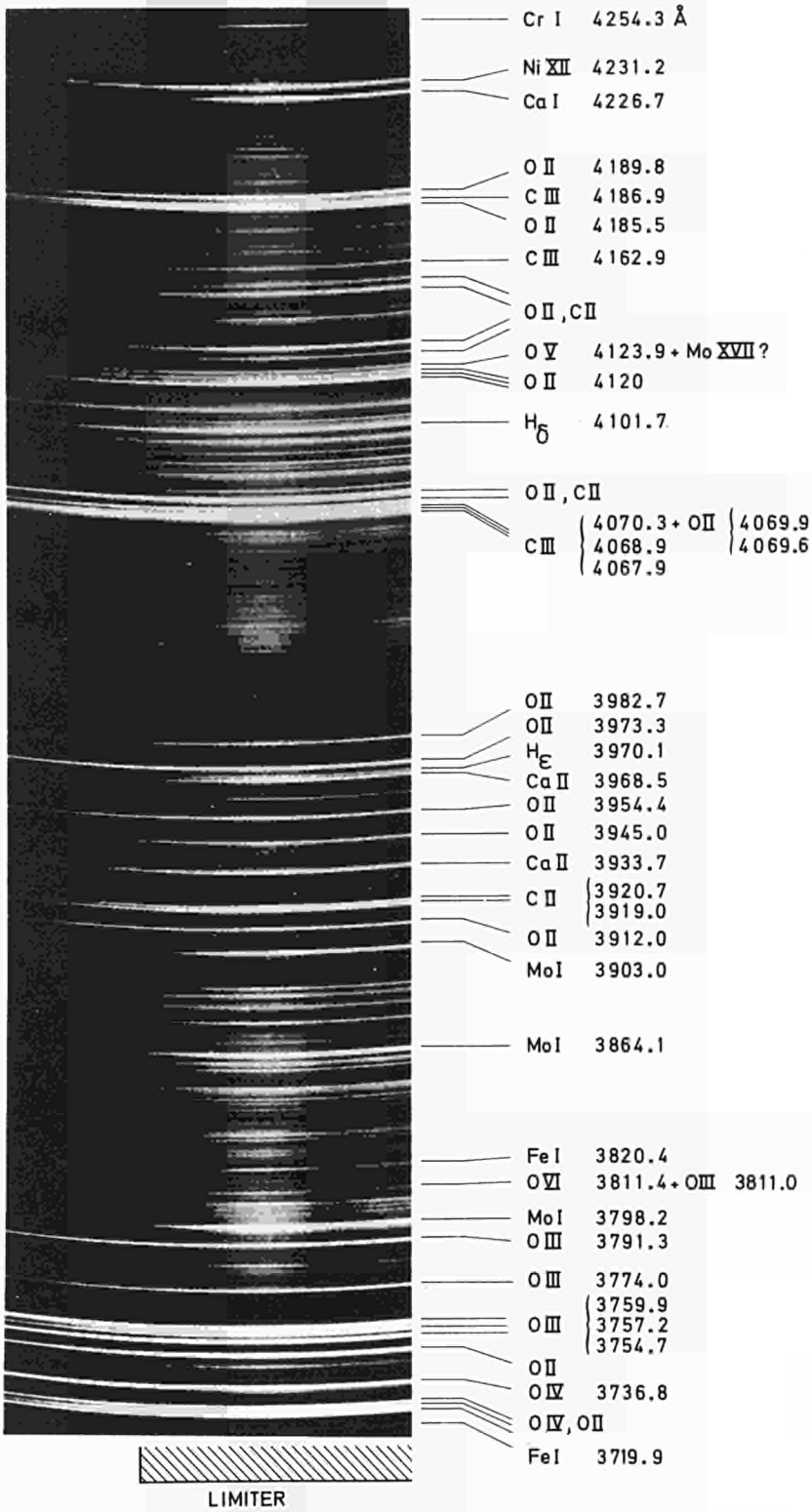

Fig. 3 Photographic spectrum recorded by the torus spectrometer during a single JET pulse. Parts of the carbon limiter and of the adjacent wall are imaged on the entrance slit. Wavelengths are given in Angstroms.

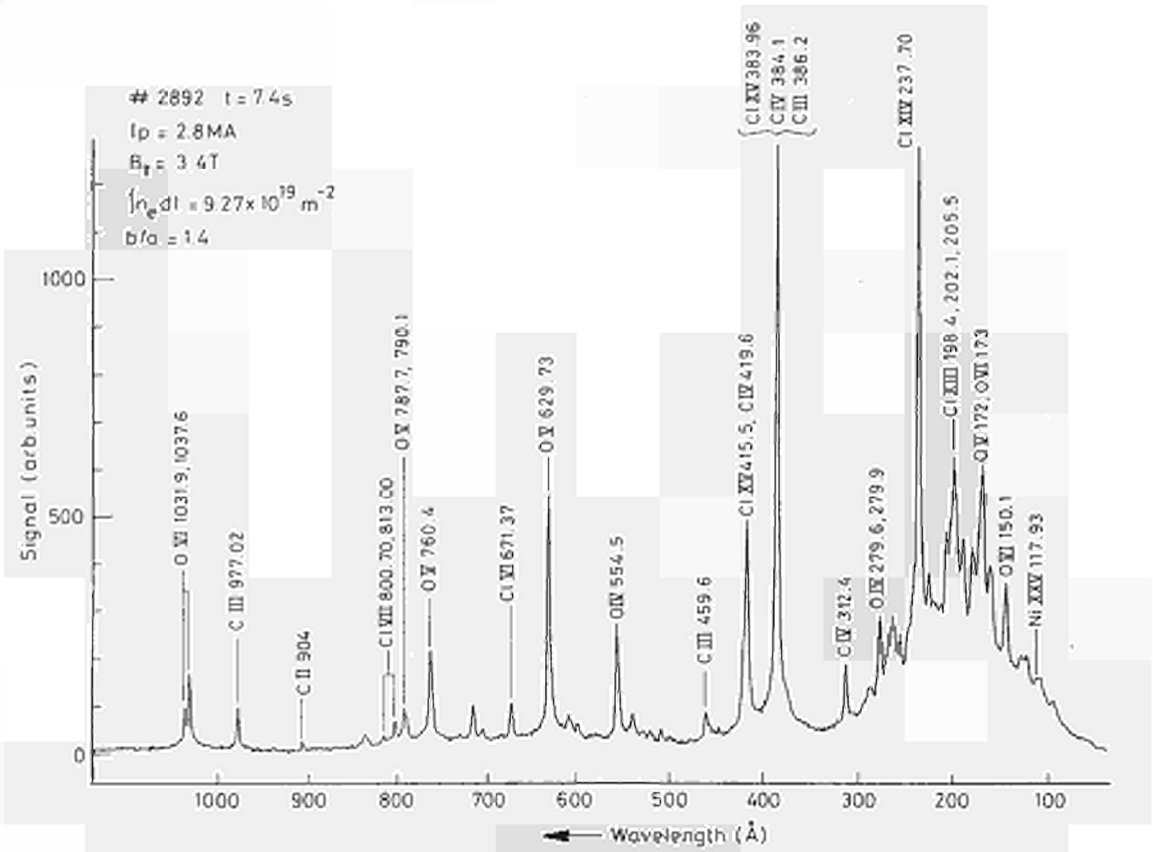

Fig. 4 VUV spectrum recorded by the survey spectrometer, integrated over 16ms during the flat-top phase of the pulse. Wavelengths are given in Angstroms.

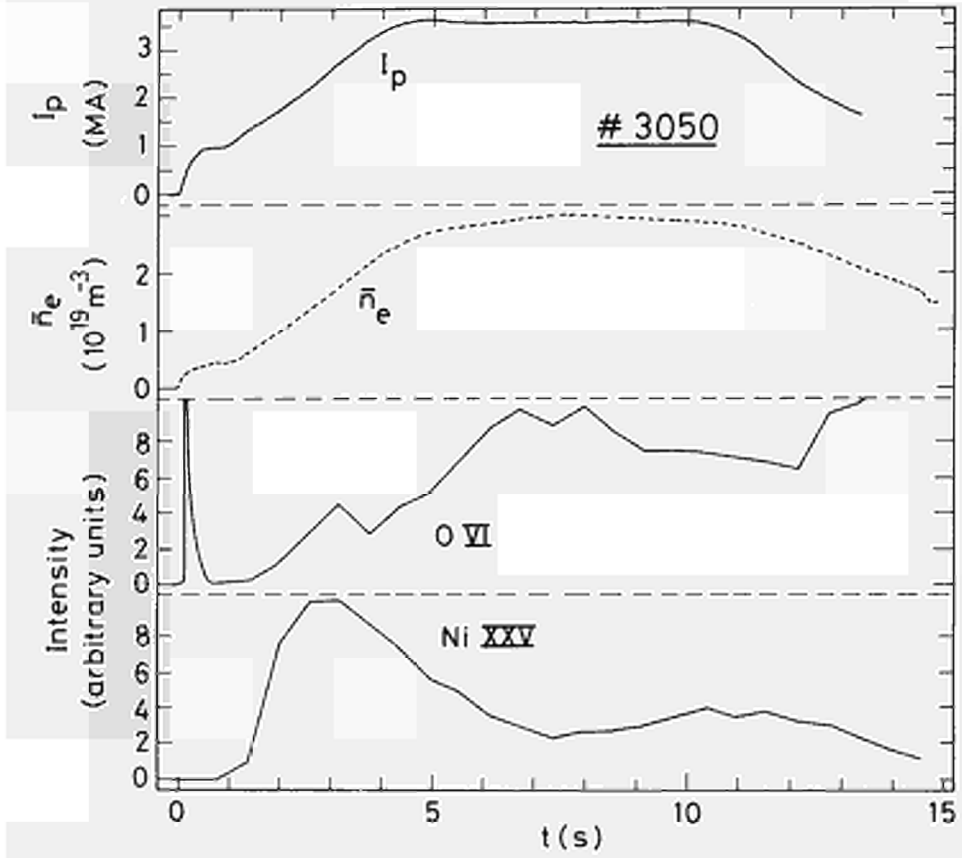

Fig. 5 Time behaviour of important VUV impurity lines. Plasma current and line average density are also shown.

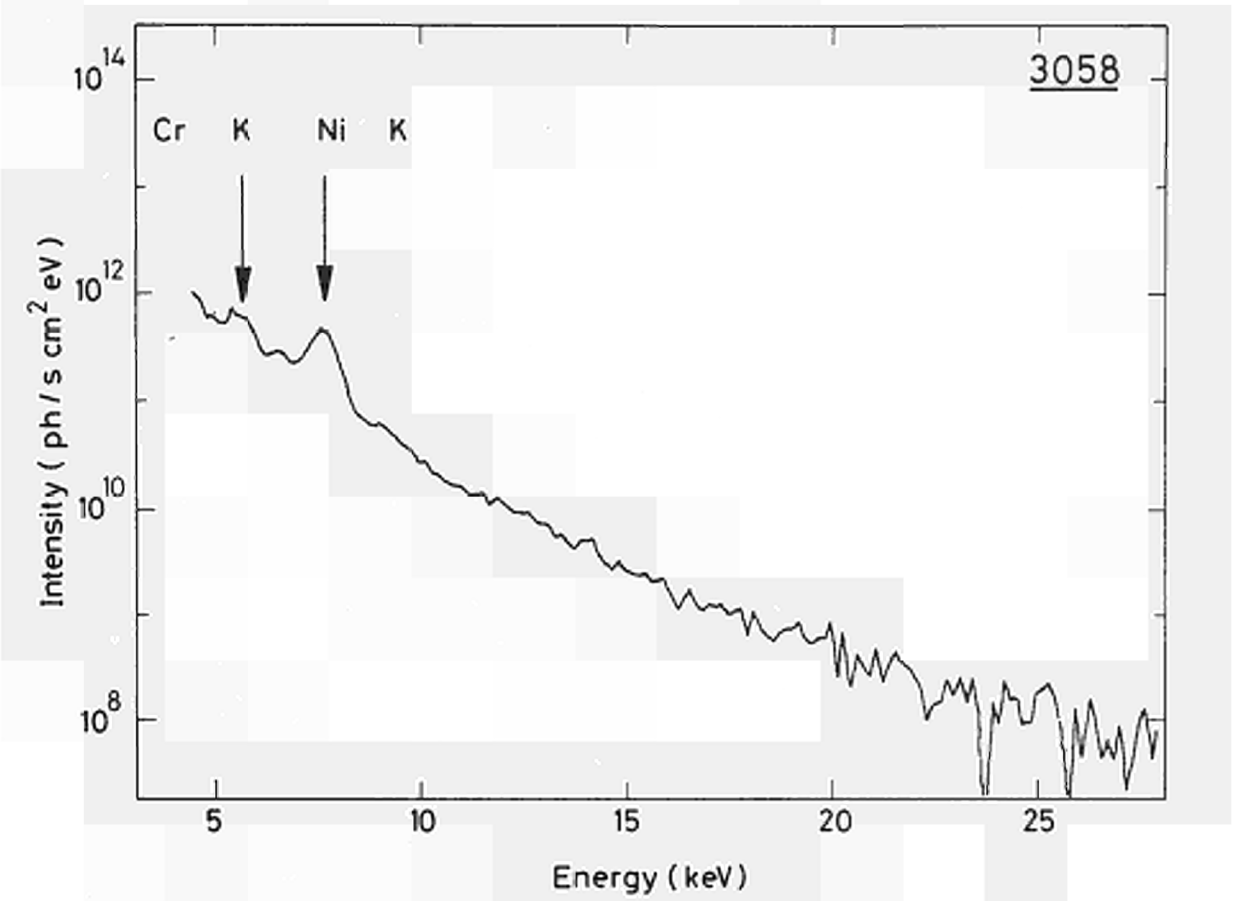

Fig. 6 Example of a PHA spectrum after carbonisation, integrated over 8s during the pulse.

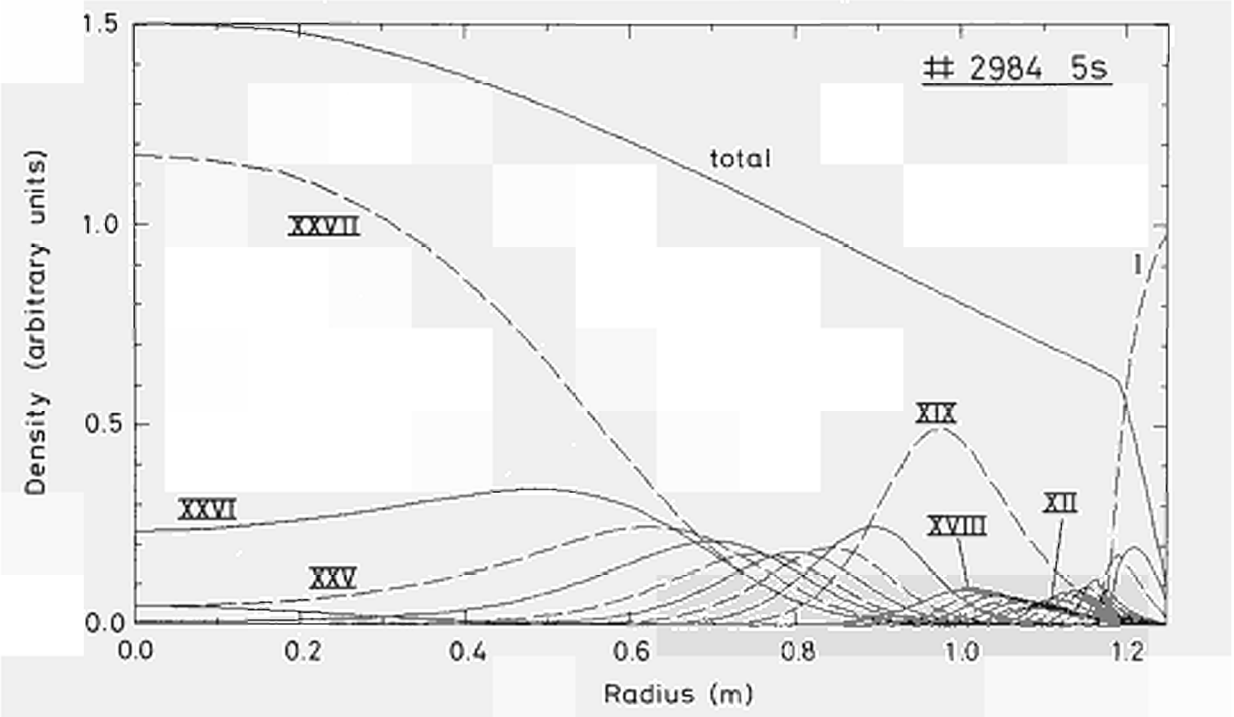

Fig. 7 Radial distributions of nickel ground state densities as calculated by the impurity transport code, using $T_{e0} = 3.3\,\mathrm{keV}$, $n_{e0} = 4 \times 10^{19}\,\mathrm{m}^{-3}$ and $D = 0.6\,\mathrm{m}^2/\mathrm{s}$.

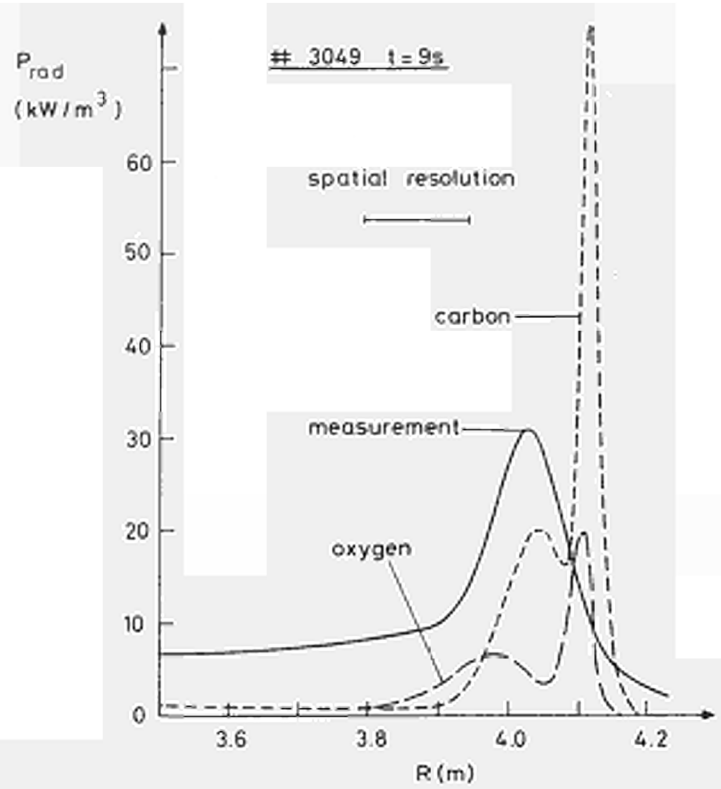

Fig. 8 Part of the Abel inverted bolometer profile of Fig. 2 versus major radius. The limiters are at 4.11 m. Calculated emission shells of carbon (3%) and oxygen (1%) are shown for comparison ($D = 0.6 m^2/s$).

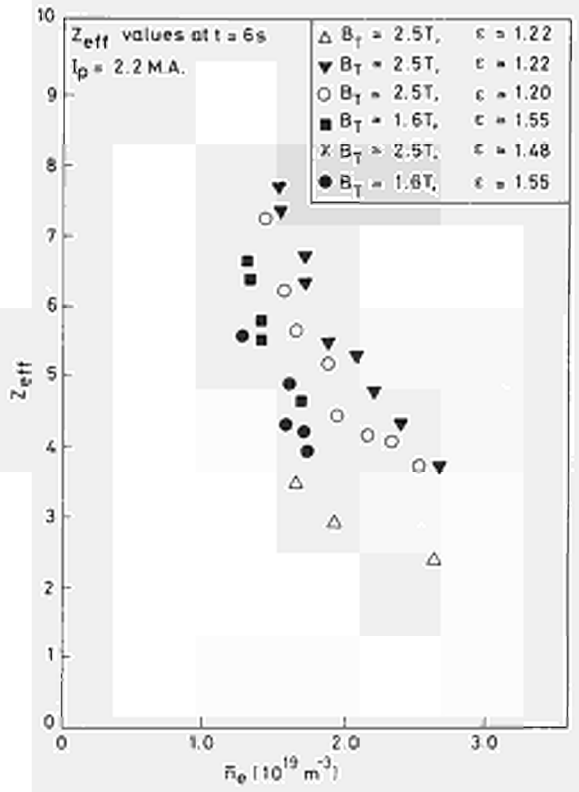

Fig. 9 Z_{eff} versus $\bar{n}_e$ for several experimental campaigns. Open triangles are for December 1983. In Spring 1984 (other symbols) higher Z_{eff} values belong to earlier operation periods.

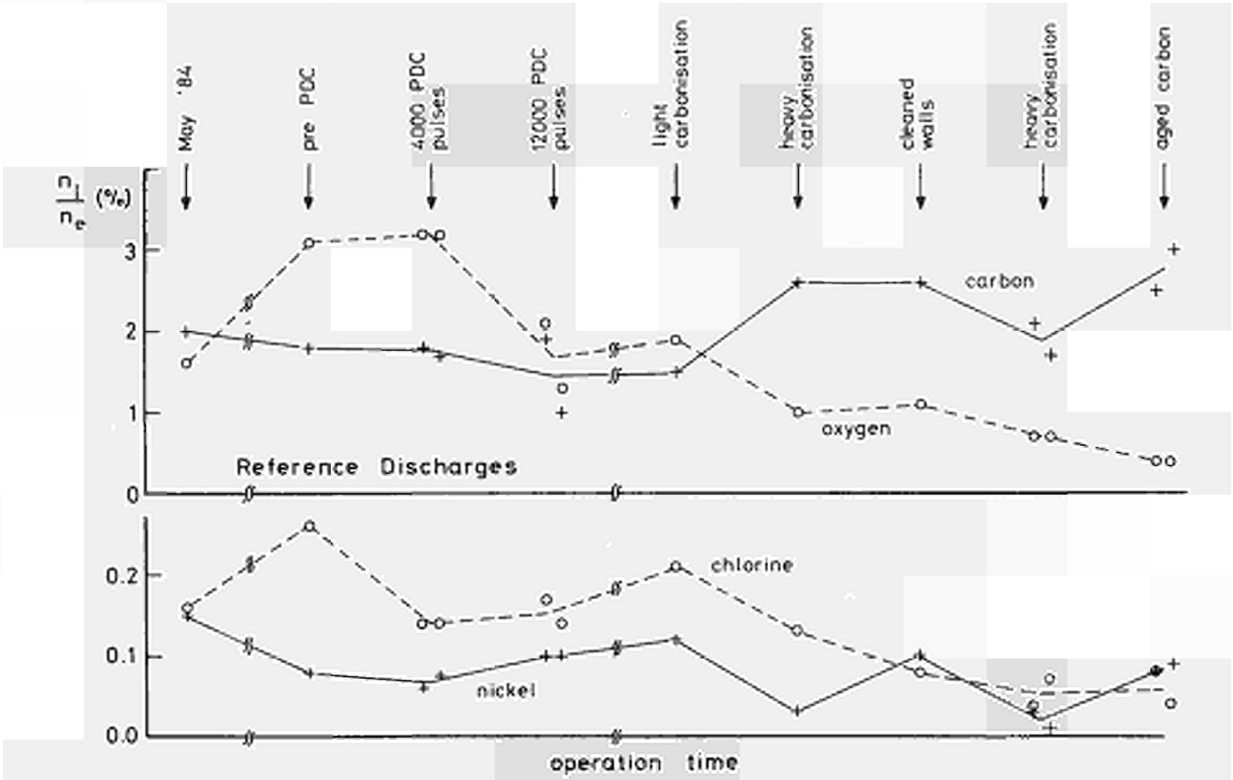

Fig. 10 Impurity levels derived from VUV spectroscopy for reference pulses during the period May—September 1984 ($I_p = 2$MA, $b/a = 2.5$T, $\bar{n}_e = 2 \times 10^{19}$ m^{-3}). The results demonstrate the consequences of PDC and carbonisation.

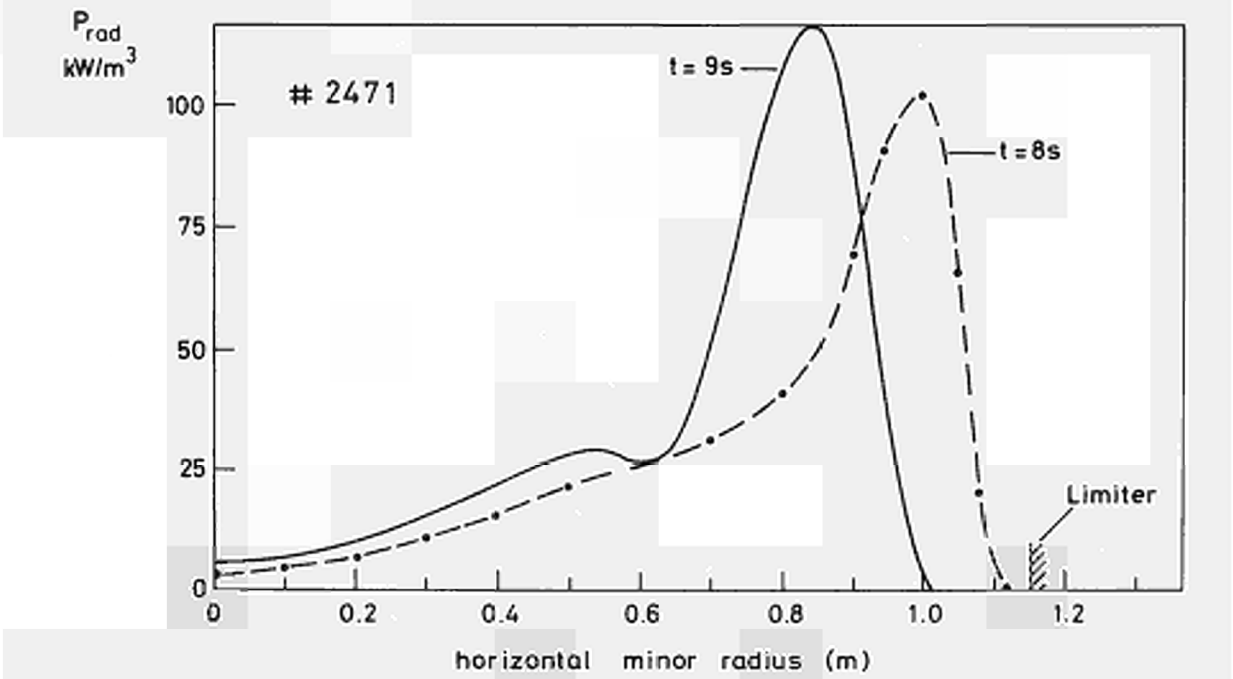

Fig. 11 Abel inverted bolometer results demonstrating the existence of a radiation mantle. It leads to a shrinking of the plasma radius and a disruption at 9.2s.

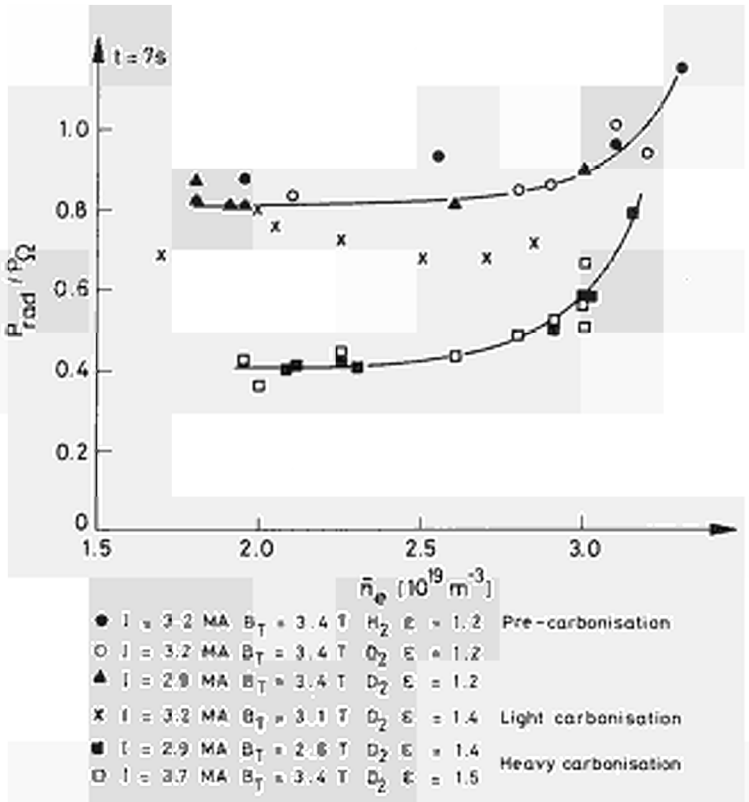

Fig. 12 Fraction of radiation power as a function of electron density before and after carbonisation.

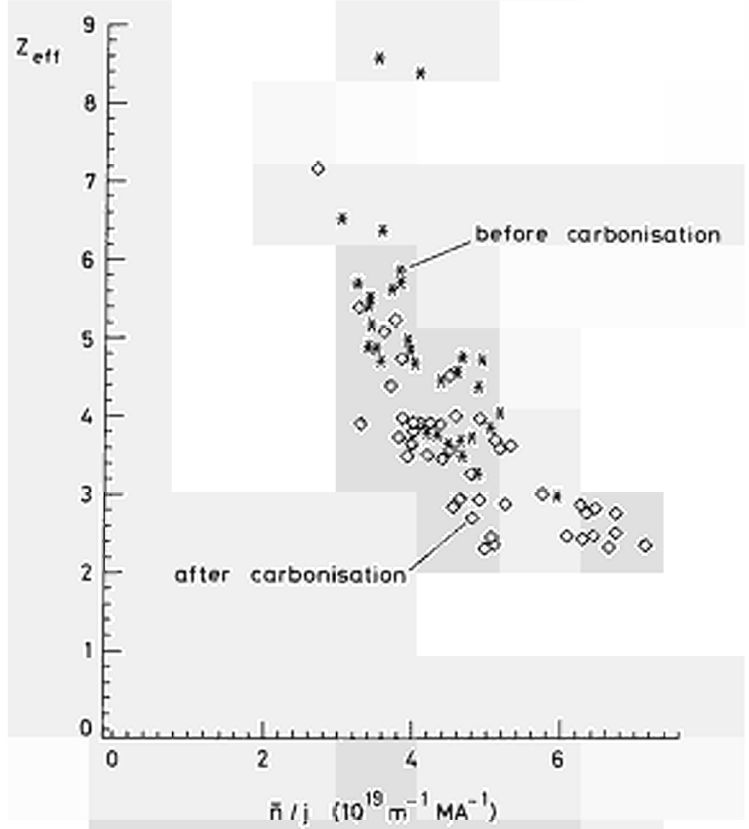

Fig. 13 Z_{eff} values for experimental periods before and after carbonisation.

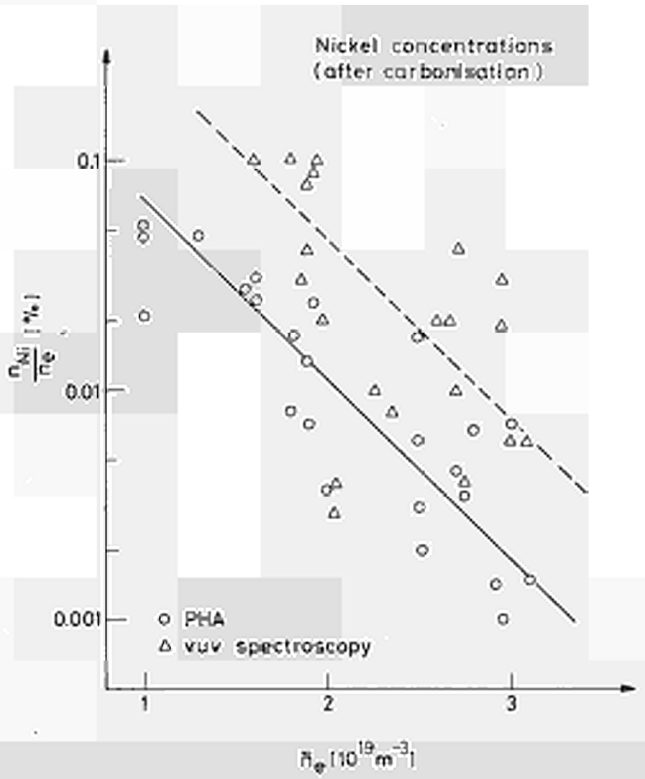

Fig. 14 Nickel concentrations derived from provisional PHA and from spectroscopy as a function of electron density. Solid and dashed lines are fitted to the respective data sets.

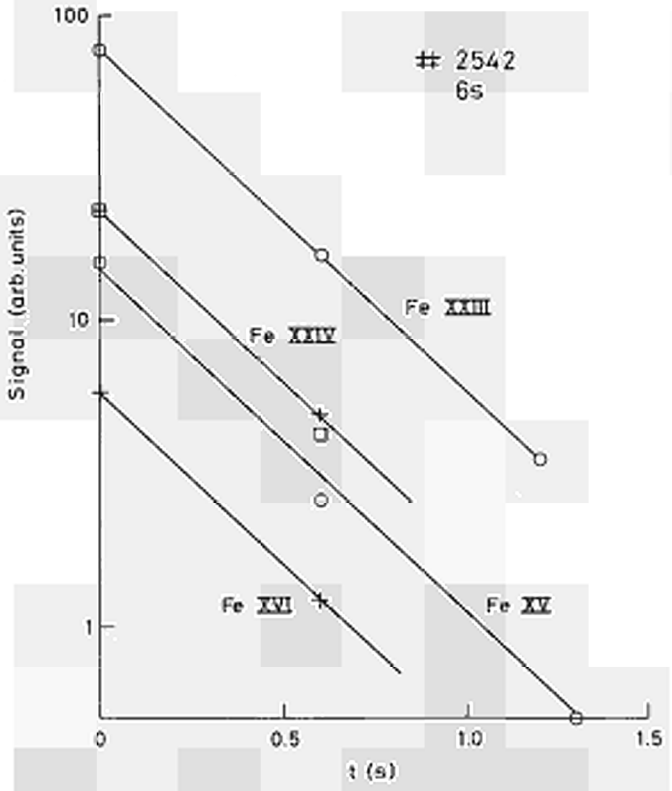

Fig. 15 Decay of iron line intensities. From the slope a diffusion coefficient of $0.6 m^2/s$ is derived.

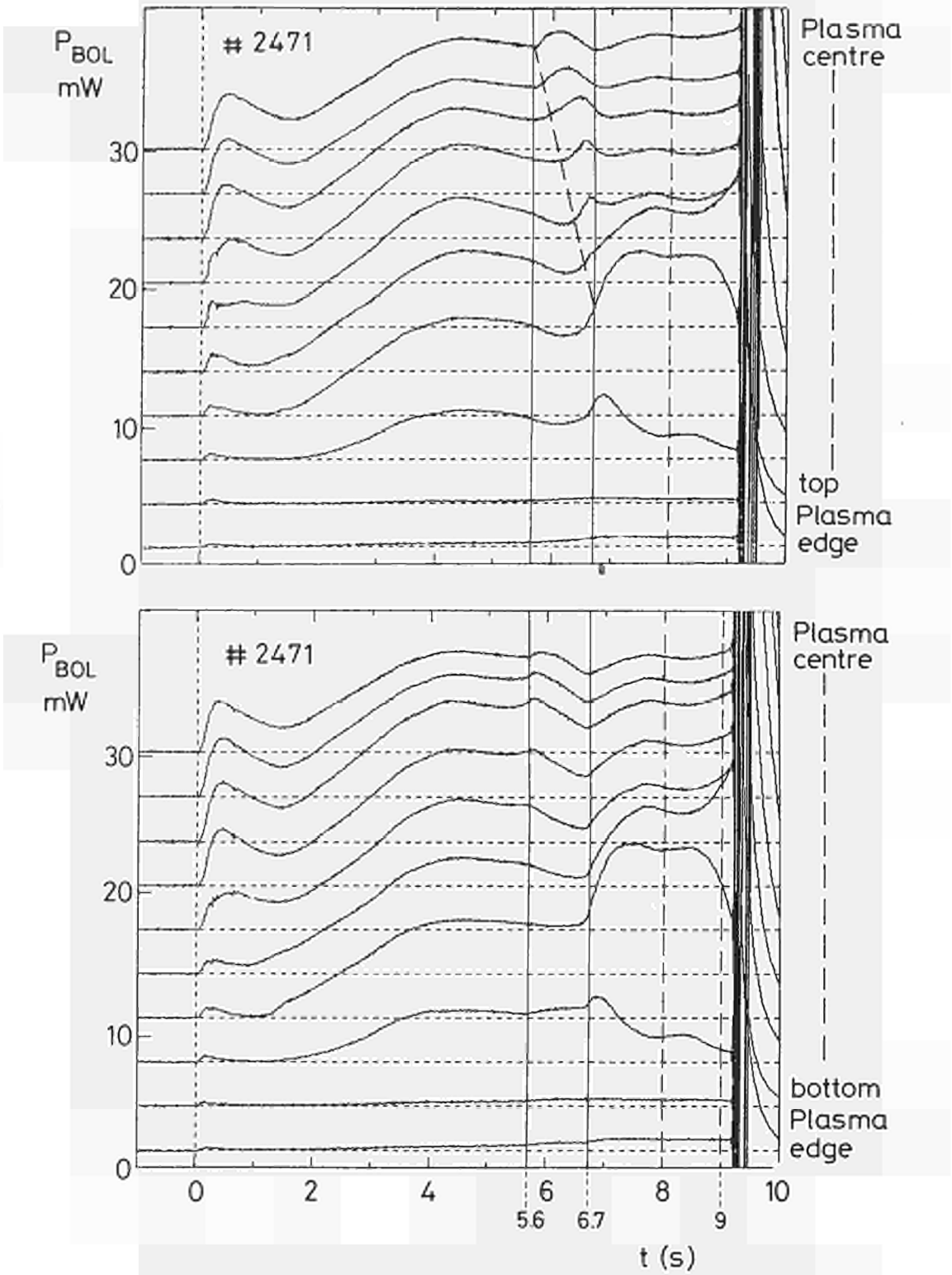

Fig. 16 Signals of the 20 channels of the horizontal bolometer camera demonstrating the development of poloidal asymmetries.

APPENDIX IV (c)
JET-P(85)10

JET Contributions to 12th European Conference on Controlled Fusion and Plasma Physics

(Budapest, Hungary, 2–6 September, 1985)

ANALYSIS OF NEUTRAL PARTICLES IN JET

S Corti, G Bracco*, M Brusati, A Gondhalekar, G Grosso+, F Hendriks°, S Segre*, V Zanza*

JET Joint Undertaking, Abingdon, Oxon OX14 3EA, UK

* on attachment from CENTRO RICERCHE ENERGIA, Euratom-ENEA Association Frascati, Italy

\+ on attachment from ISTITUTO FISICA DEL PLASMA, Euratom-CNR Association Milan, Italy

° Euratom Fellow

This paper describes features related with the analysis of neutral particles and the ion temperature in JET as measured with a passive Neutral Particle Analyser. Ten energies for two species (Hydrogen and Deuterium) are detected simultaneously so that the two energy spectra can be obtained at any time of a discharge.

An analysis code taking into account all the relevant processes, including recombination, is available. This code, using the measured neutral particle fluxes, the measured T_e and n_e profiles, taking the edge neutral density as a free parameter and assuming a T_i profile shape, allows to compute the neutral density profile and the maximum ion temperature along the line of sight. The ion and the electron densities are assumed equal throughout the calculation. The analyser used, one out of a final array of five, views a horizontal chord in the the equatorial plane of the torus at an angle of 10° with respect to a major radius /1/.

In Figure 1 typical results for a deuterium pulse are shown. The fitting of the experimental points in 1a shows a maximum ion temperature of 2.5 keV. The contribution to the neutral density due to recombination is shown in 1b while 1c and 1d show the radial location, along the line of sight, of the detected source functions. The importance of the recombination in obtaining information closer to the centre of the discharge should be noted.

Using the source function for each energy and the corresponding absolute measured flux it is in principle possible to determine an average ion temperature over the halfwidth of the source, obtaining thus ten points on the ion temperature profile. This has been done for a I=4 MA, B_T=3.4 T discharge and the resulting ion temperature profile is compared in Figure 2 with the one

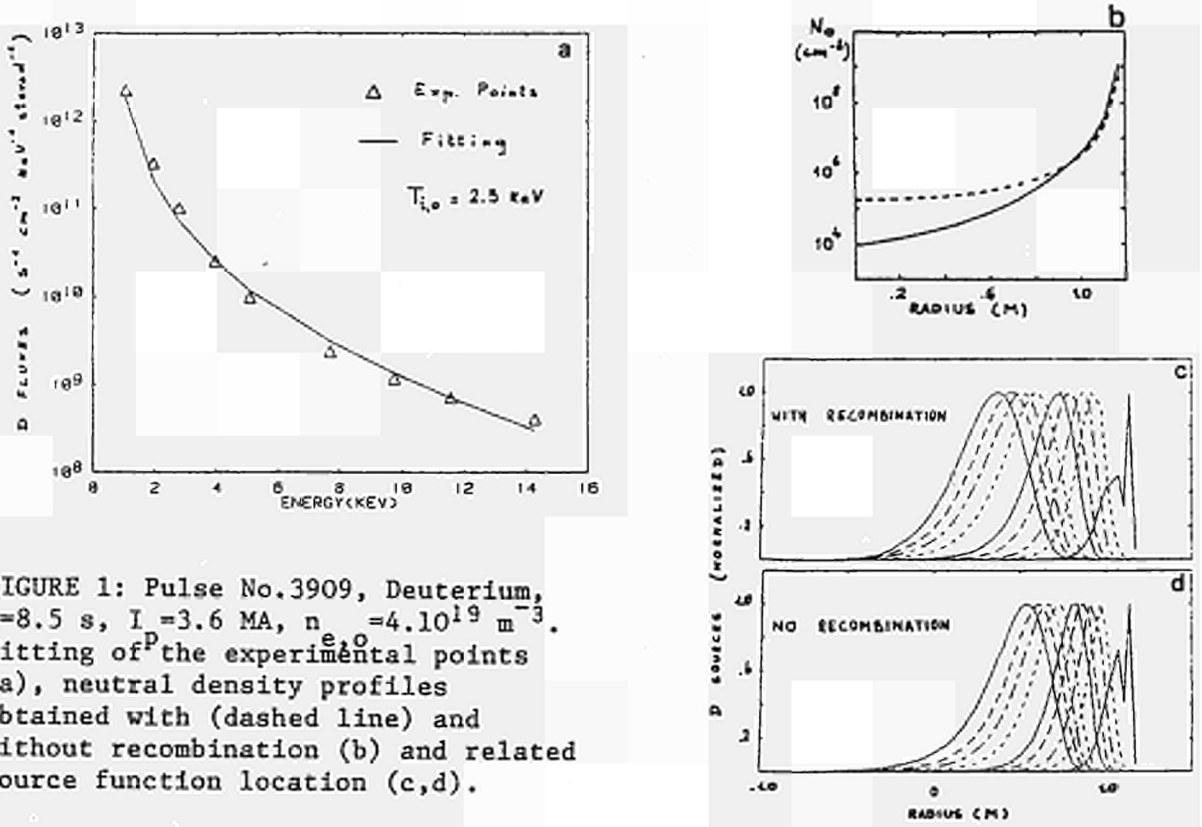

FIGURE 1: Pulse No.3909, Deuterium, t=8.5 s, I_p=3.6 MA, $n_{e,o}$=4.10^{19} m^{-3}. Fitting of the experimental points (a), neutral density profiles obtained with (dashed line) and without recombination (b) and related source function location (c,d).

obtained from transport analysis assuming an anomaly factor of 5 with respect to neoclassical ion conductivity. The horizontal error represents the halfwidth of the source function. The discrepancy between the profiles obtained in these two different ways requires further investigation, as it may be due either to departure of ion transport from the neoclassical functional dependence or to overestimating the electron temperature at the plasma edge.

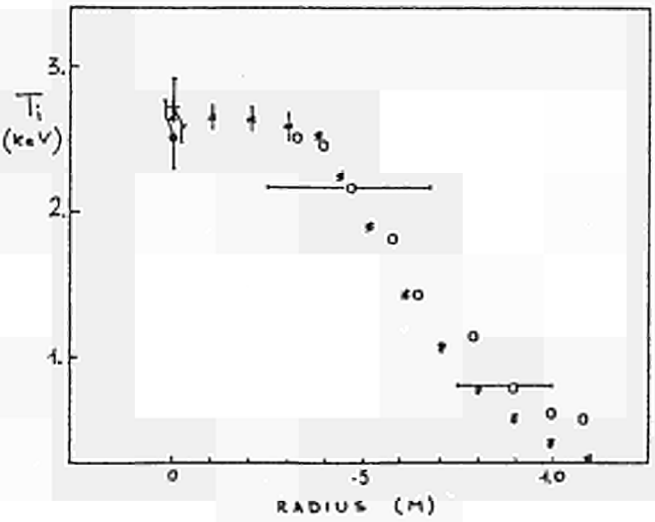

FIGURE 2: Comparison of T_i profiles from transport (*) and from local neutral sources (o) calculations. Experimental points are also shown: (+) Neutron Measurements, (•) NPA.

Some JET deuterium discharges following CH_4 carbonization, have comparable H and D concentrations due to H influx from the walls. Preliminary studies of the time behaviour of the ratio H/(H+D) at different plasma depths indicate that hydrogen reaches a stationary concentration profile in about 1s, possibly with signs of accumulation at the plasma centre.

At relatively high values of n/I, transient phenomena with strong poloidal asymmetry of the edge density and radiation (Marfes) have been observed /2/. During these events a marked enhancement of neutral particle fluxes at all energies is observed (Figure 3a).

Although the NPA is looking at the volume where marfes occur, it cannot detect particles from that zone (as shown in Figure 1c). The fact that the enhancement is observed on all channels is indicative of a modification of the neutral density beyond the zone directly affected by marfes. This is supported by a concomitant increase of the H_α measured along a vertical chord through the centre of the machine (Figure 3b).

The NPA diagnostic has been used extensively during ICRH (Ion Cyclotron Resonance Heating) studies both with He^3 and with H minority in deuterium using various types of antennae configurations (monopole, dipole, quadrupole). As an example, Figure 4a shows the ion temperature (obtained with a simple linear fitting of the measured spectra for $E \leq 2\ T_i$) when RF power is coupled through two antennae (1 MW on a quadrupole antenna between 6 and 8 seconds and 1.5 MW on a monopole between 7 and 9 seconds) for hydrogen minority heating.

Figures 4b and 4c show deuterium and hydrogen spectra.

It can be seen that the shape of the D spectra remains unchanged below 6 keV indicating that RF heating affects mainly the central ion temperature, causing probably a peaking of the profile.

The hydrogen spectra, having been corrected for background, show the appearance of an energetic tail above 7 keV with a slope corresponding to about 20 keV.

REFERENCES

/1/ G Bracco, S Corti, V Zanza et al - 'First Results from JET Neutral Particle Analyser' - JET Report JET-IR(84)04.

/2/ J O'Rourke et al - 'Poloidally Asymmetric Edge Phenomena in JET' - this conference.

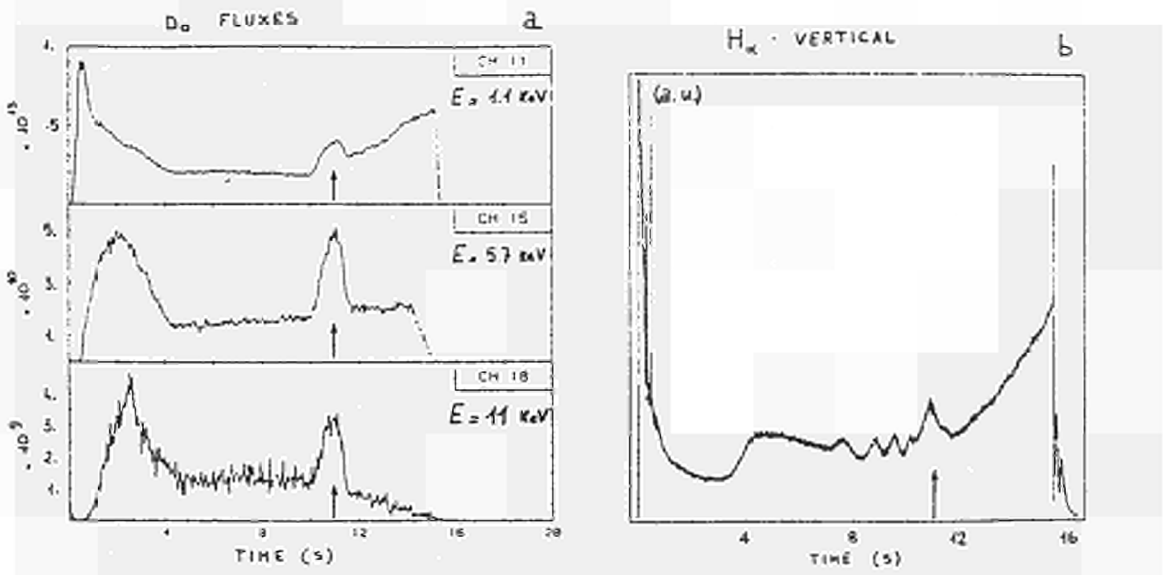

FIGURE 3: Neutral fluxes (a) and vertical H_α (b) measured during a plasma discharge showing the appearance of a Marfe around 11 s (pulse number 3428).

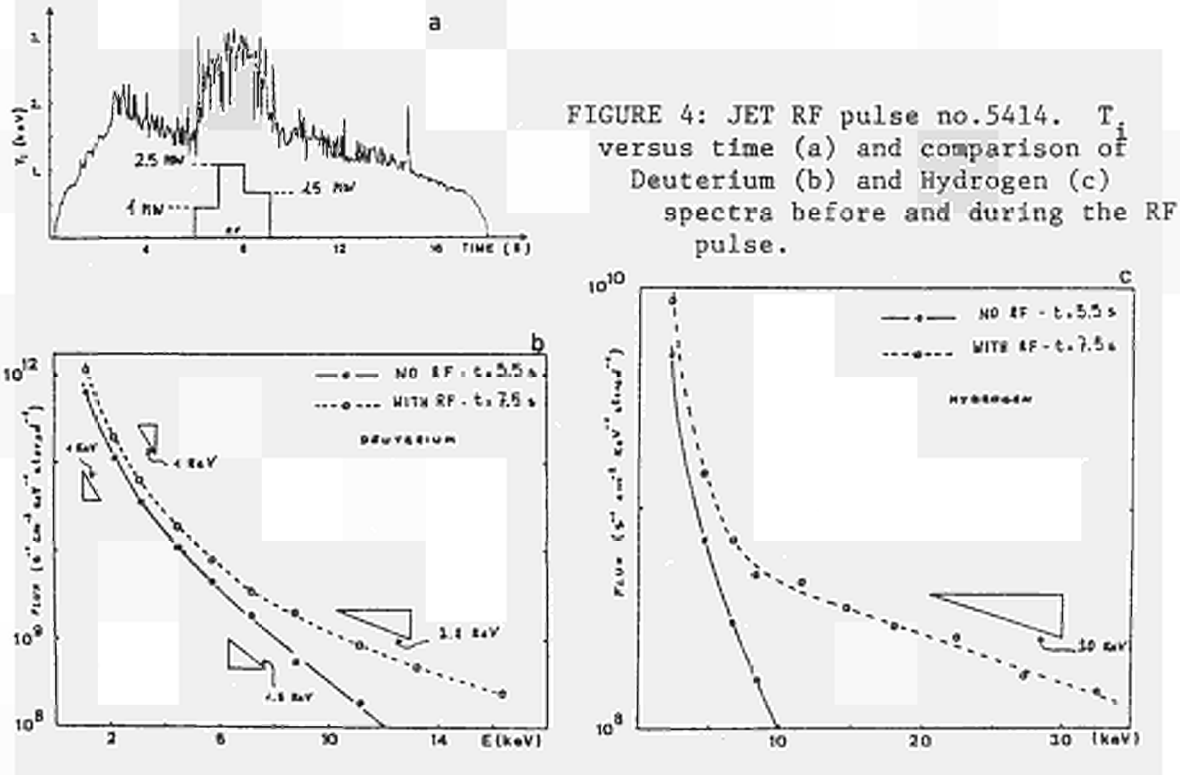

FIGURE 4: JET RF pulse no.5414. T_i versus time (a) and comparison of Deuterium (b) and Hydrogen (c) spectra before and during the RF pulse.

A Theory of Marfes

T.E. Stringer

JET Joint Undertaking, Abingdon, Oxon. OX14 3EA, UK.

Introduction A marfe is a toroidally symmetric band of enhanced radiation sometimes observed in tokamaks. It is strongly localised near the plasma edge, typically has a poloidal width of about 30°, and always occurs on the inboard side. They were first reported on Alcator C[1].

Marfes have been attributed to a radiative thermal instability[1]. As is discussed later, a local decrease in temperature leads to a local increase in radiation cooling. This destabilising effect is opposed by parallel thermal conduction. Instability can occur only near the plasma edge where parallel thermal conductivity is low. A criterion for the onset of such an instability will be derived and its saturated state studied. Theoretical predictions are consistent with experiment.

Linear Analysis of the Radiative Thermal Instability The balance between radial conduction into the edge region, enhanced radiation from the cool region and parallel conduction of energy into the cool region, is described by the total energy conservation equation:

$$3\frac{\partial}{\partial t}(nT) = \frac{\partial}{\partial s}\left\{K_{\parallel}\frac{\partial T}{\partial s} - 5nTv_{\parallel}\right\} + \frac{1}{r}\frac{\partial}{\partial r}\left\{rK_{\perp}\frac{\partial T}{\partial r}\right\} - \sum_z nn_z L_z(T) \qquad (1)$$

where $T=T_e=T_i$, s denotes distance along a field line, $K_{\parallel}$ and $K_{\perp}$ are the thermal conductivities parallel and perpendicular to the magnetic field, n_z is an impurity density, $L_z(T)$ the radiation rate, and other notation is standard. Since marfes are observed to be toroidally symmetric, the temperature and density perturbation are assumed to be functions only of poloidal angle and radius, i.e. $\tilde{T}(r,\theta,t)=\tilde{T}(r)\cos m\theta \exp(\gamma t)$. To obtain a dispersion equation for γ, Eq.(1) is linearised and combined with the continuity equation and the parallel component of the fluid equation of motion. This gives:

$$\gamma\left[\gamma^2 + \frac{5}{3}C_s^2 k_{\parallel}^2\right] = -\frac{1}{3n}\left[K_{\parallel}k_{\parallel}^2 + \frac{K_{\perp}}{\Delta^2} + nn_z\frac{dL}{dT}\right]\left[\gamma^2 + C_s^2 k_{\parallel}^2\right] + \frac{4}{3}\frac{n_z L}{M}k_{\parallel}^2 \qquad (2)$$

where $C_s^2=2T/M$ and $k_{\parallel}^2=-\partial^2/\partial s^2=m^2B_\theta^2/r^2B_\phi^2$. In deriving this equation the perpendicular heat conduction term in Eq.(1) has been replaced by $-K_{\perp}\tilde{T}/\Delta^2$, where $\Delta\cong$ the radial half-width of the perturbation, and the fractional density perturbation of the impurity is assumed equal to that of the electrons. The

condition for instability is:

$$K_{\parallel}k_{\parallel}^2 + \frac{K_{\perp}}{\Delta^2} - \frac{2nn_z}{T} + nn_z\frac{dL}{dT} < 0 \qquad (3)$$

An equivalent criterion has been derived independently by J. Neuhauser[2].

Both the parallel and perpendicular heat conduction tend to inhibit the instability, the former is usually the more important. The third and fourth terms in Eq.(3) express the change in radiation due to density and temperature variation respectively. Density varies roughly inversely with temperature as plasma moves to maintain constant pressure along the magnetic field. The temperature variation in the radiation rate for carbon in coronal equilibrium is shown by the solid curve in Fig.1. However, impurity ions near the plasma edge are generally far from coronal equilibrium. A rough approximation to non-coronal radiation may be obtained by shifting the coronal radiation curve $L_c(T)$ to higher temperatures, i.e. $L(T_e)=L_c(\zeta T_e)$, where ζ can vary from 1 to 0.3 depending on how far the ionisation distribution differs from coronal[3]. The third term in Eq.(3) is always destabilising, while the fourth is destabilising for T_e larger than the maximum in $L(T_e)$. The two terms are comparable in magnitude.

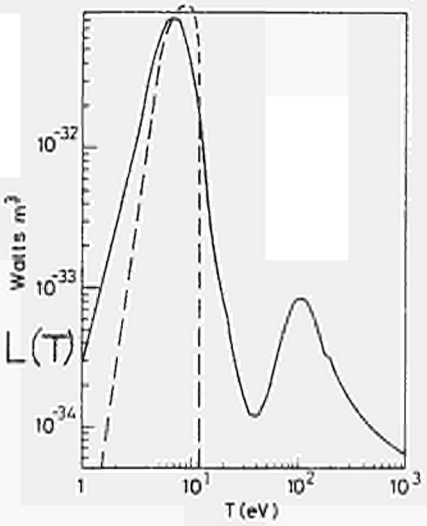

Fig.1 Coronal radiation rate for carbon (solid curve) and analytic model (dashed).

When applied to Alcator C with 1% carbon concentration and ζ=0.5, Eq.(3) predicts a critical edge density of $1.1\times10^{20}m^{-3}$ for marfe onset. This is close to that observed[1]. The measured Doppler broadening in the CIII line in JET suggests ζ=0.3. This gives a predicted critical edge density of $8\times10^{18}m^{-3}$ in JET which, although about twice that observed, is within the uncertainty in the present analysis.

The Saturated Instability This must satisfy the nonlinear steady state form of Eq.(1). An important nonlinear effect is the variation of parallel thermal conductivity with temperature, $K_{\parallel}\cong CT^{5/2}m^{-1}sec^{-1}$ To allow a simple analytic solution of Eq.(1) the following form is assumed for the radiation rate:

$$\begin{aligned} L(T) &= PT^{11/2} && \text{for } T<T_0 \\ &= bPT^2\,[T_1^{7/2}-T^{7/2}] && \text{for } T_0<T<T_1 \\ &= 0 \text{ for } T>T_1 \end{aligned}$$

where $T_1=T_0[(1+b)/b]^{2/7}$. The dashed line in Fig.1 illustrates this function for

T_0=6eV, b=0.1. The analytic solution should be at least qualitatively correct, and the scaling can be seen more clearly than in a numerical solution. Omitting the convective term, the solution of Eq.(1) is then

$$\begin{aligned} T^{7/2} &= A\cosh g\theta+H/g^2 && \text{for } \theta<\theta_0 \\ &= -B\cos(h\theta+\psi)+F/h^2 && \theta_0<\theta<\theta_1 \\ &= T_1^{7/2}+H(\theta-\theta_1)(2\pi-\theta_1-\theta)/2 && \theta>\theta_1 \end{aligned} \qquad (5)$$

where $g^2=uPT^2nn_z$, $u=7r^2B_\phi^{\,2}/2CB_\theta^{\,2}$, $H=uD$, $h^2=bg^2$, $F=h^2T_1^{7/2}-H$.

D=total conducted heat influx to the edge region/$8\pi^2rR\Delta$, where 2Δ is the radial width of the marfe. θ_0 and θ_1 are the angles at which $T=T_0$ and T_1 respectively. The boundary conditions $T(\theta_0)=T_0$, $T(\theta_1)=T_1$, and continuity of $\partial T^{7/2}/\partial\theta$ at θ_0 and θ_1 give five equations for the constants A,B,ψ,θ_0 and θ_1. Thus the poloidally asymmetric steady state, if one exists, is completely determined by the plasma parameters nT, n_z/n and D, and the radiation rate parameters P,T_0 and T_1. The steady state is arbitrarily taken to be centred around $\theta=0$, in practice its poloidal location is determined by poloidal asymmetry in the flux or impurity drifts. Figure 2 shows the predicted temperature variation for Alcator C parameters, with carbon as the radiating impurity, and several values for nT. $D=2\times10^6$w/m^3 corresponds to a total conduction influx of 200kW spread over an edge region 2.5cm wide. Asymmetric steady states become possible only when the maximum radiation rate (at T_{max} where L(T) has its maximum) exceeds the energy input. For the chosen parameters this is when $nT>2.1\times10^{20}$eV/m^3. The steady state has a central region around $\theta=0$ where $T<T_{max}$, such that radiation locally balances the energy input, and an outer region around $\theta=\pi$ where $T>T_{max}$ and radiation is less than the energy input. The surplus energy is conducted into an intermediate region where radiation is near its maximum, and locally exceeds the energy input. As nT increases, the strongly radiating intermediate region becomes narrower and moves to smaller θ until finally it reaches $\theta=0$ and the inner region disappears. The experimental marfe illustrated in Reference 2 has $nT=2\times10^{21}$eV/m^3, the radiating region extends

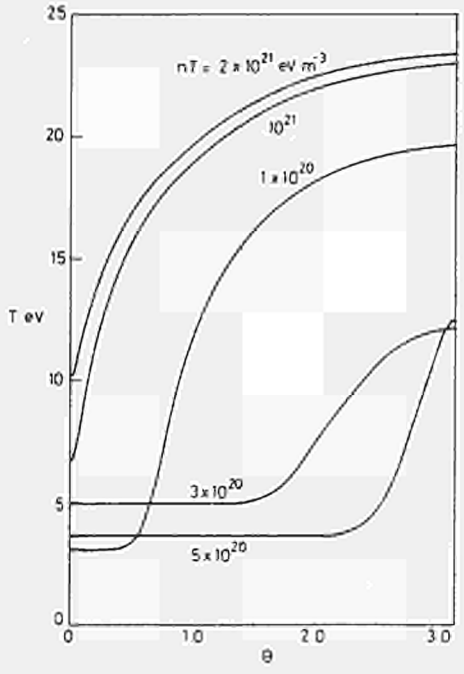

Fig.2 Stationary poloidally asymmetric temperature distributions for various nT.

poloidally over 30°, and the temperature varies poloidally by a factor of about 2 with an inverse variation in density. This is quite similar to the predicted variation in Fig.2 for the same nT value.

Acknowledgement The author is grateful to W. Engelhardt for pointing out the destabilising effect of density variation and other constructive criticism.

References

[1] LIPSCHULTZ, B. et al. Nucl. Fusion 24 (1984) 977.

[2] NEUHAUSER, J. Private communication.

[3] DNESTROVSKII, V. and PEREVERZEV, G. Nucl. Fus. 23 (1983) 633.

TWO DIMENSIONAL ANALYTIC AND NUMERICAL MODELS OF THE SCRAPE-OFF LAYER OF TOROIDAL LIMITERS

R. Simonini, W. Feneberg*, A. Taroni

JET Joint Undertaking, Abingdon, Oxon., OX14 3EA, UK
* On attachment from IPP, Garching

1. Introduction

From the classical system of equations describing the transport processes we derive a simplified system (one fluid, two spatial dimensions) of flow equations for the density n, the parallel velocity $v_{||}$, the perpendicular velocity $v_{\rho cl}$ and the pressure p in the plasma boundary layer (Section 2).

A code has been written for the solution to these equations, based on a splitting technique in spatial directions (Section 3). Classical effects are taken into account and shown to be important: they lead to radial fluxes near the limiter tip of the same order (or even larger) of the anomalous ones usually adopted, resulting in a non-symmetric layer around the limiter. Another characteristic feature of this code with respect to other 2-D codes [1-3], is the avoidance of any symmetry assumption along field lines. A JET-like plasma with one toroidal limiter has been considered in the computations reported here.

2. Description of the Physical Model

We start from the moment equations for electrons and ions given in [4], assuming toroidal symmetry. We use an orthogonal coordinate system: ρ labels the magnetic surfaces, θ is a poloidal coordinate and ϕ the toroidal one. The metric is given by $ds^2 = H_\rho{}^2 d\rho^2 + H_\theta{}^2 d\theta^2 + R^2 d\phi^2$, R being the distance from the torus axis. In the electron equations we neglect the resistivity and the external toroidal electric field, which is justified in the thermal-diffusion dominated scrape-off layer. Using an expansion in the ratio ε of the toroidal Larmor radius to the layer thickness we find that in lowest order the flow is parallel to the magnetic field. From the toroidal component of the electron equations of motions we find the flow velocity $v_{\rho cl}$ perpendicular to the magnetic surfaces:

$$v_{\rho cl} = \frac{c}{enB_\phi H_\theta} \frac{\partial}{\partial\theta} (m_i n v_{||}{}^2) - 0.71 \frac{c}{eB_\phi H_\theta} \frac{\partial T_e}{\partial\theta} \qquad \ldots (1)$$

here c is the light velocity, e the electron charge, m_i the ion mass, B_ϕ the toroidal magnetic field, T_e the electron temperature. The first term in eq (1) gives the contribution of a perpendicular electric current related to the inertial term of the ions, while the second comes from parallel thermal diffusion.

Assuming $T_e = T_i = T$ and one fluid, one is left with the system:

$$\sqrt{g} \frac{\partial n}{\partial t} = - \frac{\partial}{\partial\rho} \left[\frac{\sqrt{g}}{H_\rho} n v_\rho \right] - \frac{\partial}{\partial\theta} \left[\frac{h\sqrt{g}}{H_\theta} n v_{||} \right] + \sqrt{g}\, S_i$$

$$\sqrt{g}\,\frac{\partial(nv_{\parallel})}{\partial t} = -\frac{\partial}{\partial\rho}\left[\frac{\sqrt{g}}{H_\rho} nv_\rho v_{\parallel}\right] - \frac{\partial}{\partial\theta}\left[\frac{h\sqrt{g}}{H_\theta} nv_{\parallel}^2\right] + H_\rho h\,\frac{\partial R}{\partial\theta} nv_{\parallel}^2 + \frac{2}{m_i}\frac{\partial}{\partial\theta}\left[\frac{h^2\sqrt{g}}{H_\theta^2}\eta_o\frac{\partial v_{\parallel}}{\partial\theta}\right]$$

$$- \frac{2}{3m_i}\frac{h\sqrt{g}}{H_\theta}\frac{\partial}{\partial\theta}\left[\eta_o\frac{h}{H_\theta}\frac{\partial v_{\parallel}}{\partial\theta}\right] - \frac{2}{m_i}\frac{h\sqrt{g}}{H_\theta}\frac{\partial p}{\partial\theta} + \sqrt{g}\,F_{\parallel}$$

$$3\sqrt{g}\,\frac{\partial p}{\partial t} = \frac{\partial}{\partial\rho}\left[\frac{\sqrt{g}}{H_\rho} q_\rho\right] + \frac{\partial}{\partial\theta}\left[\frac{\sqrt{g}h}{H_\theta} q_{\parallel}\right] - \frac{\partial}{\partial\theta}\left[\frac{5\sqrt{g}h}{H_\theta} v_{\parallel} p\right] + \frac{2\sqrt{g}}{H_\theta} hv_{\parallel}\,\frac{\partial p}{\partial\theta} + \sqrt{g}\,Q. \qquad \ldots (2)$$

Here $p = nT$, $\sqrt{g} = H_\rho H_\theta R$, $h = B_\theta/B$ is the ratio of the poloidal to the total magnetic field, while $v_\rho = v_{\rho cl} + v_{\rho an}$, $v_{\rho an}$ being an anomalous transverse diffusive velocity $v_{\rho an} = D/(nH_\rho)\,\partial n/\partial\rho$; D can be any anomalous diffusion coefficient. Here we choose for simplicity an Alcator-Intor form $D = D_{AI}/n$ with constant D_{AI}. η_o and $q_{\parallel}$ are the classical viscosity and parallel heat flux as given in [4]. q_ρ is the transverse heat flux, that we choose to be anomalous, again of the Alcator-Intor type: $q_\rho = \chi_{AI}\,\partial/\partial_\rho(p/n)$. S_i, $F_{\parallel}$ and Q are related to the neutral background and radiation losses. Here we assume $F_{\parallel} = 0$, while S_i and Q come from a simplified analytic background neutral model, relating the neutral density to their mean free path.

The model described above, with proper boundary conditions (see Sections 3 and 4), is on one side sufficient to study the effect of the classical term $v_{\rho cl}$ and on the other side contains, from the mathematical and numerical point of view, most of the features that are present in more complex boundary models. For this reason, it has been chosen as a test model for the present 2-D limiter edge code.

3. Numerical Method

The system of equations (1) and (2) requires a careful choice of the numerical scheme because it is not of the type solved by standard methods of numerical fluid dynamics. In fact, not only does it present a mixture of terms with hyperbolic and parabolic character, but the relative importance and even the presence of these terms depend on the direction considered. This must reflect on the choice of both the numerical method and the proper boundary conditions. We decided to adopt a splitting technique along directions as the one that can best treat the anisotropy due to the magnetic field. Thus, the per-se interesting sets of the 1-D parallel and perpendicular equations can be solved independently, and, moreover, the technique and the code can be easily extended to include additional equations (e.g. $T_e \neq T_i$, impurities).

A staggered finite difference grid is used for spatial discretisation to avoid unstable wriggles in the solution. Good resolution near the limiter is achieved by a non-uniform grid. Different terms can be centered in space and time in a different way by prescribing a set of parameters. Implicitness is treated by linearisation and iteration. An important feature characterising this code with respect to others (see e.g. [1-3] is the possibility to combine a periodicity condition for the plasma with given boundary conditions for the limiter, thus avoiding any assumption of symmetry along field lines. This is of course necessary to study the effects of eq. (1).

A full 2-D Monte-Carlo code is at present being interfaced to the fluid code to treat the background neutrals, with the aim to allow benchmark computations to calibrate simpler models of neutrals.

4. Numerical Results

To test the code and to study the effects of $v_{\rho cl}$ we have considered a simple configuration with a toroidal limiter that in the poloidal plane maps

as in Fig. 1. Dimensions are JET-like:

$$R_o = 300cm,\ \rho_{MP} = 110cm,\ \rho_L = 130cm,\ \rho_W = 150cm,\ \rho_L(\pi - \theta_L) \simeq 40cm$$

These assumptions, in particular circular magnetic surfaces, are not essential to our code. Non-circular plasmas can be treated by supplying the appropriate metric coefficients (possibly tabulated). An extension to two toroidal limiters and different limiter and wall shapes is being implemented.

The following boundary conditions have been considered:

$\rho = \rho_{MP}, \rho_W;\ -\pi \lesssim \theta \lesssim +\pi$	: given n, T; $v_{\|\|}$ advected by v_ρ or computed through $\partial v_{\|\|}/\partial\rho = 0$.
$\theta = \pm\pi;\ \rho_{MP} \lesssim \rho < \rho_L$	: periodicity.
$\rho = \rho_L,\ -\pi \lesssim \theta \lesssim -\theta_L$ or $\theta_L \lesssim \theta \lesssim \pi$	: n, T are computed by interpolation from the values at $(\rho_L, \pm\theta_L)$; $v_{\|\|}$ either advected or computed as above.
$\rho_L \lesssim \rho < \rho_W;\ \theta = \pm\theta_L$	: n advected by $v_{\|\|}$; $v_{\|\|}$ computed by the free surface condition [1],[5] $2p = \eta_o\, h/H_\theta\, \partial v_{\|\|}/\partial\theta$, $v_{\|\|} \lesssim c_s$; $q_{\|\|} = \beta n v_{\|\|} T$, $\beta \simeq 1 - 5$, $T \gtrsim T_W$.

The transition of $v_{\|\|}$ from the sound velocity c_s to zero at the limiter tip is represented by a linear decay along ρ over 2 or 3 steps ($\simeq$ 2cm). The width of this transition region influences the details of the nearby profiles, but not the general pattern. Similarly, we have found that reasonable changes in the values of T_W (2 - 10eV) and n_W (10^{10} - 10^{11} cm^{-3}) do not influence the results noticeably. More important can be the changes in the background neutral model and in particular the recycling model at the limiter. For this reason benchmark computations and/or coupling with a Monte-Carlo neutral code are required.

Within the frame of our present model and assumptions, the importance of $v_{\rho cl}$ is illustrated in Figs. 1-4. Figures 1-3 map n, $v_{\|\|}$ and T in a typical case ($n_{MP} = 10^{13}$ cm^{-3}, $T_{MP} = 400eV$) with $v_{\rho cl}$. Here $D_{AI} = 4000cm^2/s$, $\chi_{AI} = 5 \times 10^{17}$ $cm^{-1}s^{-1}$. T near the limiter tip varies from $T_u = 32eV$ upwards to $T_d = 25eV$ downwards. More significant is the change of particle flux from $\phi_u = 4.0 \times 10^{18}$ to $\phi_d = 2.5 \times 10^{18}$ $cm^{-2}s^{-1}$. The up-down asymmetry does of course decrease as $v_{\rho an}$ increases, but it is still noticeable at D_{AI} as large as $40{,}000cm^2/s$. In this case we find T_u=32eV, T_d=29eV, $\phi_u = 2.9 \times 10^{18} cm^{-2}s^{-1}$, $\phi_d = 2.5 \times 10^{18} cm^{-2}s^{-1}$.

For comparison, Fig. 4 shows the pattern of the parallel velocity when the classical term is absent (dashed lines represent negative velocities).

In conclusion, even if these results are to be considered as preliminary only, due to the simplifying assumptions in models and geometry, they show that classical effects can indeed play a role in the boundary layer. Moreover, they illustrate the potential capabilities of the code which is at present being adapted to more realistic JET situations.

References

[1] Igitkhanov, Y.L., Kukushkin, A.S., Pigarov, A.Y., Pistunovich, V.I., Proc. 11th European Conf. on Controlled Fusion and Plasma Physics, Aachen, 5-9 September 1983.

[2] Braams, B.J., Ibidem.

[3] Petravic, M., Heifetz, D., Post, D., Proc. 10th IAEA Int. Conf. on Plasma Physics & Controlled Nucl. Fusion Research, London, 12-19 Sept. 1984.

[4] Braginskii, S.I., Rev. of Plasma Physics, edited by Leontovich, M.A., (Consultant Bureau, New York, 1965), Vol 1, p 205.
[5] Landau, L., Lifchitz, E., Mecanique des Fluides, Editions MIR, Moscow, 1971.

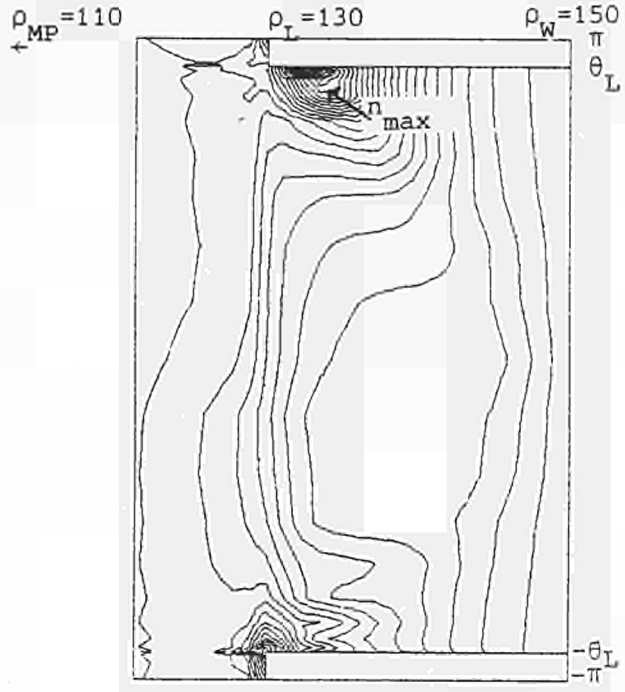

Fig 1: Density (cm^{-3})
n_{max} = 2.6 x 10^{13} Δn = 7.2 x 10^{11}

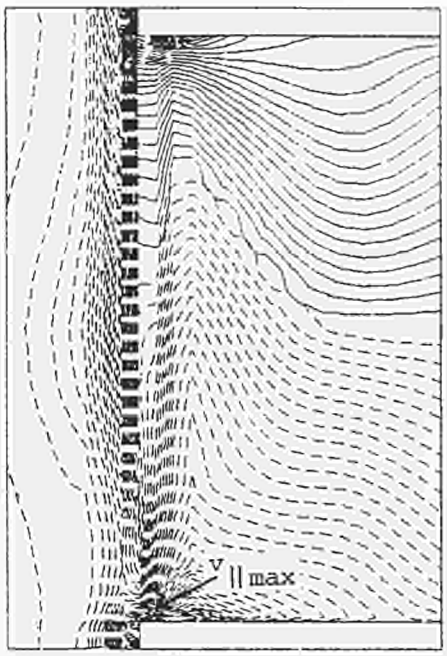

Fig 2: Parallel flow velocity (cm/s)
$v_{\|max}$ = 5.0x10^{6} $\Delta v_{\|}$ = 1.6x10^{5}

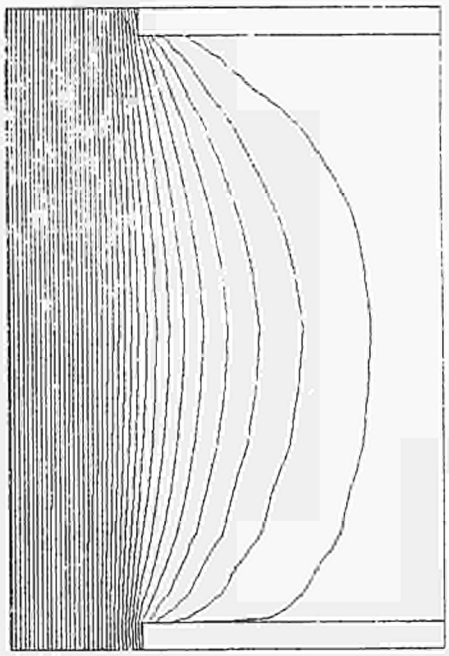

Fig 3: Temperature (eV)
T_{max} = 189, ΔT = 5.2

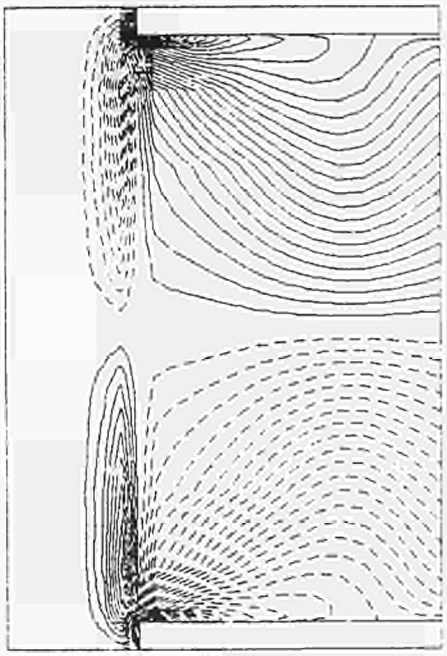

Fig 4: Parallel flow velocity (cm/s) when v_{pol} = 0
$v_{\|max}$ = 4.8x10^{6}, $\Delta v_{\|}$ = 1.3x10^{5}

TRANSPORT CALCULATIONS FOR JET DISCHARGES WITH ICRH

A. Taroni, A.E.P.M. Abels van-Maanen*, W. Core, D.F. Düchs, T. Hellsten, D.G. Muir, P.M. Stubberfield, F. Tibone, M.L. Watkins.

JET Joint Undertaking, Abingdon, Oxon., OX14 3EA, UK
* On attachment from Mathematical Institute, University of Oxford, UK.

1. Introduction

In this paper we discuss the results of 1-D and 1½-D transport codes in simulating JET discharges and in predicting future JET performance.

In Section 2 ohmic plasmas are studied with particular emphasis on the possible importance of ion thermal transport, especially at the highest JET densities. In Section 3 the transition from ohmic to auxiliary heated discharges (ICRH) is simulated. Results are compared with observations in JET. Extrapolations to higher levels of additional power are briefly discussed in Section 4.

2. The Ohmic Phase

The transport models used to simulate JET ohmic plasmas (including target plasmas for ICRH) are basically those discussed in [1]. In particular, electron energy diffusion coefficients of the Alcator-Intor (χ_{eAI}) and of the Coppi-Mazzucato-Gruber (χ_{eCMG}) form are considered. Classical energy transfer between electrons and ions and neoclassical resistivity η_{neo} are assumed. Impurities are treated either as in [1] or without assuming coronal equilibrium. Results given in this section are shown not to be sensitive to the choice.

The dependence of computed results on the ion thermal conductivity has been studied taking $\chi_i = \alpha\chi_{iCH}$, χ_{iCH} being the Chang-Hinton neoclassical expression [2]. Results are illustrated in Fig. 1, showing observed and computed peak temperatures as a function of the line-averaged electron density $\bar{n}_e$ for various values of α. At the highest densities, the maximum temperature difference computed with $\alpha = 1$ and with a model of sawtooth activity based on Kadomtsev's reconnection scheme (with flattening of both T_e and T_i profiles) is $\Delta T \equiv T_{eo} - T_{io} \lesssim 400$eV. An anomaly factor $\alpha \gtrsim 10$ is required to produce $\Delta T \gtrsim 1$keV at intermediate and high densities. At the same time χ_e must be reduced by a factor up to 3 with respect to the values given in [1].

The need for large anomaly factors, if confirmed, would mean that anomalous ion thermal conductivity, possibly having a functional form different from neoclassical, could play an important role in determining JET performance. On the other hand, Fig. 1 shows that the conventional picture with $\chi_i \sim 3\chi_{iCH} < \chi_e$ produces results within the error bars, albeit with ΔT consistently towards the lower limits.

Another important result to be pointed out is that the high ohmic electron temperatures and values of Z_{eff} from Bremsstrahlung as observed now in JET are compatible with neoclassical but not with Spitzer's resistivity η_{Sp}. This result differs from that reported in [1] when lower temperature plasmas with higher values of Z_{eff} were available for simulation, and neither η_{neo} nor η_{Sp} could be excluded.

3. ICR Heated Plasmas

RF heating of JET plasmas is simulated by a model for additional power sources for the electrons and ions, and by allowing for an enhancement of

transport losses during RF pulses.

In order to determine the auxiliary power deposition profile, we derived a simplified model for use in transport codes and containing as much as possible of the information provided by 'stand-alone' codes treating different aspects of the RF heating problem for an assumed background plasma. This model can be summarised as follows:

- the additional power is uniformly deposited within a rectangular portion (the same for electrons and ions) of the poloidal plasma section;
- the absorption region is bounded by major radii corresponding to the position of the ion-ion hybrid and the ion cyclotron resonance for the minority species, and by a height Z determined by ray tracing calculations ($Z \sim 1.5$m);
- direct heating of the electrons by mode conversion using the Budden formulae, and minority ion heating by ion cyclotron damping are estimated [3];
- heating of the background plasma ions and of the electrons is then estimated using a steady-state solution to a Fokker-Planck equation for the energy distribution function of the minority species.

Confinement degradation during RF heating has been simulated through an enhancement of the ohmic electron thermal diffusivity by a power-dependent factor, along the lines suggested by the "Principle of Profile Consistency" [4].

These models must be tested against observations and can be used in a predictive way only for studies of sensitivity of results to the assumptions they involve. Both purposes have been pursued by undertaking an extensive series of computations. Our findings are summarised in the following.

Assuming that most of P_{rf} (the total RF-power coupled to the plasma) is deposited in the central region of the plasma, as suggested by theory, a degradation of energy confinement is required to produce variations in T_{eo}, T_{io} and $\langle T_e \rangle$ comparable to the experimental ones. Furthermore, numerical results are in better agreement with observations when the power globally coupled to the electrons, P_{rf}^e, is not less than that to the ions, P_{rf}^i. This is illustrated in Fig. 2 for the case of ^{3}He minority heating, under the following assumptions:

- strong ion transport ($\chi_i > \chi_e$) as described in Section 2, but no further degradation of χ_i during RF pulses;
- $\chi_e = C \cdot \chi_{eCMG}$, with $C \sim 1$ during the ohmic phase but $C > 1$ during RF heating (scaling roughly as $C \sim (P_{oh} + P_{rf})/P_{oh}$).

Similar results have been obtained for the case of H-minority heating, with substantially different target plasmas.

Enhanced particle (including impurities) influxes at the plasma boundary allow simulation of the experimentally observed increases in line-averaged $\bar{n}_e$ (up to 30% when $P_{rf} \sim 5$MW) and total radiated power (without significant changes in Z_{eff} and in P_{rad}/P_{input}).

Our main conclusions, namely the need for transport degradation during RF heating and $P_{rf}^e \gtrsim P_{rf}^i$, are stable against model variations as long as central power deposition is retained. If, however, a large fraction of the absorbed power ($\gtrsim$ 50% when $P_{rf} \sim 2$MW) is assumed to be deposited in the plasma external region, where radiation dominates, then both peak and average temperature increase can be simulated without degrading χ_e.

The evolution of the central electron temperature constrains the power to the electrons in the central region to a minimum of $\sim$ 50% P_{rf}, as mentioned above. In addition, the moderate saturation of T_{eo} during sawtooth rise

suggests that electron transport is strongly reduced towards the plasma centre, and even degradation does not play a significant role there.

4. Extrapolation to Higher Levels of RF Power

The picture emerging from the previous Sections indicates that it is only reasonable to predict ranges of possible performance that take into account variations of all important parameters in the model, and possibly of the model itself. It is practically impossible to follow such a procedure systematically. The only way to face the problem would consist of treating all of the parameters within a given model on the same basis, and changing them randomly within reasonable ranges and constraints.

A few preliminary results using different scalings of χ_e with additional power are shown in Fig. 3 for P_{rf} = 5, 10, 15MW. They refer to two sets of transport assumptions for two different target plasmas: the 'large' $\chi_i \geq 10\chi_{iCH}$ with $\chi_e \sim \chi_{eCMG}$ when $\Delta T \sim 1.5$keV and $Z_{eff} \sim 4.0$ (Fig. 3a) and the 'standard' $\chi_i \sim 4\chi_{iCH}$ with $\chi_e \sim \chi_{AI}$ when $\Delta T \sim 0.6$keV and $Z_{eff} \sim 2.5$ (Fig. 3b).

References

[1] Behringer, K.H. et al., in Plasma Physics and Controlled Nuclear Fusion Research (Proc. 10th Int. Conf., London, 1984) 1, IAEA, Vienna (1985) 291.

[2] Chang, C.S. and Hinton, F.L., Phys. Fluids, 25 (1982) 1493.

[3] Brambilla, M., Lallia, P.L. and Thomsen, K., Private communication (1985).

[4] Coppi, B., Comments Plasma Physics and Controlled Fusion, 7 (1982) 1.

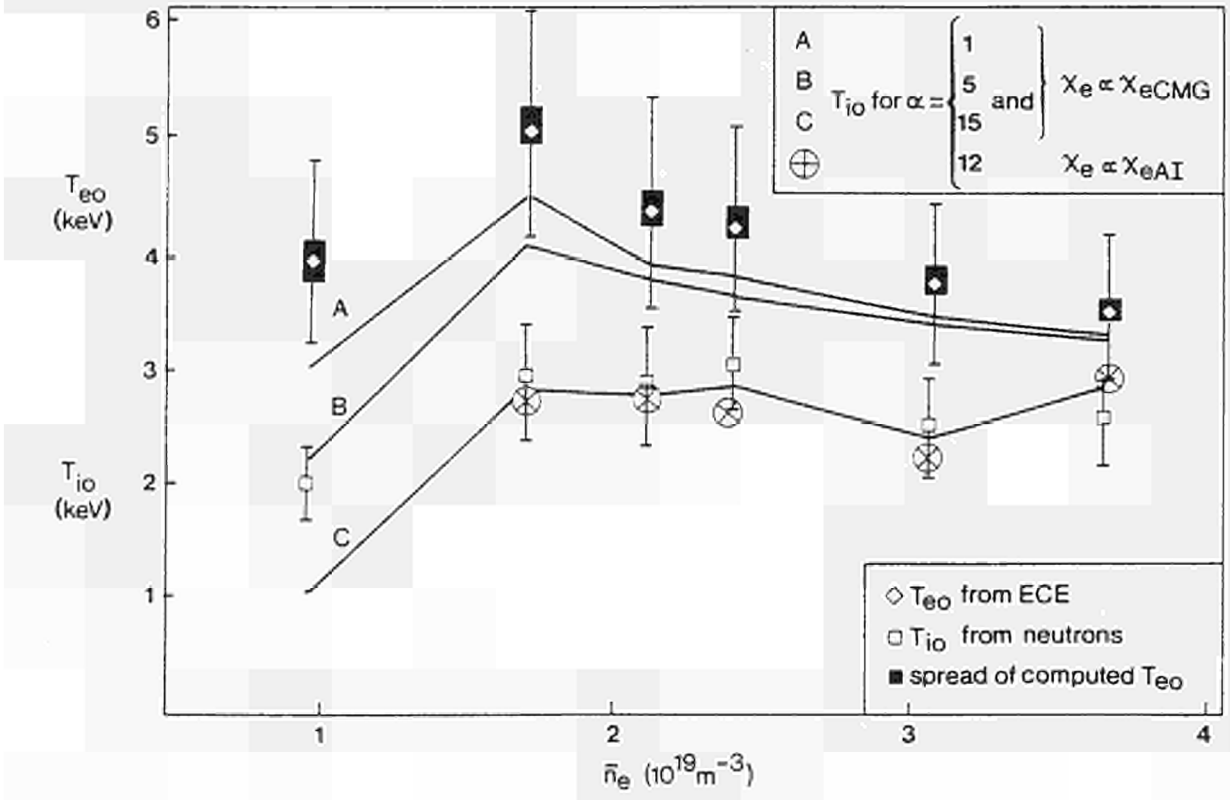

Fig 1: Observed and computed central (sawtooth averaged) temperatures. Results A, B, C were obtained with a 1-D code, ⊗ with a 1½-D code and non-coronal impurity radiation. B_t = 3.4T, I_p = 3.0MA except for the lowest density (I_p = 1MA) and the highest density (I_p = 3.6MA) case.

Fig 2: Computed and experimental peak temperatures for different levels of RF power with P_{rf}^{i}/P_{rf} = 25%(A,A'), 50%B,B'), 75%(C,C') and degraded(——) and undegraded (---) electron transport.

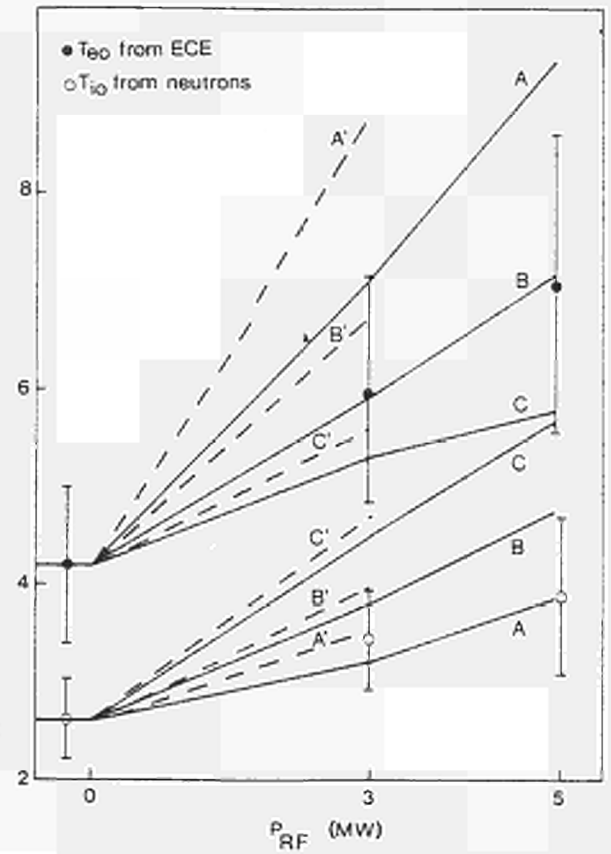

Fig 2

Fig 3: Predictions for P_{rf} up to 15MW based on plasmas with B_T=3.4T and

a) I_p=4MA, $\bar{n}_e \simeq 2.6.10^{19} m^{-3}$, $Z_{eff} \simeq 4$, $\chi_e = \chi_{eCMG} \cdot (P_\Omega + P_{rf})/P_\Omega$, α=12;

b) I_p=3.6MA, $\bar{n}_e \simeq 3.10^{19} m^{-3}$, $Z_{eff} \simeq 2.5$, $\chi_e = \chi_{eAI} \cdot \int_0^\rho P_{tot}^{e}(\rho)\,dV / \int_0^\rho P_\Omega(\rho)\,dV$, α=4.

A,B,C as in Fig 2. B' corresponds to P_{rf}^{i} = 50% P_{rf} and degradation saturated at 10MW.

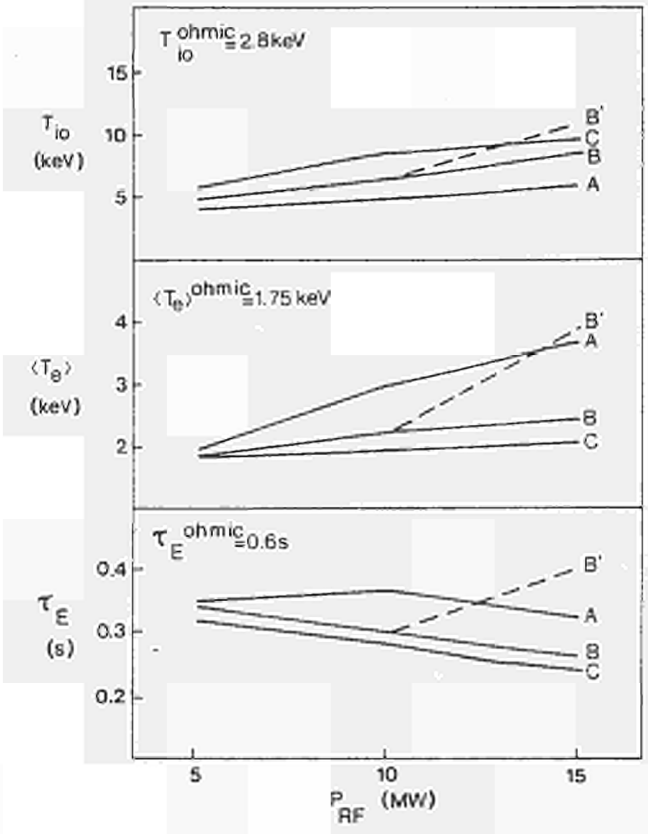

Fig 3a

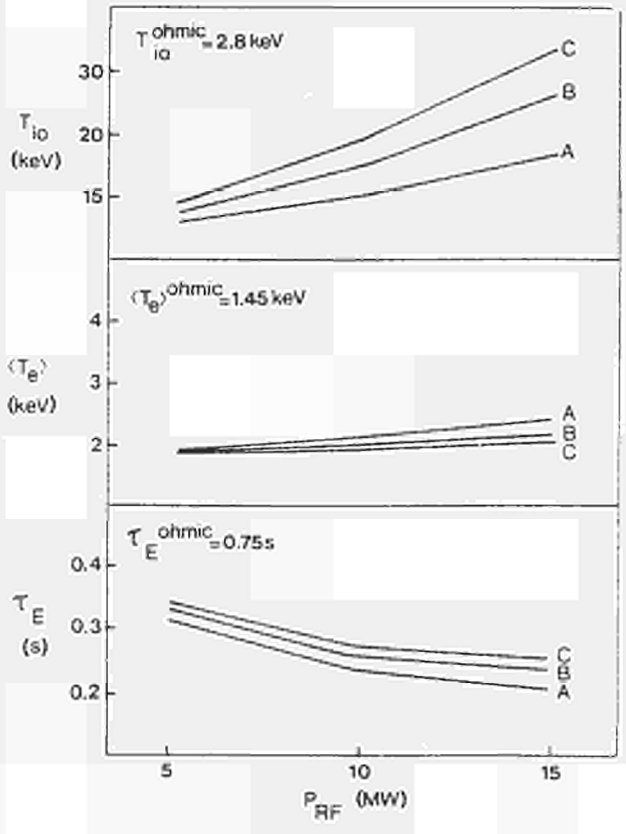

Fig 3b

DENSITY LIMIT DISRUPTIONS IN JET

J. Wesson, C. Gowers, W. Han*, F. Mast#, F. Nave, M. Turner*, M. Watkins

JET Joint Undertaking, Abingdon, Oxon., OX14 3EA, UK
* Culham Laboratory, Abingdon, Oxon., OX14 3DB, UK
# On attachment from IPP, Garching.

Abstract

The experimental observations on density limit disruptions in JET are consistent with a model in which radiation losses lead to a strongly mhd unstable configuration.

Introduction

The operating regime in JET has a disruption density limit given approximately by

$$\left[\frac{\bar{n}}{10^{19}}\right] < 12\,\frac{B_T}{R_o q_c} \qquad \ldots (1)$$

where $\bar{n}$ is the mean electron density, B_T the toroidal magnetic field, R_o the major radius of the plasma and $q_c = 2AB_T/\mu_o IR_o$, A being the plasma area and I the plasma current. For a given value of plasma current the highest electron density is achieved at disruptions on the current fall, that is for currents lower than the peak current. Figure 1 shows a plot of such disruptions in the Hugill diagram.

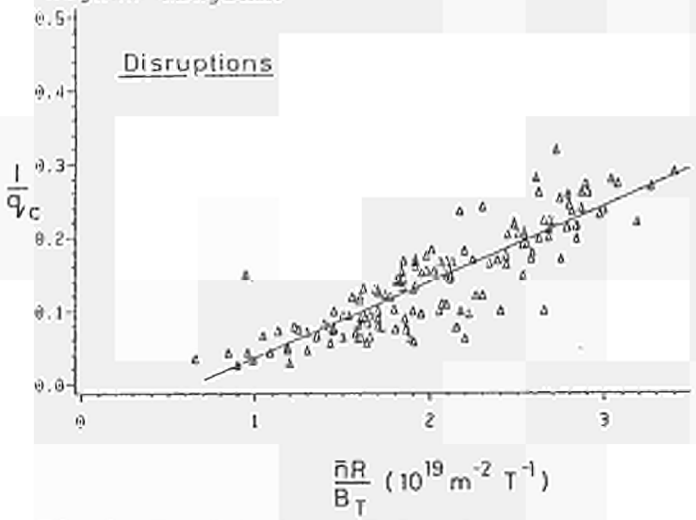

Fig 1: Hugill plot of density limit disruptions.

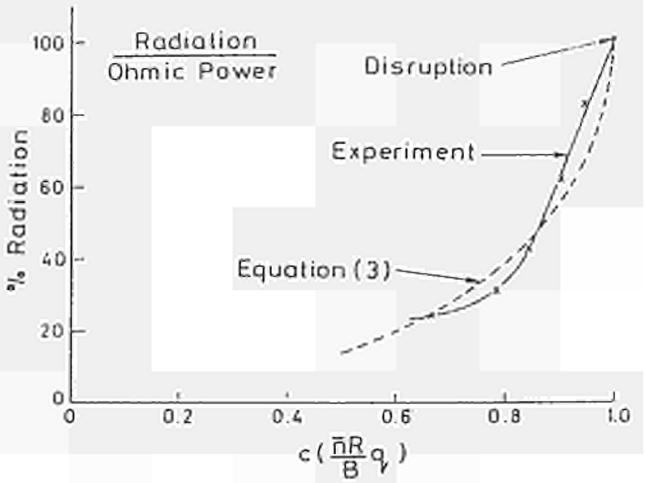

Fig 2: (Radiated power/ohmic power) against $(\bar{n}R/B)q$.

Radiation [1-7]

It is found that prior to density limit disruptions, the total radiation in the plasma increases, reaching a value ~ 100% of the input power at the time of disruption. This radiation comes mainly from the edge of the plasma. The relationship between this variation in radiated power and the quantity $\bar{n}Rq_c/B_T$ can be seen from a simple model. Inside the radiating layer the radiation losses are balanced by thermal conduction, and taking the layer to be thin

$$K \frac{d^2T}{dr^2} = R(T) f n_e^2$$

where K is the thermal conductivity, R(T) the radiation parameter and f the ratio of impurity ion density to electron density. Integration of this equation across the layer gives the radiated power as a fraction, ϕ, of the total plasma heating power.

$$\phi = 1 - \left[1 - \frac{8\pi^2 AKR_1 f n_e^2}{P^2}\right]^{\frac{1}{2}} \qquad \ldots (2)$$

where $R_1 = \int_o^\infty R \, dT$, P is the plasma heating power per unit length and A is the plasma area.

Now $2\pi R_o P = VI = V2AB_T/\mu_o R_o q_c$ where V is the loop voltage, and substitution into equation (2) gives the relationship between ϕ and $n_e R_o q_c / B_T$,

$$\phi = 1 - \left[1 - \alpha^2 \left[\frac{n_e R_o q_c}{B_T}\right]^2\right]^{\frac{1}{2}} \qquad \ldots (3)$$

where

$$\alpha^2 = 8\pi^4 K R_1 f (\mu_o R_o / V)^2 / A.$$

This relationship is complicated but it can be seen from equation (3) how the observed growth of the radiation fraction ϕ can occur as the disruption parameter $\bar{n} R_o q_c / B_T$ is increased. Figure 2 shows the result of a bolometer measurement of ϕ as a function of $\bar{n} R_o q_c / B_T$ during a particular discharge together with a normalised plot of equation (3) assuming α is a constant and that $n_e \propto \bar{n}$.

Stability to contraction

When $\phi = 1$ the plasma is thermally disconnected from the limiter. This may or may not lead to a contraction of the plasma. Some understanding of this question can be obtained from a simple model in which the plasma is taken to be circular and the radius, a_p, of the radiating layer is taken as the dependent parameter. Thus the energy balance equation may be written

$$\frac{d}{dt}(\pi a_p^2 \varepsilon) = I^2 R_p(a_p) + 2\pi \left[- c n_e(a_p) a_p - K \frac{T_R}{a - a_p} a_p\right] \qquad \ldots (4)$$

where ε is the average plasma energy density, I is the plasma current and R_p the plasma resistance per unit length. The second term gives the radiation loss, the linear dependence on n_e coming from the analysis outlined above, and the last term gives the thermal conduction loss from the layer, T_R being the temperature of the peak in the radiation parameter and a the radius of the limiter. Linearisation of equation (4) with constant I leads to the stability equation:

$$\gamma \tau_E = \tfrac{1}{2}\left[\frac{a_p}{R_p}\frac{dR_p}{da_p} - \phi\left[1 + \frac{a_p}{n_e}\frac{dn_e}{da_p}\right] - (1 - \phi)\frac{a}{a - a_p}\right].$$

where γ is the growth rate and τ_E is the energy confinement time.

It is seen that under normal circumstances, with ϕ well below unity, the last

term dominates because of the small denominator $a-a_p$. The plasma is then stable to contraction. However as ϕ approaches unity this term goes to zero. The plasma is then unstable to contraction if

$$-\frac{a_p}{n_e}\frac{dn_e}{da_p} > 1 - \frac{a_p}{R_p}\frac{dR_p}{da_p}$$

It is very difficult to determine this criterion theoretically because of the complexity of physics involved. However the experimental results indicate that both stable and unstable behaviour is possible. Figure 3 shows the contraction of the radiation layer observed before a disruption and Figure 4 shows the contraction of the electron temperature profile.

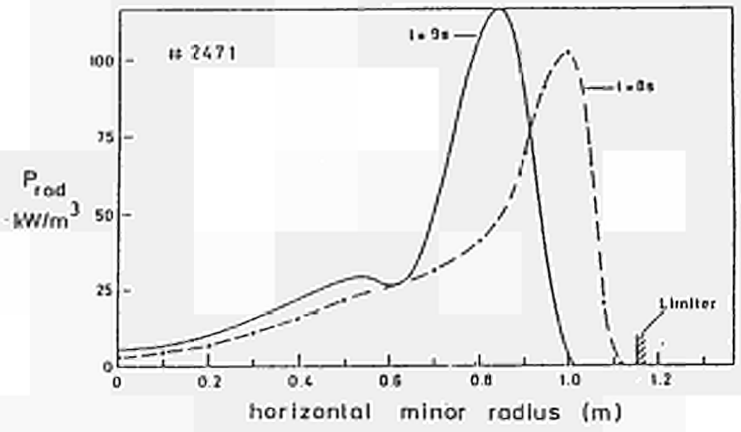

Fig 3: Radiated power against radius before disruption.

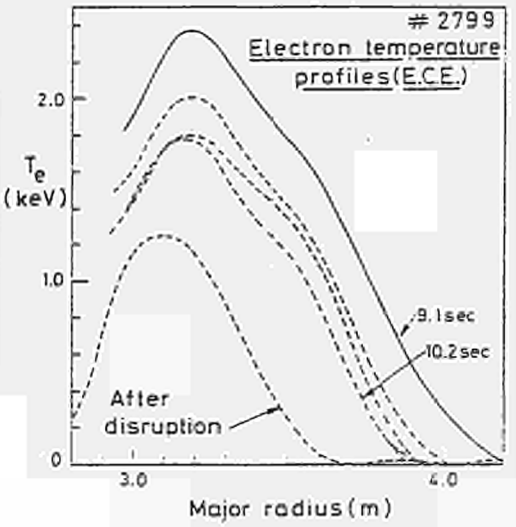

Fig 4: Electron temperature profiles

Disconnection and disruption

Contraction of the temperature profile leads to an increasingly unstable current profile and ultimately disruption can result [8]. The condition for 100% radiation as given by equation (3) is

$$\frac{n_e R}{B_T} = \frac{1}{\alpha}\frac{1}{q_c} . \qquad \ldots (5)$$

It is clear that the form of this relation is similar to that of the disruption boundary shown in Figure 1. However what is plotted in Figure 1 is the instant of disruption whereas condition (5) is the condition for 100% radiation. These must be separated in time by a time $\gamma^{-1} \sim \tau_E \sim 1$sec. A consistent description requires therefore that there should be an event prior to the disruption which marks the onset of the contraction. A candidate for this is the onset of a hesitation in the density $\bar{n}(t)$, which is observed typically 1 second before the disruption as shown in Figure 5. In Figure 6 the hesitation onsets are plotted for discharges during a given period of operation.

In many discharges no disruption occurs and the time trajectory in the Hugill diagram follows the direction of the hesitation and disruption lines. It seems likely that these are cases where the 100% radiation limit is reached but where the plasma is stable to contraction.

Simulation

A computer calculation has been carried out to simulate the disruption model outlined above. The code uses the large aspect-ratio, circular approximation. Maxwell's equations are solved together with an energy transport equation including the effects of impurity radiation losses. The self-consistent quasi-linear tearing mode island growth and the effect of the m=1 mode are followed

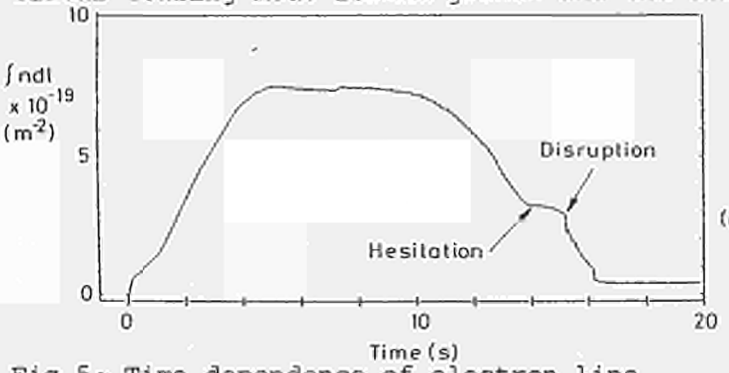

Fig 5: Time dependence of electron line density showing hesitation before disruption.

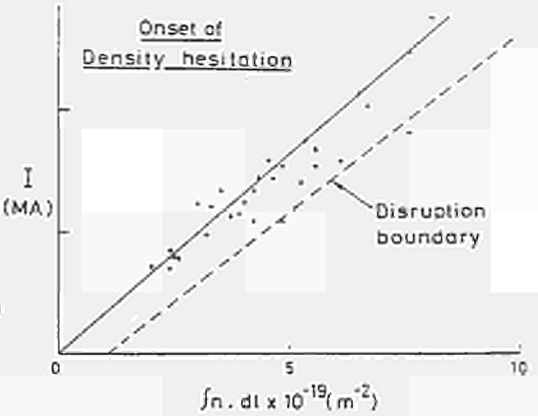

Fig 6: Hesitation onsets plotted in $(I, \int n\, d\ell)$ diagram.

in time. Figure 7 gives results from these calculations showing the inward movement of the radiating layer leading to a disruptively unstable current profile.

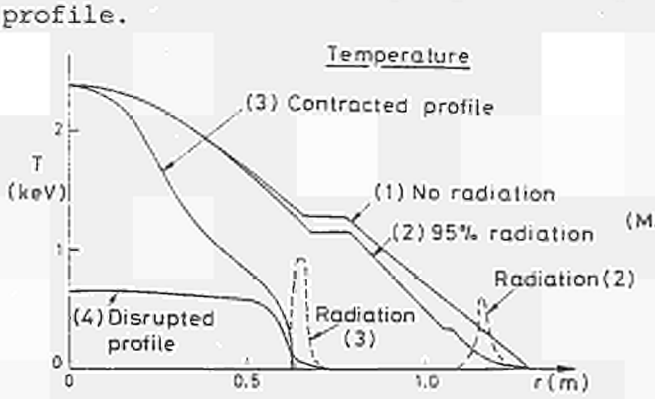

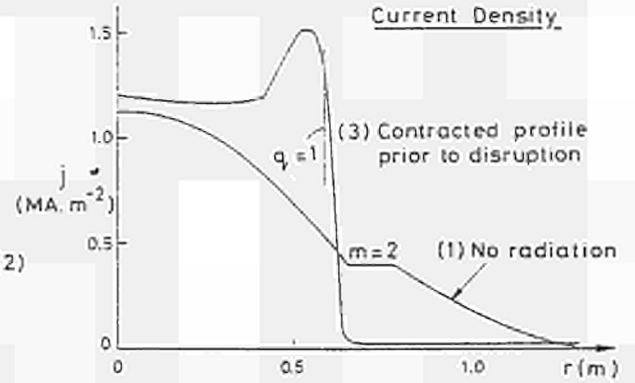

Fig 7: Plots of simulation results showing time development of the temperature and current density.

Acknowledgements

The authors would like to thank the ECE group in JET for Figure 4.

References

[1] Gibson, A., Nucl. Fusion, 16 (1976) 546.

[2] Rebut, P.H. and Green, B.J. in Plasma Physics and Controlled Nuclear Fusion Research (Proc. 6th Int. Conf. Berchtesgaden, 1976) 2, IAEA, Vienna (1977) 3.

[3] Gibson, A. and Watkins, M.L. in Controlled Fusion and Plasma Physics (Proc. 8th European Conf. Prague, 1977) 1 (1977) 31.

[4] Watkins, M.L., Physics Reports 37 (1978) 111.

[5] Igitkhanov, Yu.L. et al., Nucl. Fusion 18 (1978) 415.

[6] Ohyabu, N., Nucl. Fusion 9 (1979) 1491.

[7] Ashby, D.E.T.F. and Hughes, M.H., Nucl. Fusion 21 (1981) 911.

[8] Turner, M.F. and Wesson, J.A., Nucl. Fusion 22 (1982) 1069.

EFFECT OF PARTICLE TRAPPING IN ICRF-BEAM HEATED TOKAMAK PLASMAS

T. Hellsten, K. Appert*, W. Core, H. Hamnén, S. Succi*

JET Joint Undertaking, Abingdon, Oxon., OX14 3EA, UK.

* CRPP, Lausanne, Switzerland.

Introduction

As is well known, the combined effects of resonant ion interaction with a magnetoacoustic wave and the Coulomb scattering processes leads to the development of anisotropic distributions with the most energetic particles in deeply trapped orbits [1]. However, in an actual tokamak, trapped particle effects modify the tail formation process, and hollow distributions with the most energetic ions in banana orbits with their tips on or near the resonance layer are obtained. The effect of particle trapping in the tail formation process during second harmonic frequency heating are shown in Figs. 1 and 2.

In this paper we report the results of a numerical study of trapped particle effects on the tail formation process, heating efficiency, and thermonuclear yield in fundamental minority/second harmonic, and RF/beam-plasma hybrid systems.

Computational Considerations

The Fokker-Planck code used in the investigation is the BAFIC code which is based upon the finite element code BACCHUS [2] which numerically solves the time dependent equation:

$$\frac{\partial f}{\partial t} = C(f) + Q(f) + S,$$

where $f = f(v_{\parallel}, v_{\perp}, t)$ is the resonant ion distribution function; C, Q, are the bounce-averaged linearised Coulomb scattering and quasi-linear RF operator in cylindrical coordinates in velocity space $(v_{\parallel}, v_{\perp})$, S is a source term describing neutral beam injection.

The fusion rates are calculated using the Asher-Peres cross sections [3] and takes into account the finite temperature of the bulk plasma ions.

For the fundamental minority systems, we have examined the configurations: (i) minority ^{3}He(5%) in a deuterium plasma, with $n_e = 3\times10^{13}cm^{-3}$, and $T_e = T_D = 5keV$; (ii) the beam/RF-plasma hybrid systems of 125keV ^{3}He injection into ^{3}He (5%)/deuterium admixture. These configurations give rise to the important thermonuclear reaction $^3He+D\rightarrow{}^4He+H$. The contribution to the total fusion yield due to the bulk plasma D/D reactions are not included in these particular calculations.

For the second harmonic heating configurations, we have directed our investigation towards systems based upon a deuterium plasma with 125keV D-injection, $n_e = 3.5\times10^{13}cm^{-3}$, and initial species temperatures $T_e = T_D = 5keV$. For these systems the fusion yield is restricted to the reaction $D+D\rightarrow{}^3He+n$, and the D/^{3}He reactions are not included in the calculations done.

Finally, in each RF/beam-plasma hybrid system examined, a co/counter injection beam configuration at angles 45° and 135° to the main toroidal magnetic field and a beam current corresponding to a power density of $0.1W/cm^3$ is assumed.

Conf. on Contr. Fus. & Plasma Phys., Aachen (Sept.1983), paper B29.
[3] ASHER-PERES J. Appl. Phys., 5 (1979).

Figure Captions

Fig.1: Contour plot of the velocity distribution formed during second harmonic heating of deuterium for ε=0. Configuration parameters $n_e = 3.5\times10^{13}cm^{-3}$, $T_i = T_e$=5keV, P_{RF}=0.26W/cm³, $V_o^2 = kT_i/m_i$.

Fig.2: The distortion of the velocity distribution due to trapping effects. The full line indicates the separation between the regions of trapped and passing particles. The broken line separates the heated particles from the non-heated particles. For this case P_{RF} = 0.38W/cm³ and ε = 0.1 the other parameters are as in Fig.1.

Fig.3: The absorbed power for second harmonic heating as a function of $|E_+|^2$. The full line indicates the absorption by a Maxwellian velocity distribution and the broken line RF-absorption by the plasma beam distribution neglecting RF-modifications.

Fig.4: The logarithm of the velocity distribution along the perpendicular axis in the absence of trapping effects for second harmonic heating with and without neutral beam injection. Neutral beam injection alone is also shown. The beam injection angle 90°, power 0.23W/cm³, and the RF electric field is the same for the two cases and corresponds to absorption 0.53W/cm² and 0.95W/cm³, respectively.

Fig.5: The effect of particle trapping on the fusion yield during fundamental ICRF heating of a ^{3}He/D plasma is shown. The beam injection angles are 45° and 135°; injection energy 125keV, and the power corresponds to 0.1W/cm³.

Fig.6: The effect of particle trapping on the fusion yield during second harmonic heating of deuterium. The effect of energy clamping of the injected deuterium beam is also shown. The injection parameters are those of Fig.5.

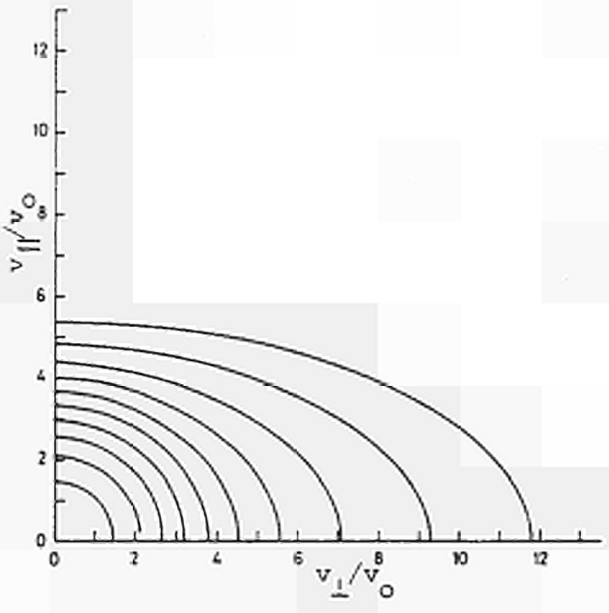

Fig.1

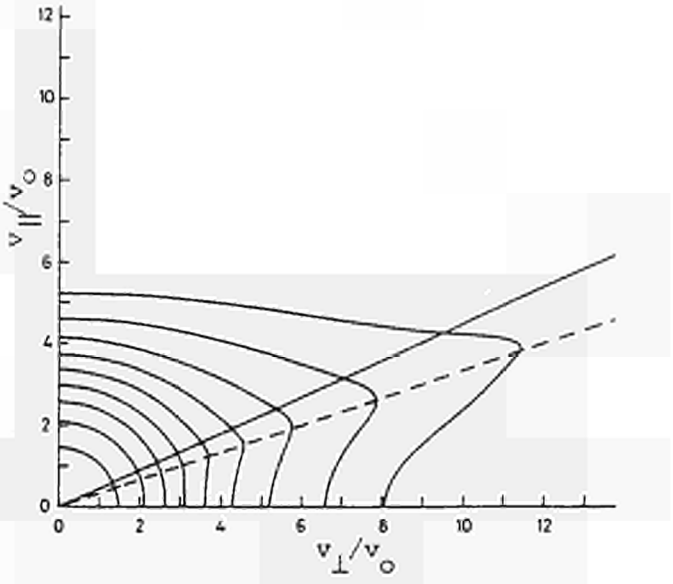

Fig.2

Numerical Results and Discussion

Since cyclotron absorption at the second harmonic resonance is proportional to $J_1^2(k_\perp v_\perp/\omega_{ci})$, a build up of the tail leads to a stronger absorption of the wave energy for a given value of E_+. In Fig.3 we have compared the power absorbed by a Maxwellian velocity distribution and that reached by steady state second harmonic heating, versus $|E_+|^2$. The square of the electric field is here normalised to the corresponding power absorption due to second harmonic heating for a Maxwellian velocity distribution. The deviation from the 45° line is a measure of how the dielectric tensor obtained using the actual velocity distribution deviates from that calculated using a Maxwellian velocity distribution.

The presence of neutral beam heating leads to a further enhancement of the tail and power absorption, Figs.3,4. The absorbed power for a given electric field increases linearly with the beam current. In Fig.3 the power absorption due to second harmonic heating for a constant beam power and having $\varepsilon=0$, where ε is the inverse aspect ratio, is shown. The dashed line in Fig.3 is the power absorption for second harmonic heating due to the increase of the $\beta_\perp$ due to the beam alone.

For heating at the fundamental and second harmonic frequencies the fusion rates have been calculated, and are shown with those obtained in the beam systems, Figs.5,6. The effect of trapping is not very important for the reaction rates. A slightly higher rate is obtained for a finite aspect ratio. This can be understood by the fact that in the case of finite trapping the power is being distributed over fewer particles than for $\varepsilon=0$. Since a fraction of the order of $\sqrt{\varepsilon}$ of the total number of particles does not interact with the wave field, these fewer heated particles will then acquire greater energy. Due to the rapid increase of the cross-section with energy a further enhancement of the thermonuclear yield is obtained.

When varying the injection angle, it is found that the fusion rate is not too sensitive a function of the injection angle. The highest rates are achieved for injection in the parts of the velocity space where $v_\parallel/v_\perp > \sqrt{\varepsilon}$. The lowest fusion yields are obtained for parallel injection. In the finite aspect ratio situation, direct injection into the region of velocity space where no RF interaction occurs is also ineffective.

Conclusions

For the scenarios discussed here, the calculations indicate that trapped particle effects are not very important in the calculation of the fusion yield and bulk plasma species heating rates. Second harmonic heating leads to important modifications of the plasma's dielectric properties through the change in distribution function. These modifications are strongly dependent on the wave electric field. Combined neutral beam and second harmonic further enhances these modifications, which for practical power levels cannot be represented by a linear treatment.

We may note here that in order for second harmonic heating of deuterium to be successful, the β-value of the plasma has to be large, and the level of the hydrogen impurities low. A small amount of hydrogen will change the polarisation of the electric field near the second harmonic cyclotron resonance of deuterium, so that the E_+ component diminishes. This will then reduce second harmonic heating. Instead, fundamental heating of hydrogen will occur.

References

[1] STIX, T.H. Nucl. Fusion, 15, 737 (1975).
[2] APPERT, K., KRITZ, A.H., SUCCI, S. and VACLAVIK, J. Proc. of 11th EPS

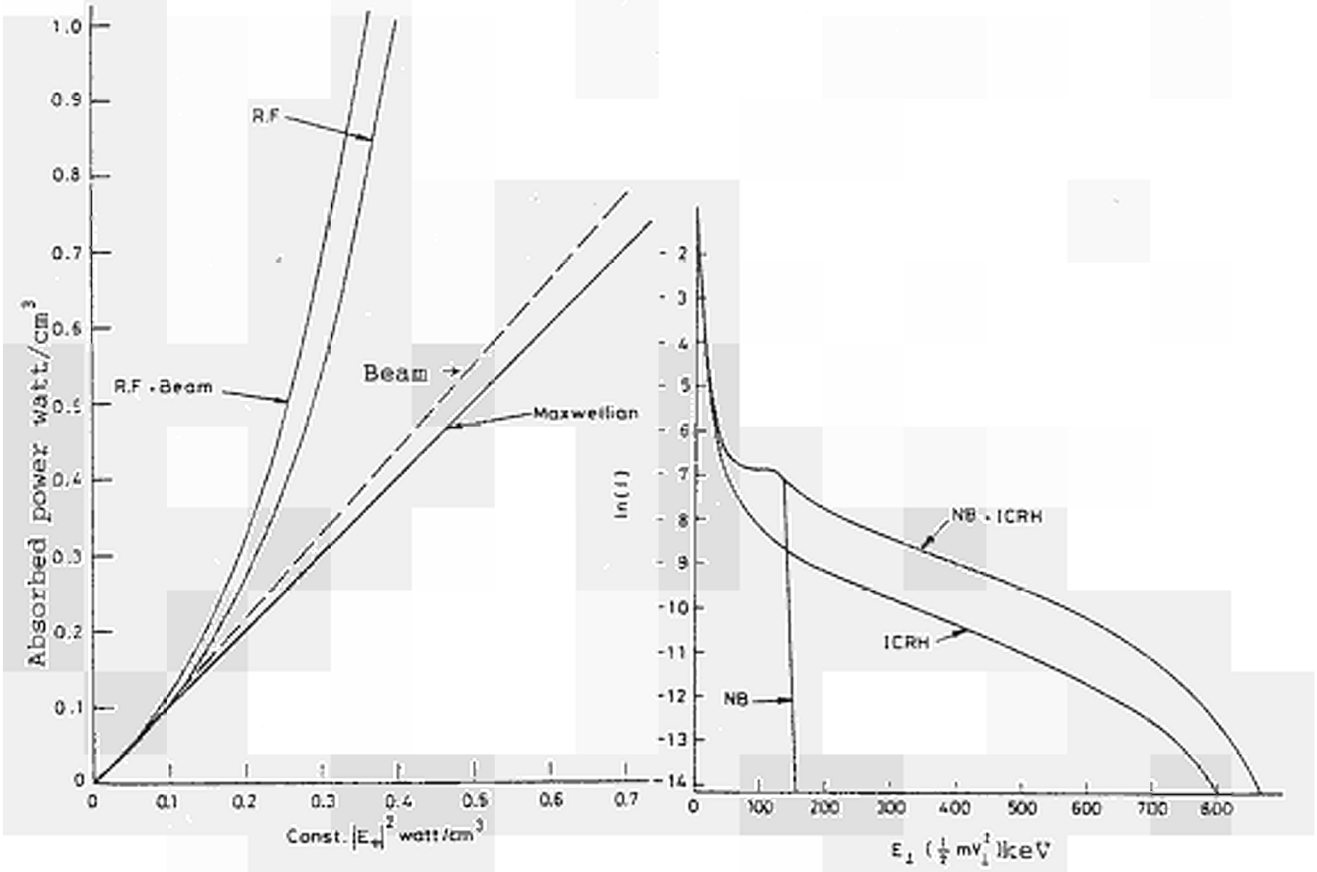

Fig. 3

Fig. 4

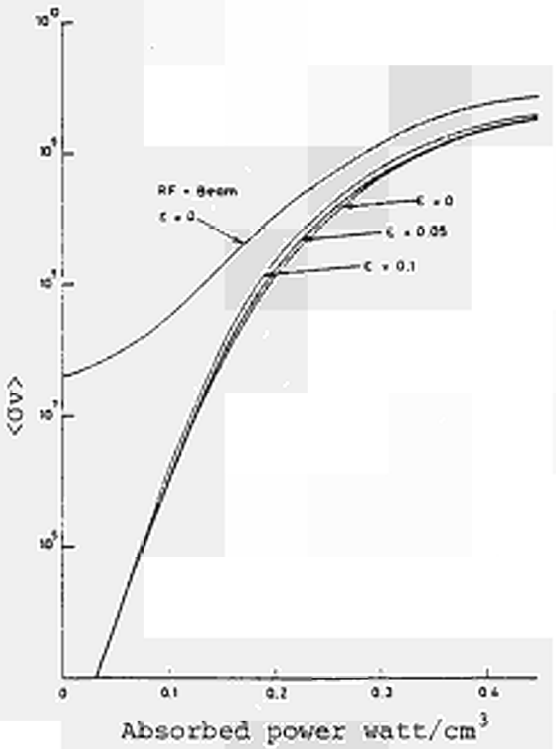

Fig. 5

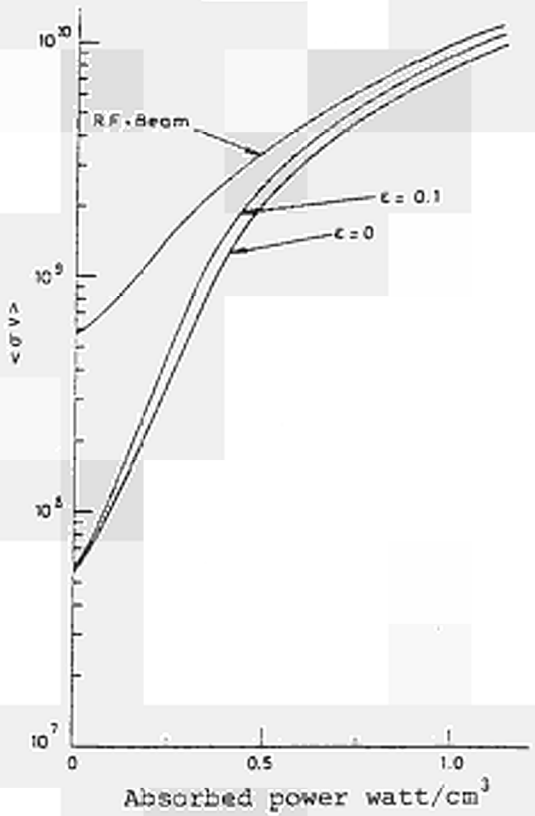

Fig. 6

GLOBAL ENERGY CONFINEMENT STUDIES IN OHMICALLY HEATED JET PLASMAS

J.G. Cordey, D.V. Bartlett, R.J. Bickerton, M. Brusati, D.J. Campbell, J.P. Christiansen, S. Corti, A.E. Costley, A. Edwards, S. Ejima#, J. Fessey, M. Gadeberg*, A. Gibson, R.D. Gill, N. Gottardi, A. Gondhalekar, C.W. Gowers, F. Hendriks, O.N. Jarvis, E. Källne, J. Källne, S. Kissel, L. de Kock, H. Krause+ E. Lazzaro, P.J. Lomas, F.K. Mast+, P.D. Morgan, P. Nielsen, R. Prentice, R.T. Ross, J. O'Rourke, G. Sadler, F. Schueller, M.F. Stamp, P.E. Stott, D.R. Summers A. Tanga, P.R. Thomas, G. Tonetti†, M.L. Watkins

JET Joint Undertaking, Abingdon, Oxon., OX14 3EA, UK

On attachment from: # G.A. Technologies, San Diego, USA; * EURATOM-Risø Association, Risø National Laboratory, Roskilde, Denmark; + EURATOM-IPP Association, IPP Garching, F.R. Germany; † EURATOM-Suisse Association, CRPP, Lausanne, Switzerland.

Abstract: Systematic scans of the plasma density n have been completed for a large variety of plasma conditions in JET. The toroidal field B, the safety factor q, the elongation K, the major radius R and the minor radius a have all been varied. It is shown that the resulting data set contains two important parametric constraints, one which is a direct consequence of the ohmic heating, relates the electron temperature T_e to the variables n, B, q, K and a further constraint which relates the effective plasma charge Z_{eff} to the same set of variables.

Subject to these constraints, the global energy confinement time τ_E is found to scale as $(nB)^{1/2}\ (q)^{1/3}\ R^{1.7}\ a^{1.3}$ and this empirical scaling is shown to be consistent with low β-collisional transport.

I General Plasma Characteristics and Parametric Constraints

An extensive series of experiments have been carried out during 1985 to determine the particle and energy confinement properties of ohmically heated discharges in JET, a preliminary account of the scaling of the global energy transport is given in this paper, other aspects such as local transport, plasma resistivity etc. are treated elsewhere [1-2].

The main plasma parameters line average density $\bar{n}$, plasma current I and toroidal field B were varied in the ranges given in Table I. The plasma geometry was also varied from fully elliptical to small circular plasmas (a=0.8m) limited on the inside wall and on the limiter; Fig. 1 shows the outer flux surface for these three cases. The discharges had long flat tops in current, density and temperature, 4-12 secs, which was sufficient in all but the 3.5 and 4MA discharges for the magnetic field diffusion to have been completed before the end of the flat top. The data for the scaling studies are extracted close to the end of the flat top, and the data set consists of some 200 shots.

Table I: Parameter Ranges

$$1.7 < B < 3.4T;\ 1 < I < 4MA;\ 0.5 \times 10^{19} < \bar{n} < 3.6 \times 10^{19}\ m^{-3}$$
$$1 < K(= b/a) < 1.7;\ 0.8 < a < 1.23m;\ 2.5 < R < 3.4m;\ 2 < Z_{eff} < 8$$
$$1.7 < q(= BA/\mu RI) < 12;\ 1.5 < \hat{T}_e < 6keV;\ 1 < \hat{T}_i < 3keV$$

All of the discharges exhibited strong sawtoothing behaviour on the flat top and the electron temperature profile which was measured by the ECE diag-

nostic, showed the characteristic flattening in the $q < 1$ region. Profiles for the three types of geometry are shown in Fig. 2. The calibration of the ECE system was checked with the single point Thomson scattering system [3]. The remainder of the data for the study was obtained from the following diagnostics, 2mm and far infra-red interferometers for the line average electron density, NPA and neutron yield for the ion temperature, visible Bremsstrahlung for the effective plasma charge Z_{eff}, VUV and visible spectroscopy for the carbon to oxygen density ratio and metal concentration. The range of variation of these parameters is also given in Table I.

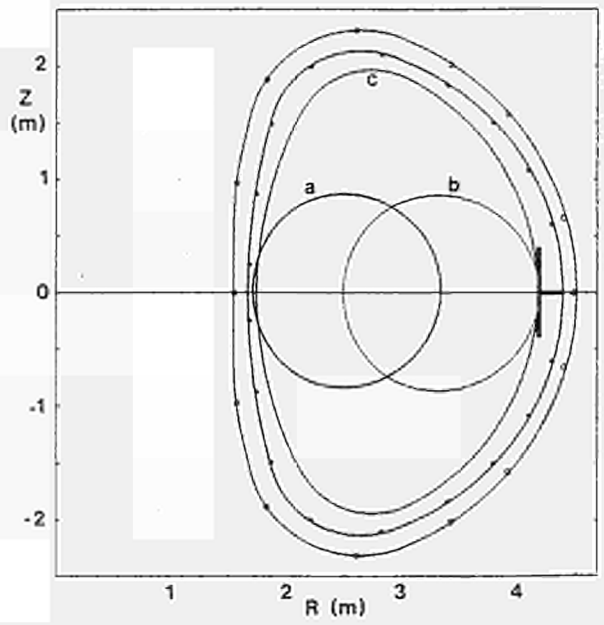

Fig 1: Outer flux surfaces for three extreme geometries a) R=2.5m, a=0.8m; b) R=3.4m, a=0.8m; c) R=2.95m, a=1.23m K=1.7.

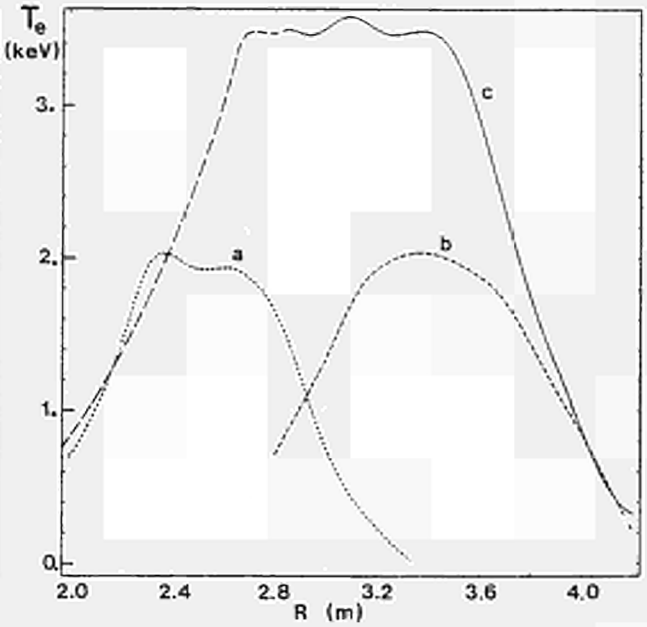

Fig 2: Typical electron temperature profiles for the geometries of Fig 1. The dotted portion of C is an extrapolation around the flux surfaces.

In any scaling study it is essential to first identify the independent variables and determine the parametric relationships that exist between these variables and the dependent variables. The independently controllable variables are $\bar{n}$, B, I, R, b, a; actually these are not fully independent since certain combinations violate stability limits. To enable comparisons to be easily made with the dimensional constraints [4] imposed by the various theoretical models the above set is replaced by $\bar{n}$, B, q_{cyl}, R, a, K.

Inspection of the data set shows that there is a strong relationship between the volume average electron temperature and the independent variables, which is a direct consequence of the ohmic heating. This ohmic heating scaling law for the JET data set is

$$\bar{T}_e \propto B^{1.8}\, \bar{n}^{-0.6}\, q^{-1.0}\, K^{0.8} \qquad \ldots (1)$$

and the fit is shown in Fig. 3. A similar scaling law was obtained by Pfeiffer and Waltz [5] in their study of confinement in small ohmically heated tokamaks, the main difference is the dependence on magnetic field which is much stronger in JET and apparently also in other large tokamaks [6,7].

There is also a further parametric relationship in the data set between the effective plasma charge Z_{eff} and the independent variables. This is

$$Z_{eff} \propto B\, \bar{n}^{-0.9}\, q^{-0.7}\, K^{0.5} \qquad \ldots (2)$$

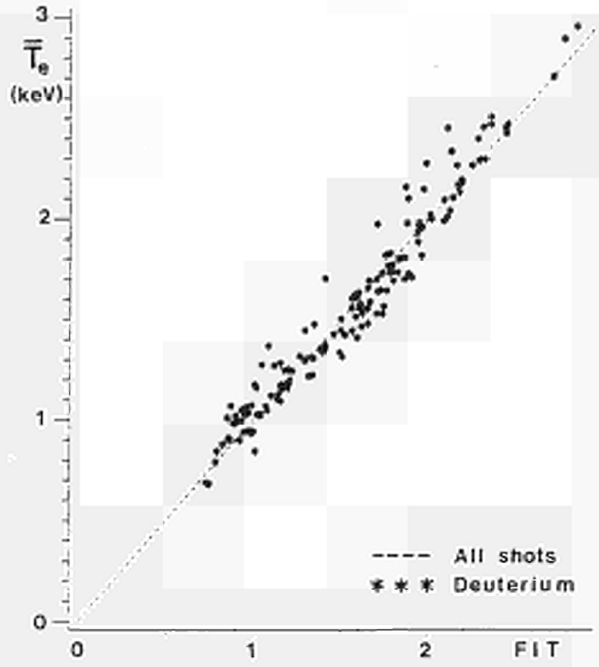

Fig 3: The ohmic heating constraint, average electron temperature versus the best fit:

$\bar{T}_e \propto B^{1.8}\ \bar{n}^{-0.6}\ q^{-1.0}\ K^{0.7}$

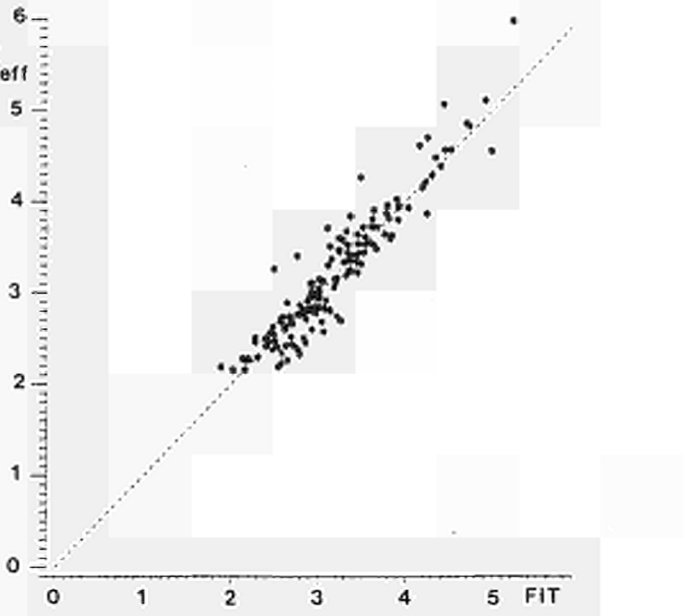

Fig 4: Effective plasma charge Z_{eff} versus the best fit:

$Z_{eff} \propto B\ n^{-0.86}\ q^{-0.7}\ K^{0.48}$

it is somewhat weaker than the ohmic constraint but nevertheless is statistically significant as the fit of Fig. 4 shows. This constraint can also be re-expressed in the form $Z_{eff} \propto P_\Omega / \bar{n}$ where P_Ω is the ohmic input power suggesting that the origin of this relationship is that the density of impurities in the plasma is related to the power flux on to the walls and limiter. It was not possible to obtain the dimensional scaling of either of these constraints due to the small range of R and a covered by the data set.

II The Scaling of the Global Energy Confinement Time

The global energy confinement time is defined as $\tau_\varepsilon = 3/2 \int n(T_e + T_i)\ dv/P_\Omega$ where the volume integral is taken over the magnetic surfaces. The variation of τ_ε with density is shown in Fig. 5 for a few of the scans with different magnetic field, current and plasma dimensions. For the range of density explored by JET the τ_ε is found to scale fairly weakly with density increasing as $\tau_\varepsilon \propto n^{1/2}$, and even this weak dependence comes mainly from the ions. This latter point is demonstrated in Fig. 6 which shows that the dependence of the electron energy confinement time $\tau_{\varepsilon e}$ (= $3/2 \int n\ T_e\ dv/P_\Omega$) upon density is very weak indeed.

Applying regression analysis to the full data set gives

$$\tau_\varepsilon \propto (nB)^{1/2}\ (q)^{1/3}\ R^{1.7}\ a^{1.3} \qquad \ldots (3)$$

the fit is shown in Fig. 7. This scaling is similar to that found in TFTR [6], except the q dependence is weaker and the B dependence stronger. The cubic dimensional dependence is close to that found by Pfeiffer and Waltz [5], the main difference between that initial study and present studies in larger tokamaks [6,7] is the B and q scaling. Interestingly, expression (1) also satisfies the constraints imposed by low-β collisional theory $\tau_\varepsilon \equiv 1/B\ F(nL^2, B^4L^5)$. The other theoretical scalings considered by Connor and Taylor [4] give a significantly poorer fit.

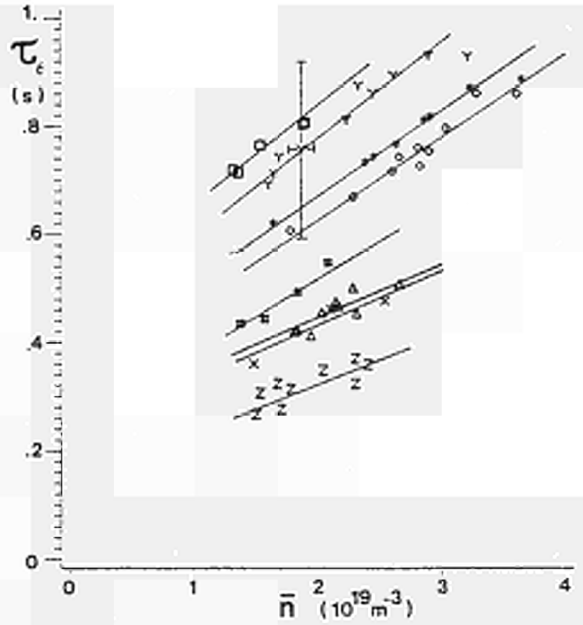

Fig 5: Global energy confinement time τ_ϵ versus line average electron density $\bar{n}$.

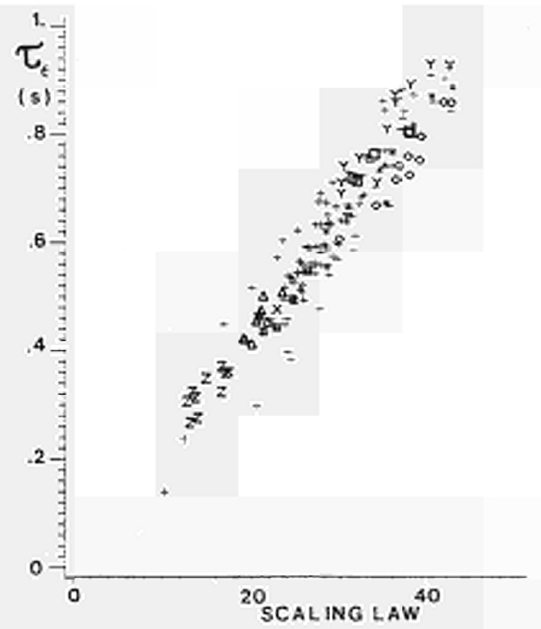

Fig 7: Global energy confinement time τ_ϵ versus best fit (symbols as Fig 5, other pulses +).

K=1.5, R=3.0m, a=1.2m, ◇ B=3.4T, I=4MA; ✱ B=3.4T, I=3.5MA; Y B=3.4T, I=3MA; □ B=3.4T, I=2MA; # B=2.5T, I=3MA; △ B=1.7T, I=2.5MA; K=1.0, X B=2.5T, I=1MA, R=3.4m, a=0.8m; Z B=2.9T, I=1MA, R=2.5m, a=0.8m.

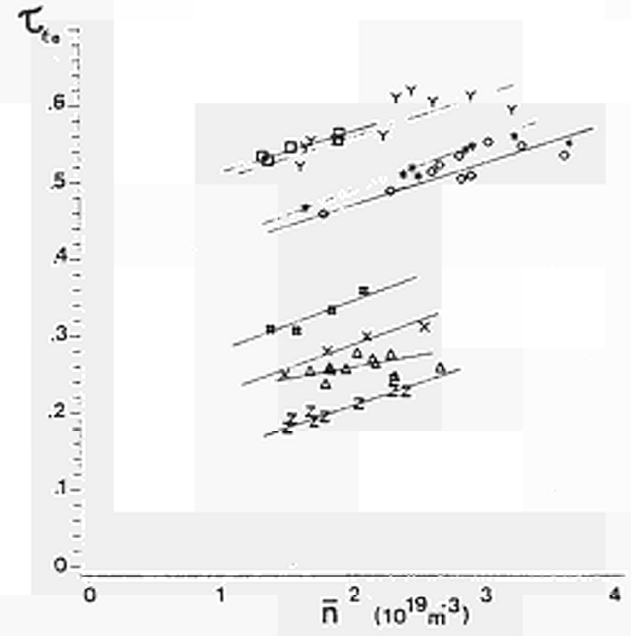

Fig 6: Electron energy confinement time versus density (symbols as Fig 5).

References

[1] Brusati, M. & Cordey, J.G., Transport analysis of JET discharges, EPS, Budapest (1985), paper 189.

[2] Christiansen, J.P. et al., Resistivity and field diffusion in JET, EPS, Budapest (1985), paper 177.

[3] Costley, A.E. et al., Electron temperature measurements in JET, EPS, Budapest (1985), paper 186.

[4] Connor, J.W. & Taylor, J.B., Nucl. Fusion, 17, 1047 (1977).

[5] Pfeiffer, W. & Waltz, R.E., Nucl. Fusion, 19, 51 (1979).

[6] Efthimion, P.C. et al., Plasma Physics and Controlled Nuclear Fusion, IAEA Conf., London, 1984, paper A-I-2.

[7] Ejima, S. et al., Nucl. Fusion, 22, 1627 (1982).

RESISTIVITY AND FIELD DIFFUSION IN JET

J.P. Christiansen, D.J. Campbell, J.G. Cordey, S. Ejima*, E. Lazzaro

JET Joint Undertaking, Abingdon, Oxon., OX14 3EA, UK.

* General Atomic Co., San Diego, USA.

Abstract: Studies have been made of parallel plasma resistivity and magnetic field diffusion in JET discharges. In these discharges plasma elongation, plasma current and toroidal field are varied. The first study includes comparisons of Spitzer resistivity and neoclassical resistivity derived from several diagnostic measurements during the flat top of the current waveform. In the second study field diffusion is followed for discharges in which the plasma current is programmed to rise from one flat top to another flat top level.

1. Resistivity and Z_{eff}

The following expressions are used to define the Spitzer resistivity $\eta_{\parallel}^{0}$ and the neoclassical resistivity $\eta_{\parallel}^{*}$ in terms of Z_{eff} and electron temperature T_e:

$$\eta_{\parallel}^{0} = \frac{m_e^{1/2} e^2}{3 \varepsilon_0^2 \pi^{3/2}} Z_{eff} \alpha(Z_{eff}) \frac{\ell n \Lambda_{ei}}{T_e^{3/2}} \qquad \ldots (1)$$

$$\eta_{\parallel}^{*} = g \eta_{\parallel}^{0}, \qquad \ldots (2)$$

where [1] $$\alpha(Z_{eff}) = 0.29 + 0.46/(1.08 + Z_{eff}), \qquad \ldots (3)$$

and $$g = (1 - f_T/(1 + \xi \nu_*))^{-1}, \qquad \ldots (4)$$

f_T, ξ and ν_* being given in [2]. Ohms Law is integrated over the plasma cross section as

$$I_\phi = \int E_\phi/\eta_{\parallel} \, da, \qquad \ldots (5)$$

where I_ϕ is the plasma current and E_ϕ the toroidal electric field.

Assuming a uniform Z_{eff} we can determine two estimates of Z_{eff} from (5) using for $\eta_{\parallel}$ either (1) or (2). These values of Z_{eff} are referred to as Z_{Spi} and Z_{Neo} respectively. A third estimate of Z_{eff} is found from visible Bremsstrahlung data collected from a vertical sight line. This estimate referred to as Z_{Vis} is evaluated from

$$Z_{Vis} = C B_\nu (\int n_e^2 g_{ff} T_e^{-1/2} \, dl)^{-1} \qquad \ldots (6)$$

where C is a constant, B_ν the brightness and the integration taken along the viewing line. The variation of the Gaunt factor g_{ff} with T_e is accounted for and typically varies from 4.5 in the centre to 1.5 at the edge. ECE electron temperature data is used [3] and the density profile is matched to data from a single sight line interferometer.

2. Comparison of Estimates of Z_{eff}

From studies of 600 JET discharges it is found that Z_{Neo}, the value of Z_{eff} derived from (5) using neoclassical resistivity (2) is a factor 0.8-1.2 times Z_{Vis} given by (6). The values of Z_{Spi} are larger than Z_{Vis} by a factor 1.5-3. Figure 1 shows Z_{Neo} and Z_{Spi} plotted against Z_{Vis}; each point in Figure 1 represents a JET discharge value calculated 1 second before the end of the current flat top. The difference between Z_{Neo} and Z_{Spi} is approximately a factor 2 and is mostly due to electron trapping in a tight torus, i.e. the term f_T in (4) is typically 0.5 and ν_* is usually below 0.1. However, some JET discharges also included amongst the points in Figure 1 have low values of field-current with T_e in the range 1-1.5keV. For such discharges ν_* is of order 0.2-0.5 and the reduced effect from trapping yields a ratio Z_{Spi}/Z_{Neo} of order 1.5. The dependence of resistivity upon ν_* is apparent from Figure 1 and shows up as a smaller spread in the Z_{Neo} values for a given Z_{Vis} than it does for the corresponding values of Z_{Spi}.

3. Field Diffusion

In three JET discharges the plasma current has been programmed to rise from one flat top level of 1MA to a second flat top level of 2MA. During this current rise phase lasting 2 seconds the plasma shape is approximately constant. Parallel resistivity is studied both during the current rise phase and during the subsequent penetration phase at 2MA. A sequence of MHD equilibria [5] are calculated from magnetic pickup coil and flux loop data. The internal inductance ℓ_i calculated for these equilibria falls from 1.6 to 1.05 during the current rise as shown in Figure 2. Approximately 1.4 seconds after the end of the rise phase the current is fully penetrated and ℓ_i has increased to its final value of 1.25. The period of 1.4 seconds is marked in Figure 3 as the time taken for the loop voltage on the plasma surface to approach the loop voltage on axis. From the calculated flux function ψ, current density J_ϕ and electric field $E_\phi = -\partial\psi/\partial t$ we form the ratio $\eta_M = E_\phi/J_\phi$ as a function of space and time. The ratio η_M is then compared with space-time dependent values of $\eta_{\shortparallel}^0$ and $\eta_{\shortparallel}^*$ as given by Eqs.(1) and (2). The latter values are calculated from ECE temperature profiles and $Z_{eff} = Z_{Vis}$ is assumed. Figure 4 shows the ratios $\eta_M/\eta_{\shortparallel}^0$ and $\eta_M/\eta_{\shortparallel}^*$ against major radius at a particular time during the current rise. The vertical bars indicate the time variation of these ratios.

4. Discussion

Both studies show that the resistivity inferred from Z_{Vis} or determined from MHD equilibria is within a factor 0.85-1.15 equal to the neoclassical value given by (2) and higher by a factor 1.4-2.6 than the Spitzer value given by (1). This applies to plasmas in a steady state and plasmas with applied external electric fields. The variations from discharge to discharge in Z_{Neo}/Z_{Vis} (Figure 1) are due to experimental errors in T_e(10%) [3], errors on the n_e profile assumption used in (6) as well as unknown variations in impurity contents, e.g. metal vs carbon; the Gaunt factor g_{ff} used assumes an atomic Z^2 in the range 4-9. The variations with time of the ratio $\eta_M/\eta_{\shortparallel}^*$ (Figure 4) are mainly subject to errors in T_e and errors arising from the equilibrium fit to the magnetic data: errors on current density J. We conclude that the parallel resistivity in JET is close to neoclassical especially, since the ratio $\eta_M/\eta_{\shortparallel}^0$ (Figure 4) clearly exhibits the lack of trapping effects. This result should be compared with a Doublet III study [5] in which trapping was found to be far less dominant.

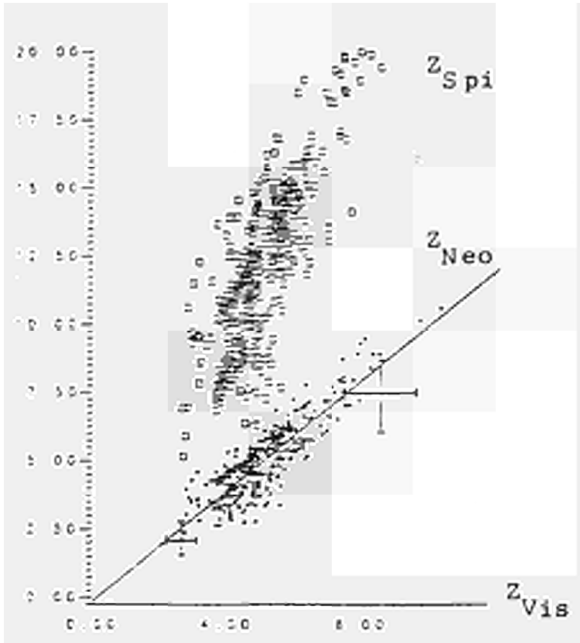

Fig 1: Estimates of Z_{eff} calculated using (1) □ and (2) * versus Z_{eff} from (6). Each point represents a flat top value from a JET discharge.

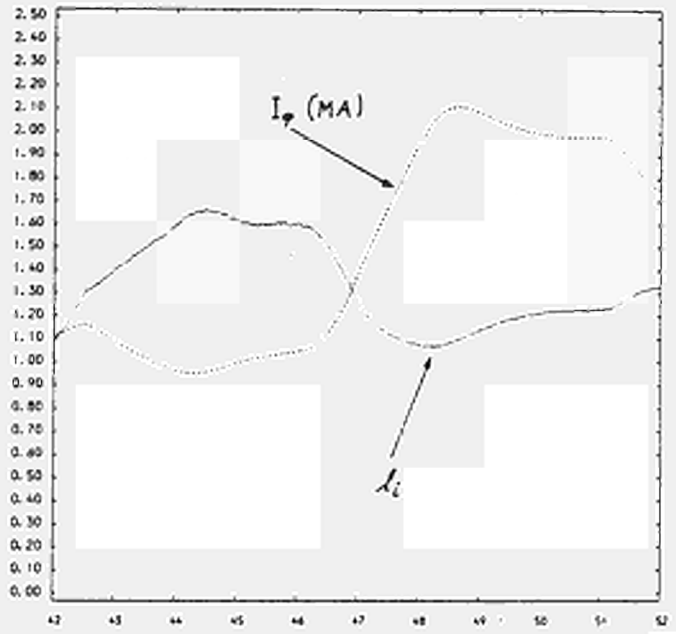

Fig 2: Internal inductance ℓ_i and plasma current I_ϕ in MA as functions of time for shot 4896.

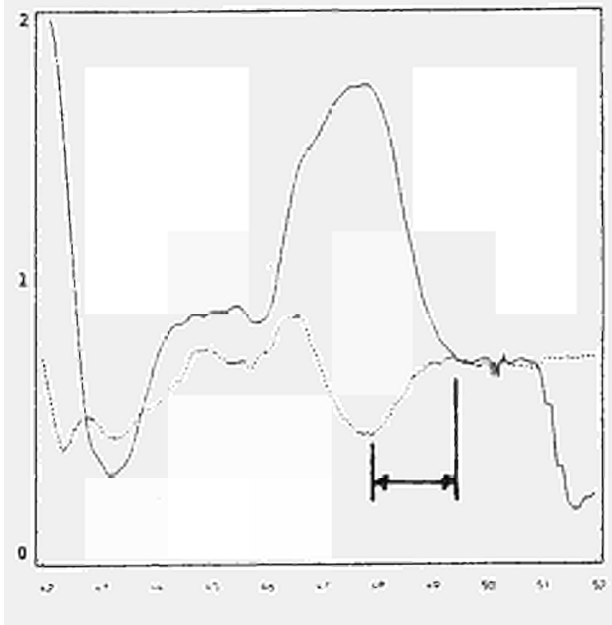

Fig 3: Loop voltages on plasma surface (solid line) and on axis (dashed line) versus time for shot 4896.

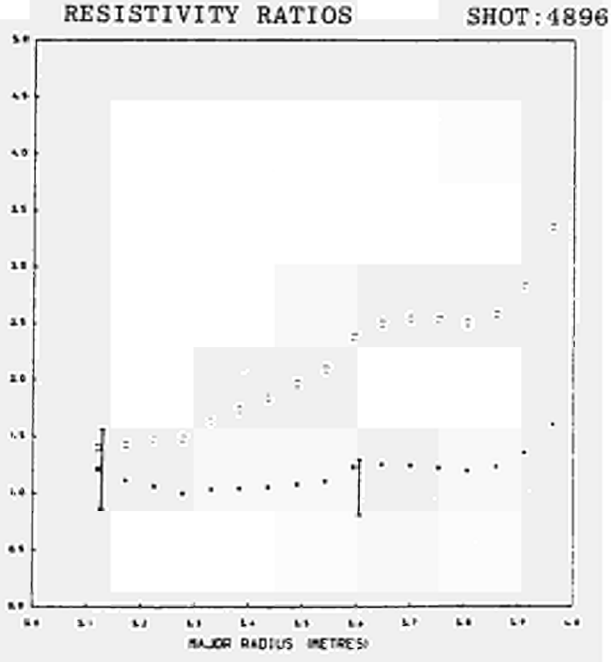

Fig 4: The ratios $\eta_M/\eta^*_{||}$ (asterisks) and $\eta_M/\eta^\circ_{||}$ (squares) versus minor radius at 47 sec. The vertical bars indicate time variations during current ramp.

References

[1] F.L. Hinton, R.D. Hazeltine, Rev. Mod. Phys., 48, 239 (1976).
[2] S.P. Hirshman, D.J. Sigmar, Nucl. Fusion, 21, 1079 (1981).
[3] A.E. Costley et al., Electron Temperature Measurements in JET, EPS, Budapest (1985), paper 186.
[4] M. Brusati et al., Comp. Phys. Reports 1, 345 (1984).
[5] R.D. Stambaugh et al., Nucl. Fusion, 22, 395 (1982).

LIMITS IN EVALUATING ENERGY LOSS PROFILES FROM BOLOMETRIC MEASUREMENTS AT JET

N Gottardi, H Krause*, K F Mast*

JET Joint Undertaking, Abingdon, Oxon, OX14 3EA.
* On assignment from Max-Planck-Institut für Plasmaphysik, Garching, FRG.

ABSTRACT In JET three pin-hole type bolometer cameras observe one poloidal cross-section of the plasma from three different viewing positions. A simple projection method is used to test the consistency of the assumed shape of isoemissivity surface with the integral measurements. If consistency is found a generalized Abel inversion can be performed. In a considerable number of discharges the surfaces of constant emissivity do not coincide with the magnetic flux surfaces. Besides the obvious asymmetry due to limiter and R.F. antenna, a strong ($\tilde{>}$ 30%) up/down asymmetry and MARFEs are presented as examples. A neoclassical explanation for the up/down asymmetry is proposed.

Radiation losses play an essential role in the measurement of energy balance of tokamak plasmas. Bolometers measure the plasma emissivity only integrated along the lines of sight. Local emissivities, however, are wanted for the energy balance. A local emissivity can be obtained either by tomographic methods or through assumptions on the geometry of the isoemissivity surfaces. In JET, with the present arrangement (maximum 34 lines of sight from only three view points [1], tomographic methods yield an unsatisfactory spatial resolution. A resolution of 10 cm would require several hundred bolometer channels distributed rather homogeneously around the plasma cross-section. Assumption of the surface geometry reduces the two-dimensional to a one-dimensional problem, and in JET a resolution of about $\sim$ 10 cm is possible. This can be achieved with the help of a generalized 2-step inversion method [2] which can be applied to any set of nested contour lines. Usually the geometry has been assumed to be that of the magnetic flux surfaces derived at JET from magnetic measurements [3]. This assumption is not justified in general. We check the validity of this by utilizing the first step of the above mentioned inversion method. In this step all sight lines are projected to a common virtual observation point each line remaining always tangent to the same contour line. This procedure transforms also the integrated signals. If the assumed geometry is correct all transformed signals which are tangent to the same contour line must coincide. To illustrate this let us consider an observation plane (Fig. 2) with viewing lines (S_1-S_5) and selected isoemissivity surfaces (σ_0-σ_5) each of which is tangent to one of the viewing lines. The spaces between adjacent σ are the pixels in which the emissivity ε is considered constant. If the total length of viewing line S_i inside pixel ε_k is denoted by A_{ik} then the line integrated intensity I_i is given by

$$I_i = \Sigma A_{ik} \varepsilon_k \qquad (1)$$

Straightforward inversion of this linear system, where A is a lower-triangular matrix, would yield the emissivity ε from the measurements I but the resulting emission profile would be too discontinuous due to noise in the measurements and the pixel spacing too irregular.

A method of spatial smoothing and interpolation of the measured I is therefore needed. Since measurements result from cameras with different

points of view interpolation between data from different cameras are not directly possible. Following a suggestion [4] the data from all cameras is therefore projected first into the viewing frame of a virtual camera at an arbitrary position, eg the position of a real camera.

Let T_1-T_5 be a set of view lines emerging from the pin-hole P (cf. Fig.2) of a virtual camera, each T_i chosen to be tangent to the isoemissivity surface σ_i. The virtual intensities I' are then given by

$$I'_i = \Sigma B_{ik} \varepsilon_k \qquad (2)$$

with the B_{ik} being the total length of I'_i inside pixel ε_k. From Eq.1 and Eq.2 then follows the projection of real intensities into virtual ones

$$I' = B \cdot A^{-1} \cdot I \qquad (3)$$

In this way all measurements can be represented as a function of a single coordinate. Cubic splines and/or Chebyshev polynomials are used to fit a smooth curve through all the data. At this stage it can be checked if the assumed isoemissivity surfaces are adequate by inspection of the deviations of the I' from the fit curve. In many cases a consistent set of I' can be achieved by the elimination of single strongly affected channels (eg limiter effects). Inversion then proceeds by sampling the fit curve on a fine numerical grid and solving a matrix equation (as in Eq.1) for the samples.

Fig.3 illustrates this technique applied to an assumed hollow emissivity profile with the real camera geometry for a set of isoemissivity surfaces taken to be the magnetic flux surfaces of an actual pulse (cf. Fig.1). After projection of the (calculated) line averaged data on to the virtual camera the resulting inversion of the fit curve reproduces the initial profile very well.

Fig.4 shows the procedure using actually measured intensities. The pulse shows a typical level of data scatter between the different cameras after projection which still allows a satisfactory inversion result. Some evident deviation might be explained by the nearness of structures (limiter, RF antenna) to the observation plane.

For plasmas in the vicinity of the density limit MARFEs are frequently observed in JET. Details can be found in [5].

Differences of more than one order of magnitude are observed when the plasma is limited by the inside column of the torus rather than by the outside limiters. Those channels viewing the region where the plasma touches the wall both in the horizontal cameras and the vertical camera then show drastically enhanced signals.

A similar observation holds for discharges with an internal separatrix whose flux surface geometry is similar to the one in Fig.1. Here the plasma streaming along the separatrix to the top and bottom wall of the vessel causes drastic local radiation which shows on some vertical and horizontal channels at about five times the intensity of a normal central channel while not affecting the majority of channels.

Fig.5 gives a typical example of significant ($\sim\pm25\%$) up/down asymmetry. One possible explanation for this type of asymmetry is given by an analytical one-dimensional neoclassical two-fluid model [6,7]. It considers a radial electric field which gives rise to diamagnetic rotation of the bulk plasma and of the impurities with different velocities corresponding to their different electric charge Z.

The friction force between impurities and the bulk plasma then results in a pressure gradient of the impurities in poloidal direction due to finite aspect ratio effects. With the assumption of constant temperature on flux surfaces and negligible radial transport the relative variation of impurity density n_z/n_z on a flux surface can be derived. This variation is then expanded in a Fourier series with respect to the poloidal angle Θ. There are two toroidally symmetric first order Fourier terms representing up/down asymmetry (first term) and inward/outward asymmetry (second term).

$$\tilde{n}_z/n_z = 2\frac{r}{R_o}\frac{\Omega}{1+\Omega^2}\sin\theta - 2\frac{r}{R_o}\frac{1}{1+\Omega^2}\cos\theta \qquad (4)$$

The parameter Ω is given by

$$\Omega = \frac{\omega_H \tau_{HH}^{b/a}}{r\, Z^2}\frac{r^2}{q(r)R_o^2}\frac{P_H(r)}{dP_H/dr} \qquad (5)$$

with P_H pressure of H, ω_H H^+-gyrofrequency, τ_{HH} H^+-collision time, b/a axis ratio of ellipse.

Eq.4 shows that the up/down asymmetry changes sign with the toroidal magnetic field. The inward/outward asymmetry represents always an impurity accumulation at the torus inside plasma edge.

With Nickel and Carbon as typical JET impurities Ω is estimated to be in the range of 2 to 3. Eq.4 then predicts up/down asymmetries larger than inward/outward asymmetries which in JET could easily be masked by effects of localised plasma-wall interactions, eg by limiters. For up/down asymmetries Eq.4 gives a scaling law

$$(\tilde{n}_z/n_z)_{max} \approx \frac{2r}{R_o\Omega} \approx \frac{r^4}{T_e^{3/2}}\frac{B_T n_e}{I_p^2(r)\, b/a} \qquad (6)$$

Since absolute numbers for n_e and T_e are quite uncertain at the plasma edge the measured maximum up/down asymmetry in the emissivity $\tilde{\varepsilon}/\varepsilon$ which is expected to scale with $\tilde{n}_z/n_z$ is normalised to one for one time in a pulse and the subsequent development of density, temperature and current in this pulse is used to compare the normalised asymmetry with Eq.6. Fig.6 shows good agreement between the prediction and the experimental points.

For high densities and/or low T_e Eq.4 predicts small up/down and large inward/outward asymmetries. This could explain why MARFEs nearly always form at the torus inside plasma edge.

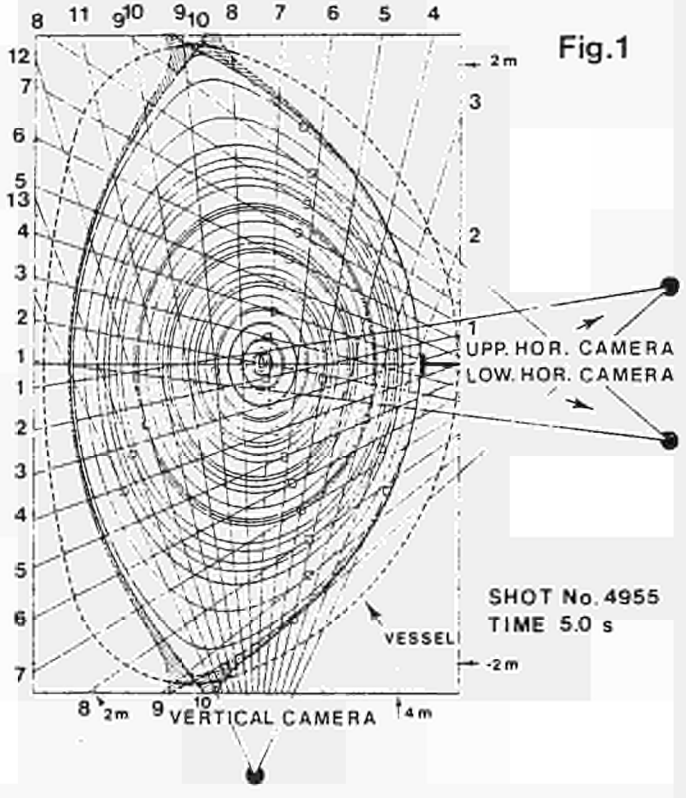

Fig.1

FIG.1 Arrangement of bolometer channels in JET.

REFERENCES

[1] K F Mast et al., Proc. of the 5th Top. Conf. on High Temp. Pl. Diagn., 1984 Tahoe City, USA.

[2] N Gottardi. Evaluation of local distributions from line Integrated Measurements, JET Report, in prep.

[3] J Blum et al., JET Contract No. JT3/9008; Jan. 1985.

[4] W Engelhardt, private communication.

[5] J O'Rourke et al., Poloidally Asymmetric Edge Phenomena in JET, this conference.

[6] K Feneberg et al., Radiation Asymmetries in JET, JET report, to be publ.

[7] K Feneberg et al., Poloidal Asymmetric Impurity Radiation in ASDEX in the Presence of Neutral Injection, this conference.

ACKNOWLEDGEMENT

The authors thank D F DUchs for many discussions and S Springmann for improving flux surface handling routines.

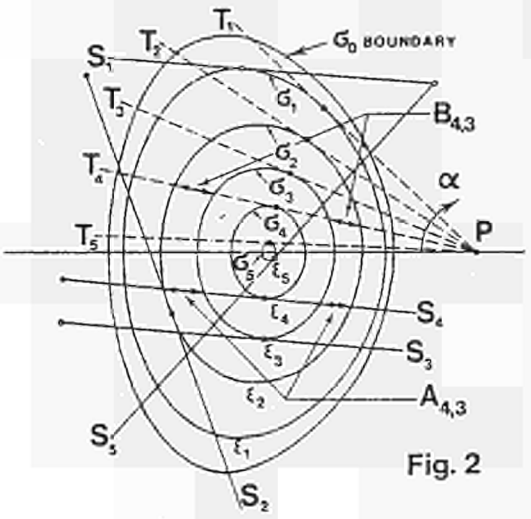

Fig. 2

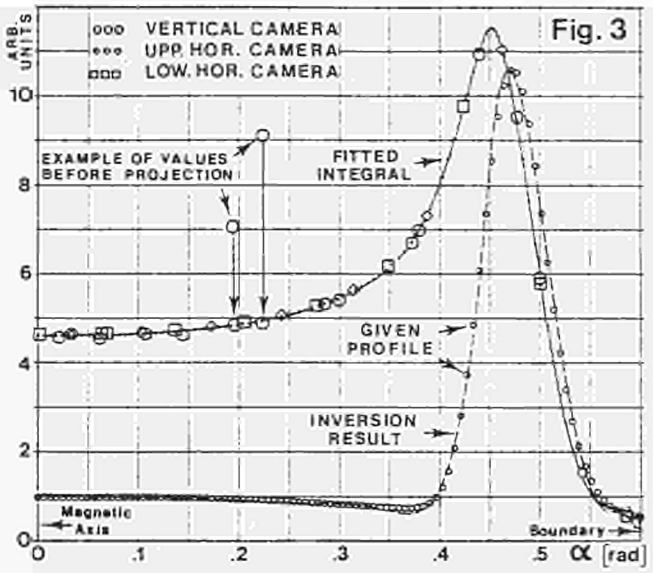

Fig. 3

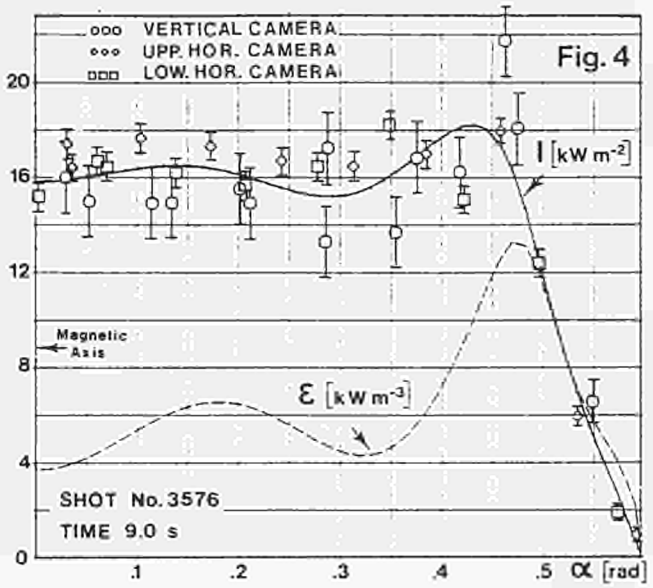

Fig. 4

FIG.2 Isoemissivity lines and the projection of real view lines into a virtual camera.
FIG.3 Generalised Abel inversion for an assumed initial emissivity distribution; α as in Fig.2.
FIG.4 Measured data from three bolometer cameras projected into the viewing frame of a virtual camera in the equatorial plane outside the plasma and resulting local emissivity; α as in Fig.2.
FIG.5 Up/down asymmetry evident in data from the upper and lower horizontal camera; α as in Fig.2.
FIG.6 Normalised neoclassical prediction and normalised experimental data for the up/down asymmetry.

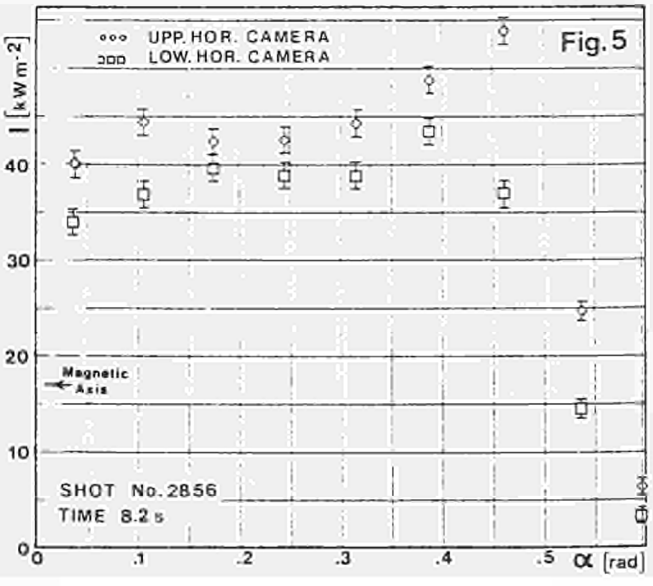

Fig. 5

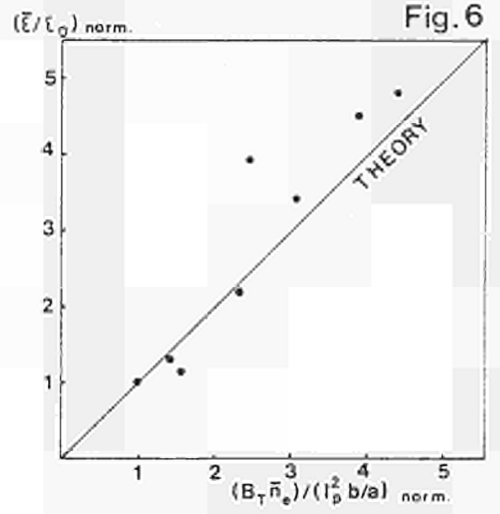

Fig. 6

THE FORMATION OF A MAGNETIC SEPARATRIX IN JET

A. Tanga, D.J. Campbell, B. Denne, A. Gibson, N. Gottardi, A. Kellman†, E. Lazzaro, K.F. Mast, G. McCracken*, P. Noll, F.C. Schüller, P. Stangeby*, D.D.R. Summers, A.J. Tagle, P.R. Thomas, M. Valisa

JET Joint Undertaking, Abingdon, Oxon, OX14 3EA, U.K.
*UKAEA Culham Laboratory, Abingdon, Oxon, OX14 3DB, U.K.
†G.A. Technologies, P.O. Box 85608, San Diego, Ca. USA

Introduction

The goal of increasing the quality of confinement in tokamaks has led to a renewed interest in the "divertor" and "magnetic limiter" configuration in which the plasma boundary is defined by a magnetic separatrix, detached from the material limiter and the vacuum vessel. Such a configuration may afford improved thermal insulation of the plasma as well as reduced contamination from impurities. The region at the plasma boundary may be able to sustain a high edge temperature with a large temperature gradient when substantial additional heating is applied. Such a so-called "H mode" shows a much reduced radial transport compared to the "L mode" (1,2,3). In this paper the initial results and the experimental observations on the formation of a magnetic separatrix in ohmic JET discharges are presented.

Analysis of the magnetic configuration

The transformation of a closed plasma boundary into one with a separatrix can be regarded as an extreme case of plasma shaping for which a particular mode of operation of the poloidal circuit is required. A poloidal cross section of the JET configuration is shown in Fig.1. The iron circuit, the equilibrium coil PF4 and the shaping doublet PF2 and PF3 are clearly shown. The field produced by the coils PF2-PF3 is largely quadrupolar and is suitable for the control of the plasma elongation. A field is also produced by the primary coil, especially when the primary carries its full current, due to the local saturation of the iron.

This field has a strong hexapolar component and changes the triangularity of the plasma. In practice, a stagnation point can be produced near the top-bottom of the vessel by cancelling the predominantly horizontal plasma poloidal field.

The relative contribution of the field produced by the coil PF2 and of the primary can be seen by plotting the horizontal field produced by the current in the coil PF2 in the top of the vessel for a case in which the current of the primary was large and a case in which the current of the primary was zero.

This effect is shown in Fig.2 in the upper and lower curve, respectively. The formation of a magnetic separatrix is possible, either by having a large current in the coil PF2, or at the end of a long plasma current pulse due to the effect of the field produced by the primary. The combination of these two fields makes possible the formation of a magnetic separatrix at large values of plasma current.

The magnetic diagnostic of the configuration is based on the equilibrium identification calculations performed with the JET code IDENT B suitably modified for accurate determination of the field null location. As reported elsewhere (4,5), the code solves an inverse equilibrium problem finding the free boundary solution of the Grad-Shafranov equation which fits best the magnetic measurements of flux and poloidal field. To locate the separatrix in the first approximation, an initial run of the code is made.

Using a spline interpolation routine the separatrix line is traced and its

intersection with the equatorial plane is taken as a new boundary position. The successive runs converge easily to the solution, if the initial case is not pathological. As a consequence, the relevant parameters of the flux and current distribution such as the safety factor at the magnetic axis, the value of poloidal beta and that of the internal inductance are determined, within the accuracy of the magnetic data (6).

Experimental results

The separatrix configuration has been maintained for several seconds on discharges with plasma currents of 1.5MA and 2.0MA. The value of the toroidal field was 2.6T, the line average density was $1.0.10^{19}m^{-3}$.

In the 1.5MA discharge shaping has been obtained by applying a pulse on the coils PF2-PF3 only, with nearly zero current in PF1. A plot of the poloidal flux contours is shown in Fig. 3.

The separatrix configuration for the discharges at 2.0MA plasma current has been obtained all along the final five seconds of a tokamak discharge lasting for twenty seconds, needed to bring the current in the primary coil to a high negative value. The poloidal flux plot is shown in Fig. 4.

The presence of the two null points located approximately 10-15cm inside the vessel is apparent. The plasma is well detached from both the limiter and the inner vessel. This was also confirmed by the absence of H_α emission from these surfaces. The high value of triangularity $\delta = 0.46$ for the discharge in Fig. 4 is a consequence of the hexapolar moment produced by the PF1 coil. The IR camera viewed a poloidal section of the vessel.

Areas of intersection of the plasma with the inconel protection plates were clearly visible. In Fig. 5, the intensity along the poloidal cross section of the vessel is shown. The intensity, within a window centred around the wavelength of 0.9μ, shows two maxima separated by 24cm which are in correspondence of the left and right intersection of the magnetic separatrix with the bottom of the vacuum vessel, in good agreement with the plot of the poloidal flux. The properties of the edge plasma during the 1.5MA experiments have been measured using an array of four Heat Flux/Langmuir probes as described in ref. (7). Three probes face the ion drift side and are located at distance 1,4,8cm from the array tip and one facing the electron drift direction is located 1cm from the array tip. The major radius position of the probe on the torus was $R_p = 3.252m$ and the array was moved up-down in the vertical direction between $1.71 < Z < 1.76$, Z being the distance between the probe array tip and the equatorial plane of the machine.

Fig. 6 gives an example of the ion saturation current density (particle flux density) radial profile. As can be seen, the e-folding length on the electron-drift side $\lambda = 57mm$ is about twice that on the ion drift side, $\lambda = 28mm$. The reasons for this difference are still under investigation. Measurements of radiated power have been performed by a multi-channel array bolometer camera, described elsewhere (8).

The signals along the viewing lines pointing to the regions of the X point were up to ten times larger than the average.

The generalised Abel inversion of the radial profile, excluding the channels affected by the enhanced radiation around the X points shows that, for the 1.5MA discharges, most of the radiated power comes from the outer regions of the plasma. The total radiated power can be described as the sum of the power which is radiated by the whole valome of the plasma ≅450kW and the power which is radiated in the regions of the X points ≅250kW. The total ohmic input power was 780kW.

A preliminary analysis of the spectral lines of the impurities shows that the nickel content of the discharge was very low and well below 0.1%, whilst the concentration of oxygen and carbon was of the order of 1%; both these values are comparable with the concentrations of an equivalent limiter JET

discharge.

References

1) F.L. Hinton et al, in Plasma Physics and Controlled Nuclear Fusion, Tenth Conference proc., London 12-19 Sep. 1984, IAEA Vienna 1985, vol.II p.3.
2) M. Okabayashi et al, ibid., vol.I p.229.
3) C.E. Singer et al., to be published in Nucl.Fus.
4) J. Blum, J. Le Foll, B. Theoris, JET Workshop on Magnetic Measurements Culham 1980.
5) M. Brusati et al, Comp. Phys. Rep. 7-8 345 (1984).
6) M. Brusati et al, Proc, Workshop on Diagnostics for Fusion Reactor Conditions, Vienna 1982 p.235.
7) P.C. Stangeby et al, this conference.
8) N. Gottardi, H. Krause, K.F. Mast, this conference.

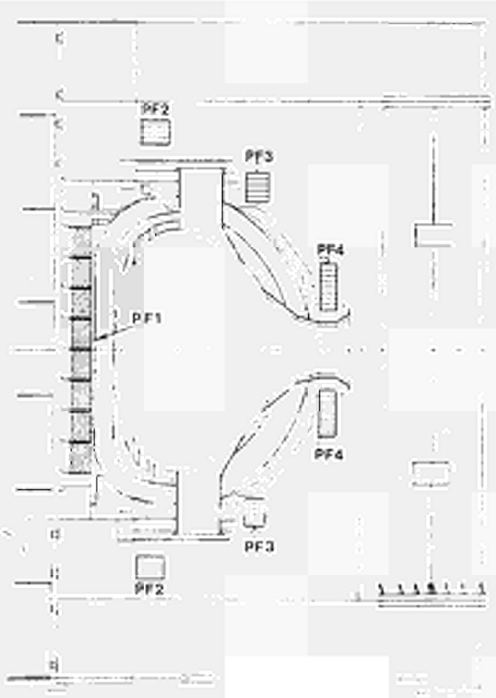

Fig. 1
Cross section of JET showing position of poloidal field coils (PF).

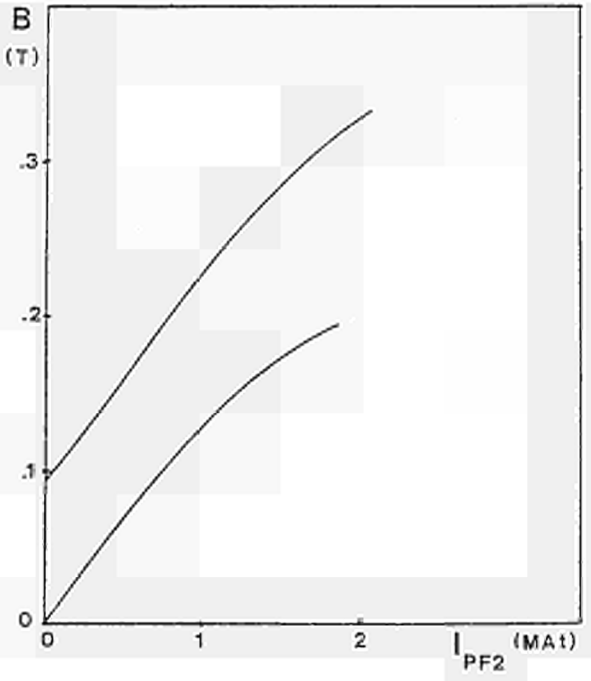

Fig. 2
Horizontal field produced by the PF2 coil current at the tip of the vessel (T). Upper curve is with a large primary current, lower curve is with zero primary current.

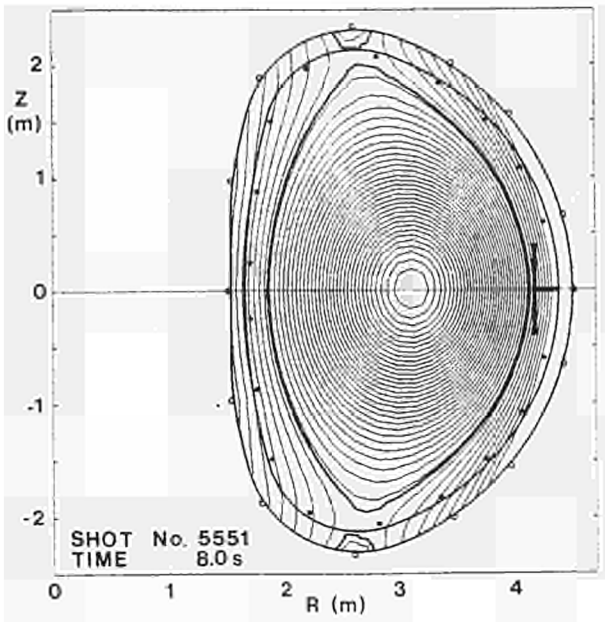

Fig. 3
Poloidal flux contours in the plasma: current 1.518MA, poloidal beta 0.26, internal inductance 1.29, plasma elongation 1.75.

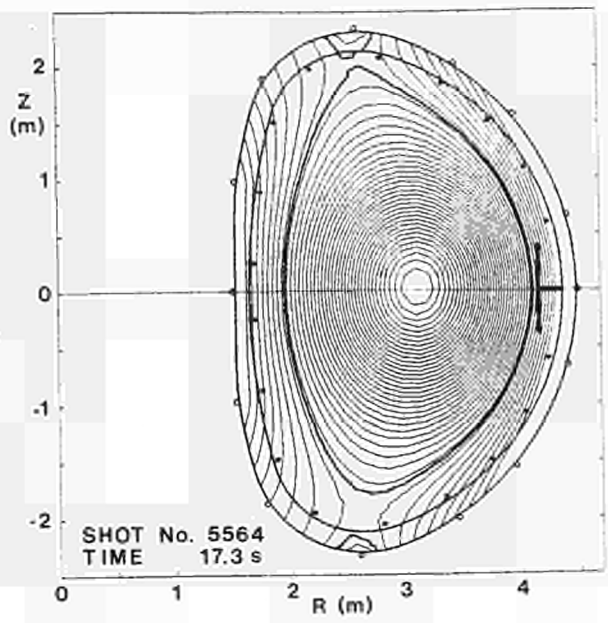

Fig. 4
Poloidal flux contours in the plasma: current 1.995MA, poloidal beta 0.09, internal inductance 1.4, plasma elongation 1.8.

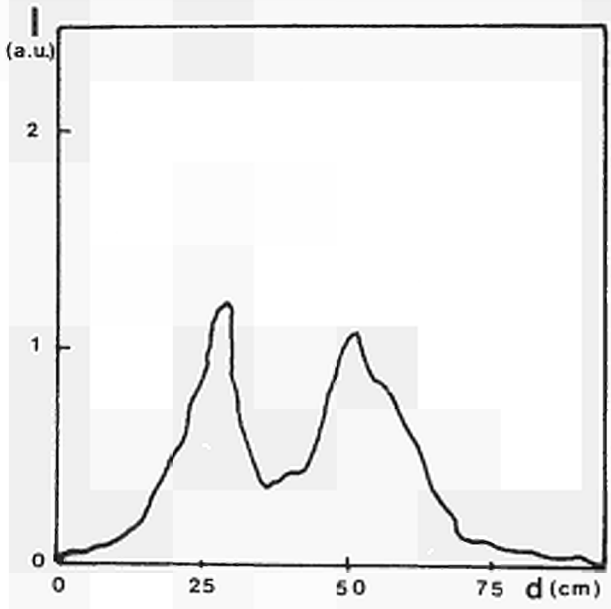

Fig. 5
Intensity of infrared emission along the protection plates as a function of the distance.

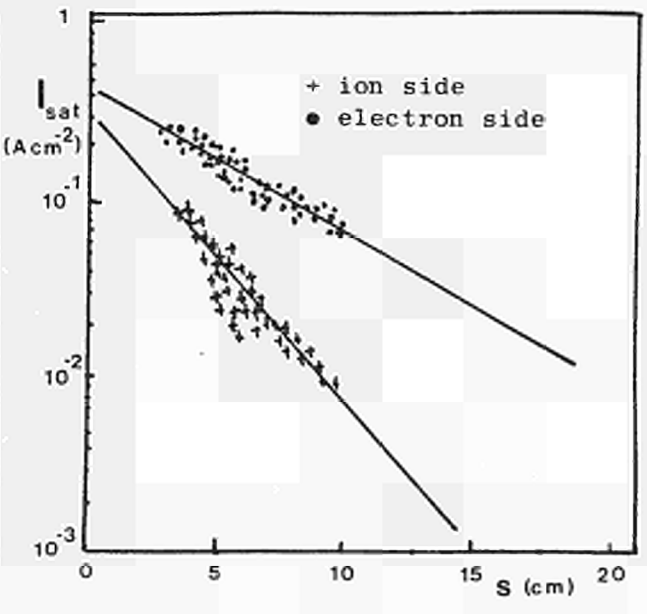

Fig. 6
Ion saturation current measured in the plasma scrape-off layer versus the distance from the plasma edge.

RECYCLING, ISOTOPIC EXCHANGE AND DENSITY BEHAVIOUR IN JET DISCHARGES

P D Morgan, S Corti, J Ehrenberg*, M J Forrest+, A Gondhalekar, C W Gowers, G Magyar, J J O'Rourke, M F Stamp, D D R Summers, A Tanga, M L Watkins

JET Joint Undertaking, Abingdon, Oxon OX14 3EA, UK
* on attachment from Euratom-IPP Association, Max-Planck-Institut für Plasmaphysik, D-8046 Garching, FRG
+ on attachment from Euratom-UKAEA Association, Culham Laboratory, Abingdon, Oxon OX14 3DB, UK

INTRODUCTION

An understanding of recycling and particle confinement in tokamak discharges is an important prelude to achieving successful density control. Likewise, knowledge of isotopic-exchange processes permits a rapid and efficient changeover in the plasma hydrogenic content, when interchanging the working gas between H_2 and D_2.

The study reported is based mainly on measurements using optical spectroscopy. Details of the apparatus are to be found in /1/. Absolute H_α or D_α intensities, measured simultaneously at the graphite limiters, antennae, inner and outer walls and at upper and lower walls, yielded the neutral influxes. Other selected spectral lines were used to obtain impurity influxes. A 7-channel interferometer provided electron density profiles, while information about H or D effluxes was obtained using a neutral particle analyser (NPA).

RESULTS

The temporal behaviour of plasma current and electron line density is shown in Fig.1(a). The evolution of the line density closely follows that of the current. Also shown, as a broken line, is the evolution of $n_e.\ell$ if it were determined only by the initial torus prefill and the subsequent gas puff. To a reasonable approximation, the H_α or D_α signals from the limiters follow the current, while those from the wall, after the initial breakdown, tend to remain constant until a few seconds before the discharge ends /2/.

During current rise a substantial desorption of gas occurs. From particle balance /2/, the recycling coefficient

$$R = \Sigma S_i / (\Sigma S_i + \Phi_g - dN_e/dt)$$

is deduced to be > 1. It has the general form shown in Fig.1(b). ΣS_i is the electron production rate from ionisation of the recycled hydrogenic and impurity fluxes, Φ_g is the gas flux introduced by puffing, mostly during current rise, and N_e is the plasma electron content. The global particle confinement time $\tau_p \triangleq R\ N_e/\Sigma S_i$ may also be evaluated, and permits deduction of the characteristic time for density change, $\tau^* = \tau_p/(1-R)$.

With no gas puffing, during the current plateau the plasma density is approximately constant, indicating that $R \sim 1$ (Fig.1). During this stationary phase, for sequences of shots in which the average density $\bar{n}_e$ is varied, to a good approximation the hydrogenic influxes from the limiters and wall vary quadratically with $\bar{n}_e$ (Fig.2) over the density range covered. The limiters are the main source of recycled particles. The ratio of limiter to wall flux

varies with plasma current and elongation, b/a, but is generally in the range 3-15:1, during the current plateau. Since the total limiter area is $\lesssim$ 1% of the plasma surface area, the corresponding H_α or D_α brightness ratio is in the range 300-1500:1. Fig.3 shows the variation of τ_p with $\bar{n}_e$ during the plateau, for several series of shots. Proton dilution by the impurities has been taken into account. For $\bar{n}_e \gtrsim 10^{19}$ m^{-3}, τ_p decreases with increasing density, but at lower densities the dependence is reversed /2/. The high density regime is consistent with the plasma becoming impervious to the penetrating neutrals and the recycling becoming predominantly an edge effect.

During the discharge termination phase the plasma current is ramped down to zero in $\sim$ 5s. There is a simultaneous decrease in plasma density (Fig.1(a)) indicating that $\sim$ 2-5x10^{20} particles/s are pumped by the torus and its accessories, with concomitant decreasing influx from the limiters. A recycling coefficient < 1 is inferred during this phase (Fig.1(b)). In contrast, the H_α or D_α signal at the wall remains unchanged for several seconds following the start of current ramp-down, before steadily increasing as the discharge ends. In many discharges, particularly those at higher density, there is a sudden decrease in the influx from the limiters accompanied by a simultaneous increase in the influx from the wall and a peaking of the density profile. This is described in detail in /3/ - this conference - and is attributed to the formation of a 'marfe'.

On changing the working gas from H_2 to D_2, without conditioning the vacuum vessel, within $\sim$ 10 discharges the concentration ratio $n_D/(n_D + n_H)$ is found to be $\gtrsim$ 0.9, from measurements of the neutral influx and efflux. However, for a series of discharges following carbonisation of the vessel, by glow discharge cleaning in H_2 and $\sim$ 5% CH_4, the situation is different. The deposited carbon traps considerable amounts of H_2. On changeover, it is observed that $n_D/(n_D + n_H)$ is only $\sim$ 0.5 after 10 discharges and that it takes a further 20-30 shots to increase the ratio to $\gtrsim$0.9.

ICRH experiments have been performed on JET, using ^{3}He as a minority species. Controlled quantities of this gas are injected into the vacuum vessel towards the end of the current ramp-up. From interferometry, the increase in the plasma electron content is consistent with all of the helium entering the plasma. The increase in electron density penetrates to the plasma centre in approximately 0.5s, which is on the same time scale as the particle confinement time. Using H as minority, the application of a 2s 2.5 MW square pulse of RF power to the antenna resulted in brighter D_α signals, by a factor of $\sim$ 3 at the wall and $\sim$ 2 at the limiters. The RF power caused τ_p to drop to about half its former value of $\sim$ 0.35s, in $\sim$ 0.5s. After the pulse τ_p recovered to its previous value on the same time scale.

DISCUSSION

The gas desorbed during current rise, due to the increasing power loading and rising temperature of the graphite limiters, generally accounts for a significant fraction of the plasma density achieved during the plateau, and limits the density range over which JET can operate - typically a factor of 2 at fixed current. For mid-range densities desorption contributes $\sim$ 50% of the plasma electron content (Fig.1(a)) the amount decreasing during the course of a long series of discharges. Overnight glow discharge cleaning replenishes the source. During a discharge, additional gas is puffed in to achieve the desired density. In the case of discharges at the high end of the density range, more gas is admitted to the torus than enters the plasma, which becomes increasingly impervious to the neutral atoms.

The observed dependence of the recycled flux Φ on $\bar{n}^2$ during the current plateau (Fig.2) is predicted by a simple transport model /4/. In it, the inward flux of neutrals penetrating the plasma, and ionised within a short

distance of the boundary, is balanced by the diffusion of electrons at the edge with an anomalous diffusion coefficient of order 0.4 m^2/s. Since $\tau_p = V\bar{n}_e/S\Phi$, where V is the plasma volume and S the surface area, a consequence of the dependence $\Phi \propto \bar{n}_e^2$ is that $\tau_p \propto 1/\bar{n}_e$, which is in reasonable agreement with the results in Fig.3.

No clear explanation can be offered at present for the temporal variation of the recycling coefficient during a discharge. Similar behaviour has been observed on ASDEX and TFTR. Considering R to comprise two components, one possibility is that at the limiters R_L is > 1, decreasing from a high value during current rise, as the gas available for desorption becomes progressively less, whereas at the wall R_W is < 1. Under this hypothesis, during current rise the limiter recycling would dominate, while during the plateau the desorption from the limiters is approximately equal to the wall pumping. During current decay the safety factor at the edge q increases, broadening the scrape-off layer and increasing plasma-wall interaction, while the limiters cool and release less gas. In this phase, the role of the wall would dominate. However, the abrupt change in R at initiation of current ramp-down (Fig.1) is not understood. Transport code modelling /5/ indicates that in order for the ohmic power to exceed the radiated power during current decay, which is the experimental observation, a density decay is necessary. For the specific case of Pulse No.3050, using a non-coronal radiation model for carbon impurities, a decay in the electron content in the range $2\text{-}4\times10^{20}$ s^{-1} is required, which agrees well with the measured rate, $\sim 3\times10^{20}$ s^{-1}.

The observed behaviour on changing the working gas from H_2 to D_2 can be explained on the basis of an isotope exchange model /6/. The main assumption is that the limiters, with which the plasma mainly interacts, are saturated with hydrogen. This is then exchanged with deuterium, in accordance with the local mixing model /7/; hence, a recycling coefficient of unity is assumed. The calculated influx ratio $\Phi_H / (\Phi_H + \Phi_D)$ has been compared with measurements from the NPA and with H_α/D_α intensity ratios determined by spectroscopy /8/, for a sequence of discharges. Good agreement was obtained between theory and experiment for the temporal evolution of the ratio during a discharge and throughout the sequence. The model also describes the shot-to-shot behaviour of the flux ratio for the case of carbonised walls.

CONCLUSIONS

The gross recycling and particle confinement properties of JET discharges have been evaluated, from considerations of particle balance applied to spectroscopic and interferometric measurements. This has resulted in an improved understanding of the behaviour of particle fluxes from various locations in the torus, the role of fuelling and of density control. Measurements made following a change in the working gas from hydrogen to deuterium, and the results from a model of this process, have provided an insight into the mechanisms of isotopic exchange.

REFERENCES

/1/ P D Morgan et al, Rev.Sci.Instrum. 56, (5) part 2, 862, (1985).
/2/ A Tanga et al, JET Report JET-P(84) 09, (1984).
/3/ J O'Rourke et al, paper 190 this conference, (1985).
/4/ W Engelhardt and W Feneberg, J Nucl.Mat. 76 & 77, 518, (1978).
/5/ D G Muir and M L Watkins. To be published.
/6/ G M McCracken et al, Nucl.Fusion 18, 35, (1978).
/7/ B L Doyle et al, J.Nucl.Mat. 93 & 94, 551, (1980).
/8/ J Ehrenberg, JET Report JET-DN-E(84) 07, (1984).

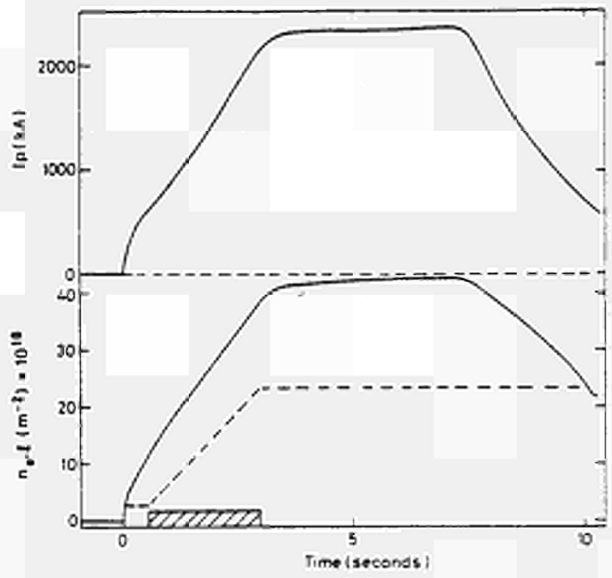

(a)

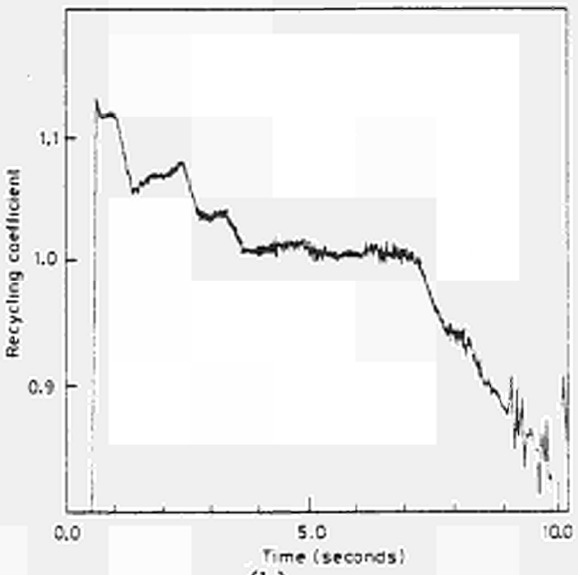

(b)

Figure 1 (a) Plasma current I_p and electron line density $n_e.\ell$ (solid line) during a discharge in H_2. Shaded area indicates waveform of gas puff. B_T = 2.5T, b/a = 1.2. Further details given in text. (b) Global recycling coefficient R versus time, for same discharge.

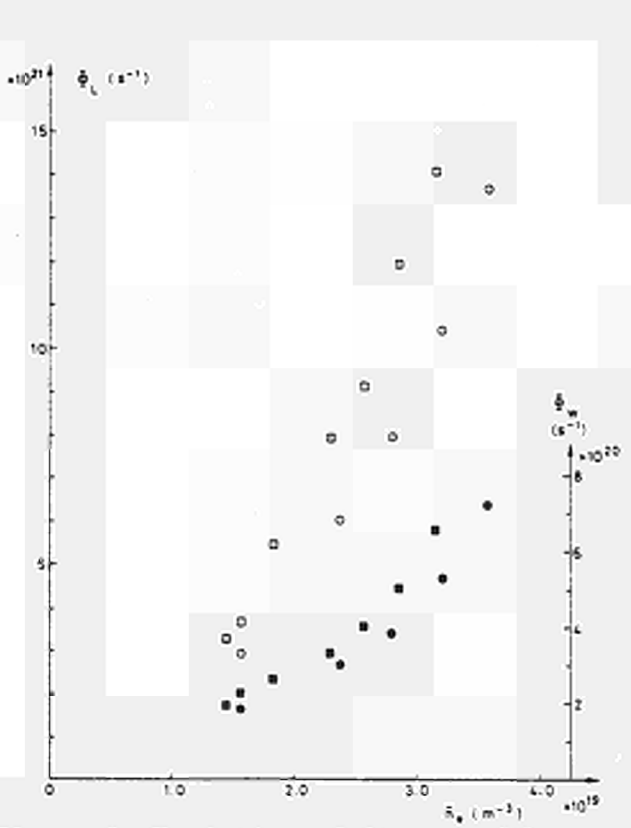

Figure 2 Variation of limiter (L) and wall (W) influx with average density during the current plateau, for 2 series of shots in D_2. Open symbols - Φ_L, solid symbols - Φ_W. O : Ip = 3.6 MA, □ : Ip = 3.0 MA. B_T = 3.4T, b/a = 1.5.

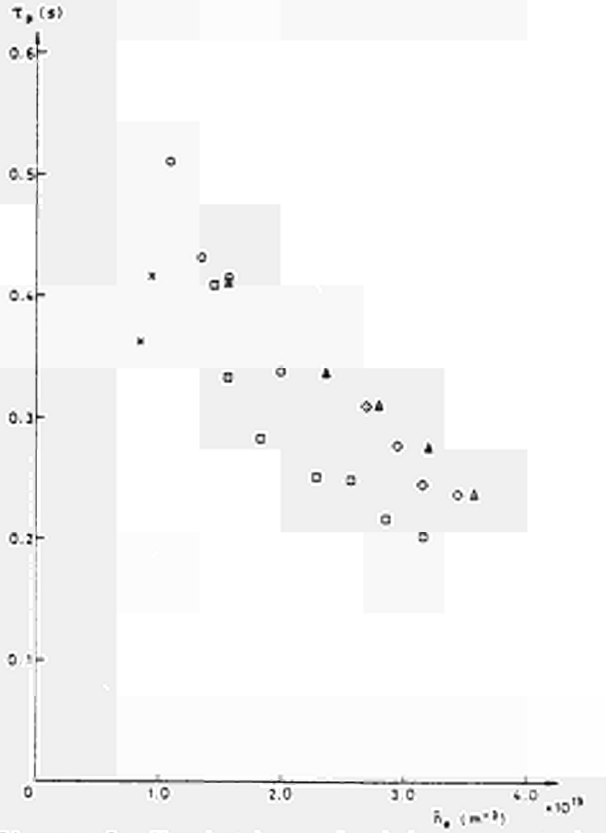

Figure 3 Variation of global particle confinement time with average density during the current plateau, for 5 series of shots in D_2. Plasma current: ◇ - 4.0 MA, Δ - 3.6 MA, □ - 3.0 MA, O - 2.0 MA and X - 1.0 MA. B_T = 3.4T, b/a = 1.5.

SPECTROSCOPIC MEASUREMENTS OF THE IMPURITY CONTENT OF JET PLASMAS WITH OHMIC AND RF HEATING

B Denne, K H Behringer, W Engelhardt, R D Gill, N C Hawkes[+], E Källne[o], H Krause*, G Magyar, M Mansfield, K F Mast*, C De Michelis, P D Morgan, D Pasini†, N J Peacock[+], H P Summers

+ JET Joint Undertaking, Abingdon, Oxon OX14 3EA, UK
EURATOM-UKAEA Association, Culham Laboratory, Abingdon, Oxon OX14 3DB, UK
* EURATOM-IPP Association, IPP Garching, Federal Republic of Germany
o EURATOM-CEA Association, Fontenay-Aux-Roses, France
† Stipendiary of the Natural Sciences and Engineering Research Council of Canada

INTRODUCTION

Knowledge of the impurity concentrations in the JET plasmas is based mainly on the analysis of resonance line intensities in the VUV, with additional information coming from measurements of soft x-ray spectra.

The plasma impurity content is monitored routinely by a McPherson Model 251 VUV broadband spectrometer, covering the wavelength range 100-1700 Å by means of two interchangeable gratings and equipped with a multi-channel detector. The spectrometer views a horizontal central chord in the torus midplane. Up to 128 spectra are recorded during a plasma discharge, allowing the study of the time evolutions of various spectral line intensities.

A relative calibration of the spectrometer sensitivity has been obtained by studying transitions between charge-exchange populated, excited levels in C VI and O VIII during neutral beam injection on the ASDEX tokamak. The absolute sensitivity is derived from the H_α-L_β branching ratio using a special H_α monitor along the same line-of-sight.

The soft x-ray spectra over the range 4-30 keV are recorded by a HgI_2 detector viewing the plasma in the horizontal mid-plane through Al, Be and air absorbers. The detector has an energy resolution of 0.6 keV at 6 keV, which is sufficient to separate the groups of He-like metal impurities in the plasma. The spectra show both continuous emission and the characteristic K-lines of Ni and Cr. The latter are used to calculate the nickel concentrations in the centre of the plasma.

METHOD OF ANALYSIS

A transport code is used for the interpretation of JET VUV line intensities. It solves, in cylindrical co-ordinates, the coupled set of continuity equations for the individual ionisation stages, taking into account ionisation, recombination and diffusion processes. The code predicts the radial distribution of ground state densities and emission shells, line-of-sight integrals of selected lines and local as well as global radiation losses caused by line emission.

The ionisation rate coefficients are calculated as proposed by Lotz /1/. For Na-like ions, correction factors for inner-shell ionisation have been evaluated and implemented in the code. The Burgess formula /2/ is used for the dielectronic recombination rates, taking into account modifications by Merts et al /3/ and a density dependence according to Post et al /4/. The

resonance line excitation rates required are mostly found in the literature for light impurity ions, otherwise the $\bar{g}$ approximation is used. For the actual analyses, T_e profiles from the ECE diagnostic were used. Electron density profiles were taken from the multi-channel DCN interferometer. The conditions at the plasma edge were estimated from Langmuir probe measurements in the scrape-off layer.

The impurity ion fluxes are described by an anomalous diffusion coefficient D and a convective term $V_D = - 2Dr/a^2$, leading to moderately-peaked profiles for the total impurity ion densities. The analyses of several accidental injections of iron and nickel into the JET plasmas resulted in diffusion coefficients of 0.6-1.0 m^2/s, as found in many other tokamaks. $D = 0.6\ m^2/s$ is used in the code.

Several ionisation stages of important impurities have been investigated routinely, in order to check the consistency of the analysis method. For ions with metastable levels, the population of these has been assessed by measuring the intensities of transitions within the metastable spin system. The number densities in the metastable levels have been added to the ground state densities. Results calculated from different ionisation stages of the same element are consistent to within about a factor of two. The total radiated power, calculated from the measured impurity concentrations, agrees well with the bolometer measurements. Z_{eff} values, derived from the spectroscopic analyses, are usually within ± 1 of the Z_{eff} results obtained from visible bremsstrahlung. The remaining difference is probably due to uncertainties in the light impurity levels, which are obtained from the plasma edge.

Nickel concentrations have been evaluated from the x-ray spectra during 4 s of the flat tops of the plasma pulses, using theoretical excitation rates for the four main lines in Ni XXVII and using the electron temperatures as obtained from the high energy tail. Coronal ionisation equilibrium is assumed to predict the total nickel concentration. The respective results agree with those of VUV spectroscopy within the mutual error limits, although the results from the x-ray spectra have a tendency to be somewhat lower.

RESULTS

The main impurities in JET are C (2-3%), O (1-4%), Cl and metals (a few tenths of a percent).

Nickel is the most important metal impurity. In addition, chromium and some iron are observed. Ni and Cr are the main constituents of the Inconel vessel wall, and the Faraday shields of the ICRH antennae are made of Ni. During glow discharge cleaning and also normal tokamak operation these metals are deposited on to the graphite limiters, which thus become the main source of the metal impurities.

Studies of the general impurity behaviour for a variety of ohmic plasmas have shown that the concentrations of light impurities are fairly insensitive to plasma current and electron density, but increase with electron density close to the density limit. Chlorine shows a similar behaviour. The metal impurities are especially prominent in low-density plasmas. They increase with plasma current, but decrease with electron density, particularly steeply near the density limit.

Carbonisation of the vacuum vessel walls has been carried out on several occasions. The purpose of the carbonisations has been to assess the influence of an all-carbon wall on plasma behaviour and metal impurities; also to remove oxygen and chlorine.

Spectroscopically, the carbonisation brought about a large reduction in metals. This is consistent with the observation of hollow bolometric radial profiles and an appreciable decrease in radiated power from the plasma centre. Generally, the total radiated power decreased to about 50% of the ohmic input

power after carbonisation, to be compared with typically ∿ 70% radiated power before carbonisation. Both figures hold for low and intermediate electron densities.

After carbonisation oxygen and chlorine are somewhat reduced.

The effect of carbonisation on the impurity line intensities is shown in Fig.1 for three selected lines: Ni XXV 117.93Å, O V 629.73Å and C IV 312.43Å. All the points plotted are for plasmas with B_T=3.4 T, I_p=2.8 MA and $\bar{n}_e$=2.3-2.6x10^{19} m^{-3}. The vertical dashed line between shots #4202 and #4228 indicates where carbonisation took place (6 hours of glow discharge cleaning in deuterium doped with 12% methane). A drastic decrease in the Ni-signal is seen immediately after carbonisation. However, within the following 20-25 shots, the Ni-signal recovers to the level before carbonisation. This behaviour is consistently observed for heavy carbonisations. However, after a recent, much heavier carbonisation (48 hours of glow discharge cleaning in deuterium doped with 17% methane) the reduction in nickel persisted for approximately 2 weeks of operation (∿ 200 shots).

Analysis of the plasma impurity content before carbonisation (shot #4186) and immediately after (#4228), reveals a practically unchanged carbon concentration (2.3% → 2.5%), a slight decrease in oxygen content (1.4% → 1.2%), a factor of 2.5 decrease in chlorine (0.1% → 0.04%) and a factor of 4-5 decrease in nickel concentration (0.09% → 0.02%).

During 1985, ICRH experiments have started on JET/5/. The maximum power available from the RF-generators was 6 MW (3 MW per antenna) of which up to 80% was coupled to the plasma.

Figure 2 shows the relative increase of radiated power, line-integrated electron density and two impurity line signals (C IV 384.1Å and Ni XXV 117.93Å) as a function of RF-power coupled to the plasma. ^{3}He minority heating was used with B_T = 3.4 T and I_p = 4 MA.

The radiated power increases linearly with RF-power. The fraction of the total input power lost by radiation is ∿ 50% both before and during RF. The increase in line-integrated electron density, $\bar{n}_e \ell$, is approximately constant above 2 MW of RF power. The C IV and Ni XXV line intensities (corrected for the density increase during RF by dividing by $\bar{n}_e \ell$) indicate that there is no appreciable increase in impurity concentrations during ICRH, within the RF power range investigated. It should be pointed out, that since the electron density profile changes during RF in the sense that the edge density increases (flatter profile), correcting the line intensities to the local change in n_e rather than $\bar{n}_e \ell$ would have the effect of increasing the Ni XXV points somewhat and decreasing the C IV points. The Z_{eff}, as measured from the visible bremsstrahlung, does not change significantly during RF.

Analysis of the impurity concentrations before and during ICRH for one of the pulses with 5 MW RF-power gives the following results: the carbon and oxygen concentrations do not change (3% C and 0.8% O), also the chlorine concentration stays constant (0.06%) while the metal concentration increases slightly during RF. The metal concentration obtained from the VUV is in good agreement with that obtained from the soft x-ray measurements.

REFERENCES

/1/ W Lotz, Lab.Reports IPP 1/62 (1967) and IPP 1/76 (1968), Garching, Germany.

/2/ A Burgess, Astrophys.J. 141, 1588 (1968).

/3/ A L Merts, R D Cowan, N H Magee, Los Alamos Scientific Laboratory Report LA-6220-MS (1976).

/4/ D E Post, R V Jensen, C B Tarter, W H Grasberger, W A Lokke, Atomic Data and Nuclear Data Tables 20, 397 (1977).

/5/ J Jacquinot, invited paper, this conference.

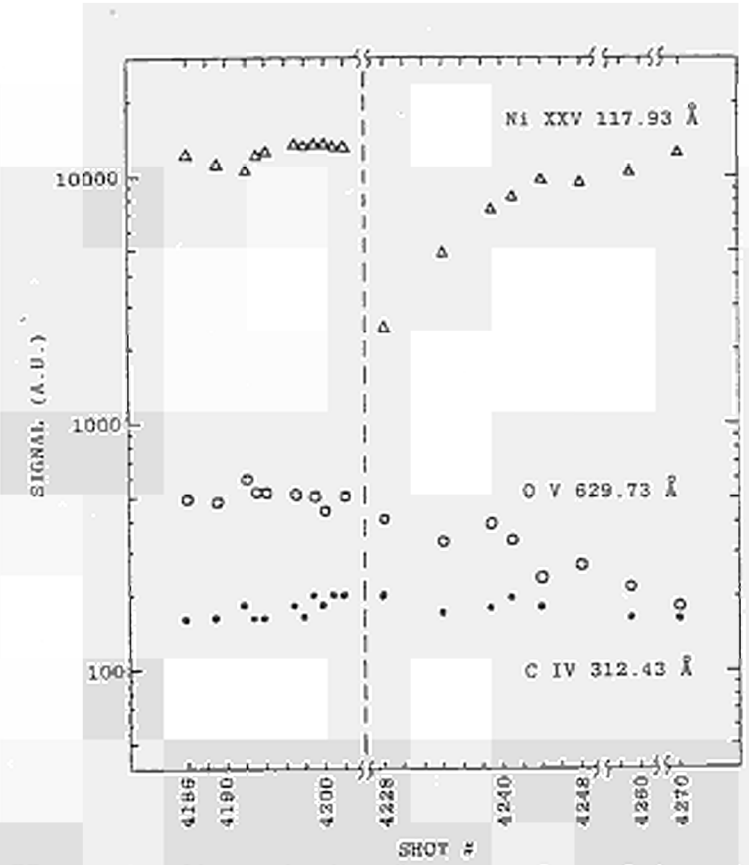

FIGURE 1 The effect of wall carbonisation on selected impurity line intensities.

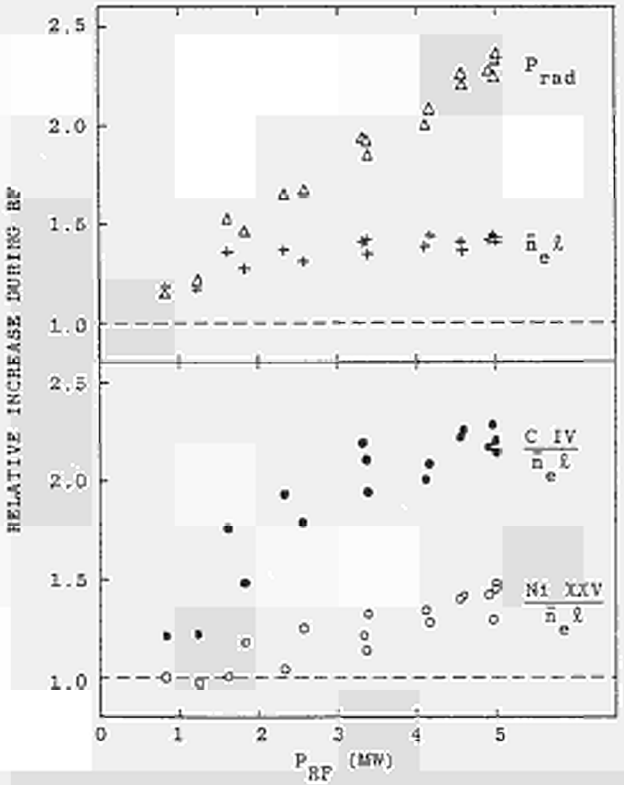

FIGURE 2 Relative increase in radiated power, line-integrated electron density and C IV and Ni XXV line intensities during ICRH, as a function of RF power.

ANALYSIS OF SAWTOOTH INSTABILITIES IN JET

D J Campbell, D V Bartlett, C Best, M Brusati, J P Christiansen, S Coda, J G Cordey, A E Costley, L de Kock, P A Duperrex*, A Edwards, J A Fessey, R D Gill, A Gondhalekar, C W Gowers, J Hugill+, A Hubbard°, O N Jarvis≠, S E Kissel, E Lazzaro, P D Morgan, R M Niestadt≠, J O'Rourke, Th Oyevaar≠, H W Piekaar≠, A Pochelon*, R Prentice, R T Ross, G Sadler, M F Stamp, T E Stringer, D Summers, G Tonetti*, B J D Tubbing≠, M Valisa, P van Belle and J A Wesson,

JET JOINT UNDERTAKING, ABINGDON, OXON, OX14 3EA, UK

* On attachment from EURATOM-SUISSE Association, CRPP, CH-1007, Lausanne Switzerland.

\+ On attachment from EURATOM-UKAEA Association, Culham Laboratory, Abingdon, Oxon, OX14 3DB, UK.

° On attachment from Imperial College of Science and Technology, University of London, London, UK.

≠ On attachment from EURATOM-FOM Association, Instituut voor Plasmafysica, Rynhuizen, Nieuwegein, The Netherlands.

1. INTRODUCTION

Sawtooth instabilities /1/, which are observed in virtually all JET 'flat-top' discharges, have been investigated with a wide range of diagnostics: electron cyclotron emission, neutron emission, soft x-ray diodes, density interferometry and reflectometry, H_α and impurity emission, magnetic pick-up coils, and limiter viewing camera. Aspects of sawtooth activity studied include the onset of sawteeth at early discharge times, MHD oscillations associated with sawteeth, sawtooth fall times, 'giant' (double) sawteeth, and the variation of sawtooth behaviour when additional heating (ICRH) is applied. It is found that sawtooth behaviour in JET is not satisfactorily described by conventional models /2/ of the sawtooth instability.

2. INSTRUMENTATION

Second harmonic, extraordinary mode ECE is used to determine the temporal evolution of the electron temperature in JET /3/. An absolutely calibrated Michelson interferometer measures the electron temperature profile with a scan time of 15 ms. A static Fabry-Perot interferometer and, more recently, a twelve channel grating polychromator /3/ provide high time resolution measurements of the variation of electron temperature at predetermined radii. Both instruments may be scanned across the plasma on a shot-to-shot basis. Ion temperature measurements are obtained from a neutron total yield monitor /3/.

A provisional 4-channel surface barrier diode array viewing just above and below the JET midplane provides measurements of soft x-ray emission. Density measurements are obtained from a seven-channel far-infrared interferometer, and a single channel 2-mm interferometer. Although the latter instrument measures the line integral of the electron density along a vertical chord, correlations of sawtooth measurements with the soft x-ray and ECE measurements reveal that it is a sensitive detector of sawtooth activity and

associated MHD oscillations. In addition, a microwave reflectometer monitors the variation of plasma density near the plasma edge.

Edge diagnostics available include H_α and impurity line emission, infrared thermography of the limiters, and magnetic pick-up coils.

3. SAWTOOTH ACTIVITY IN OHMIC DISCHARGES

Analysis of sawtooth behaviour in JET indicates that two distinct sawtooth regimes exist during ohmic discharges. During the current rise phase (which lasts several seconds), and during the current flat-top in discharges with high values of q_{cyl} ($\sim$10), sawteeth are generally preceeded by a growing odd m (presumably m=1) oscillation with a frequency in the range 0·1-1 kHz. At such times the electron temperature profile is very peaked and the sawtooth inversion radius may be only 10 cm. Figure 1(a) shows a striking example, measured by 2 mm interferometry, in which the MHD oscillation frequency decreases during successive sawteeth. The corresponding electron temperature profile is shown in Figure 1(b) (note that R_o = 2.96 m and a = 1.25 m).

During the current flat-top in most JET discharges, a second sawtooth regime is observed: sawtooth behaviour may be very irregular with 'single' and so-called 'giant' sawteeth /4/ occurring, apparently at random. The principal characteristic of this regime is that precursor oscillations are invariably absent, though successor oscillations are often observed. In addition, 'giant' sawteeth exhibit a partial sawtooth which i) does not penetrate to the plasma axis, ii) may occur on either the high-field or low-field side of the plasma axis, and iii) within the resolution of the diagnostics ($\lesssim$5 cm), has the same inversion radius as the full sawtooth. Figure 2 shows such a sawtooth measured by the twelve-channel ECE grating polychromator. Note that only every second channel is shown.

There are several possible explanations for the lack of precursor oscillations in this regime: there may be no magnetic island; an island may exist but be locked; there may be a very small rotating island which is beyond the resolution of the diagnostic instrumentation; or the growth time of the island may be so short that no significant rotation occurs before the disruption. These possibilities are currently under investigation, but it is clear that there is a discrepancy between these observations and the conventional picture of the sawtooth instability /2/. Similar discrepancies have been observed previously in TFR/5/.

A further aspect of sawtooth activity in JET not explained by the conventional model is the collapse time. Figure 3 shows a time interval of 1 ms around the collapse of central electron temperature. This observation was obtained from an ECE Fabry-Perot with signal bandwidth of 100 kHz and a sampling rate of 40 kHz. The electron temperature profiles obtained from the Michelson interferometer before and after the sawtooth collapse are also shown. It is clear that the collapse time is $\sim$100 μs. Typical sawtooth collapse times in JET lie in the range 100-200 μs, though a range of times of up to 1 ms have been observed within a single discharge. The model of the sawtooth collapse due to Kadomtsev /2/ predicts that

$$\tau_c \sim (\tau_R \tau^*)^{\frac{1}{2}} \qquad (1)$$

where τ_R is the resistive diffusion time, and τ^* the Alfven transit time in the helical magnetic field B* associated with the sawtooth. For the discharge parameters relevant to the case shown in Figure 3, and making the simplest assumptions about the development of B*, equation (1) gives $\tau_c \gtrsim 10$ ms.

4. SAWTOOTH ACTIVITY WITH ADDITIONAL HEATING

During additional heating experiments in JET, carried out with up to 5 MW of ICRH for periods of 1 - 3 seconds /3/, sawtooth activity exhibits the same

basic behaviour as in ohmic discharges, though with some modifications. The most striking of these is a substantial increase in sawtooth amplitude. Whereas the electron temperature fluctuation due to sawteeth in ohmic discharges is $\lesssim$ 15%, during ICRH the fluctuation on axis rises to 30 - 50% of the maximum electron temperature. By comparison, the ion temperature fluctuation shows a modest increase from $\lesssim$ 10% during ohmic heating, to 10 - 15% during ICRH (while the average ion temperature on axis may show a substantial increase of order 30%)

The sawtooth inversion radius increases slightly during ICRH, but this may simply reflect an acceleration of the gradual expansion of the inversion radius which occurs during the current flat-top. In addition, the sawtooth period increases slightly relative to the ohmic phase, and giant sawteeth with a period $\sim$ 300 ms have been observed. However, the details vary depending on the target plasma, heating mode, antenna coupling, and power level.

A remarkable feature of this heating regime is the observation at relatively low values of q_{cyl} (I_p = 4 MA, B_T = 3.4T, q_{cyl} = 3.3) of a large saturated MHD oscillation preceding the sawtooth collapse. This mode may exist in a saturated state for up to half the sawtooth period, with an amplitude $\gtrsim$ 30% of the sawtooth amplitude. An example of this phenomenon is shown in Figure 4. Correlation of soft x-ray and ECE signals indicate that this is an n = 1, m = 1 mode.

5. PLASMA DIAGNOSIS BY SAWTEETH

Analysis of the measured changes in temperature and density associated with sawteeth permits the determination of plasma parameters inaccessible to conventional diagnostic techniques. The use of the sawtooth heat pulse to investigate thermal diffusivity is well known /6/ and has been applied to JET plasmas /3/.

Measurements of sawtooth fluctuations in the line integrated density have been used, together with some modelling assumptions about the variation in the electron density profile, to investigate particle convection in the centre of the discharge. It is found that the fuelling of the core of the discharge, and restoration of the peaked density profile between sawteeth can be explained by the neoclassical pinch effect /7/, with pinch velocities in the range 5 - 10 x 10^{-2}m/s. The role of this effect in the buildup of the plasma density profile is still under investigation.

Study of the periodic electron and ion temperature variations during sawteeth allows the different components of the energy balance in the central region to be distinguished. Using an axial current derived from the condition that q = 1 on axis, ohmic heating during sawteeth can be derived. The mean rate of increase in the electron temperature during the sawtooth recovery phase then gives a measure of the central resistivity and hence of Z_{eff}. Thus, for a typical JET ohmic discharge, this yields Z_{eff} (o) = 5 compared with $\bar{Z}_{eff}$ = 4, derived from the neoclassical resistivity, and Z_{eff} = 3, calculated from visible Bremsstrahlung measurements.

REFERENCES

/1/ S von Goeler et al, Phys. Rev. Lett. 33 1201 (1974).
/2/ B B Kadomtsev, Sov. J. Pl. Phys. 1 389 (1975).
/3/ For additional details see papers 142 (B J D Tubbing et al), 185 (O N Jarvis et al), 186 (A E Costley et al) and the invited paper by J Jacquinot at this Conference.
/4/ W Pfeiffer, G A Technologies Report GA - A16994 (1983).
/5/ M A Dubois et al, Nucl. Fus. 23 147 (1983)
/6/ M Soler and J D Callen, Nucl. Fus. 19 703 (1979).
/7/ F L Hinton et al, Phys. Rev. Lett. 29 698 (1972).

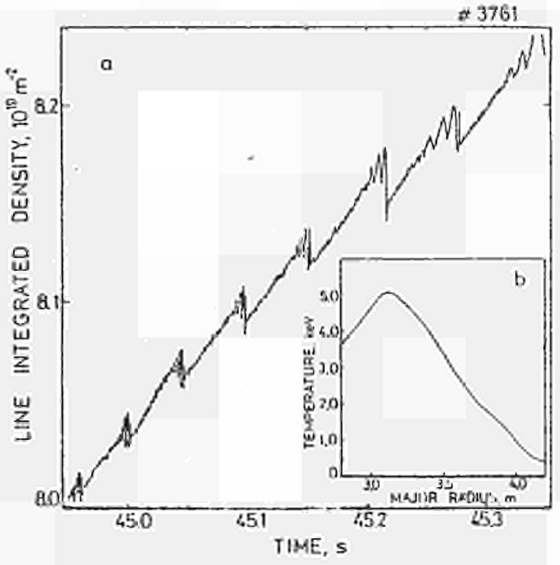

Figure 1: (a) Sawteeth density fluctuations measured by 2 mm interferometry during the rise phase of a JET discharge. (b) Temperature profile at this time measured by an ECE Michelson interferometer.

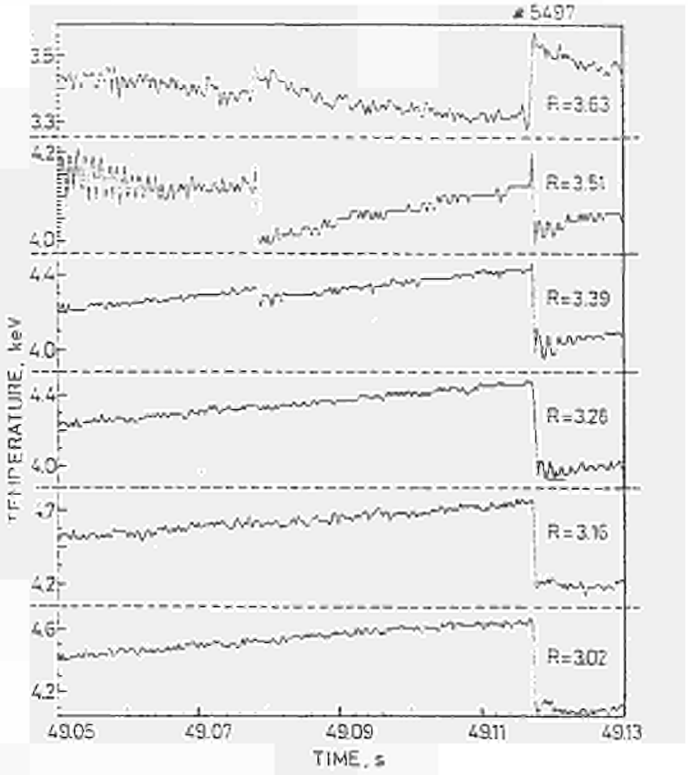

Figure 2: Partial and complete temperature sawteeth measured by an ECE grating polychromator.

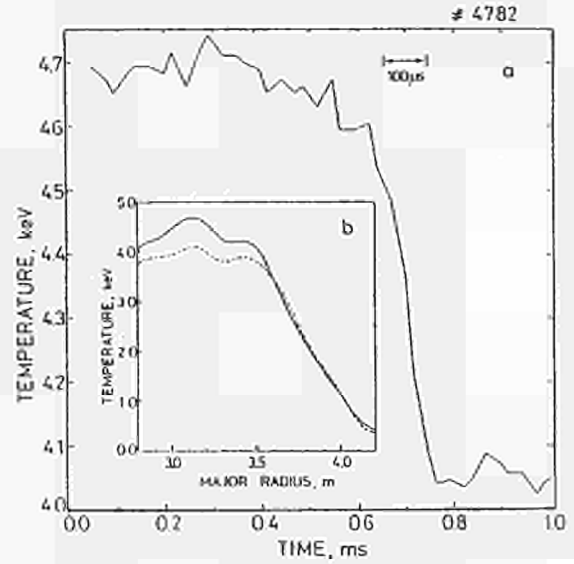

Figure 3: (a) A time interval of 1 ms around the collapse of a sawtooth measured by an ECE Fabry-Perot interferometer. (b) The temperature profiles measured before (solid lines) and after (dotted lines) the collapse, measured by an ECE Michelson interferometer.

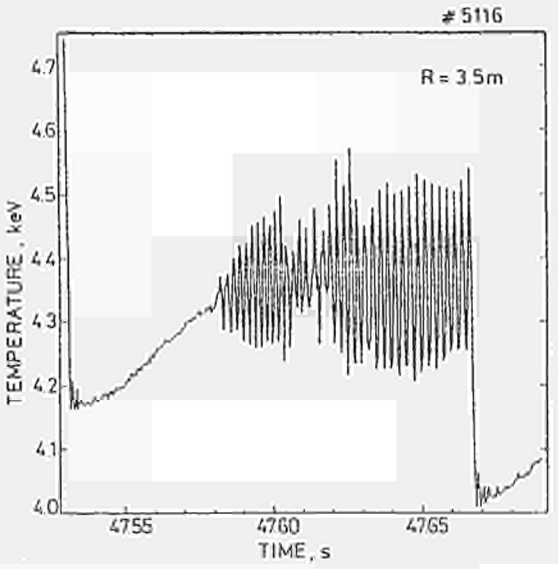

Figure 4: Sawtooth measured by an ECE Fabry Perot interferometer, during ICRH, showing large saturated MHD oscillation.

IMPURITY FLUXES IN THE BOUNDARY LAYER OF JET

J.P. Coad, G.M. McCracken*, S.K. Erents*, J. Ehrenberg+,
L. de Kock, P.C. Stangeby*+, T. Tagle,
JET Joint Undertaking, Abingdon, Oxon. OX14 3EA, U.K.
* Culham Laboratory, Abingdon, OX14 3DB, U.K.
+ M.P.I. für Plasmaphysik, 8046 Garching bei München, W. Germany.
*+ Aerospace Institute, University of Toronto, Canada.

INTRODUCTION

Impurity elements are observed in the JET plasma, typically at 1 to 4% for light elements (O and C) and up to 0.2% for medium weight elements (such as Cl and Ni) leading to Z_{eff} values between 2 and 5 for most discharge conditions. For densities above $3\times10^{19}m^{-3}$ power is radiated from the outer regions by O and C and the contribution of metals can be neglected.

Surface analysis of the limiter tiles after operating has shown a certain spatial distribution[1] indicating migration from the wall to the limiter and erosion and redeposition during plasma discharges. However, a post-mortem analysis only gives an integrated picture of very complex sequences of operation. The information from the limiter has been supplemented by the use of collector probes which were exposed to different types of cleaning and tokamak discharges to show how these types of operation affect the impurity production. The measurements were carried out using the vertical probe drive which normally operates as a Langmuir probe.[2]

EXPERIMENTAL

(a) Method

The probe is mounted vertically near the top of the torus on a long bellows as shown in Figure 1. When operating in tokamak discharges the probe head can be inserted to within 1.5 m of the midplane, and is preset at the required distance from the predicted last closed surface. Figure 1 shows that the head can be covered over with a cap which carries small samples of various materials to act as collectors for subsequent surface analysis: this device has been used to monitor carbonisation of the vessel (see below).

On removal from the torus, the collectors, or the surfaces of the probe assembly itself, have been analysed using Auger Electron Spectroscopy (AES), Rutherford Backscattering (RBS) and Nuclear Reaction Analysis (NRA). Spatial resolution employed in the RBS and NRA was approximately 1mm (the diameter of the particle beam) and in AES was about 5μm (the diameter of the electron beam). Information on the depth distribution of the elements can be gleaned directly from RBS and NRA spectra, whilst in AES (which only samples from a depth of 1 to 2nm) depth profiles are obtained by successive analysis and surface erosion by ion bombardment.

(b) Results of Exposure to cleaning and tokamak operations

The probe has been exposed to (i) 70 hours of glow discharge cleaning (GDC) (2A at 380 V in 10^{-3} m bar of H_2), (ii) 2800 pulses of pulse discharge cleaning (PDC) (of 150 m secs and peaking at 50 KA, plus 30 pulses of $\sim$ 600 msecs peaking at 250 KA), and (iii) 60 tokamak discharges in September 1984. The results of RBS analysis are shown in the table below, and compared with graphite samples from the limiter and to long-term samples (LTS) from the wall.

	GDC	PDC	Tokamak Discharges	Integrated deposit Limiters	LTS
Ion Fluence m^{-2}	1.6×10^{22}	1.2×10^{23}*	-	-	
Time exposed	70 hrs	2800 pulses	~60 discharges	March - September 1984	
Ni+Cr(atoms m^{-2})	4×10^{19}	2.8×10^{21}	$0.8-1.2\times10^{21}$	3.5×10^{21}	$10^{21}-10^{22}$
Heavy species Z > 70			4×10^{19}	?	?
O (atoms m^{-2})	1×10^{20}	3×10^{20}	?	5×10^{20}	?

* From H_α at the wall.

Following the tokamak discharges (in deuterium) the deuterium content of the surface was also measured, as well as the carbon on the tungsten probe elements. The carbon on the elements was 5-8 x 10^{22} atoms m^{-2}, whilst the D was ~3 x 10^{22} on the graphite body of the probe.

(c) Carbonisation of the JET vessel

The JET vessel was 'carbonised' on occasions near the end of the 1984 operational period, by adding 3% methane to the usual GDC discharges (in hydrogen), and the impurity levels before and after treatment were monitored by VUV broadband spectroscopy.[3] Following 'carbonisation' metallic impurities such as nickel were typically reduced immediately by a factor of 5. Oxygen was reduced from 1.7 to 0.7% for reference discharges (2MA plasma current at an electron density of 2 x $10^{19}m^{-3}$) and to ~ 1% from perhaps as high as 4% for high density discharges (~ 3MA, ~ 3 x $10^{19}m^{-3}$) and chlorine was reduced by similar factors. Carbon levels increased slightly for reference discharges and decreased slightly for high density discharges. After 'carbonisation' the plasma power loss mechanisms changed markedly, with much more power going to the limiters.

The 'carbonisation' thus significantly improved the impurity situation. During the 1985 programme, the 'carbonisation' has been monitored using the surface probe, samples of Si, Ni and inconel being exposed on five occasions. Since deuterium plasmas have been used in the 1985 programme, deuterium has replaced hydrogen as the carrier gas, and the methane levels employed are either 2.15 or 12%: the wall temperature has also increased from 250 to 300°C. Figure 2 shows profiles for oxygen and carbon in inconel samples (a) as received, without any exposure in the torus, (b) after 8 hours GDC 'carbonisation' at 4A and 380V in 2.15% CH_4, and (c) after a similar exposure in 12% CH_4. For comparison (d) shows the carbon profile in nickel after 8 hours in 2.15% CH_4, and (e) shows the composition of an inconel long-term sample exposed throughout the 1984 programme. Note that the 'carbonisation' does not always produce a layer of carbon over the surface and in any case is certainly not uniform over the JET vessel due to the positioning of the discharge electrodes. Basically the treatment removes the surface oxide and carburizes the near-surface region. Tokamak operation following carbonisation is difficult for several pulses due to outgassing from the walls.

DISCUSSION

GDC and PDC each cause large amounts of metal and oxygen to move around the vessel, and some oxygen is removed from the torus by reaction to form H_2O

and CO. Nevertheless the oxygen and metal concentrations observed on the probe after the "cleaning" are also likely to arise at the limiters. They are a significant part of the equilibrium concentrations which are observed after tokamak discharges (and which clearly are soon established in the boundary layer as seen on the probe).

Similar deuterium concentrations were found on the probe after tokamak discharges to those on the limiter [1]. The carbon concentration was a factor of 3-4 greater than the deuterium. Although some of the carbon may have been displaced locally from the body of the probe, it shows that co-deposition of deuterium and carbon is the main mechanism for deuterium incorporation with important implications for recycling calculations, and eventually for the tritium inventory.

The 'carbonisation', is seen to have a marked effect on the oxygen level on the surface, and whilst significant carbon penetrates a clean inconel sample, comparison between (b) and (e) in Figure 2 suggests the carbon level on the actual wall is unlikely to be significantly affected by the process.

What happens on the limiter during carbonisation to dramatically change subsequent tokamak operation? The majority of the surface is already carbon, and the metallic deposits on it are probably also thoroughly mixed with carbon: thus the carbon content of the surface is probably little changed. However, the oxygen concentration on the surface should have been reduced and calculations of sputtering rates based on precarbonisation discharges suggest that much of the carbon entering the discharge results from sputtering by oxygen.

The combination of the lower oxygen level and the consequential reduction in sputtered carbon then leads to the immediate reduction in radiated power and increased limiter temperature observed. However, the total carbon level seen by VUV does not fall significantly, which suggests another removal mechanism for carbon from the limiter becomes significant at these high fluxes: it cannot be normal chemical sputtering as the correct behaviour with limiter temperature is not observed. The benefits of 'carbonisation' last for many tens of discharges, which is most unlikely to be due to an overlayer of carbon on the limiters (which might be $\sim$50 monolayers thick) due to the rate of sputtering and redeposition on the surface. However, the immediate increase in limiter temperature (from $\lesssim$ 500°C to $\sim$1500°C) due to altered sputtering coefficient caused directly by the carbonisation could cause evaporation from, or diffusion into, the limiters of the metallic impurities, resulting in medium to long-term benefits.

CONCLUSIONS

Probe measurements, allied to limiter and wall analysis and spectroscopy show that GDC and PDC cause significant contamination of the limiters without significant removal of the oxygen.

'Carbonisation' does reduce oxygen from surfaces in the torus and this may be the cause of its beneficial effect in JET in 1984, when carbon overlayers were probably not produced. (However, if carbon overlayers can be produced they might well produce further benefits).

Tokamak discharges in JET seem to produce similar levels of impurities on all parts of the torus ($\sim 10^{21}$ atoms m^{-2} for nickel) suggesting some form of equilibrium. Deuterium levels also reach a uniform value of $\sim 3 \times 10^{22}$ atoms m^{-2} due to codeposition with carbon, except where significant heating occurs [1]

REFERENCES

(1) J. Ehrenberg et al - this conference
(2) P. Stangeby et al - this conference
(3) K. Behringer et al - JET - P(85)08

FIGURE 1

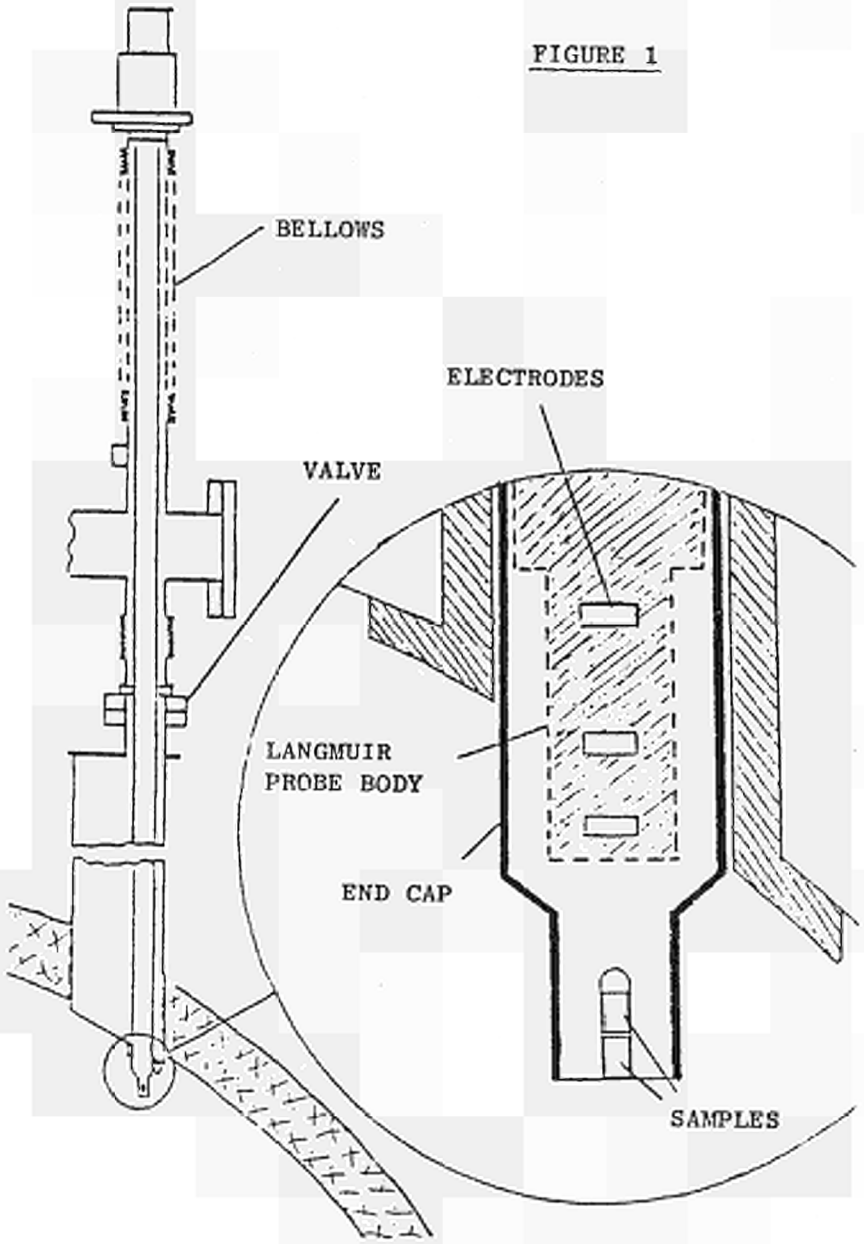

FIGURE 2

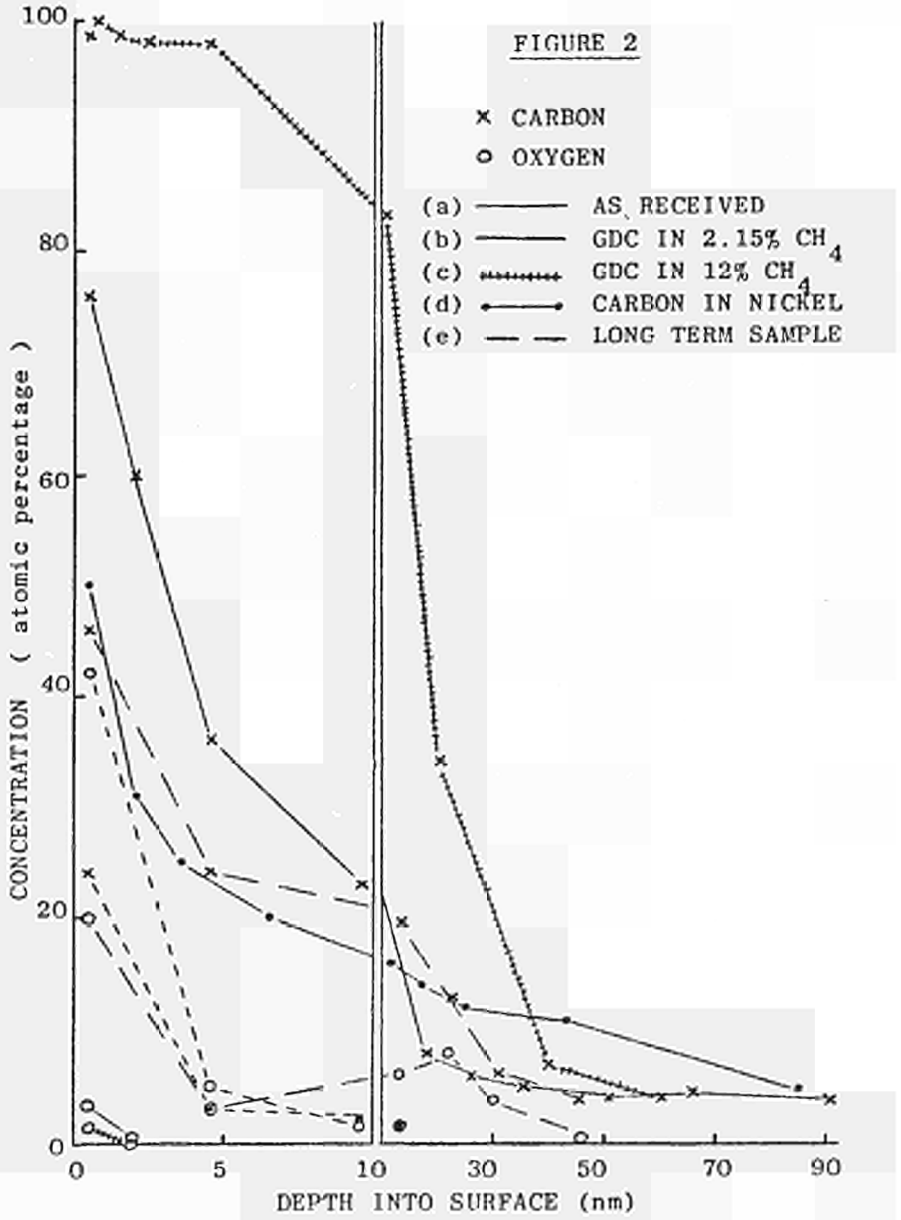

Erosion and Redeposition of Wall and Limiter Material in JET

J Ehrenberg*, R Behrisch*, P Martinelli*, H Kukral*,
G M McCracken°, J P Coad, L de Kock

JET Joint Undertaking, Abingdon, Oxon, OX14 3EA, UK
*Max-Planck - Institut für Plasmaphysik, 8046 Garching bei Munchen, FRG
°Culham Laboratory, Abingdon, OX14 3DB, UK

I Introduction

Study of walls and limiters of plasma machines by means of surface analysis techniques provides valuable information for the understanding of the causes of impurity fluxes into the plasma which is one of the most important problems in today's fusion research. Therefore, surface analyses of JET graphite limiters have been performed /1,2,3,/ after the experimental periods in 1983 as well as in 1984. In addition graphite and metal long term samples (LTS) have been analysed. They were uniformly distributed over the vessel wall and placed well in the shadow of the bellow shields . They have been exposed to all 1984 discharges, in order to monitor effective erosion and redeposition of wall material in an extended run of the machine.

II Experimental techniques

Quantitative surface analyses have been performed by means of two accelerator based techniques, namely Proton Induced X-Ray Emission (PIXE) analysis with 1.5 MeV protons and Rutherford Backscattering Spectrometry (RBS) with 2.5 MeV ^{4}He -ions. PIXE detects metallic contaminants up to depths of several μm below the surface, whereas RBS is most sensitive in more shallow regions ($\lesssim$400nm).

III Analysis Results and Discussion

All deposits found either on the limiter or on the LTS must be regarded as nett deposition, as these surfaces were also subject to erosion.

Limiters.- Fig.1 shows the toroidal distributions of metallic deposits on the 1983 and 1984 limiters as measured in both cases near the plasma midplane position. The most abundant elements are the constituents of the main wall material (Inconel 600) present in their correct ratios on the 1983 limiter and with deviations from this on the 1984 limiter. The other elements are trace elements in either inconel or carbon and have also been detected on the 1984 limiter. Not shown is oxygen, which is present with more than 10^{20}atoms/m^2. Mo was introduced into JET by an accidental contamination of the graphite limiters during manufacture. Contamination with wall materials (Ni,Fe,Cr) occurs during glow- and pulse-discharge cleaning runs [4] as well as in plasma disruptions or by runaway electrons where high power loads may hit the wall causing melting and evaporation. During normal tokamak discharges wall erosion by charge exchange neutrals may also contribute, whereas erosion by hydrogen ions may be negligable because of the low energies involved/5/. However, wall erosion by impurity impact, such as by O, C or Ni atoms cannot be excluded. Metal deposition on the limiters was found to have three different forms: firstly, between about 100mm and 350mm deposition on the centre tile (tile 4) of both limiters is mainly in the form of atomic layers,

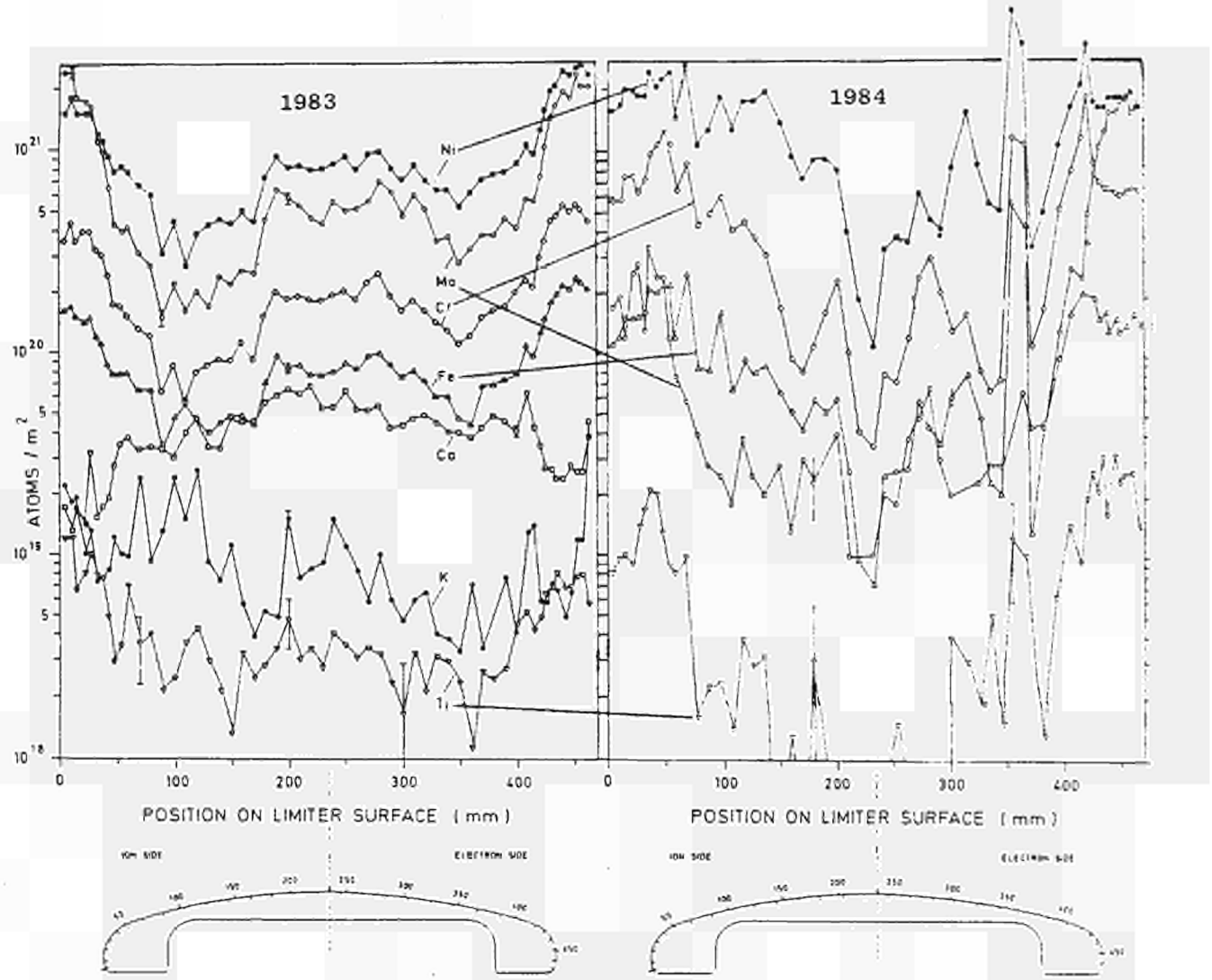

Fig. 1 Toroidal distribution of metallic contaminants on two JET graphite limiter tiles (plasma midplane) from two experimental periods.

secondly the side edges on the '83 limiter are contaminated with small metal droplets having diameters in the range of µm, and finally metal splashes of about 100 µm in diameter are present on both limiters but are much less frequent than the small droplets.

The zones on either side of the centre of the tile where the layer deposition is found correspond to the areas of plasma contact (and thus greatest heating) on the tile. The areas correlate with the "footprints" on the limiter seen by recycling light at λ = 900nm by means of a CCD video camera /6/: Maxima of intensities are in the regions 100 mm to 200 mm and 250 mm to 350 mm defined in Figure 1. Here, erosion may be larger than on more remote locations such as the limiter side edges.

The mechanism of droplet formation on the limiter side edges is not yet understood. However, they may constitute an effective source for metal erosion by evaporation as they might have poor thermal contact to the surrounding material.

During 1984 the limiter was exposed to about 400 discharges, with maximum surface temperatures towards the end of this period of 1800°C, whereas in 1983 there were only 200 discharges and the temperature was always <650°C. As the limiter is the only source of molybdenum, much more is likely to have been removed during 1984 than in 1983, as is confirmed in Fig.1. However the Ni concentrations are comparable in the two cases, with a tendency for greater Ni levels in the zones of high heat load in 1984.

Careful examination of the deposits by RBS and PIXE/7/ has shown that the Ni on the 1984 limiter is distributed to larger depths in the graphite than in the 1983 limiter. This would be expected due to the higher temperatures in that period (particularly after carbonisation of the vessel in Sept. 1984 - see reference 4). Thus, Ni is reduced at the very surface and has diffused deeper into the bulk and subsequently is less accessible for plasma erosion. This might have contributed to the conditioning of the '84 limiter.

Long term samples (LTS)

Examination of the inconel deposits on carbon LTS (Fig.2) revealed the following general trend in the distribution around the JET vessel: differences of deposited amounts are large in the poloidal direction whereas toroidally the distribution is more uniform. At the inside wall, the large deposits correlate with visible wall damage by gross melting which is also strongest there. A source-sink correlation is also observed on those LTS which have been placed closest to the Ni limiters which were retracted 9 cm behind the graphite limiters at the outer vessel wall. There, the ratio [Cr]/[Ni] (Fig.2) shows an enrichment of Ni compared to every other position. In addition, Mo was found predominantly on the outer wall samples which have been closest to the graphite limiters. From the Mo distribution on the limiter, it can be assumed that Mo erosion takes place predominantly during plasma discharges (see also Fig.1).

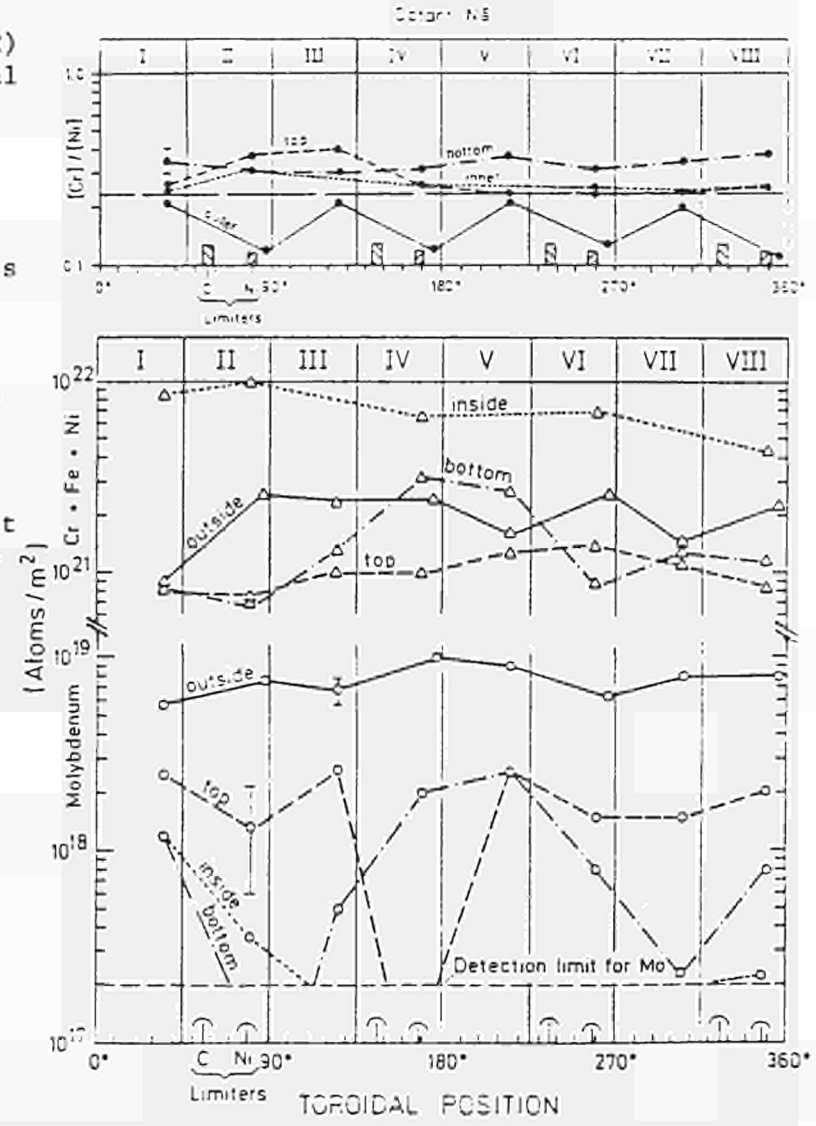

Fig. 2 Toroidal distribution of metallic contaminants as found on carbon long term samples which have been distributed around the JET vessel wall. Top, etc. denotes the position in the vessel.

However, redeposition did not occur uniformly over the torus, but is concentrated on the outer wall at the midplane. Mo from the carbon limiters appears to travel further toroidally than Ni from the Ni limiters, since the latter shows an immediate response on those LTS which have been positioned close to the Ni limiters (see the Cr:Ni ratio in Fig.2). This may reflect the different distances of the respective sources from the scrape-off layer: as stated above the Ni-limiter was retracted by ∿9cm behind the leading edge of the C-limiter. Thus the ionisation of eroded Mo is more likely than the ionisation of Ni from the Ni-limiters, and so transport of Mo would be more affected by the plasma and the magnetic field, resulting in a larger fraction of Ni being deposited as neutrals at wall positions close to this particular source.

In general it is believed that wall erosion may affect the plasma directly but also contaminates limiters with wall material thus partially losing the advantage of the carbon limiters being a low-Z material.

IV Conclusions

Examination of the JET graphite limiters shows that they constitute an important source for metal fluxes into the plasma. The amounts and distributions of deposits depend on the actual surface temperature which has been reached. Analyses of JET carbon Long Term Samples show a close correlation between metal erosion sources and redeposition sinks. Toroidally redeposition of wall material is rather uniform, whereas poloidally large differences exist.

V Acknowledgement

For helpful collaboration and discussions we would like to thank:
P. Børgesen from IPP/Garching, M. Braun and B. Emmoth from AFI Stockholm, K. Erents and D. Goodall from Culham Laboratories and C. Lowry, P.C. Stangeby, P.E. Stott and D. Summers from JET.

VI References

/1/ G.M. McCracken - private communication
/2/ J. Ehrenberg and R. Behrish IPP-JET Report No.23, May 1984
/3/ J. Ehrenberg, R. Behrisch, P. Martinelli and H. Kukral IPP-JET Report 29 May 1985.
/4/ J.P. Coad et al, this conference.
/5/ P.C. Stangeby et al, this conference.
/6/ D. Summers - private communication.
/7/ J. Ehrenberg and P. Børgesen "Effective Depth Distribution of Ni on the JET graphite limiter". presented at the 7.Int.Conf. ION BEAM ANALYSIS Berlin 7-12 July 1985, F.R.G., to be published in Nucl. Instr. Meth.B

ION TEMPERATURE AND DENSITY MEASUREMENTS IN JET USING NEUTRON DIAGNOSTICS

O N Jarvis, G Gorini, M Hone, J Källne, V Merlo, G Sadler, P van Belle
JET Joint Undertaking, Abingdon, Oxon, OX14 3EA, UK

Introduction Two neutron diagnostic systems are in use on JET for determining the ion density and temperature for deuterium plasmas. The first comprises three sets of fission counters [1], each mounted on a separate magnet limb on the horizontal midplane of the machine, to measure the instantaneous neutron emission from the plasma. The second is a ^{3}He ionization chamber spectrometer[2] located in the well-shielded Roof Laboratory about 20 m above the midplane of the machine and viewing the plasma through a collimator (set in the floor of the Roof Laboratory) aligned with a vertical diagnostic port in the vacuum vessel.

The neutron emission is related to the volume integral over the plasma of the product $n_d^2 \langle\sigma v\rangle$, where n_d is the deuterium ion density and $\langle\sigma v\rangle$ is the plasma reactivity. For a Maxwellian plasma the reactivity varies with temperature as T_i^α, with $\alpha \sim 4.0$ for $T_i = 3$ keV. Thus, assuming that the spatial profiles of density and temperature for electrons, which are measured routinely, apply also to ions with only the scale factors differing, then the neutron emission measurements provide an estimate for the product of central parameters $\hat{n}_d^2 \hat{T}_i^\alpha$.

The ^{3}He chamber possesses excellent energy resolution (42 keV at 2.5 MeV) and is thus able to measure the thermal broadening of the thermonuclear neutrons, which should exhibit a nearly Gaussian energy spectrum [3] with fwhm = $82.5\sqrt{T_i}$, with T_i in keV. The primary result from the spectrometer is therefore a value for $\hat{T}_i$ which can be used in conjunction with the neutron emission measurements to determine $\hat{n}_d$.

Neutron Emission Each set of fission counters comprises a ^{235}U fission chamber and moderator, engineered to give a flat energy response, and a ^{238}U fission chamber which has a neutron energy threshold at about 1 MeV. Both counters operate simultaneously in pulse counting and current modes to provide coverage for neutron emission intensities from 10^{10} to 10^{22} neutrons/sec. Present yields from deuterium plasmas rarely exceed 10^{14} neutrons/sec.

The ^{235}U fission counters have been calibrated with both a ^{252}Cf radioisotope neutron source and a pulsed 14 MeV neutron tube by placing them, separately, at a large number of positions within the vacuum vessel. The vessel is effectively enclosed within the copper toroidal field coils and an iron support structure in which the voids are filled with high density borated concrete. This copper/iron/concrete blanket is about 40 cm thick and effectively inhibits neutron leakage from the vacuum vessel except through the various penetrations. Because of this blanket, it is clear that those neutron which reach a fission counter do so only after having scattered a few times from the material surrounding the vacuum vessel before leaving through the large diagnostic port closest to the counter and scattering in or near the port closure plate into the direction of the counter. We have found that the counter response as a function of source position is remarkably insensitive to

neutron energy and that the positional dependence is easy to model in terms of the toroidal co-ordinates. With the aid of this model, the total neutron emission from a deuterium plasma of known dimensions can be determined from the fission counter response to an absolute accuracy of ± 10%.

Figure 1 shows the time dependence of the central ion temperature $\hat{T}_i$ for discharge number 3050 as determined from the neutron emission measurements. The analysis incorporates two significant assumptions: (i) that the d-d fusion reactivity is an accurately known function of temperature, and (ii) that the deuterium ion density is half the electron density.

Neutron spectrometry In principle, analysis of the data obtained with the ^{3}He spectrometer is particularly straightforward: the neutron energy spectrum is assumed to be Gaussian in shape [3] so the measured detector response function is convoluted with a Gaussian neutron energy spectrum appropriate to a trial temperature T_i and a maximum likelihood optimization of T_i is performed to obtain the best fit with the measured pulse-height spectrum. In practice, entirely satisfactory fits have been obtained, but only after very careful measurements of the detector response function were made. It should be noted that it proved not to be acceptable to adopt the response function reported in the literature [4] for a ^{3}He spectrometer with identical specification to ours. The source of difficulty is not the determination of the fwhm of the full-energy peak in the counter (from the n + ^{3}He → p + t + 0.764 MeV reaction) but rather that of determining the precise shape of the apparently insignificant low-energy tail due to the wall-effect in the ionization chamber. The relative magnitude of this wall effect increases with neutron energy. It was also found that appreciably better counting statistics were required to determine T_i to a given accuracy than was predicted [5] on the basis of a simple Gaussian-shaped response function. This prediction connects the required accuracy ($\Delta T_i/T_i$), the spectrometer resolution (R), the width of the neutron spectrum (W) and the necessary total count in the measured neutron energy spectrum through

$$N = 2\,[T_i/\Delta T_i]^2\,[1 + R^2/W^2]^2$$

where it is assumed that R is known precisely and that both spectrometer response and neutron spectrum are Gaussian in form. For R = 42 keV, W = 143 keV (T_i = 3 keV), we should be able to ignore R^2/W^2 and to deduce that a 10% measurement requires only 200 counts. In practice we find we need at least 600 counts. This finding is also attributed, at least partially, to the low energy wall effect tail in the spectrometer resolution function; taking moments about the centroid of that portion of the repsonse function contributing to the measurement so as to obtain an "equivalent Gaussian" shows that R is comparable with W. Thus, we have found that the spectrometer wall effect is already very important and can be expected to become more so as ion temperatures rise and neutral beam heating with deuterium beams is introduced.

Of the many plasma discharges now analysed, one sequence of 3 MA discharges (numbers 3447 to 3052) is outstanding because of their very long plasma duration, with flat-tops extending over 8 seconds (see Figure 1). These discharges used ohmic heating only and the plasmas were formed under identical conditions. It has been observed that in a sequence of repeated discharges the total neutron emission per discharge has been reproduced to ± 1%, implying a very high order of reproducibility in the machine control elements. The

individual discharges in the selected sequence were analysed and flat-top temperatures in the range 2-3 keV have been deduced, but with only ± 20% accuracy. A considerably improved accuracy is achieved by summing the individual spectra to obtain 1000 counts in the peak, as shown in Fig. 2.

Analysis of the summed spectrum gives a time averaged ion temperature of 2.73 ± .18 keV. This result refers to the line-integrated neutron emission along a vertical chord and can be converted to the required central temperature by multiplying with the factor 1.08 ± .02 obtained from numerical studies on plasmas with density and temperature profiles similar to those on which the measurements were made. The short period temperature variations, such as those due to sawteeth, are not significant for ohmically heated plasmas as can be seen from the detailed time dependence in T_i measured by the fission counters (see Fig. 1).

Density fraction The mean value for the central ion temperature of 2.95 ± .21 keV obtained from the spectrometer is to be compared with the mean temperature of 2.64 keV derived from the fission counters on the assumption of a density ratio $\hat{n}_d/\hat{n}_e = 0.5$. Adoption of the spectrometer value permits the density fraction to be refined to $\hat{n}_d/\hat{n}_e = 0.47 \pm .08$ for the discharge sequence studied. The uncertainty quoted here is determined primarily by the temperature measurement but includes contributions for the absolute calibration of the fission counters and for the uncertainty in the basic d-d fusion cross-sections.

References

1. M T Swinhoe and O N Jarvis, Nucl.Instrum.Meth. in Physics Research 221 (1984) 460.

2. Jordan Valley, Emek Hayarden, Israel. Spectrometer type FNS-1.

3. H Brysk, Plasma Physics 15 (1973) 611.

4. W A Fisher, S H Chen, D Gwinn and R R Parker, Nucl.Instrum.Meth. in Physics Research 219 (1984) 179.

5. O N Jarvis in Diagnostics for Fusion Reactor Conditions, EUR 8351-EN, Vol. 1 (1984) 353

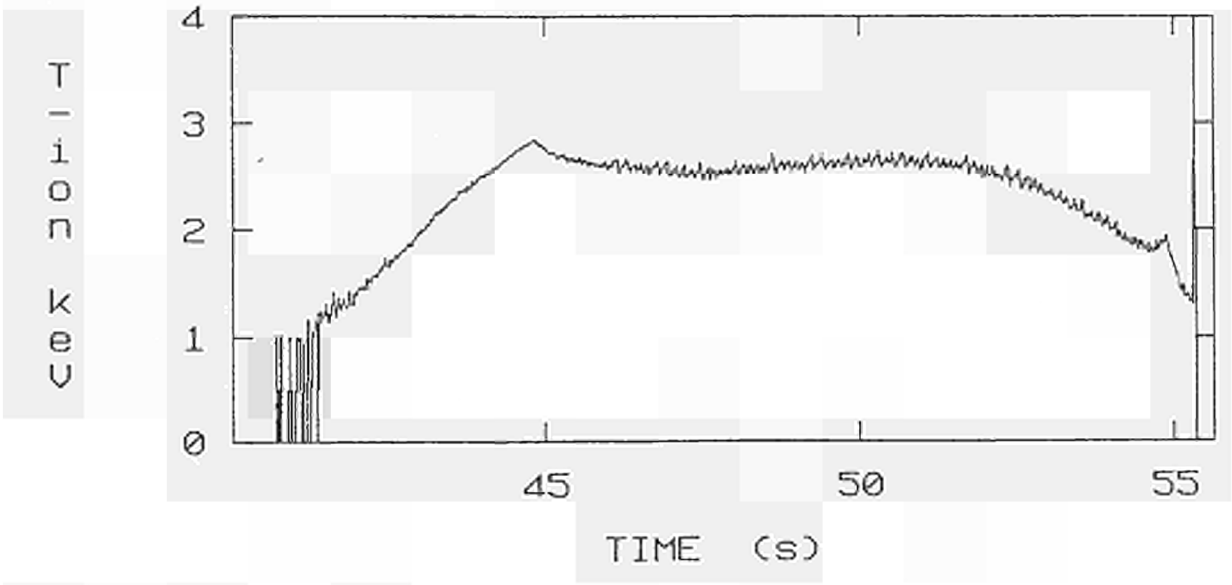

Figure 1 The central ion temperature determined from the neutron emission measurements for discharge number 3050, with a toroidal field of 3.4T and a plasma current of 3.6MA. The plasma is formed at time 40 seconds.

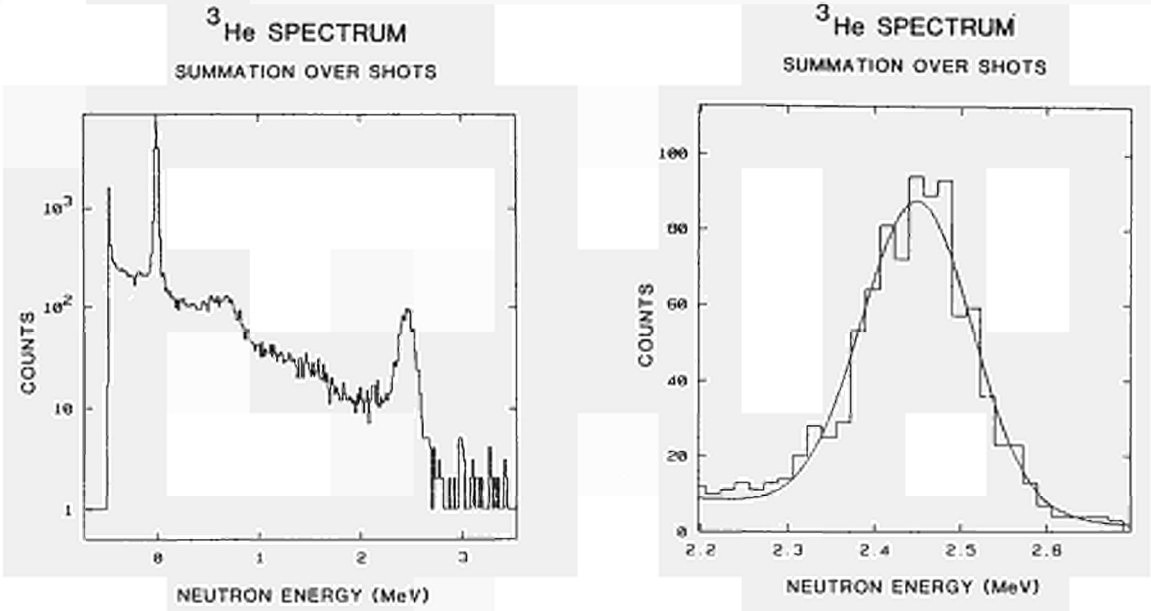

Figure 2 The pulse-height spectrum obtained with the ^{3}He ionization chamber for the sum of six discharges (numbers 3447 - 3052). Discharge numbers 3447-3052. Note that the thermal neutron peak (left picture) appears at a pulse-height equivalent to 764 keV. The excellent fit to the 2.5 MeV thermonuclear peak (right picture) substantiates the claim for a Maxwellian ion energy distribution.

ELECTRON TEMPERATURE MEASUREMENT ON JET

A E Costley, E.A.M. Baker†, M. Brusati, D V Bartlett, D J Campbell
G Decker+, M Gadeberg*, R D Gill, E Källne, S Kissel, P Nielsen,
D Pasini# and R Prentice

JET JOINT UNDERTAKING, ABINGDON, OXON, OX14 3EA, UK.

* On attachment from the Risø National Laboratory, Denmark
\+ Permanent address: University of Düsseldorf, West Germany
\# Permanent address: University of British Columbia, Vancouver, Canada.
† Permanent address: National Physical Laboratory, U.K.

1. INTRODUCTION

The electron temperature on JET is measured routinely using two independent diagnostics: a single point Thomson scattering system and a spatial scan electron cyclotron emission (ECE) system. In addition, some measurements of the electron temperature have been made with a preliminary soft x-ray pulse height analysis (PHA) system.

In this paper these three diagnostics are described. Results obtained with the diagnostics are presented and compared, and some examples of the use of the measurements in the study of plasma physics phenomena on JET are given.

2. THE SINGLE POINT THOMSON SCATTERING SYSTEM

The Thomson scattering system has the conventional 90° scattering geometry/1/. Light from a ruby laser (λ = 694.3 nm) illuminates the plasma along a vertical chord. The laser has two operating modes: a single pulse mode giving one 20J pulse during a JET discharge and a multipulse mode with lower energy and repetition rates up to 1Hz. The scattering volume (2 mm diameter by 50 mm length) can be chosen to at be one of seven discrete locations in the equatorial plane of the torus. The scattered light is collected by an array of large mirrors arranged as a double Newtonian telescope, and is transmitted to the spectrometer with F number of 10. The spectrometer consists of three prism spectrometers in series, the first two constituting a notch filter for the ruby wavelength. The scattered light is detected with ten photomultipliers fitted with GaAs photocathodes.

The laser and spectrometer are located outside the biological shield so the diagnostic will be compatible with the active phase of JET operation. Alignment systems employing HeNe laser beams keep the diagnostic aligned to the torus. The entire diagnostic is operated automatically through the JET computer system (CODAS).

Temperatures in the range 0.5 - 6 keV have been measured. The sensitivity of the diagnostic allows measurements at densities as low as $3 \times 10^{18} m^{-3}$. The temperatures are obtained by a conventional non-linear least squares fit of the data to tabulated theoretical spectra. The tabulated spectra are calculated using a complete relativistic analysis. The accuracy in the measurement is typically ± 10%.

3. THE SPATIAL SCAN ECE SYSTEM

The spatial scan ECE system has been designed to measure the spatial dependence of the electron temperature in the poloidal cross-section/2/. It is a flexible system; for example it has two operating modes. In the first, the spatial dependence of the electron temperature is measured along ten different chords in the plasma with moderate time resolution ($\lesssim$ 15 ms). In the second, the time dependence of the temperature at specific locations in the plasma is measured with a high time resolution ($\lesssim$ 20 μs).

The first element in the system is an antenna array mounted inside the torus vacuum vessel which views the plasma along 10 different chords in the poloidal cross-section. The radiation is transmitted through crystal quartz vacuum windows and then along oversized aluminium waveguide (S-band) to the measurement area outside the biological protection wall, where the spectrometer and detection systems are located. These consist of four low resolution rapid-scan Michelson interferometers, one high resolution rapid-scan Michelson interferometer and six rapid-scan Fabry Perot interferometers all fitted with liquid helium cooled indium antimonide detectors. The system is operated through CODAS and is compatible with the active phase of JET operation.

One of the 10 planned channels of the system has been operated routinely since the autumn of 1983. It is fitted with a low resolution Michelson interferometer and this is used to measure the ECE radiation emitted in the range 70 GHz < f < 350 GHz. (typically $f_{ce} < f < 4f_{ce}$). The line of sight is 13 cm below the mid-plane and parallel to the major radius. From the emission measured around $f = 2f_{ce}$ the spatial profile of the electron temperature is obtained using the established frequency to space, and intensity to temperature transformations. In the analysis full account is taken of the internal magnetic fields in the plasma due to the plasma current. The spatial resolution in the measurement is $\sim$ 15 cm and the time resolution is $\sim$ 15 ms, and typically 320 temperature profiles are acquired on a JET discharge. The system is calibrated using large area black-body sources. The uncertainties in the measurement are such that the relative shape of the profile is obtained to an accuracy of ± 10% and the absolute level to ± 20%.

In addition measurements have been made of the time dependence of the temperature at specific locations in the plasma with one of the Fabry-Perot interferometers. In this case the time resolution is $\lesssim$ 20 μs and the sensitivity is such that temperature fluctuations of $\lesssim$ 5 eV can be measured. Further measurements of the time dependence of the electron temperature at specific radial locations have also been made with a 12 channel grating polychromator/3/.

4. THE SOFT X-RAY PHA SYSTEM

The preliminary PHA system measures the spectrum of the soft x-ray emission in the energy range 4 - 30 keV. The line of sight is defined by a

set of apertures and is along the major radius. The detector is a mercuric iodide detector/4/ and the plasma is viewed through a 200 μm beryllium window. A composite absorber of beryllium, aluminium and air is used to reduce the sensitivity of the system at low energies and to allow observation of the helium like nickel lines and the continuum emission at higher energies. Both the metal concentration and the electron temperature are extracted from the measurements. Since the measurement is a line of sight integral the analysis takes account of the radial variations of both the plasma temperature and density. The central electron temperature deduced from this analysis is found to be insensitive to profile effects. The accuracy of the measurement is typically ± 10%.

In recent experiments the diagnostic has been optimized for the determination of plasma impurity concentration by employing absorbers which restrict the energy range to 4 - 12 keV. Under these conditions the diagnostic is not so well suited to the measurement of the electron temperature and so the uncertainty in the determination of this parameter is higher.

5. RESULTS AND COMPARISONS

Temperatures measured by the Thomson scattering and ECE systems have been compared over a wide range of plasma conditions; 1 MA < I_p < 5 MA, 2T < B_T < 3.4T, 1 x $10^{19}m^{-3}$ < $n_e(o)$ < 5 x $10^{19}m^{-3}$, 0.5 keV < $T_e(o)$ < 6 keV, 2 < Z_{eff} < 5. For the bulk of the data (> 90%) agreement is obtained to within the stated uncertainties; frequently the measurements agree to within 10%. A more limited comparison has been made including results from the preliminary PHA system. Again agreement to within the stated uncertainties is usually obtained. The main conclusions to be drawn from these agreements are (i) that the diagnostics are operating correctly and (ii) that the plasma is thermal. This latter conclusion arises from the fact that these diagnostics are sensitive to different parts of the electron velocity distribution. Examples of the comparisons are shown in Figures 1 and 2.

Extensive use of the measurements has been made in studies of many plasma physics phenomena on JET: for example, measurements have been made of the time and space dependence of the electron temperature during sawteeth oscillations, Figure 3. Note the flattening of the profile after the disruption and the lack of precursor MHD oscillations/5/. Other phenomena studied with the diagnostics include energy confinement, MHD activity and disruptions. The measured temperature profiles (provided by the ECE system) have also been used in plasma optimization studies: it has been observed that the T_e profile shape at early times is important to subsequent plasma behaviour. An example is shown in Figure 4. More details of the comparisons, and further examples of the use of the measurements will be given in the poster presentation.

REFERENCES

/1/ P Nielsen, Proc, Course on Diagnostics for Fusion Reactor Conditions, Vol 1, Pages 225 - 259, Varenna, 1982.

/2/ A E Costley et al. Proc. 4th International Workshop on Electron Cyclotron Emission and Electron Cyclotron Resonance Heating, pages 1 - 10, Rome, 1984.

/3/ B J D Tubbing et al. paper 142, this conference.

/4/ A J Dabrowski et al. IEEE Trans. Nucl. Science NS-28, 536, 1981.

/5/ See also paper by D J Campbell et al, paper 182, this conference.

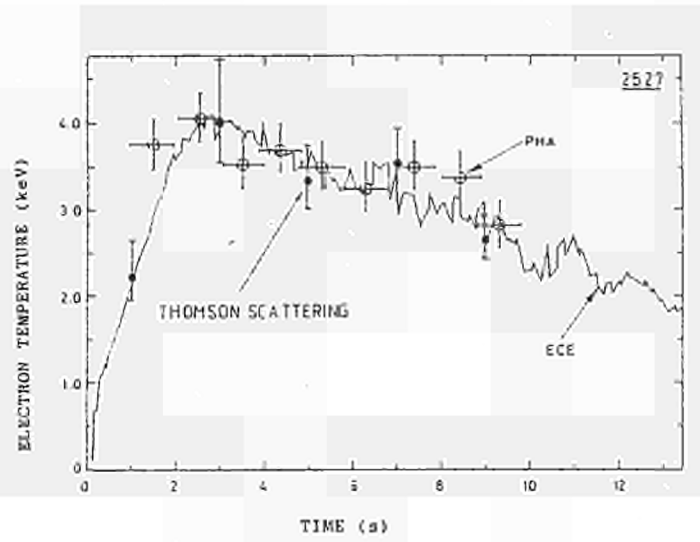

Fig 1: Electron temperature measured by Thomson scattering, ECE and soft x-ray (PHA) on a typical JET pulse, B_T=2.8T, I_p=2.2MA.

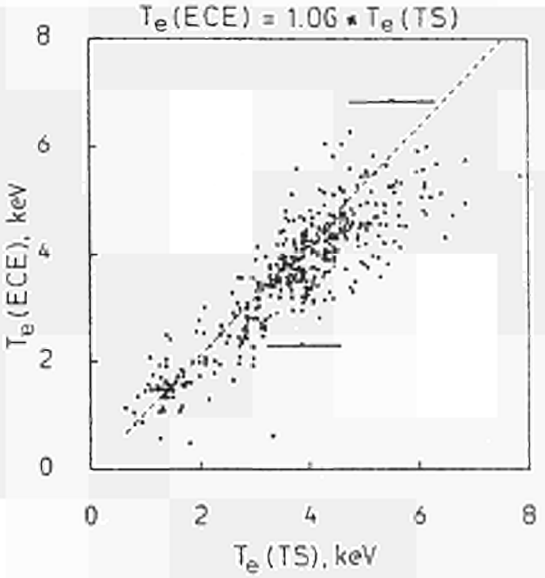

Fig 2: Electron temperature measured by ECE versus electron temperature measured by Thomson scattering. 415 independent measurements are included in the comparison. The slope of the best fit line is $T_e(ECE)=1.06T_e(TS)$.

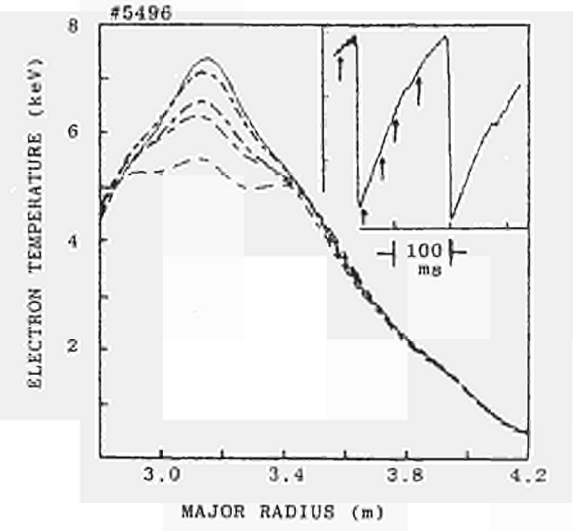

Fig 3: The time dependence of the electron temperature profile during a single sawtooth oscillation on a JET discharge (3.4T, 3.9MA) with 4MW of ICRH. Inset shows the time dependence of the electron temperature at R=3.1m. Measurements made with the ECE system.

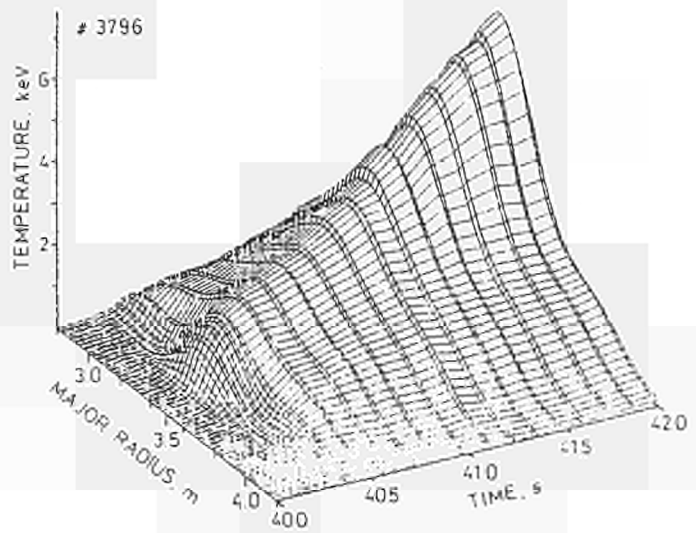

Fig 4: The time dependence of the electron temperature during the early phase of a standard JET discharge, B_T=3.4T, I_p=2.8MA.

Density, Temperature and Power Measurements in the JET Edge Plasma using Heat Flux/Langmuir Probes

P.C. Stangeby[+], S.K. Erents*, J.A. Tagle, G.M. McCracken*, L. de Kock
JET Joint Undertaking, Abingdon, OX14 3EA, U.K.

Introduction

The properties of the edge plasma in JET have been measured for ohmic discharges, with plasma currents Ip = 1-4MA, B_T = 2.6 - 3.4T, using a probe consisting of four combination Heat Flux/ Langmuir detection elements. The individual tungsten elements are as shown in Fig 1. The operation and interpretation of the probe is described further in Ref 1. Three sensing elements face the ion drift direction and are located at distances 1,4 and 8 cm from the end of the probe housing which is fabricated from a 30 mm diameter graphite rod. One sensor, 10 mm from the end, faces the electron drift direction. Each sensor was repeatedly biased with a linear voltage ramp, -100V to + 10V, every 50 ms. The power deposited on each sensor was inferred from the rate of temperature rise of a chromel-alumel thermocouple spot-welded to the back of each 1 x 5 x 10mm^3 tungsten sensor plate.

A typical JET discharge current is shown in Fig 2. During the current rise the plasma vertical elongation increases, typically to b/a ≅1.5, then is roughly constant during the current flat-top before decreasing again; Fig 2 shows an example of the vertical position of the last closed flux surface (separatrix) at the probe location R_p = 3.25m. The probe was inserted from the top of the torus, and was thus sensitive to the changing probe-separatrix distance, $Z_p - Z_s$, during the discharge. The location of the separatrix is calculated for frequent time intervals during JET discharges using magnetic pick-up coil data.

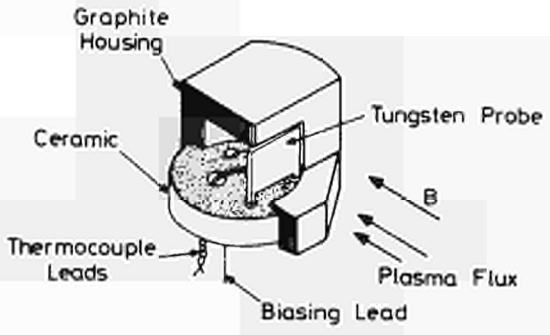

1. Individual sensing element.

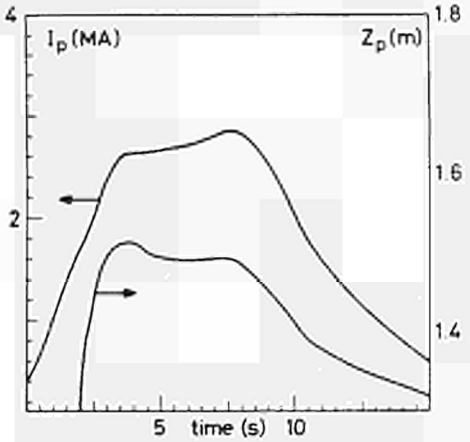

2. Typical time trace of plasma current I_p and vertical position of plasma edge at the probe Z_p.

+ and University of Toronto Institute for Aerospace Studies M3H 5T6
* Culham Laboratory, Abingdon OX14 3DB

The probe vertical position Z_p can be varied between one discharge and the next. Probe data was interpreted as a function of the distance between sensing element and the boundary $r=Z_p-Z_s$.

Experimental Results

Because of (a) the radial separation of the sensors on the probe housing and (b) the variation of Z_p-Z_s during a discharge, a radial profile of plasma temperature etc. could be obtained for each discharge. Fig 3 gives an example of such radial profiles. The ion saturation current density I^+_{SAT} (particle flux density), electron temperature T_e and floating potential V_f for each element were obtained by fitting each 50 ms Langmuir I-V characteristic to the function $I=I^+_{SAT}[1 - \exp(e(V-V_f)/kT_e)]$; only data points for $V \leq V_f$ were employed since it was found that the I-V characteristic departed from true exponential behaviour above V_f, giving spuriously high values of T_e. Values of ion temperature T_i were deduced from measurements of the deposited heat flux density P_d, T_e and I^+_{SAT}. Plasma density was calculated from $I^+_{SAT} = 0.5 n_e c_s e$ where $c_s = [k(T_e+T_i)/m_i]^{\frac{1}{2}}$.

The radial electric field was calculated from $E_r = -dV_f/dr + \frac{d}{dr}[(kT_e/2e) \ln[(2\pi m_e/m_i)(1+T_i/T_e(1-\delta_s)^{-2}]$, where δ_s is the coefficient of secondary electron emission.

Fig 4 gives radial profiles of I^+_{SAT} for two sets of plasma current: $I_p \sim 1$MA (q_s=10-11) and ~ 3MA (q_s=3-4). As can be seen the e- folding length of the profile for lower current discharges is about double that of the higher current shots. This is evidently a direct result of the change in connection length $L=\pi R q_s$ and the relation between the scrape-off and connection lengths: $\lambda = (D_\perp / Lc_s)^{\frac{1}{2}}$. A value of $D_\perp \cong 0.5 m^2/s$ is thus obtained which agrees with spectroscopic (impurity transport) measurements on JET.

Virtually no probe data was obtained within the last scrape-off width of the plasma boundary. Radial profiles of $n_e(r)$ and $T_e(r)$ were extended to r=0 by supplementing the probe data with spectroscopic measurements made at the limiters of heat flux (infra red camera) and particle flux (H_α emission). An example of such complete radial profiles is given in Fig.5. Since the magnetic flux lines for a typical discharge of b/a =1.5 are radially compressed by a factors of 2 in going from the probe position at the top of the torus to the limiter position at the outer mid-plane, the radial scale in Fig 5 is about half that in Fig 3.

Discussion

Impurity generation. The impurity influx rates (carbon, oxygen, metals) from the walls and limiters are measured spectroscopically. The radial profiles of Fig 5 were used to calculate the carbon sputtering rate at the limiter due to deuterium ion impact and it was found that this only accounts for a fraction of the impurity influx. The measured influx can be accounted for by including impurity (O,C), sputtering.

Impurity screening. The ionization of impurity neutrals entering the scrape-off layer, SOL, from the walls and limiters was calculated using Fig 5. Fig 5 was also used to calculate the rate of removal of impurities by convection to the limiters and diffusion into the core plasma. It was found that although impurity influxes from the walls and limiters can be comparable, the SOL effectively shields the core plasma

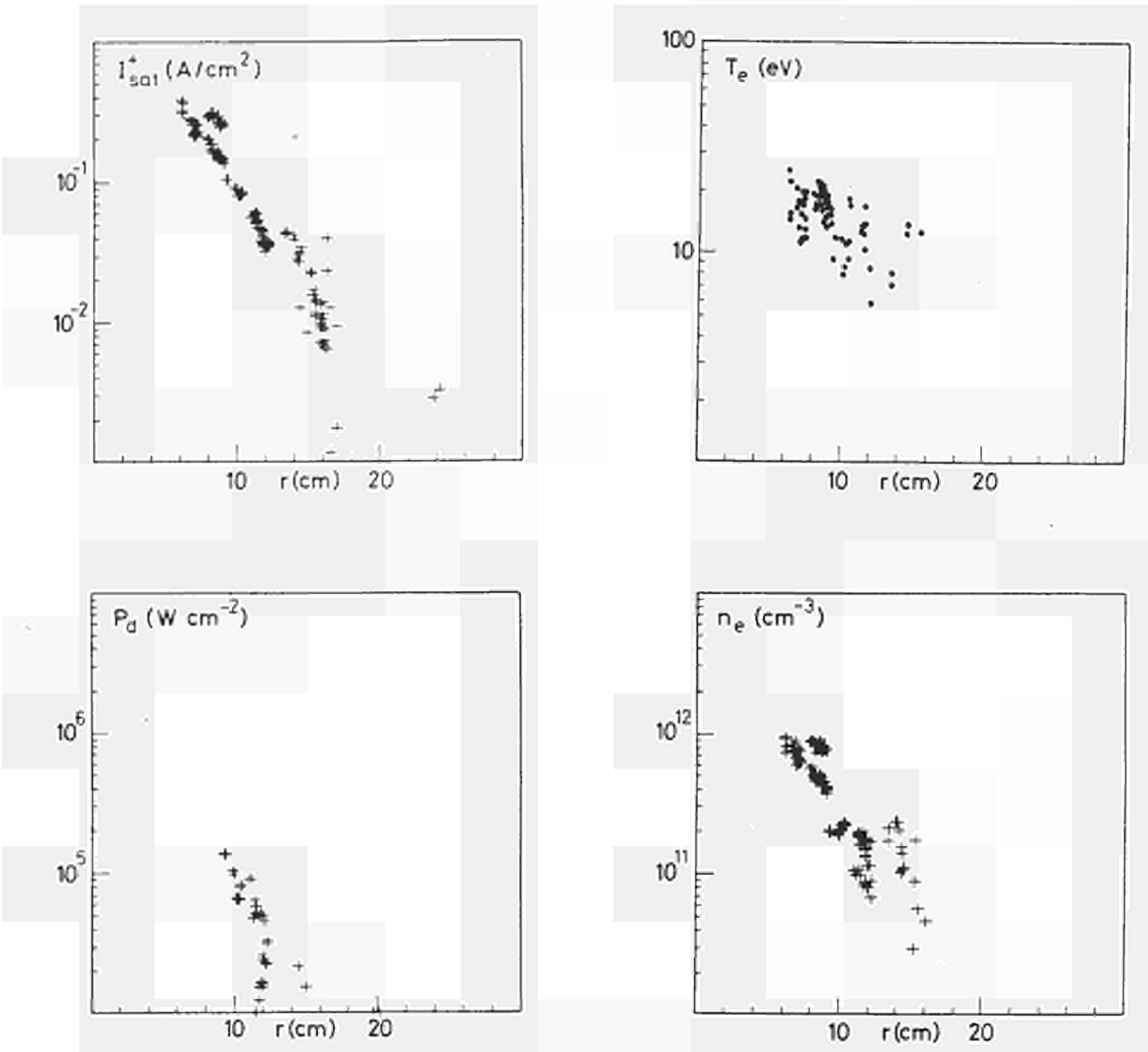

3. Radial profiles for a single shot (NO.3756). I_p = 3 MA, B_T = 3.4T, b/a = 1.5, $\bar{n}_e \ell$ = 8x10^{19}m^{-2}.

from the wall impurities. The shielding of the limiter impurities is partial. The known carbon generation rate at the limiters together with the profiles of Fig 5 give a carbon concentration in the core plasma of 2 - 4%, which is consistent with the spectroscopic estimates and measurements of Zeff (bremsstrahlung).

Hydrogen fueling efficiency. The ionization of deuterium molecules entering the SOL was calculated using the profiles of Fig 5. A fraction of the ionization occurs in the SOL itself, reducing the fueling efficiency of the core plasma.

Poloidal $\vec{E} \times \vec{B}$ drifts. The radial electric field, $\sim 10^3$V/m, causes a poloidal $\vec{E}\times\vec{B}$ drift of $\sim 10^3$m/s which greatly exceeds the radial out-drift $D_\perp/\lambda \cong 10$m/s. If this poloidal drift varies poloidally it would result in the mix of plasma between adjacent flux tubes i.e. tubes which strike one of the four small (40x80 cm) limiters on the first pass and ones

which miss. This may explain the apparent existance of a single effective connection length on JET of $L = \pi R q_s$, rather than the multiplicity expected from the magnetic topology and limiter geometry.

Parallel-field T_e-gradients and Edge Impurity Radiation. When the quantity $Z_{eff} L n_e / T_e^2 \gtrsim 10^{17} m^{-3} eV^{-2}$ then parallel field T_e- gradients will exist along the SOL due to finite electron heat conduction[2]. When the quantity $n_z L / T_e^{3/2} \gtrsim 10^{16} m^{-2} eV^{-3/2}$, where n_z is the impurity density, then impurity radiation dominates the SOL energy balance[2]. The n_e, T_e profiles of Fig 5 indicate that both these criteria are approached for $r \cong 50$ mm. The formation of MARFE 's which are observed in JET is believed to be associated with such effects[3].

Conclusions. Radial plasma profiles have been measured in the JET scrape-off layer for ohmic discharges and have been found to explain observed impurity levels in the central plasma, as well as several properties of the scrape-off layer.

Acknowledgements
Technical assistance by A. Stevens, J. Vince, D. Wilson, J-P. Jeral, K. Slavin, W. Dearing, G. Matthews is gratefully acknowledged. PCS wishes to acknowledge personal support from the National Research Council of Canada.

Reference

1. P.C. Stangeby, G.M. McCracken, S.K. Erents, G. Matthews, J. Vac. Sci, Technol. A2 (1984) 702.
2. P.C. Stangeby, Phys. Fluids 28 (1985) 644.
3. B. Lipschultz et al, Nucl. Fusion 24 (1984) 977.

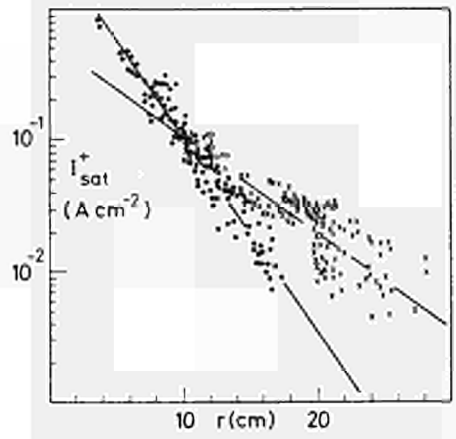

4. Radial profiles of I^+_{SAT}. Points for $I_p = 3$ MA, $q_s = 3$-4. Crosses for $I_p = 1.1$ MA, $q_s = 10$-11.

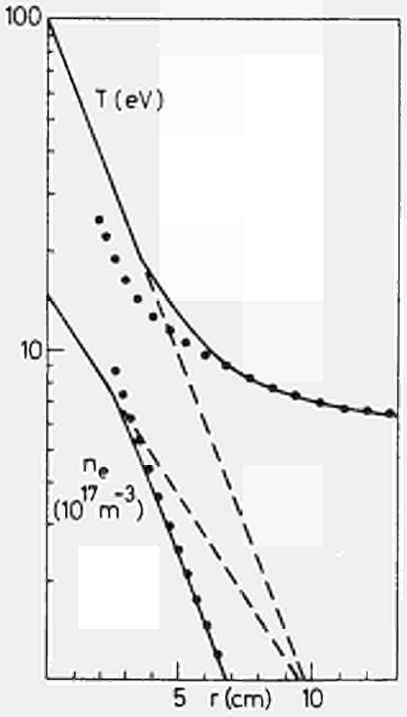

5. Radial profiles constructed from combined limiter and probe data. At the mid-plane. Points from probe data. Broken lines from limiter data. $\bar{n}_e^{\ell} = 7.5 \times 10^{19} m^{-2}$, $I_p = 2.8$ MA.

Experimental Observations of Disruptions in JET

F C Schüller, F Alladio[+], D Campbell, F Crisanti[+], L de Kock, H Krause[o], P Lomas, M Malacarne, F K Mast[o], M F F Nave, R Niestadt*, P Noll, H W Piekaar*, P R Thomas, J Thompson, G Tonneti[#], B Tubbing*, J Wesson

JET Joint Undertaking, Abingdon, Oxon OX14 3EA
[+]Euratom - ENEA Association, Frascati, Italy
[o]Euratom - IPP Association, Garching, Fed. Rep. Germany
[*]Euratom - FOM Association, Nieuwegein, The Netherlands
[#]Euratom - Suisse Association, Lausanne, Switzerland

1 Introduction

The main aim of JET is the study of plasmas in which α-particle heating is a significant part of the input power and this depends on reaching a value of the product $\bar{n}_i T_i \tau_E > 5.10^{21} m^{-3} s^{-1}.keV$. With ohmic heating alone all 3 parameters are about a factor 3 too small. The maximum value of $\bar{n}$ reached up until now is $3.75\ 10^{19} m^{-3}$ and limited by the high density disruption. It has been shown elsewhere that additional heating brings this limit up with a factor 1.5 to 2 which is not enough. Moreover it is undesirable to induce a disruption at every pulse when heating is switched off. Study of high density disruptions is therefore a key issue for JET.

2 Disruption Database

A database has been developed in order to document the occurrence of disruptions. For every disruptive pulse 16 plasma quantities are stored at 3 moments in time:

a) the moment of energy quench is undistinguishable from the start of the current quench and is defined as the plasma current data point where after $dI/dt < -0.4I$;
b) one time slice preceding a) because often diagnostics are wiped off during the energy quench.
c) The start of the MHD-precursor (m=2/n=1) defined as the time slice in which the MHD-activity is twice as large as the average over the preceding second.

3 Operational Window

The database can be used for the construction of Hugill-diagrams. Fig. 1 gives as an example the 1984 disruptions in the $(1/q_\psi)$ - $(\bar{n}R/B)$ plane. Two categories can be observed:

a) disruptions connected to the rise phase or early flat-top: their probability is enhanced by increasing current ramp-rates [1] and shows a maximum around $q_\psi \cong 3.3$ although these disruptions may occur at any q-value.
b) high density disruptions. It is shown [2] that these disruptions occur when the radiative loss about equals the input power. Low Z radiation is dominant. The fact that also in JET these disruptions follow the well known diagonal in the Hugill diagram can be described by a simple model: assume that the input power is dissipated within the q=2 surface and the

radiative loss takes place outside this surface. When radiation is 100% of the input power a disruption will occur. If one takes the empirical dependence of the input power on B, q and dimensions and for the low-Z radiation the corona-model predictions for the second "helium-like" radiation peak one finds the following for JET:

$$\bar{n}R/B = 1.2 10^{20} \; B_t^{-3/4} \; q_\psi^{0.1} \; [(q_\psi - 2)\,(Z_{eff} - 1)]^{-\frac{1}{2}} \qquad (1)$$

Curves of this dependence for typical values of B_t and Z_{eff} are shown in the diagram. In 1985 the Murakami parameters obtained are about 20% higher than in 1984. The record value being 4.7 $10^{19} m^{-2} T^{-1}$ was obtained without disruption at low B_t=1.7T and q_ψ=3.2.

4 Precursors

On a timescale of about 1 sec before disruption noticeable changes in the plasma edge can be observed: changes in the recycling pattern, i.e. reduction at the limiter, increase at the wall, increase in low Z radiation, increase in $\beta_{pol} + \ell_i/s$. Often this leads to a development of a "marfe", sometimes to the development of a growing cool plasma mantle leading to a thermal collapse. On shorter timescales (100 to 500ms) an increase in MHD - activity mainly m=2/n=1 leads finally to a disruption in most cases with the mode locking to a "standing wave". this mode-lock occurs always in the same toroidal location. This preference can either be explained by a toroidal asymmetry in the poloidal field distribution or by the fact that the position control acts on magnetic signals from one toroidal location.

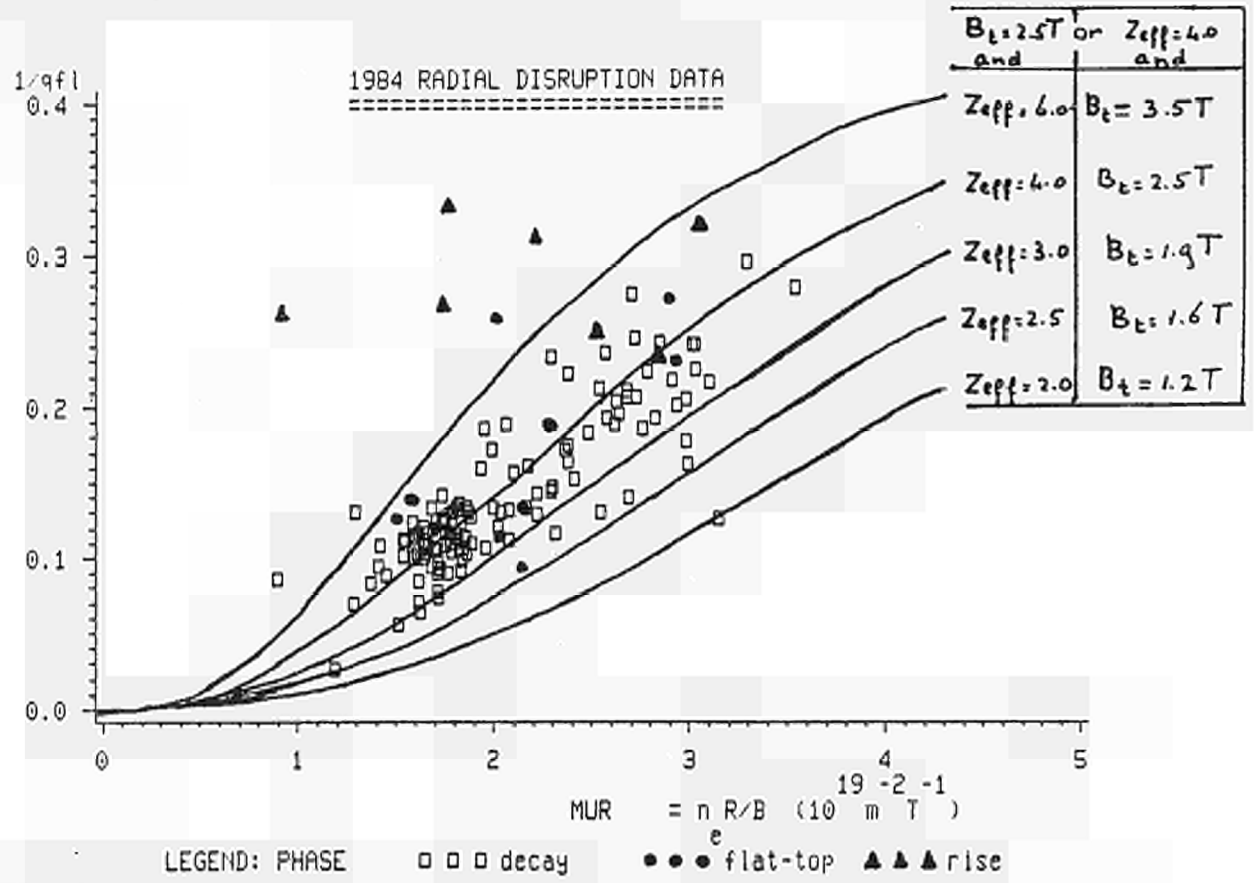

Fig. 1
Hugill diagram for 1984 disruptions. The drawn lines give the results of eq.(1) for a few combinations of toroidal field and Z_{eff}-values.

5 Energy quench

From fast e.c.e - measurements [3] the width of the magnetic island can be estimated as being the width of the shoulder in the Te-profile at the q=2 radius. A few ms before the final collapse the width starts to grow rapidly such that Te inside the q=2 surface decreases by several 100eV and outside increases with a similar amount. This time scale is in good agreement with the scaling law [4].

$$(\gamma)^{-1} \equiv \tau_\sigma^{3/5} \cdot \tau_{pol.Alfvén}^{2/5}$$

However the final collapse occurs on a much faster timescale: T_e drops over the whole cross-section to a flat profile of about 100eV within one data sampling time of 200μsec. The data suggests that this collapse occurs when the magnetic island has grown so far that it either touches the limiter or contacts the q=1 surface.

6 Current-quench

Depending on the magnitude of the energy quench and the plasma current level at disruption the subsequent current quench is "soft" (decay time around 300ms) if the position control circuitry is able to maintain control by ramping down the vertical field fast enough. If the power amplifier comes into saturation position control is lost and the current quench is much faster. Current quenches up to~180MA/s have been observed. Fig. 2 illustrates the difference between slow and fast current quenches by showing the magnetic surfaces as calculated from the magnetic diagnostics. In Fig. 3 the influence of the voltage capability of the position control power amplifier on the $\dot{I}$-value as function of the current value at the moment of

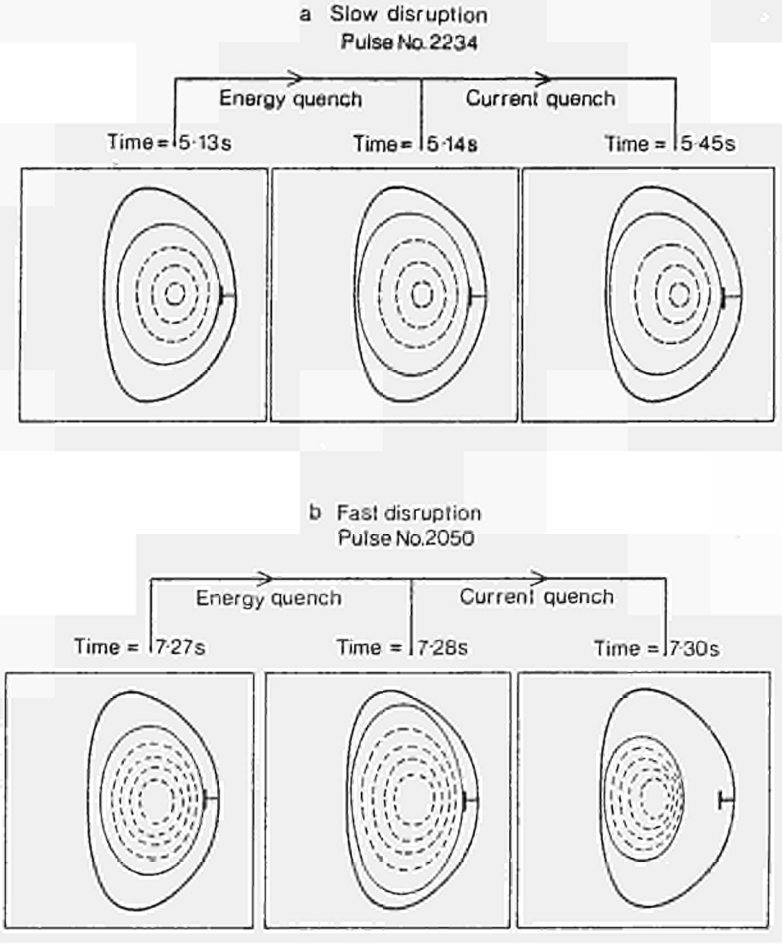

Fig. 2 Examples of a slow and a fast current quench. The magnetic surfaces are reconstructed from magnetics by the ODIN-code. Note the blow-up during the energy quench and the loss of position in the fast quench example
case a: I=1.5MA; $\dot{I}$=4MA/s
case b: I=1.9MA; $\dot{I}$=56MA/s
B_t=2.5T; q_{cyl}=4.8 for both.

disruption is shown. A high voltage capability (●) lowers I compared with a low capability (▲). The ohmic driving voltage during the rise-phase is about 4 x larger than during the flat-top. Therefore the input power is higher which slows the current quench of rise-phase disruptions (x) down compared with quenches occurring in the flat-top or decay-phase. This again raises the chance that position control is maintained.

References

[1] F C Schüller et al. This conference.
[2] J Wesson et al. This conference.
[3] B Tubbing et al. This conference.
[4] J D Callen et al. IAEA 8th Int. Conf. Plasma Physics and Contr. Nucl. Fus. Brussels [1980].

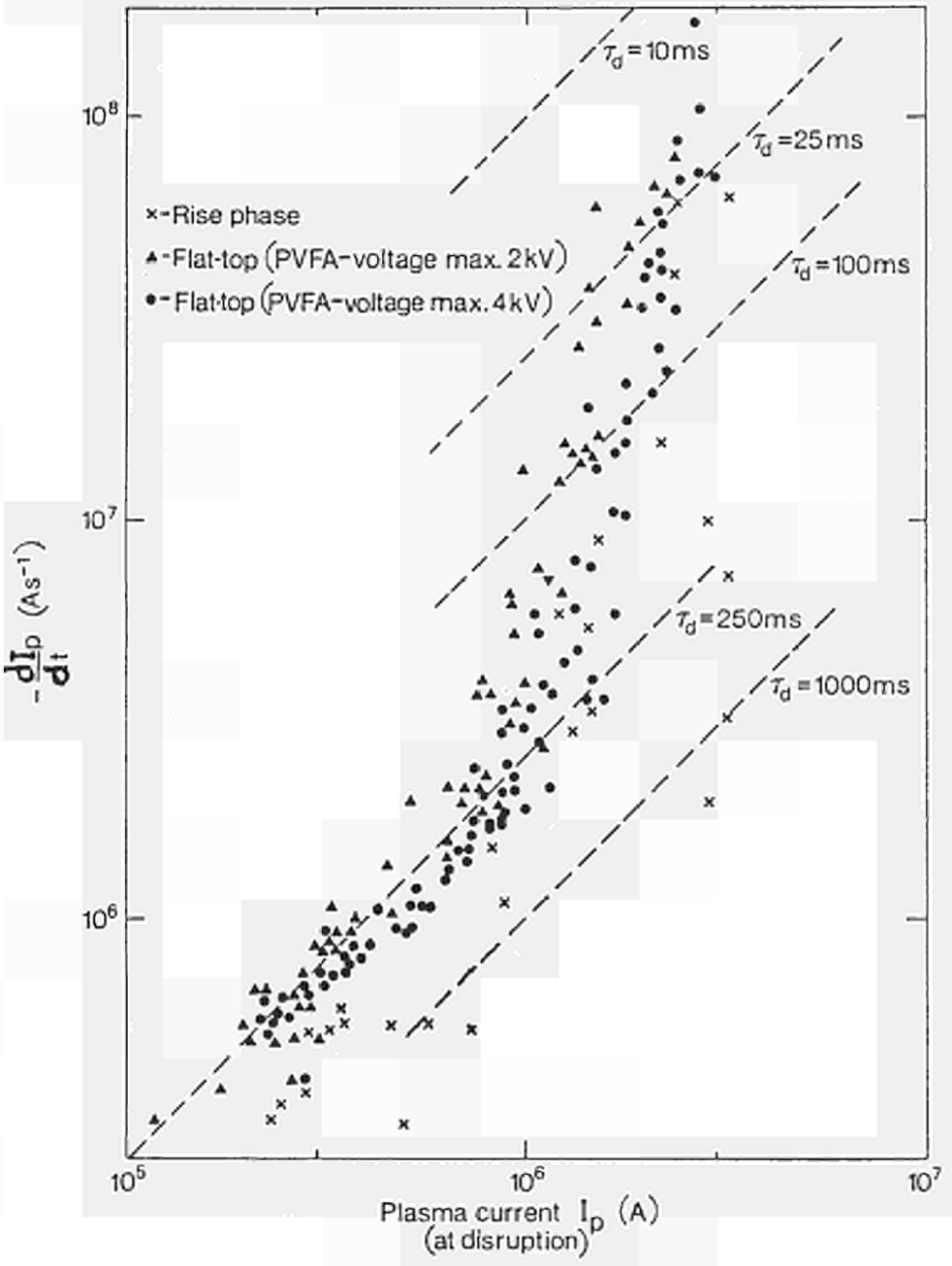

Fig. 3
The current quench rate as function of the current at disruption. As long as the position is controlled the decay rate is given by a time constant of about 250ms. Above 1MA this becomes difficult and the decay-rate is enhanced by the loss of position.

Transport Analysis of JET Discharges

M. Brusati, J.G. Cordey

JET Joint Undertaking, Abingdon, Oxon. OX14 3EA, UK.

Abstract: Local transport studies of JET ohmically heated plasmas show that ion losses in the region $r/a<2/3$ exceed electron losses when the local electron density is greater than a critical value which increases with the plasma current I_p.

Both ion and electron losses in the $1<q<2$ region are due to thermal conduction, the ion conductivity being several times neoclassical, the departure from the neoclassical value increasing monotonically with I_p.

The total energy confinement time τ_E of this region is up to 1.1sec; τ_E scales as $n_e^{0.6}$, and no clear dependence on plasma current is found.

I Local plasma energy balance

Ohmic plasmas have been obtained in JET over a wide range of plasma parameters:

$$1.7<B_t(T)<3.4;\ 1.0<I_p(MA)<4.0;\ 0.5\times10^{19}<\bar{n}_e(m^{-3})<3.6\times10^{19}$$
$$2.0<T_e(keV)<7.0;\ 1.5<T_i(keV)<3.0;\ 2<Z_{eff}<5$$

The plasma balance is calculated at several time points during the current flat top by the 1½D time dependent transport analysis code JICS. The current and mean density waveforms have a flat top of at least 5sec. The high current discharges ($I_p>3$MA) do not reach a steady state, the surface voltage exceeding the resistive voltage on axis means that inductive effects have to be taken into account when analysing the plasma equilibrium.

The ion and electron energy equations are solved in the flux surface geometry which is determined from the magnetic data and the equilibrium identification code IDENTB [1]. Other diagnostic information input to JICS include the electron T_e profile from ECE, density n_e from 2mm and FIR interferometry, ion temperature T_i from c-x and neutron yield, radiation losses from bolometry, effective ion charge Z_{eff} from visible bremsstrahlung; information on the average ion species is obtained from VUV and visible spectroscopy, and on particle recycling at the edge from H_α monitors. The results presented here are restricted to the region of the plasma where the radiation is small; this extends up to 2/3 of the average plasma minor radius. Thus more than 150 discharges were analysed to cover the above range of parameters.

In JICS the ion energy equation is given by:

$$\frac{dE_i}{dt} = P_{ei} + P_{cx} + P_{cv} + P_{cd}\ .$$

The electron-ion coupling P_{ei} is assumed to be classical; the convection P_{cv} is determined from the particle balance and the charge exchange term P_{cx} relies on the self consistent calculation of the neutral density profile; this is computed by the code FRANTIC [2]; the boundary neutral flux is given by the H_α intensity.

The conduction term P_{cd} is derived from multiple times of the neoclassical

conductivity; the results presented here have been obtained using the Chang-Hinton formulation of the conductivity [3]. Equation (1) is solved for T_i adjusting the multiplier until agreement is found between the calculated central ion temperature and the measured one.

Results of the analysis are shown in fig.1a for a I_p=4.0MA, B_t=3.4T plasma; ion losses are due mainly to conduction, P_{cv} and P_{cx} being negligible. To reproduce the measured central ion temperature it is necessary to use a large multiplier for the ion conductivity. The "anomalous" ion transport, including MHD driven ion losses [4] within the q=1 region, can be up to an order of magnitude higher than neoclassical, the departure from neoclassical increasing with plasma current.

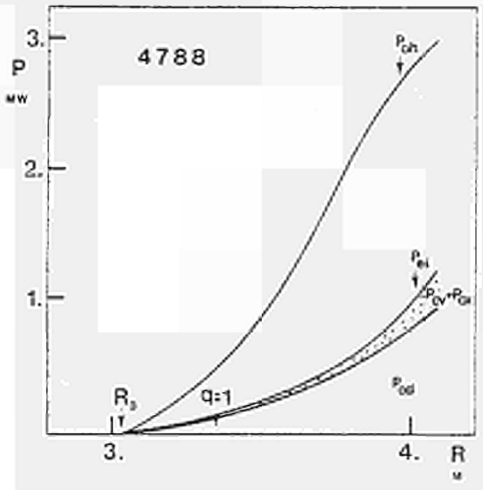

Fig.1a

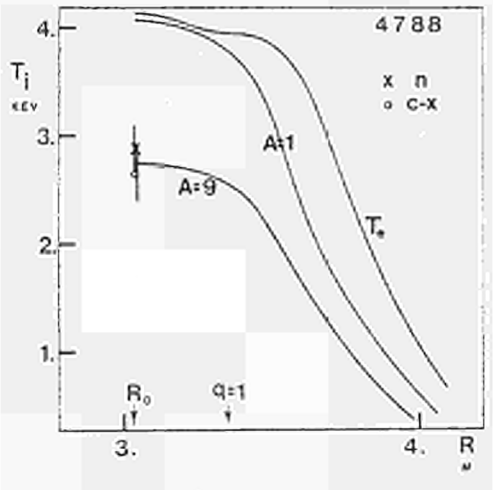

Fig.1b

This treatment of the ion heat diffusion does not allow any further conclusion on its nature but the relative importance of electrons and ions in plasma confinement can be investigated by comparing P_{ei} with the main electron losses.

The electron energy equation is:

$$\frac{dE_e}{dt} = P_{OH} + P_{RAD} + P_{ei} + P_{cv} + P^e_{CD} + P_{iz} \qquad (2)$$

P_{RAD} is the radiation loss, P_{cv} the convection, defined similarly to the ion term, P_{iz} the ionization term.

The ohmic term P_{OH} is computed from the local current density and electric field, derived from the time derivative of the poloidal flux [1]. In JET the resistive voltage is 0.5-0.8V on axis, increasing with poloidal flux to 1.-1.5V at the plasma edge, resulting in up to 3.2MW coupled to the electrons at I_p= 4.0MA with $Z_{eff}\sim 3.0$.

Equation (2) is solved for the electron heat diffusion term P^e_{CD}. The power balance is shown in fig.2a for the same discharge as in fig.1. The ohmic power is lost mainly by coupling to the ions and heat conduction.

The role of electrons and ions in plasma confinement is assessed by comparing electron heat losses P^e_{CD} with P_{ei}. This is shown in fig.3 where P^e_{CD}/P_{ei} is plotted for a large number of discharges against local electron density for various currents at B_t=2.5 and 3.4T. The scatter of the data reflects the uncertainty on the ion neoclassical term, most of which is due to experimental

errors in the region outside the plasma volume considered. The density at which $P^{e}_{CD}/P_{ei}=1$ increases with I_p, from $\sim 1.5\times10^{19}m^{-3}$ at I_p=2MA to $\gtrsim 3.\times10^{19}m^{-3}$ at I_p=4MA, apparently saturating at high current. No toroidal field dependence can be resolved within the data scatter.

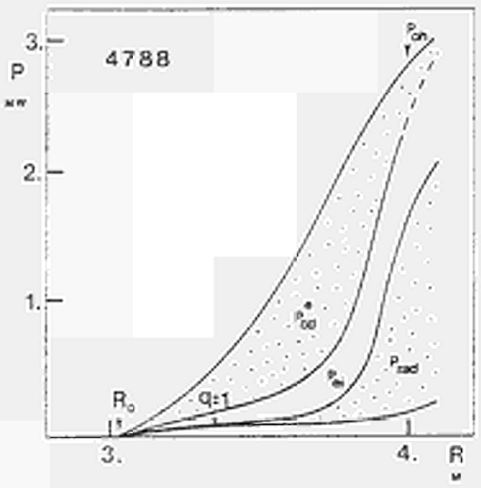

Fig.2a

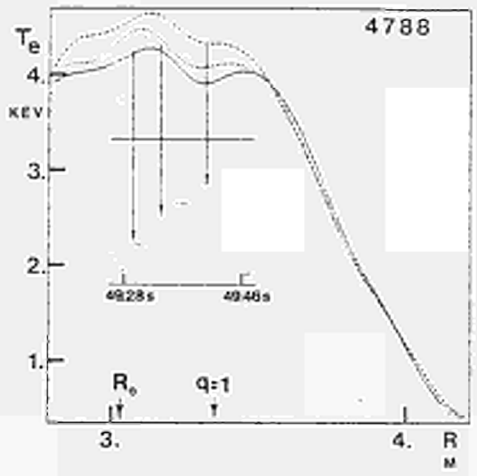

Fig.2b

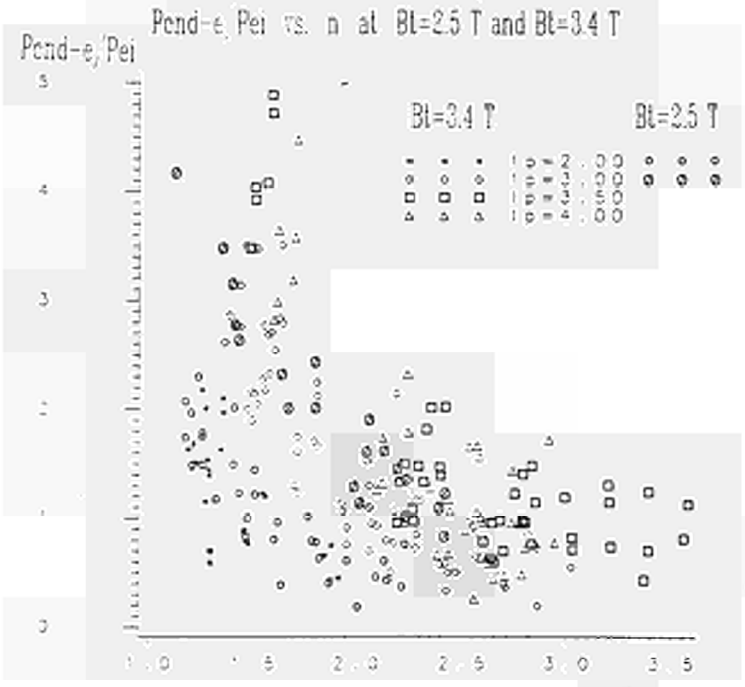

Fig.3

II Plasma Confinement Scaling

The plasma energy confinement in the inner volume V is:

$$\tau_E = \frac{\frac{3}{2}\int_V (n_e T_e + n_i T_i)dv}{P_{OH} - \frac{3}{2}\frac{d}{dt}\int_V (n_e T_e + n_i T_i)dv}$$

Density scans were performed on JET at different B_t and I_p values. No clear dependence was found for the confinement of the inner plasma on I_p, in contrast with previous results [5]. The scaling of τ_E with density is shown in fig.4; τ_E appears to scale as $n_e^{0.6}$; uncertainties at higher densities (~30%) are related to higher ion losses.

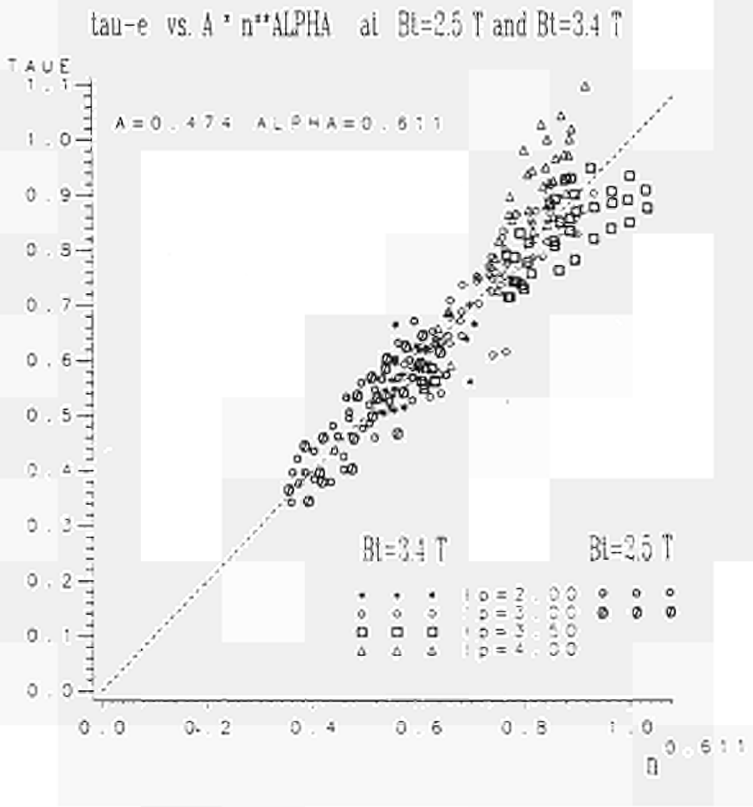

Fig.4

Summary

It is found that in JET ohmic plasmas, ion losses exceed neoclassical values and become dominant, at higher plasma currents, at lower electron densities than previously reported [6]. The total energy confinement time in the radiation free region of the plasma scales less than linearly with n_e, without saturation effects at higher densities. No clear dependence is observed as yet on plasma current and toroidal field.

References

[1] BRUSATI, M. et al. Comp. Phys. Report 1, (1981) 345 and references therein.

[2] TAMOR, S. Journal of Comp. Physics 1 (1981) 104.
GOLDSTON, R., TOWNER, H. Private communication.

[3] CHANG, C.S., HINTON, F.L. Phys. Fluids 25 (1985) 1493.

[4] CORDEY, G.G., STRINGER, T.E. To be published.

[5] EFTHIMION, P.C. et al. "Plasma Physics and Controlled Nuclear Fusion Research", London 1984, Vol.1, IAEA-CN-44/A-I-2 page 29.
EJIMA, S. Nucl. Fusion 22 (1982) 1627.

[6] GONDHALEKAR, A. et al. "Plasma Physics and Controlled Nuclear Fusion Research", Innsbruck 1978, Vol.1, IAEA-CN-37/C-4, page 199.

POLOIDALLY ASYMMETRIC EDGE PHENOMENA IN JET

J O'Rourke, D Campbell, B Denne, A Gondhalekar, N Gottardi, H Krause*, G Magyar, M Malacarne, F Mast*, P Morgan, M F Nave, F C Schüller, M Stamp, D Summers

JET Joint Undertaking, Abingdon, OX14 3EA, UK
* On attachment from IPP-Euratom Association, 8046 Garching, RFG

ABSTRACT

JET discharges near the density limit frequently form a region of high-density strongly radiating plasma localised at the plasma edge, on the small major radius side. A detailed description of such an event is presented. The onset of such an event coincides with a decrease in the kinetic energy content of the discharge. The asymmetric state initiates a transition of the discharge to a new poloidal symmetric state characterized by high edge radiation and decreased interaction with the limiters. The concomitant modifications of the density and energy dynamics of the discharge are observed.

INTRODUCTION

In this paper we present observations of the formation and evolution of regions of high density and enhanced radiation localised at the edge of JET plasmas, on the small major radius side. Similar events in ALCATOR C discharges [1] have been termed 'marfes' and the same designation is adopted here.

'Marfes' in JET occur near the density limit of the operating regime (see Figure 1). They have been observed to form during all phases of JET discharges: current rise, flat-top and decay. No correlation has been observed with details of vessel conditioning history. Beyond the general characteristics mentioned in the proceeding paragraph, 'marfes' exhibit a varied phenomenology. For consistency we shall concentrate in the following on a typical 'marfe' which occurred during pulse 3428. Important differences with observations of other 'marfes' in JET will be pointed out.

STRUCTURE

Figure 2 shows the position, in a poloidal plane, of the 34 chords of the bolometer arrays and the 7 vertical chords of the far infrared interferometer. These diagnostics are separated toroidally by 135°. Also shown is the plasma boundary (deduced from magnetic measurements) for pulse 3428 (at t=10 s).

Figure 3 shows the time evolution of the plasma current, the line integrated electron density along 3 interferometer chords, the poloidal β and the radial position of the inside plasma boundary at z=o. The radial position of the outside plasma boundary is at the limiter. At 10.1 seconds, the line integrated density on the innermost chord (R=1.883 m, 0.1 m inside the plasma boundary at z=o) rises by nearly 10^{19} m^{-2} in 300 msec. This event is clearly poloidally asymmetric (as no corresponding change occurs on the outer interferometer channels) and is not due to motion of the plasma boundary. Figure 4 shows the evolution of bolometric and spectroscopic signals.

Comparison of signals from single bolometers situated toroidally around the plasma confirms that the 'marfe' is axisymmetric. At its onset the 'marfe' is most pronounced on channels V12-V14, UH2-UH6 and LH1-LH4. By referring to Figure 2, one deduces that it is localised poloidally between Θ=145° and Θ=210°. Figure 5 (however taken from a different pulse) shows the relative increase in several spectral line intensities during a 'marfe' as a function of the ionization potential of the emitting ion. Probe measurements yield a temperature at the plasma boundary of about 50 eV. The enhancement of lines with ionization potentials of about 100 eV shows that the 'marfe' is situated within the plasma boundary. Localisation of the 'marfe' inside the plasma boundary permits us to interpret the line integrated density as a mean density in the 'marfe' of at least $1.2\times10^{19}m^{-3}$. The density at the centre of the discharge is $2\times10^{19}m^{-3}$. The line-integrated density through the 'marfe' location exhibits large (10%) modulations both prior to and during the 'marfe'.

DENSITY DYNAMICS AND TRANSITION TO A NEW POLOIDALLY SYMMETRIC STATE

The increase in poloidal β during the current decay is arrested when the marfe occurs (see Figure 3). The increase in the rate of loss of kinetic energy which this implies can be interpreted as due to the increased rate of loss of bulk plasma particles.

A horizontally viewing analyser in the mid-plane shows a large ($\sim$x2) enhancement of the neutral particle efflux at all measured energies (2-15 keV) during a 'marfe' (see S Corti et al, this conference). D_α light from the initial 'marfe' location is not monitored in this pulse, but as the 'marfe' spreads into the line of sight of vertically viewing D_α monitors, an increase in D_α light is observed. This supports the hypothesis that there is an increased source of neutrals at the wall.

The end of the 'marfe' usually coincides with a sudden increase in C III signal (Figure 4) and a burst of D_α light from the inner wall. The radiation asymmetry subsides by spreading poloidally beginning at about 10.5 sec. This is best seen on the vertical bolometer channels (Figure 4). At about 11.3 sec this asymmetry is no longer observed and the 'marfe' is terminated. The density asymmetry, evidenced by the innermost interferometer channel, subsides simultaneously with the radiation asymmetry.

The end of the 'marfe' coincides with an increase in the total radiated power, and a progressive shrinking of the radiating shell away from the plasma edge. The electron density profile also becomes increasingly peaked. Figures 6 and 7 compare the density and radiation profiles at 10 sec (before the 'marfe') and 12 sec (after the 'marfe').

The D_α and C_{III} light measured at the vessel wall continue to rise, while that at the limiter decreases, indicating that the wall is becoming a relatively more important source of electrons compared with the limiters. We refer to this as detachment from the limiters.

Taking as definition of the global particle confinement time, τ_p, the equation

$$\dot{N} = -\frac{N}{\tau_p} + \phi_\ell + \phi_\omega + \phi_g$$

where N is the total number of electrons, and ϕ_ℓ, ϕ_ω and ϕ_g are the limiter, wall and external fluxes, assuming that the wall flux is uniform everywhere, and accounting for the presence of impurities, we obtain τ_p = 0.60 sec before the 'marfe' and τ_p = 0.93 sec after. No attempt is made to estimate the

confinement time during the 'marfe', since the assumption of uniformity is not valid.

This change in plasma behaviour can be seen very clearly in the evolution of the discharge in the Hugill diagram (Figure 8). At the end of the 'marfe', the Murakami parameter begins to increase, and the discharge evolves towards the density limit.

Not all 'marfe' events lead to detachment of the plasma from the limiters, although this is often the case. Further elucidation of such a bifurcating process requires a more detailed knowledge of the parameters at the plasma edge.

CONCLUSION

In the 'marfe' state, a discharge is characterised by poor particle confinement. The end of a 'marfe' frequently signals the transition to a state of increased particle confinement and decreased interaction with the limiters.

[1] B Lipschultz, B La Bombard, E S Marmar, et al., Nuclear Fusion, Vol.24, No.8 (1984) 997.

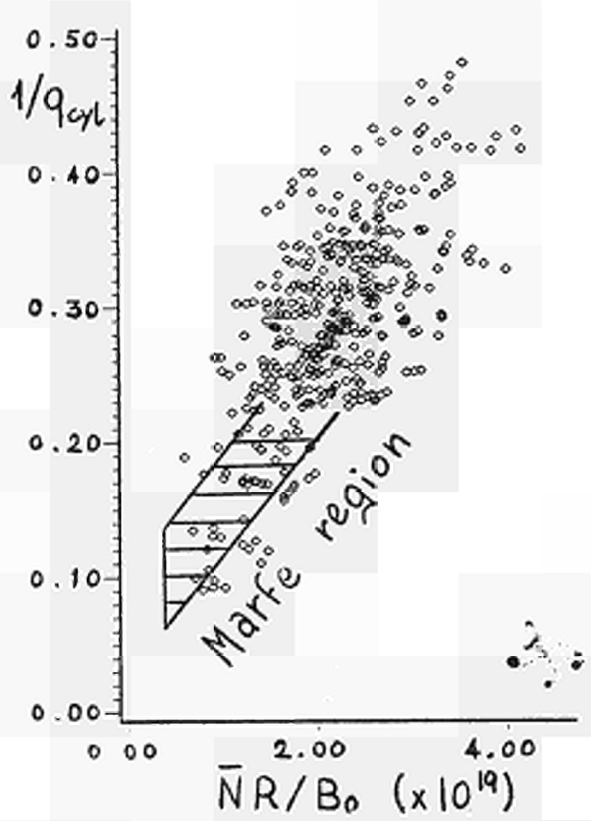

FIGURE 1: Marfes in JET operating regime.

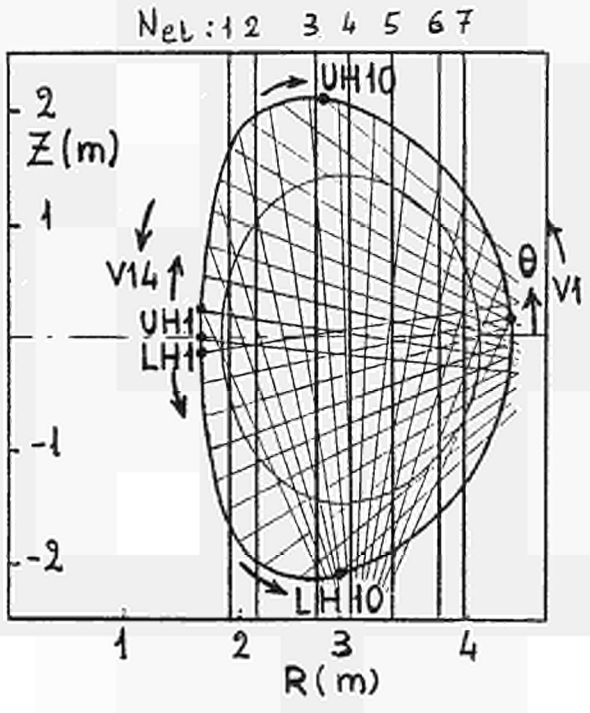

FIGURE 2: Layout of bolometer and interferometer arrays.

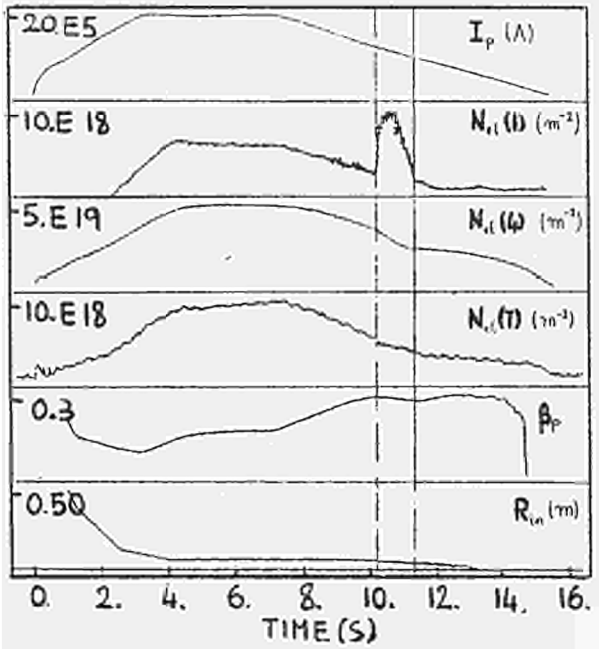

FIGURE 3: Evolution of JET pulse 3428.

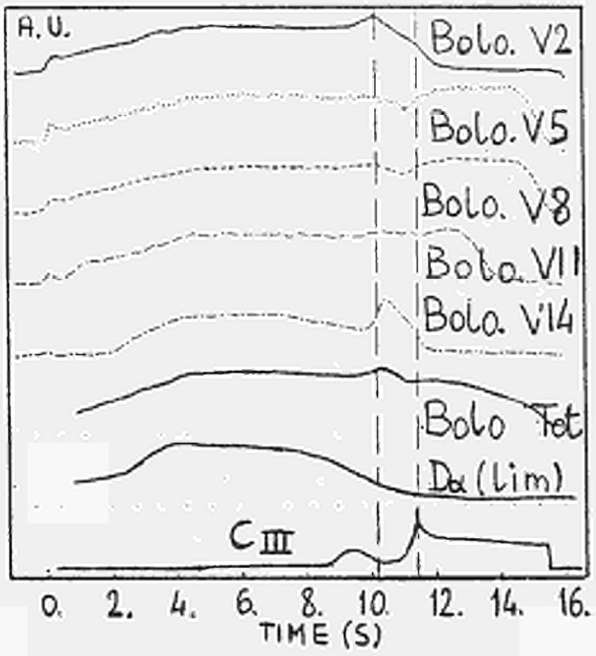

FIGURE 4: Some bolometric and spectroscopic signals.

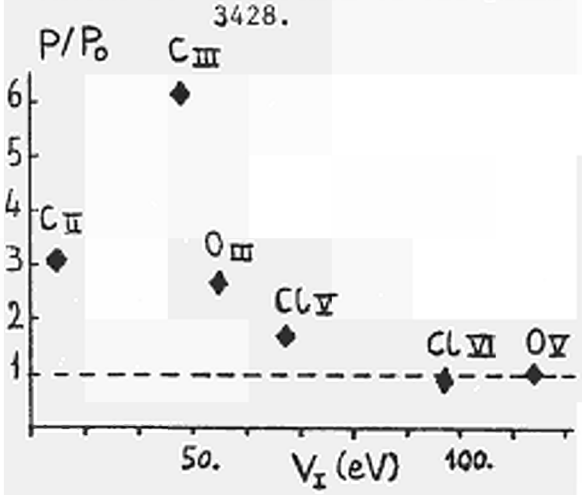

FIGURE 5: Enhancement factor for some impurity lines.

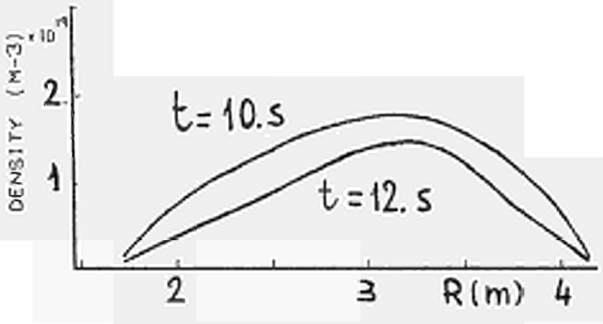

FIGURE 6: Density profiles.

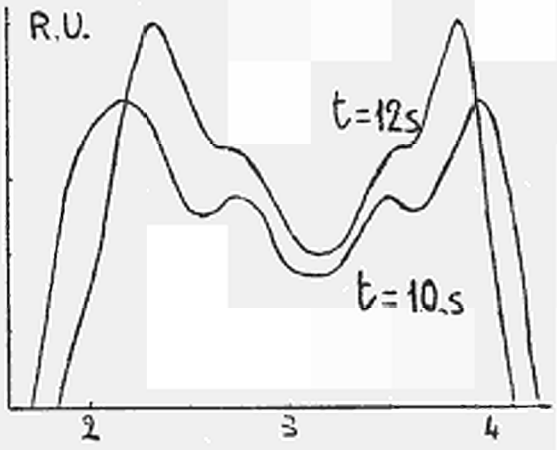

FIGURE 7: Bolometric profiles.

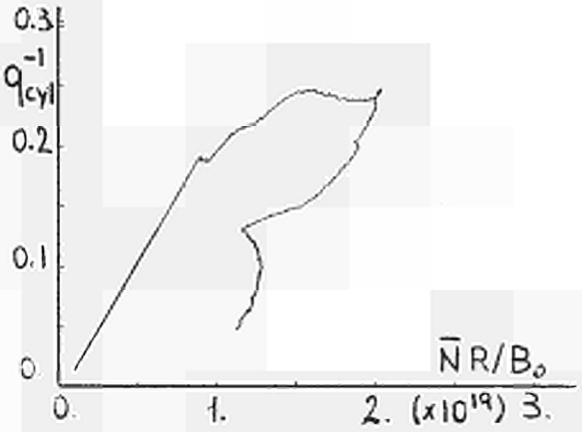

FIGURE 8: Hugill diagram evolution.

VOLT-SECONDS CONSUMPTION OF JET DISCHARGES

P R Thomas, J P Christiansen and S Ejima†
JET Joint Undertaking, Abingdon, Oxon OX14 3EA, UK
†GA Technologies, San Diego, CA 92138, USA

Introduction

JET has been designed to contain plasmas where α-particle heating is a significant part of the power balance. To do this it must be capable of operation at high enough plasma current to trap the 3.5MeV α-particles and for long enough for them to slow down and impart their energy to the plasma. The full performance specification of the device was for 4.8MA plasma current. This has recently been exceeded, albeit with little flat-top. The behaviour of other limiter tokamaks with intense additional heating indicates that still higher current might be necessary to obtain the thermonuclear yield required for an observable level of α-particle heating. Therefore the volt-seconds consumption of JET discharges is of interest because it will, in part, determine the ability of the machine to meet its design goals. Also the performance of JET should guide the design of the next generation of machines such as INTOR and NET.

JET has operated at plasma currents in the range 1-5MA, toroidal fields 1.3-3.4T, elongation ratios 1.05-1.85 and mean densities $0.75\text{-}3.5\times10^{19}m^{-3}$. The minor radius was typically 1.16-1.22m corresponding to major radii 3.01-2.95m. Most discharges had the same start-up conditions and so were used to determine the dependence of the flux consumption on the flat-top plasma-parameters. A smaller selection of discharges, in which the break-down voltage and current ramp-rate were varied have been used to determine the sensitivity of the flux consumption to these parameters.

Volt-seconds Consumption at the End of the Flat-top

Two codes have been used to fit parameterisations of the plasma current density to the magnetic diagnostic signals. The internal inductance ℓ_i and β_T can be separated reliably when the elongation ratio is $\gtrsim$1.3. The FAST code[1] uses an analytic expression for the separation and is routinely used on all JET discharges of more than 1MA. ODIN[2] solves the Grad-Shafranov equation with a four parameter representation of the current distribution. It is only used for single time-slices of a small number of discharges. The results from both codes show that ℓ_i depends only on $q_{cyl}=2AB_T/\mu oI_pR$, where A is the poloidal cross-sectional area. Most of the points group together very tightly except for those with b/a<1.3, where the value of ℓ_i is not reliable. ℓ_i is well represented by

$$\ell_i \tilde{\sim} 0.9 + 0.05q_{cyl} \quad . \qquad (1)$$

The ODIN results yielded an estimate for the flux difference between the magnetic axis and the plasma surface. This was found to be related to the internal inductance by

$$\psi_i \tilde{\sim} \mu o\, I_p\, R\, (\ell_i/2 + 0.3) \qquad (2)$$

When equation (2) was compared with the volt-seconds consumed at the end of the flat-top, it was found that a simple model described the resistive consumption on axis,

$$\psi_r = V_\ell(0)t + \psi_{bd} , \qquad (3)$$

where V_ℓ is the loop voltage on axis at time t near the end of the flat-top and ψ_{bd} is a "breakdown" loss. The flux swing measured at the plasma surface is compared with $\psi_i+\psi_r-\psi_{bd}$ in figure 1. The model for the resistive loss gave surprisingly good agreement with the data considering that $V_\ell(0)$ was taken constant and the current penetration was not complete in many of the high current, high field discharges. ψ_{bd} was found to be typically 1-3Wb. The points with the largest flux swings include 2MA discharges with a total pulse duration of 20 seconds to the end of the flat-top and a 5MA pulse with little flat-top.

Dependence on Breakdown Voltage and Current Ramp-rate

The dependence of the volt-seconds consumption on breakdown voltage has been determined by varying the premagnetisation current of the ohmic primary and measuring the total flux swing at the end of the flat-top of 2MA discharges. At breakdown the premagnetisation current is diverted through a resistor across the primary whose value determines the breakdown voltage and decay time. As a consequence, increasing the breakdown voltage with the resistance fixed also increased the plasma current ramp-rate. Therefore the flux consumption of a series of discharges with constant breakdown conditions and a varying ramp-rate was studied to separate the two effects.

The total flux-swing is plotted against breakdown voltage in Figure 2. The filling pressure was increased in proportion to the breakdown voltage. It may be seen that as the breakdown increased from 8 to 27 volts the flux consumed went up by 2.5Wb. Since the 2.5Wb loss corresponds to one third of the extra flux obtained by raising the premagnetisation current, this limits the plasma current that is achievable.

The effects of varying the current ramp-rate after breakdown are illustrated in Figure 3. The flux consumed at the end of the current rise and the end of the flat-top is plotted against ramp-rate. The flux is a decreasing function of ramp-rate at the end of the rise because of the drop in inductance and the reduced time for resistive dissipation. However at the end of the flat-top this difference has disappeared because the current has penetrated. The "path independence" of the flux consumption has been confirmed in other discharges where the current was increased half-way through the flat-top. We would conclude form this that the increased losses during the breakdown voltage scan occurred at breakdown and not in the current rise.

Summary and Conclusions

It has been found that the total flux consumption of a JET discharge is well represented by a simple model for the internal flux and resistive consumption on axis (see Figure 1). To a good approximation, the flux

consumed after current penetration is complete is independent of the current ramp-rate up to 2.0MA.s^{-1}. Lowering the breakdown voltage from 27 to 8 volts saved 2.5Wb.

Under normal operating conditions, only half the maximum magnetising current is used. A further increase of the magnetisation current does not raise the plasma current significantly because of the increased breakdown losses. The flux that is unavailable because of the extra losses and the limit on the maximum stable current ramp-rate amounts to some 8 Wb or 10 seconds flat-top at 5MA, 3.4T. Making use of this flux is now the main aim of the future development of the JET ohmic heating circuit. The success of the simple model for flux consumption encourages us to believe that 7MA operation is possible in JET with $\beta_p \sim 1$.

References

[1] M Brusati, J P Christiansen, J G Cordey, K Jarrett, E Lazzaro, R T Ross, Comp. Phys. Rep. 1 (1984) p345.

[2] By F Alladio and F Chrisanti, CRE-Associazione Euratom-ENEA, Frascati, Italy.

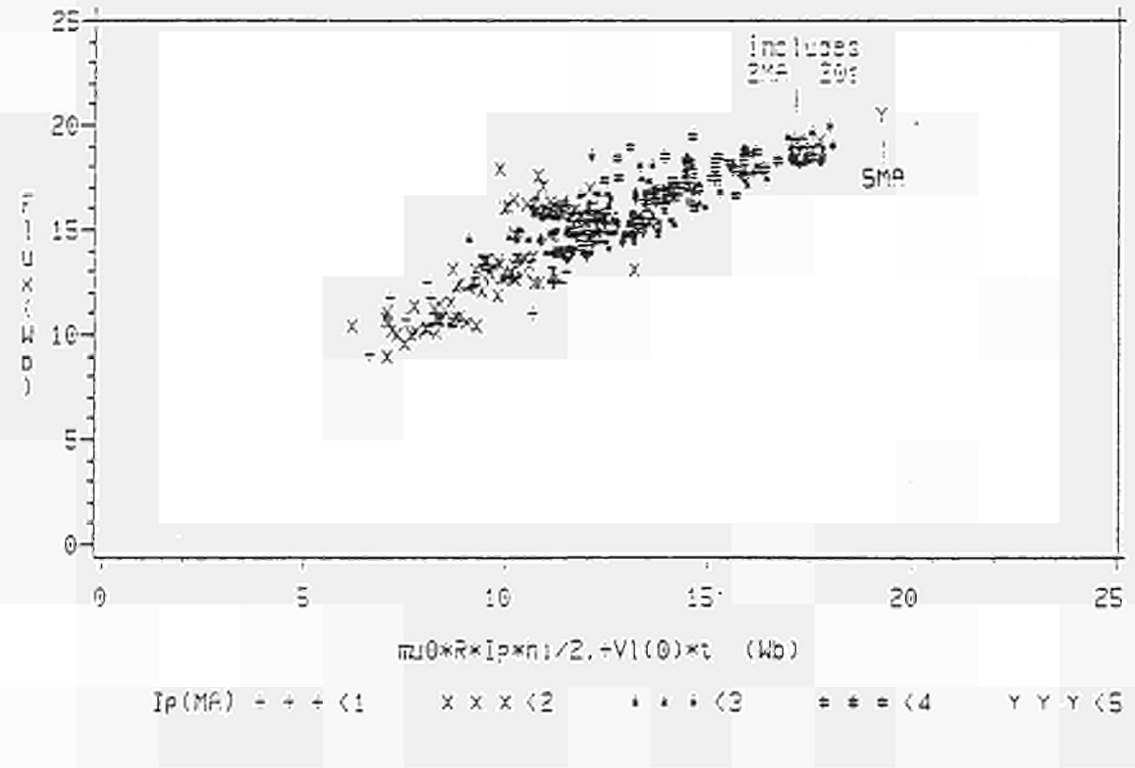

Figure 1
The flux swing measured at the plasma surface against the simple model given in equations 2 and 3. Points with different plasma currents are distinguished.

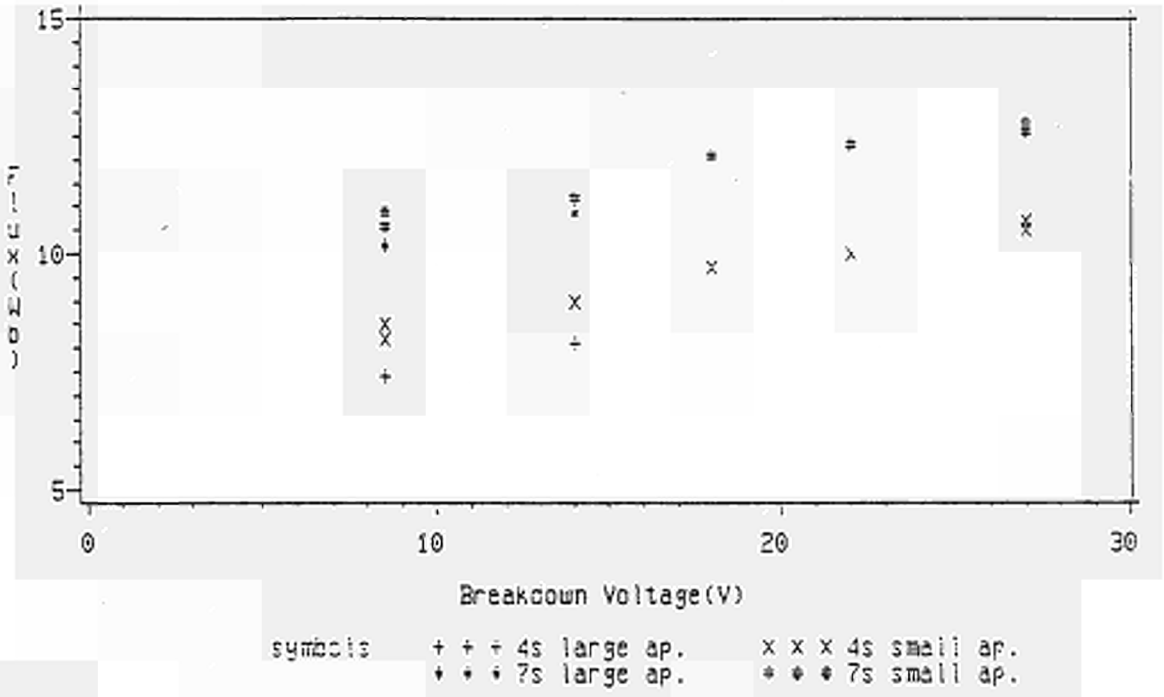

Figure 2
The surface flux swing against breakdown voltage for a series of 2.1MA, 2.6T, b/a=1.38 discharges. The measurement times were 4 and 7s after breakdown and the initial minor radius was either 0.8m (small) or 1.05m (large) minor radius. The filling pressure was increased with the breakdown voltage to keep $E/_p \approx 1.5 \times 10^4 V.m^{-1}mb^{-1}$.

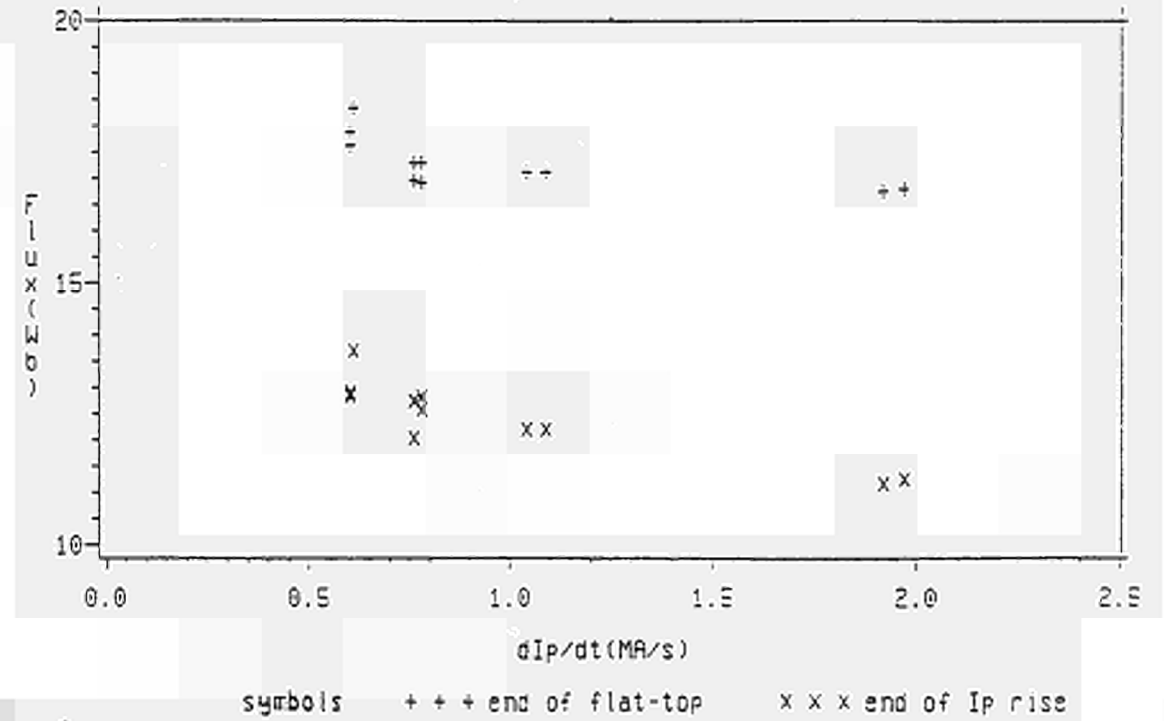

Figure 3
The surface flux-swing against current ramp-rate for discharges with I_p=2.6-2.8MA, a=1.16m and b/a=1.37. The two sets of points correspond to the end of the current rise and the end of the flat-top.

Plasma Evolution and Skin-Effects in JET

F C Schüller, P R Thomas, A Kellman*, E Lazzaro, P Lomas,
H W Piekaar+, A Tanga
JET Joint Undertaking, Abingdon, Oxon OX14 3EA
*GA Technologies, La Jolla, Cal. USA
+Euratom-FOM Association, Nieuwegein, The Netherlands

Introduction

The evolution of a plasma pulse in JET can be described by defining a number of phases and transitions between them (TABLE I). In the following the experimental conditions for successful transitions will be given and it will be shown that skin current effects are important.

Breakdown/Townsend Phase

The only two necessary conditions to enter this phase are:

a) A poloidal field null should be somewhere in the vessel. This requires an accuracy of the vertical field control of $2 \cdot 10^{-3}$T.

b) $E_t/p > 5 \cdot 10^3$ Vm^{-1} $mbar^{-1}$

Whilst obtaining some breakdown is not difficult, the sustainment and transition to the next phase was not always successful. The usual predictions of the charged particle loss rate along magnetic field lines intersecting the vessel wall allows for JET a ratio of $B_\perp/B_t$ of 10^{-2}. In reality for sustainment it is found that the area within which $B_\perp/B_t < 10^{-3}$ must be a substantial fraction of the vessel cross-section. These requirements became even more stringent when the vessel was dirty. Lowering the prefill in order to raise E_t/p didn't help, but increasing E_t was very effective. This lead to the hypothesis that it was not the loss-rate which was too high but the ionisation-rates which were too low compared with expectations. It is a well known effect in gaseous discharges that inelastic electron-impurity collisions deplete the high energy tail of the electron velocity distribution thereby lowering the ionisation rate for a given E/p. The condition to reach the next phase can only phrased qualitatively:

c) the applied loop voltage should be large enough to ensure sufficient ionisation in the presence of impurities and the cross-sectional area within which $B_\perp/B_t < 10^{-3}$ should be at least substantial.

Cold Coulomb Collisions Phase In contrast with the preceding phase here it is the energy balance which controls the evolution since the plasma has to burn through the low Z radiation barrier. Only rarely does this phase fail to reach the next phase but the quality of the plasma can affect the success of further stages. Depending on wall conditions one can raise $\dot{I}$ from near to zero to 5MA/s by decreasing the prefill, increasing E_t, or increasing the aperture. However too large $\dot{I}$ leads to excessive MHD-activity, strongly hollow Te-profiles and extra impurity influx. Too low $\dot{I}$ costs V.sec. [1]. Emperically it is found that:

d) a successful end of the cold radiative phase is obtained by tuning prefill and initial aperture such that with given loop voltage the resulting $\dot{I}$ is between 2 and 3 MA/s.

Magnetic Field Diffusion Phase - Inward. In this phase the current ramp-rate has been varied under different conditions: constant/expanding aperture. constant/ramped toroidal field, low/high $\partial\bar{n}/\partial t$:

- with constant aperture and B_t current ramp-rates up to 1MA/s didn't show MHD-activity nor anomalous penetration [2]. Above 1MA/s some MHD can be observed but not enough pulses are available yet for extensive study. Scaling experiments in ASDEX [3] predicted MHD-activity and anomalous penetration from 0.8MA/s upwards and disruptions above 1.3MA/s.
- With expanding cross-section ramp-rates up to 2MA/s didn't show any MHD-activity. In these pulses q_a was kept close to constant. Similar effects could be obtained by simultaneous ramp of I and B_t. Both methods require some extra initial V.sec. because of low initial $\dot{q}_a$, but the overall gain in flat-top duration is still positive.
- strong inward diffusion of particles has been observed which means a VxB-term in Ohm's Law of near equal magnitude to the applied E_t. Simultaneous ramp of n and I seems to facilitate simultaneous inward diffusion of particles and field.
  e) strong gas introduction is beneficial but the density limit is somewhat lower than in later phases and should obviously be avoided.

Relaxation Phase. In this first part of the flat-top net inward particle diffusion stops and the VxB-term in Ohm's law becomes neglectable. Skin current effects die down on a timescale between 1 and 4 seconds: ℓ_i still increases; the sawtooth inversion radius continues to increase; the shaping coil current has to increase to keep the elongation constant. An increase and then decrease of MHD-activity is noticeable (see Fig. 1) if $\dot{I}$ was large in the preceding rise-phase. Seemingly the profile relaxes from one stable situation with skin-current to another stable one without skin current by passing through an unstable situation. Quite often this passage leads to a disruption just about 1 sec into the flat-top:

  f) Ramp-rates above 1MA/s with constant B and aperture during the rise-phase enhances the chance of disruption in the early flat-top.

Stationary Phase: The confinement results obtained during this phase are described elsewhere [4]. Sometimes the relaxation took so much of the flat-top duration that no stationary state was reached.

Diffusive Decay Phase In this phase skin-effects as well as outward particle and energy diffusion are coupled:

- o high values of $\Lambda=\beta_p+\ell_i/2>2$;
- o sawteething goes on for seconds during current-decay;
- o the density decreases proportional to I_p with no change in profile; as in the rise-phase this means that VxB is very important in Ohm's Law and for the magnetic field diffusion rate;
- o close to the high density limit sometimes "marfes" occur i.e. strong poloidal asymmetries in density and radiation distribution. These change the density decay markedly and might initiate a high density disruption [5] See Fig. 1 at t=15.5.

Table I
Evolution of JET Pulses showing correspondence between control technical phases and physics processes.

Machine Control Phases	Physics Process Phases
t=0.0	t=0.0
Fast Rise: o no current feedback o Ohmic drive by $V=V_1 \exp[-t/t_1]$ $6<V<30$; $0.2<t_1<0.85$s; $1<\dot{I}<5$MA/s o no density control before t=0.2 filling pressure 10^{-5}-10^{-4}mb H_2/D_2 o position control when $I>100$kA $0.4<a<1.0$ o mostly constant B_t: $0.15<B_t<3.4$T sometimes $\dot{B}=0.5$T/s	Breakdown/Townsend Phase o ionisation by electron neutral collisions competes with particle loss along field lines o $I_p<100$kA; $\bar{n}<10^{18}m^{-3}$
t=0.4-0.8	t=0.02-0.05
	Cold Coulomb Collision Phase: o low Z-radiation competes with ohmic input o $I_p<300$kA; $\bar{n}<10^{19}m^{-3}$; $T<50$eV
	t=0.1-0.3
	Magnetic Diffusion-Inward: o inward diffusion of B_{pol}, particles and energy o diffusion equation coupled: VxB not neglectable in Ohms Law o classical or anomalous skin diffusion
Slow Rise: o current feedback requested $0.2<\dot{I}<2.0$MA/s o density feedback: $0.1<\dot{\bar{n}}<1.10^{19}m^{-3}s^{-1}$ o position and shape feedback: expanding aperture a=0.8→1.2m o toroidal field normally constant: $1.3<B_t<3.4$T sometimes $\dot{B}=0.5$T/s	
t=2.5-6.0	t=2.5-6.0
	Relaxation Phase: o magnetic diffusion without strong driving terms
	t=(2.5-6)+(1-4)
Flat-top: control facilities identical to Slow Rise with appropriate control parameters kept constant	Stationary Phase o time-derivatives small in balance equations o at a high current this phase cannot be reached
t=8.0-20.0	t=8.0-20.0
Termination: o no current feedback Ohmic drive negative due to coil resistance: $-1.5<V<0$; $-1<\dot{I}<-0.3$MA/s o no density control: all gas feed stopped o full position and shape feedback o toroidal field decoy with	Diffusive Decay Phase o outward diffusion of B_p, n and T o again strong skin effect: o high $\Lambda=\beta_p+\ell_i/2>2$ o $n \propto I$ unless "marfes" o again VxB important o surplus particles pumped by wall?
t=12.0-25.0	t=12.0-25.0
End of Plasma: $I_p=0$	

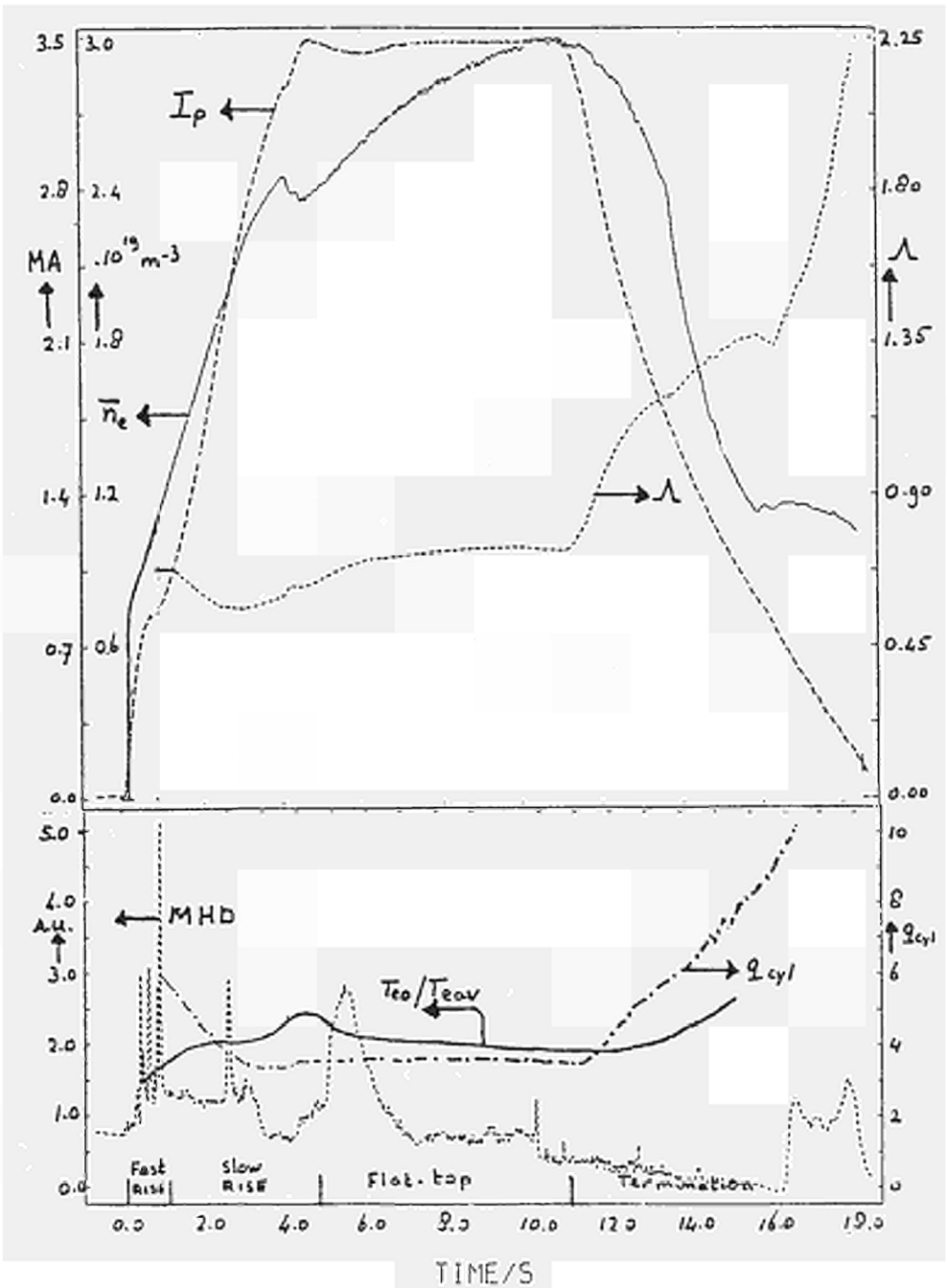

Fig.1. The evolution of pulse 5507: I(t) and $\bar{n}(t)$ as given; B_t=3.4T; R=2.98m; a=1.20m; b/a=1.47; T_{eo} (t=10)=3.5KeV. Note the MHD-activity during: a)fast-rise; b)slow-rise when I>1.0MA/s; c)the relaxation phase; d)the termination phase when a "marfe" has spoiled the density decay.

References:

[1] P R Thomas et al. This conference.
[2] J P Christiansen et al. This conference.
[3] F Karger et al. Post Dead-line paper EPS Conference Aachen 1983.
[4] J G Cordey et al. This conference.
[5] J O'Rourke et al. This conference.

IMPURITY SOURCES AND IMPURITY FLUXES IN THE JET TOKAMAK

M F Stamp, K H Behringer, M J Forrest*,
P D Morgan, H P Summers

JET Joint Undertaking, Abingdon, Oxon OX14 3EA, UK
* EURATOM-UKAEA Association, Culham Laboratory, Abingdon, Oxon OX14 3DB, UK

INTRODUCTION

Spectral lines from hydrogen and low ionization stages of impurities (C, O, Cl, Cr, Ni) have been studied routinely in JET by means of visible spectroscopy. The plasma light, collected along selected chords terminating on the upper torus walls (vertical chords) or on carbon limiters or an RF antenna (horizontal chords), is relayed to spectrometers or narrow band interference filters outside the torus hall by about 100 m long optical fibres. Since the use of fibres restricts the wavelength range to $\lambda > 380$ nm, a close coupled spectrometer is mounted on the torus, viewing a carbon limiter in the extended range down to about 200 nm. Calibrated signals from these instruments are used for determining the local influxes Γ of hydrogen and impurities from walls and limiters, and for calculating the integral fluxes ϕ by multiplying by the respective areas.

METHOD OF ANALYSIS

The neutral particles are ionized in a narrow shell at the plasma periphery. Under the usual conditions of negligible recombination, the ionisation rate per unit surface area, integrated over the shell width, equals the neutral influx density Γ_o. Since ionisation and excitation rates are closely correlated, Γ_o may be derived from the line-of-sight intensities of neutral line emission, essentially by multiplying the number of photons by the ratio of ionisation coefficient S over excitation coefficient X. Within certain limitations, spectral lines from low ionisation stages can also be used for flux measurements. The results are less localised and corrections must be made for losses in lower ionisation stages. According to transport calculations, these corrections are small for limiter fluxes and about a factor of two for wall fluxes in the cases discussed here.

The majority of the observed atoms and ions have metastable levels with high statistical weights in an alternative spin system from that of the ground level. Therefore, the influxes of ground state and metastable state particles have been measured separately. This is done by analysing lines of the different spin systems, relying on the fact that excitation rates within a spin system are much larger than inter-system excitation rates. According to the present analysis, the population of metastable levels in O II, O III and C III is comparable to the ground state population, while it is much lower in C II and Cr I. In the latter cases it appears sufficient to investigate the ground state system only, in order to obtain the influx density.

The excitation rate coefficients required, mainly non-dipole transitions, were calculated by an atomic physics code. In some cases, the results are confirmed by more elaborate treatments available in the literature (eg Mann

/1/ for C II). Ionisation rate coefficients are taken from Lotz /2/. As an example, Fig.1 shows the S/X ratio for C II 657.8 mn (ground state system), C II 514.5 mn (metastable system) and Cr I (ground state system) as a function of temperature. In the analysis, temperatures for the plasma boundary have been taken from ECE and Langmuir probe measurements.

RESULTS

As demonstrated by the signals in Fig.2, the influxes of hydrogen and light impurities (C, O, Cl) scale roughly with $\bar{n}_e^2$. They are insensitive to the plasma current I_p. This means that light impurity production does not depend on temperature but on the number of recycling hydrogen particles. Throughout the JET operation period, ϕ_C was in the range 10-20% ϕ_H, with about equal contributions from walls and limiters. For oxygen, wall and limiter fluxes were also found to be about equal, but their magnitude was much more variable, ie $\phi_O \tilde{\sim}$ 20% ϕ_H after a major opening of the torus and $\phi_O \tilde{\sim}$ 2% ϕ_H after long operation and repetitive carbonisation of the vacuum vessel. During the JET start-up phase, chlorine influxes were observed, which were comparable to the hydrogen fluxes. ϕ_{Cl} decreased rapidly during operation and as a consequence of cleaning methods; it is now below 1% ϕ_H. All light impurity influxes from the top and bottom of the vessel increased substantially with reduced plasma-wall distance, ie large values of the vertical plasma dimension b. This behaviour is shown in Fig.3.

The carbon limiters have been identified as the main source of metal impurities in JET. During the first weeks of operation with new carbon tiles metal influxes from the limiters were not measurable. Later on, the graphite was coated by wall material (Inconel 600) as a consequence of tokamak operation and glow-discharge cleaning. Then, metal fluxes of 2% ϕ_H were observed for $\bar{n}_e = 2.10^{19}$ m^{-3} and $I_p = 2$ MA. This production yield can be explained by a combination of hydrogen and impurity sputtering at $T_e \tilde{\sim}$ 100 eV, even if the carbon surface is only partly covered by metals. The metal influxes increased with I_p and, as shown for chromium in Fig.2, decreased with $\bar{n}_e$. The signals from the torus walls were usually below the detection limit, ie less than 10% of the limiter fluxes.

The consequences of pulse-discharge-cleaning (PDC, 12000 pulses) and of carbonisation of the vessel walls are demonstrated in Fig.4. Carbon and oxygen fluxes were lower after PDC, but higher chromium signals indicated an increased metal deposition on the limiter surface. Carbonisation lead to a substantial reduction of oxygen, chlorine and chromium signals. Although the carbon flux was higher, the resulting plasmas were cleaner as demonstrated by lower Z_{eff} values from visible bremsstrahlung and radiated power. Because of the latter fact the limiters heated up to temperatures of 1700 K and a sudden increase in metal influx was observed, which is attributed to metal evaporation. During these limiter temperature excursions the carbon influx, as derived from C II signals, followed the electron density in the usual way. There was no indication of the existence of chemical sputtering expected to occur around carbon surface temperatures of 900 K. On the other hand, the high carbon yield measured could be indicative of a temperature independent chemical release mechanism.

During ICRF heating of JET plasmas, the limiter fluxes of deuterium and light impurities behave normally, ie scale with $\bar{n}_e^2$. However, the wall fluxes increase substantially and approximately linearly with RF power, as shown in Fig.5. For $P_{RF} \tilde{\sim}$ 5 MW, the deuterium wall flux is about 5 times higher and the carbon wall flux is 7 times higher than before RF. Impurity influxes from

the antennae show the same behaviour as the limiters, but with an additional small power-dependent influx when the antenna is active. From these results, an increase in light impurity content in the plasma must be expected, which may only be small due to the efficient screening of wall influxes. Metal influxes appear to be almost unaffected by RF heating. Z_{eff}, measured from bremsstrahlung, shows very little increase during RF heating.

All the results and trends of impurity influxes, discussed in this paper, are in good agreement with the impurity density behaviour in the plasma interior, as described in "Spectroscopic Measurements of the Impurity Content of JET Plasmas with Ohmic and RF Heating", B Denne et al, at this conference.

REFERENCES

/1/ J B Mann, quoted in Los Alamos Scientific Laboratory Report, LA-6691-MS (1977).

/2/ W Lotz, Lab. Reports IPP 1/62 (1967) and IPP 1/76 (1968), Garching, Germany.

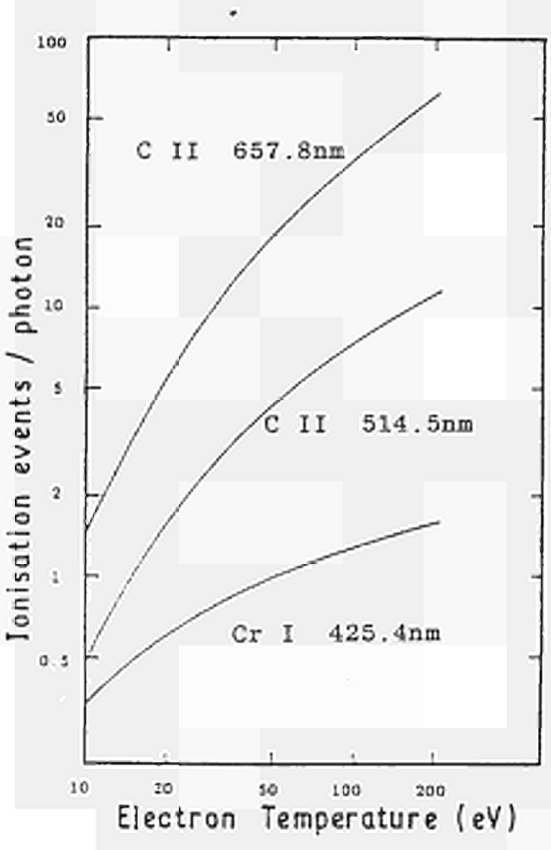

Fig.1 : S/X ratio calculated for C II (metastable system 514.5nm and ground state system 657.8nm) and for Cr I (ground state system).

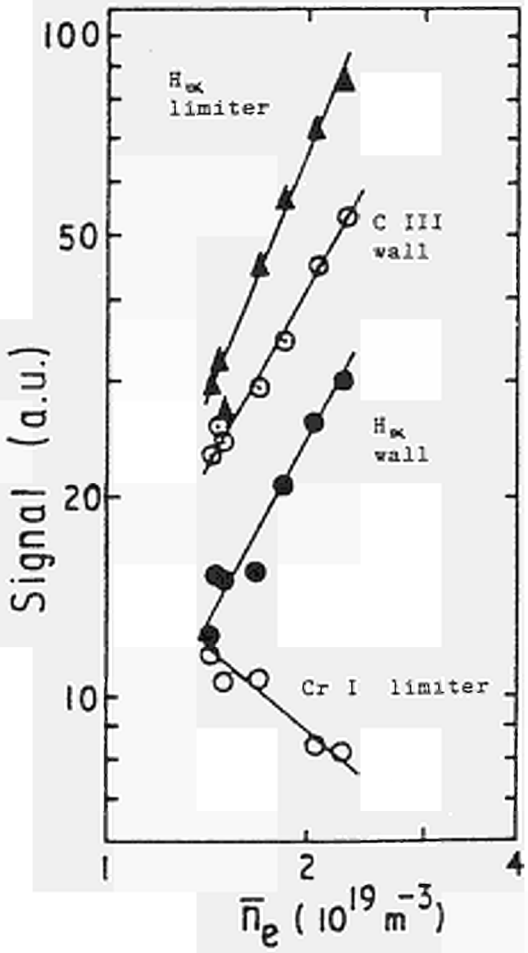

Fig.2 : Variation of hydrogen and impurity influxes with average electron density, $\bar{n}_e$. The data is from similar pulses (#1885-1895) with I_B=1.9-2.2MA, B_T=2.5T, b=1.29m, b/a=1.2.

Fig.3 : Variation of carbon influx with plasma height b. The vessel wall is at 2.1m. The data was taken during the current flat-top, where I_p = 3MA, B_T = 2.6T, a =1.16m.

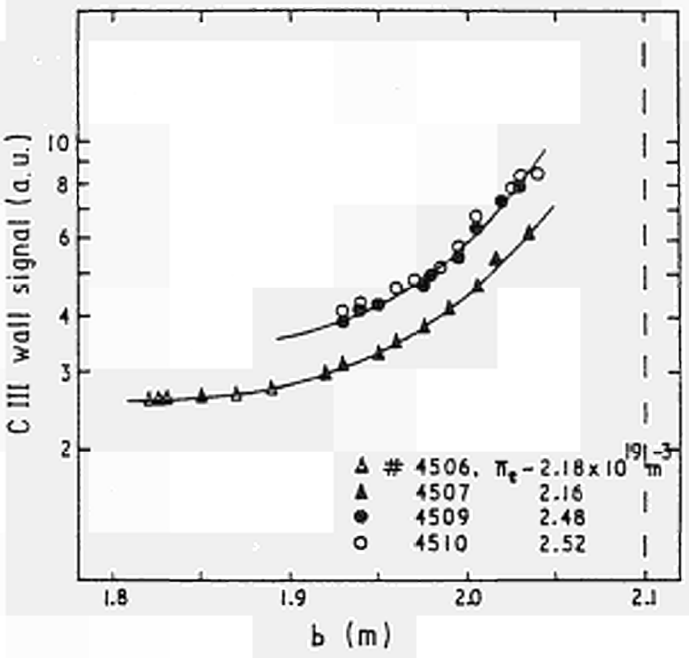

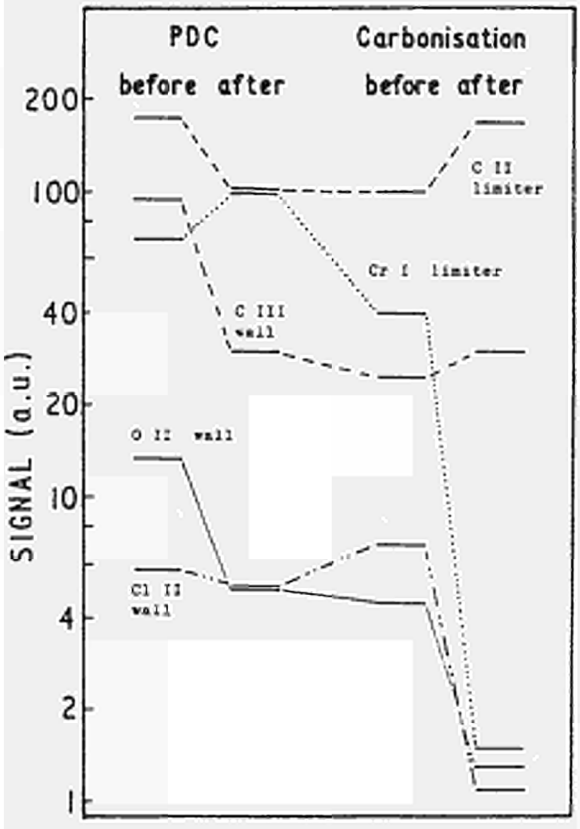

Fig.4 : Changes in impurity influx for reference discharges (I_p ≃ 2.5MA, B_T = 2.6T, $\bar{n}_e$ = 2.0x10^{19} m^{-3}, β_p = 1.5-1.6m, b/a =1.4) as a result of PDC and carbonisation.

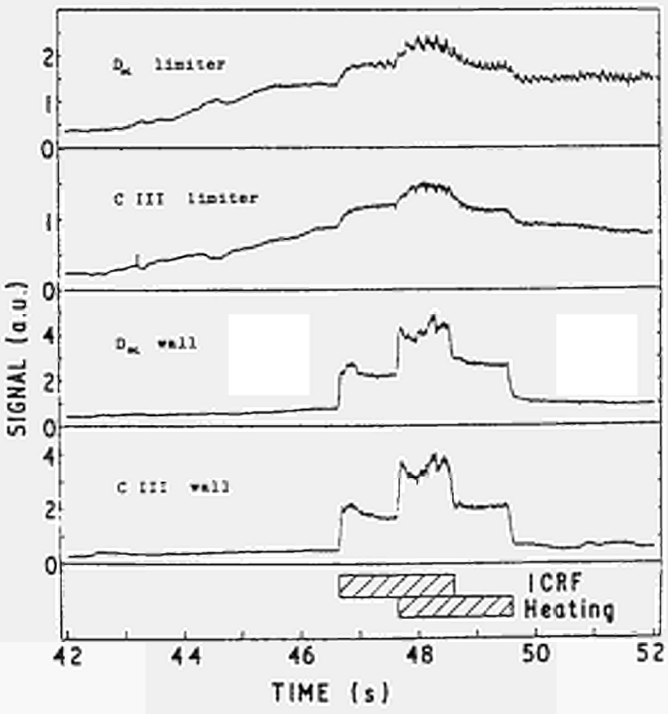

Fig.5 : Carbon and deuterium influxes during a RF heated discharge. Two antennae each couple 2.5MW for two seconds into the plasma. The RF pulses have a one second overlap.

PLASMA-ANTENNA COUPLING AND THE RELATED SCRAPE-OFF LAYER STUDIES ON JET

M. Bureš, M.P. Evrard*, J. Jacquinot, P.P. Lallia and F. Sand

JET Joint Undertaking
Abingdon
Oxon, OX14 3EA, UK

* ERM/KMS, Brussels, Belgium

Introduction

During the first six months of 1985 the four types of different RF antenna configurations [1] were tested on JET. The antenna preformance in terms of coupling efficiency and plasma heating was investigated. In this paper we present the results on plasma-antenna coupling and also discuss the modification of scrape-off layer by RF power. The coupling resistance was measured as a function of plasma-antenna distance at different plasma densities, magnetic fields, frequencies and power levels. The experiments were performed in a deuterium plasma with Helium and Hydrogen gas as minority species. The resonances of RF field in the toroidal cavity were observed when the minority concentration was varied. The maximum power delivered to the transmission line, when operating both antennae was 5.5 MW.

Coupling Efficiency

To assess the overall efficiency of the antenna performance, two antennae were investigated. First antenna with two conductors can be phased either in monopole or dipole configuration (AØ1M, AØ1D) while the second one, having four conductors, can be phased either as dipole or quadrupole, i.e,. AØ2D and

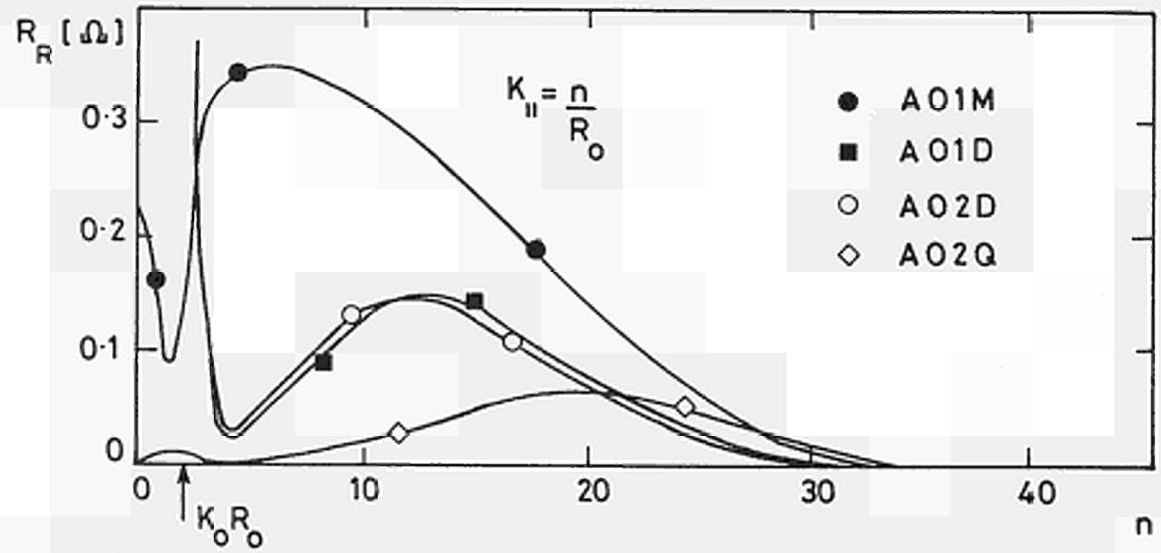

Fig. 1 Radiation resistance spectra for the AØ1 monopole, AØ1 dipole, AØ2 dipole and AØ2 quadrupole antenna configurations. The spectra are symmetric about n = 0.

AØ2Q. The radiation resistance spectra corresponding to the four antenna configurations are shown in Fig.1 as function of the toroidal mode number n. The variation of R_R at low n values are due to the coaxial modes. At present there is no evidence that these modes are excited in JET and when comparing with experimental data, these modes are excluded from model. The coupling resistance was measured by the directional couplers on the transmission line and includes the line and antenna losses $R_s = R_L + R_A \simeq 0.6\ \Omega$ (at 33 MHz). The resistance of the 80 m long transmission line is $R_L \simeq 0.35\ \Omega$. The power coupling efficiency becomes $\eta = P_{Pl}/P_{Gen} = 1 - R_s/R_c$, where $R_c = 2\,P_{Gen}\,(Z_o/\hat{V}_L)^2$. Here $Z_o = 30\ \Omega$ is the characteristic impedance of the line and $\hat{V}_L$ is the maximum voltage. Each antenna is powered by two generators and thus the power

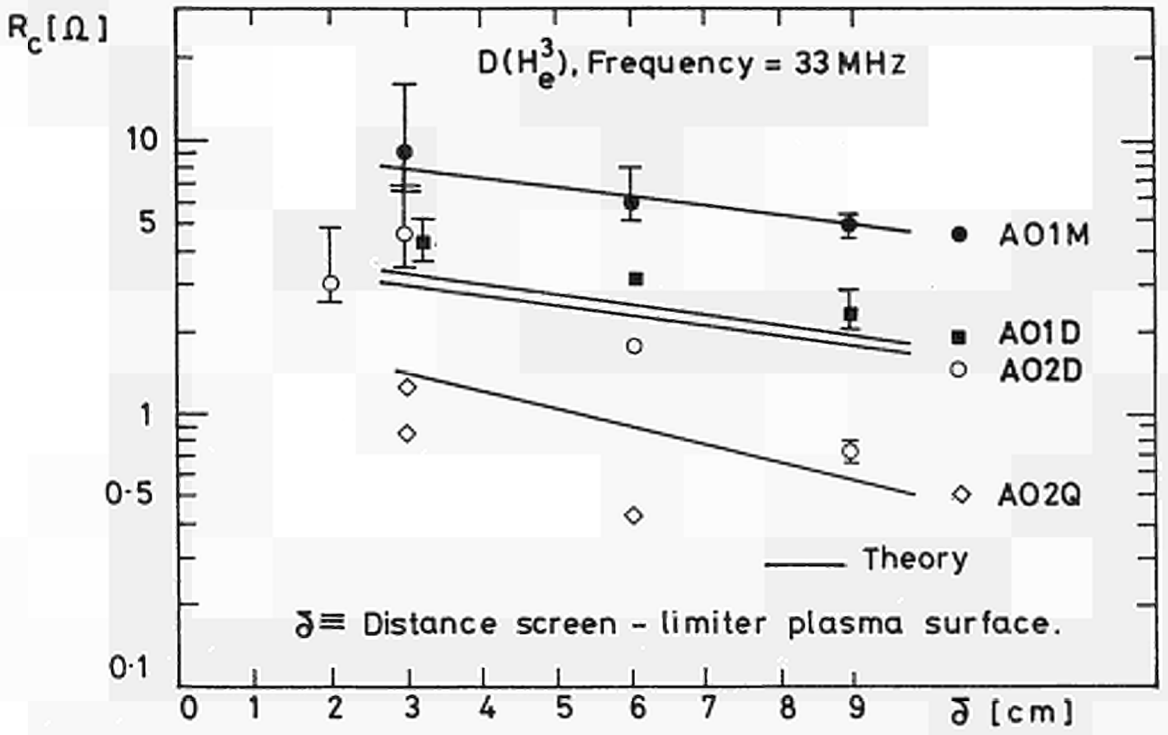

Fig. 2 Coupling resistance as a function of distance antenna screen-limiter plasma surface.

delivered per unit becomes $P_{TOT}(MW) = R_c\ (\Omega)$ when the maximum voltage on the line is $\hat{V}_L = 30$ kV. The coupling efficiency at $\delta = 3$ cm ranges from $\eta =$ 40-60% for quadrupole, 80-92% for dipole and 92-96% for monopole configuration. The tuning is performed close to the generator. The coupling resistance as function of distance screen-limiter plasma surface is plotted in Fig 2. The measured resistances are averaged over the duration of RF pulse (typically 1-2 secs). The indicated range of values reflects the variation of plasma densities over the whole period of operation, i.e., the average density being in range $\langle n_e \rangle \simeq 1.3 - 3.4 \times 10^{19}\ m^{-3}$. The inverse dependence of coupling resistance on δ is clearly seen. The plotted values apply to the $D(H_e^3)$ operation at frequency f = 33 MHz. The 3D theoretical coupling model [2] predicts the measured values with a fair accuracy. The low coupling achieved by the quadrupole antenna could be attributed to the uncertainty about the current distribution in the antenna conductors. Using the prematching stubs close to the antenna, which lower the voltage and therefore the losses of the line, allow for 2 MW of RF power delivered to the quadrupole antenna system. The coupling efficiency in this case becomes $\eta = 0.75\%$.

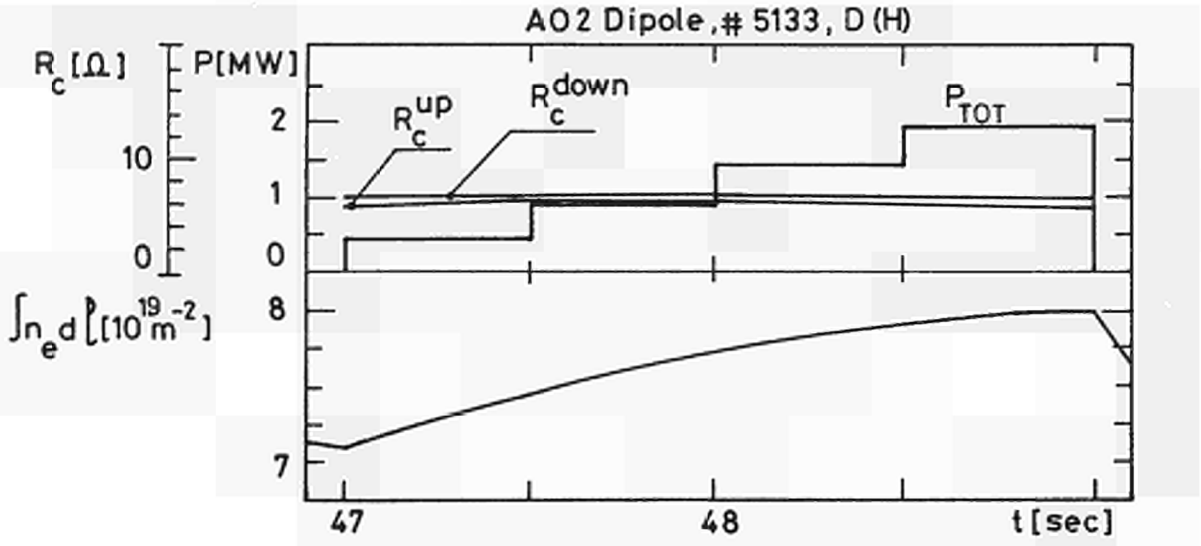

Fig. 3 Coupling resistance, power delivered by generator and plasma line density evolution during the RF pulse.

The low values of coupling resistance at δ = 2 cm were obtained during 1 day operation with typical line density being in the range $\int n_e dl \approx 4\text{-}5 \times 10^{19}$ m^{-2}. Because the antenna was acting as limiter, the scrape-off density e-folding length was $\lambda_n \cong 0$. The coupling resistance is not sensitive to the RF power level as can be seen from Fig 3. The power was increased in 4 steps up to $\approx$ 2 MW. The plasma line density increases by $\approx$ 15% while the coupling resistance remains practically constant.

Scrape-off Layer

During the operation it was observed that the coupling resistance is a function of plasma density measured before the application of RF, as shown in Fig 4. There is an indication that, in JET the discharges with higher densities tend to have a flatter profile. One might be tempted to correlate the coupling resistance to the average density and/or to the flatness of the density profile. However, the calculations indicate that the most important parameters are the density at the plasma surface defined by limiter and the density e-folding length λ_n in the scrape-off. Indeed a typical scrape-off density in JET being $n(a) \cong 3 \times 10^{18}$ m^{-3} is the cut-off density for the $k_{\parallel} = 6$ m^{-1} implying that the $n \leqq 25$ modes (Fig. 1) have its cut-off within the scrape-off. The resistance increase $\approx$ 0.7 Ω per 10^{19} m^{-2} of the line density (measured at the central chord) should be attributed to the corresponding increase of n(a). During the RF pulse the density increase is a function of RF power and can become $\Delta\int n_e dl / \int n_e dl \approx 40\%$ with $\Delta\int n_e dl \cong 2.3 \times 10^{19}$ m^{-2} in the discharges with carbonized wall. The remarkable result is that the coupling resistance during the RF pulse is not correlated to this density increase. We suggest that n(a) is not increased correspondingly which could be explained by the locally Rf enhanced particle diffusion due to the increased fluctuation level or by the recycling due to the fast neutrals. The difference between the resistances observed during the D(H) and D(He^3) operations at 33 MHz cannot be explained only by the change of the magnetic field which is required to maintain the resonance zone in the centre of the plasma cross section. The low values of R_c at the frequencies 26 MHz and 47 MHz illustrate the increased mismatch between the antenna and transmission line when going away from the antenna resonance.

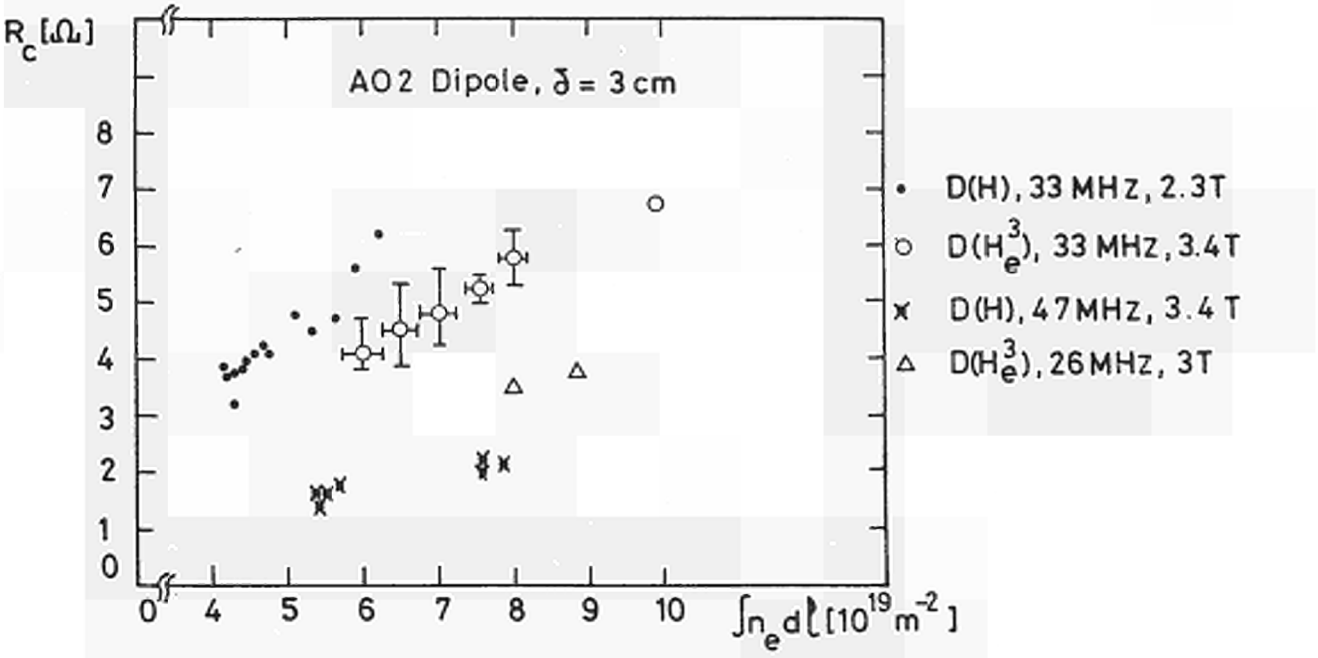

Fig. 4 Coupling resistance as a function of line density measured before the application of RF pulse at different conditions as indicated in the inset.

Toroidal Cavity Modes

During the early operation, one conductor of the AØ2 antenna was used as magnetic probe to pick up the magnetosonic signal excited by the second antenna. When the plasma did not contain the minority species the measured signal was modulated by the appearance of the toroidal cavity modes. The same modulation was observed on the reflected voltage measured on the transmission line. When the Helium minority was injected the modulation decreased as a function of He^3 concentration. At the optimum concentration estimated to be $n_{He^3}/n_e \cong 8\%$, the cavity fields were completely damped.

Conclusions

The coupling resistances measured on the AØ1 and AØ2 antennae allow for the efficient coupling of RF power. The efficiencies $\eta \gtrsim 95\%$ were readily achieved and practically all the RF power which is generated can be coupled to plasma. The measured values show a reasonable agreement with the predictions based on present coupling theories. The dependence of coupling on the scrape-off conditions is observed. The antenna loading conditions allowed for long RF pulses $1 \text{ sec} \leq \Delta t \leq 4 \text{ sec}$.

Acknowledgments

We thank Dr V.P. Bhatnagar for providing us with the computer program [2] developed at ERM, Brussels.

References

[1] Jacquinot J., Arbez J., Beaumont B., Hanley E., Kaye A.S., Lallia P.P. Plancoulaine J., Sand F., Walker C.I., in Proceedings of the 4th Inter. Symp. on Heating in Toroidal Plasmas (Rome 1984) II, 1244.

[2] Bhatnagar V.P. et al, Nuclear Fusion, Vo. 22, No. 2 (1982) 280.

A TWELVE - CHANNEL GRATING POLYCHROMATOR FOR MEASUREMENT OF ELECTRON TEMPERATURE IN JET

B J D Tubbing*, E Barbian*, D J Campbell+, C A J Hugenholtz*,
R M Niestadt*, Th Oyevaar*, H W Piekaar*

JET Joint Undertaking, Abingdon, Oxon, OX14 3EA
* on attachment from FOM Instituut voor Plasmafysica, 'Rijnhuizen',
Nieuwegein, The Netherlands

1. INTRODUCTION

A twelve-channel grating spectrometer for electron cyclotron emission measurements has recently been installed and put into operation at JET. The first measurements have yielded a wealth of information in particular about sawtooth behaviour.

2. THE SPECTROMETER

The spectrometer measures the electron-temperature as a function of time at twelve radial positions along the line of sight of the antenna, using the second harmonic, extraordinary mode e.c.e. emission. It is a grating instrument of the conical diffraction type with twelve exit channels. A prototype is described in [1]. Rotation of the grating allows for shifting of the set of twelve radial positions on a shot to shot basis. The typical spatial range is of the order of 70 cm for a particular grating angle.

Plasma radiation is collected by one of the horizontal JET ECE antennae and transmitted to the spectrometer via an oversized (S band, 34x72 mm) waveguide system approximately 40 m long [2]. The spatial resolution perpendicular to the line of sight is about ±8 cm. The spatial resolution along the line of sight is about ±3 cm as determined by the spectrometers resolving power ($\sim$60).

The grating is used in first order. The spectrometer is also sensitive however to frequencies diffracted in higher grating orders. These frequencies are rejected by low-pass filters, consisting of unidirectional gratings mounted on S band waveguide bends. Two such filters in cascade provide sufficient suppression in the stop band [3].

A radiation chopper with a 95% duty-cycle is incorporated in the feeding waveguide in order to enable signals to be corrected for drift of the amplifiers.

The diffracted radiation in the exit waveguides of the spectrometer is detected by InSb detectors at liquid helium temperature. The electronic signals are amplified, a low-pass filter is applied and the signals are digitised. The maximum electronic bandwidth is 200 kHz, the maximum sampling rate is 1 MHz and there is 16 k words of memory installed for each channel. The noise of the system when expressed in plasma temperature, is about 30 eV r.m.s. at 10 kHz electrical bandwidth.

Calibration of the system is carried out by cross-calibration with the standard JET ECE Michelson interferometer [4].

3. A MAJOR DISRUPTION

The spectrometer has proved to be capable of following the rapid evolution of the temperature profile during major disruptions. An example is provided in Figure 1. The sampling time is 200 μs in this case. The centre of the discharge is approximately at 3.01 m and the limiter is at 4.174 m. Eleven channels cover the range of radii from 2.95 to 3.86 m. In the first stage of the disruption, the central temperature collapses. The effect of the rapid loss of confinement propagates inwards with a velocity of about 1 m/ms. The collapse of the central temperature is shown by the solid lines in the figure. From these successive profiles, it can be seen that the central temperature drops from about 1.7 keV to about 0.9 keV and that over 75% of the minor radius the temperature becomes nearly constant. Outside a radius of 3.7 m, the temperature increases by about 0.2 keV or 30%. Prior to this first phase of the disruption, the central region had a temperature gradient of about 2 keV/m, whereas at the end of this phase the gradient is almost zero. The collapse takes about 600 μs. For the next 400 μs the profile is stationary, existing in a second plateau stage. Then within 200 μs the central region reheats, while maintaining the flat profile; the temperature rises from 0.9 keV to 1.2 keV. This can be seen by comparing the profiles of Figure 1 (broken and solid lines). Finally, a second collapse occurs as shown by the broken line in Figure 1. Within 400 μs nearly all thermal energy is lost. The plasma current was observed to start decaying from this time onwards, going from 2.2 MA to zero in about 40 ms.

4. SAWTOOTH BEHAVIOUR IN THE INNER REGION

Sawtooth activity in JET, which is discussed in detail in [5], has been studied with the grating spectrometer. Figure 2 shows the temperature evolution at 5 different positions during part of a pulse. 2 MW of ICRH is applied at this time. The current centre is at 3.02 m major radius. The toroidal field is 2.0 T. The short straight lines in the traces are not real, but are interpolations across chopper spikes. The noise on the signals is the noise of the amplifiers and detectors.

The figure shows a common phenomenon: two normal and one partial sawtooth (47.45 sec) collapse, the partial one being followed by an oscillation which is probably m=1. The inversion radius at 0.5 m can clearly be distinguished. Comparing sawtooth amplitudes at different positions shows that the inversion radii for the normal and the partial sawteeth are equal to within 4 cm. Sometimes it was observed on other discharges that the partial sawtooth collapse affects the plasma only at major radii $R > R_o$. At radii $R < R_o$ the collapse is not seen and the temperature is affected only by the subsequent oscillation. The oscillation has it's largest amplitude at $R - R_o = 0.26$ m, well inside the inversion radius. It is remarkable that the oscillation on the inversion radius is very small: i.e. about 50 eV (2.5%).

5. SAWTOOTH BEHAVIOUR IN THE OUTER REGION

The sawtooth collapse perturbs the temperature profile by flattening it up to the so-called mixing radius, on a timescale of the order of 0.1 ms. On a much slower timescale the perturbation relaxes by a diffusive process with a heat conduction coefficient $\chi_e(r)$ [6] [7]. For radii outside the mixing radius this effect manifests itself as a heat-pulse propagating outwards. The delay time $t_p(r)$ between the collapse of the sawtooth and the time of the maximum of this pulse for a given minor radius r yields information about $\chi_e(r)$.

Figure 3 shows the temperature evolution for 5 different radial positions. These traces are obtained from the data by averaging over 10 sawteeth,

synchronising them by triggering on their fast edges. In addition digital filters are applied to reduce the noise, especially in the outer channels. The traces are recorded during application of 1.5 MW ICRH and similar traces were obtained for the ohmic phase.

The $t_p(r)$ values for both cases are shown in Figure 54. It is clear that the pulse propagation velocity is very similar for both cases, although the sawtooth amplitude is greatly enhanced by the ICRH. (Central ΔT_e = 500 eV for the ohmic phase and ΔT_e = 1500 eV during ICRH.) It is observed that the mixing radius shifts slightly outwards during the ICRH.

In order to derive χ_e from the measured $t_p(r)$ values a simulation program is used that numerically solves the diffusion equation, in a cylindrical geometry, for given density and initial temperature perturbation profiles. It is assumed that $\chi_e(r)$ is inversely proportional to the density profile n(r).

$$\chi(r)_e = \frac{\chi_{eo}\, n_o}{n(r)} \qquad n(r) = n_o\,(1 - 0.99(\tfrac{r}{a})^2)^{\frac{1}{2}}$$

where χ_{eo} and n_o are central values of χ_e and n. The line drawn in Figure 5.2 shows the $t_p(r)$ for a simulation with χ_{eo} = 1.5 m^2/s n_o = 2.9 x $10^{19} m^{-3}$ and mixing radius r_m = 0.66 m.

Figure 5 shows the corresponding $\chi_e(r)$ in the relevant region of the plasma. The χ_e value is significantly larger than χ_e values obtained from transport codes [8].

ACKNOWLEDGEMENTS

We are indebted to Dr T E Stringer for his co-operation in the heat-pulse studies, to Dr D A Boyd for his analysis of the major disruption data, and to Dr D V Bartlett, Dr A E Costley and Dr S E Kissel for sharing the calibration data from the Michelson interferometer.

REFERENCES

[1] R M J Sillen, H W Piekaar, Th Oyevaar and W Werner, A F.I.R Grating Polychromator Using Conical Diffration as a Diagnostic Tool for E.C.E Plasma Measurements. Infrared Physics, 24, 6, 511 (1984).

[2] E A M Baker et al., Proc. 4th Int. Workshop on ECE and ECRH. Frascati (1984)

[3] E Barbian, D J Campbell and G de Zwart, to be published.

[4] A E Costley et al., Paper 186 this conference.

[5] D J Campbell et. al., Paper 182, this conference.

[6] G Jahns et al., Internal Disruptions in Tokamaks, Nucl. Fusion 18, 5 (1970).

[7] T Bell et al., Measurements of χ_e in ISX-B Beam-Heated Discharges by Heat-Pulse Propagation, Nucl. Fusion, 24, 8 (1984).

[8] M Brusati, J G Cordey, Paper 189, this conference

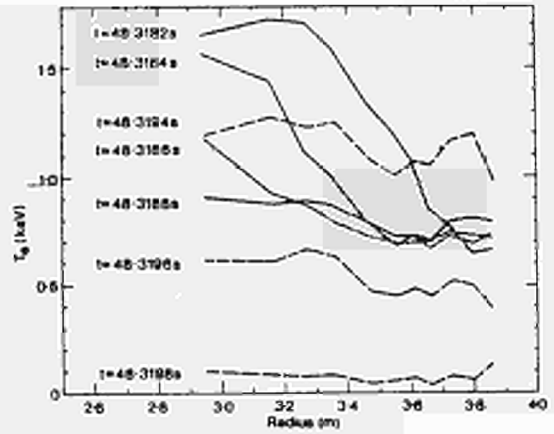

Fig. 1 Profiles during a disruption.

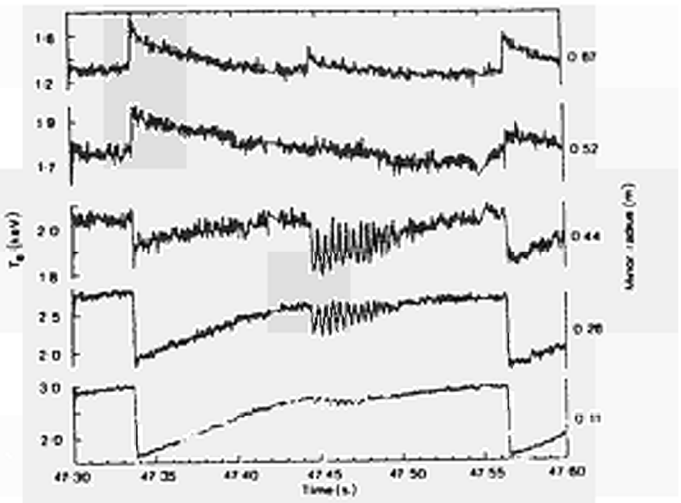

Fig. 2 Sawteeth inside the mixing radius

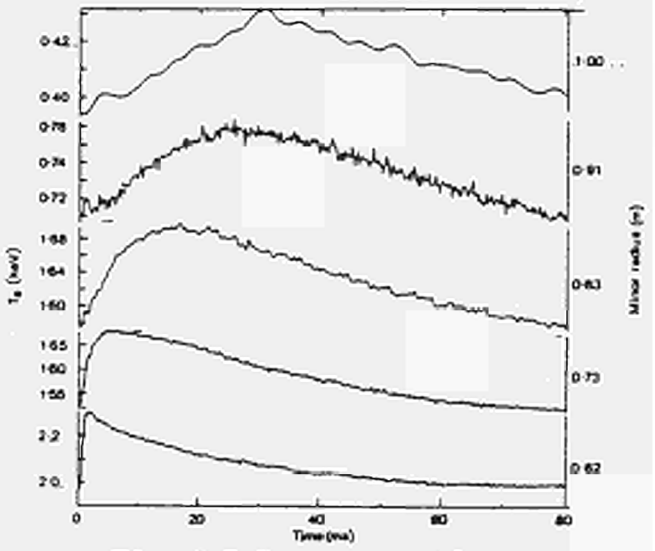

Fig. 3 Pulse propagation

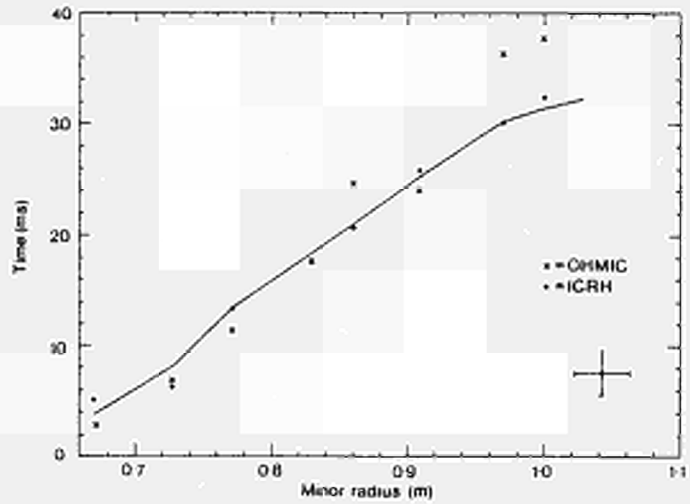

Fig. 4 The time delay values

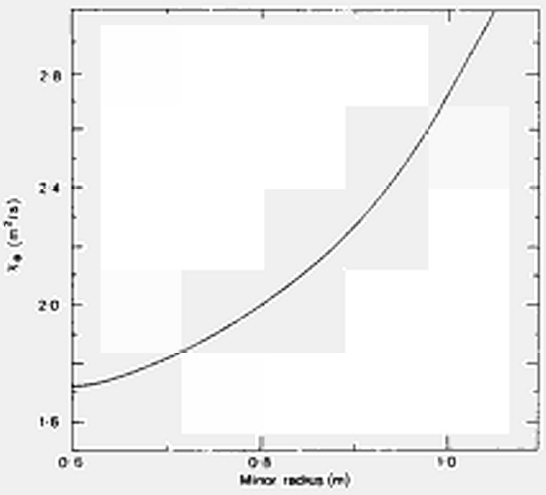

Fig. 5 Heat conductivity ceofficient

ELECTRON POWER DEPOSITION PROFILE DURING ICRF HEATING ON JET

D.J. Gambier[+], D.V. Bartlett, M. Bureš, D.J. Campbell,
G.A. Cottrell, J. Jacquinot, S. Kissel, P.P. Lallia,
R. Niestadt[++], F. Sand, K. Thomsen, B.J.D. Tubbing[++]

JET Joint Undertaking
Abingdon, Oxon, OX14 3EA, UK

[+] Association Euratom CEA sur la Fusion,
Fontenay aux Roses, (France)
[++] FOM Instituut voor Plasmafysica,
Rynhuizen, Nieuwegein, The Netherlands

Abstract

The first measurements of the electron power deposition profile for ICRF heating on JET [1] are presented. In the two-ion regime (H or He^3 in D-H or D-He^3 plasmas), it is found that the power deposited directly to the electrons is strongly peaked within the volume limited by q = 1. Indeed, 'giant' sawteeth have been induced by application of RF at megawatt power levels. The sawtooth amplitude and period appear dependent on both the location of the cyclotron resonance layer and $k_{//}$ spectrum of the antenna.

Introduction

For the minority heating scenario on JET, theoretical models of ICRF [2] predict that when the wave is launched from the low field side, a large fraction of the energy is absorbed in a single transit. As the absorption occurs within the cyclotron resonance layer, it is expected that the power absorbed by the electrons is strongly peaked at the location of the cyclotron layer. Moreover, k-shaping appears crucial for the energy deposited on the electrons [maximum at $k_{//} = 0\ m^{-1}$ for a standard JET ICRF plasma].

The results presented here were obtained during experiments at multi-megawatt ICRF power levels [1]. The main objectives of these experiments were to: (i) study the power deposition profile on the electrons and compare it with a computed ohmic case, (ii) study the effect of the location of the cyclotron resonance layer on sawtooth oscillations, (iii) observe the effect of k shaping on the power deposition profile.

The electron temperature T_e was measured by electron cyclotron emission (ECE) in the second harmonic extraordinary mode, using three different instruments: a 12-channel grating polychromator [3], a Michelson interferometer and a Fabry-Perot interferometer. The Fabry-Perot and the polychromator are cross-calibrated against the Michelson which is absolutely calibrated [4].

A variety of sawtooth behaviour is observed in ohmic plasmas [5]. During ICRF heating at the plasma centre, both the sawtooth amplitude and period may increase by a factor of two or more. The sawtooth oscillation is observed on most of the diagnostic signals, including the line-integrated density, the bolometer signal and (less markedly) the magnetic β.

Power deposition profile

The spatial distribution of the absorbed RF power is determined from the change in $dT_e(r,t)/dt$ measured at the beginning of the sawtooth. As the

electron temperature profile is flat inside the q = 1 surface at this time, the thermal losses may be neglected and the slope of T_e, together with the evolution of $n_e(r,t)$ permits the determination of the total power deposited on the electrons. This hypothesis that the electron thermal losses are low (compared to the input power) is confirmed by the observation that the sawteeth seldom reach saturation.

To deduce the RF power deposition profile, we subtract the quantity $\frac{3}{2}\, d(n_e T_e)/dt$ during the ohmic plateau (before the onset of the RF) from the value obtained during the RF heating. This difference is $P_{RF} + \Delta(P_{ei} - P_{rad} - P_\Omega)$. The ohmic deposition profile is deduced from the q-profile obtained by a numerical analysis of the ohmic discharge. In Fig. 1, we show the ohmic and RF deposition profiles calculated in this way for a D-He^3 plasma with 2.4 MW coupled RF power and 2 MW ohmic power (see Table, case a). The sawtooth inversion radius is at R = 3.6 m and the plasma centre at 3.07 m (the limiter radius is 4.24 m).

The ohmic power density decreases from 0.08 MW/m^3 at the plasma centre to 0.07 MW/m^3 at the inversion radius, while the RF power density falls from 0.09 MW/m^3 to 0.001 MW/m^3. This corresponds to a 15% and a 98% variation respectively, and implies that 0.5 MW of ICRF power is deposited on the electrons within the inversion radius, ie. 20% of the coupled RF power. Assuming a deuterium plasma with 10% He^3, is in fair agreement with the predictions of ray tracing codes [2].

Assuming the ohmic deposition profile is known, it is possible to compute [6] the local confinement time during a sawtooth ($\tau_{st}(r)$) and the average confinement time (after sawtooth averaging) $\bar{\tau}(r)$. Considering the power balance representing the electron temperature during a sawtooth, as well as for T_e averaged at the same radial position, it is possible to derive both the confinement time and the power deposited on electron assuming a simple conservation of (τ_{st}, $\bar{\tau}$) in both ohmic and RF discharges. We supposed $\tau_{st}(\Omega) = \tau_{st}(\Omega + RF)$, which is equivalent to the statement that the losses inside the q = 1 surface are independent of the T_e profile outside q = 1. It then appears (Fig. 1) that this approximation is in agreement with the method of slope subtraction, suggesting that the central confinement time is not strongly affected in the presence of ICRF power, in accordance with plots of the overall increase of T_{eo} with ICRF power [7].

Effect of resonance location on sawtooth activity

The radius of the hydrogen cyclotron resonance, R_{CH}, in a D-H plasma was varied by changing the toroidal magnetic field. Three different radii were used (R_{CH}=3.25, 3.5 and 3.7 m) at constant RF power ($\simeq$ 1.0 MW) and central density (2×10^{19} m^{-3}). The time derivative of the magnetic beta was similar in the three cases ($d\beta/dt$ = constant), as was the change in total energy content ($\Delta\beta \simeq 2 \times 10^{-4}$).

The ion temperature increase, deduced from the neutron ratio, is maximum when the cyclotron layer is located close to the centre of the plasma and smoothly decreases as R_{CH} increases (0.4, 0.3 and 0.2 keV). On the other hand, the electron behaviour is dramatically affected when R_{CH} is increased (Fig. 2).

The central electron temperature (measured by the Fabry-Perot) shows a decreasing sawtooth amplitude and period as R_{CH} moves towards the q = 1 surface. This is shown in Fig. 2. At the largest RF heating radius, the sawteeth are comparable to those observed in the ohmic heating case. However, the bottom of the small RF heating sawteeth is higher than for the large sawteeth, the two effects cancelling so as to give the same volume average temperature in the three cases.

Effect of the antenna k-spectrum on the electron power deposition profile

Using two sets of antennae [1], a monopole (M) and a quadrupole (Q), we were able to shape the $k_{//}$ spectrum emitted by the antenna [$k_{//}$ spectrum centred on 0 (M) and peaked around 7 m^{-1} (Q)]. In the same D-H plasma (see Table, case c), we compared the effect of the two antennae at the same power coupled to the plasma (P_{RF} = 0.8 MW).

Concerning the power deposition profile on electrons (Fig. 3), we expect, from the theoretical point of view, to observe the profile peak for the Q-antenna to be closer to the cyclotron layer and to be wider ($\omega - \omega_{ci} = k_{//} V_{th}$). Indeed, we observe that the power deposition profile in the quadrupole case is shifted towards the resonant layer (R = 3.24 m) by 15 cm while the width at half profile is 20 cm and 25 cm for the M and Q-antennae respectively. The power deposited on the electrons can be roughly estimated as 300 kW in the monopole case and 600 kW in the quadrupole case. Finally the amplitude and period of the sawteeth reach the values [M : 1.1 keV, 130 ms; Q : 0.75 keV, 110 ms].

Although a general observation is that the slope of T_{i_0} at the onset of the RF power and $T_{i\ max}$ are comparable for both the M and Q-antennae, the evolution of the magnetic beta is noticeably different. The slope $d\beta/dt$ at the onset of RF in both D-H and D-He^3 plasmas is higher in the Q-case than in the M-case at the same power [$\dot{\beta}Q/\dot{\beta}M \simeq 1.2 - 2.0$] while $\Delta\beta Q/\Delta\beta M \simeq 1.4$ (case c). This observation indicates that the efficiency of the Q-antenna is greater than the M-antenna.

Conclusions

The RF power deposition profile on the electrons is strongly peaked on JET and appears to be affected both by the localisation of the minority cyclotron resonance layer and the value of the $k_{//}$ spectrum of the antenna. Further experiments, including RF amplitude modulation, will be carried out, and are currently being investigated.

Table : JET ICRF Discharges

case	min	B_T(T)	ν(MHz)	R_{CH}(m)	I_p(MA)	V_L(V)	$T_{eo\Omega}$(keV)	$T_{io\Omega}$(keV)
a	He^3	3.4	33	3.23	2.8	0.7	4	2.2
b	H 5%	2.3	33	3.28	2.0	0.8	2	1.7-1.8
c	H 5%	2.0	29	3.24	2.0	0.75	1.8	1.8

References: [1] J. Jacquinot et al., invited paper, this conference.
[2] M. Brambilla, IPP JET rep. 22 Garching 1984.
[3] B.J.D. Tubbing et al., paper 142, this conference.
[4] A.E. Costley et al, paper 186, this conference.
[5] D.J. Campbell et al, paper 182, this conference.
[6] D.J. Gambier, Thèse d'état 1985.
[7] P.P. Lallia, private communication.

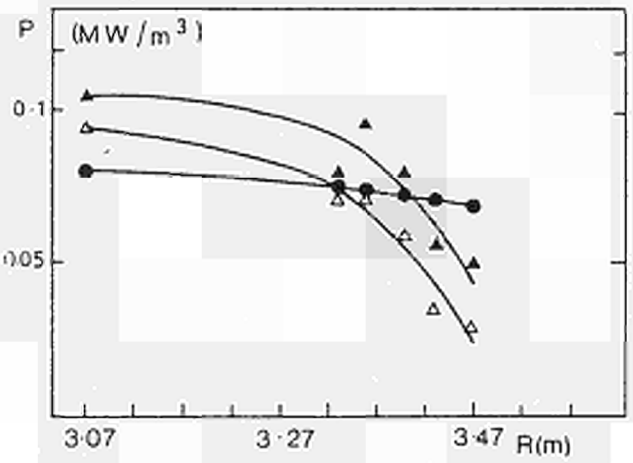

Fig.1. Power deposition profile on electrons

D–He³ P_{RF} = 2·4 MW

● ohmic

△ slope subtraction

▲ τ_{st} = const

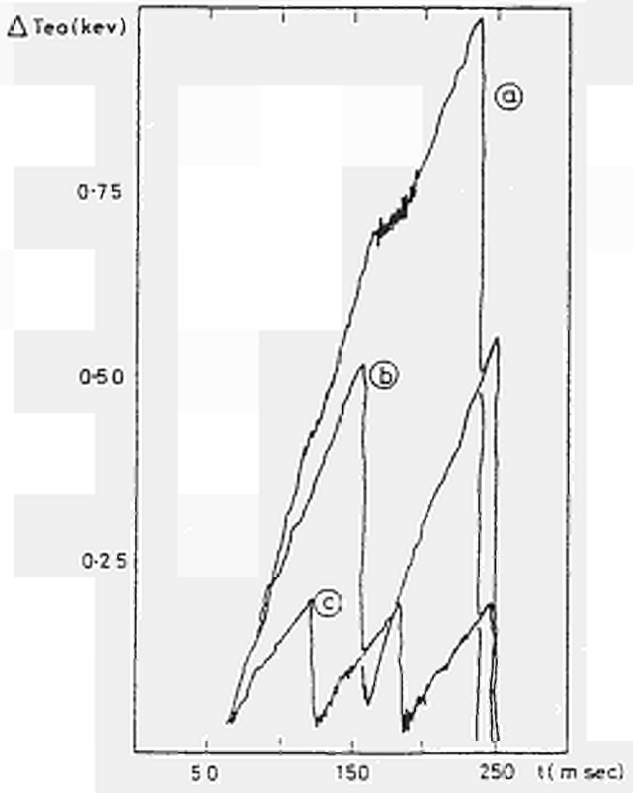

Fig. 2 : Sawtooth evolution vs. time (P_{RF} = 1 MW)
a- B_T = 2.3T (R_{CH} = 3.3 m)
b- B_T = 2.45T (R_{CH} = 3.5 m)
c- B_T = 2.6T (R_{CH} = 3.7 m).

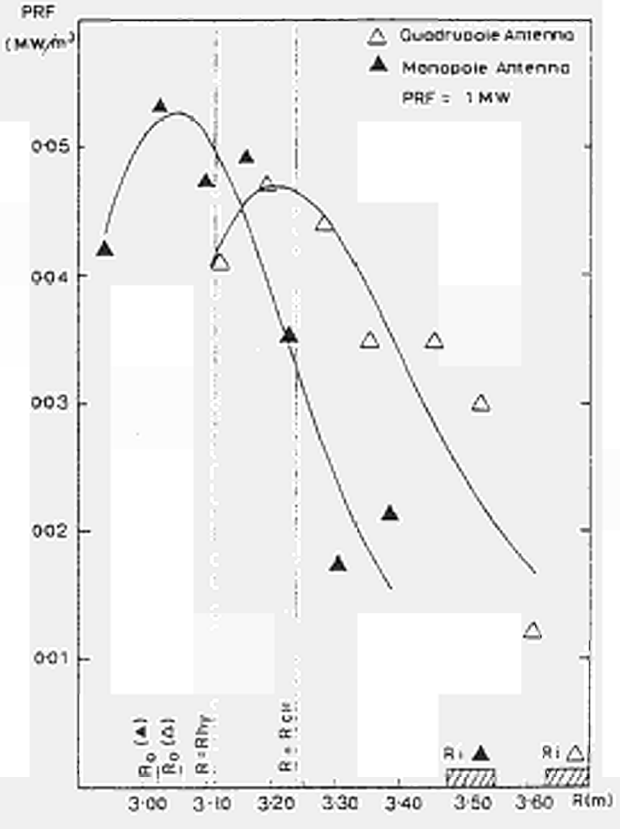

Fig. 3 : Power deposition profile for two $k_{//}$-spectrum [$k_{//}$ centred on 0 m^{-1} (▲) and 7m^{-1} (△)]

STUDIES OF EDGE PHENOMENA IN JET WITH VISIBLE SPECTROSCOPY

P G Carolan*, M J Forrest*, N C Hawkes* and N J Peacock*
JET Joint Undertaking, Abingdon, Oxon OX14 3EA, UK
*Culham Laboratory, Abingdon, Oxon OX14 3DB, UK
(EURATOM/UKAEA Fusion Association)

INTRODUCTION

Visible spectroscopy affords an effective means of studying edge phenomena in JET, by monitoring the behaviour of lowly ionised or neutral states. Here we report on the following edge related topics. (a) effect of RF heating on minority species; (b) MARFES, and (c) Zeeman splitting of impurity lines.

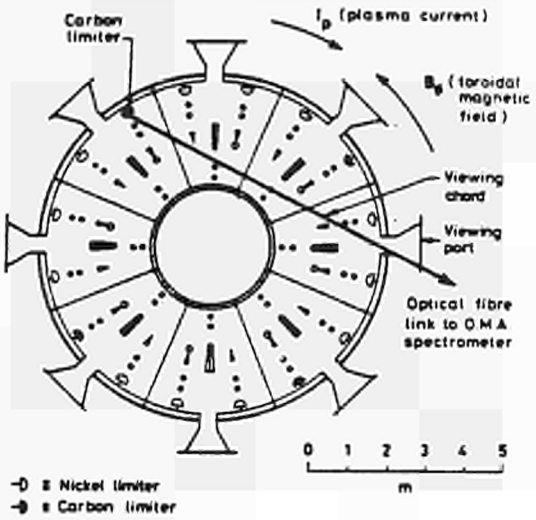

Fig.1 The tangential viewing optics arrangement in JET which obtains a clear view of the carbon limiter.

The experimental arrangement is shown in Fig.1. Light from a tangential chord viewing a carbon limiter is coupled by 120 metres of high transmission 1 mm quartz fibre to a Czerny-Turner spectrometer. A calibrated Optical Multichannel Analyser (OMA) samples 16 nm increments of the output spectrum with a resolution of 0.03 nm and a variable time resolution (set to 196 ms). The available spectral range has been surveyed and the main impurities identified. Impurity atoms and ions of the usual impurities such as O, C, Cr with multiplets conveniently close to the Balmer Series are routinely monitored. The survey aspect of the diagnostic is particularly valuable however in detecting unexpected elements or unforeseen plasma or impurity behaviour.

RESULTS

(a) Effect of RF Heating on the Plasma Edge

RF heating power on JET is coupled to the plasma by minority heating of H or $^3_2$He. Extensive line shape studies have been made of the HeII 468.5 nm line before and during the RF heating pulses. Because there is a significant change in the HeII line shape during high power RF injection, it is possible to evaluate edge plasma heating for a wide range of launched powers and for the various antennae configurations. The analysis is based on a two gaussian best fit programme used after the observed spectral line has been deconvolved using the measured instrumental function. Figure 2a and 2b, show two gaussian fits for the 468.5 nm line before and during RF heating which combined a dipole 0.7 MW, and a monopole 1.75 MW into a 2.8 MA plasma. In each case the two gaussians represent a family of gaussians associated with a cold outer edge region and a hotter zone a few cm inside. The outer zone remains cold (80 eV) before and during RF, presumably because of the heat sink effect of

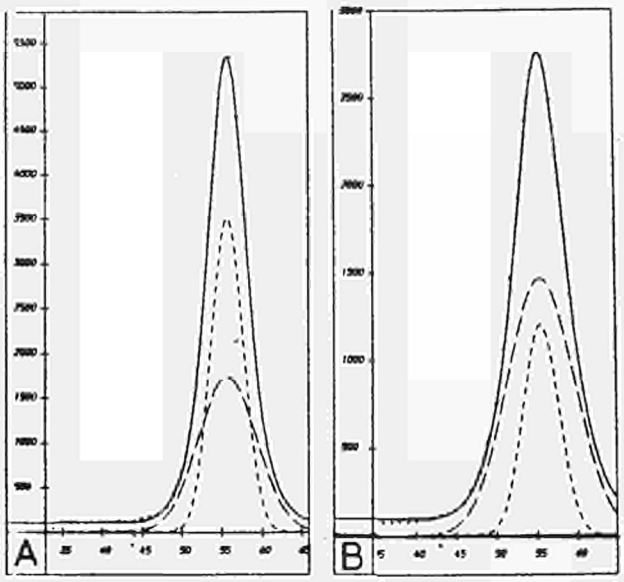

Fig.2 Two Gaussian fits on the HeII 468.5 nm line for (A) before the RF amd (B) during the heating pulse. The solid line is the sum of the two gaussians fitted on the data points while the long and short dashed curves are the 'hot' and 'cold' individual Gaussians components. The offset between the data curve and the two Gaussians has been added for clarity.

effect of the limiters. In contrast the 'hot' zone shows an increase of temperature from 244 eV to 310 eV. From inspection of the areas under the gaussians, it can be seen that before heating they are roughly the same whilst during the RF pulse the hot component is three times that ascribed to the cold edge.

The effect of RF power from the dipole (2.75MW) and then the monopole (2.64MW) antennae in the same plasma shot (3.4T 4MA) is shown in Fig.3. In this example the two gaussian fit reveals an outer layer around 100 eV before and during the pulse - the hotter inner layer remains around 400 eV until the monopole pulse is applied when it increases to ≃ 550eV. The dipole which was switched on 1 second earlier has little effect.

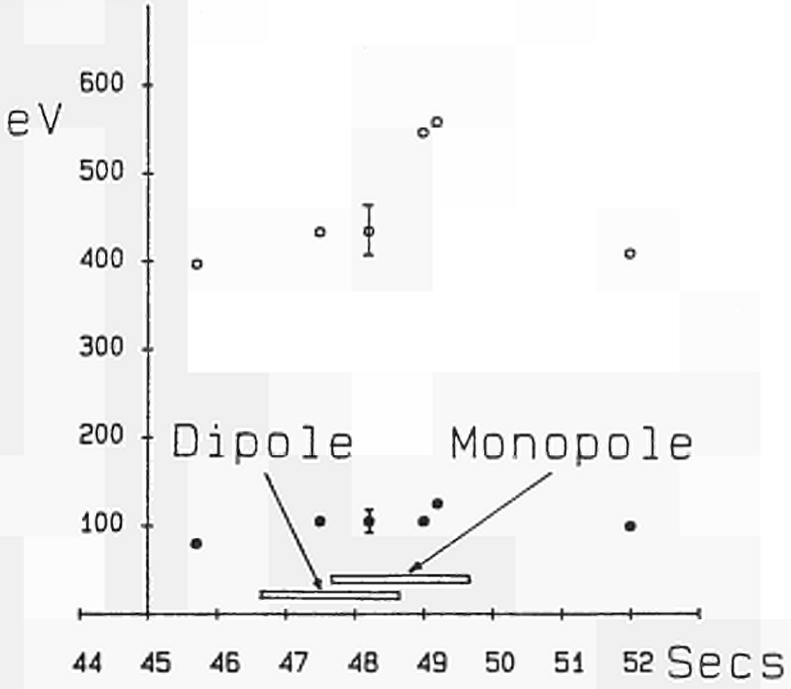

Fig.3 Variation of temperature in the outer edge (filled circles) and hotter inner zone (open circles) for times that span pre RF, dipole emission (D), monopole emission (M) and post RF.

Transport codes indicate that HeII would only exist for a few cm inside the plasma boundary, therefore our measurements show considerable increases in edge temperature for some antenna configuration. The evaluation of the effect of antenna geometry on edge heating is an ongoing study. The results described are for two RF heating experiments and are given to illustrate the value of line shape analysis to determine temperatures in an area normally difficult to diagnose.

(b) MARFES

A MARFE, first reported in Alcator[1] is currently conceived as a toroidally symmetric but poloidally asymmetric band of enhanced radiation - apparently peculiar to tokamaks. MARFE's in JET are characterised by rapid changes in the line emission from low ionisation states of low Z impurities, accompanied by an increase in the n_e and the bolometer signal on the inner edge of the plasma. These are discussed at length [2](this conference) the results in this section represent additional material.

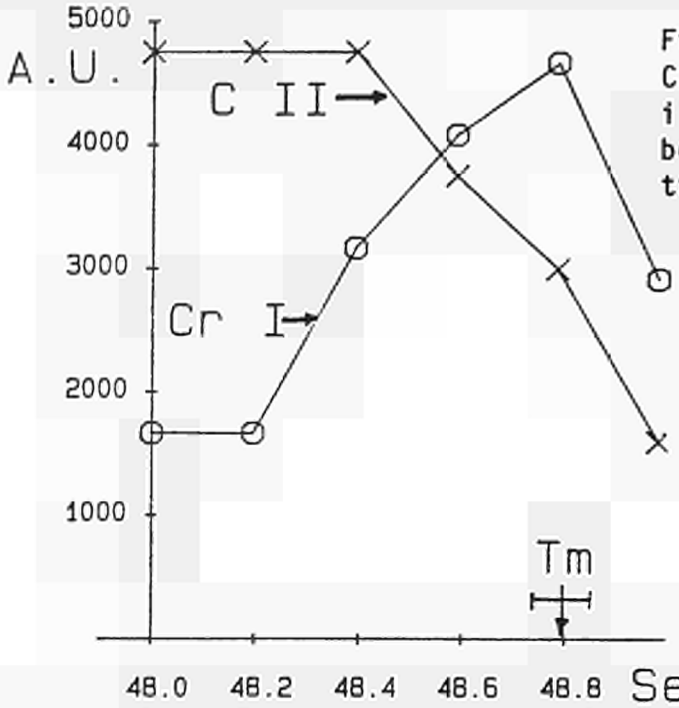

Fig.4 Time history of CII and CrI line intensities illustrating precursor behaviour relative to the MARFE time T_m.

The references[e.g.1] report no change in Te or radiation in the central plasma or in the outer edge. Our findings are contrary to the latter, in that significant changes in the line emission from the plasma in close proximity to the limiter are observed. From comparisons with other lines of sight it has been determined that the tangential viewing chord employed is dominated by limiter rather than wall effects (see next section). Figure 4 shows a time sequence in 200 ms steps illustrating a characteristic drop in CII intensity. The MARFE time as detected by the inboard n_e interferometer channel is indicated. Within the limits of our timing accuracy ± 50 ms it appears that MARFES are signalled some 200 ms earlier by changes in the outer edge emission than by the inner edge interferometer channel. This effect is corroborated by a vertically viewing optical fibre, with photomultiplier detection, which show changes in H_α and CIII intensity some 50 ms after outer edge changes. There is also evidence that the drop in edge CII intensity is preceded by a two fold increase in the Cr influx by some 200 ms, but it is unlikely that this would have a significant effect on the plasma edge behaviour.

(c) Zeeman Splitting

To date Zeeman splitting of the spectral lines HI (6563), CII (5132.9, 5133.3, 5146, 5151, 6578 and 6583), CIII (4794, 4810 and 4819) and Cr I (4254, 4274 and 4289) has been observed[2] in the JET plasma. A representative time sequence of spectra is illustrated in Fig.5 for the CIII triplet at the

termination phase of a discharge. The observations are of particular importance in determining the sources of impurity influx since the location of the emitting regions can be determined from the magnitude of the splitting and the known toroidal field distribution. Localisation of the impurities has been determined at the limiters and at the inside plasma periphery both at the setting up and termination phases. The source of impurities which show Zeeman splitting depends on the initial time history of the plasma profile and the plasma excursions or expansion during termination. The Chlorine spectrum shown in Fig.5 located the influx region at the inner periphery thus showing that the plasma vessel, rather than the limiters, was contaminated at this time (these results were from a discharge which had relatively high Cl influx that was later substantially reduced with the consequent reduction to negligible levels of the line intensities.)

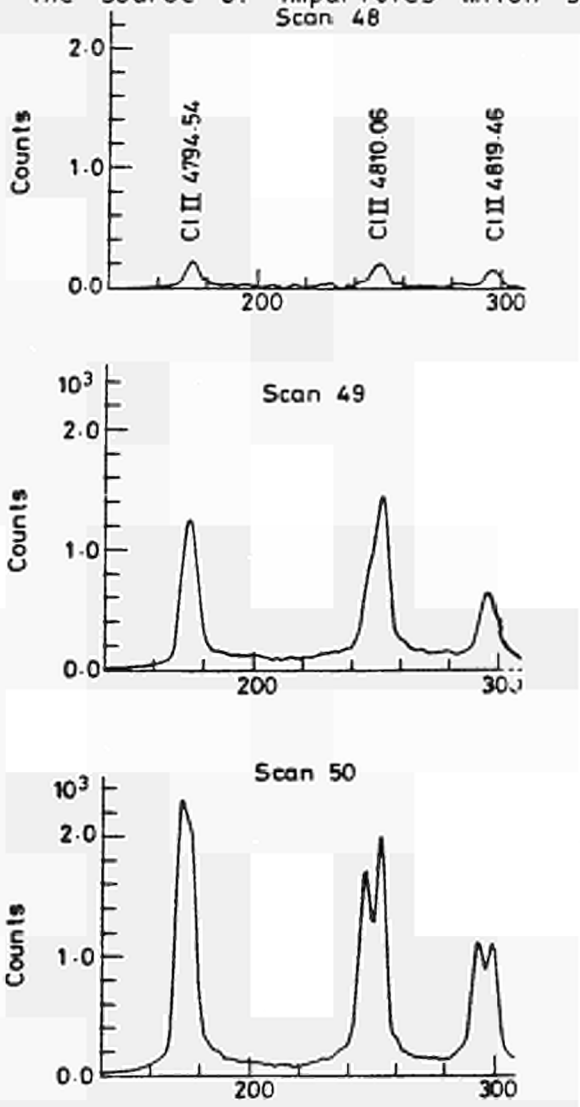

Fig.5 A time sequence in 196 ms increments for the Cl II triplet at the termination of the JET discharge. The Zeeman splitting on the third frame indicated the influx of Cl was from the inner wall.

CONCLUSIONS

Visible spectroscopic observations of the JET plasma edge shows significant heating in the edge vicinity during rf heating (for certain antenna configurations), they detect MARFE behaviour before changes in n_e are seen and the source of impurity influxes are localised from Zeeman splitting.

ACKNOWLEDGEMENTS

The authors wish to thank the whole JET operational team for their support, but in particular Drs K H Behringer, P D Morgan, M F Stamp and W W Engelhardt.

REFERENCES

1. B Lipschultz, B LaBombard et al, Nucl Fus 24 No.8 (1984) 997.
2. J O'Rourke et al Paper 190 this conference.
   P G Carolan, M J Forrest, N J Peacock and D L Trotman, JET preprint
3. JET-P(85)05, accepted for publication in Plasma Phys and Cont Fusion.

APPENDIX IV (d)
JET-P(85)15

Latest Results from JET

R J Bickerton et al

Invited Paper to the 12th European Conference on Controlled Fusion and Plasma Physics
(Budapest, Hungary, 2—6 September, 1985)

LATEST RESULTS FROM JET

R.J. Bickerton, F. Alladio[1], D.V. Bartlett, K. Behringer, R. Behrisch[2], E. Bertolini, C. Best, T. Bonicelli, G. Bracco[1], M. Brusati, D.J. Campbell, P.G. Carolan[3], J. Christiansen, P. Chuilon, J.P. Coad, J.G. Cordey, S. Corti, A.E. Costley, F. Crisanti[1], C. deMichelis[4], B. Denne, K.J. Dietz, D.F. Duechs, P.A. Duperrex[5], A. Edwards, S. Ejima[6], W.W. Engelhardt, J. Ehrenberg[2], S.K. Erents[3], B.T. Ericksson, M.J. Forrest[3], M. Gadeberg[7], A. Gibson, R. Gill, A. Gondhalekar, D. Goodall[3], N. Gottardi, C. Gowers, B.J. Green, G. Grosso[8], N.C. Hawkes[3], J. Hemmerich, F. Hendricks[9], M. Huart, M. Huguet, J. Jacquinot, O.N. Jarvis, E.M. Jones, E. Kallne, J.C. Kallne, A. Kellman[6], S. Kissel, L. de Kock, H. Krause[2], H. Kukral[2], P. Lallia, J. Last, E. Lazzaro, P. Lomas, G. McCracken[3], G. Magyar, M. Malacarne, M. Mansfield, V. Marchese, P. Martinelli[2], F.K. Mast[2], P.L. Mondino, P.D. Morgan, A.W. Morris[3], G. Murphy, M.F.F. Nave, P. Nielsen, R.M. Niestadt[10], P. Noll, J. O'Rourke, D. Pasini[11], N.J. Peacock[3] H.W. Piekaar[10], A. Pochelon[5], R. Prentice, P.H. Rebut, D.C. Robinson[3], R. Ross, G. Sadler, A. Santaguistina, F.C. Schueller, S. Segre[1], M.F. Stamp, P. Stangeby[12], C.A. Steed, P.E. Stott, T.E. Stringer, D. Summers, H.P. Summers, J.A. Tagle[13], A. Tanga, A Taroni, P.R. Thomas, K. Thomsen[9], G Tonetti[5], B.J.D. Tubbing[10], M. Turner[3], M. Valisa[9], P. van Belle, H. van der Beken, M.L. Watkins, J.A. Wesson, V. Zanza[1].

JET JOINT UNDERTAKING, Abingdon, Oxfordshire, United Kingdom

1 Euratom-ENEA Association, Frascati, Italy
2 Euratom-IPP Association, Institut für Plasmaphysik, Garching, Federal Republic of Germany
3 Euratom-UKAEA Association, Culham Laboratory, Abingdon, UK
4 Euratom-CEA Association, Fontenay aux Roses, France
5 Euratom-Suisse Association, CRPP CH-1007, Lausanne, Switzerland
6 G.A. Technologies, P.O. Box 85608, San Diego, Ca., USA
7 Euratom-Danish Association, Risø, Denmark.
8 Euratom-CNR Association, Instituto di Fisica del Plasma, Milan, Italy
9 Euratom Fellow
10 Euratom-FOM Association, Rynhuizen, The Netherlands
11 University of British Columbia, Vancouver, Canada
12 Permanent address, Aerospace Institute, University of Toronto, Canada
13 On leave from UNESA-ASINEL, Spain

ABSTRACT

In the last year, JET tokamak performance has been progressively raised, culminating in operation at the full design level of 5MA plasma current in a toroidal field at 3.4T. Plasma control has been improved with the plasma current, position, shape and line-average electron density all now controlled by feed-back systems. By glow discharge cleaning in hydrogen/methane mixtures, the interior of the vessel has been coated with carbon (carbonisation). This reduces the fraction of power radiated to ≤50% at intermediate densities and raises the density limit for disruption by 10%. Operation over a wide range of parameters, including varying major and minor radii, has given data for more extensive scaling studies. With ohmic heating, the maximum global energy confinement time is 0.8 ± 0.1s and the maximum central ion-temperature ~3.0keV. The highest ($\hat{n}\ \hat{\tau}_E\ \hat{T}_i$) product is reached with ohmic heating in a deuterium plasma and is ~$6 \times 10^{19} m^{-3} s$ keV ±20%

KEYWORDS

Thermonuclear Fusion Research; Tokamaks; Joint European Torus; Plasma Diagnostics, plasma.

INTRODUCTION

The main parameters of the Joint European Torus (JET) are shown in Table 1. Typical pulse durations are 15s with current flat-top times of 5s or greater. The aims of the last year of ohmic operation have been to extend the operating range to the full design values, to get cleaner plasmas than hitherto and to establish a wider data base for scaling studies. All these aims have been achieved to some extent. Details of the JET apparatus and earlier results have been given by Rebut and Green (1984) and Rebut et al (1985).

TABLE 1 JET Parameters

Parameter	Design Value	Operational Values
Plasma minor radius (hor)	1.25m	0.8 - 1.2m
Plasma minor radius (vert)	2.10m	0.8 - 2.1m
Plasma major radius (R)	3.0m	2.5 - 3.4m
Toroidal magnetic field at R=3.0m	≤3.45T	≤3.45T
Plasma current (I_p)	≤4.8MA	≤5.0MA

TABLE 2 JET Carbonisation History

Glow discharge voltage 400V: Gas Pressure ~ 5.10^{-3}mbar

Date (number of Sessions)	Gas Mixture	Discharge Current (A)	Wall Temp (°C)	Duration (hours)
Aug 84 (2)	H_2-3%CH_4	3	250	1
Sept 84 (1)	H_2-3%CH_4	3	250	6
Jan 85 (1)	D_2-2%CH_4	5	300	6
Feb 85 (2)	D_2-2%CH_4	5	300	8
Mar-May 85 (5)	D_2-12%CH_4	5	300	6
Late May 85 (1)	D_2-17%CH_4	6	300	48

MACHINE OPERATION

Figures 1(a) and (b) show toroidal and poloidal cross-sections of the JET device. During 1985, the machine operated with 4 carbon limiters, 4 nickel limiters and 2 RF antennae

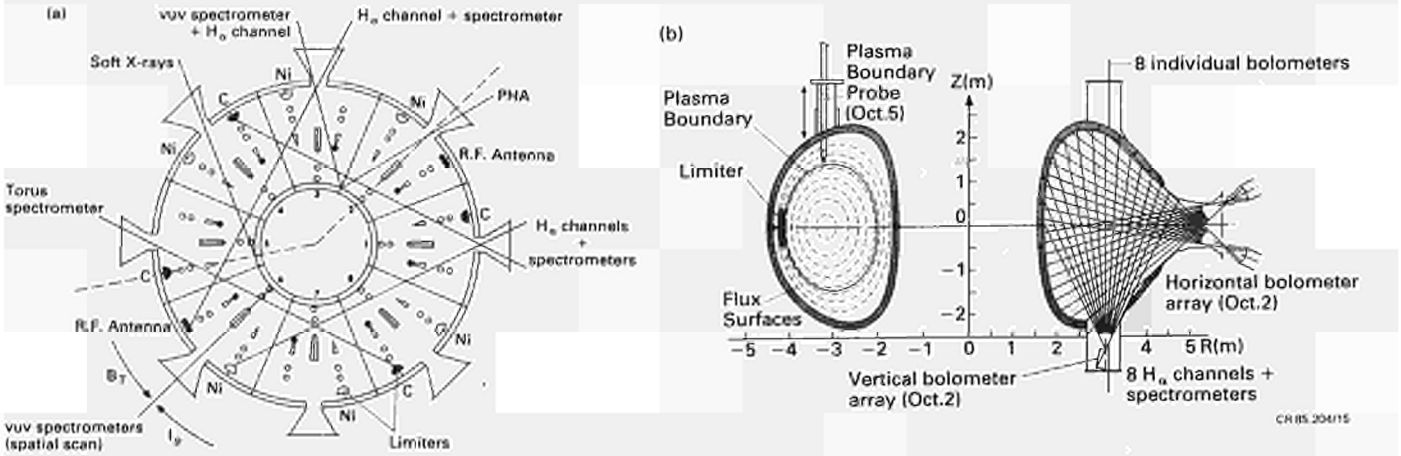

Fig. 1. (a) Toroidal and (b) Poloidal cross-section of the JET machine, showing the line-of-sight of various diagnostics. In (b), the left-hand poloidal cross-section is taken through Octant No. 5 (marked as the dotted line in (a)); and the right-hand poloidal cross-section is taken through Octant No.2 (shown as the dotted line in (a));

installed on the outer equatorial plane. The carbon limiters were the effective ones with the nickel limiters withdrawn 4cm behind. The antennae were also 2cm behind the carbon limiters for most of the operation. In addition the small major radius side of the interior of the vacuum vessel was covered to a height of ± 1m by carbon tiles for the 1985 operations. Figure 2 shows the vessel interior where all these features can be seen. The interior vessel wall was maintained at a temperature of about 300°C for all the experiments reported here. The base pressure was typically 10^{-7}mbar, comprising 10^{-7}mbar of hydrogen and 10^{-9}mbar of residual impurities. The vessel was conditioned by glow discharge cleaning in hydrogen, deuterium/methane or hydrogen/methane mixtures.

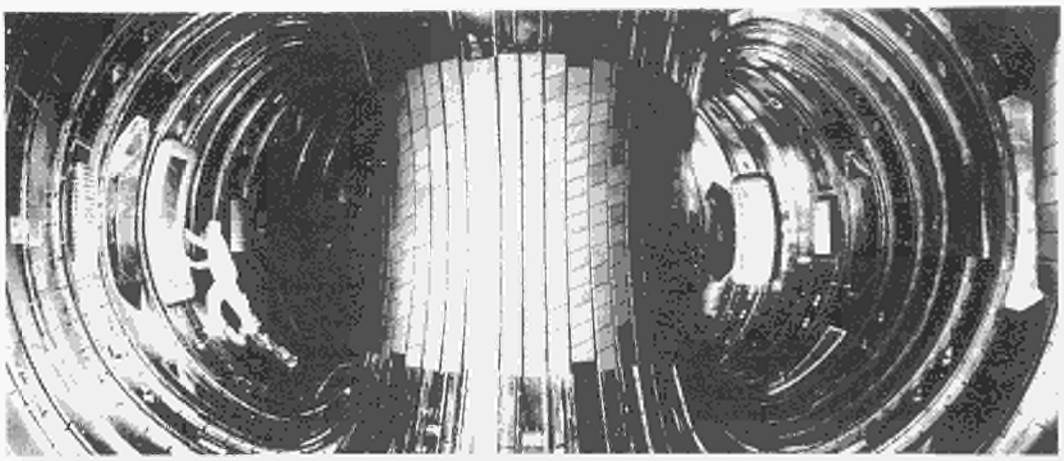

Fig. 2. Photograph inside the JET machine, showing the relative orientation of the two RF antennae, and the nickel and carbon limiters. The extent of the carbon protection tiles on the inner wall is also shown;

DIAGNOSTICS

a) The torus is equipped with 18 poloidal field pick-up coils inside each octant, continuous loops around the symmetry axis and local flux loops on the exterior surface of the vacuum vessel, enabling determination of plasma current, loop voltage, plasma boundary and the internal flux surfaces.

b) The electron temperature $T_e(r)$ profile is measured by an absolutely calibrated electron cyclotron emission (ECE) system viewing along several major radius chords in and close to the mid-plane. Michelson and Fabry-Perot interferometers and an echelon grating polychrometer are used to give varying frequency coverage and time resolution. The electron temperature is also measured by a single point Thomson scattering system, at a fixed point on the equatorial plane at a frequency of ~1Hz throughout the pulse. The 'fixed' point can be changed between pulses. Generally good agreement is obtained between the two methods (Costley et al 1985).

c) The electron density $n_e(r)$ is measured by a single channel 2mm microwave interferometer, and a seven channel far infra-red laser (190μm) interferometer system.

d) The ion temperature T_i is measured by a mass-selecting neutral particle analyser viewing the plasma along a chord in the mid-plane (Corti et al., 1985). In deuterium the ion temperature is also deduced from the neutron yield and from the energy distribution of the emitted neutrons with a ^{3}He spectrometer (Jarvis et al., 1985).

e) The effective ion charge Z_{eff} is deduced from the bremsstrahlung continuum intensity at 523nm viewed along a vertical chord. The electron temperature and density profiles from other diagnostics are used in the analysis.

f) The radiated power is measured by bolometers viewing along 34 chords at one poloidal location and by single bolometers in each octant. Assuming constant emissivity on magnetic surfaces, the multiple chord data is Abel inverted to give local radiated power densities (Gottardi et al., 1985).

g) The temperature and power flux in the scrape-off plasma have been measured with a single Langmuir/bolometer probe inserted from the top of the vacuum vessel (Stangeby et al., 1985).

h) Soft X-ray measurements have been made with diodes viewing the plasma horizontally on the mid-plane through various filter thicknesses. There is also a single chord pulse-height analyser system which gives a measure of metal ion concentrations (K-lines) and a secondary measurement of electron temperature (continuum).
i) Visible spectroscopic observations (viewing the plasma through ~100m of optical fibres) yield data on H_α emission and the influx of light impurities from the limiters and the walls. Two close-coupled spectrometers cover the ranges 200-700nm and 10-170nm yielding information on impurity species and ion states from which the central impurity concentrations can be deduced (Denne et al, 1985, Stamp et al, 1985).
j) Surface probes can be introduced into the torus to determine the nature of machine surfaces after glow-discharge cleaning and/or plasma operation (Coad et al., 1985). Long term samples, distributed over the interior vacuum vessel, are analysed after each experimental period.
k) An infra-red camera system (sensitive around 900nm) observes the emission from a carbon limiter. In some cases, this emission reflects the rise in surface temperature up to ~1500°C. In other cases, the temporal behaviour of the emission is not consistent with a temperature rise but may be due to emission from carbon lines or excited molecules. The two cases can be clearly distinguished.

PLASMA CONTROL

The plasma current time dependence is determined by a combination of pre-programming and feedback control of the excitation of the flywheel generator in the poloidal field circuit. The plasma density is also feedback controlled by varying the gas introduction rate according to the line density measured by the 2mm microwave interferometer. Since density can only be added in a controlled way, the system is ineffective when the gas release rate from wall and limiters is too high or is increased uncontrollably. Examples are the density rise accompanying sudden increases in power input from RF heating or large gas releases from walls and limiters immediately after carbonisation.

The plasma position and shape is determined in real-time from the magnetic signals. The radial position is maintained by a feedback system controlling coil PF4 voltage (Fig. 3). Up-down plasma symmetry is maintained by a similar system driving differential currents in

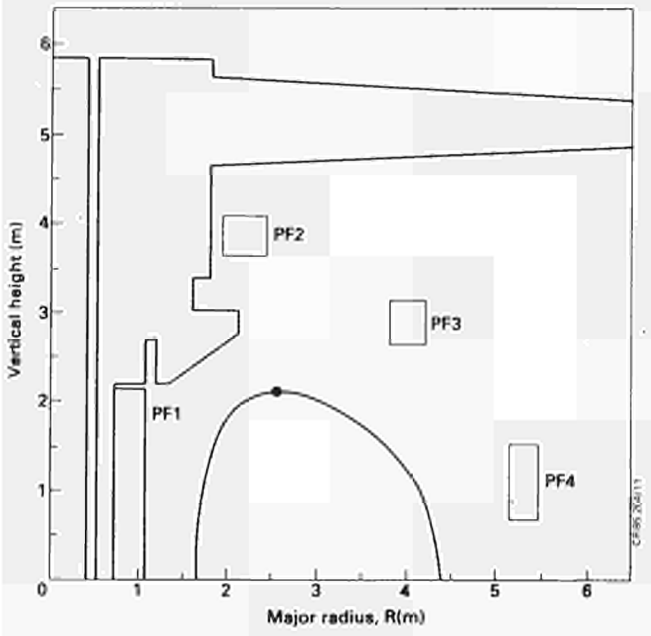

Fig. 3 Poloidal cross-section of JET machine showing relative positions of poloidal magnetic field coils 1,2,3 and 4;

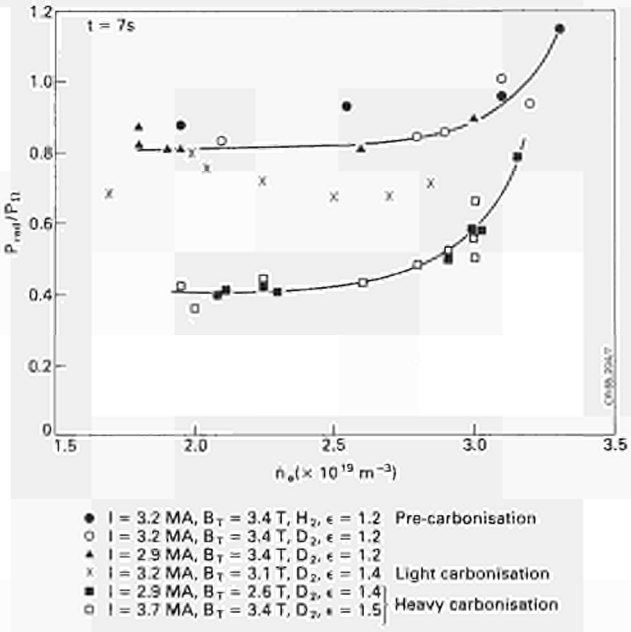

Fig. 4. Ratio of radiated power, P_{rad}, to ohmic input power, P_Ω, versus average electron density, $\bar{n}_e$, before and after carbonization;

sections of coils PF3 and PF4. The plasma shape is primarily determined by the proximity of plasma to the unsaturated parts of the iron magnetic circuit, ie by the plasma size, and by the magnitude of the quadrupole poloidal field generated by feedback - controlled opposite currents in the coils PF3 and PF4. With these feedback systems and under normal operating conditions, the flat-top current is held within 5% of the desired value, the radial position to ± 3cm, the vertical position to ± 1cm and the elongation ratio to within 5% of the pre-set value.

The initial "fast-rise" phase of JET operation is made by first charging the inductive store represented by the primary coil PF1 up to a pre-set current and then opening a switch across a resistor in the circuit. The higher the value of the resistor the higher the voltage applied at breakdown but also the faster the rate of plasma current rise in this phase. Experiments have shown excessive disruptive behaviour if the current rise rate exceeds ~1MA/s, probably due to skin currents and multi-valued q versus radius. To achieve adequate breakdown and a slow rise rate requires the charging current in PF1 coils to be limited to ~50% of its design value. Hence, only 25 of the theoretically available 34Vs can be used. For this reason, the record peak current of 5MA can be maintained at present only for about 1s. Modifications are planned to enable the resistor value to be reduced with time, giving a high breakdown voltage and a sufficiently slow current rise rate. Experiments on the breakdown phase are described in the papers (Thomas et al, and Schüller et al, 1985).

VERTICAL INSTABILITY

During one pulse in 1984, the growth rate of the vertical instability exceeded the capacity of the feedback system. The plasma current centre moved downwards 1m. without significant reduction in current (~2.6MA). Unexpectedly, very large forces (~300 tonnes) were transferred to the vacuum vessel causing significant displacements and a slight permanent distortion. The transfer of forces is now believed to be due to poloidal currents flowing radially through the plasma and returning in the rigid vessel sectors. Since then the vacuum vessel mounting has been considerably strengthened, with 16 tie-bars connecting the main ports to the iron limbs, restraining vertical motion and hydraulic dampers restraining the top and bottom vertical ports against sudden radial movements. Experiments with deliberately induced vertical instabilities at low currents have shown torus displacements reduced by a factor of ~3, when normalised to the square of the plasma current. Studies of these results and the growth rate dependence have lead to the imposition of an operating limit,

$$I_p^2 \, (b/a - 1.2) < 5.0 \; (MA^2) \qquad (1)$$

From this expression, it is clear that a current of 5MA cannnot be used with full plasma elongation (b/a~1.6). This limitation may be raised after further strengthening of the torus mounting and/or through a better understanding of vessel stresses. However, it seems likely that operation at currents of ~7MA will have to rely on a feed-back system with sufficient redundancy to protect the vacuum vessel from damage.

CARBONISATION AND IMPURITIES

"Carbonisation" of the torus interior is achieved by glow discharge cleaning in a mixture of hydrogen or deuterium and hydrogenic methane (CH_4). The carbonisation history of JET is shown in Table 2.

Analysis of samples exposed to carbonisation shows that carbon is diffused into the surface of inconel with a 100% coverage of the surface only being achieved in the case of the heavy carbonisation in 1985 ie. with 12% CH_4, 6 hrs or 17% CH_4, 48 hrs. (Coad et al., 1985).

Even before carbonisation, carbon was an important plasma impurity, due to the presence of carbon limiters and protection plates. The carbon concentration in the plasma core is

usually 2-3% n_e, and the limiters are the main source of carbon influx. Depending on the vacuum vessel cleanliness, 1-4%n_e of oxygen is found for which limiters and walls are both important sources. A few tenths of a percent of chlorine is believed to originate from torus washing after a vacuum opening. Concentrations of these light impurities are fairly insensitive to plasma currents and electron density. They increase in cases of stronger plasma-wall interaction, eg high elongations, and when approaching the density limit.

Nickel is the most important metal impurity. In addition, some chromium and iron are observed. Nickel and chromium are the main constituents of the Inconel vessel walls. The Faraday shields of the ICRH antennae present in the machine for 1985 operation are made of nickel. Metal impurities are especially prominent in low density plasmas. Their concentrations increase with plasma current, but decrease with plasma density, particularly steeply near the density limit for disruption.

During initial operation with new carbon tiles on the limiters, metal concentrations in the plasma were very low. After several weeks operation, the tiles become coated with metals probably due to strong plasma-wall interactions in disruptions. After some time, the metal deposit comes to an equilibrium level of ~10^{21} atoms/m^2, (found by surface analysis of limiter tiles after the 1983, 1984 and 1985 operation periods (Ehrenberg et al., 1985)). At this stage, the carbon limiters are the main sources of metal influx into the plasma. However due to the specific deposit topography, there is still about 90% carbon on the exposed surface.

After the initial contamination of the limiters, carbonisation was used routinely in 1985 to produce discharges with low metal content, and has been the most successful cleaning technique in JET so far. Before carbonisation JET plasmas had high radiation levels (70-100% P_Ω) and Z_{eff} was typically 4-5 or higher.

Carbonisation (first carried out in August 1984) led to an immediate reduction of metal concentrations and radiated power. Oxygen and chlorine reduced gradually after repetitive carbonisation to values below 1% and 0.05% respectively. After such repetitive carbonisation, P_{RAD} was only 40%P_Ω at moderate densities (ie the same value as with new limiter tiles) and 80%P_Ω at high density. The fraction of radiated power over input power versus electron density is shown in Fig. 4 (before and after a relatively light 1984 carbonisation). Z_{eff} was 3-4 for moderate and 2-3 for high electron densitites in the carbonised case.

Metal concentrations, derived from VUV spectroscopy, are about five times lower after a standard JET carbonisation (12% CH_4,6 hrs) but they recovered after some 20 plasma pulses to their previous level. A particularly heavy carbonisation carried out in 1985 (17% CH_4,48 hrs) resulted in a two orders of magnitude reduction in metals and a recovery time of ~200 plasma pulses. In 1984, the reduction in the fraction of power radiated for moderate densities lead to a clear heating of the limiter surface to 1800°C and metal was observed to evaporate from the surface. In 1985, even with low radiated fraction this heating has not been seen, presumably because of the proximity of relatively large antennae taking some of the load. The effect of the carbonisation on the Hugill diagram is shown in Fig. 5.

Carbonisation points are plotted indiscriminately without regard to the intensity used or the number of pulses after the treatment. However it can be seen that carbonisation extends the density limit by ~10%. Fig. 6 shows the radiated power profiles before and after carbonisation for similar plasma parameters. There is a reduction in the power radiated from the plasma core and a narrowing of the annular radiating zone surrounding the plasma.

Carbonisation is effective in reducing metal concentrations temporarily and oxygen on a longer timescale, but it leads to high carbon concentrations and thus a dilution of the working gas. For Z_{eff} ~3 and a carbon/oxygen ratio of 3:1, about 40% of the plasma electrons originate from impurities. Such depletion can be seen when comparing the neutron

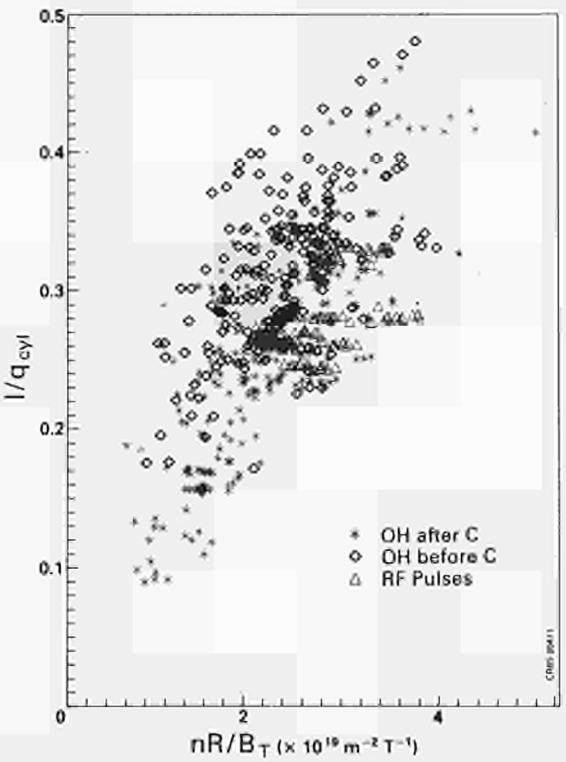

Fig. 5. Hugill-Murikami diagram of $1/q_{cyl}$ versus nR/B_T for ohmic plasma before and after carbonization and during R.F. heating.

yield with the ion temperature from the neutron spectrum. Agreement between the ion temperature deduced from the yield and that measured requires a deuteron/electron density ratio of typically 0.5 in the plasma core. Hydrogen release from the deposited carbon also makes density control difficult in the first few shots after carbonisation. However carbonisation is the only means found so far for reducing the radiated power once the limiters have become coated with metals.

Figure 7 shows Z_{eff} from bremsstrahlung measurements versus the ratio $\bar{n}_e/\bar{j}$ where $\bar{j}$ is the mean current density in the plasma, both before and after carbonisation. Carbonisation reduces Z_{eff} slightly but the minimum value is still high at ~2.5. To reduce this further, it is planned to surround the plasma more completely with low Z material, ie more carbon tiles. Other measures under discussion include gettering with beryllium or chromium and the use of beryllium limiter tiles.

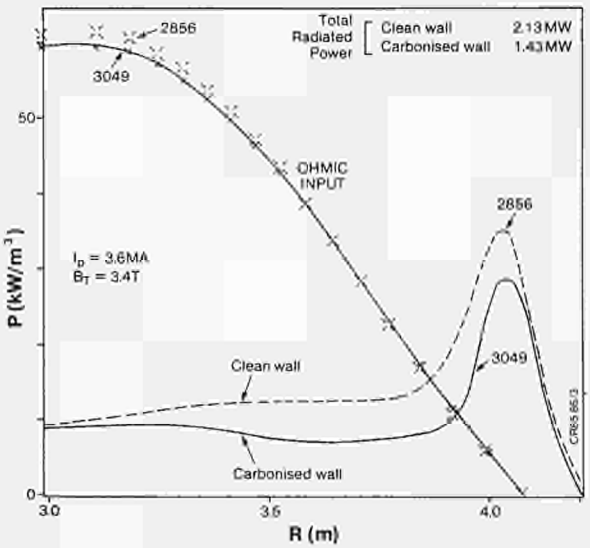

Fig. 6. Input ohmic power, P_Ω, and radiated power, P_{rad}, profiles for Pulse No: 2856 (before carbonization) and Pulse No: 3049 (after carbonization);

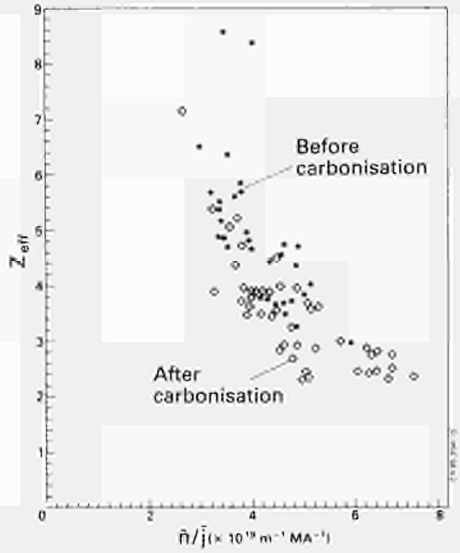

Fig. 7. The effective ion charge, Z_{eff}, from Bremsstrahlung measurements versus the ratio of average density, $\bar{n}$, to average current density, $\bar{j}$, both before and after carbonization;

EDGE PARAMETERS

Measurements of plasma parameters in the scrape-off layer of JET discharges have been performed in limited cases with an array of Langmuir and heat flux probes. An example is shown in Fig. 8 at I_p = 2.8MA, where the extrapolated plasma parameters at the plasma boundary are T_e ~100eV; n_e ~$2\times10^{18}m^{-3}$. The scrape-off layer profiles of $n_e(r)$ and $T_e(r)$, such as Fig. 8 (I_p ~2.8MA, $\bar{n}_e$ ~ $3\times10^{19}m^{-3}$,b/a~1.5,) have been used to calculate impurity generation rates due to sputtering of the limiter which are then compared with the spectroscopically observed influx. Only a small fraction of the impurity production at the limiters can be accounted for by hydrogen or deuterium impact. Under some conditions, the observed fluxes can be shown to be in rough agreement with carbon and oxygen ion sputtering.

The scrape-off layer $n_e(r)$ and $T_e(r)$ profiles were also used to calculate the shielding of the main plasma from impurities generated at the walls and limiters, and to compute the impurity content of the discharge. It is found that the scrape-off layer shields the main plasma quite effectively from impurities generated at the walls and that the principal, direct source of impurites in the core is due to the limiter. The values of n_e and T_e at the limiter tip are sufficiently high that all limiter impurities are ionised within a few centimetres of the limiter. The shielding of these limiter impurities is therefore approximately species-independent. The impurity density in the plasma can be estimated by balancing the impurity influx Γ_j particles from the limiters against the diffusive outflow,

$$\frac{n_j D}{\lambda_i + \lambda_{so}} = \frac{\Gamma_j}{A}$$

where n_j is the density of impurity species j in the plasma, λ_i the ionisation length for the impurity entering the plasma, λ_{so} the scrape-off layer thickness, D the diffusion coefficient for particles and A the plasma surface area. For JET, this gives $n_j \approx 10^{-3}\Gamma_j$ m^{-3}. Such concentrations are in agreement with measured values of Z_{eff} (~3) in such discharges.

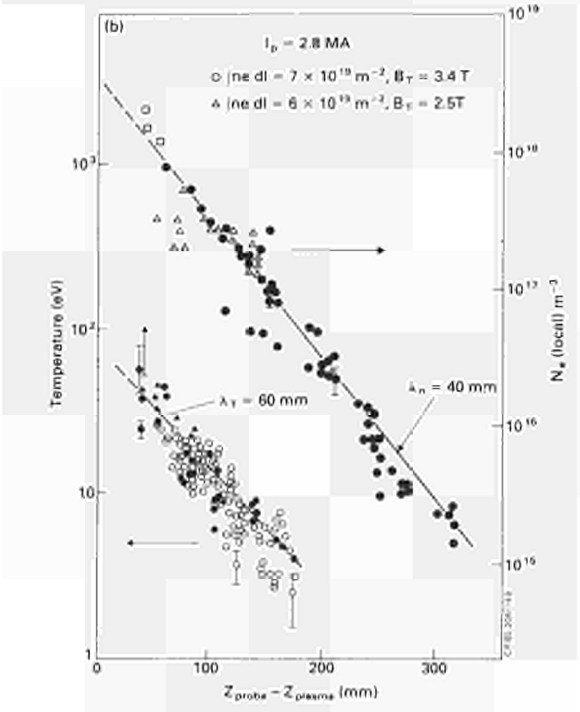

Fig. 8. Profiles of $T_e(z)$ and $n_e(z)$ for a standard I_p = 2.8MA discharge. All data was taken on the ion-side probes and during the discharge flat-top.

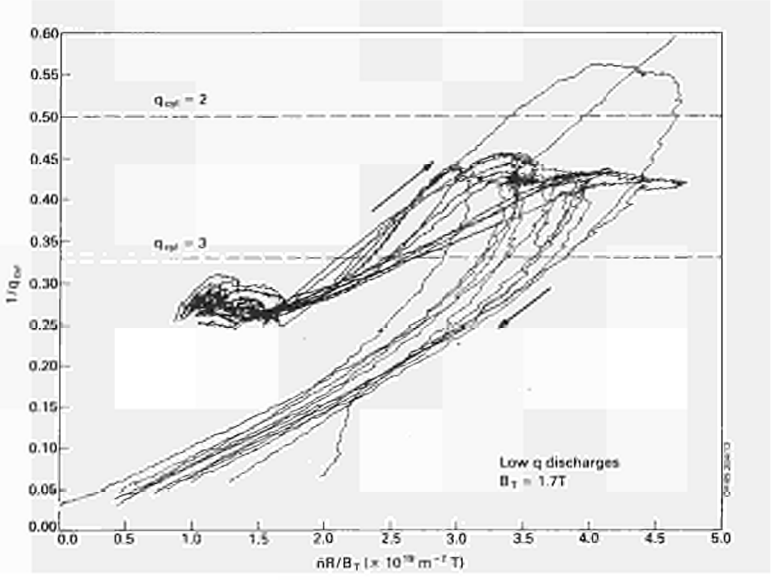

Fig. 9. Time trajectories in Hugill space ($1/q_{cyl}$ versus $\bar{n}R/B_T$) of low q discharges (B_T=1.7T) Current decay phase is lower bundle of trajectories;

Combining the H_α flux measured on the limiter and the power loading deduced from the surface temperature measurement at λ ~900nm reasonable agreement is obtained with the data from the Langmuir probe. The scrape-off layer thickness deduced from the thermal "footprint" on the limiter is in good agreement with the Langmuir probe measurements after correction for compression of the flux surfaces near the limiter on the mid-plane of the vessel.

Since the plasma-limiter contact dominates the influx of low and high Z impurites the limiter surfaces have been analysed by a variety of techniques and substantial coverage by (wall) metals was found after operations in 1983, 1984 and 1985. The surface concentration reflects broadly the plasma footprint on the limiter surface and the coverage is about 2.10^{21} atoms/m^2 for the colder edges down to 2.10^{20} atoms/m^2 in the hottest areas. Large ($\geq$ 100μm: splashes) and small (~1μm) droplets are found in certain areas of the surface. On the limiter edges, an anomalously high concentration of D_2 (5.10^{21} atoms/m^2) was found and this is attributed to co-deposition of D_2 and carbon. The deuterium inventory in the limiters is ~10 times that in the plasma for one shot. Thus, the limiters represent a potential source for uncontrolled gas release if they become sufficiently hot.

DENSITY LIMITS

From the Hugill diagram (Fig. 5) it can be seen that the density limit (n_L) for ohmic discharges before carbonisation was

$$\bar{n}_L(m^{-3}) = 1.0\times10^{20}\ \frac{B(T)}{R(m)\ q_{cyl}}$$

and increases by about 10% after carbonisation. Although this is a small effect, there is a more important change from an operational point of view. Disruptions at the density limit after carbonisation tend to be slower and Marfe-like compared with hard disruptions before carbonisation.

At the density limit both before and after carbonisation, the contribution from metal impurities is small. The results are consistent with a model (Wesson et al, 1985) in which a density disruption occurs, whenever the radiated power from the annular zone outside the q_ψ=2 surface approaches 100%of the total input power. If the radiation is assumed to come from helium-like states of light impurities (Schüller et al, 1985, Gowers et al, 1985) then a fair agreement between experiment and observation is obtained. Since in this model $n_L\alpha(P/f)^{1/2}$ where P is the total input power and f the fractional impurity content, there should be no difficulty in raising the density limit by the required factor of 2 when the power input is increased from the present (ohmic) values of ~3MW up to a total of about 35MW. This assumes that, as in the present RF (< 5MW) experiments, f remains independent of P. Density limit disruptions may be of the Marfe (Stringer, 1985) type with strong initial poloidal asymmetries in the annular radiating layer or more conventional with approximate symmetry. (More details are given in O'Rourke, et al. 1985).

CURRENT LIMITS

With the density significantly less than the limiting density the discharge still disrupt in about 7% of cases over the whole data set. The probability of disruption peaks at ~20% for $3.2<q_{cyl}<3.5$. However, discharges have been made with q_{cyl} ~1.6 (q ~2.2) at 3.25MA in 1.7T field, without disruption. From this evidence, a 7MA discharge should be possible using the full aperture in JET. Concern about potential damage from disruptions or vertical instabilities precludes operation at this level for the present. Fig. 9 shows some of the trajectories in Hugill space of low q_{cyl} discharges. Note a common feature of tracking down the density limit line, as the discharge current and correspondingly $1/q_{cyl}$ fall at the end of the current pulse.

The time constant of the current quench phase depends whether the equilibrium field system can respond fast enough to maintain position control (Schüller et al., 1985). For currents <1MA, this control is maintained and the quench time is a constant 250ms. For currents >1MA, this becomes increasingly difficult and in the worst case the current fell from 3MA to zero in 10ms. In these "lost equilibrium" cases, the discharge moves rapidly to the small major radius side of the torus axis, interacting strongly with the inner wall. In such cases, the photoneutron production may reach 3.10^{14}/disruption with accompanying local photo-activation of the torus wall.

SAWTEETH

Sawteeth oscillations are seen on the signals from soft X-rays, neutrons, electron temperature, ion temperature and electron density in flat-top discharges for which q_{cyl} at the boundary is less than 12. Fig. 10 shows an example of sawteeth on the central electron temperature as measued by electron cyclotron emission. In many discharges, sawteeth are aperiodic and complex. In a simple case, the sawtooth period τ_{ST} is correlated with the global energy confinement time τ_E and for a particular data set the period of simple sawteeth scales as τ_{ST}/τ_E = 0.13±30%. More commonly, in JET, the behaviour is dominated by giant sawteeth having roughly twice the period of the simple sawteeth (Campbell et al, 1985).

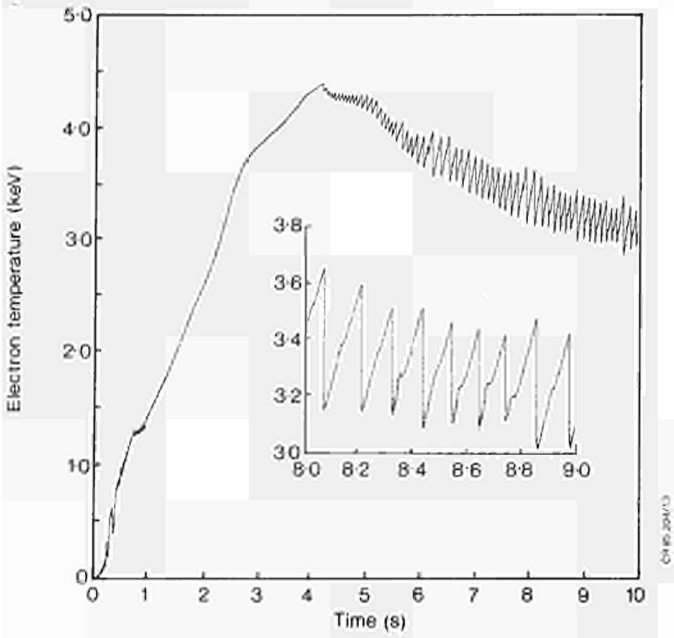

Fig.10. Central electron temperature, from ECE diagnostic, as a function of time (over 10s) showing sawtooth behaviour. The inset shows expended timescale (over 1s);

By using the fast electron cyclotron emission grating polychromator (Tubbing et al, 1985), it is possible to track the passage of the thermal wave excited by the sawtooth collapse in the plasma core. The observed propagation can be interpreted to give the effective electron thermal diffusivity $\bar{\chi}_{ep}$ and this can be compared with the value $\bar{\chi}_{eE}$ deduced from the global energy confinement time ($\bar{\chi}_{eE} = a^2/4.\tau_E$), typical results from a single shot during RF heating (1.3MW) and after RF during the Ohmic phase are

	$\bar{\chi}_{ep}$	$\bar{\chi}_{eE}$	$\bar{\chi}_{ep}/\bar{\chi}_{eE}$
RF	$3.5m^2s^{-1}$	$1.6m^2s^{-1}$	2.2
Ohmic	$3.4m^2s^{-1}$	$1.0m^2s^{-1}$	3.4

The reason for these differences is not known. A possible explanation is that the equilibrium profile is close to a state of marginal stability and any perturbation causes an enhancement in the thermal loss mechanisms. Another possibility is that there is an inward thermal pinch term analogous to that found for density diffusion.

HIGH CONFINEMENT AND HIGH CURRENT SHOTS

Figs. 11, 12 and 13 show a consistent set of data for a high confinement time shot. The discharge current is held at 3.6MA for a time of 6s. The minor radius is 1.2m and the elongation ratio b/a ~1.5. Towards the end of the current flat-top, the ohmic input power is 2.4MW and Z_{eff} ~2.6 (q_{cyl} ~ 3.5). Note the initial overshoot in central electron temperature which is not reflected in the volume average electron temperature. This is the consequence of the flattening with time of the electron temperature profile that can be seen in Fig. 13. Figure 14 shows the current wave-form for a 5MA shot. To minimise the chances of disruption these shots were run at intermediate density so that the corresponding global confinement time is not remarkable at ~0.5s. Nevertheless, these shots show the technical feasibility of full design performance in JET. Longer flat-top times will be feasible when, after circuit modification, the full volt-second capability can be used effectively.

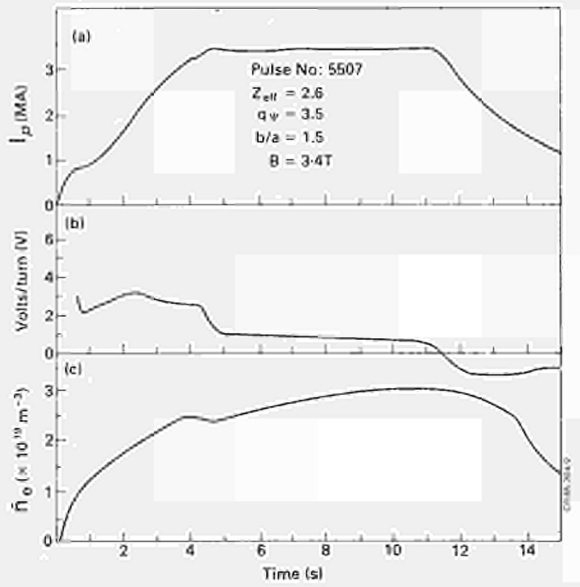

Fig.11. Pulse No:5507: (a) Current, (b) Volts per turn, and (c) Line average electron density versus time;

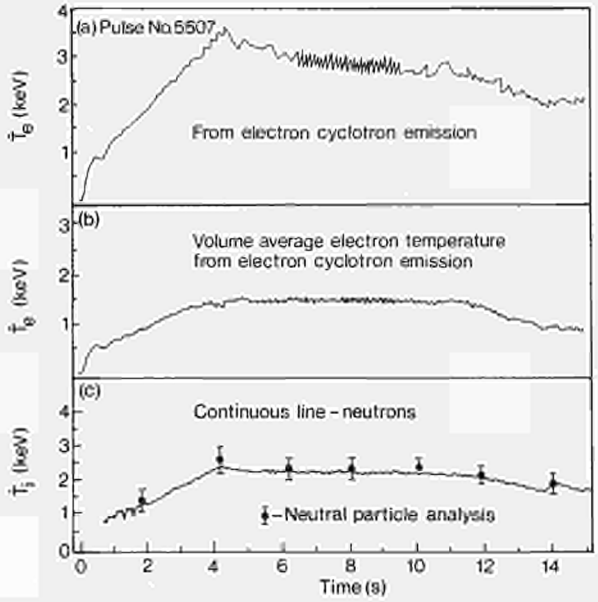

Fig.12. Pulse No:5507: (a) Peak electron temperature; (b) volume averaged electron temperature (from ECE); (c) Peak ion temperature versus time;

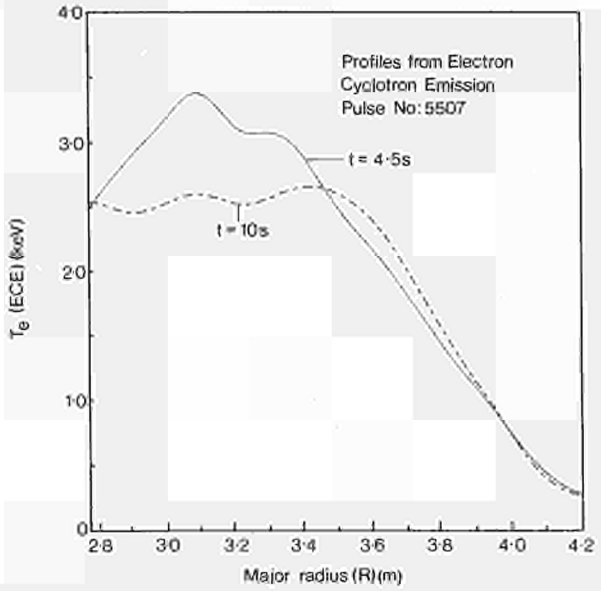

Fig.13. Electron temperature (T_e) profiles, from ECE measurements, at t=4.5s and t=10s in Pulse No:5507;

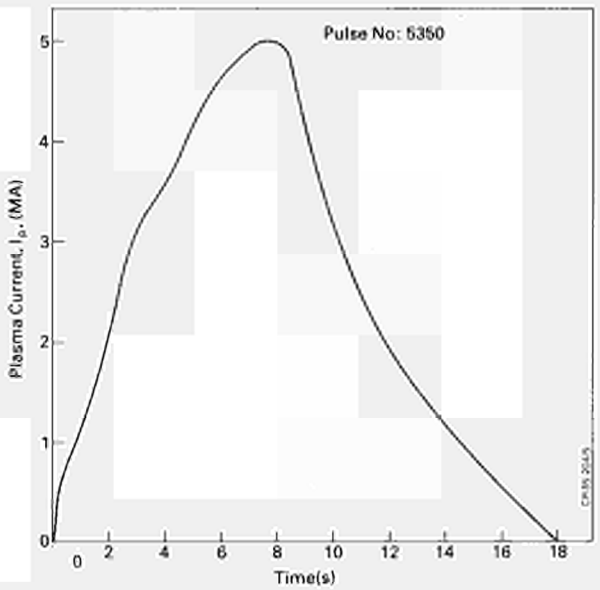

Fig.14. Plasma Current versus time for Pulse No:5350 showing achievement of 5MA plasma current;

CONFINEMENT TIME AND LAWSON PARAMETERS

The global confinement time (τ_E) is calculated near the end of the current flat-top when quantities are in an equilibrium state. τ_E is defined by $\tau_E=(W_e+W_i)/P_{input}$, where W_e and W_i are the electron and ion energy contents in the plasma. W_e is calculated simply using the known electron density and temperature profiles integrated over the volume of the derived magnetic surface. The ion energy content is calculated using the measured (NPA) central ion temperature, assuming that the radial profile has the same form as the electron temperature together with the ion density (n_i) from,

$$\frac{n_i}{n_e} = \frac{n_D}{n_e}(1+Y) + \frac{n_o}{n_e} + \frac{n_c}{n_e}$$

(n_D, n_o and n_c are the deuteron, oxygen and carbon ion densities, respectively)

n_D/n_e is derived from the neutron yield using the neutral particle analyser ion temperature, Y is the ratio of hydrogen to deuterium (normally 5%) and the ratio n_o/n_c is calculated from the spectroscopic data. Together with the equation for charge neutrality

$$n_D + n_o\,8 + n_c\,6 = n_e$$

this determines n_i/n_e

The global confinement data for discharges in JET is plotted versus the scaling $R^2a\bar{n}q_{cyl}$ in Fig. 15. This is not the best regression fit to JET data but is shown here for comparison with earlier results from JET and TFTR. The best regression fit now shows a weaker dependence on density than found previously (J G Cordey et al, 1985). This may reflect the greater variation with density of the fraction of power radiated (Fig. 4) since the first carbonisation in late 1984.

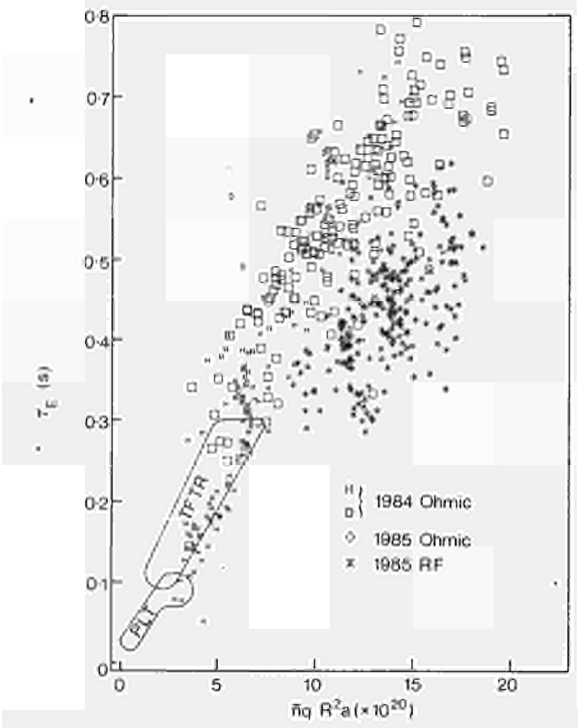

Fig.15. Global energy confinement time, τ_E, versus the scaling factor $\bar{n}qR^2a$ for both Ohmic and RF heated plasmas. The data from PLT and TFTR are shown for comparison;

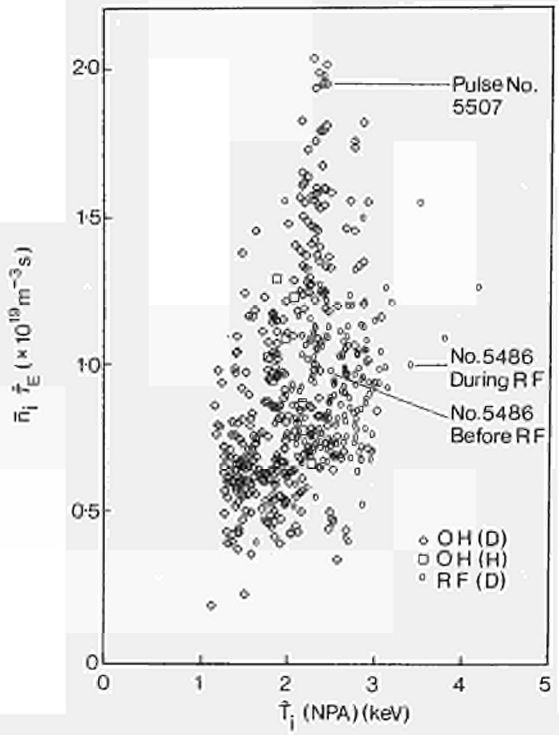

Fig.16. Lawson diagram of $\hat{n}_i\hat{\tau}_E$ versus $\hat{T}_i$(NPA) for both hydrogen(H) and deuterium(D) plasmas during ohmic and RF Heating. Pulse No:5507 and Pulse No:5486 (both before and during RF heating) are highlighted;

In Fig. 16 the performance of JET is plotted in the Lawson plane of $\hat{n}_i\hat{\tau}_E$ versus $\hat{T}_i$. Here n_i is the central hydrogen isotope density (usually significantly less than the electron density). τ_E is the central energy confinement time and T_i the central ion temperature. For a limited number of shots $\tau_E(\Psi)$ has been calculated where

$$\tau_E(\psi) = \frac{3/2 \int_0^{\Psi} n_e T_e + n_i T_i)\, dV}{P_\Psi}$$

P_Ψ is the power input inside the flux surface Ψ. P_Ψ is calculated from the known loop voltage and the current distribution deduced from magnetic measurements. $\tau_E(\Psi)$ is found to have a broad maximum inside the plasma half-radius, such that $\tau_E(\Psi) \sim 1.3\ \tau_E$ where τ_E is the global confinement time defined earlier. This ratio has then been applied to all the analysed shots on the Lawson diagram. The measured density profile generally has the form

$$n_e = \hat{n}\ (1 - r^2/a^2)^{\frac{1}{2}}$$

giving a ratio $\hat{n}/\bar{n}$ of $4/\pi$ where $\bar{n}$ is the line-average value.

The effect of RF heating in raising the central ion temperature can clearly be seen. The performance of ohmic heating plasmas is typically 20-40% higher in τ_E with deuterium rather than hydrogen plasmas, under similar conditions. With RF no attempt was made to increase the density above the Ohmic limiting value. In addition, RF was usually applied to standard ohmic plasmas with modest densities, ie discharges in which the ohmic confinement time was typically ~0.5s and not the highest attainable. Coupled with the observed degradation in τ_E when heating is applied, this leads to the RF discharges having the highest $\hat{T}_i$ but only modest $\hat{n}\,\hat{\tau}_E$. The highest value of the product $\hat{n}\,\hat{\tau}_E\,\hat{T}_i$ is ~6 $\times 10^{19} m^{-3} s$ keV, obtained with Ohmic heating. For the RF cases, τ_E is calculated assuming that all the power launched from the antennae is absorbed by the plasma. At present, power accounting is not accurate enough to prove this assumption.

MAGNETIC SEPARATRIX OPERATION

However, with this assumption, the first results with RF heating (Jacquinot et al, 1985) on JET show confinement time degradation similar to that seen on other machines with neutral beam or ion cyclotron resonance heating into limiter-bounded plasmas (Goldston 1984).

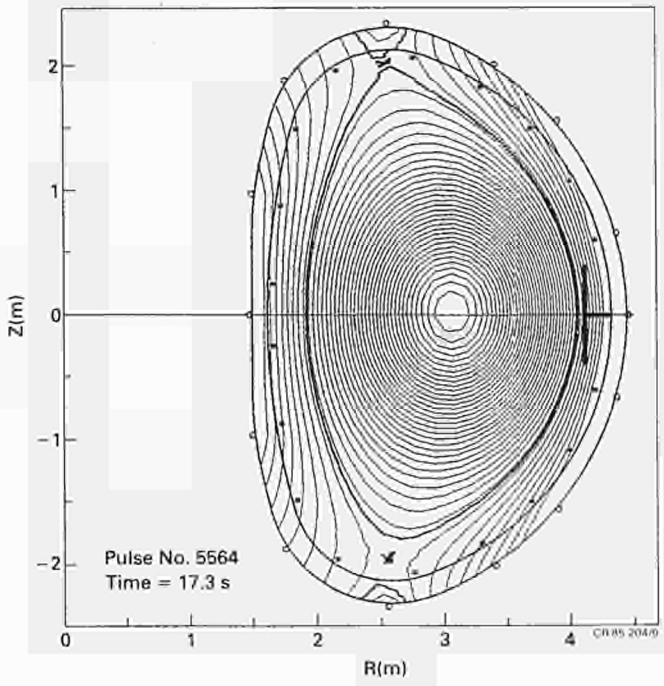

Fig.17. Pulse No:5564: (I_p=2MA, B_T=2.6T) showing formation of magnetic separatrices inside the vacuum vessel.

Starting with ASDEX, several tokamak devices (DIII,PDX) have shown that confinement can be greatly improved if the plasma is bounded by a magnetic separatrix. The JET poloidal field coil configuration allows the formation of a magnetic separatrix with two stagnation (or X-points) at the top and bottom of the vacuum vessel as an extreme case of plasma shaping. Experiments during Ohmic heating only have demonstrated this mode of operation and a number of technical questions relating to the up-down stability and the heat loads on the vessel have been studied (Tanga et al, 1985). Figure 17 shows the flux-contours for such a case at a current of 2MA in a field of 2.6T. The stable configuration was maintained by feed-back for several seconds. The corresponding plasma elongation is 1.7-1.8. In the region around the X-points, ~30% of the input power is radiated while interaction with the mid-plane limiters stops. The conduction/convection losses to the top and bottom of the vessel are estimated to be only 10-20% of the total power input. We believe that JET can be operated in this mode transiently for several seconds at a current level of 4MA without modification to the existing poloidal field coil system.

SUMMARY OF CONCLUSIONS

1) The electron density, plasma current, plasma position and shape are now controlled by feedback systems.
2) A 5 MA discharge has been achieved with a flat-top duration of ~1s. To extend this duration, the poloidal circuit will be modified to enable use of the full volt-seconds capability of the machine, consistent with breakdown and current rise-rate limitations.
3) The vessel supports have been strengthened so that performance at these higher levels was possible without risk of mechanical damage if vertical position control was lost. To go to full aperture plasmas at 5MA, further strengthening of the torus mounting will be required. To go to 7MA will require a feedback system with redundancy to minimise the risk of damage due to loss of position control.
4) Carbonising the vacuum vessel has both reduced Z_{eff} and given a modest increase in the critical density for disruption. However, the light impurities in the centre cause a considerable reduction (50%) in the ratio of deuteron to electron density. Immediately after carbonisation, breakdown and density control are difficult due to the release of retained hydrogen.
5) The observed density limits are consistent with the radiated power outside q=2 equalling the total input power at the limiting line in the $1/q_{cyl}$ vs $\bar{n}R/B$ plane. If this is the case, substantial increases in the density limit will be possible with full additional heating power, provided that the fractional impurity content does not increase with power.
6) JET has been operated down to q_{cyl}~ 1.6 (q_ψ = 2.2) at 3.25MA without disruption. On this basis, it should be possible to achieve 7MA in JET using full field and full aperture.
7) Sawtooth periods on JET are roughly linearly related to the global energy confinement time. Study of the heat pulse propagation shows an electron thermal diffusivity 2-4 times that deduced from the global energy confinement time.
8) By operating at full field, high aperture, and density near the limiting value, global energy confinement times of about 0.8s have been achieved with ohmic heating.
9) The highest central ion temperature of 4keV is achieved with RF heating. The best combination of Lawson parameters is obtained with ohmic heating, $\hat{n}\,\hat{\tau}_E = 2.2 \times 10^{19} m^{-3} s$ and $\hat{T}_i$ ~2.6keV, giving a product ($\hat{n}\,\hat{\tau}_E\,\hat{T}_i$) of ~$6 \times 10^{19} m^{-3} s$ keV.
10) Preliminary studies have demonstrated experimentally the ohmic operation of JET with a magnetic separatrix. This configuration when used with additional heating may permit an H-mode regime of confinement to be reached.

ACKNOWLEDGEMENTS

The authors wish to acknowledge the hard work and devotion of the many staff at all levels who built, modified and operated the machine for these experiments.

REFERENCES

Campbell,D.J., Bartlett,D.V., Best,C., Brusati,M., and coworkers. Proc. 12th European conference on Controlled Fusion and Plasma Physics (Budapest, Hungary, 1985). Vol 9F, Part 1, p. 130

Coad,J.P., McCracken,G.M., Erents,S.K., Ehrenberg,J., de Kock,L., Stangeby,P.C., Tagle,T. Proc. 12th European Conference on Controlled Fusion and Plasma Physics (Budapest, Hungary, 1985). Vol 9F, Part 2, p. 571

Cordey,J.G., Bartlett,D.V., Bickerton,R.J., Brusati,M., and coworkers. Proc. 12th European Conference on Controlled Fusion and Plasma Physics (Budapest, Hungary, 1985). Vol 9F, Part 1, p. 26

Corti,S., Bracco,G., Brusati,M., Gondhalekar,A., Grosso,G., Hendriks,F., Segre,S., Zanza,V. Proc. 12th European Conference on Controlled Fusion and Plasma Physics (Budapest, Hungary,1985). Vol 9F, Part 1, p. 219

Costley,A.E., Baker,E.A.M., Brusati,M., Bartlett,D.V., and coworkers. Proc. 12th European Conference on Controlled Fusion and Plasma Physics (Budapest, Hungary,1985). Vol 9F, Part 1, p. 227

Denne,B., Behringer,K.H., Engelhardt,W., Gill,R.D., and coworkers. Proc. 12th European Conference on Controlled Fusion and Plasma Physics (Budapest, Hungary, 1985). Vol 9F, Part 1, p. 379

Ehrenberg,J., Behrisch,R., Martinelli,P., Kukral,H., McCracken,G.M., Coad,J.P., de Kock,L. Proc. 12th European Conference on Controlled Fusion and Plasma Physics (Budapest, Hungary, 1985). Vol 9F, Part 2, p. 575

Goldston,R.J., (1984). Plasma Physics & Controlled Fusion, 26, 1A, 87

Gottardi,N., Krause,H., Mast,K.F. Proc. 12th European Conference on Controlled Fusion and Plasma Physics (Budapest, Hungary, 1985). Vol 9F, Part 1, p. 30.

Jacquinot,J., Anderson,R.J., Arbez,J., Bartlett,D., and coworkers. Special Issue of the Journal of Plasma Physics and Controlled Fusion. To be published

Jarvis,O.N., Gorini,G., Hone,M., Kallne,J., Merlo,V., Sadler,G., van Belle,P. Proc. 12th European Conference on Controlled Fusion and Plasma Physics (Budapest, Hungary, 1985). Vol 9F, Part 1,p. 223

O'Rourke,J., Campbell,D., Denne,B., Gondhalekar,A., and coworkers. Proc. 12th European Conference on Controlled Fusion and Plasma Physics (Budapest, Hungary, 1985). Vol 9F, Part 1,p. 155

Rebut,P-H., and Green,B.J. (1984). Plasma Physics and Controlled Fusion,26, 1A,1.

Rebut,P-H. et al., (1985). Plasma Physics and Controlled Nuclear Fusion, IAEA,(London) Vol.1,11.

Schueller,F.C., Alladio,F., Campbell,D., Crisanti,F., and coworkers. Proc. 12th European Conference on Controlled Fusion and Plasma Physics (Budapest, Hungary, 1985). Vol 9F, Part 1,p. 151

Schueller,F.C., Thomas,P.R., Kellman,a., Lazzaro,E., Lomas,P., Piekaar,H.W., Tanga,A. Proc. 12th European Conference on Controlled Fusion and Plasma Physics (Budapest, Hungary, 1985). Vol 9F, Part 1,p. 287

Stamp,M.F., Behringer,K.H., Forrest,M.J., Morgan,P.D., Summers,H.P. Proc. 12th European Conference on Controlled Fusion and Plasma Physics (Budapest, Hungary, 1985). Vol 9F, Part 2,p. 539

Stangeby,P.C., Erents,S.K., Tagle,J.A., McCracken,G.M., de Kock,L. Proc. 12th European Conference on Controlled Fusion and Plasma Physics (Budapest, Hungary, 1985). Vol 9F, Part 2, p. 579

Stringer,T.E. Proc. 12th European Conference on Controlled Fusion and Plasma Physics (Budapest, Hungary, 1985). Vol 9F, Part 1, p. 86

Tanga,A., Campbell,D.J., Denne,B., Gibson,A., and coworkers. Proc. 12th European Conference on Controlled Fusion and Plasma Physics (Budapest, Hungary, 1985). Vol 9F, Part 1, p. 70

Thomas,P.R., Christiansen,J.P., Ejima,S. Proc. 12th European Conference on Controlled Fusion and Plasma Physics (Budapest, Hungary, 1985). Vol 9F, Part 1,p. 283

Tubbing,B.J.D., Barbian,E., Campbell,D.J., Hugenholtz,C.A.J., Niestadt,R.M., Oyevaar,Th., Piekaar,H.W. Proc. 12th European Conference on Controlled Fusion and Plasma Physics (Budapest, Hungary, 1985). Vol 9F, Part 1,p. 215

Wesson,J., Gowers,C., Han,W., Mast,F., Nave,F., Turner,M., Watkins,M. Proc. 12th European Conference on Controlled Fusion and Plasma Physics (Budapest, Hungary, 1985). Vol 9F, Part 1,p. 147

APPENDIX IV (e)
JET-P(85)18

Magnetic Topology, Disruptions and Electron Heat Transport

P. H. Rebut and M. Brusati

Invited Paper to the 12th European Conference on Controlled Fusion and Plasma Physics
(Budapest, Hungary, 2–6 September, 1985)

MAGNETIC TOPOLOGY, DISRUPTIONS AND ELECTRON HEAT TRANSPORT

P. H. Rebut, M. Brusati
JET Joint Undertaking, Abingdon, Oxon OX14 3EA, UK

Abstract

JET results are presented which show a "profile consistency" of the electron temperature under a variety of plasma conditions.

This experimental fact is interpreted as due to a topology of the magnetic field lines where ordered structures such as laminar surfaces and magnetic islands coexist with ergodic domains.

The development of this concept identifies different plasma regions according to the value of the safety factor and relates the observed degradation in confinement time, when Additional Heating is applied, to the plasma entering a multiphase state where the electron temperature gradient is limited by a critical value defined by the global plasma parameters. A preliminary scaling law for the electron temperature is proposed which indicates a strong favourable dependence on major radius and plasma current.

Losses due to atomic processes at the plasma edge give rise to thermal instabilities with low m numbers, which induce ergodic regions. Plasma disruptions could be considered as the effect of these very low number instabilities ($m = 2, 3$).

The near future JET experimental programme is briefly described and possible ways of improving the plasma confinement are presented.

Keywords

Tokamak, JET, Magnetic Topology, Disruptions, Electron Heat Transport, Additional Heating, Scaling Laws, Electron Temperature Profile.

I) Introduction

Plasma discharges in tokamaks exhibit a variety of phenomena (anomalous thermal diffusion, degradation of confinement with additional heating, sawteeth oscillations, disruptions) and different regimes (L and H modes) which have so far eluded a satisfactory theoretical explanation.

Some of these phenomena are generally attributed to changes in magnetic topology: appearance of magnetic islands (disruptions, sawteeth) or formation of a separatrix at the plasma edge (H mode).

In this paper we try to analyse some of the consequences of topologies which include ergodization of magnetic field lines. The ergodicity is produced by the interaction of several sets of magnetic islands.

The occurrence of three types of topologies, main magnetic surfaces, magnetic islands and regions of ergodic field lines, can have major effects on the plasma and could be the main cause of the complex behaviour observed experimentally.

Except for the largest islands these different topologies affect mainly the electrons due to the small Larmor radius and mobility along field lines. The ratio between the parallel and perpendicular electron thermal conductivities is $\chi_{\parallel}/\chi_{\perp} \simeq 10^{14}$ in JET and a small displacement of the field lines can modify completely the main perpendicular electron heat transport.

The existence of magnetic islands can also arise from ergodic magnetic fields and can only be maintained at the expense of the energy confinement time.

In this paper we shall see how the experimental results obtained on JET could be described by such a concept.

We are still far from being able to explain these aspects of plasma physics quantitatively, but the general conclusion we can draw so far points in the right direction. Major work remains still to be done to justify some of the hypotheses and conclusions; nevertheless we shall tentatively present them.

II) JET experimental results: the electron temperature profile

Most of the results which will be described here have been obtained during the 1985 JET operation with ohmic and RF heating. We limit ourselves to a study of the electron behaviour mainly through the ECE diagnostic which provide a spatial and temporal resolution of the electron temperature (Costley et al., 1985).

The electron temperature on JET shows a strong "profile consistency"; this has already been seen on other toroidal devices (Coppi, 1979).

CR85.223

In the absence of sawteeth, electron temperature profiles are similarly independent of the plasma conditions: this can be seen in figs. 1,2 where the electron temperature profile is shown for two JET discharges with plasma currents of respectively 1.12 MA and 2.82 MA. In the latter case (2.82 MA), the profile at $t = 6$ s corresponds to the beginning of the current flat top when a strong skin effect prevents a large $q = 1$ region from developing. Under these conditions the two temperature profiles can be superimposed within the experimental uncertainty. Later on at $t = 8.5$ s, the current has diffused further into the plasma centre and a large $q = 1$ sawteeth region develops, cutting the temperature profile at a lower value.

The electron temperature behaviour can be revealed further by studying the profile evolution when an RF heating pulse is applied. Fig. 3 shows the time evolution of the central electron temperature when RF is applied at $t = 6.25$ s for 2 seconds. Large sawteeth of 1.5 keV develop with partial or full reconnection. The bottom of the sawteeth in case of full reconnection shows no increase in electron temperature. The related temperature profiles are shown in fig. 4 where case (a) corresponds to the sawtooth start-up both in ohmic and in RF heated phases.

The profiles (b) and (c) are measured at the top of the sawteeth and refer respectively to an ohmic discharge with 1.58 MW of input power and to an RF heated discharge where a total of 3.4 MW is applied. The total amplitude of the sawteeth reach 2 keV and depends strongly on the power input; the rate of temperature increase dT_e/dt seems to be proportional to the heating power density.

The confinement time in the sawteeth zone ($2.7\,\text{m} < R < 3.6\,\text{m}$) between two relaxations is very long with no sign of degradation. Outside the $q = 1$ region, the temperature profile does not vary when the power is increased by more than a factor of two with the exception of small variations after the collapse of the sawtooth (heat pulse) as shown in fig. 5. During this time the electron thermal conductivity varies by more than a factor of 2 on average when RF is applied and by almost an order of magnitude (>7) when comparing ohmic and RF heating phases. It follows that the thermal conductivity does not seem to be a useful physical quantity.

The heat flow equation:

$$\Phi_e = \chi_e \nabla T_e \tag{1}$$

must be replaced, outside the $q = 1$ region, by an equation of the type

$$T_e = T_c \tag{2}$$

or

$$\nabla T_e = \nabla T_c \tag{3}$$

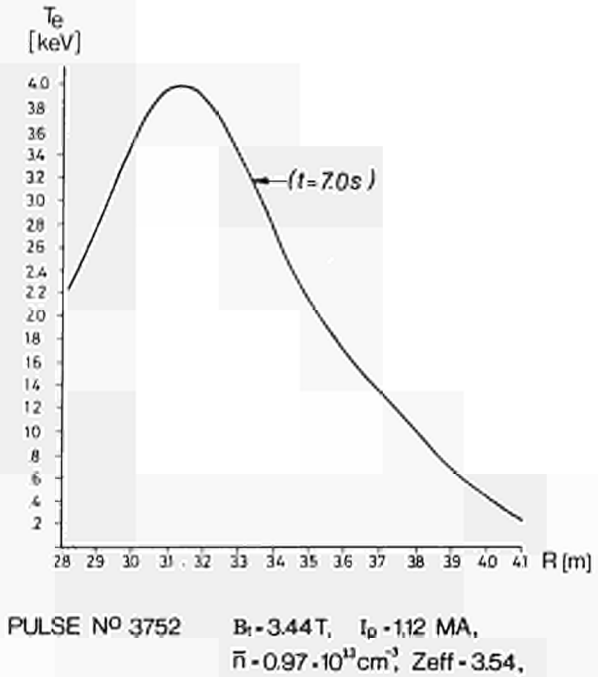

Fig. 1. Typical electron temperature profile for a high q value.

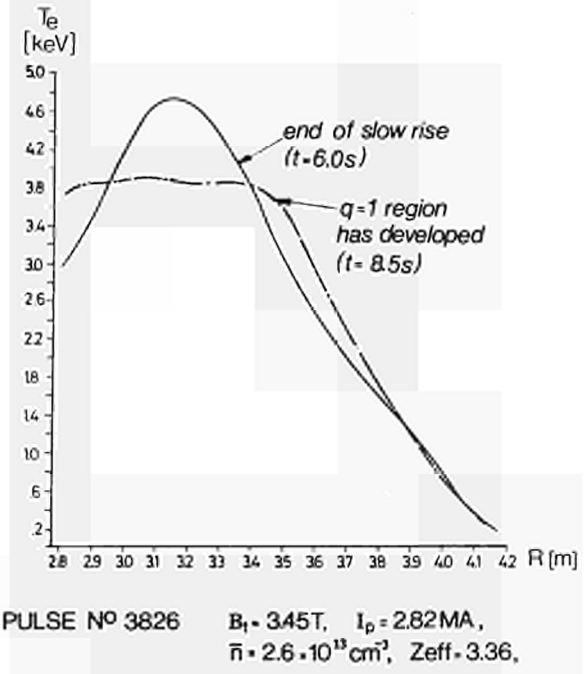

Fig. 2. A similar profile is obtained for a much lower q value when the $q = 1$ region has not yet developed (end of slow rise). Subsequently, the effect of sawtoothing is to cut the central region of the profile at a lower temperature value.

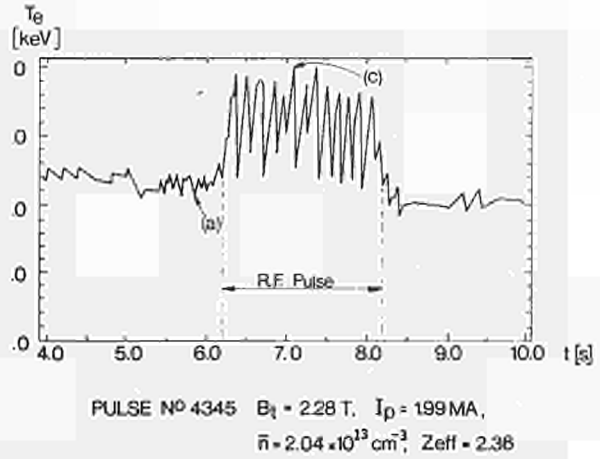

Fig. 3. Evolution of the central electron temperature when an RF pulse is applied, in which giant sawteeth are observed. The temperature collapse at the end of the sawteeth is not always complete but occasionally full reconnections do occur which lower the central temperature to ohmic values.

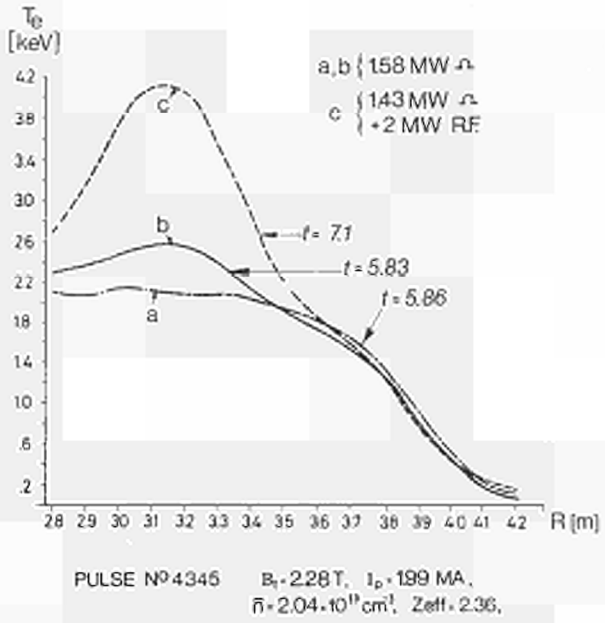

Fig. 4. The electron temperature profile under different conditions: (a) at the end of a sawtooth after full reconnection; (b) at the peak of a sawtooth during ohmic heating; (c) at the peak of a sawtooth during RF heating. The profile outside the $q = 1$ region (sawteeth region) does not vary significantly with or without additional heating (confinement degradation). The central zone ($q = 1$) does not exhibit such a behaviour.

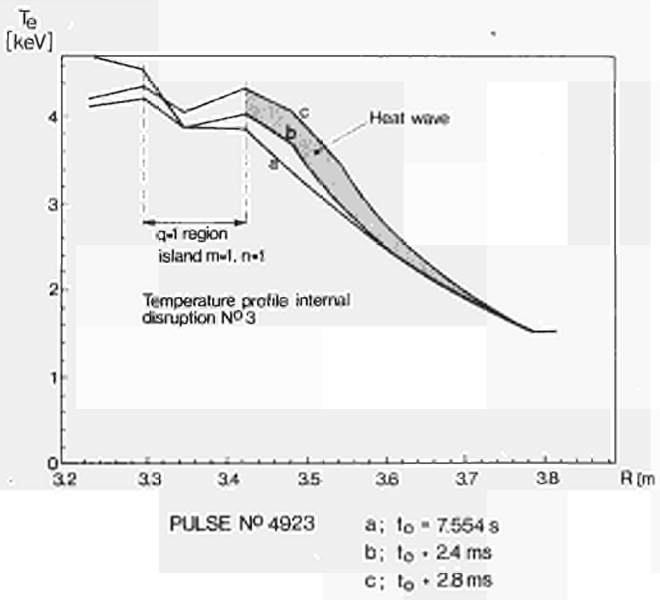

Fig. 5. Heat wave in JET after a sawtooth collapse. It propagates from $R \simeq 3.58$ m to $R \simeq 3.74$ m in 0.4 ms (≃40 cm/ms). The change in the temperature profile is small (~0.5 keV over ~4 keV).

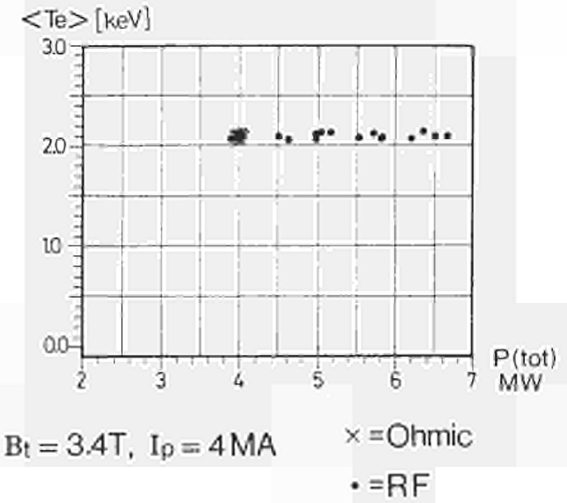

Fig. 6. The average electron temperature does not vary appreciably when the total RF input power varies from 4 to 6.6 MW.

where T_c depends on the plasma parameters and not on the power input. This is confirmed by the evolution of the volume average electron temperature when the RF power is varied, for constant values of the machine parameters (magnetic field, current and density).

The volume average temperature is shown in fig. 6 as a function of the total power input. As can be seen, there is no variation over a wide range of power. The increase in the sawteeth region is compensated by a small temperature decrease caused by a density build-up during the RF pulse.

If the experimental evidence generally supports these facts, the concept of energy confinement time in predicting the plasma performance becomes doubtful and must be replaced by a concept of central electron temperature capability of the device.

A scaling law has been obtained on JET by regression analysis giving the dependence of the electron temperature at the $q = 1$ surface, or at the plasma centre if $q > 1$, on global parameters.

The result of this analysis is shown in fig. 7. The q dependence in this formula has been included to take into account the "cutting" of the temperature profile by the sawtooth relaxation.

The scaling law for the electron temperature at the $q = 1$ surface could be:

$$T_e = 0.66 \frac{I_p^{1.5} B_t^{0.5} (R/a)^{1.4}}{r^{0.9} n^{0.7} K^{0.25}} \log\left(\frac{q_c + 0.8}{1.8}\right) + T_p \qquad (4)$$

[T_e, T_p (keV), I_p (MA), B_t (T), r (m) and n (10^{19} m^{-3})]. Here r is the radius defined by the condition $T_{e|r} = 0.5\, T_{e|q=1}$ and T_p is a pedestal which defines the electron temperature where atomic processes become

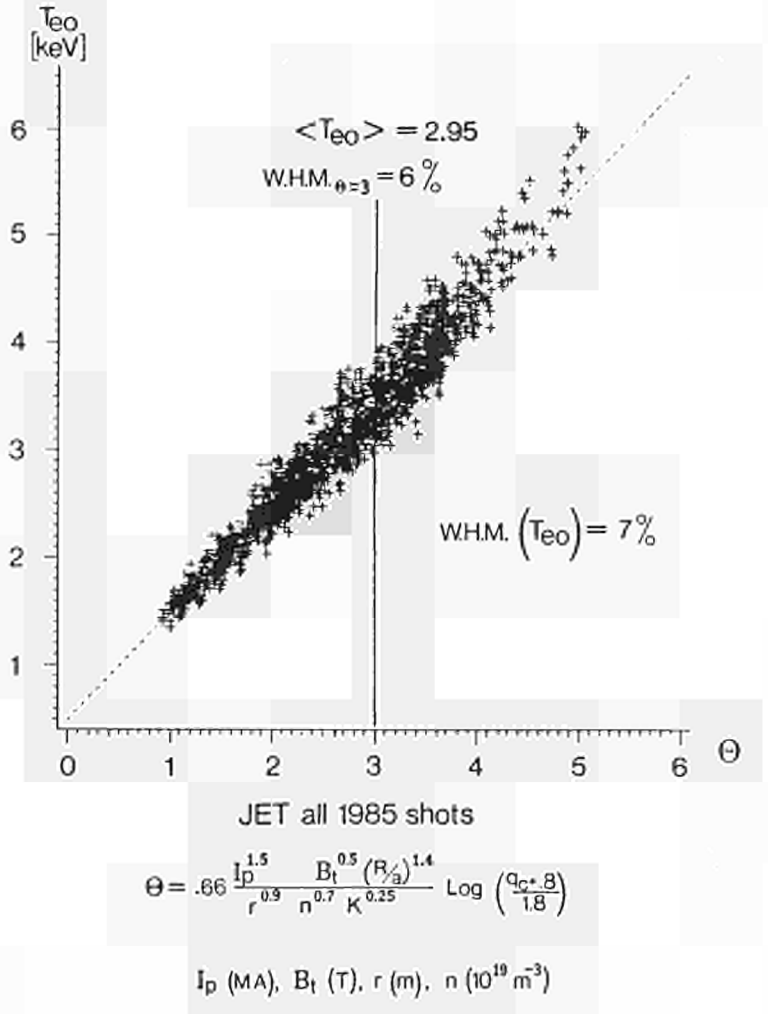

Fig. 7. Scaling law for the electron temperature on JET as a function of machine parameters. The dependence on the cylindrical q (q_c) takes into account that the critical temperature profile is cut by the $q=1$ region. For a given toroidal field the maximum temperature is obtained for $q = 3.5 - 4$. In this formula r is the radius defined by $T_e = 0.5\, T_e$ ($q=1$), where a strong temperature gradient exists.

significant ($0.3\ \text{keV} < T_p < 0.5\ \text{keV}$).

Even if the statistical error is small, the values of some of the exponents are difficult to assess due to experimental correlations between the independent variables (e.g. n and Z_{eff}).

In conclusion, three regions can be identified in the plasma:

1) the sawteeth region ($q \simeq 1, q' \simeq 0$) where $\nabla T_e = 0$ after a full reconnection. The amplitude of the sawteeth depends directly on the heating power and long confinement time with no degradation is observed between two relaxations.
2) The "confinement" zone, not dominated by atomic processes, which is characterized by a "critical" electron temperature profile largely independent from the power input. In this zone the diffusion equation (1) must be replaced by Eqs. (2) or (3) which describe a thermostatic system (two phase equilibrium)
3) An edge region where atomic processes are dominant (radiation, ionization) due to plasma-wall interaction and where a poor confinement is generally observed.
4) If, in addition, the results obtained on ASDEX (Wagner et al., 1982; Keilhacker et al., 1984) and on PDX (Kaye et al., 1983) are considered, a fourth domain could be envisaged with good confinement properties around the separatrix with steep temperature gradients.

III) Non dimensional analysis

A meaningful scaling law can be constructed using non-dimensional parameters (Beiser and Raab, 1961; Kadomtsev, 1975; Connors and Taylor, 1977). In regions wher atomic processes do not play any rôle (thus excluding the plasma edge) the non-dimensional parameters can be classified into two groups:

1) shape parameters, defined as ratios of two components of the same physical quantities and which generally describe the geometry of the plasma or its composition.
2) Structural parameters, constructed from different physical quantities. Relations between the structural parameters reflect the physics which is involved.

The following table shows the non-dimensional parameters needed to describe the physics of a steady state tokamak including Additional Heating.

Group 1

Description	Parameters	
a) geometry	$q,\ R/a,\ r/a,\ rq',\ r\nabla T/T,\ r\nabla n/n$	(5)
b) composition	$m_e/m_i,\ T_e/T_i,\ Z_{eff},\ n_e/n_i$	(6)

Group 2

Description	Parameter	
a) ideal MHD	$\beta \equiv 8\pi nkT/B_t^2$	
b) resistive MHD	$\Delta^* \equiv \eta J/B_p v_{th} \sim \eta/qr\sqrt{2kT_e/m_e}$	
c) heating	$\Pi \equiv 8\pi R\mathcal{P}_e/B_t^2\sqrt{2kT_e/m_e}$	
d) finite Larmor radius (Vlasov equation)	$\Omega \equiv 2m_e kT/q_e^2 B_t^2 r^2$	(7)
e) charge separation (relativistic effects)	$\Gamma \equiv 2kT/m_e c^2$	
f) collisions (granular effects)	$\zeta \equiv q_e^2/rm_e$	

If the shape parameters are initially neglected, or if only plasmas with the same "shape" are considered, comparisons could be expressed only by relations between the structural parameters. In the following we will neglect also the numerical constants in the different relations.

Taking into account the number of independent variables which can be constrained externally, the physics of magnetic confinement can be summarized by only two relations among the five structural parameters.

The first relation is the one which defines the electrical resistivity:

$$\Delta^* = \zeta r^{-2} \equiv \frac{m_e c^2 e^2}{4rk^2T^2} \equiv \Delta^+ \rightarrow \eta \sim T^{-3/2}. \tag{8}$$

Then the electron temperature can be related to the input power. Neglecting relativistic effects and taking collisions into account by replacing Δ^* with Δ^+ we have:

$$g^*(\beta, \Omega, \Pi, \Delta^+) = 0. \tag{9}$$

In the ohmic heating case, an extra relation defines the power input:

$$\Pi = \Delta^+ \tag{10}$$

Under these conditions it is impossible to distinguish between collisionality and heating and the confinement time degradation with additional heating will strongly depend on the relative weight of Π and Δ^+ in Eq. (9).

The electron temperature profile in the "confinement" zone is found to be largely independent of the input power and the function g^* is independent of Π. Eq. (9) becomes:

$$g(\beta, \Omega, \Delta^+) = 0. \tag{11}$$

Eq. (10) implies a full degradation of the energy confinement time. Such a law may apply only in a restricted region as the parameter Δ^+ varies over a wide range between plasma centre and edge. A relation between β, Ω, Δ^+ in the form of a power law is only valid asymptotically and does not necessarily apply for large variations of some of the parameters. In fact, the scaling given in fig. 7 could be given by the relation:

$$\Omega^{1/3}\beta^{2/3} = \Delta^{+(\sim 0)} = \text{const.} \tag{12}$$

The dependence on Δ^+ is weak but the relative weight of Ω and β is difficult to assess due to the observed coupling between density and impurity level. A more complicated dependence for the electron temperature is expected when edge effects are taken into account.

IV) Magnetic Topology

It is generally thought that the topology of magnetic field lines plays a major role in determining tokamak behaviour; internal disruptions (sawteeth), and major disruptions are attributed to a rearrangement of the magnetic structure due to the growth of large magnetic islands. Further, more complicated geometries could arise where ergodic field lines and small size islands co-exist. These structures could be responsible for some of the phenomena observed in tokamaks, such as anomalous heat conduction, degradation of confinement with additional heating, L and H mode transitions.

The basic topology can be computed from a very simple set of equations in slab geometry, but the resulting mapping is indeed very general:

$$\frac{dx}{dz} = \Sigma_j A_j \cos(m_j y - n_j z); \qquad \frac{dy}{dz} = x \tag{13}$$

where x and y are the coordinates of the cross section. The equation

$$x_j = \frac{n_j}{m_j} \tag{14}$$

defines the centre of a set of magnetic islands and A_j is the amplitude of the magnetic field perturbation. The different mappings shown in fig. 8 correspond to a set of three islands with same amplitude $A_j = A$, same m number ($m = 1$) and different n numbers ($-1, 0, 1$). The size of the ergodic regions increases when the amplitude of the perturbation increases. In an early phase the ergodicity is confined around the separatrices (a); subsequently, it expands over a continuous zone embedding the islands (b): in this phase secondary islands are created. Finally for large perturbations the interaction region is fully ergodized and the island structure disappears (c).

We can define an overlapping parameter:

$$\gamma = \frac{\varepsilon_j + \varepsilon_{j+1}}{\delta_{j,j+1}} \tag{15}$$

where

$$\varepsilon_j = 2\sqrt{\frac{A_j}{m_j}}; \qquad \delta_{j,j+1} = \left|\frac{n_{j+1}}{m_{j+1}} - \frac{n_j}{m_j}\right| \tag{16}$$

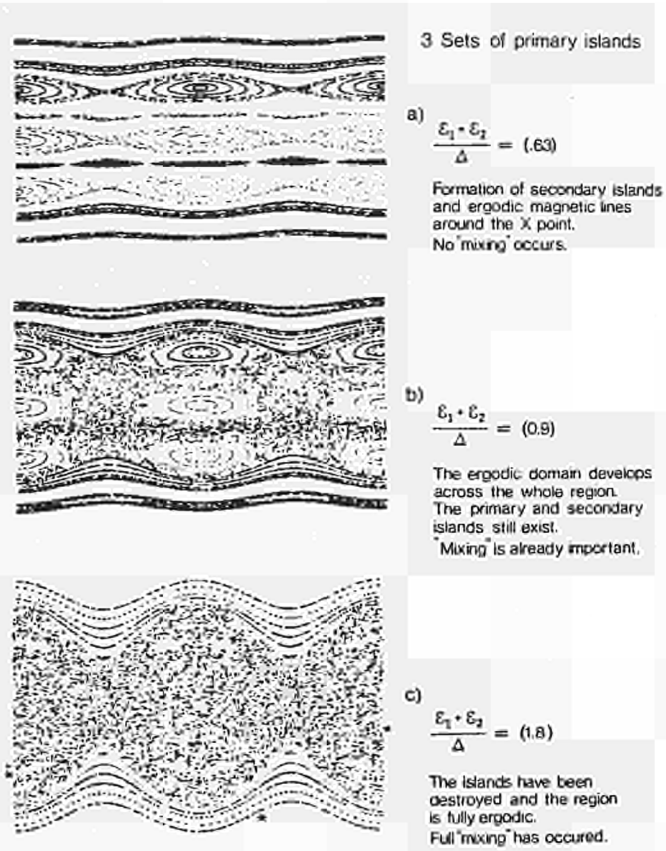

Fig. 8. Interaction of magnetic islands showing the creation of ergodic field lines.

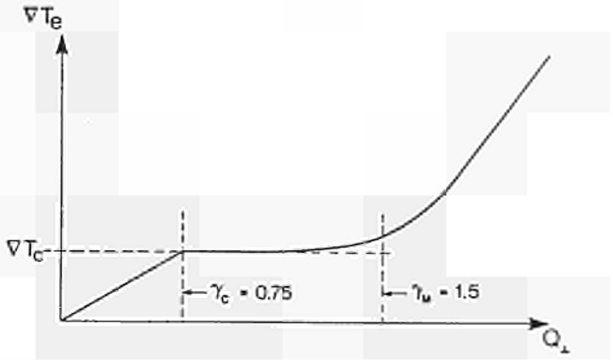

Fig. 9. Variation of ∇T_e as a function of the heat flux $Q_\perp$ at the onset ($\gamma = 0.75$) and saturation ($\gamma \simeq 1.5$) of the ergodization (schematic).

ε is the island size and δ the separation between adjacent islands.

The ergodic regions around the separatrices join together when the magnetic islands start to overlap. Due to the presence of secondary islands the overlapping starts at a value of γ somewhat lower than 1 ($\gamma = 0.75$). For $\gamma \simeq 1.5$, the island structure is destroyed even if the diffusion of ergodic field lines has not reached a saturated state.

The following relation between γ and A was used in the computation:

$$\gamma = 4\sqrt{A} \tag{17}$$

In a tokamak

$$\varepsilon^2 = 4\frac{R}{m}\left|\frac{\tilde{B}q^2}{B_t q'}\right| \tag{18}$$

and

$$\delta \simeq \frac{3q^2}{mq'} \tag{19}$$

where $q = m/n$ is the safety factor and $\tilde{B}$ is the perturbing radial field.

When $\gamma = 0.75$ the corresponding critical perturbing field $\tilde{B}_c$ is given by:

$$\frac{\tilde{B}_c}{B_t} \simeq 0.3\frac{q^2}{Rq'm^3} \tag{20}$$

From these considerations follows that a continuous sequence of states can arise in a magnetically confined plasma, from a laminar state with nested magnetic surfaces and non overlapping islands to a fully ergodized state. The transition which occurs when the ergodic regions around the separatrices join together for $\gamma \gtrsim 0.75$ may induce a complete change in the confinement properties of the plasma.

The equivalent mean perpendicular thermal conductivity $\bar{\chi}_\perp$ has been calculated for a fully developed ergodic domain (Rechester and Rosenbluth, 1978). Calculations are not available yet for the transition region where magnetic islands and ergodic field lines co-exist but an estimate of the transport when the electron mean free path is smaller than a few times $2\pi R$ can be made following the previous scheme.

If we assume that, in the overlapping region, the electrons "can choose" to pass on either side of a set of islands each time they cross the separatrix, we obtain, for $\gamma > \gamma_c = 0.75$:

$$Q_\perp = S\chi_\parallel \nabla T_e \frac{\tilde{B}^2}{B_t^2}\left(\frac{\gamma - \gamma_c}{\gamma}\right)\left(1 - \log\frac{\gamma - \gamma_c}{\gamma}\right)^{-2} \tag{21}$$

where S is the average surface of the ergodic region. When the electron mean free path is much longer than mR, $\chi_\parallel$ has to be replaced by:

$$\alpha(\gamma) n v_{th} \tfrac{2}{3} mR \tag{22}$$

where α is a numerical factor.

If γ_m is a value for the overlapping parameter at which full ergodization occurs for a given mode number m, saturation is reached and the heat flow $Q_\perp$ is again proportional to the temperature gradient ∇T_e. This is schematically shown in fig. 9 where a limiting value $\gamma_m = 1.5$ is assumed. The saturation level depends also on electron temperature and density and it increases with density at high temperatures (Eq. 22).

To calculate the ergodization of the field lines self consistently, it is necessary to relate the perturbing magnetic field to the plasma current, which in turn requires a non-linear calculation of the island size either in a saturated or in a transient phase. The very existence of the islands could even be linked to the plasma transport properties inside the islands and in the surrounding ergodic regions. According to the island size, several phenomena could contribute to these patterns, such as tearing and micro-tearing modes or thermal instabilities. We will try to assess the potential role of some of these phenomena in creating the described topologies in tokamaks.

Assuming that the perturbing magnetic field is due to the presence of islands, its value can only be a few times (Eq. 20) the critical value $\tilde{B}_c$. As a consequence, for high m numbers ($m > 20$), the heat flow can not be strongly influenced by ergodicity.

As an example, in JET, with $S = 100\,\mathrm{m}^2$, $\nabla T_e \cong 6\,\mathrm{keV/m}$, $T_e \cong 3\,\mathrm{keV}$ and an ergodic region of a few tenths of the total plasma volume, a perturbation level of 3×10^{-5} leads to a heat flow in excess of 5MW.

The following conclusions can be drawn from these considerations:

—the interaction of sets of magnetic islands produces a surrounding ergodized region for $\gamma > \gamma_c \simeq 0.75$.
—The mixing of magnetic field lines in the ergodized region can be thought of as a new phase in the plasma.
—Ergodization does not occur when $q' \simeq 0$ due to the lack of overlapping ($\gamma \ll \gamma_c$), e.g. in the sawteeth region, with no degradation of confinement.
—High q and q' values limit the island size and force high m numbers. Islands would generally not contribute to the transport and would disappear under these conditions (e.g. X points).

V) Thermal Instabilities

The existence of islands with closed magnetic surfaces surrounded by ergodic zones could result from the different thermal properties of these two magnetic topologies.

When islands are large enough they can provide a good thermal insulation and under or overheating can develop. This would change the local resistivity and modify the current distribution (Rebut and Hugon, 1984), with stabilising or destabilising effect depending upon the sign of the related current, as compared to the sign of the shear q'. The importance of this effect is measured by the value of the parameter N:

$$N = -6\pi \frac{J_0 r_0}{B_t}\frac{\mathcal{P}_v}{\chi_\perp T_e}\frac{Rq^2}{q'} \tag{23}$$

where $\mathcal{P}_v$ is the net input power to the electrons in the island excluding the conduction contribution and $\chi_\perp$ is the average "perpendicular" electron thermal conductivity in the ergodic region. We can distinguish different conditions:

a) small shear ($q' \simeq 0$): N becomes very large and instabilities can develop with either under or overheating

even if the surrounding region is not ergodic and $\chi_\perp$ is small (fig. 10). In the sawteeth region $q' = 0$, there are no adjacent islands and ergodization cannot develop, but the island growth could be limited by MHD effects. This may explain the good confinement time in this region between the sawteeth collapse and the fact that no degradation of confinement is observed.

A feedback in the $q = 1$ region acting on the local current distribution or on the plasma resistivity may stabilize the sawteeth leading to higher temperatures.

Good plasma confinement could be obtained by controlling the current profile in order to have $q' \simeq 0$ and $q \neq 1$ over a wide area. This requires current and temperature profiles not to be coupled through the resistivity; non-thermal current carrying electrons sustained by current drive or slide-away regimes could be a possible scheme.

b) Normal condition ($q' > 0$): in this case only underheating instabilities can develop in a tokamak. This occurs in the edge regions where losses due to atomic processes overcome the local plasma heating. The island size is only limited by its self destruction either by ergodization or disruption (fig. 11). These phenomena can arise only for small m numbers:

$$m \leqslant 5, 6 \tag{24}$$

The plasma current density is small for $q > 2$ and it is easy to get into a situation where underheating occurs ($\mathcal{P}_0 < 0$). In this case, islands develop centered on magnetic surfaces with rational q values corresponding to small m numbers ($q = 2, 3, 5/2 \ldots$).

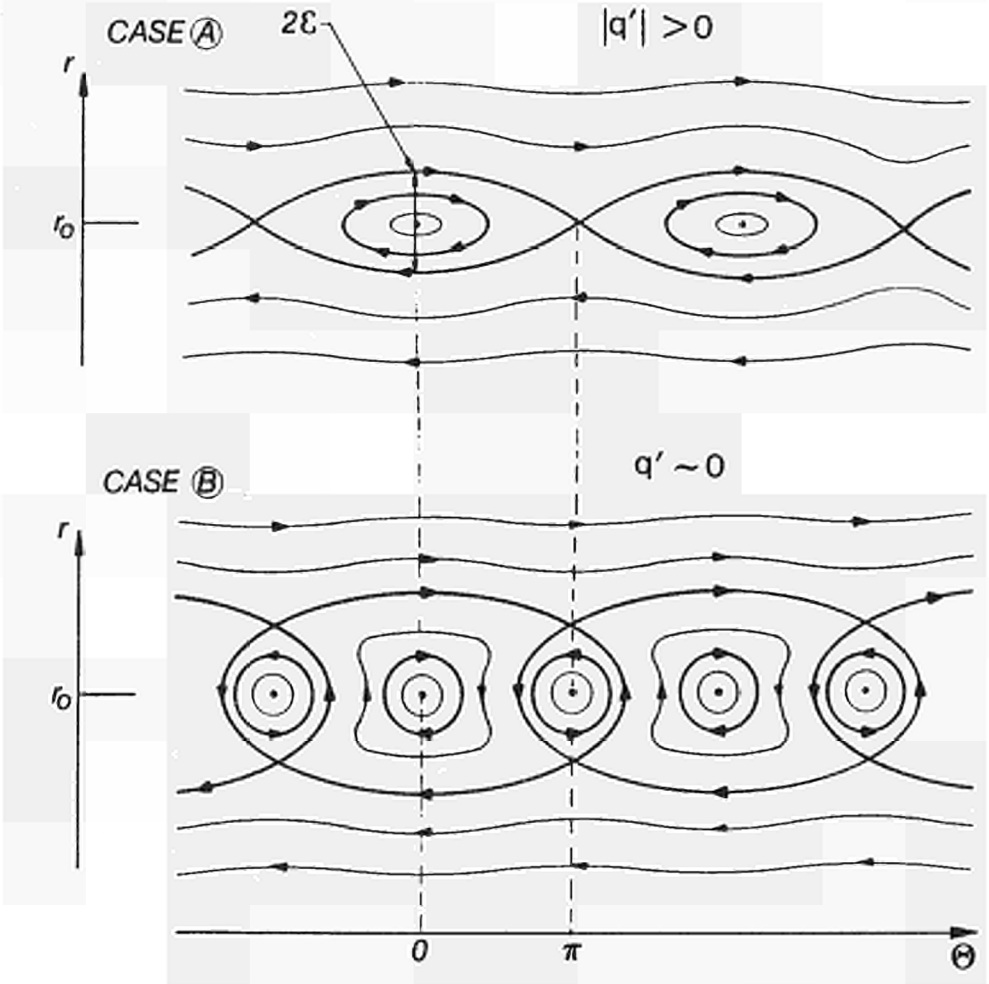

Fig. 10. Island topology in presence of shear (A). When the shear is weak (B) more complicated topologies can exist with islands twisting in opposite directions.

Islands developing at $q = 2, 3$ can grow very large bridging the $q = 1$ region to the plasma edge; this in turn redistributes current and electron temperature profiles ($J_\parallel \simeq$ const. along a given magnetic field line) leading to disruption (Kadomtsev, 1976), a condition for which could then be written as

$$\mathcal{P}_v < 0 \qquad \text{at } q = 2 \tag{25}$$

or, in non dimensional parameters

$$\Pi < 0 \qquad \text{at } q = 2 \tag{26}$$

c) High q values ($q > 5{,}7$ imposes $m > 5{,}7$): in this condition thermal instabilities cannot arise any more and have no effect on confinement.

In summary the plasma can be divided into several regions (fig. 12):

—a sawteeth region with $q \simeq 1$ and $q' \simeq 0$
—a confinement region with $q > 1$
—an edge region defined by $\mathcal{P}_v < 0$ with poor confinement properties.
—when a separatrix does exist a fourth region must be considered with large values of q, where good confinement could be restored.

VI) Confinement region and temperature gradient

This region extends from $q \gtrsim 1$ to $q \gtrsim 2$ (Eq. 25) or up to the X point in case of H mode. It is characterized by the fact that the electron temperature profile is relatively insensitive to the power flow; this suggests a marginal condition for the plasma, i.e. this region is marginally ergodic with $\gamma \simeq 1$. The change in ergodicity produced by a small increase in island size may explain variations in heat flow leaving the profiles unaffected.

Saturated micro-tearing modes could be responsible for the topology in this region; magnetic islands are

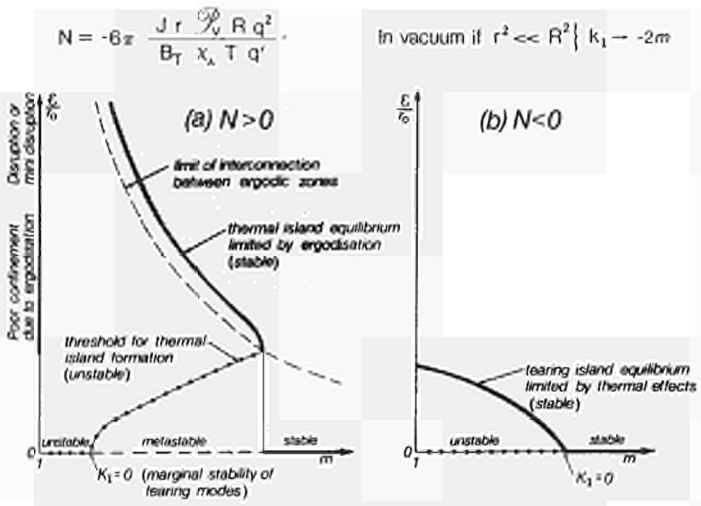

Fig. 11. Existence domain for thermal instabilities and their coupling with the tearing mode. The metastable nature of some equilibria should be noted when thermal effects give rise to instabilities.

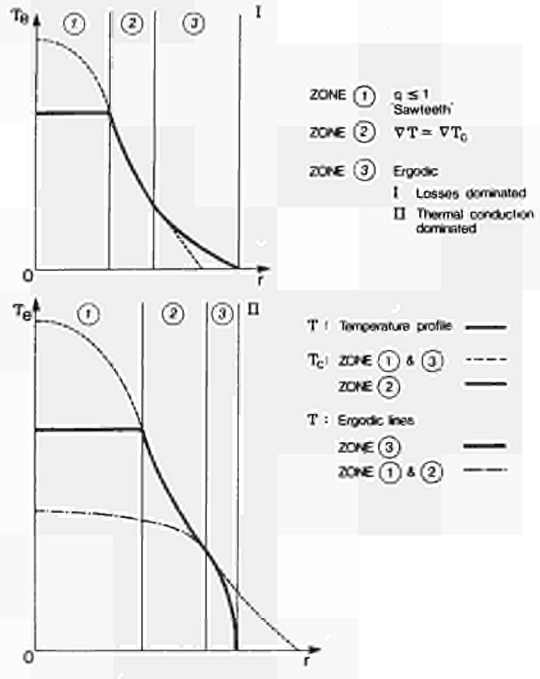

Fig. 12. Different zones in a plasma: the respective confinement properties differ strongly. In zone 1 the temperature profile is controlled by sawteeth activity ($q' \simeq 0$, $q \simeq 1$). In zone 2 a critical temperature profile is established, defined by the equation $\nabla T_e = \nabla T_c$ ($\gamma \simeq 1$). In zone 3 edge effects dominate (e.g. thermal islands, case I) or the plasma is in a regime where ergodicity is saturated when $\nabla T_e > \nabla T_c$ ($\gamma = \gamma_m$, case II).

sustained through energy conversion by the electron temperature gradient and the current flowing along magnetic field lines balances the velocity dependent electron diffusion.

The amplitude of micro-tearing modes and related island size have been calculated both in the linear case (Hazeltine et al., 1975) and including some non linear effects (Samain, 1984), but these studies do not take explicitly into account the ergodic topology, which can have a decisive influence on the electron behaviour and on the onset of micro-tearing instabilities.

We have made the hypothesis that the plasma finds itself in a multiphase state when the temperature gradient approaches a critical value ∇T_c. It seems then logical to assume that the relative size ε/r of the islands is a direct function of $r\nabla T/T$ and depends on the structural parameters β, Ω, Δ^+; the critical temperature gradient is defined by the condition $\gamma \simeq 1$.

In JET, islands with halfwidths $\varepsilon \simeq 1$ cm and m numbers between 10 and 15 would be necessary to explain the observed behaviour.

In order to fully justify this hypothesis, experimental measurements of islands in the plasma are needed or a self consistent computation of islands surrounded by ergodic field lines should be done. Some experimental measurements already indicate that magnetic field fluctuations are correlated with the energy confinement time.

Heat waves arising after the collapse of a sawtooth could be interpreted as an increase of the ergodization in the confinement region due to a small redistribution of the parallel current generated in the plasma centre; this in turn increases the perturbing magnetic field and the ergodization level.

VII) Conclusions

The effect of structured topologies of confinement could explain the behaviour of tokamak plasmas. Attention has been focused in this paper on the electron behaviour and some of the conclusions are still of a speculative nature. In particular, the local electric field resulting from thermo-electrical effects in the ergodic region must be included. The effect of these topologies and of the resulting electric field on the ion population has not been assessed at all.

Nevertheless, the description presented of a magnetically confined plasma seems promising and links together several phenomena which, up to now, seemed uncorrelated.

The main conclusions can be summarized as follows.

Three regions can be generally distinguished in a plasma:

a) a central region where $q \simeq 1$, dominated by sawteeth: the confinement time is long (classical?) between the relaxation of the sawteeth and no degradation is observed during sawteeth. No ergodic domain can generally develop. Feedback control of the sawteeth or current profile control may prove feasible and lead to much higher central temperature values; a factor of two seems achievable.

b) A confinement region where the temperature gradient is established: an equilibrium may exist among laminar surfaces, magnetic islands and ergodic domains. This equilibrium defines a critical temperature which is maintained when the heating rate changes. High energy electrons may be responsible for this behaviour.

c) An external region dominated by atomic processes and power losses associated with the plasma edge: underheating instabilities can grow if resonant surfaces with low rational number are present. In particular, disruptions could occur if:

$$\mathcal{P}_v < 0 \qquad \text{at } q = 2$$

This condition leads to a Murakami type of limit for ohmic heating.

The nature of impurities and the edge values of density and temperature may define the critical density at which a tokamak can work. Low Z wall material like beryllium and high edge temperatures associated with strong edge pumping may help to achieve higher plasma densities, along with high speed pellet injectors.

d) When a separatrix is present a fourth region can exist where the electron temperature is high enough for the plasma not to be dominated by power losses due to atomic processes; significant levels of ergodization leading to large heat flows cannot take place in conditions of high shear and high q numbers and a steep local temperature gradient may be established (H mode).

Different methods to improve plasma confinement will be tried on JET:

i) a high speed pellet injector is under development in a cooperative effort between JET and several

European Laboratories.

ii) Studies are under way for establishing a separatrix inside the JET vacuum vessel at high plasma current values (Tanga et al., 1985).

iii) JET has been operating in the last period with walls covered with low Z material and preparation for beryllium operation is progressing.

iv) A significant part of the next operating phase of JET will be devoted to a better understanding and control of the plasma current density profile, by varying the energy deposition profile and allowing for current drive operation within the flexibility of the JET ICRH system.

If the concepts which have been presented here are supported by experimental evidence and if the scaling of the temperature holds, it is possible to conceive a reactor as a large major radius tokamak with no Additional Heating and without problems of burn control.

VIII) Acknowledgements

Valuable discussions with A. Samain, J. Jacquinot and P. Lallia are gratefully acknowledged. We wish also to thank B. Keen for his help in editing this article.

IX) References

Beiser, A. and Raab, B., *Phys. Fluids,* **4** (1961) 177.

Connors, J. W. and Taylor, J. B., *Nuclear Fusion,* **17** (1977) 1047.

Coppi B., *Proc. Physics of Plasmas close to Thermonuclear conditions, Varenna (Italy) 1979,* Vol. II, p. 479.

Costley, A. E. et al., *12th European Conference on Controlled Fusion and Plasma Physics, Budapest, September 1985,* Vol. 9F, Part 1, p. 227.

Hazeltine, R. D. et al., *Phys. Fluids,* **18** (1975) 1778.

Kadomtsev, B. B., *Proc. 6th IAEA Conf on Plasma Physics and Controlled Nuclear Fusion Research (Berchtesgarden, F.R.G., 1976),* Vol. 1, p. 555.

Kadomtsev, B. B., *Fiz. Plazmy,* **1**, (1975) 531; [*Sov. Phys.–J. Plasma Phys.*, **1** (1975) 295].

Kaye, S. et al., *Proc. 11th European Conference on Controlled Fusion and Plasma Physics, Aachen 1983,* Vol. I, p. 19.

Keilhacker M. et al., *Proc. 10th Conf. on Plasma Physics and Controlled Fusion Research (IAEA) London 1984,* IAEA-CN-44/A-II-1.

Rebut, P. H. and Hugon, M., *Proc. 10th Conf. on Plasma Physics and Controlled Fusion Research (IAEA) London 1984,* IAEA-CN-44/E-III-7.

Rechester, A. B. and Rosenbluth, M. N., *Phys. Rev. Lett.*, **40** (1978) 38.

Samain, A., *Plasma Physics and Controlled Fusion,* **26** (1984) 5.

Tanga, A. et al., *12th European Conference on Controlled Fusion and Plasma Physics, Budapest, September 1985,* Vol. 9F, Part 1, p. 70.

Wagner, F. et al., *Proc. 9th Conf. on Plasma Physics and Controlled Fusion Research (IAEA) Baltimore 1982,* Vol. I, p. 43.

APPENDIX IV (f)
JET-P(85)20

ICRF Studies on JET

J. Jacquinot et al

Invited Paper to the 12th European Conference on Controlled Fusion and Plasma Physics
(Budapest, Hungary, 2—6 September 1985)

ICRF STUDIES ON JET

J Jacquinot, R J Anderson, J Arbez, D Bartlett, B Beaumont[1], K Behringer, E Bertolini, V P Bhatnagar[2], T Bonicelli, G F Bosia, H W Brinkschulte, M L Browne, M Brusati, M Bureš, D Campbell, J P Christiansen, C O A Christodoulopoulos, P Chuilon, R Claesen, J P Coad, J G Cordey, S Corti, A Costley, G Cottrell, B Denne, K Dietz, S Ejima[3], S K Erents[4], B T Eriksson, M Evrard[2], K Fullard, D Gambier[1], R D Gill, N Gottardi, B Green, G Grosso[5] N C Hawkes[4], T Hellsten, J L Hemmerich, M Huguet, O N Jarvis, E Jones, A S Kaye, H Kimura[6] J de Kock, L de Kock, H Krause[7] P P Lallia, J Last, E Lazzaro, P J Lomas, G Magyar, M Mansfield, V Marchese, F K Mast[7] G M McCracken[4], P Mondino, P Morgan, R M Niestadt[8], J O'Rourke, H Piekaar[8], J Plancoulaine, P H Rebut, G Rhoden, G Sadler, F Sand, A Santaquistina, M S Schmid, F Schueller, S Segre[5], A Sibley, M F Stamp, C A Steed, P E Stott, D Summers, A Tanga, J A Tagle[9], P R Thomas, K Thomsen[10], B J D Tubbing[8], M Valisa, H Van der Beken, M Watkins, T J Wade, C I Walker

JET Joint Undertaking,
Abingdon, Oxfordshire, OX14 3EA, U.K.

ABSTRACT

Two antennae have been installed in JET and operated to the maximum design capability of the generators. 4.5 MW, 10 MJ have been coupled to the plasma which heated up to a maximum stored energy of 3 MJ with central temperatures of T_{e0} = 5 keV and T_{i0} = 4 keV without increase of the relative impurity concentration. Degradation of energy confinement is observed according to an L mode scaling. The effect of $k_{//}$ shaping is discussed using a quadrupole antenna. Hydrogen and Helium 3 minority heating regimes give similar results.

KEYWORDS

JET; Tokamak; Plasma Heating; ICRH; Confinement; Energy; Deposition.

INTRODUCTION

The JET programme of extension to full performance is based on two different plasma heating methods:

- Neutral Beam Injection (NBI) with a total of 10 MW, in two units, of "high grade power"
- Ion Cyclotron Range of Frequency (ICRF) with a total of 15 MW, in ten units, of "high grade power"

where in both cases "high grade power" refers to the power deposited in the plasma centre, defined as 25% of the plasma volume. For ICRF, it was estimated that this specification would require 30 MW at the output of the RF generator plant.

---

[1]From EUR-CEA Association, Fontenay-aux-Roses, France
[2]From LPP-ERM/KMS; EUR-EB Association, 1040 Brussels, Belgium
[3]From GA Technologies Inc., PO Box 85608, San Diego, California 92138, USA
[4]From EUR-UKAEA Association, Culham Laboratory, Abingdon, Oxon OX14 3DB, UK
[5]From EUR-ENEA Association, Frascati/Roma, Italy
[6]From JAERI, Naka-Gun, Ibaraki-Ken, Japan
[7]From EUR-IPP Association, Garching, Federal Republic of Germany
[8]From EUR-FOM Association, Rijnhuizen, Postbus 1207 - Edisonbaan 14, NL-3430 BE Nieuwegein, The Netherlands
[9]On leave from UNESA-ASINEL, Madrid, Spain
[10]From Risø National Laboratory, Roskilde, Denmark

The physics of NBI heating is solidly documented and well proven by experiments where it is normally the major heating method. However, the high injection energies required for penetration of large plasmas sharply decrease the neutralisation efficiency with serious consequences on the technological complexity and cost of the system. Nevertheless, good progress has been achieved and the first NBI unit will be used during the next JET operation programme. On the contrary, the efficiency of ICRF does not, in theory, appear to be penalized by the increased plasma size. However, the method is based on physics processes which are far more complex and remain somewhat unclear despite the remarkable progress achieved recently. Therefore the two methods appear complementary; when used separately, a larger domain of plasma operation can be explored; when used simultaneously, synergistic effects may be expected on wave damping and current drive.

On the technical side, the JET ICRF system will deliver, when completed, 30 MW in 10 antennae and will be operated in pulses lasting 20 s. Each unit can be operated at any particular frequency chosen between 23 to 57 MHz. Groups of units can also be operated at the same frequency and phase locked. Compared to the previous generation of experiments, this implies a formidable increase in the size of the system: in particular, the amount of energy delivered to the plasma will be increased by nearly three orders of magnitude.

On the physics aspect, the relative importance of basic processes are greatly modified by the large size of JET:

(i) For the first time, the wavelength inside the plasma becomes small (1/5) compared to the plasma radius. This will decrease the importance of diffraction effects and allow focusing effects analogous to geometrical optics. This effect is illustrated in Fig. 1. The main component of the group velocity is along the density gradient and the wave is strongly focused in a poloidal plane although significant divergence occurs in the toroidal plane. Full wave calculations confirm this conclusion which has the consequence of a highly peaked deposition profile when the cyclotron layer passes in the vicinity of the magnetic axis.

(ii) Both larger size and higher temperature increase the wave damping at each pass across the damping zone. For JET ohmic plasma parameters, nearly single pass damping is achieved in the case of Hydrogen minority heating; the ^{3}He minority case is somewhat less effective (50% of power damped per pass) but is still far greater than in smaller experiments.

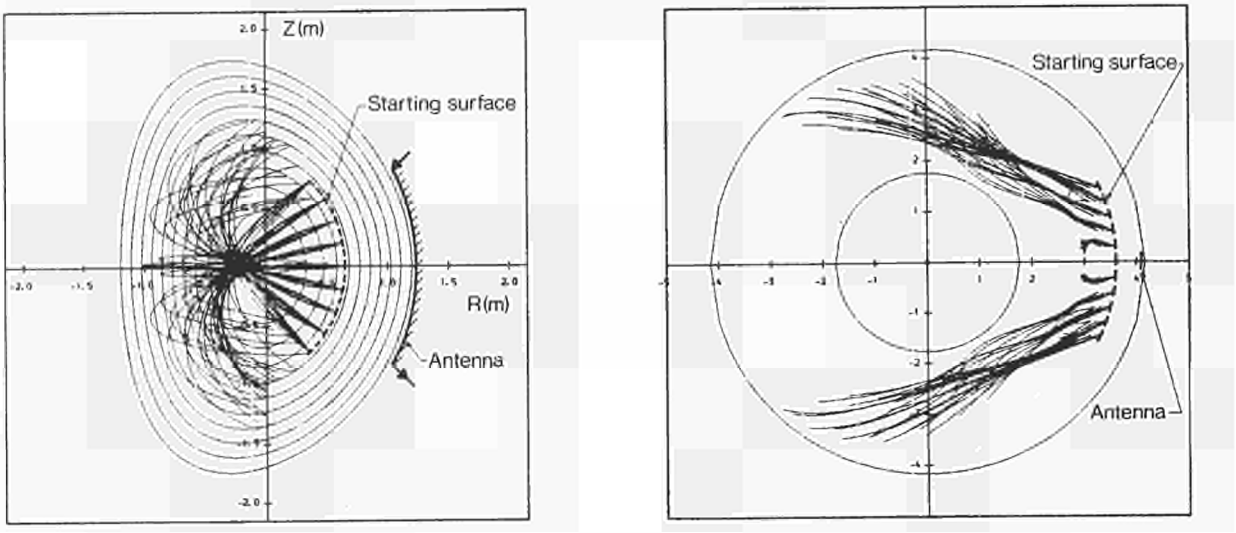

1a Poloidal Projection 1b Toroidal Projection

Fig. 1. Ray tracing calculation illustrating, for JET conditions, focusing of the wave energy in the poloidal plane and divergence in the toroidal direction. Reflection on the high field side is also shown.

The construction of the ICRF system, organised in three successive stages, started at the end of 1982. Operation with the first stage, consisting of two units, began in 1985. A description of the system, the plasma antenna coupling and preliminary results after the first four months of operation were presented in a recent publication (Jacquinot et al, 1985). In this companion paper, we concentrate on the analysis of the results relevant to ICRF physics and to confinement under additional heating.

EXPERIMENTAL SET-UP

Two antennae (Arbez et al, 1984) are installed on the low field side of the torus and at diametrically opposed toroidal locations (Fig. 2). Additional thermal protection is provided by four movable carbon limiters normally introduced for the high power experiments 16 to 26 mm further inside the torus. In these conditions, the thermal load is shared by all six limiter structures. The antenna electrostatic screen is 17 mm in the shadow of the carbon frame. Made of nickel bars, it is designed as a wave polariser transparent to the wave electric field corresponding to the polarisation of the fast magnetosonic wave. This is achieved by inclining the nickel bars at 15° to the horizontal.

The screen, housing and coaxial feeds of the two antennae are identical. However, they differ in the configuration of the central conductors (Fig. 3). The antenna, referred to as A_{01}, is made of two single turn coils. When the coils are fed out of phase (configuration A_{01_M}, "Monopole"), the two current elements reconstruct the conventional single turn normally used in ICRF experiments. In-phase feeds, ($A_{01}D$, "Dipole"), however, eliminate coupling to modes with large poloidal wavelength (m = 0 modes). The antenna referred to as A_{02}, is made of four single turn coils with internal connections producing two poloidal dipoles, separated toroidally by a distance of 20 cm and fed as previously by two coaxial lines. Fed in phase ($A_{02}D$), this configuration is similar to $A_{01}D$ but with a somewhat larger equivalent width. Feeding out of phase ($A_{02}Q$) in a "quadrupole mode" radiates a spectrum which is depleted for both long poloidal and toroidal wavelengths. With $A_{02}Q$, the peak radiation occurs for a toroidal wave number of 7 m^{-1}, a spectrum comparable to the conditions generated by the phased array of JFT 2M (Mori, 1984), which considerably reduced impurity release.

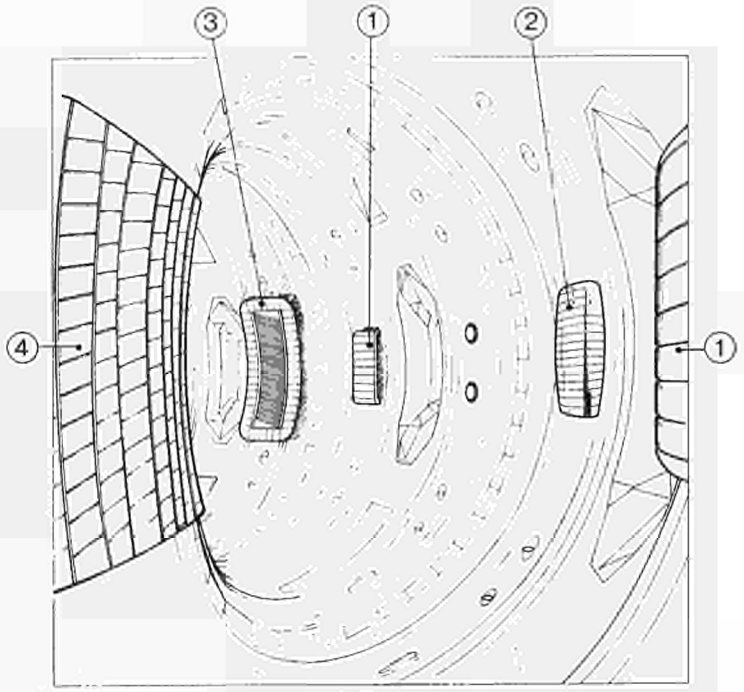

Fig. 2. View of the JET vacuum vessel showing one of the 2 diametrically opposed antennae protected by a picture frame of carbon tiles. Nickel and carbon limiters are located on either side of the antenna. Nickel limiters were retracted during operation. The inner vessel central column on the left is covered with carbon tiles.

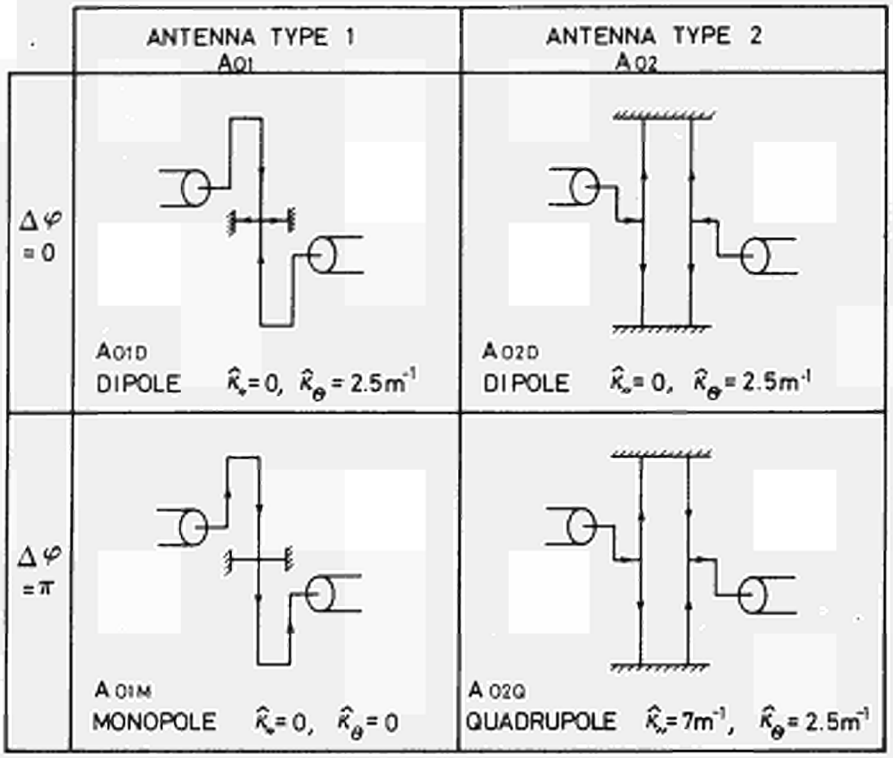

Fig. 3. Sketch of the RF current paths for the 2 antennae in the 2 possible states of phasing. $\hat{\kappa}$ indicates the peak value of the radiated spectrum.

Each coaxial feed is connected through a long (84 m) coaxial transmission line to a 1.5 MW amplifier (Wade et al, 1984). The two amplifiers feeding an antenna form a unit driven at the same frequency and locked either in phase or out of phase with respect to each other. Impedance matching is achieved by impedance transformation caused by a fine frequency tuning (± 0.9 MHz) and by an adjustable stub placed along the main transmission line. The principal features of the RF system are summarised in Table 1.

Table 1 Main Features of the RF Power System

Frequency	23 to 57 MHz in 8 pre-set channels
Power	3 MW per unit in 2 outputs provided VSWR < 1.5
Pulse Length	20 seconds
Duty Cycle	1/30
Transmission Lines (2 per unit)	ϕ = 230 mm, 30 Ω, Length 84 m, 3 bars overpressure in dry air
Matching	Single stub and frequency tuning

MEASUREMENT OF LOSSES AND COUPLED POWER

The net RF power delivered by the generator $P = P_{inc} - P_{refl}$ is measured by directional couplers on the line and cross calibrated by calorimetric measurements by diverting all the RF power into a dummy load. The losses in the transmission lines and in the antenna, mainly in the screen, are deduced from the equivalent resistance of the system

$$R = 2\ PZ_o^2/V_M^2$$

where V_M is the peak voltage along the coaxial line and Z_o its characteristic resistance.

The measurement of R with plasma (R_p) or without it (R_v) provides the value of the wave power effectively launched inside the torus. Throughout this paper this power will be referred to as P_{RF}.

$$P_{RF} = \eta \,.\, P\ ;\ \eta = (R_p - R_v)/R_p$$

Both antennae have R_V values of 0.6 Ω at 33 MHz when matching is achieved at the generator end, 85 m from the antenna tip. It drops to about 0.2 Ω when the matching element is located close to the antenna. As discussed by Bureš et al, 1985, the values of R_P vary widely depending on the antenna type, the distance between the plasma edge and the antenna, and finally, the edge density profile. As expected, quadrupole phasing considerably reduces the coupling; η is only 30% (far matching) or 75% (close matching). In the other conditions (Monopole and Dipole), η is about 90%.

The coupling resistance R_P appears fairly constant during a 2 s RF pulse; however in the case of significant heating in the plasma centre, R_P shows an "inverted sawtooth" behaviour in close correlation, after a delay of 40 ms, with the sawtooth relaxation of the central electron temperature (Jacquinot, 1985). Strong sawtooth activity is also observed in the intensity of the light emitted from the limiter, the antenna tiles and its screen. These observations suggest that the burst of heat generated after the crash of the sawtooth releases gas from the carbon tiles which contributes to an increase of density.

EXPERIMENTAL CONDITIONS

So far, ICRF has been operated with vessel walls and antennae heated to 300°C and carbonised walls, although the carbonisation was in some cases fairly old (∿ 15 days). The frequency is normally chosen to match, near the magnetic axis, the fundamental resonance of the Hydrogen or Helium 3 minority. After glow discharge cleaning, the background hydrogen concentration settles to 3 to 5% of the Deuterium density. It was found difficult to modify the concentration by Hydrogen injection without significant change to the plasma density. The ^3He minority is injected about 2 s before the RF pulse and its concentration is monitored by measuring the corresponding increase of electron density. The usual concentration ranges from 5 to 10% of the Deuterium density. The effect of Helium injection is quite apparent as it effectively damps the toroidal resonance in the cavity formed by the torus chamber. Cross-talk between the antennae is also reduced by more than an order of magnitude. The initial period of operation of ICRF heating on JET which is the subject of this paper, was essentially devoted to technical commissioning of the equipment with the plasma and no systematic variation of the plasma parameters could be attempted. Nevertheless, a variety of conditions were explored, as summarised in Table 2. It can be seen that the exploration of the parameters is only in the range of a factor of 2 for the most important parameters such as P_{RF}/P_Ω, I_p, $n_e\ell$. Other parameters (such as q and ellipticity) essentially stayed constant.

RESPONSE OF THE PLASMA TO AN RF PULSE

Figures 4 to 7 illustrate the variation of the plasma parameters by an ICRF heating pulse. The minority is Hydrogen with $n_h/n_d = 4\%$; $B_\phi = 2$ T ; $I_p = 2$ MA and $n_e\ell = 6.4 \times 10^{19} m^{-2}$. The antennae are either used simultaneously during an overlapping period of 1 s (Figs. 4 & 5) or separately in consecutive identical shots (Figs. 6 & 7). The illustration in Figs. 4 & 5 corresponds to the highest ratio of RF power to ohmic power achieved so far on JET (2.5). In this case, the time average central electron temperature rose from 1.8 keV to about 3 keV (Fig. 4b). The volume average temperature (Fig. 5a) underwent a smaller relative increase from 0.8 to 1.1 keV. As the plasma heated up, giant sawtooth disruptions of the central electron temperature developed, reaching in some cases, a temperature excursion of 1.5 keV.

Table 2 Experimental Conditions during ICRF Heating

Frequency (MHz)	25 30 33 47
Coupled Power, P_{RF}	$\leq$ 4.5 MW
P_{RF}/P_{Ω}	$\leq$ 2.5
Majority Ions	Deuterium
Minority Ions	Hydrogen or Helium 3, $\frac{n}{n_e} \sim$ 2.5 to 5%
Plasma current (MA), I_p	2 to 4
Magnetic field (T), B_ϕ	2 to 3.4
Electron line density, $n_e\ell$ (m^{-2})	6×10^{19} to 1.2×10^{20}
Z_{eff} (from Bremsstrahlung)	3 to 5
Ellipticity	1.4 to 1.5 (Horizontal dimension 2.3 m)

During the rise of a sawtooth, the electron temperature profile (Fig. 4a) becomes steeper inside the q = 1 magnetic surface. After its collapse, it takes a shape similar to the pre-RF phase. At the highest heating level achieved, the regularity of the sawteeth is broken by the appearance of a sub-harmonic modulation which periodically creates very long sawteeth reaching 250 ms, a value to be compared to 100 ms before RF is applied.

As mentioned earlier, the heating pulse is accompanied by an increase of line density (+ 18% in the case of Fig. 4) possibly resulting from the desorption under increased thermal loading of the limiter tiles and antenna structures.

The increase of central deuteron temperature deduced from the neutron flux and from the Neutral Particle Analyser, NPA, (Corti, 1985) is comparable to the increase of central electron temperature (Fig 5b). There is no evidence of deviation from a Maxwellian energy distribution as seen from both the NPA and from the neutron spectrum. On the contrary, the Hydrogen minority energy spectrum measured by the NPA shows a high energy tail with a slope corresponding to an apparent temperature of 15 keV. The overall effect of impurity production is measured by the evolution of the Bremsstrahlung emission in the visible spectrum. The value of Z_{eff} does not change appreciably when RF is applied. Bolometric measurements along several vertical and horizontal chords show that most of the radiated power is coming from the plasma periphery. The power radiated from the centre does not exceed 10% of the input power and this ratio does not appreciably change during the heating phase. The same conclusion applies to the total radiated power which remains a constant or slightly decreasing fraction of the total input power (Fig. 8). Spectroscopic analysis (Stamp et al, 1985, Denne et al, 1985) confirms the general conclusion that the relative concentration of impurity does not increase with RF and that impurity radiation never plays a significant role in the energy balance in the central part of the plasma.

The heating efficiency and the dynamic response of the plasma parameters are similar when the resonating minority is changed from Hydrogen to Helium 3. However, in agreement with basic damping mechanisms, the Hydrogen high energy tail disappears and the production of 14 MeV protons from D-^{3}He reactions increases sharply, implying the development of an energetic Helium 3 population.

POWER DEPOSITION PROFILE AND POWER ACCOUNTABILITY

The slope measurements of the initial electron temperature increase just after the crash of a sawtooth offer a direct determination, assuming adiabatic heating, of the net power density transferred from the RF to the electrons. The heating deposition profile inside the q = 1 surface has been determined by such a method (Gambier et al, 1985) using a 12 channel ECE polychrometer (Tubbing et al, 1985). The results presented in Fig. 9 show the very peak deposition profile in agreement with the ray tracing expectations and full wave calculations mentioned in the introduction. The heating profile of the quadrupole is somewhat wider, in

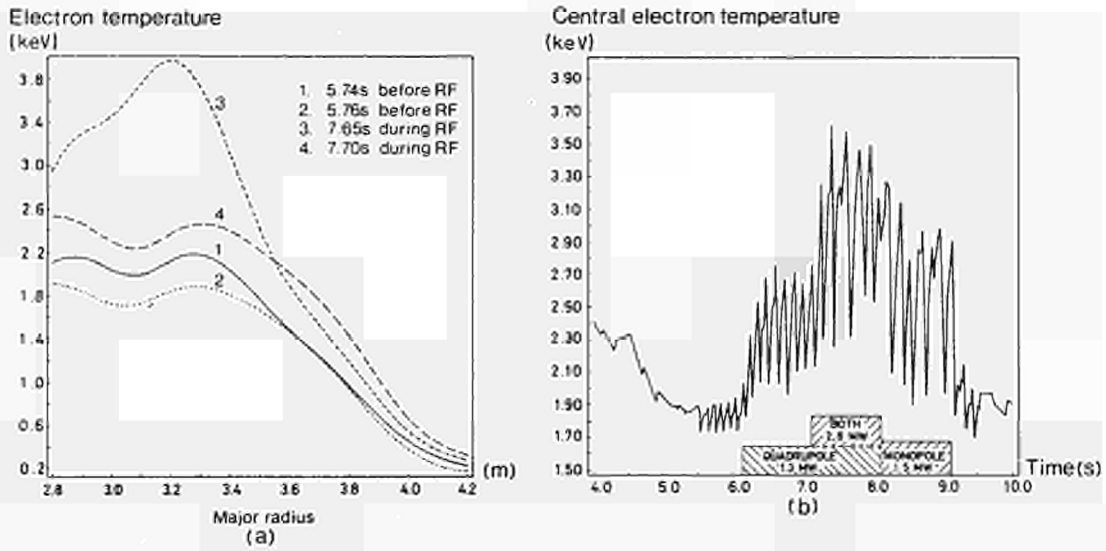

Fig. 4. Electron temperature measurements deduced from the Michelson interferometer.

(a) Temperature profiles measured at the top and at the bottom of a giant sawtooth.
(b) Evolution of the central electron temperature showing the difference in period of the giant sawteeth with the antenna type.

B_ϕ = 2 T, I_p = 2 MA, $n_e\ell = 6.4 \times 10^{19} m^{-2}$, Hydrogen minority n_H/n_D = 4%.

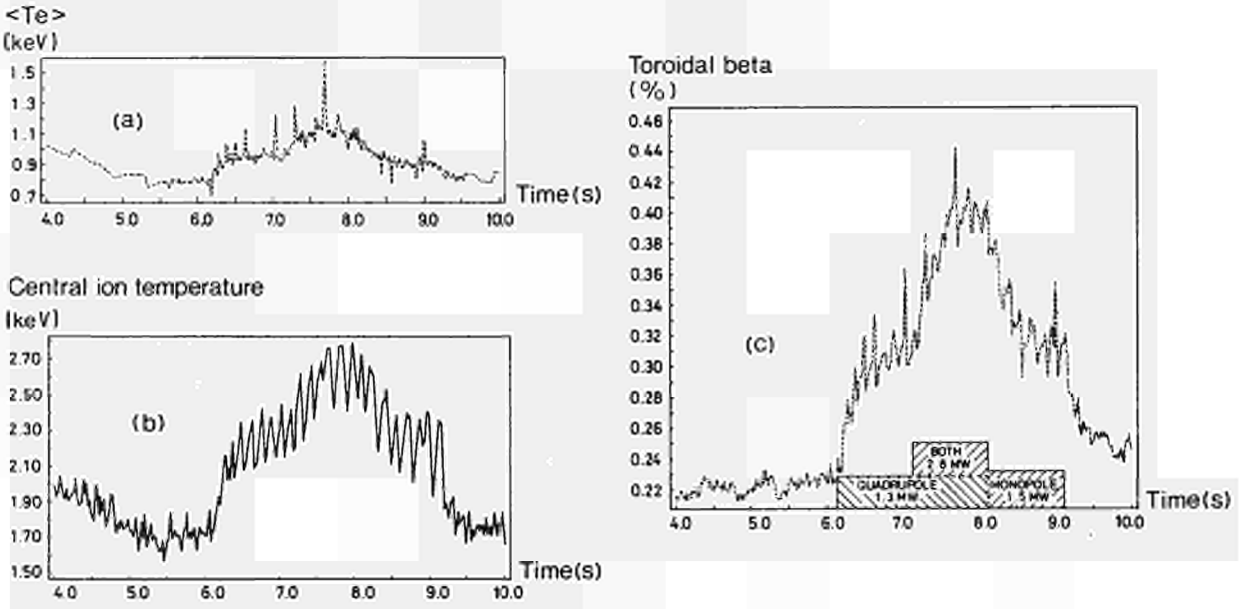

Fig. 5 (a) Evolution of the volume average electron temperature.
(b) Evolution of the central ion temperature deduced from the neutron flux and the density.
(c) Evolution of the plasma kinetic pressure normalised to the toroidal magnetic field pressure.

Same conditions as Fig. 4.

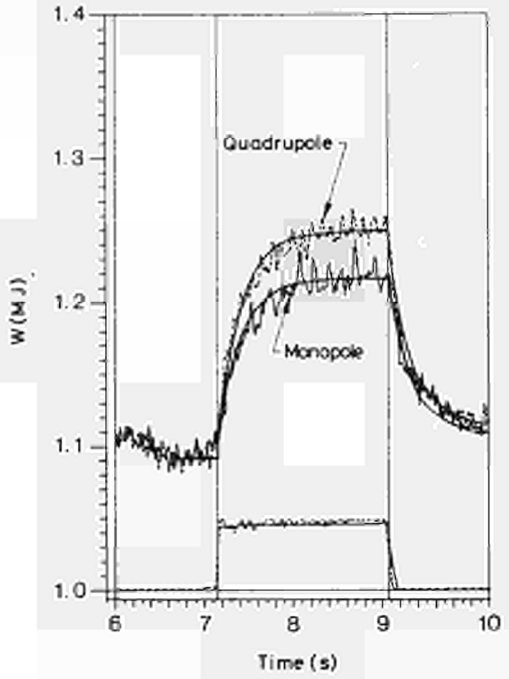

Fig. 6 Time evolution of the stored energy deduced from magnetic signals. RF parameters of Fig. 9 and the same plasma conditions as Fig. 4. Each experimental signal is compared to values (smooth curves) given by equations 1 and 2 (see text) with τ_{ad} = .25 s and P_{abs}/P_{RF} = 0.75 for both monopole and quadrupole.

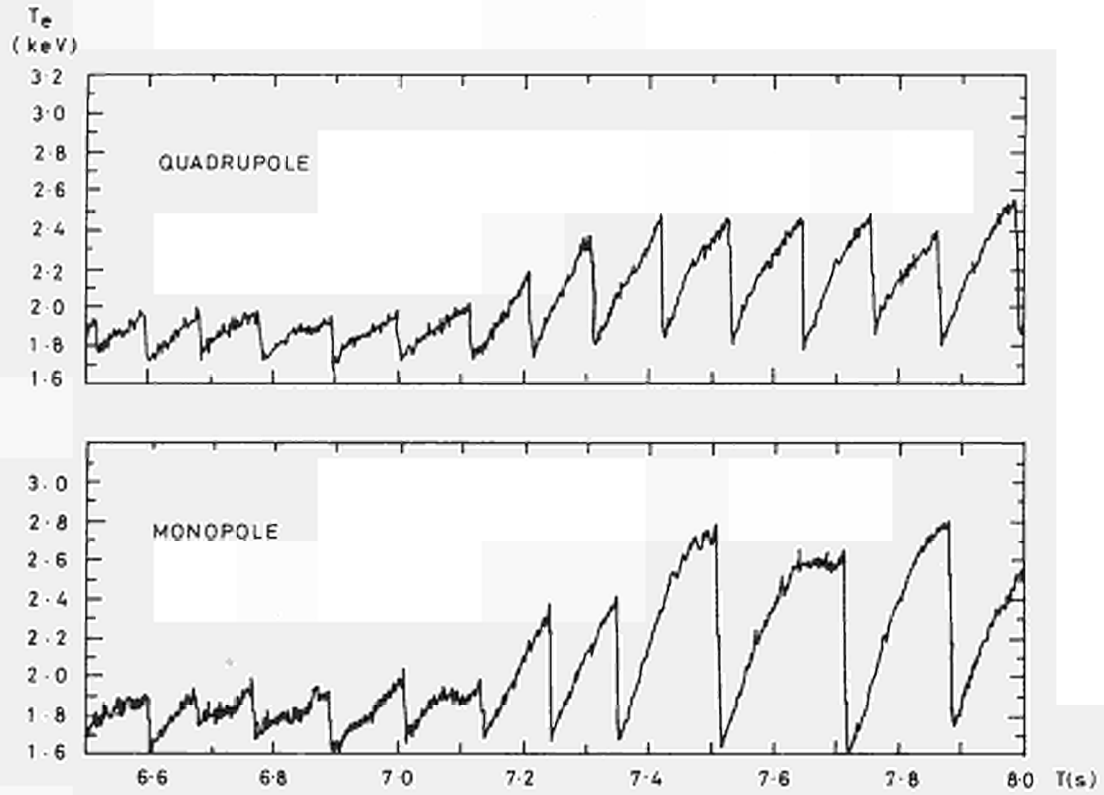

Fig. 7 Evolution of the electron temperature in the vicinity of the magnetic axis R = 3.11 m. RF is turned on at 7.1 s. The two discharges are consecutive, one with the quadrupole, the other with the monopole. The slope of the sawteeth is similar but the period and the shape of the relaxation is quite different.

agreement with the expected increased Döppler effect due to the larger mean $k_{//}$ radiated by this antenna. Confirmation that this peaked deposition profile is related to the localisation of the cyclotron layer R_{CH} is obtained by varying R_{CH} (Fig. 10) and by observing that the large internal sawteeth disappear as soon as R_{CH} is out of the q = 1 surface. In this experiment, the increase of plasma stored energy remained constant when R_{CH} was changed from 3.1 m to 3.7 m.

Integrating these experimental profiles over the q = 1 volume leads to a net power transferred to the electrons inside this volume of approximately 45% (monopole) or 35% (quadrupole) of the total coupled power. Extending the volume of integration outside the q = 1 volume by extrapolation of the curves has no effect on the value given for the monopole but rises to 45% for the quadrupole value. Estimating the net power transferred to the deuterons from the rate of rise of T_i and assuming the same profile of increase gives a total power transfer in the range of 70% of the coupled power.

An independent estimate of the power absorbed in the plasma may be obtained from the stored energy deduced from magnetic signals (Fig. 6). Trying to fit the evolution of the signal with a form of the type

$$\text{During RF} \quad W = W_o + P_{abs}\,\tau_{ad}\,[1 - \exp(-t/\tau_{ad})] \qquad (1)$$

$$\text{After RF} \quad W = W_o + P_{abs}\,\tau_{ad}\,\exp(-t/\tau_{ad}) \qquad (2)$$

we find the best fit for the conditions of Fig. 6:

(i) $P_{abs}/P_{RF} \cong 75\% \pm 15\%$ for both monopole and quadrupole

(ii) $\tau_{ad} = 225$ ms ± 25 ms

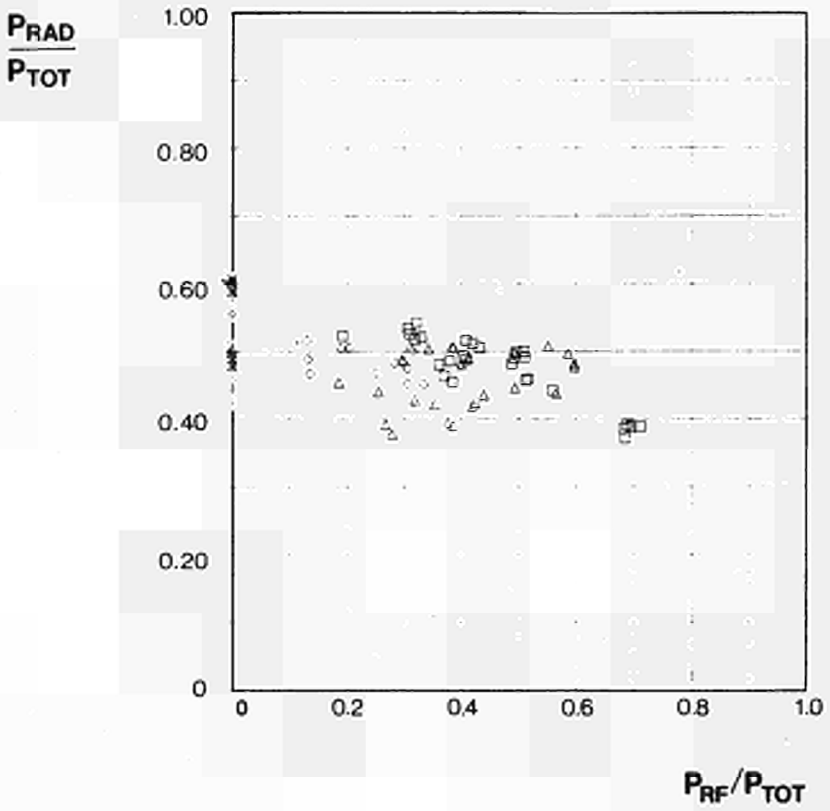

Fig. 8 Total radiated power normalised to the total input power versus the launched RF power (same normalisation).

△ = 3.4 T ; 4.0 MA
◇ = 3.1 T ; 2.7 MA
□ = 2.0 T ; 2 MA
× = ohmic cases (before RF)

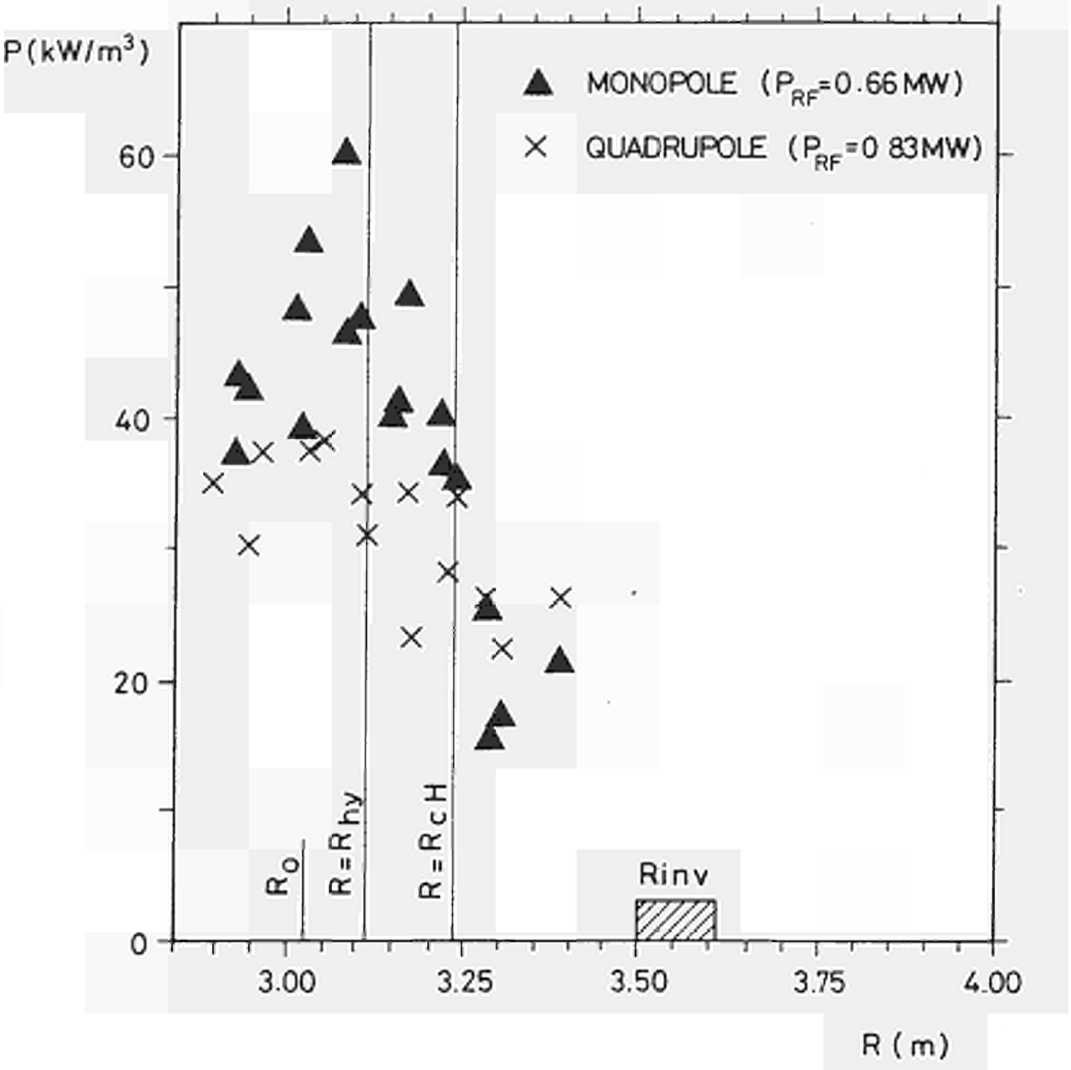

Fig. 9 Net electron heating power density deduced from the slope of the electron temperature sawteeth. The profile is obtained in a single shot with a polychromator. Various positions refer to : R_o : magnetic axis, R_i : inversion radius, R_{hy} : hybrid resonance, R_{CH} : Hydrogen cyclotron resonance.

τ_{ad} has the physical meaning of a confinement time of added power. A similar value is deduced independently from dW/dP_{TOT} (Fig. 12a). When compared to the ohmic confinement time of 480 ms, it implies directly, without the need for power calibration, a serious degradation of the energy confinement, although the net effect on the global confinement time (400 ms) during the heating, is fairly small due to the modest power level used in this particular experiment.

When P_{RF} is increased from 1 MW to 3 MW τ_{ad} remains unchanged but P_{abs}/P_{RF} increases slightly by about 10%. Also note that a unique value of τ_{ad} represents equally well the rise of the stored energy when RF is turned on (equation 1) and its decay when RF is turned off (equation 2). This excludes any direct effect of the RF waves on energy confinement.

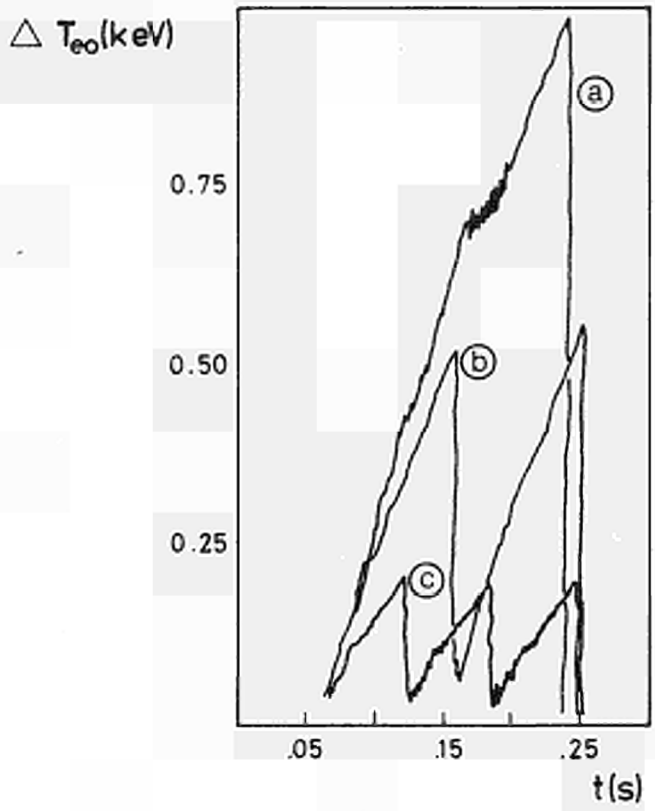

Fig. 10 Variation of the central electron temperature during sawteeth for three positions of the cyclotron resonance (a) R_{CH} = 3.3 m (close to the magnetic axis); (b) R_{CH} = 3.5 m (edge of the q = 1 surface); (c) R_{CH} = 3.7 m (outside the q = 1 surface). The bottom of the traces have been adjusted to the same level.

Due to the global nature of equations 1 and 2, the physical meaning of P_{abs} is not very accurate but can be interpreted as the power absorbed in the plasma core which is confined during a time comparable to τ_{ad}. Any power deposited on the edge or in the scrape off layer will not contribute to P_{abs}. P_{abs}/P_{RF} determined by this global method is comparable to the previous estimate of the power deposited inside the q = 1 volume. This implies that the additional power deposited inside this volume is confined with a characteristic time τ_{ad} and that the remainder of the power which is deposited in more peripheral regions escapes with a shorter time constant, say $\tau_{ad} \lesssim 50$ ms. More specific analysis will have to await a more extended data base and a more complete determination of power deposition by other methods such as power modulation.

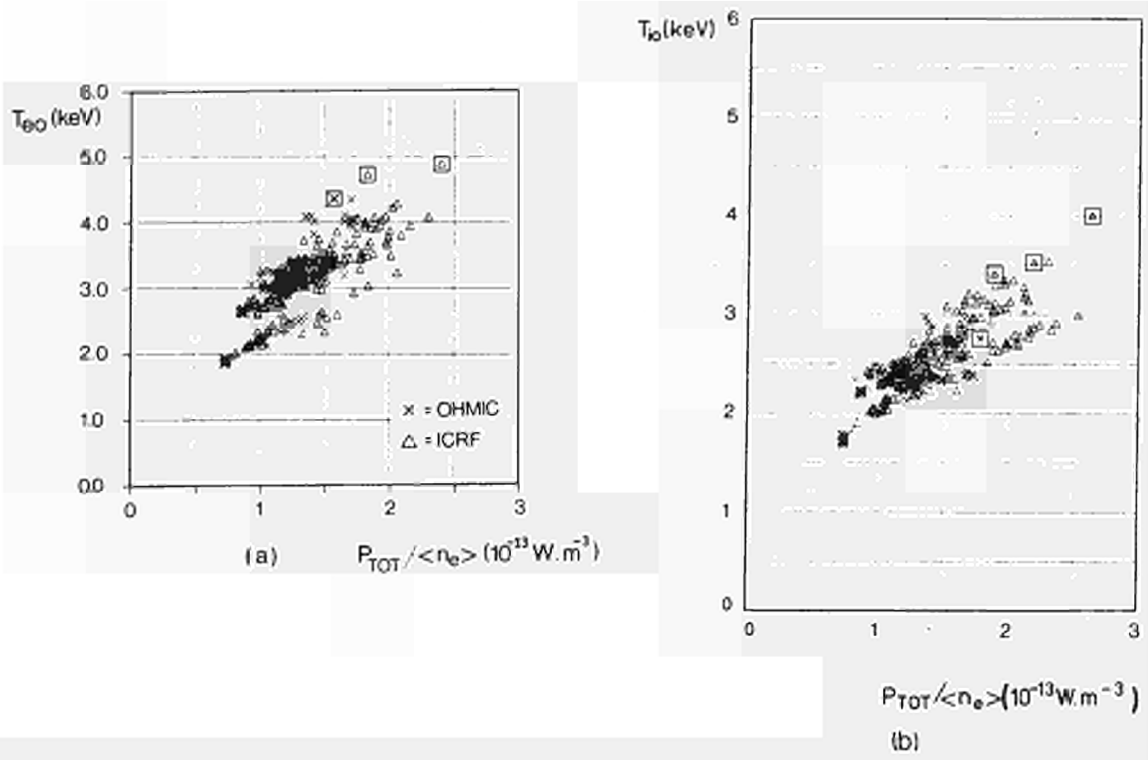

Fig. 11 Central electron (Fig. 11a) and ion (11b) temperatures (time averaged on the sawteeth) versus the total power normalised to the average electron density. △ : during RF (all data), × : before RF: ⊠ ; ⍓ refer to experiments just after the end of a 4 MA current rise.

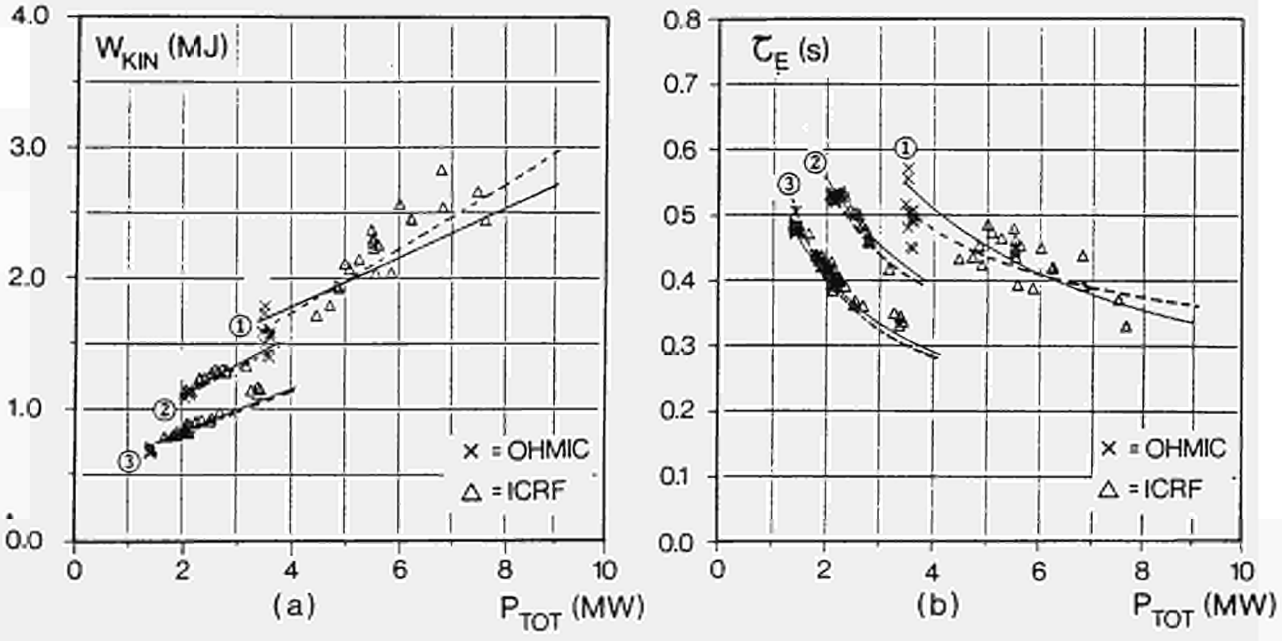

Fig. 12 Stored kinetic energy (a) and energy confinement time (b) versus total power $P_{TOT} = P_{RF} + P_{\Omega}$

1 : 3.4 T : 4.0 MA
2 : 3.1 T : 2.7 MA
3 : 2.0 T : 2.0 MA

× ohmic cases (before RF)
△ during RF

------ "Saturating L mode" scaling

_____ Normal L mode scaling (see text)

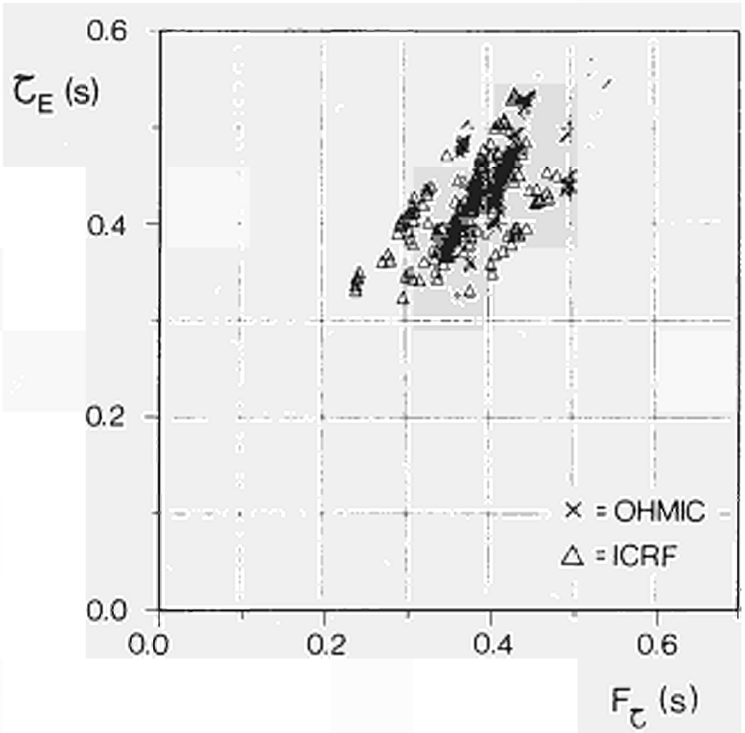

Fig. 13 Comparison of the observed energy confinement times to the Kaye-Goldston empirical law

$$F_\tau = 2.77 \times 10^{-5}\, I^{1.24}\, P_{TOT}^{-0.56}\, B_\phi^{-0.09}\, R^{1.65}\, a^{-0.49}$$

△ all RF data

× ohmic values before RF

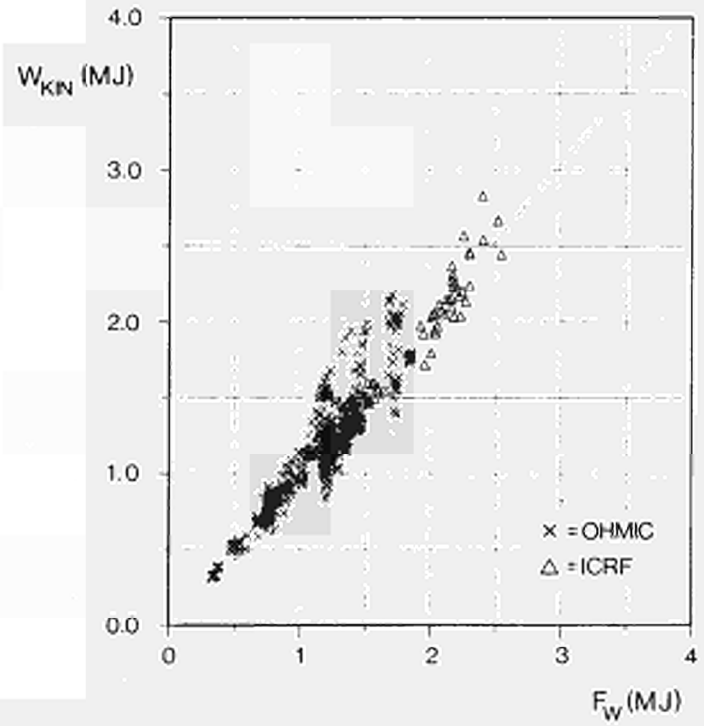

Fig. 14 Comparision of ohmic and RF data to an L mode scaling law

$$F_W = 0.34\, (I_p B_\phi^{0.5}/P_{TOT})^{0.5}$$

COMPARISON OF THE ANTENNA CONFIGURATIONS

Some small difference in heating efficiency between the monopole and dipole configurations can be noted in favour of the monopole. However, the largest differences arise when the quadrupole is used:

(i) The energy deposition profile is wider (Fig. 9).

(ii) The sawtooth relaxation has a smaller amplitude and a smaller period (Fig. 7). The bottom of the sawtooth rises with the quadrupole while it remains almost constant with the other configurations. However, the ion and electron central temperatures, when time averaged over a sawtooth period, are unchanged. The same conclusion applies to the stored energy.

(iii) Although the plasma density increase is insensitive to the configuration used, the scrape off density nearly doubles with the quadrupole, while it remains constant or slightly decreases with the monopole. Recycling on the limiters is also larger with the quadrupole.

SCALING LAWS

Figures 11, 13 and 14 represent all the experimental results obtained with ICRF. The central electron temperature (time averaged on the sawteeth) appears to scale linearly with $P_{TOT}/\langle n_e \rangle$ (where $P_{TOT} = P_{RF} + P_{\Omega}$) (Fig. 11a). A similar behaviour of the central ion temperature is observed (Fig. 11b).

The stored kinetic energy also exhibits a linear scaling with P_{TOT} (Fig. 12a) although the lines do not go through the origin, indicating degradation of overall confinement times. These are represented on Fig. 12b and compare two scaling laws obtained by the regression technique:

Law 1 $\tau_E = 0.34\ (I_p B_\phi{}^{0.5}/P_{TOT})^{0.5}$ "L" mode scaling" ;

Law 2 $\tau_E = (0.095 + 0.29/P_{TOT})\ (I_p B_\phi{}^{0.5})^{0.5}$ "Saturating L mode"

With the present level of RF power, it is impossible to distinguish between the depressing "L mode" scaling, which steadily degrades with P_{TOT}, and the more cheerful "Saturating L mode" behaviour which has been reported on PLT (Hosea, 1985). The general behaviour reported here is in no way different from observations from smaller experiments; this is well illustrated by comparing our results to an earlier scaling law (Kaye and Goldston, 1985) based on smaller sized tokamaks. Their law is in fair agreement with the data base, although on the low side (Fig. 13). Note that the extent of this preliminary data base is not sufficient for a precise determination of the I_p and B_ϕ dependence.

Finally, we note that the results are well represented by laws where only $P_{TOT} = P_{RF} + P_{\Omega}$ appear. In other words, the additional power appears to continue a degradation already started with P_{Ω}. This suggests that a unique law could well describe both ohmic and RF heated plasmas. Such an attempt is illustrated in Fig. 14 where all the 1985 data base for ohmic and RF data is fitted against an "L mode law" (Law 1). The representation is certainly reasonable and does show that the RF family of points merges nicely with the ohmic crowd. Similar information is obtained from the propagation of the heat pulse generated by the crash of the sawtooth. The heat pulse travels towards the plasma edge at the same speed when ICRF is present (Tubbing et al, 1985) although the amplitude of the sawtooth was 3 times larger. As discussed by Rebut (1985), the degradation of confinement appears to occur outside the $q = 1$ surface where the electron temperature gradient is stiffly regulated.

CONCLUSIONS

(a) Two ICRF units have been operated on JET without major difficulties. After only a short operating period, the power launched by the antenna reached the design capability of the generators. 4.5 MW and 10 MJ have been coupled during a standard 4 MA, 3.4 T discharge.

(b) Steady state central temperature values (time averaged on the sawteeth) have reached T_{e0} = 4.1 keV, T_{i0} = 3.5 keV at a density $\langle n_e \rangle = 3.5 \times 10^{19} m^{-3}$ which is close to the maximum density reached on JET. The stored energy was 3 MJ. At the end of the current rise of 4 MA discharges, record temperatures of T_{e0} = 5 keV and T_i = 4 keV have been obtained.

(c) Relative impurity concentration and Z_{eff} remained constant during the heating and radiation does not play a significant role in the energy balance in the plasma centre.

(d) Heating deposition appears well localised in the centre when the cyclotron resonance crosses the magnetic axis. In this case, 50% or more of the coupled power, depending on the antenna configuration, is deposited inside the q = 1 surface and very large sawteeth with subharmonic structures are observed.

(e) Energy degradation with power is evident from the time evolution of the signals. Assuming that all the coupled RF power is absorbed in the plasma core, similar "L mode" scaling laws to those found in previous tokamak experiments are obtained. For P_{RF}/P_{Ω} = 2.5, the maximum operating value, the gross energy confinement time was only 60% of the ohmic value.

(f) The heating efficiency does not seem to depend on the choice of the resonating minority. Shaping of the parallel wavelength spectrum generated by the antenna has consequences on the power deposition on the electrons.

REFERENCES

Arbez, J., B. Beaumont, A. Franklin, E. Hanley, J. Jacquinot, A. Kaye, H. Panissié, J. Plancoulaine, C. Walker (1984). *Proceedings of the 13th Symposium on Fusion Technology (SOFT)*, (Varese).

Bures, M. et al. (1985). *Proc. EPS 12th European Conference on Controlled Fusion & Plasma Physics, (Budapest), Vol 9 F*, Part II, 148

Corti, S. et al. (1985). *ibidem*, Part I, 219

Denne, B. et al. (1985). *ibidem*, Part I, 379

Gambier, D. et al. (1985). *ibidem*, Part II, 152 *(Erratum: Fig. 3 of this paper as well as the comparison of antennae should be replaced by Fig. 9 and the paragraph on "Power Deposition Profile and Power Accountability" of the present article)*

Hosea, J. et al. (1985). *ibidem*, Part II, 120

Jacquinot, J. et al. (1985). *Invited lecture at the Inst. of Physics Conference, Glasgow, to be published in the Journal of Plasma Physics and Controlled Fusion, Pergamon Press.*

Kaye, S. M. and R. J. Goldston (1985), *Nuclear Fusion 25*, 65.

Mori, M. et al. (1984), *Proceedings of the 10th Int. Conf. on Plasma Physics and Controlled Nuclear Fusion Research*, (London).

Rebut, P-H. and M. Brusati (1985), *Invited Paper at the EPS 12th European Conference on Controlled Fusion & Plasma Physics, (Budapest)*

Stamp, M. et al. (1985), *Proc. EPS 12th European Conference on Controlled Fusion & Plasma Physics, (Budapest), Vol 9 F*, Part II, 539

Tubbing, B. et al.(1985). *ibidem*, Part I, 215

Wade, T., R. J. Anderson, G. F. Bosia, M. Schmid (1984). *Proceedings of the 13th Symposium on Fusion Technology (SOFT)*, (Varese).

APPENDIX IV (g)
JET-P(85)25

Sawtooth Oscillations

J. A. Wesson

JET Joint Undertaking
(Abingdon, Oxfordshire, U.K.)

Paper Presented to the 12th European Conference on Controlled Fusion and Plasma Physics
(Budapest, Hungary, 2–6 September, 1985)

Abstract

The present model of sawtooth oscillations does not appear to be consistent with experimental observations on JET. An alternative theory is proposed, offering possible explanations for the basic aspects of the observed behaviour.

Introduction

There are three basic questions concerning sawtooth oscillations:

1. What instability drives the oscillations?
2. What is the mechanism of the collapse?
3. Why does the oscillation have the form of a relaxation?

In the most generally accepted theory an m=1 instability occurs at the end of the ramp phase as q falls below unity in the core of the plasma. The plasma is then restored to stability during the collapse phase by a fast reconnection of the magnetic field which returns q to a value above unity.

This model does not provide completely satisfactory answers to the basic questions and in the case of JET appears to be in direct conflict with the experimental results.

The basic questions will be considered in turn and answers will be suggested. Some of these constitute firm results backed by calculations, others are more tentative ideas which remain to be tested.

In any event no complete solution is offered and indeed it might be that the sawtooth behaviour is dependent on the circumstances and in particular on the size of the machine.

1. The Instability

If there is a q=1 surface in the plasma it is potentially unstable to both ideal and resistive m=1 instabilities. However, if the rapidity of the observed sawtooth collapse is to be explained in terms of a rapid magnetic reconnection as proposed by Kadomtsev (1975), it would appear to require the narrow current layer induced by an ideal mode (an ideal mode is an instability of a resistive plasma resulting from violation of the ideal mhd stability criterion).

In a "cylindrical tokamak" the potential energy of the ideal m=1 mode (Shafranov, 1970) is negative if

$$\int_0^{r_1} \left(rp' - \frac{B_\theta^2}{2\mu_0}(1-q)(1+3q)\right) r\,dr < 0$$

where p is the pressure, B_θ is the poloidal magnetic field and r_1 is the radius of the q=1 surface. Thus in the usual simple case $p' < 0$ and $q < 1$ for $r < r_1$, the ideal m=1 is unstable.

However in toroidal geometry there is a stabilising effect (Sykes and Wesson, 1974). This has been calculated by Bussac et al. (1975), and for current profiles having the form

$$j = j_o(1-r^2/a^2)^\nu \qquad (1)$$

The m=1 mode is stable if

$$\beta_p' < \beta_{pc}'$$

where

$$\beta_p' = \frac{2\mu_o R^2}{r_1^2 B_\phi^2} \int_o^{r_1} (-dp/dr)\, r^2 dr$$

R being the major radius and B_ϕ the toroidal magnetic field. For cases of interest the critical value β_{pc}' lies in the range 0.2 to 0.3 for $r_1/a < 0.3$.

Sawteeth occur in JET for values of β_p' much less than this critical value, a typical value of β_p' for ohmic discharges immediately prior to the collapse being 0.05. Thus if an ideal mhd mode is occuring, there is a discrepancy to be explained.

An explanation is to be found in the q profiles implied by equation (1). These profiles have $1-q(0) \simeq \frac{1}{2}\nu(r_1/a)^2$ and this is typically 0.1. On the other hand the experimental change in q during the sawtooth can be estimated and the value is given by

$$\delta q \simeq \frac{\delta T}{T} \cdot \frac{\tau_s}{\tau_R}$$

where $\delta T/T$ is the fractional change in temperature, τ_s is the sawtooth period and τ_R ($= \mu_o \sigma\, r_1^2/4$) is the characteristic resistive diffusion time. Since $\delta T/T \sim 0.1$ and $\tau_s/\tau_R \sim 0.1$, δq is $\sim 10^{-2}$. This means that the values used in the theory might make it inapplicable to the actual experimental case. The theoretical model has therefore been modified and the stability limits have been recalculated.

The modified j(r) and q(r) profiles are illustrated in Figure 1. The j profiles have the form of equation (1) outside the q=1 surface and inside the q=1 surface they are taken to be parabolic corresponding to q profiles of the form

$$q = \frac{q_o}{1 - (1-q_o)r^2/r_1^2} \qquad (r < r_1)$$

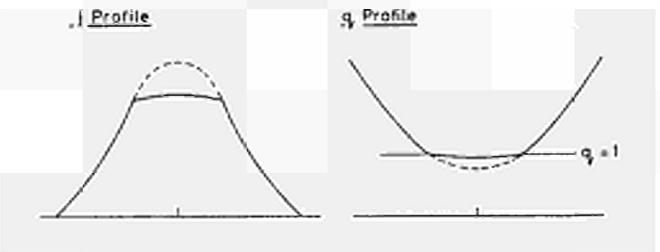

Figure 1: j and q profiles

The results are shown in Figure 2.

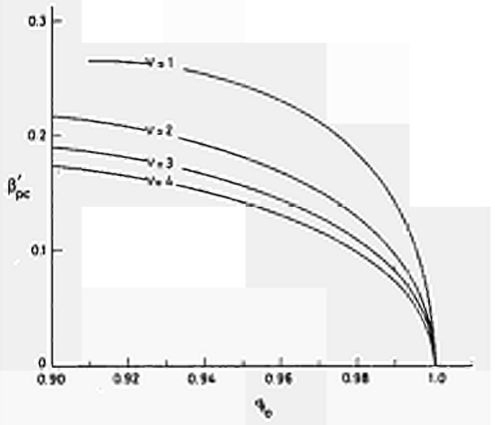

Figure 2: Critical β'_p against q_o

It is seen that for a fixed value of r_1 the critical $\beta'_p \to 0$ as $q_o \to 1$. This explains therefore how an ideal m=1 mode can occur with very small values of β'_p.

2. The Mechanism

The central problem in finding a suitable mechanism for the sawtooth collapse has always been that of explaining the timescale. The table below presents the difficulty.

Characteristic Times for JET Sawteeth

Collapse time	$\tau_c \sim$ 100μs
Resistive time	$\tau_R \sim$ 1s
Alfven* time	$\tau_A^* \sim$ 30μs
Kadomtsev time	$\tau_c^K \sim$ 5ms

The collapse time is smaller by a factor 10^{-4} than the resistive time which would characterise a gross reconnection. The explanation proposed by Kadomtsev (1975) was that a narrow current layer is involved and that this introduces a characteristic time $\tau_A^* \sim r_1/(B_\theta(1-q)/\sqrt{\mu_o \rho})$, the collapse time being given by $\tau_c^K \sim (\tau_R\ \tau_A^*)^{1/2}$. The value given in the table assumes $1-q \sim 10^{-2}$ but the large discrepancy between τ_c and τ_c persists even for much larger 1-q.

However the introduction of the concept of small 1-q now allows a completely different model. Consider the idealised case where q=1 everywhere inside the inner region. The absence of shear would then allow interchange of flux tubes without line bending, leading to a rearrangement of the temperature and density profiles on an inertial timescale. An estimate of this timescale for the instability gives $\tau_c \sim$ 100μs, in agreement with the observed τ_c. Now in reality there will be some shear and the energy of the instability must overcome this in the non-linear phase. Preliminary estimates indicate that this is possible.

This model leads to a completely different picture of the plasma motion. To see this it is necessary to return to the theory of the instability. The potential energy may be written

$$\delta W = \delta W_2 + \delta W_4$$

$$= \frac{\pi^2 B_\phi^{\ 2}}{2R} \int (1 - 1/q)^2 \left(\frac{d\xi}{dr}\right)^2 r^3 dr \ + \ O(\varepsilon^4)$$

where the expansion is in the inverse aspect ratio $\varepsilon = a/R$. In order to remove the contribution of the positive definite δW_2, the trial function shown in Figure 3 is used. This has $d\xi/dr=0$ except for $q \to 1$, corresponding to a rigid shifting of the $q < 1$ core. However for $1-q < \varepsilon$ this expansion fails and a new calculation is required. An idea of the effect can be obtained from a cylindrical calculation and eigenfunctions for cases with $q_o=0.6$ and $q_o=1$ are shown in Figure 4. Both cases have $r_1/a = 0.3$.

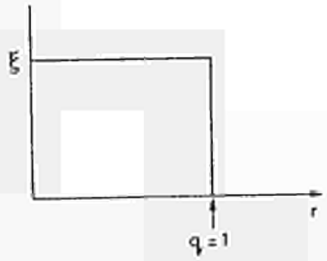

Figure 3: Rigid shift trial function

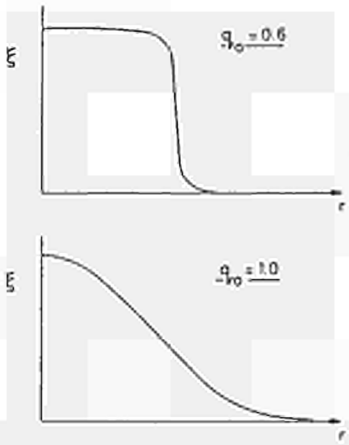

Figure 4: Eigenfunctions for $q_o=0.6$ and $q_o=1.0$

It is seen that the eigenfunction for $q_o=1$ is completely different from the rigid shift and corresponds to a circulatory motion with two cells as illustrated in Figure 5(a). Figure 5(b) shows how such a motion for $q_o \simeq 1$ would rearrange the plasma temperature and density during the collapse. The result is reminiscent of the bubble formation described in a different context by Kadomtsev and Pogutse (1973).

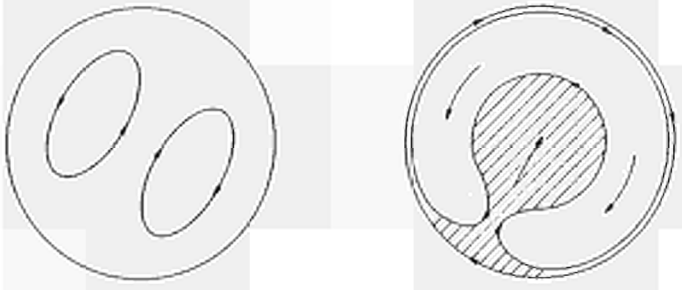

(a) Flow Pattern

(b) Rearrangement of Field and Plasma

Figure 5: Behaviour of m=1 mode for $q \simeq 1$.

Thus, in this model, the answer to the question - How does the reconnection occur on the

very short timescale? - is that it doesn't. The reconnection takes place slowly during the ramp phase.

3. The Relaxation

The fact that the m=1 instability gives rise to a relaxation oscillation has never been explained. The simpler behaviour of a saturated mode would probably have been predicted in the absence of experimental evidence. A consequence of this is that it is not clear why the sawtooth collapse occurs when it does rather than at some other time.

A clue to this behaviour is suggested by the sawtooth behaviour in JET when ICRH heating is switched on. It is seen from Figure 6 that although the sawtooth amplitude increases by a factor of about 5, the period is almost unchanged. This shows that it is not the plasma pressure which determines the collapse. It seems therefore that the energy reservoir built up during the ramp phase is released by a magnetic trigger.

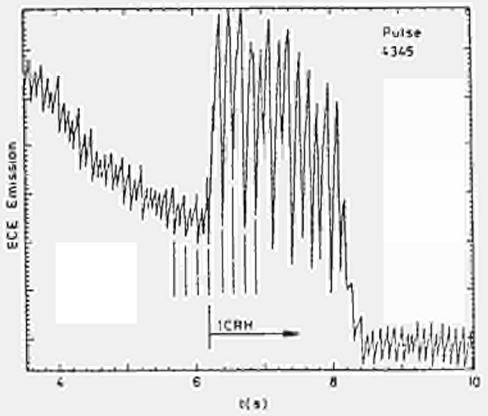

Figure 6: ECE emission when ICRH is switched on (JET)

What is needed is a sudden gross instability brought about by a small change in q. It is expected that the q profile will fall as current enters the central region during the ramp phase. Three possible types of behaviour are illustrated in Figure 7. The first two of these are unsatisfactory but the third offers the possibility of a satisfactory trigger.

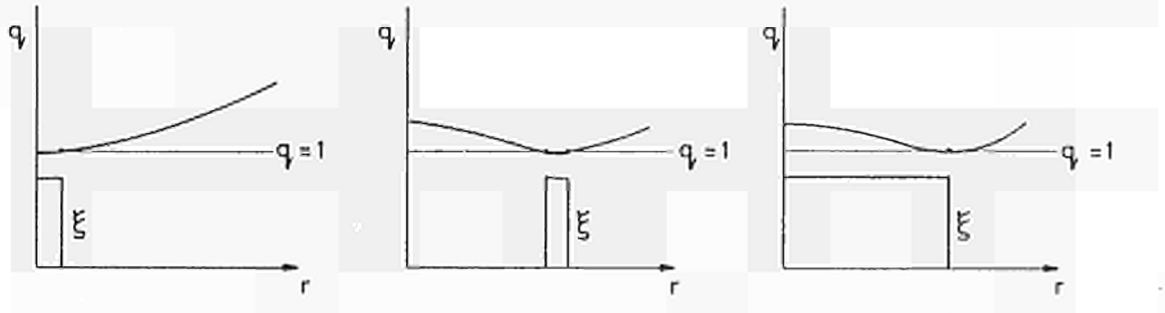

Figure 7: Possible displacements, ξ, as q reaches unity.

In case (i) q reaches unity on the axis and, even if unstable, would only lead to a soft localised instability. In case (ii) an off-axis minimum with a localised displacement, ξ, leads to a similar result. The third case however, gives a gross instability as q reaches unity off axis, the appearance of a resonant surface in the plasma allowing a displacement of the type shown.

To illustrate this, descending profiles of type (iii) have been studied in the cylindrical case and the suddeness of the onset of inertial growth rates is shown in Figure 8. An off-axis minimum in q might be expected from the inward resistive diffusion of a current "skin" into the instability region during the ramp phase.

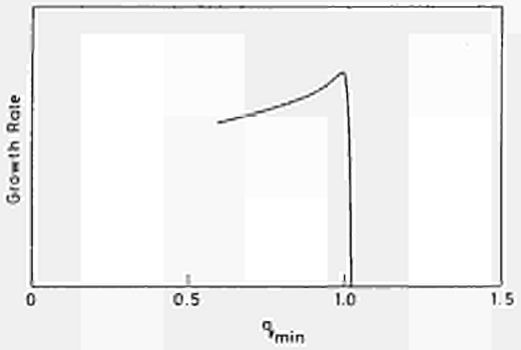

Figure 8: Growth rate against q_{min}

Summary

1. An ideal m=1 mode is predicted when flattening of the q profile is allowed for.

2. In a q flattened core an ideal instability can produce the sawtooth collapse on an inertial timescale. Reconnection does not occur during the sawtooth collapse but on a longer timescale during the ramp phase.

3. A destabilising potential energy builds up during the ramp phase to be released by a magnetic trigger. Such a trigger is provided by an off-axis minimum in q.

Acknowledgement

The author is grateful to F. Nave and P. Kirby for help with the numerical calculations, to J. Hastie and A. Samain for stimulating discussions and to the ECE Group in JET, particularly D. Campbell, for the use of their experimental results.

References

Bussac, M.N., Pellat, R., Edery, D. and Soule, J.L., Phys. Rev. Letts. 35 (1975) 1638.
Kadomtsev, B.B., Sov. J. Plasma Phys. 1 (1975) 389.
Kadomtsev, B.B. and Pogutse, O.P., 6th Eur. Conf. on Contr. Fus. and Plasma Phys., 1973, Vol. 1, p 59.
Shafranov, V.D., Sov. Phys. Tech. Phys. 15 (1970) 175.
Sykes, A. and Wesson, J.A., Nucl. Fusion 14 (1974) 645.

APPENDIX IV (h)
JET-P(85)26

JET Contributions to the 11th Symposium on Fusion Engineering

(Austin, Texas, U.S.A., 18–22 November, 1985)

CONTENTS

Preprints of articles to be published in the Proceedings of the 11th Symposium on Fusion Engineering.

OPERATION AND DEVELOPMENT PLANS OF JET

E. Bertolini
JET Joint Undertaking, Abingdon (OX), U.K.

ABSTRACT

The main objective of the Joint European Torus (JET) experiment is to obtain substantial alpha heating of a D•T plasma in this tokamak device. To reach this goal, the experimental programme is laid down in four phases, and in each phase the machine improvements and modifications required for the following phase are implemented and tested. JET has been operational since June 1983 and since January 1985 experimental work has been carried out in two shifts (16 hours/day).

The key experimental results, in the Ohmic Heating conditions, exceeded expectations, allowing a fusion parameter of $(\hat{n}_{iD}\ \tau_E\ \hat{T}_i) = 0.5\ 10^{20} m^{-3} skeV$ to be reached. Preliminary experiments with ICRH heating have produced ion temperatures up to 4 keV using less than 20% (≤5 MW) of the additional heating power which will be eventually available.

It has become apparent, however, that further enhancements of the machine are necessary to enable JET to reach its ultimate goal. A number of modifications/improvements are now being considered (some of which are already being implemented): modifications to the poloidal electromagnetic system to allow plasma currents up to 7MA, long pulses (>30s) at reduced currents, and to obtain a magnetic limiter configuration with two X-points up to currents of 4MA; modification to the vessel to improve mechanical stability against vertical disruptions, to protect the walls facing the "X-points" and to allow density increase and control by means of pellet injection and pumping panels and/or pumped limiters; use of the RF power to control sawteeth oscillations and the plasma current profiles (by current drive).

At the same time, the existing programme of increasing additional heating power up to 25MW ("high grade" power in the plasma) or above, by both neutral injection and ion cyclotron radio-frequency heating will continue expeditely.

For active phase (D•T) operation, most of the remote handling tools required are now available and some have already been used, while the design, technical specification and prototype work for the tritium plant is proceeding.

1. INTRODUCTION

The JET (Joint European Torus) tokamak experimental facility represents the main component of the European fusion research programme, coordinated by the European Atomic Energy Community (Euratom), aiming to prove the feasibility of nuclear fusion as a viable source of energy.

Among the three large tokamaks in operation in the world at present (TFTR in the United States, JT-60 in Japan and JET in Europe), JET is the one with the largest plasma volume, the longest pulse time, the highest current capability and is the only one allowing significant elongation of the plasma cross section. In spite of the lower toroidal magnetic field, it should allow the closest performance to the thermonuclear ignition regime. Finally it has been conceived, designed and constructed to carry out a comprehensive experimental programme using deuterium-tritium fuel.

The main objectives of JET are the following studies:

a) plasma processes and scaling laws in operating regimes close to those needed in a thermonuclear reactor;
b) interaction of the plasma with the torus walls, which controls the plasma purity;
c) methods of heating the plasma to temperatures approaching those required in a reactor (ohmic heating, neutral beams and radio frequency additional heating);
d) behaviour of energetic alpha particles produced by the fusion process of deuterium and tritium nuclei and consequent plasma heating.

While for the first three objectives, substantial contributions are expected from other experiments and in particular from the other large tokamaks, the last objective is peculiar to JET (and to some extent TFTR), in that a full deuterium-tritium operation phase has been planned and prepared in detail since the conception of JET and throughout the design, construction and project development phases for $10^3 - 10^4$ pulses.

A cross-section of the JET tokamak is shown in Figure 1, indicating the D-shaped features of the machine (toroidal coils, vacuum vessel and plasma), the primary winding of the transformer (coils 1 and 3), the plasma shaping and positioning windings (coils 2, 3 and 4) and the large vessel access ports for neutral injectors, remote handling tools, pumping and diagnostics. The main parameters are shown: the large plasma volume of more than $150 m^3$ and the plasma current of 4.8MA, already exceeded in operation, are worthy of mention.

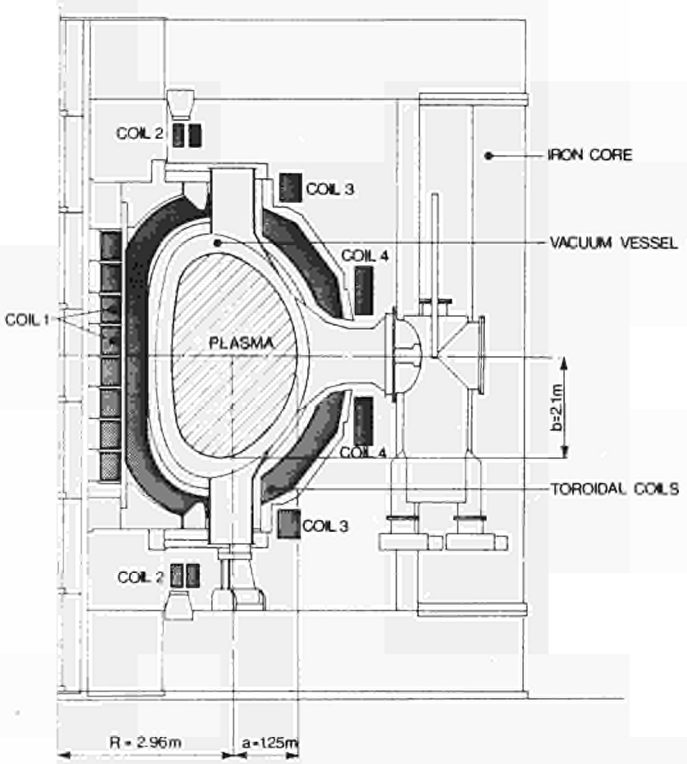

Figure 1. Cross sectional view of the JET Tokamak.

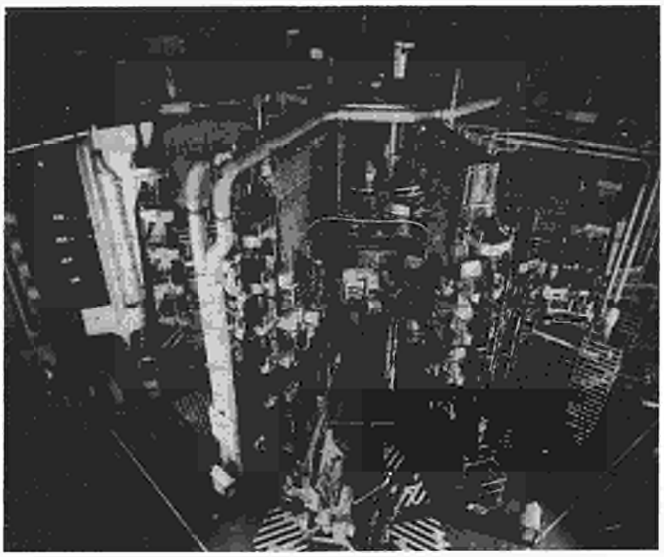

Figure 2. View of the machine in its present status in the Torus Hall.

The machine in its present status, is shown in Figure 2: besides the large number of diagnostics installed, three ion cyclotron radio-frequency heating (ICRH) antennae and one neutral injection box with eight injectors, are now operational.

A view of the vacuum vessel (Figure 3) indicates its large volume and shows one of the eight graphite limiters, two of the three RF antennae, and the graphite tiling of the inboard wall and of the vessel octant joints.

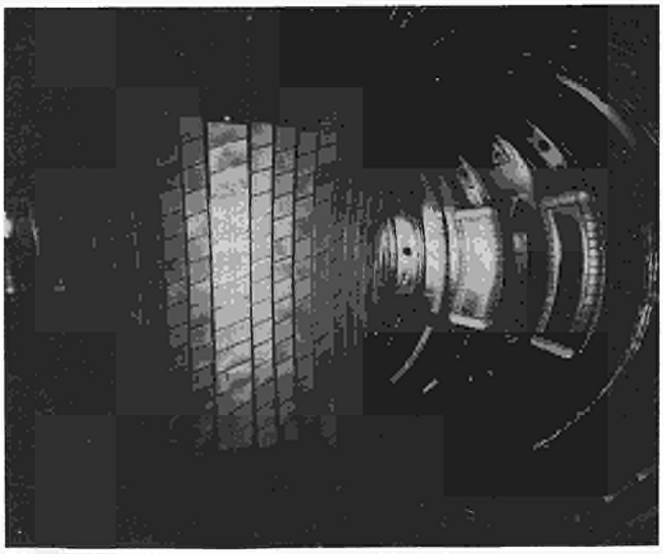

Figure 3. View of the inner walls of the vacuum vessel.

While the tokamak assembly and its surrounding plasma diagnostics are the heart of the JET facility, there are essential auxiliary subsystems distributed all over the site (see Figure 4), such as power supplies, additional heating equipment, computer networks, cooling and heating plants, etc.

The European Associated Laboratories are participating in the JET experimental programme by providing key diagnostics and visiting staff involved in the preparation of the experiments, in the daily operation of the machine and in the evaluation of the results.

The design features and the construction of the JET Tokamak and its main subsystems have been described in several reports and publications in great detail [1, 2, 3, 4, 5, 6, 7, 8].

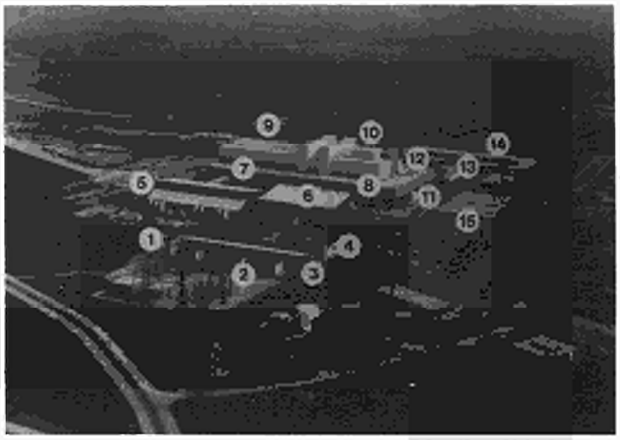

1. 400kV Incoming Line and Substation.
2. 400kV/33kV Transformers.
3. J5 Building: 33kV Switchgears.
4. Outdoor Additional Heating AC/DC Convertors.
5. J3 Building: Toroidal and Poloidal Generators.
6. J4 Building: Toroidal AC/DC Convertors.
7. J1NWE Building: Ohmic Heating Circuit and Plasma Position and Shape Control AC/DC Convertors.
8. J1NWW Building: Neutral Injection Protection Circuits and Radio Frequency Generators for Additional Heating.
9. J1 Building: Assembly Hall.
10. J1 Building: Torus Hall with the JET Tokamak.
11. J1WW Building: Machine Services.
12. J1SW Building: The Diagnostics Hall.
13. J2 Building: The JET Control Room.
14. K1 Building: Offices.
15. J6-11 Building: Offices.

Figure 4: Aerial View of the JET Site, showing the layout of the main auxiliary subsystems.

2. RESEARCH PROGRAMME AND OPERATION

2.1 Experimental and Development Programme

The JET Experimental Programme started in June 1983, when the first tokamak operation was achieved, with the machine in its basic configuration: ohmic heating, quasi circular plasma cross section, hydrogen gas and essential diagnostics. The experimental programme had to be harmonized with a huge development programme (requiring investment close to the original construction cost of the tokamak system available for the first plasma), in order to bring JET to the configuration required for attempting its ultimate goal: plasma heating with alpha particles. The above investment was primarily for neutral beams at 80kV (hydrogen) and 160kV (deuterium), ion cyclotron radio-frequency at 25-55MHz; extension of the power supplies, D-shape plasma cross section control, first wall protection, remote handling equipment, tritium plant and for a large number of sophisticated diagnostics.

The experimental and development programme was set up in four phases, as shown in Table I, where during each phase the devices necessary for the following phase have to be procured, installed and commissioned during major shutdowns between phases. It was understood, however, that besides the major additions indicated in Table I, further machine

Table I: JET Experimental and Development Programme.

1983	1984	1985	1986	1987	1988	1989	1990
	PHASE 1	PHASE 2A	PHASE 2B			PHASE 3	PHASE 4
	OHMIC HEATING	ADDITIONAL HEATING (NI & RF)				FULL POWER	TRITIUM
	HYDROGEN	HYDROGEN	DEUTERIUM			DEUTERIUM	DEUTERIUM TRITIUM
		S	S	S	S	S	S
	FIRST PLASMA	∘ 2 A_0 ANTENNAE ∘ C TILES ∘ 4 C LIMITERS	∘ 3 A_0 ANTENNAE ∘ FIRST NI BOX ∘ MORE C TILES ∘ 8 C LIMITERS	∘ 6 A_1 ANTENNAE ∘ SECOND NI BOX ∘ BELT LIMITERS ∘ ALL DIAGNOSTICS	FIRST NI BOX 160 kV	∘ 10 A_2 ANTENNAE ∘ SECOND NI BOX 160 kV ∘ REMOTE HANDLING ∘ "D-T" DIAGNOSTICS	∘ TRITIUM PLANT

S: SHUTDOWN

development and modification should be considered in the light of the experimental results and performance obtained from JET (and other tokamaks), to give the best chance of success to the deuterium-tritium operation phase.

Due to the dual purpose of the present phase (experimental and development), the concept of the organisational structure of the JET Joint Undertaking for the construction phase has been broadly retained, since, below the Technical and Scientific Departments level the Divisions still represent the heart of the JET structure, insofar as each one is homogenous in tasks and competence [8]. The success in the operation of JET is therefore the result of a cooperative effort of the whole JET Team, involving personnel of all Divisions having equipment actually used in operation and/or specific technical and scientific responsibilities. This approach has proven effective in providing a clear direction to the work and in maintaining a high momentum toward the key goal of JET.

2.2 Organization of Operations

Since January 1985, JET has operated in two shifts, as follows [9].

There are cycles of six weeks operation followed by two weeks of maintenance and necessary re-commissioning. Each operational week is made up of 4 days of Tokamak Operation in two shifts (06.30 - 22.30) followed by a week-end available for essential small repairs, inspection and minor maintenance and a Monday "extended hours" (08.00 - 18.30) for plasma "re-start". However, the tokamak control room is manned around the clock by two shift technicians for surveillance of auxiliary equipment constantly kept operational (such as vacuum pumps, electronics, etc) and to perform special tasks outside tokamak operation, such as wall carbonization, glow discharge cleaning, etc.

The key shift duties are those of: the Session Leader, who is responsible for preparing the pulse schedule and of carrying out the agreed experimental programme for the shift: the Engineer in Charge, who approves the schedule of pulses and is responsible for the machine operation and for the safety of the equipment and of the personnel: the Physicist-in-Charge, who is responsible for the physics measurements and for the operation of diagnostics. In addition a key role in the operation of the machine is played by the Power Supply Engineer, by the Control and Data Acquisition Duty Officer and by the three Console Operators. Finally the required diagnostics are monitored by a suitable number of Physicists, according to the type and the amount of equipment required.

A comprehensive picture of the staff required to be rostered for each shift in the control room and in other areas, including on-call duties, is shown in Table II.

The "Next Pulse" is decided by the Session Leader upon the measurements displayed in "real time" during the pulse and upon data elaborated by the local computers. Only if further information is required, the full set of data (analysed by IBM and Cray computers off line) have to be evaluated before allowing the next pulse.

The "decision making process" for establishing the programme of an experimental period in between shutdowns, from the general guidelines to the detailed daily schedule of pulses, is summarized in the following.

The main goal of an experimental period is bound to be the one set up in the terms of reference of JET for the phase concerned: for instance optimization of the ohmic heating performance and experiments with 3MW (2 antennae) of ICRH (see Table I, Phase II A, Nov 1984-June 1985).

Table II. Composition of a shift rota.

Duties	Location		
	Cotrol Room	Site	On Call
Session Leader	1	-	-
Engineer in Charge	1	-	-
Physicist in Charge	1	-	-
Torus Operators	3	1	1
Power Supply Engineer	1	-	-
Power Supply Operators	1(+1*)	1	1
CODAS Duty Officers	2	5	-
RF Heating	-(+2*)	1*	-
NI Heating	-(+2*)	1*	
Physics Operation	1	-	-
Diagnostics	2(+10**)	-	-
Theory	1	-	-
Radiological Protection	-	-	1
Totals	14 (29)	7(9)	3

* Additional Heating Programme
** Full Diagnostic Programme

The Director nominates, for a typical period of six months, two Programme Leaders, who are responsible for proposing and guiding the experimental programme toward its agreed goal. The Experiments Committee, chaired by the Director, is the body where the proposals for experiments, the whole procedure and necessary changes are discussed. Its members are the Director, the Department Heads, the Division Heads, the Programme Leaders, the Session Leaders, and the Topic Leaders. The Experiments Committee meets, typically, twice per month during operation. The Director nominates the Session Leaders, Engineers-in-Charge and Physicists-in-Charge. The nomination of the remaining rota personnel is the responsibility of the Divisions. The overall organisation of the shift rota and of the machine operation is the responsibility of the Machine Operations Group, while the Physics Operations Group plays a key role in the planning and in the coordination of the experiments. The detailed daily programme of the week is defined at the Coordination Meeting held on the preceding Friday. A key role in the formation of the experimental programme, made up of a number of scientific topics, and in the evaluation of the results, is also played by the Topic Leaders: they are the spokesmen of "spontaneous groups" built up around key topics agreed at the Experiments Committee. They report at a Science Meeting a first analysis of results, usually during the two maintenance and commissioning weeks, and therefore they report about results obtained in the previous six weeks of tokamak operation.

3. KEY TECHNICAL AND SCIENTIFIC RESULTS

3.1 Machine Conditions

Machine conditions have been progressively improved from the date of the first plasma (June 1983) to the end of the 1985 shutdown (October 1985). This progress can be broadly represented by the increase of plasma current values and/or flat top times (see Figure 5).

Machine conditions during the January-June 1985 campaign of experiments are summarized in the following.

a) Electromagnetic Systems

The Toroidal Magnetic Field was operated up to its maximum design value of 3.45T (67kA of magnet current). As for the Poloidal Magnetic Field, the maximum value of the design current was reached in the transformer coil P1, (i.e. 40kA at the end of the pulse for each of the two sections, upper and lower, connected first in parallel and, after February 1985,

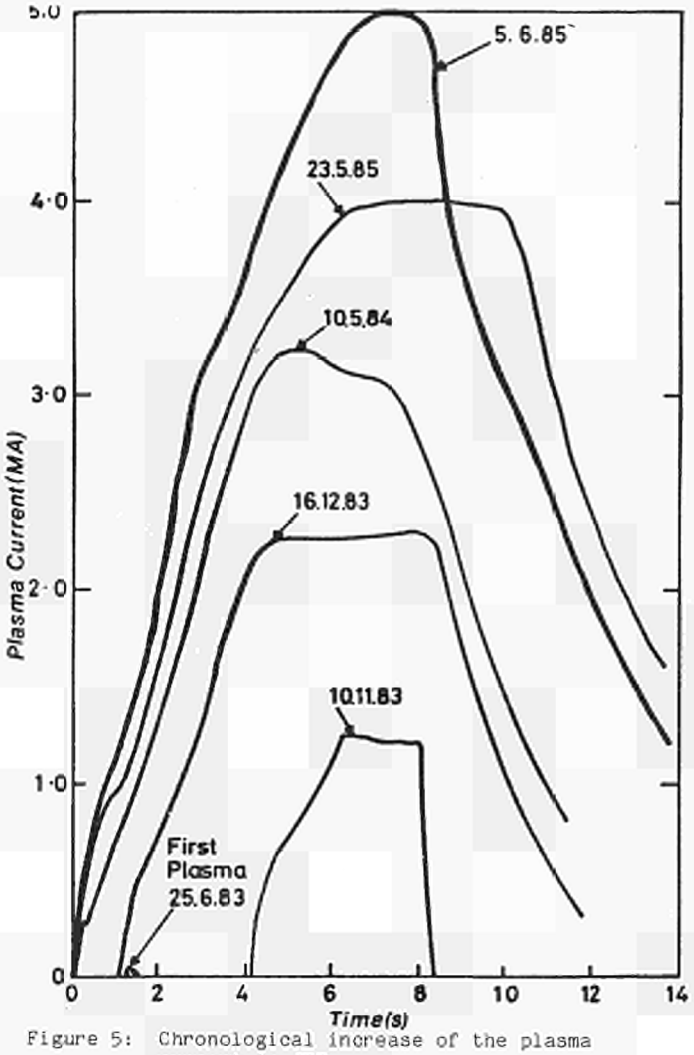

Figure 5: Chronological increase of the plasma current in JET.

in series). However, only half of this current value was used during premagnetization of the coil P1, due to the necessity to have a breakdown despite the presence of transformer stray fields and to limit the plasma current derivative typically at 1MA/s [10]: only about 75% (26Vs) of the design flux swing (34Vs) was therefore available, thus limiting the plasma current flat top length at the maximum plasma current achievable.

b) Plasma Control

The Plasma Control [3,11] is achieved in a conventional way, by using magnetic probes and flux loops as sensors to provide the feedback signals which, combined with pre-programmed functions, produce the control voltages to the relevant power supplies which, in turn, supplies the appropriate current profiles to the poloidal coils (see Figure 1).

The Plasma Current Control is obtained by acting on the excitation current of the dedicated poloidal flywheel generator, which supplies the magnetizing coils (P1 and P3). The flat top values of the plasma currents were within $\pm$5% of the pre-set values.

The Plasma Radial Position Control is determined by controlling the voltage in the P4 poloidal coils. The accuracy obtained has been within $\pm$3cm, over a plasma radius "a" up to 1.2m ($\pm$2.5%).

The Plasma Vertical Position Control is determined in a similar manner, by controlling the voltage at appropriate windings of coils P2 and P3. The accuracy obtained was $\pm$1cm. Plasmas with vertical semiaxis "b" up to ~2m could be produced and maintained. Since a vertical disruption experienced during 1984 at I_p= 2.6MA, inducing large forces in the vessel, improvements were made on the response time of the active control system (from ~4ms to ~2ms) and on the support of the vessel. However, further improvements are now considered (see Sect 4) and the plasma elongation has been limited according to the semi-empirical formula: $I_p^2\left(\frac{b}{a}-1.2\right) \leq 5(MA)^2$, where I_p is the plasma current and $\frac{b}{a}$ is the elongation ratio. Plasma Shape (elongation) Control was also available by controlling the currents in appropriate sections of coils P2 and P3, within the limitations imposed by the above formula: for currents up to 3MA, elongations up to 1.7 were achieved and satisfactorily controlled.

Finally, the Plasma Density, measured by a single channel (vertical chord), 2mm interferometer, was feedback controlled by controlling the rate of gas inlet.

c) Vacuum Vessel

There were four Carbon Limiters symmetrically assembled on the equatorial plane of the vessel and two Radio Frequency Antennae, usually operated 2cm behind the limiter radius, in the opposite position, each on the same octant as a limiter. Four Nickel Limiters were always located about 4cm behind the carbon limiters. Since the relatively frequent radial disruptions always terminate the plasma on the inner walls, these have been covered by carbon tiles to a height of $\pm$ 1m (see Figure 3). This tiling can also be used as limiters defining the magnetic surface adjacent to the vessel inner walls: this configuration has been used for minor radius and major radius scaling experiments.

The vessel usually operates with wall temperatures between 250°- 300°C (by blowing hot nitrogen between the two vessel walls), with ports at 130°-150°C (by electric heating), with base pressure of 10^{-7}mbar of hydrogen and of 10^{-9}mbar of residual impurities. The vessel is conditioned by glow discharge cleaning in hydrogen and/or deuterium.

Gas Introduction is achieved by four injection modules, each permitting fast puffing for pre-filling, and controlled addition of gas during the pulse: the valves are fully metallic since they have to be bakeable up to 300°C and tritium compatible.

JET usually operates with carbonized walls since it has been shown that this type of wall conditioning reduces considerably (at least temporarily), the level of metallic impurities and of oxygen and chlorine as well, leading to Z_{eff}= 2.5 - 4, according to the plasma density level. Carbonization is usually performed once or twice per week and it is achieved by glow discharge cleaning in a mixture of hydrogen (or deuterium) and methane [12]

d) Diagnostics

The major diagnostics to measure essential plasma parameters are the following [13,14]:

The Magnetic Measurements for the plasma current position and shape: there are 18 pick up coils and 14 saddle loops for each vessel octant and 12 full flux loops around the whole vessel.

The Electron Density Profile $n_e(r)$ is measured by a single channel 2mm microwave interferometer and a seven channel far infra-red laser interferometer.

The Impurity Level Z_{eff} (effective ion charge) is evaluated from the bremsstrahlung continuum viewed along a vertical chord.

The Electron Temperature Profile $T_e(r)$ is measured by an absolutely calibrated electron cyclotron emission system along a number of major radius chords and by a single point Thomson scattering (the "fixed point" can be changed in between pulses).

The Ion Temperature T_i is measured by a neutral particle analyser along a chord in the mid plane of the machine. In deuterium it can also be measured by the neutron yield with a ^{3}He spectrometer.

The energy confinement time τ_E is calculated as the ratio between the total plasma thermal energy and the total input power.

3.2 Statistics

JET pulses are divided into Commissioning Pulses (which are the pulses performed to test subsystems, to prepare the machine and to check the correct operation with plasma, of all subsystems together) and into Tokamak Pulses (which are pulses performed according to the daily programme).

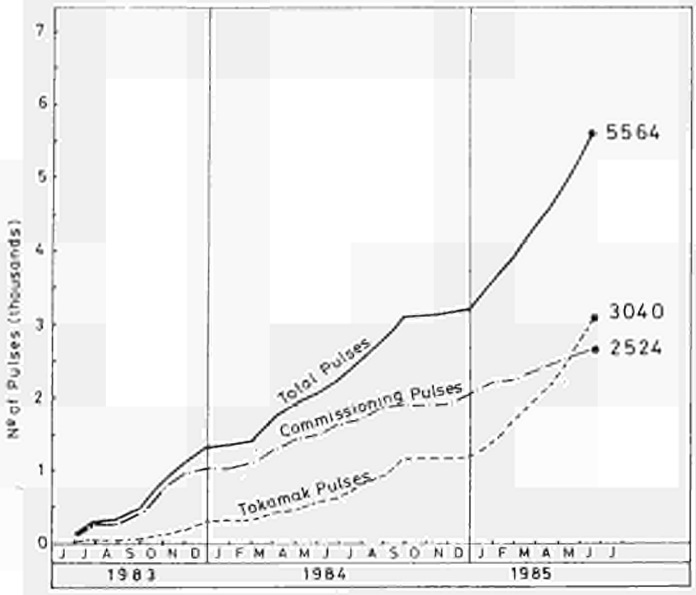

Figure 6: Some stastistics about the JET pulses.

As can be seen from Figure 6, during 1985 the number of Tokamak pulses was much larger than the number of commissioning pulses, due to the completion of the commissioning at full performance of most subsystems and to their improved reliability. Also the percentage of successful pulses has been increased for the same reasons, namely, for the commissioning pulses, 52% in January-February 1985 to 70% in April-June 1985 and for the Tokamak pulses 77% and 84% respectively [9].

3.3 Results

During the operating period, January-June 1985, two experimental programmes have been undertaken: the Ohmic Heating programme aimed at maximizing the tokamak performance with the machine in the configuration already described [13] and the Radio Frequency programme aimed at the commissioning of the ICRH system (2 A_0, radiation cooled antennae) and subsequently at plasma heating studies up to 5MW of additional heating power coupled with the plasma [15,16,17]. These programmes would run on alternative days in two shifts.

The parameter range in which the machine has been operated compared with the design values, is shown in Table III. Two typical and fully reproducible discharges have been used mainly as target plasma for RF heating experiments: B_{TO}=3.4T, I_p=2.8MA (elongation ~1.5) and I_p=4.0MA (elongation ~1.4) respectively, with minor plasma radius a ~1.2m. Operation was performed with a deuterium plasma.

The optimisation of the Ohmic Heating discharges [13] was performed at full toroidal magnetic field (3.4T) with plasma current below 3.7MA and limited elongation at high current, in order to avoid vertical instability and to reduce the number of radial disruptions at high current when attempting to maximize the plasma density. Central average electron temperatures up to $\bar{T}_{eo}$=4.0keV and central average ion temperatures up to $\bar{T}_i$=3.0keV, average electron densities up to n_e=3.5 $10^{19}m^{-3}$ and effective ion charges as low as Z_{eff}=2.5, were systematically achieved. The global energy confinement time over the whole plasma volume was as high as 0.8s in the best discharges. Finally the best value of the fusion

Table III. Parameter range explored in operation.

Parameter		Unit	Operational		Design	Potentials
			Ohmic Heating	Additional Heating		
Major Radius	R	m	2.5-3.1	3.0	2.96	2.96
Minor Radius	a	m	0.8-1.2	1 -1.2	1.25	1.25
Elongation	k	-	1.2-1.7	1.4-1.5	1.68	1.7
Toroidal Field	B_T	T	2 -3.4	2 -3.4	3.45	3.8
Plasma Current	I_p	MA	1.5-5	2 - 4	3.2-4.8	7.0
Pulse Flat Top Time	t	s	1 -20	4 -10	20 - 12	30 (I_p < 3MA)
ICRH Power (Plasma)	P_{RF}	MW	-	5	15	>15
NI Power (Plasma)	P_{NI}	MW	-	-	10	>10

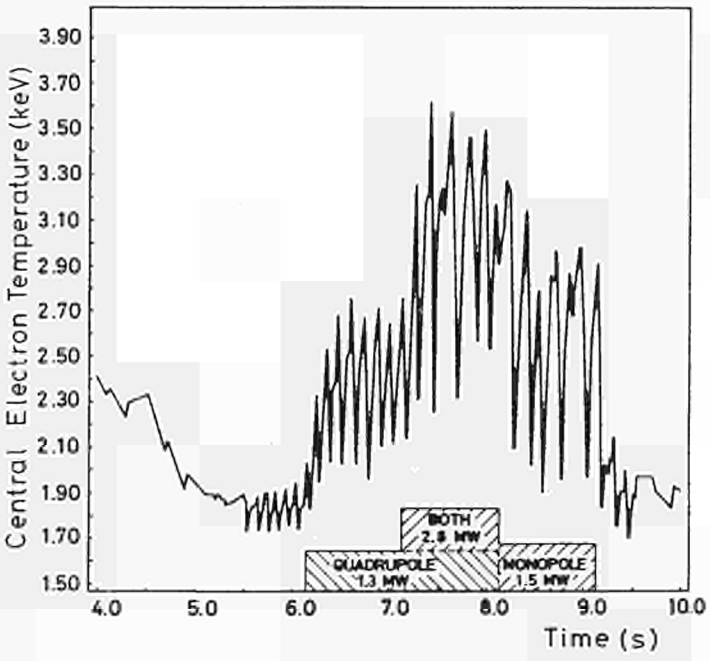

Figure 7: Electron temperature sawteeth with Ohmic Heating and with RF Heating.

product ($\hat{n}_{iD}\ \tau_E\ \hat{T}_i$) was 0.5 $10^{20} m^{-3} s$ keV, a factor of about 20 below the level at which, in a deuterium-tritium gas mixture, fusion reactions would have a clearly measurable impact in the plasma energy balance, thus allowing study of alpha particle confinement and heating.

The discharges at plasma currents above 3.7MA were performed at lower densities and at reduced elongations for the reasons mentioned previously, in order to set up a 4.0MA, 4s flat top, target plasma for RF heating experiments and to test the capability of the overall machine up to 5.0 MA.

Most of the Radio Frequency Heating programme was devoted to the technical commissioning of the equipment with plasma [15]. The plasma parameters were modified only by a factor of 2: an optimization of the plasma performance with RF was not attempted, as far as the density limit was concerned. As a consequence, the best value of the fusion product ($\hat{n}_{iD}\ \tau_E\ \hat{T}_i$) obtained in ohmic heating discharges was not even reached.

There is a clear effect in raising the average central electron (up to 5.0 keV) and ion (up to 4.0keV) temperatures. However large sawteeth develop, as soon as the RF power is injected (see Figure 7). The average electron density (without attempting to reach the density limit), was close to that reached in ohmic heating discharges (3.5 $10^{19} m^{-3}$). Moreover no evidence of appreciable increase of Z_{eff} was noticed up to 5MW of RF power and 10MJ of RF energy coupled with the plasma. However, an expected degradation of the energy confinement time up to 40% (with P_{RF}/P_{Ω}=2.5) was noticed ("L mode").

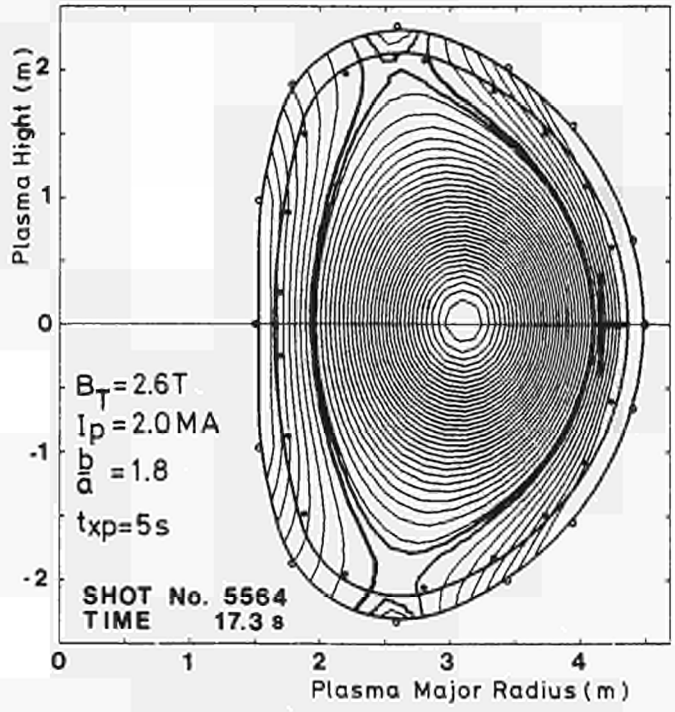

Figure 8: Magnetic limiter configuration with two X-points obtained in JET.

Although these results are of a preliminary nature, they appear to be similar to those obtained in other tokamaks with additional heating (neutral injection and ion cyclotron resonance).

It has been shown, however, in ASDEX, PDX and DIII tokamaks that the degradation of the confinement with additional heating can be greatly reduced ("H" mode) if the plasma magnetic configuration contains one or two X-points in a magnetic limiter mode of operation. Therefore, during June 1985, the formation of a Magnetic Separatrix with X-points at the top and bottom of the vessel was attempted and successfully obtained in JET [18] at a plasma current of 2MA, with a toroidal magnetic field of 2.6T (see Figure 8).

The level of plasma performance was kept low in order to limit mechanical stresses in case of vertical instability and to limit the heat load on the unprotected vacuum vessel wall. As a by-product of these experiments, long pulses (>20s) were obtained, because, in order to produce the required magnetic configuration with these X-points in the previously described machine conditions, the flat top current in the coils P1 had to reach values close to its maximum (40 kA) in order to partly saturate the upper and lower collars of the iron core (see Figure 1).

4. FUTURE DEVELOPMENT

4.1 Implication of the experimental results.

The analysis of the results so far obtained with JET, on one side indicates performances exceeding expectations (plasma temperatures and confinement in ohmic heating), but on the other shows that additional improvements/modifications of the machine are necessary in addition to those already part of the JET development programme, to bring the ultimate machine performance close to ignition. The problems encountered are mainly concerned with the density limit and control, with plasma MHD behaviour, with the amount and behaviour of impurities and with transport. In particular the confinement degradation with additional heating calls for modes of operation where the plasma current density and the electron temperature are decoupled.

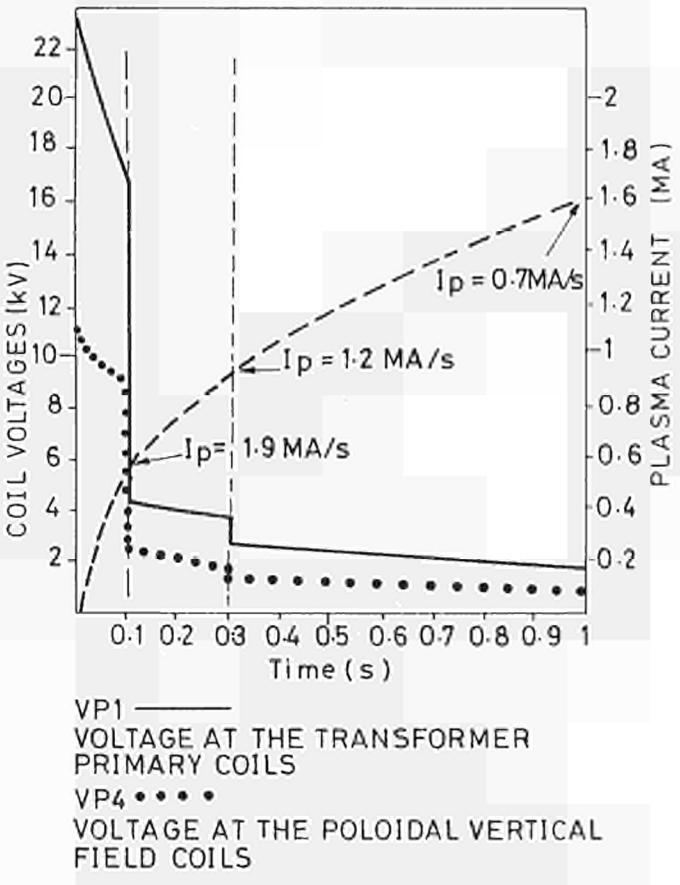

Figure 9: Voltage profiling during plasma breakdown and early fast rise phase.

Fortunately, the design concept of JET allows a good degree of flexibility for modifications and improvements, without affecting the basic structure of the machine, thus requiring limited additional resources and time. However, the implementation of such enhancements require a reappraisal of the development plan shown in Table I.

4.2 JET Development and Enhancement

In the following the present JET development and enhancement programme is briefly described:

a) Electromagnetics

A full use of the transformer flux capability of JET (34 Vs) requires to reach a plasma current of about 1.5 MA at the end of the "fast rise" phase of the discharge. Therefore a relatively high breakdown voltage (40V, i.e. -24kV across the magnetizing coils P1 and P3) is required to pass quickly through the radiation barrier, but within a time of 100-300ms the voltage must be greatly reduced in order to limit at about 1MA/s the rate of rise of the current to avoid early disruptions [10]. In order to control the radial position of the plasma during the fast rise phase a suitable voltage with the same pattern is supplied at the coils P4 (see Figure 9). These voltages will be achieved by modifying the poloidal power supply system with the addition of a set of thyristor switched resistors to supply coils P1 and, most probably, a resistor divider to supply coils P4.

These modifications are expected to allow plasma currents of 5MA for several seconds, peak plasma currents approaching 7MA and very long pulses (above 30s) at moderate currents (~3MA) and toroidal magnetic fields (<3T).

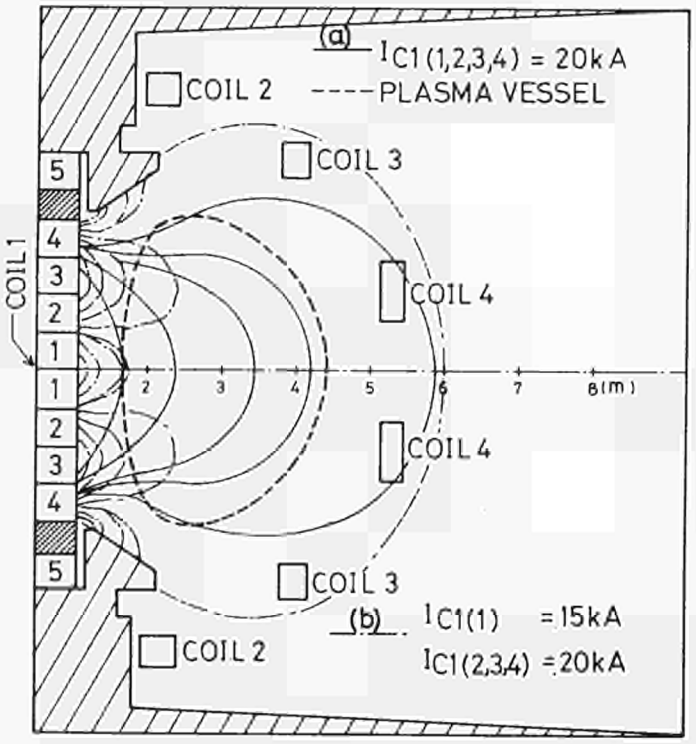

Figure 10: Example of computed poloidal field mapping without (a) and with stray field correction (b).

When the two P1 coil sections were connected in series and electrically disconnected from P4, (February 1985), difficulties in the start-up of the plasma current were encountered due to the enhanced adverse effect of the stray magnetic fields with the reduced voltage available across P4 coil at breakdown [10]. The possibility of reducing these stray fields at breakdown is now considered by limiting the current in the two central pancakes of coil P1: Figure 10 shows the field mapping without and with this additional facility [19], which would require a ~5kV, ~10kA, thyristor controlled power supply and new busbar connections. The two available spare pancakes may be added, top and bottom of the P1 coils and energized: this would further reduce the stray fields and provide compensation for the volt-second loss, due to the above tailoring of the stray fields.

The increased plasma current capability should allow increase of the density limit and the global energy confinement time.

The JET electromagnetic system, with the additions mentioned above, allows the production of a magnetic limiter configuration (with the plasma detached from the outer wall limiter) with two X-points [19] at plasma currents approaching 4 MA (see Figure 11), allowing operations at the high plasma temperatures produced by additional heating, possibly without an appreciable degradation of the energy confinement time ('H' mode).

All these additional features of the JET magnetic configuration could be available after the 1986-87 shutdown.

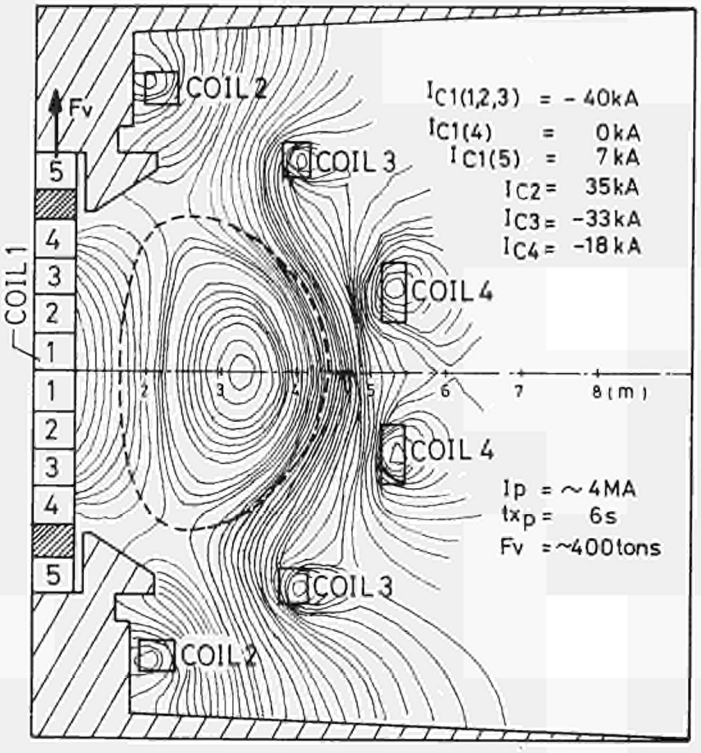

Figure 11: Computed magnetic limiter configuration at I_p~4MA.

b) Vacuum Vessel and First Wall

The original flexible vessel supports in the mid plane of the vessel (4 at each octant) were not sufficient to cope with the associated stresses from plasma vertical instabilities. Additional supports, consisting of two rigid vertical supports at the bottom edge of each of the eight main horizontal ports plus a set of shock absorbers (top and bottom) at the vertical ports, have been fitted during the 1984 shutdown (see Figure 12). However if currents above 3MA (and up to 7MA) are produced with design elongation values (1.6-1.7), the mechanical capability of the vessel must be improved by new special supports at top and bottom of the vessel (See Figure 12). The design is underway and will be implemented during the 1986-87 shutdown. It should allow to withstand forces up to 1600 tons, which can be expected in the event of a vertical instability at 7MA and full elongation [20].

Graphite tiling and wall carbonization have assisted the reduction of impurity content, (allowing somewhat higher density limits) and the tiles have provided an efficient local wall protection. Consequently eight octant joints were covered by graphite (instead of inconel) protection plates during the 1985 shutdown, while the vessel bellows will be covered during the next 1986-87 shutdown (leading to 100m^2 covered , i.e. 50% of the wall surface). In addition, the number of graphite limiters has already been increased from four to eight.

In order to cope with the additional wall power loading caused by increasing the additional heating power to the plasma, two toroidal belt limiters (to be covered by graphite or beryllium tiles) are under manufacture: these are made up of 16 sections each and located at the top and bottom of the ports in the meridian plane on the outer walls of the machine (see Figure 13). The belt limiters (surface area of 18m^2 with graphite, 13.8m^2 with beryllium) will be installed during the 1986-87 shutdown and will replace the eight existing limiters (surface area 2.56m^2).

In addition graphite tiles have been installed on the outer wall at the point of impact of the tangential neutral beams.

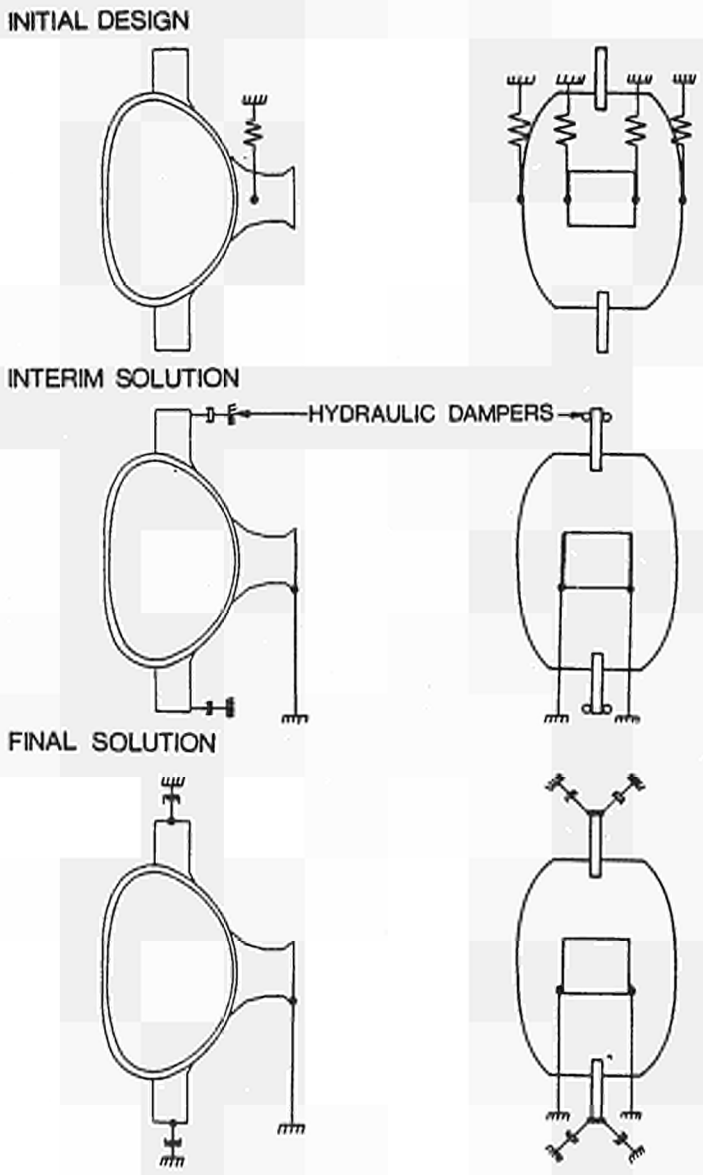

Figure 12: Vacuum vessel supports installed at the vessel ports.

It is believed, however, with some supporting evidence obtained with experiments performed on the ORNL ISX-B tokamak, that a better solution might be to replace the graphite tiles of the belt limiters with beryllium tiles. This would be due to the lower Z of the beryllium and to its property of reducing oxygen. Four beryllium evaporators will also be installed in order to coat the (remaining) carbon tiles and the vessel surface with a layer of beryllium. The beryllium tiles have already been ordered, together with the evaporators and the equipment necessary to handle beryllium in the vacuum vessel.

A design is underway for the protection of the walls facing the X-points: the structure of the protection plates could be similar in design to the one shown for the belt limiters, with cooled fins and graphite and/or beryllium covering tiles. These plates will be installed most likely during the 1988 shutdown [12,21].

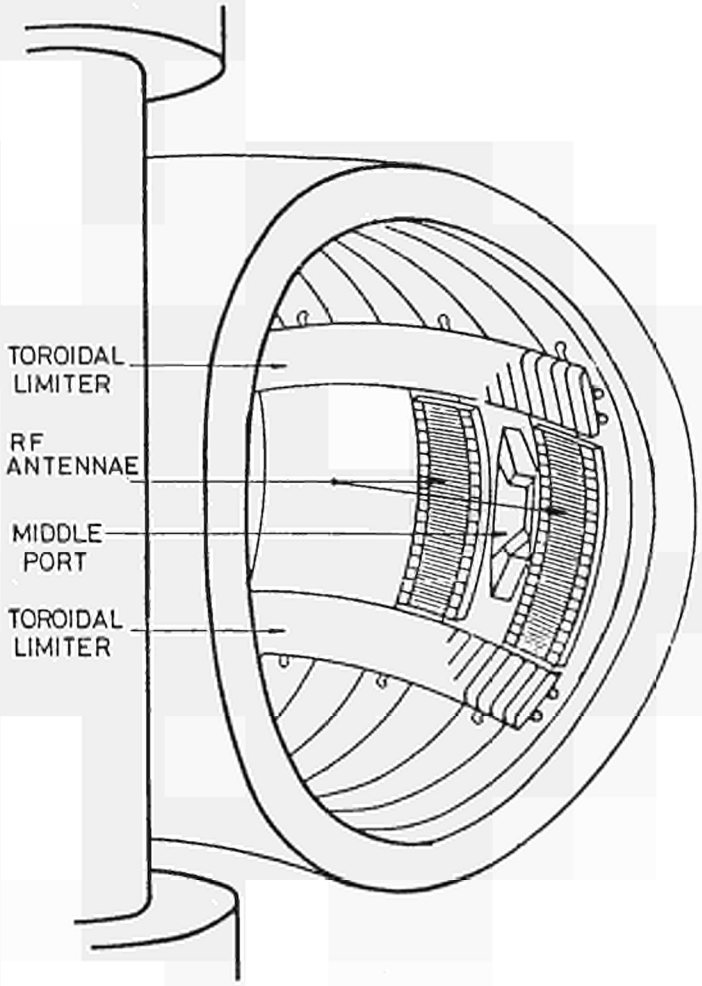

Figure 13: Sketch of the two belt limiters under construction.

Finally pumping panels and/or pumped limiters may be installed on the outer walls, to reduce the plasma density in a controlled way, by intense pumping at the edge of the plasma. Small pump limiter probes (120mm diameter) have been installed during the recent shutdown and they should allow an assessment of the principle of plasma exhaust control. Pumping panel (graphite) experiments will also be carried out [12, 21].

The other facility planned to increase and control the density are Pellet Injection techniques, in which the density is increased in the plasma centre by injecting, at suitable speed, solid pellets of hydrogen isotopes into an existing plasma.

Preliminary experiments will be carried out during late 1986 by using a 1-2km/s single pellet launcher, capable of pellet diameters up to 4mm. After the 1986-87 shutdown, a triple barrel system, 2.6, 4, 6mm pellet diameter, at a repetition rate up to 5 per second, at speeds approaching 2km/s, will be used. This programme will be carried out through a cooperation with the USA Department of Energy. Since JET may eventually need multipellet injection at higher speed (5km/s or above), a cooperative programme is underway with other European Laboratories concerning: the possibility of accelerating pellets up to 3mm diameter with arc heated guns (RISO), the development of a cryogenic pellet production unit to be used with any accelerator systems under consideration (CENG) and investigation of various stages of a piston driven scheme with plastic pellets of equivalent mass (EMI). The final multi-pellet, high speed JET pellet injection, tritium compatible, system should be available before the start of the D+T phase [22].

c) Additional Heating

The progressive increase of the additional heating power in JET, with both neutral injection and ICRF heating methods, represents the main part of the JET experimental and development programme shown in Table I and it will be maintained.

Experiments with three RF antennae up to ~5MW of "high grade" power, (i.e. the power deposited in the central region of the plasma) and with the first Injection Box made up of eight, 80kV, 60A injectors, up to ~5MW of "high grade" power, (i.e. considering only the full energy components), will be carried out during the 1985-86 period of operation. The installation and commissioning of the second Box is well underway and it will be available by May 1987 after the next shutdown. The work necessary for the future operation of the 16 beams at 160kV, 30A is also well in hand [5,17].

The RF heating programme will be slightly modified. Only eight antennae (and not ten) will be eventually installed without reducing the planned total "high grade" power of 15MW ($8A_1$, water cooled, antennae). This is possible because the antennae and the transmission lines, as built, have a power capability well above 3MW and therefore modifications required are in the power supplies and in the RF generators only. In particular new tubes, capable of handling a power above 2MW (present ones operate at 1.5MW), have been ordered. The overall result should be the same power to the plasma at reduced cost.

The additional heating should not only allow a substantial increase in plasma temperatures, but also in the plasma densities whose optimization has not yet been attempted. Moreover it has been suggested [23] that with the increase of the additional heating power above a certain level, the degradation of the energy confinement time may be greatly reduced.

With more RF heating power available, preliminary experiments in setting up the conditions for the stabilization of the sawteeth and for the control of the plasma current density profiles should be performed in 1986. Studies are underway to assess the capabilities for current drive, for the control of the current density profile, of the JET ICRH system or other methods (ECRH and LHRH) [24]. The location of the antennae has been revised. They will be installed in four pairs, equally spaced on the outer walls of the vacuum vessel: two of the existing three antennae are already installed in this position (see Figure 3), allowing an assessment of some of the technical and physics issues on the capability of JET ICRH system for current drive.

d) Diagnostics

Only minor modifications to the already established diagnostics development plan are foreseen. In fact, sawtooth oscillation measurements, to be used for feedback stabilization, may require four extra diodes to upgrade the X-ray diagnostic already available, although existing diagnostics, like ECE, could be used for the same purpose and will be tested. The timing of the 14 MeV neutron diagnostic may be re-scheduled in accordance with the modifications to the JET development plan now being considered.

e) Remote Handling and Tritium

The main reason for the these enhancements is to improve the chances of success of D+T operation in JET. The remote handling programme is continuing expeditiously and the tritium plant programme is also proceeding.

In order to appreciate the full commitment to the deuterium-tritium operation phase in JET, one needs to consider the layout of the buildings, i.e. the Hot Cell, with the sliding doors and roof beams, the Torus Hall with the special 2.5m thick walls, the 100m long RF and NI high voltage power transmission lines, to cope with the mandatory requirements of "no" power supplies or electronics too close to the tokamak, the use of helium (now implemented) instead of nitrogen/air for the vessel temperature control, because helium is a low "Z" material and has no activation problems.

A large investment has been made in the remote handling programme and this is continuing.

Besides the claim of having considered the remote handling [1] requirements in all key design issues of the JET tokamak, all the required specific devices have been designed (and some of them are operational already), such as:

"Transporters", to move components which will need to be replaced and to position the servomanipulators and other tools; they are the Main 150t Crane, the Telescopic Arm, the Turret Truck, the Low Level Transporter and the Articulated Boom [25], which has already been successfully used for removing and positioning limiters and RF antennae during the 1985 shutdown (see Figure 14). "End Effectors", dedicated to special lifting and operation, such as the force reflecting servomanipulators, the limiter gripper and the RF antenna grabber; "Special Tools", to perform dedicated operations in restricted spaces, like the

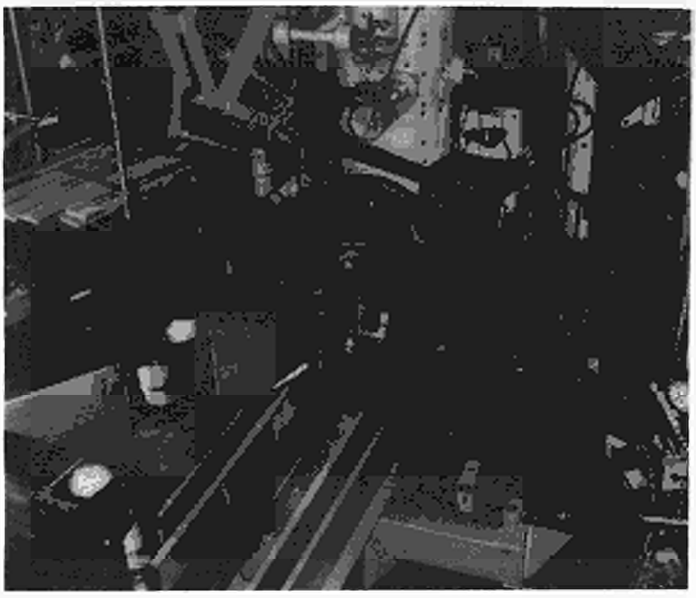

Figure 14: The articulated boom during the removal of a Nickel Limiter.

welding trolley, already used to weld two vacuum vessel octants and the cutter. Four stations for "In Vessel Inspection", consisting of stainless steel tubes terminating in glass cylinders, fitted already in 1984, have been successfully used to take black and white pictures of the critical parts of the vessel after operation [7].

On tritium recycling plant [8, 26] its basic design has been fully defined. It will reprocess and separate the gases into hydrogen isotope fractions ready for re-use in plasma pulses. The choice of recovery of the tritium has been made basically on economic grounds, since the cost of machine exhaust gas disposal would have been more than twice compared with a gas recovery and recycling plant. The tritium inventory of the plant is expected to be 10g (100,000 Ci) which is much less than would need to be kept on site if the once-through principle was used. The basic choices for the tritium plant have been secondary containment, cryogenic techniques for tritium recycling and gas chromatography for isotope separation. Prototypes for key special components, fully designed by JET, such as valves, D+T transfer pumps and accumulating panels are being manufactured and their testing should provide further information for the final design.

4.3 Experimental Programme 1986 and Beyond

The experimental programme from November 1985 to December 1986, will be focussed on the issues shown in Table I, i.e. the progressive enhancement of the additional heating power with RF and NI [27, 28, 16] up to ~10MW in the plasma core, allowing an assessment of maximum temperatures and densities achievable when $P_{AH} >> P_{\Omega}$. But at the same time key issues related to the new machine enhancements under consideration, will be addressed such as: plasma start up, magnetic limiter ("X-points"), pumping panels, the current drive concept for the control of the current profiles and sawtooth stabilization.

The impact on the JET Experimental and Development Plan shown in Table I, of the key issues described before (and summarized in Table IV) is now being discussed by the JET supervisory bodies in order to assess technical and scientific merits and cost and time implications.

5. CONCLUSIONS

JET, has been operational for more than two years. The sound technical performance and the good overall reliability of the various subsystems has permitted start of regular two shifts (16h/day) operation since January 1985.

The goals of both the development and experimental programmes planned so far, have been achieved and the main physics results can be summarized with the highest value of the fusion parameters obtained in Ohmic Heating ($\hat{n}_{iD}\ \tau_E\ \hat{T}_i$ = ~0.5 $10^{20} m^{-3} s$ keV), and with central average ion temperatures of 4 keV, obtained with less than 20% of the total additional heating power, which will eventually be available.

However the experimental results recently obtained (in JET and other Tokamaks) indicate that some machine enhancements must be introduced in JET if the ultimate goal (show alpha particle heating) is likely to be achieved.

Due to the key design features of JET and to its plasma size, the machine has flexibility which allows these enhancements to be implemented without affecting the basic structure of the apparatus.

These enhancements are: the modification of the poloidal coils and related power supplies configuration in order to allow the full use of the flux available, allowing plasma currents up to 7MA to be reached (or alternatively long pulses at lower currents) and to allow the generation of open poloidal field configurations ("X-points") to assess the "H" mode plasma heating up to plasma currents of 4 MA; the above performance can be achieved with the associated development on the vessel, i.e. additional mechanical supports to withstand vertical instabilities, toroidal belt limiters and protection plates facing the two X-points; moreover to optimize and control the density, pellet injectors, pumping panel and pumped limiters systems, have to be installed; together with the progressive upgrading of the additional heating power, RF will be used to stabilise sawteeth and the requirements of current drive for current profile control will be assessed; the diagnostics foreseen will be progressively added.

All this work is aimed at bridging the gap between the present value of the fusion parameter and that required to start a meaningful D+T phase, where alpha particle heating ($\hat{n}_{iD}\ \tau_E\ \hat{T}_i$ = ~ 0.5 $10^{21} m^{-3}$ skeV) is clearly shown. The remote handling development is well advanced already and the tritium plant programme will be pursued at the pace required by the updated JET experimental and development programme.

Table IV: Summary of the technical and scientific issues now under consideration for JET. (● fully defined, o not fully defined yet)

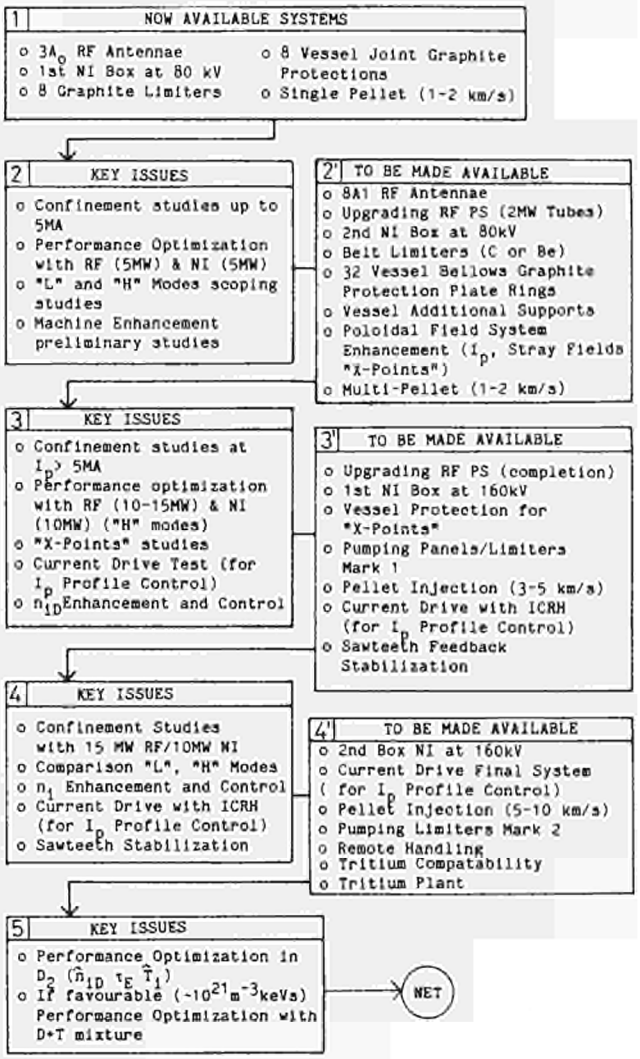

ACKNOWLEDGEMENTS

The content of this paper represents the present appraisal of the status and the prospects of JET. The information reported has been gathered, using the work and obtaining the help of many colleagues, as it appears from the references. For the up-to-date information provided and for the useful discussion, the author would like to thank M.Brusati, A.Boschi, G.Celentano, J.Dietz, A.Gibson, B.Green, H.Hemmerich, M.Huguet, J.Jacquinot, P.Kind, P.Kupschus, J.Last, E.Lazzaro, P.L.Mondino, P.Noll, T.Raimondi, W.Riediker, A.Tanga, A.Tesini. I also wish to acknowledge the guidance of R.J.Bickerton and P.H.Rebut in establishing a correlation between JET results, objectives and the necessary future development. Finally a special appreciation is due to B.Keen for carefully reading the first draft of the paper and for the many suggestions made for improving the text.

REFERENCES

1. The JET Project, "Reports of the Commission of the European Communities": EUR 5516e (1976), EUR 5781c (1977), EUR 6831en (1978).
2. Huguet M., Dietz, J.K., Hemmerich J.L., Last J.R: "The JET Machine: Design, Construction and Operation of the Major Subsystems", submitted for publication to "Fusion Technology Journal" (Sept 1985).
3. Bertolini E., Mondino P.L., Noll P: "The JET Power Supplies and Plasma Control System", submitted for publication to "Fusion Technnology Journal"(Sept 1985).
4. Van der Beken H: "The JET Control and Data Acquisition System (CODAS)" submitted for publication to "Fusion Technology Journal"(Sept 1985)
5. JET Additional Heating:
Duesing G: "The JET Neutral Beam Injection System";
Kaye A., Lallia P., Wade T: "The JET Radio Frequency Heating System";
Claesen R, Mondino P.L: "The JET Additional Heating Power Supplies"
submitted for publication to "Fusion Technology Journal"(Sept 1985).
6. Gibson A., Millward P: "Engineering Aspects of the JET Diagnostic Systems", submitted for publication to "Fusion Technology Journal" (Sept 1985).
7. Dean J.R., Raimondi T: "Measures for JET Active Operation", submitted for publication to "Fusion Technology Journal" (Sept 1985).
8. JET Joint Undertaking "Annual Report 1984", EUR 1022en, EUR-JET-AR7, August 1985.
9. Green B.J., Saunders R., Webberley D.A: "Report on 1984-1985 JET Operations", JET Internal Report - to be edited.
10. Schüller F.C, et al: "Plasma Evolution and Skin-Effects in JET", Proceedings of the 12th EPS Conference on Controlled Fusion and Plasma Physics, Budapest, 2-6th Sept 1985.
11. Noll P, et al: "Stabilization of Vertical Position and Control of Plasma Shape in JET", 11th Symposium on Fusion Engineering, Austin, Texas, 18-22nd Nov 1985.
12. Huguet M, et al : "Limiter and First Wall in JET", 11th Symposium on Fusion Engineering, Austin, Texas, 18th-22nd Nov 1985.
13. Bickerton R.J, et al: "Latest Results from JET" Proceedings of the 12th EPS Conference on Controlled Fusion and Plasma Physics, Budapest, 2-6th Sept 1985.
14. Caldwell-Nichols C.J: "Aspects of Interfacing JET Diagnostics Systems", 11th Symposium on Fusion Engineering, Austin, Texas 18-22th November 1985.
15. Jacquinot J, et al: "ICRF Studies on JET", Proceedings of the 12th EPS Conference on Controlled Fusion and Plasma Physics, Budapest, 2-6th Sept 1985.
16. Kaye A, et al: "Engineering Design and Preliminary Performance of the JET ICRF System", 11th Symposium on Fusion Engineering, Austin, Texas, 18th-22nd November 1985.
17. Claesen R, et al: "JET Additional Heating Power Supplies: Design Concept and First Operation", 11th Symposium on Fusion Engineering, Austin, Texas, 18th-22nd November 1985.
18. Tanga A, et al: "The Formation of a Magnetic Separatrix in JET", Proceedings of the 12th EPS Conference on Controlled Fusion and Plasma Physics, Budapest, 2-6th Sept 1985.
19. Lazzaro E., Tanga A: JET, Private Communication, Oct 1985.
20. Huguet M: JET, Private Communication, Oct 1985.
21. Dietz J: JET, Private Communication, Oct 1985.
22 Kupschus P: JET, Private Communication, Oct 1985.
23. Rebut P.H., Brusati M: "Magnetic Topology, Disruption and Electron Heat Transport", Proceedings of the 12th EPS Conference on Controlled Fusion and Plasma Physics, Budapest, 2-6th Sept 1985.
24. Jacquinot J: "Heating and Current Drive Scenarios with ICRF", Proceedings of the Course on Tokamak Start Up, Erice (Italy), July 1985.
25. Jones P D F, et al: "Design and Operation of the JET Articulated Boom", 11th Symposium on Fusion Engineering, Austin, Texas, 18-22nd Nov 1985.
26. Riediker W: JET, Private Communication.
27. Falter H, et al: "Operational Tests of the JET Neutral Injection System in the JET Test Bed", 11th Symposium on Fusion Engineering, Austin, Texas, 18-22nd Nov 1985.
28. Haange R, et al: "JET Neutral Injection Beamline System: Manufacture and Assembly", 11th Symposium on Fusion Engineering, Austin, Texas, 18-22 Nov 1985.

LIMITERS AND FIRST WALL ON JET

M Huguet, J A Booth, G Celentano, E Deksnis*
K J Dietz, P H Rebut, R Shaw, K Sonnenberg

JET Joint Undertaking
Abingdon, Oxfordshire, England

*Supported by National Research Council of Canada

Abstract

During the initial phase of the JET operation, graphite limiters and Inconel wall protection plates had been used. After one year of operation, some of the Inconel plates at the inboard wall were found to be significantly damaged. These plates were replaced by graphite tiles in order to eliminate one source of metallic contamination of the plasma. Operational experience with the graphite tiles has been good, and additional graphite protections have been installed recently. Further protections will be added in 1987 to cover extensively, although not completely, the walls of the vessel.

Some of the graphite tiles have also to protect the wall from the power loading of neutral particle beams. Tests have confirmed that the tiles can withstand the expected load due to beam shine-through, but they have revealed that the tiles are cracked by unattenuated beams of long duration. Alternative designs and materials are being considered and will be tested.

By the beginning of 1987, it is planned to install a toroidal belt limiter. This limiter, with a total area of 15 m^2, should be able to withstand 10 second long pulses with 40 MW of additional heating power injected into the vacuum vessel. The limiter tiles are radiation-cooled by means of a radiator comprising water cooled fins. A similar design is used for the protection frames around the ICRF heating antennae. The material used for the limiter tiles will be either graphite or berryllium. Both materials are being procured. It is also planned to use beryllium evaporators in conjunction with the belt limiter, in order to take full advantage of the gettering properties of beryllium.

Future plans include the possibility of operations with a magnetic separatrix. This will require the use of a new set of limiters in the top and bottom parts of the vessel.

Introduction

The Joint European Torus (JET) is the largest tokamak in operation, and is the central project within the fusion programme of the European Communities [1]. First operation was achieved as planned in June 1983 after a five year construction period [2-3]. During the first two years of operation, the machine has reached its full rated design performances with a maximum plasma current of 5 MA in a toroidal field of 3.4 T. Physics results have been impressive; a global confinement time of 0.8 s and a maximum central ion temperature of 4 keV have been achieved. The best combination of Lawson parameters gave a product $\hat{n}_D \cdot \hat{\tau}_E \cdot \hat{T}_i$ of 6 x 10^{19} m^{-3}.s.keV [4-5].

Impurity control which aims at reducing radiation losses from the plasma and dilution of the thermonuclear fuel, is one of the key issues to approach reactor conditions in fusion machines. Impurity control has always been one of the basic objectives of the JET experiment, and the use of low Z materials for the limiters and wall protections has been a long term policy to achieve it. This paper describes the limiters and wall protections used so far, together with the experimental evidence gained during 2 years of operation. It also describes the belt limiter to be installed in the near future, and outlines longer term development plans.

I. Graphite Limiters and Inconel Wall Protections during the initial period of operation

1. Description of Limiters and Wall Protections

During the initial phase of operation, from June 1983 to October 1984, JET operated with 4 graphite limiters and Inconel walls.

The limiters are located at the equatorial plane on the outboard wall. Each limiter is 40 cm wide and 80 cm long and consists of 8 graphite blocks shaped in the toroidal direction so as to distribute the power load. The graphite blocks are supported at the back by an Inconel structure which transfers the transient mechanical torques occurring during plasma disruptions to the vacuum vessel. The radial position of the limiters can be adjusted by 12 cm, from the outside by means of bellows. [6].

The graphite used is a fine grained, highly purified material (CL 5890 PT manufactured by "Le Carbone Lorraine") which offers satisfactory thermo-mechanical properties (table 3) and an average impurity content of the order of 20 ppm [7]. After machining, the material is cleaned, outgassed at 1250°C in vacuum, and saturated with helium around 400°C during cooling.

The inner wall of the JET vessel consists of rigid sectors made of Nicrofer 7216 LC (Inconel 600), and bellows assemblies and octant joints made of Inconel 625 (figure 1). During the initial phase of operation, the inner wall was protected by Nicrofer 7216 LC (Inconel 600) heat shields and protection plates.

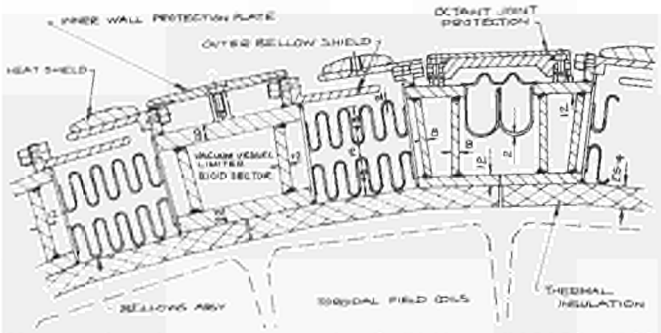

Figure 1. Cross section of vacuum vessel wall showing Inconel protections

2. Operational Experience with the Limiters

During discharges, two of the limiters were viewed by infra-red cameras. Arcing was observed during the initial phase in 1983 but ceased to be as frequent later in 1984 when baking at temperatures in the range of 300°C was introduced. The surface temperature of the limiters was typically around 800°C during the plasma current flat tops. Due to the curved shape of the limiters, heating is localised in 2 zones (figure 2) with stronger heating on the ion side for most plasma conditions. The change from near circular to elongated plasma cross sections results in an increased plasma length interacting with the limiter in the vertical (poloidal) direction.

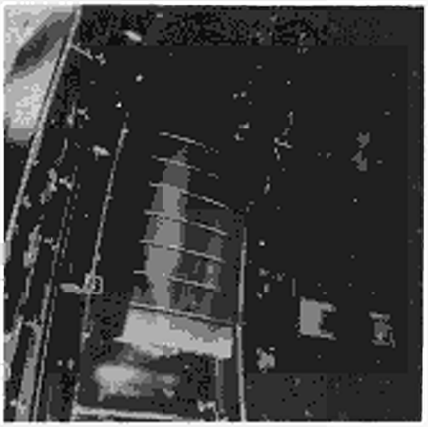

Figure 2. Graphite limiter showing plasma "footprints"

During the early phase of the JET operation, there was a relatively high (0.2%) level of metallic impurities in the plasma [8]. The carbon limiters have been identified as the main source of high Z (metallic) contamination during discharges. Contamination of the limiter by wall material is present in all tokamaks and a surface analysis of some of the JET limiter tiles confirmed the presence of metal deposits. Nickel and chromium are, as expected, the major contributors with concentrations which appear to come to an equilibrium level in the range of 10^{20} to 10^{21} atoms/m^2. In the area of plasma contact, the deposition is in the form of atomic layers, whereas on the edge small droplets (1 μm) are observed. Large droplets (100 μm) are also present [9].

Mechanisms which can be responsible for the metal coating of the limiters include the sputtering of wall material during glow discharge cleaning and tokamak discharges, and strong plasma-wall interactions such as arcing and disruptions. Fast plasma disruptions are sometimes associated with the production of spectacular metal projections originating from the inboard wall, and large photo-neutron emissions. This is explained by run-away electrons accelerated by the voltage spike during the disruption and carried to the inboard wall together with the magnetic surfaces of the plasma. This phenomenon may account for the presence of metal droplets on the limiter surface.

Another possible source of metal contamination was plasma interactions with the Inconel structures supporting the graphite limiter blocks. When the vessel was opened, discoloration marks on these structures clearly indicated that the plasma could flow behind the 75 mm thick graphite blocks. This source of contamination has now been eliminated by the recent installation of additional graphite tiles around the limiters.

During this period of operation, "carbonization" of the vessel walls has been the method used to control metallic impurities. Carbonization has been achieved by glow discharge cleaning in a mixture of hydrogen and methane [10]. Carbonization has resulted in the temporary reduction of the plasma total radiated power from typically 80% of the ohmic power input to less than 50%, and in an increase of the limiter surface temperature up to 1800°C.

3. Damage Observed on Inconel Protections

When the vessel was opened during the October 84 shut-down, significant damage was found on the Inconel protection plates. [11]. Most damage was localized at the inboard wall. Three kinds of damage could be clearly identified.

Type 1

This type of damage is characterized by a thin melted layer which extends along one edge of the protection plates. It is seen by its coloration due to a surface deposition of carbon of about 0.1 μm. The damage is found systematically on the left hand side (electron side) for plates above the equatorial plane and on the right hand side (ion side) for plates below the equatorial plane. The reason for this is not understood. The damage is not radio-active and is believed to be due to plasma discharges leaning against the inboard wall.

Type 2

This type of damage consists of melted craters surrounded by splattered metal. (Figure 3). There were approximately 50 impacts, most of them very close to the midplane. As expected, the damage was almost exclusively on the protection plates which for construction reasons project most towards the plasma.

The craters exhibited some radio-activity, the dominant contribution being Ni^{57} with a half life of 3 days, the next most radiating elements being Co^{56} (77 days) and Ni^{56} (6 days). This activation is thus to be attributed to photo-neutrons generated by run-away electrons. These run-away electrons can be accelerated to 30 or 40 MeV by the voltage spike during a disruption, and driven to the inner wall together with the magnetic configuration of the plasma.

The total energy deposited by electrons was estimated from the amount of melted metal as indicated in table 1.

Figure 3. Damage (type 2) produced by run-away electrons on inconel protection plates. Size of crater = approximately 50 mm.

Table 1. Damage due to Run-Away Electrons (October 1984)

Size of craters	5 to 50 cm^2
Amount of metal melted (per crater)	0.5 cm^3 (4g) to 3.5 cm^3 (30g)
Estimate of energy deposited (per crater)	$6x10^3$ to $4.4x10^4$ joules
Total amount of melted metal (50 craters)	1 kg
Total energy deposited (50 craters)	1 MJ

In the estimate above, the amount of metal blown away was given by the volume loss of the craters, and the thickness of the melt resolidified on the crater was measured from the grain structure of micrographs. The estimate is however rather inprecise since the temperature of the melt is not known and may have been close to boiling point in some cases.

Some of the major disruptions were accompanied by a burst of photo-neutrons. In one case, a U^{238} counter recorded 2.5×10^{13} neutrons occurring in a time less than 3 ms. An attempt has been made to calculate the energy deposited by electrons from the measurement of the photo-neutron yield. There were 22 major disruptions producing about 1.4×10^{15} neutrons in total. Assuming an energy of 30 MeV for the electrons, the total energy deposited in Inconel is estimated to be 5 MJ, i.e. 5 times more than the other estimate. The first estimate of 1 MJ is however, believed to be the most precise.

Type 3

There were 3 areas of local melting with little or no activation. Contrary to damage of type 2, these areas exhibited smooth melted craters without any spattered metal (figure 4). They were not located near the equatorial plane, indeed one of them was at the bottom of the vessel on an octant joint protection plate. This kind of damage is severe and involves as much melted metal as the most extensive single damage of type 2. Although the appearance suggests some form of arc damage, there is no satisfactory explanation for this.

Figure 4. Damage (type 3) found in the bottom part of the vessel. Size of crater = approximately 60 mm.

II. Graphite Tiles for Wall Protection

The metal contamination described in section I.2 prompted a decision to partly cover the Inconel walls of the vessel with some low Z protection. In a first step towards a low Z vessel, it was decided to cover only the inboard wall. It was felt that this would eliminate one of the most important and obvious source of metal contamination. This decision was taken well before the opening of the vessel and was, a posteriori, proven to be correct, by the damage found on the Inconel plates.

1. Choice of a Material for Wall Protections

Graphite is an obvious choice when looking for a low Z, refractory material. It can be obtained in large quantities at a reasonably low cost and is very easy to machine.

In addition to the points above, graphite offers a very attractive combination of physical and thermo-mechanical properties (table 3). The most important points are summarized below.

Due to the low density of graphite, energy deposition by run-away electrons is not limited to a small superficial spot as in Inconel, but is distributed in a deep layer. For example, the penetration depth is 80 mm

for 30 MeV electrons. As a result, graphite would suffer no damage, and the surface temperature would remain below the sublimation point for the type of heat impacts which are indicated in table 1.

Graphite has an excellent resistance to thermal loading. For a brief heat influx and a volumetric deposition of the energy, the factor of merit can be characterized by:

$$f = \frac{Rc}{\alpha E}$$

R = ultimate strength, c = specific heat, α = thermal expansion coefficient, E = young modulus. (The value of f is given in table 3).

The high specific heat of graphite minimizes the temperature rise and the high sublimation temperature reduces the erosion rate.

So far, JET has been using graphite from 2 sources only. Graphite CL 5890 PT from Le Carbone Lorraine and graphite EK 986 from Ringsdorff.

2. Design of the tiles and their attachments

For use as wall protection, the graphite is machined in tiles. The tiles are 20 mm thick and their small dimensions (typically 150 x 150 mm) make them easy to handle. To avoid the circulation of eddy currents, each tile is individually attached to the wall and there is a small gap between adjacent tiles. These gaps have been arranged so that the field lines can never penetrate between tiles (figure 6).

The attachment of the graphite tiles must be compatible with remote handling requirements. The design is shown on figure 5. On the back of the tile, an Inconel plate is screwed to Inconel rods which themselves pass through holes machined in the tile. The back plate carries two V-shaped wings which engage into and slide along V-shaped rails bolted onto the wall of the vacuum vessel. Springs provide some pressure between the back plate and the rails and stabilize the tiles. The assembly is quite easy: once inserted into the rail, the tile slides down to its position where it butts against a stop screw. Tests have shown that the operation is easily performed by a servo-manipulator.

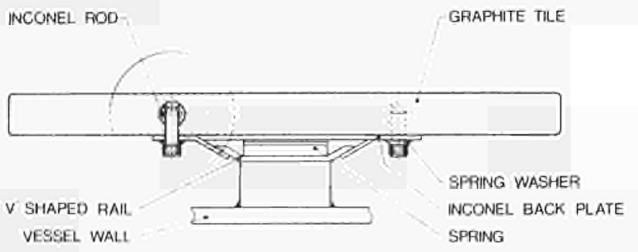

Figure 5. Attachment of graphite tiles

3. Operational Experience with Graphite Tiles

Figure 6 shows the graphite tiles installed in the vessel in October 1984. A height of 2 metres and an area of 23 m^2 is covered by a total of 960 tiles. At the same time as the tiles were installed, the limiter graphite blocks were replaced, so that only clean metal-free graphite surfaces would be present in the vessel.

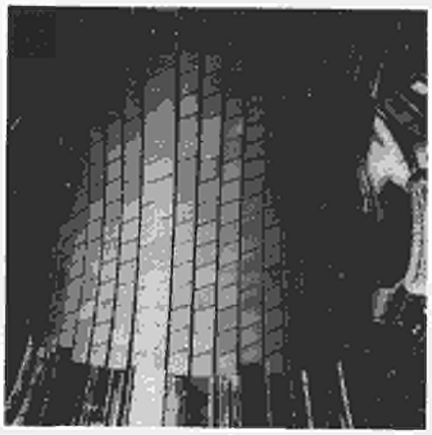

Figure 6. Graphite tiles at the inboard wall of the vessel - Status in January 1985

When operation resumed in January 1985, metal impurities in the plasma were low initially, and the total power radiated from the discharge was only 40% of the total ohmic input. However, within a few weeks, a gradual increase of metal impurities was observed and soon carbonisation (see section I.2) was the only method to control metal impurities. It must be noted that an experimental study of vertical instabilities [12] was being carried out at the same time, and the frequent occurrence of strong plasma-wall interactions at the top and bottom parts of the vessel certainly contributed greatly to metal contamination of the graphite limiters.

After 6 months of operation, in July 85, the vessel was re-opened and virtually no damage could be seen on the graphite tiles. Some signs of erosion were observed on slightly protruding edges, and 3 tiles showed minor cracks, but these may well have been caused by mishandling during assembly. This gave great confidence in the design and suitability of the tiles since during these 6 months a large number of disruptions, some at a current level up to 4.5 MA, had produced a total dose of photo-neutrons comparable to that in the previous operation period with Inconel tiles.

It is noteworthy that although the graphite tiles at the inboard wall suffered no damage during the operation period from January to June 1985, one of the graphite blocks of the limiter at octant 1, showed a cracked spot due to a heat impact (figure 7). This kind of damage on limiters had never been observed before on JET. A post mortem examination revealed that the cracks were approximately 2 mm deep and that damage was only superficial. It is tempting to put together this damage and the type 3 of damage described in section I.3. However, in this case, a run-away impact, perhaps at lower electron energy, cannot be excluded since this limiter was found to be slightly proud of the 3 other limiters.

Figure 7. Damage on graphite limiter. Size of cracked area : approximately 25 mm.

4. Further Graphite Protections

It has been mentioned in the previous section that "vertical instabilities" hitting the top or bottom parts of the vessel can contribute to the contamination of the graphite surfaces by metals. It is also at the top and bottom parts of the vessel that the plasma interacts strongly with the wall when JET is operated in the separatrix mode (see section V) [13].

Damage similar to that described in section I.3 has indeed been seen for the first time at the top and bottom parts of the vessel, after the 1985 experimental campaign during which both vertical instabilities and the separatrix mode were studied. It is therefore essential to extend further the graphite protections. For budget and time reasons the work has been planned into 2 steps. (See also table 5).

Step 1: In August 85, the Inconel octant joints protections have been replaced by graphite tiles. This makes up a configuration of 8 graphite belts in the poloidal direction.

Step 2: The Inconel heat shields protecting the bellows will be replaced by graphite tiles in January 1987. This will add another 32 graphite belts in the poloidal direction.

III Protections Against Neutral Particle Beams

1. Load Conditions at the Inboard Wall

Some of the graphite tiles face the neutral beam injector lines and must be able to withstand the power deposition associated with neutral particles. The most severe case occurs at the inboard wall of the vessel. Several load conditions can be considered:

1. During normal operation, the power loading on the wall due to the beam shining through the plasma is estimated to be less than 500 W/cm^2 for 10 seconds.

2. Neutral beam shots without plasma can give peak loads of about 2 kW/cm^2.

This situation can arise:

a) immediately after a disruption for less than 100 ms until the beam is switched off
b) during test shots for less than 500 ms
c) in case of a failure of all beam interlocks the peak load could last 10 sec.

2. Tests and thermo-mechanical analysis

Tiles have been subjected to destructive tests under neutral beam loading [14]. The interpretation of the results is difficult because damage initiation is not easy to detect and cannot be clearly associated with a particular neutral beam shot. This is because the tiles are observed through windows of the test bed target tank and only significant cracks can be seen. In addition, fatigue effects do play a role, as cracks have been seen to appear only after several identical shots. So far, only 4 tiles have been tested and the conclusions below must be considered with some caution.

a) The tiles can withstand the normal beam shine-through load. The safety factor seems adequate since no damage was produced with heat loads of 1 kW/cm^2 for 8 seconds.

b) The peak load of 2 kW/cm^2 can be resisted only for a limited time, less than 1 second, and a small number of shots. Cracks develop along the fixation holes which act as stress raisers.

These tests have been supported by finite element thermal and stress analysis. Table 2 gives the peak stresses in a solid (without holes) tile subject to a constant heat flux. It must be noted that due to the time dependant temperature distribution, peak compressive and peak tensile stresses do not appear at the same time.

Table 2. Peak Stresses in a Graphite Tile Under Thermal Load

Heat flux (W/cm^2)	Peak tensile stress (MPa)	Peak compressive stress (MPa) at front surface
500	6.3	15
1500	19	46

The holes necessary for supporting the tiles introduce a stress intensification factor for tension in the vicinity of the hole of approximately 2.2. Thus failure of the tile along the hole, as observed, is consistent with the calculation since the ultimate tensile strength of graphite is 40 MPa.

In conclusion, the present design is adequate for the normal load but would not resist a single 10 second shot at full power. To remedy this, various new solutions are being envisaged and will be tested soon. Stress can be reduced by using thinner tiles and a new design of supports without holes. Carbon fibre reinforced graphite is also being considered as an alternative material.

3. Port Protections

Some of the beam lines do not intersect the inboard wall but travel across the vessel to the outboard wall in the area of the main horizontal ports. The power flux there is less severe than at the inboard wall because of the greater attenuation through the plasma, or in the case of a shot without plasma, because of the divergence of the beams. The present design of the graphite tiles is adequate for these areas.

A difficulty arises however because the ports which have to be protected are also the access ports for personnel and later for the telescopic boom and servo-manipulator. The remote removal and re-assembly of the tiles is imperative since they are partially obstructing the passage. For this reason, the tiles are mounted on an Inconel frame which is itself attached by a system of hooks to the walls of the ports.

IV The Toroidal Belt Limiter

JET has used 4 graphite limiters from the start of operation in June 1983 to July 1985. In July 1985, 4 additional graphite limiters have been installed, thus increasing the total limiter area facing the plasma from 1.28 m^2 to 2.56 m^2. It is planned to use these 8 limiters from November 1985 to December 1986. During this period, the useful heating power into the plasma will reach 15 MW (3 MW of ohmic heating; 5 MW of neutral beams and 7 MW of ICRF) and the total power injected into the vessel will reach 20 MW (see also table 6) - The graphite limiters would be able to sustain this total power for only 3-4 seconds. However, it is expected that some of this power will be radiated to the walls.

When the additional heating power is increased to its full performance value in 1987, the thermal load will have to be taken by a larger, new type of limiter, i.e. the toroidal belt limiter.

1. Operational requirements and general description of the toroidal belt limiter

At full performance, 25 MW of useful additional heating power will be injected into the plasma, (10 MW of full energy species neutral beams and 15 MW of ICRF heating). The total power injected inside the vacuum vessel however will reach approximately 40 MW for 10 seconds. This power will be almost entirely dissipated on the limiter if radiation due to impurities can be reduced to a low level.

The geometry of the belt limiter is shown on figure 8. It consists of 2 toroidal belts above and below the main horizontal ports of the vessel. The axissymmetry is preserved everywhere except for short sections at two horizontal ports where the requirements of diagnostics viewing made it necessary to indent the profile of the limiter. With this geometry, the area facing the plasma is very large, and the surface load is low enough, even at full power, to allow an adiabatic temperature rise during the pulse, and some form of radiation cooling between pulses.

Each belt includes 858 tiles placed edge on to the plasma. The material of the tiles may be either graphite or beryllium (section IV.2). Radiation cooling of the tiles is maximized by a "radiator structure" made up of nickel fins placed between each tile. The fins are themselves welded to water-cooled tubes. In order to increase the radiative heat transfer, the side faces of the fins and of the tiles (in the case of beryllium) are coated with a black layer for higher emissivity.

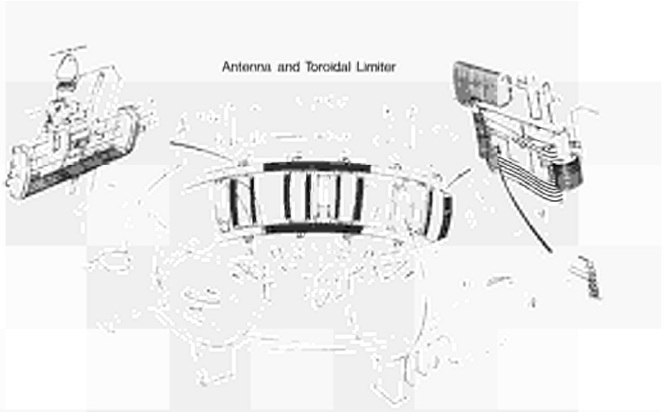

Figure 8. Toroidal geometry of the belt limiter. The ICRF antennae are shown between the upper and lower belts

This design is attractive because of the absence of critical thermal stresses and the possibility of exchanging easily some or all limiter tiles. As shown on figure 8, the belt limiter and the ICRF antennae form an integrated design wehere the limiter protects the upper and lower edges of the antennae. The limiter and antennae also share the same water cooling system. The toroidal belt limiter is now under construction and is planned to be installed in the machine by the beginning of 1987.

2. Materials for the Limiter Tiles

The material to be used for a limiter should fulfil the following requirements: low Z, high melting (sublimation) temperature, large thermal conductivity, large specific heat, good resistance against thermal shock, low erosion through sputtering (chemical or physical sputtering), low retention of hydrogen isotopes, getter action if possible.

The two materials which have been selected for JET are graphite and beryllium. The type of graphite is similar to the one described in sections I.1 and II.1. The beryllium grade is S65B from Brush-Wellman (USA). Some physical properties of these materials are shown in table 3.

From the table it can be seen that the thermal properties of graphite are superior to those of beryllium, but this advantage is offset by the better mechanical properties of beryllium, in particular the high ductility at elevated temperature.

Table 3. Physical Properties of Graphite and Beryllium. Properties Given at 300°C unless stated.

	Graphite	Beryllium
Atomic number Z	6	4
Density (g/cm^3)	1.6-1.85	1.8
Porosity (%)	15-25	0
Melting temperature (°C)	-	1277
Boiling/Sublimation temp. (°C).	4450	2770
Heat of evaporation (J/mole)	7x10	3x10
Thermal conductivity (W/m.°C)	64	128
Specific heat (kJ/kg.°C)	1.34	2.6
Expansion coefficient (x 10^6)	5.5	13
Elastic modulus (G Pa)	11	220
Ultimate tensile strength (MPa)	40	320
Elongation at 400°C (%)	0	50
Electrical resistivity (μΩ.m)	11.4	0.03
Factor of merit f (section II.1)	0.88	0.29

In addition to the physical properties which affect mostly the behaviour of the limiter, there are other properties which have a great importance for the quality of the plasma. Beryllium is a very attractive choice because of its very low Z, which means that its contribution to plasma radiation is negligible, even at high concentrations. Sputtering by hydrogen and deuterium is lower for beryllium than for graphite at the JET operating temperature [15]. Hydrogen retention and release is very important as it affects strongly the evolution of the plasma density. Studies [15] have shown that at the JET operating temperature, hydrogen retention is smaller in beryllium than in graphite. This is because hydrogen starts being thermally released at a lower temperature in beryllium. Finally beryllium can be employed as an oxygen getter because it forms a non volatile stable oxide.

From an engineering point of view, graphite is attractive since it is reasonably cheap and easy to machine, whereas, beryllium is an expensive material involving a difficult metallurgy. Another drawback of beryllium is the toxicity of its dust which imposes strict safety precautions. The precautions are well known to the beryllium industry and can be applied to JET. The ISX-B experience at Oak Ridge (see below) has been valuable in assessing safety aspects. The precautions include dust monitoring systems, decontamination procedures before entering the vessel, the use of special suits for workers inside the vessel and the careful monitoring and cleaning of tools. It must be noted, however, that for a machine like JET, which is designed for tritium operation, beryllium would not add significantly to safety problems.

Graphite has almost become a conventional first wall material in tokamaks and its use is now well documented. In the case of beryllium, the lack of experimental data prompted JET into placing a contract with the Oak Ridge National Laboratory to test beryllium as a limiter in the ISX-B machine. The results of this experiment are outside the scope of this paper and have already been reported [16]. They have shown that beryllium is suitable as a limiter and getter material.

For JET, tiles made of graphite and beryllium are now being manufactured and will be available for use in the machine by the beginning of 1987. It has not been decided yet which material will be used first. The graphite and beryllium tiles are shown on figure 10. It can be seen that the cross section of the graphite tiles is T shaped to maximize the area facing the plasma. This feature could not be retained for the beryllium tiles for cost reasons.

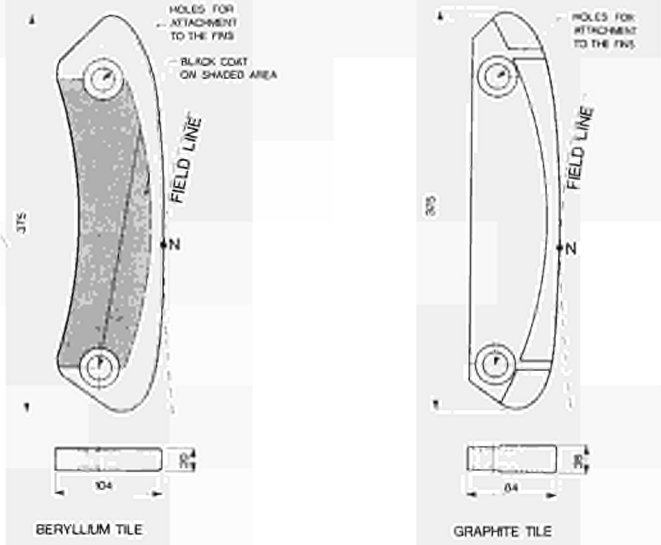

Figure 9. Graphite and beryllium tiles for the belt limiter. The point N is where the field lines are parallel to the surface of the tiles.

3. Thermo Mechanical Analysis

a) Power deposition and heat removal.

The profile of a tile, as shown on figure 9, is shaped so as to optimize the distribution of the thermal load. Figure 10 illustrates the heat flux distribution calculated for various thickness of the scrape-off layer. The peak flux is 1.6 times greater than the average flux. The profile of the tiles is asymmetrical in order to take into account the different values of the scrape-off layer thickness on each side. In the narrow gap between the upper and the lower toroidal limiter belts, the thickness of the scrape-off layer has been assumed to be in the range of 3.7 mm to 15 mm while on the other side of the belts the values are between 7.5 and 30 mm. This is due to the unequal connection length of the magnetic lines of force. The assumptions made for the incident power on each side are shown on figure 10.

Heat deposited on the tiles is radiatively transferred to the adjacent water cooled fins. The fins and the beryllium tiles are coated with a black layer which gives an effective emissivity from tile to fin of approximately 0.65. The process used for blackening are described in section IV.4.

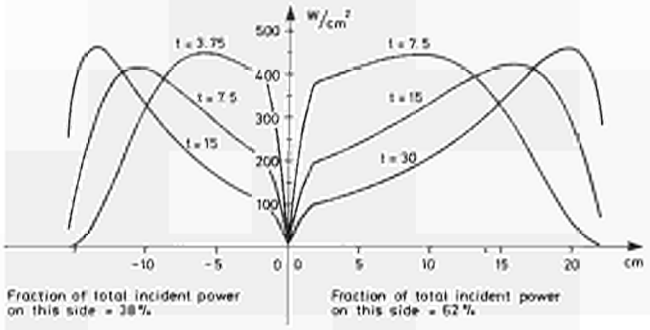

Figure 10. Heat flux distribution on beryllium tiles. The field lines are tangent to the tiles at point x = o. Total power to the limiter = 40 MW. Each curve corresponds to a scrape-off thickness t in mm.

b) Results of analysis.

Table 4 gives the basic results of the thermal and mechanical anaylsis.

Table 4. Results of Thermo Mechanical Analysis for Graphite and Beryllium Belt Limiter Tiles

	Beryllium tiles	Graphite tiles
Thickness of tiles (mm)	20	26
Total area facing the plasma (m^2)	13.8	18
Average heat flux (W/cm^2)	290	222
Expected peak heat flux (W/cm^2)	450	370
Peak surface temperature (^oC)	1000	1250
Peak compressive stresses at front surface (MPa)	plastic behaviour	21
Peak tensile stresses (MPa)		5.5

Figure 11 illustrates the evolution of the surface temperature in beryllium tiles during 10 consecutive shots at full power.

The stress pattern set up by the temperature distribution involves initially compression at the front surface and tension deeper in the material. The fixation holes have been located in areas where the stress level remains low. In the case of beryllium, plastic deformation takes place near the surface during the heat pulse, and is reversed during cool-down. This cyclic plastic strain causes fatigue cracks to develop at the heated surface. This effect has been investigated analytically and experimentally at Sandia Laboratory [17]. The study included 5000 cycles with a heat flux of 450 W/cm^2 for 10 seconds and has shown that crack growth is arrested at a depth of about 5 mm.

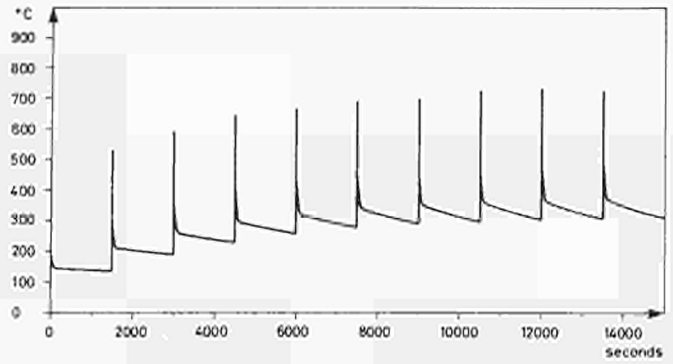

Figure 11. Evolution of the surface temperature of beryllium tiles during 10 consecutive shots.
Heat flux = 290 W/cm^2 for 10 seconds every 25 minutes.

4. Blackening of radiating surfaces

The nickel fins are coated with a black layer for higher emissivity. Several coating methods have been tested and have resulted in the selection of low pressure (100 mbar) plasma spraying of aluminium oxide. Low pressure spraying is essential to achieve good adhesion, low porosity and reduce the outgassing of atmospheric gases during plasma discharges The spraying gas is a mixture of nitrogen and helium. Helium and hydrogen were initially the preferred choice but were found to be inefficient for this process, and argon could not be considered because it is used as a test gas for leak detection in JET. Only one spraying run is sufficient to achieve a coat thickness of 15 µ. The coat is mechanically very strong and has an emissivity greater than 0.8.

The beryllium limiter tiles are blackened by using a conventional process of chromic acid anodizing in a bath.

5. Mechanical Design and Manufacture

The cooling structure, or radiator, of the belt limiter includes the fins and the water pipes. Each belt has been split into 16 sectors, for assembly reasons. Each sector is made up of 4 thick-walled (2 mm) Inconel tubes and 55 nickel fins welded to them. Nickel has been selected as the fin material because of its high thermal conductivity and its good mechanical properties even at elevated temperature. It has been specified in the quarter hard state to ensure the mechanical stability of the structure and guarantee an easy assembly of the tiles. Holes and welding lips around the holes are stamped in the fins for welding to the tubes. (Figure 12). During manufacture, each fin is precisely located by a jig and the fin to tube welds are carried out by means of automatic orbital welding machines. The water manifolds at the extremities of each sector are machined out of forged Inconel bars. They carry the water inlets and outlets and the mechanical attachments to the wall of the vessel. Differential expansion between the vessel and the water cooled structure is made possible by sliding spring loaded supports at one end. Inconel bellows are provided on the water pipework.

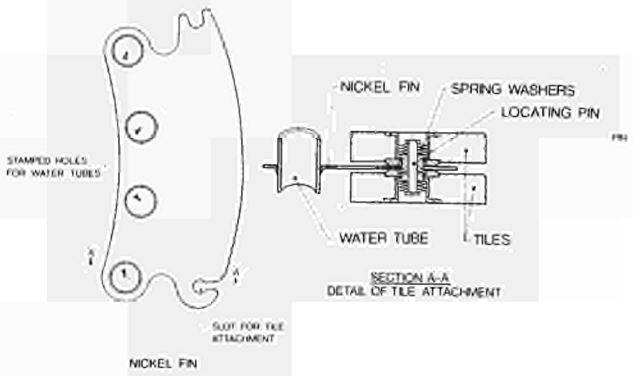

Figure 12. Cooling fin of the belt limiter and detail showing the attachment of the tiles onto the fin.

Each sector may have to be dismantled and reassembled remotely during the active phase. For this reason, the attachments include a combination of hook supports and a minimum number of well accessible captive bolts. The remote handling of the limiter sector involves the use of the articulated boom together with a special extension [18]. Cutting and welding of waterpipes inside the vessel will be carried out by special orbital tools presently under development.

The tiles (graphite or beryllium) are assembled in pairs by means of pins and locating washers (figure 12). Spring washers keep the tiles pressed against each other. For assembly, the tiles forming a pair are slightly separated with a simple tool, and inserted on either side of a fin. Slots are provided in the fin for the passage of the pins. When in position, the locating washers spring into the holes in the fin and lock the tiles in position. With this simple spring locking mechanism it is possible to replace pairs of tiles using remote handling techniques.

The electro-mechanical loading experienced by the cooling structure comes from eddy currents produced by the poloidal flux changes during plasma disruptions. These currents interacting with the toroidal magnetic field produce no net force but moments twisting each section so as to increase the toroidal flux intersected. These currents interact also with the poloidal magnetic field to produce bending moments along the cooling pipes. These currents may flow through the mechanical attachments. For this reason electrical straps have been provided to prevent arcs and any risk of spot welding of bolts. All these forces have been conservatively calculated and can be resisted by the structure.

6. Cooling System

The belt limiter and the antennae share the same cooling system. The cooling system has to provide several modes of operation and the complex transitions between these modes. The main modes of operation are as follows:

- Normal tokamak discharge: the limiter and antennae are water-cooled.
- Wall conditioning: the water is drained and the temperature of the limiter and antennae is allowed to rise up to the vessel temperature to avoid the trapping of impurities on cold surfaces.

The transition from wall conditioning back to tokamak discharge involves first a phase of nitrogen gas cooling in order to lower the temperature below 100°C, and secondly the evacuation of the system to avoid trapped gas pockets when water is re-introduced.

V Future development and Conclusions

Table 5 summarizes the installation of graphite protections on the inner wall of the JET vacuum vessel. From the table it can be seen that 48% of the total vessel area will be covered with graphite by 1987.

Table 5. Graphite Protections in JET

Description	Date of installation	Area covered (m^2)	% of vessel wall surface
Inboard wall (2 m high)	Nov.84	23	10
Octant joint protections (8 poloidal belts)	July 85	12.9	6
Neutral beam protection at horizontal port (octant 5)	July 85	3.5	2
Bellows protections (32 poloidal belts)	Jan.87	62.7	28
Neutral beam protection at horizontal port (octant 1)	Jan.87	3.5	2

Table 6. Basic parameters of the JET limiters

Description	Period of operation	Material	Area (m^2)	Total heat load (MW)
4 discrete limiters	June 83 July 85	graphite	1.28	10
8 discrete limiters	Nov. 85 Dec. 86	graphite	2.56	20
Toroidal belt limiter	From April 87	graphite	18	40
		or beryllium	or 13.8	40

It is planned to install beryllium evaporators in the vessel by the beginning of 1987. The ISX-B experiment has demonstrated that evaporation is a necessary step for the getter action of beryllium to take place. In ISX-B, this was achieved by allowing the limiter to melt locally. In JET, it is planned to control this process and avoid limiter melting by means of 4 evaporators mounted on the outboard wall. They would be retracted during discharges, but could

otherwise be pushed inside the vessel to cover the Inconel walls, the graphite tiles, and the limiter tiles (whether graphite or beryllium) with a thin layer of beryllium. At a temperature of 1050°C, the evaporation rate is expected to be 0.15g of beryllium per minute, which corresponds to the deposition of 2 monolayers onto the internal surface of the vessel. In total, the evaporator heads could operate 300 hours and deposit on average a 10μ thick layer on the vessel wall, before having to be replaced. Even in case graphite tiles are used for the belt limiter, a beryllium layer on graphite may well be self-sustaining during discharges if the deposition rate is made to balance the erosion rate.. To achieve this, it may be necessary to feed the discharge with small beryllium pellets. In conclusion the use of beryllium evaporators offers a unique combination of attractive operation features.

- low Z material (Beryllium).
- identical material for the limiter and the walls. This would simplify problems related to erosion and redistribution of wall and limiter material.
- an oxygen getter.

A new interesting mode of operation for JET is a type of magnetic limiter operation with a separatrix defining X points inside the vacuum vessel at the top and bottom parts. This configuration may induce H. mode behaviour and therefore limit the degradation of confinement time with additional heating power. This configuration has already been established in JET at a plasma current of 2 MA [13]. Further experiments are planned in 1986 at current levels of 3 MA and with some additional heating. Minor changes in the configuration of the poloidal field circuit could be implemented early in 1987 in order to bring the current capability of this configuration in the range of 4 MA. If the configuration is to be used at full power, additional graphite or beryllium protection plates will be required at the top and bottom parts of the vessel. The expected heat flux can be inferred from experimental results obtained in June 1985 and has been seen to peak sharply at the points where the magnetic separatrix intersects the wall of the vessel. The peak heat flux there should be in the range of 450 W/cm^2 for a total input power to the plasma of 40 MW. This value is similar to that of the belt limiter and should allow a design based on adiabatic heating during the pulse and cool-down between pulses. Because of the limited space available between the X points and the wall, a design based on heat conduction through pressure contacts, rather than radiation cooling is being envisaged. Such new protections could be installed at the earliest by the middle of 1988.

Fuel exhaust is of course a key issue which will have to be addressed and may become crucial when higher densities can be achieved with additional heating and pellet injection

On JET, the density decay at the end of a discharge indicates that 2-5 x 10^{20} particles are pumped by the torus walls and other internal components. This phenomenon is not well understood but is observed in other tokamaks. If JET is to achieve the high densities required for near-ignition conditions, much higher pumping rates in the range of 5 x 10^{21} particles will be required to avoid the disruptive termination of discharges.

It is planned in the near future to assess more systematically the pumping efficiency of the walls. Of particular interest is the enhanced wall pumping which has been sometimes observed on JET during plasma discharges leaning against the inner graphite wall. Wall saturation effects are expected and are an important part of this study.

In the longer term, there is at present no design available for devices such as pumped limiters. Some very preliminary work has however started on this question. Small (120 mm in diameter) pump limiter probes have been installed in August 1985. These probes are too small to contribute to density control and in any case they are not connected to fast pumping lines. They can be moved radially towards the plasma edge, and will be used to measure the evolution of the neutral gas pressure built up behind the probe heads. Some probes have been fitted with palladium membranes behind the head so as to assess the possibility of transient particle pumping.

Transient pumping, should it prove of interest, could be associated with the belt limiter. As shown on figure 12, the cooling fins have been provided with re-entrant edges on either sides. The limiter tiles could therefore be reshaped to assume the function of scoop limiter tiles and deflect particles towards pumping plates placed along the vessel wall behind the limiter tiles.

Pumping plates may also be associated with the top and bottom protections for the magnetic limiter mode of operation.

Another possibility is the installation of pumped limiters, possibly moveable limiters, at some of the main horizontal ports. Because of the large size and conductance of these ports, fast pumping could be achieved there by getter panels inside and conventional pumps outside the vacuum vessel. No design effort has been devoted to this scheme so far.

Since JET started operation in June 1983 with Inconel walls, there has been an accelerating evolution towards the use of low Z materials, in accordance with the policy defined at the start of the project. The increasing use of graphite protection offers good prospects of eliminating high Z impurities. The use of beryllium also offers the exciting possibility of reducing low Z impurities.

Plans beyond 1987 are less defined and new modes of operation such as the magnetic limiters, or new systems such as fuel exhaust, have still to be developed. Because of the size of JET, there is a long delay between the conceptual phase and the start of experiments. The development of these new systems will therefore have an impact on the long term experimental programme of JET but may also be the key to reach the goal of

near ignition conditions.

References

[1] The JET Project. Reports of the Commission of the European Communities. EUR 5516 e (1976), EUR 5781 c (1977), EUR 6831 en (1978).

[2] Rebut P H, Green B. Status and programme of JET. Plasma Physics and controlled fusion, 26, 1A, 1 (1984).

[3] Huguet M, Assembly, commissioning and first operation of JET, 10th Symposium on fusion engineering. Philadelphia, (1983).

[4] Rebut P H et al. First experiments in JET, 10th Int. Conf. on plasma physics and controlled nuclear fusion. IAEA, ondon (1984).

[5] Bickerton R, et al. Latest ohmic heating results from JET. 12th Conf. of the E.P.S. Plasma Physics, Budapest (1985).

[6] Rebut P H, Dietz K J. The first wall in JET. Status and perspectives. 12th Symp. on fusion Tech. Julich (1982).

[7] Deschamps P, Dietz K J, Yvars M, Fabrication and characterization of graphite 5890 PT, 13th Symp. on fusion Tech, Varese, (1984).

[8] Behringer K H, Impurity studies and transport code modelling. 10th Int. Cont. on plasma physics and controlled nuclear fusion. IAEA, London (1984).

[9] Ehrenberg J, et al. Erosion and redeposition of wall and limiter material in JET, 12th Conf of the EPS. Plasma Physics, Budapest (1985).

[10] Dietz K J et al. Start up and initial operation of JET. Journal Nucl. Materials 128+129 (1984) 10.

[11] Dietz K J, Sonnenberg K, Deksnis E, Shaw R. Wall protection in JET. International School of Fusion Reactor Technology. (1985). Plenum press in publication.

[12] Noll P et al. Stabilisation of vertical position and control of plasma shape in JET. 11th Symp. on fusion Engineering. Austin (1985).

[13] Tanga A, et al. The formation of a magnetic separatrix in JET. 12th Conf. of the EPS. Plasma Physics. Budapest (1985).

[14] Massmann P, (JET). Private communication.

[15] Bohdansky J, Moller W et al. Report on hydrogen retention and sputtering measurements of beryllium. JET study contract JD3/9005 with IPP, Garching.

[16] Edmonds P H et al. Technical aspects of the joint JET-ISX-B beryllium limiter experiment, J. Vac. Sci. Technol A3 (3) May/June 85.

[17] Smith M F, Watson R D. Thermomechanical testing of beryllium for limiters in ISX-B and JET, 6th Topical Meeting on Tech. of fusion energy. San Francisco, 1985. Work done under JET study contract JD3/0771.

[18] Jones P D F, Maissonier D, Raimondi T. Design and operation of the articulated boom for JET. 11th Symp. on fusion Engineering. Austin (1985).

STABILIZATION OF VERTICAL POSITION AND CONTROL OF PLASMA SHAPE IN JET

P Noll, R Aigle, M L Browne, D Corbyn, T Eriksson, C Froger, M Huguet, H Niedermeyer*, P H Rebut, A Santagiustina, L Sonnerup, J R Watkins, J Wesson

JET Joint Undertaking
Abingdon, Oxfordshire, England
*EURATOM-IPP Association, IPP,
Garching, F.R.G.

Abstract

The vertical position of the JET plasma is unstable without feedback stabilization. The growth rate can reach 150 s^{-1} for strongly elongated plasmas with elongation ratio b/a ≈ 1.8. A failure of the stabilization at large plasma current (~5 MA) can cause damage to the vessel due to large vertical forces unless the plasma elongation ratio is limited or additional vessel supports are provided. The paper outlines the shape control system and discusses the vertical instability and its stabilization.

Introduction

The JET experiment aims at achieving plasmas with parameters approaching those needed in a thermo nuclear reactor. The vessel has a small aspect ratio and a D-shaped elongated cross section to accommodate a plasma with high current (≲5 MA) at a moderate level of toroidal magnetic field (≲3.4 T). The elongated plasma shape is produced by an externally applied quadrupole magnetic field. This field and the presence of the iron magnetic circuit render the vertical position of the plasma unstable. A stabilizing circuit has therefore been built which was designed from the outset to stabilize plasmas with an elongation ratio b/a=1.6, with adequate safety margin (b/a) max = 1.9.

In the course of experiments performed in May 1984 the stabilization limit was, however, already reached in the pulse no 1947 at an elongation ratio b/a = 1.68 and the plasma became vertically unstable. The stabilization circuit was subsequently investigated and adjusted to perform as intended, so that presently plasmas with elongation ratio exceeding 1.8 can be stabilized.

The consequences of a vertical instability are of great concern. In the pulse no 1947 the current was 2.65 MA and the instability gave an estimated vertical force of ~ 250 tons at the vessel and caused large deflections and stresses. Forces of order 800 tons are expected in the event of a vertical instability at extended performance, with 5MA current and elongation ratio b/a ≈ 1.6, and these would cause a permanent deformation of the vessel.

The following courses of action have therefore been considered or started:

- automatic and operational safeguards against exceeding the stabilization limits. This concerns mainly the shaping circuit which produces the destabilizing quadrupole field.
- improvement of the reliability and, if possible, of the stabilization range of the vertical stabilization circuit.
- provision of additional vessel supports, to reduce stresses of the vessel in the unlikely event that the first two actions fail.

The shaping and stabilization circuits of JET are outlined and discussed in the following sections.

The Poloidal Magnetic Field

The poloidal magnetic field is governed by the currents in four sets of coils, the transformer or magnetising coil (M), the vertical field coil (V), the shaping coil (S) and the radial field coil (R). Each coil consists of series connected subsections of four coils which are shown as P1 to P4 in the fig. 1.

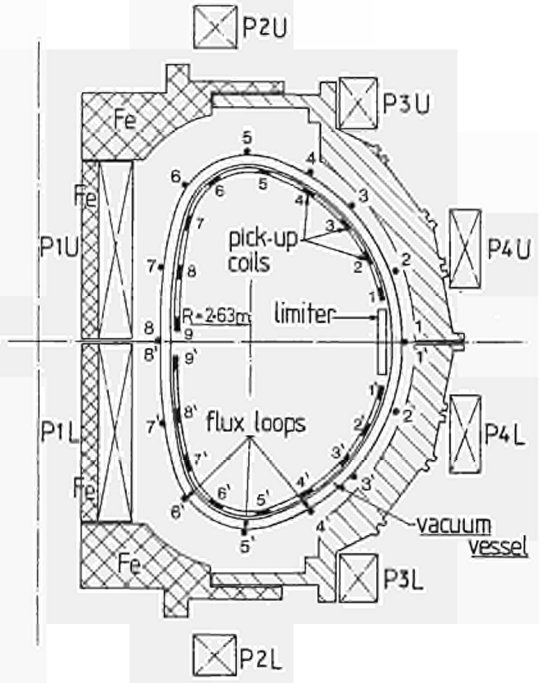

Fig. 1 Schematic section of the JET apparatus

Table 1 presents specific magnetic fields, field gradients and other parameters of

Table 1 specific magnetic fields $b_{zi} = B_{zi}/ I_i$ and field gradients $\partial b_z/\partial R$ at radius R = 3 m for typical configurations of the magnetising, vertical, shaping and radial field coils. The iron image current field caused by the plasma current is given for circular shape and parabolic current profile. The iron core is saturated.

Parameter / Function	PF coil turns	b_z or b_R (10^{-6} T/A)	$\partial b_z/\partial R$ (10^{-6} T/m/A)	Inductance (mH)	Resistance (mΩ)	Comments
M	P1M 568 P3M 4	- 0.10	+0.19	210	29	signs apply after current reversal
V	P4 78 (max 122)	+16	-0.86	117	17	
S	P2S -40 P3S +20	-1.14	+1.10	15	6	current in P2S opposite P3S, P4
R	P2R 32 P3R 40	±5.5	-	43	24	
Plasma	- -	-0.028	+0.012	0.006		minor radius a = 1.25 m

typical coil configurations as used in 1985. In the course of experiments the M, V, R-coil configurations remain unchanged while that of the S-coil is altered occasionally by choosing different turn numbers and current directions in the P2S and P3S coils.

The M-coil is connected through the ohmic heating network to the JET Poloidal Flywheel Generator Converter. It includes few turns of the coil P3M to reduce the stray field in the plasma region. The maximum current is ± 40 kA.

The V-coil is connected to a 50 Hz 2 kV/25 kA 2 quadrant thyristor power supply which is configured as a voltage amplifier with gain 300 V/V. The V-coil produces an almost homogeneous vertical field as main part of the required equilibrium vertical field.

The S-coil is connected to the same type of power amplifier as used for the V-coil, but this amplifier is configured as current amplifier with gain 4 kA/V. The purpose of the S-coil is to provide a quadrupole field for the control of the elongation ratio b/a of the plasma cross section. The contribution to the vertical field can be made relatively small.

The R-coil produces the radial field for the stabilization of the vertical plasma position. The upper and lower parts of the coils P2R and P3R are connected in series and in opposite sense. The R-coil is connected to a 50 Hz 4 kV/2 kA 4 quadrant thyristor power supply which is configured as voltage amplifier with gain 600 V/V.

Plasma Shape Control

The shape of the plasma cross section is controlled by two feedback systems which act on the vertical field (V) and the shaping field (S) coils, respectively.

Radial position control

An earlier version of this system is described in [1]. In 1985 the previous galvanic connection of the V-coil to the ohmic heating circuit was removed and the control system was slightly modified.

For radial position control the poloidal flux difference $\delta\Psi_R = \Psi(R_L) - \Psi(R_i)$ is measured between the limiter radius R_L and the desired inboard radius R_i of the limiter magnetic surface. $\delta\Psi_R$ is obtained from a linear combination of integrated signals from saddle loops mounted on an vessel octant and from poloidal field pick up coils mounted inside of the same octant, as shown in fig. 1. Two saddle loops are used which span from positions 2 to 8 and 2' to 8', resp., while the pick up coils 1, 1', 9 and 9' provide the flux extrapolation to the interior. Field gradients due to the field curvature are ignored. The inner reference radius R_i can be varied as function of time by means of a preprogrammed gain function $D\phi R$ for the pick up coil signals 9 and 9'. The flux difference signal is transmitted through a proportional/derivative controller to the vertical field amplifier. The flux error $\delta\Psi_R$ becomes zero when the inboard plasma boundary coincides with the preprogrammed radius R_i.

The feedback control is supported by a pre-programmed part of the amplifier control voltage and by the addition of a part which is proportional to the voltage at the transformer coil. These contributions can be chosen to provide a bias vertical field and to reduce control errors due to induced voltages in the V-coil during the plasma current rise. Typical control errors are $\delta R_i \approx 10^{-2}$ m during the "slow rise" and "flat top" phases. The response time upon a small step perturbation of the control voltage is ≈30 ms.

The outlined method of controlling the position of magnetic surfaces has been previously applied in the ASDEX Tokamak [2] and in other Tokamak machines.

Control of plasma elongation

In the simplest mode of operation the current in the shaping coil (S) is controlled in proportion to the measured plasma current, with a factor of proportionality which can be regulated as

function of time by a preprogrammed gain function GOH. The resulting elongation ratio b/a of the plasma cross section depends on the radial diameter 2a and on the plasma current profile. The example shown in fig. 2 illustrates the effect of an increased shaping current. The flux contours are derived from measurements with flux loops and pick up coils indicated in fig. 1 and 2.

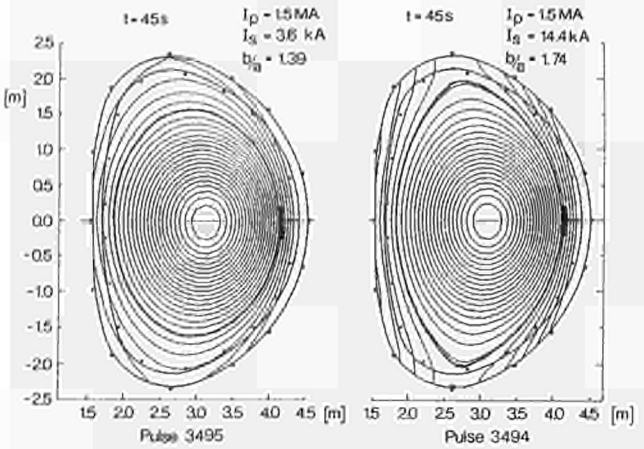

Fig. 2 Plasma shape for two different shaping currents

A potential danger of this control method arises for large plasmas in the event that the current profile becomes flatter than expected. The plasma becomes then more elongated leading to contact with the vessel at top and bottom and the limits for vertical stabilization can be exceeded.

In the feedback mode of operation the flux difference is measured between the limiter and symmetric reference points in the vicinity of flux loop positions 4 and 4' shown in fig. 1. The distance of these top/bottom reference points from the wall can be varied during pulse by a preprogrammed gain function DΦH in much the same way as the inboard reference radius R_1 is varied by the function DΦR. The flux difference signal is transmitted through a controller to the shaping field amplifier to produce a shaping current proportional to the flux difference. The controller gain is fixed but the output signal amplitude can be limited or suppressed by a preprogrammed function of time. When the flux error is zero then the plasma boundary passes through the desired top/bottom reference positions. These positions are normally chosen in such a way that the outboard plasma boundary matches the shape of antennae for high frequency heating. The vertical plasma diameter can still vary to some extent with changing plasma parameters because the reference points for shape control are usually further outwards than the plasma centre.

So far, no integral control was used. The resulting control error of a desired increment of the plasma/wall distance at positions 4,4' (fig. 1) is about 10%. The measured response time upon a small step of the desired distance is about 20 ms, in reasonable agreement with simulation results

Interactions of Control Systems

The feedback control systems for radial position, plasma elongation and plasma current are magnetically coupled. The interactions with the current feedback system are not critical because the current control system has a slow response of about 0.5 s. The coupling between radial position and elongation control has caused large amplitude oscillations of both systems in an experiment where the usual shaping field configuration given in table 1 was replaced by the coil P3 (fig. 1) which has a 0.4 times smaller field index. The experiment was continued using the simpler pre-programmed control mode for the shaping field. Electronic decoupling would be required for feedback control of the plasma elongation in cases where the shaping coil has a small field index.

Stabilization of the Vertical Plasma Position

Feedback Circuit

The radial flux $\delta\Psi$ is measured between two symmetric positions at distances $\pm$ h from the mid plane by a combination of integrated signals from saddle loops spanning from positions 4 to 4' and 6 to 6' (fig. 1) and from pick up coils at interior positions 4, 4', 6 and 6'. The separation 2h of the equivalent differential flux loop is about 3.2m if field gradients are ignored. To lowest order the flux Ψ corresponds to a vertical plasma displacement

$$\delta Z_p = h\delta\Psi/(2\mu_o I_p R) \qquad (1)$$

from the mid plane, where I_p = plasma current, R = 3m. The measurement sensitivity $\delta\Psi/\delta Z_p$ is however substantially smaller when the strong non uniformity of the poloidal field along the poloidal circumference of elongated plasmas is taken into account.

For feedback stabilization a flux error signal proportional to $\delta\Psi$ is transmitted through a proportional/derivative controller to the radial field amplifier in order to apply a corrective voltage at the radial field coil. The use of derivative control is equivalent to a direct transmission of the effective differential loop voltage $\delta\dot{\Psi}$. It corresponds to velocity feedback and is essential for the stabilization. The proportional control is only needed to define the position.

Simplified System Analysis

Several studies have been performed for the design of the stabilization circuit. We outline a simplified analysis which assumes a rigid plasma displacement and ignores eddy currents in the mechanical shell. The stabilizing eddy currents in the vessel are assumed axisymmetric and toroidal.

The circuit equations for the R-coil and vessel currents are

$$\begin{aligned} A_{rr}\dot{I}_r + A_{rv}\dot{I}_v + A'_{rp}I_p\dot{Z}_p &= V_r \\ A_{rv}\dot{I}_r + A_{vv}\dot{I}_v + A'_{vp}I_p\dot{Z}_p &= -I_vR_v \end{aligned} \qquad (2)$$

$\pm I_r$ = Ampere turns in the upper/lower half of the R-coil

± I_v = differential vessel current in the upper/lower half
Z_p = plasma displacement
V_r = applied voltage per turn at the R-coil
A_{rr} = 14.6 μH = R-coil inductance, one half only, reduced for single turn in each half
A_{vv} = 4.2 μH = vessel inductance, one half only, for current I_v
A_{rv} = 4.2 μH = mutual normalised inductance, one half
$A'_{rp} = A'_{vp}$ = 1.4 μH/m = flux change in one half of the R-coil and the vessel for unit displacement parameter $I_p Z_p$ = 1 MA.m
R_v = 1 mΩ = vessel resistance (one half) for current I_v

The plasma force balance can be written in the form

$$A'_{rp} I_r + A'_{vp} I_v + A''_{pp} I_p Z_p = 0 \qquad (3)$$

where

A''_{pp} = normalised plasma self force due to the quadrupole component of the equilibrium field and due to iron image current fields produced by the displacement

The values for A_{rr}, A_{rv}, A_{vv}, A'_{rp}, A'_{vp} are derived from previous field computations. They are independent or only weakly dependent of the plasma shape and current profile, in contrast to the plasma self force coefficient. For a full size D shape plasma with parabolic current profile a value $A''_{pp} \approx 0.23$ μH/m^2 was computed.

For the case that the R-coil voltage is kept zero the equations 2, 3 yield an exponential growth of the displacement with an instability growth rate γ given by

$$\gamma T_v = \frac{A''_{pp} - (A'_{rp})^2/A_{rr}}{(A'_{vp})^2/A_{vv} - A''_{pp}} \qquad (4)$$

where $T_v = (A_{vv} - A_{rv}^2/A_{rr})/R_v \approx 3$ ms
= characteristic time for the decay differential vessel currents or the penetration of radial flux.

One obtains $\gamma \approx 135\ s^{-1}$ for a full size D shaped plasma. When $A''_{pp} < (A'_{rp})^2/A_{rr} \approx 0.13$ μH/m^2 the induced currents in the R-coil are sufficient to stabilize the plasma. In JET this is the case when the plasma elongation ratio b/a is < 1.2, with large diameter 2a ≈ 2.4 m. When $A''_{pp} > (A'_{vp})^2/A_{vv} \approx 0.47$ μH/m^2 the plasma is unstable on a MHD timescale and stabilization becomes impossible.

The dependence of A''_{pp} on the plasma shape can be anticipated from an approximate expression which is applicable for plasmas with flat current profile and small elongation ratio b/a of the semi axis a, b:

$$A''_{pp} \approx \frac{\mu_0 R}{4\bar{a}^2}\left(\frac{b}{a} - 1\right) + \frac{\mu_0 R}{2a_m^2} - \frac{\mu_0}{4R}\left(\frac{3}{4} + \ln\frac{8R}{\bar{a}} - \frac{17}{16}\right) \qquad (5)$$

where $\bar{a} = (a + b)/2$ and $a_m \approx 3$ to 4 m = average effective distance of the magnetic circuit from the plasma centre. A''_{pp} and γ increase with increasing elongation ratio and decreasing size $\bar{a}$.

When feedback stabilization is applied using a PD-controller the system behaviour can be approximately described by the closed loop transfer function

$$V_1 \approx -V_0 \cdot \frac{1 + sT_D}{1 + sT_D + s\frac{T_D}{G_0}(sT_v - \gamma T_v)(1 + sT_A)(1 + sT_u)} \qquad (6)$$

where s = Laplace parameter

V_0 = voltage perturbation at the input of the radial field amplifier
V_1 = feedback or error voltage
$V_0 + V_1$ = control voltage
T_D = 80 ms = derivative time constant of controller
$T_A \approx 2$ ms = amplifier response time
$T_u \approx 1.5$ ms = combined delay time due to filters in the feedback electronics and due to second order time lags in the amplifier
G_0 = adjustable low frequency open loop gain without plasma, i.e. for $\gamma T_v = -1$

From (6) one finds that the loop gain G_0 must be chosen between the limits

$$\gamma T_v < G_0 < \left(\frac{T_v}{T_A} + \frac{T_v}{T_u}\right)(1 - \gamma T_A)(1 - \gamma T_u) \qquad (7)$$

in order to stablize the plasma position, for example $0.45 < G_0 < 1.9$ for $\gamma = 0.15\ s^{-1}$. Normally the loop gain is chosen $G_0 \approx 1$.

In practice, the stabilization range is narrower than estimated from (7), with the parameters listed above. In the particular case of the pulse no 1947, the amplifier response time was $T_A \approx 4$ ms and the plasma became instable with growth rate $\gamma \approx 0.13 s^{-1}$. The critical loop gain ($G_{crit} \approx 1.1$ from (7)) was obviously smaller than the chosen one. Since then the amplifier response was improved so that presently $T_A \approx 2$ ms.

Experimental Tests

The stabilization range was tested at different plasma parameters by injection of a small step perturbation V_0 at the amplifier input and by observation of the feedback voltage V_1. The fig. 3 shows the step response with a strongly elongated plasma with parameters $I_p = 1.5$ MA, $B_T = 2.6$ T, a = 1.18 m, b/a = 1.67, $\gamma \approx 150\ s^{-1}$ (from instability tests). At low loop gain a large amplitude low frequency oscillation is excited, at higher gain and in the vicinity of the upper stabilization limit the excited eigenmode has a higher frequency and a smaller relative amplitude. A rough extrapolation of the damping ratio to zero gives an estimated stabilization range $0.45 < G < 1.4$ while the equation (7) predicts $0.45 < G < 1.9$. The best value of G_0 appears to be ≈ 0.8, and this has been chosen in more recent experiments.

Experiments aimed at producing highly elongated plasmas with a separatrix gave further information on the stabilization

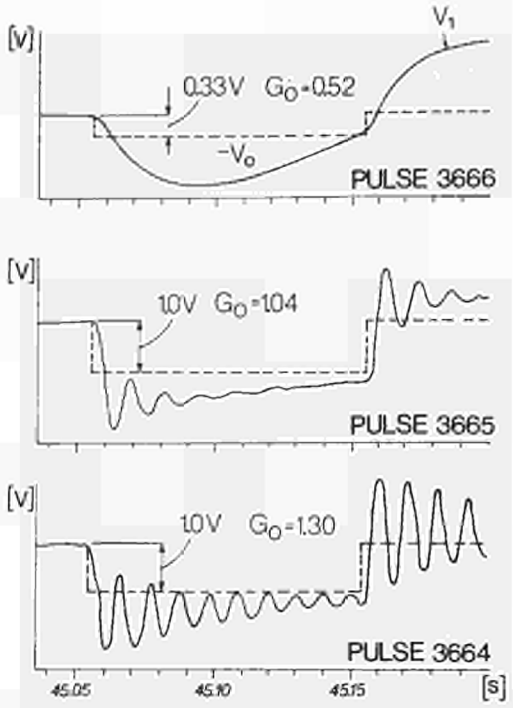

Fig. 3 Step response of the feedback voltage V_1 for different values of the open loop gain G_o. Plasma elongation ratio b/a = 1.67

limits: at G_o = 1.04 the plasma became vertically unstable with a growing eigenmode f = 80 Hz when the elongation ratio reached a value b/a = 1.86. At G_o = 0.78 the plasma became unstable at a somewhat larger ratio b/a = 1.92, starting with a growing eigenmode of low frequency f = 12 Hz. This indicates that a slight improvement was achieved by the reduction of the loop gain.

The vertical instability

Large vertical forces at the vessel can result from a malfunction of the stabilization. The vertical instability was therefore examined at different plasma parameters at low current level in order to establish safe operational limits. For this purpose the feedback stabilization was disabled during the current flat top at a time t = 45.05s (5.05s after plasma start up).

The fig. 4 shows, as example, the displacement of the effective current centre and the plasma current in a pulse with large plasma size and elongation. Initially the current centre moves downwards with approximately exponential growth while the radial position and the current remain unchanged. This is followed by a rapid current quench and an inward plasma displacement.

The vertical force on the vessel F_v and a decomposition of vertical forces acting on the plasma are shown in fig. 5, for the pulse exemplified in fig. 4.

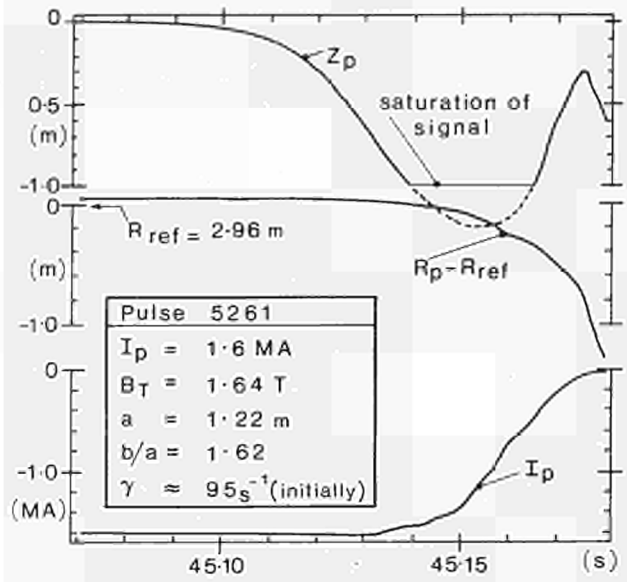

Fig. 4 Vertical and radial displacement of the current centre when the stabilization is disabled at t = 45.05s

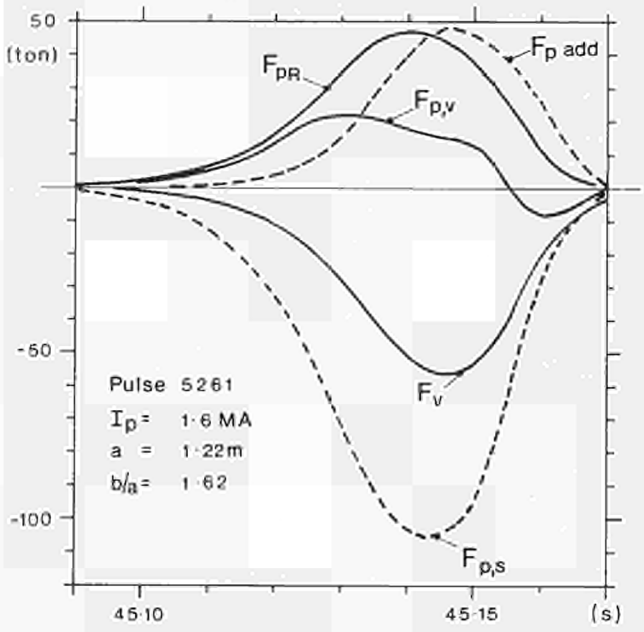

Fig. 5 Vertical forces on the vessel F_v and the plasma F_{pi} during a vertical instability. F_{ps} = self force, F_{pr} = force from R-coil, F_{pv} = force from vessel differential currents, F_p add = force needed for the balance $\sum F_{pi} = 0$.

The forces are evaluated from measurements using a simplified model in which stabilizing eddy currents in the mechanical shell and saddle shaped currents in the rigid sectors of the vessel are ignored.

The plasma force balance can be written

$$F_p = F_{ps} + F_{pr} + F_{pv} + F_{p\,add} = 0, \qquad (8)$$

where $F_{ps}=2A''_{pp}I_p^2Z_p$ = destabilizing self force of the plasma

$F_{pr}=2A'_{rp}I_pI_r$ = stabilizing force from R-coil current I_r

$F_{pv}=2A'_{vp}I_pI_v$ = stabilizing force from differential vessel current I_v

$F_{p\,add}$ = additional force, not accounted for by I_r and I_v

A''_{pp} is evaluated from (4), using the measured growth rate γ, and also cross checked against computed values at similar parameters. The current I_v is deduced from the loop voltages at poloidal positions 3,5,6,3',5',6' (fig. 1) using the known vessel toroidal resistance per unit poloidal length. It is found in all experimental tests that an additional force $F_{p\,add}$ must be postulated during the later stages of the instability when the displacement exceeds typically 0.5 m. From theoretical studies it is concluded that the magnitude of $F_{p\,add}$ is substantially larger than that of stabilizing forces arising from saddle shaped eddy current in the mechanical shell and the rigid vessel sectors. A possible mechanism for the additional force is represented by poloidal currents which can arise from the plasma motion across the toroidal field when the plasma comes in contact with the vessel walls at top or bottom. These currents could flow across the plasma and return through the vessel, but no measurement is presently available to confirm their existence.

The vessel force F_v shown in fig. 5 is derived from the relation

$$F_v=-\pi R_o I_v \tilde{B}_r - F_{p\,add} \approx F_{ps}+F_{pr}+\pi\bar{a}_v A''_{pp} I_p I_v \quad (9)$$

which is applicable as long as the contribution from the net toroidal vessel current set up by the current quench can be neglected. In (9), $\tilde{B}_r$ is the first Fourier harmonic of the radial field at the vessel and $\bar{a}_v \approx 1.75$ m is the average minor radius of the vessel. The last term of (9) is found to be significantly smaller than the first and second terms, so that an upper limit of the vessel force is represented by the plasma self force, reduced by the stabilizing force of the R-coil current.

A theoretical estimate of the vessel force can be derived from the equations (2,3,9) by setting $V_r = 0$ (feed-back disabled). In the case that poloidal stabilizing currents are ignored one obtains, before the current quench,

$$F_v=K.I_p^2Z_p(t).\gamma T_v.(1+\gamma T_v)^{-2} \quad (10)$$

where $K = 2(A'_{vp})^2.(1-A_{RV}^2/A_{vv}A_{rr})/A_{vv}$.
This suggests that the maximum vessel force should depend mainly on the normalised growth rate γT_v and on the displacement reached before the current decrease.

Experimental results obtained for different plasma diameters and elongation ratios are shown in fig. 6. The growth

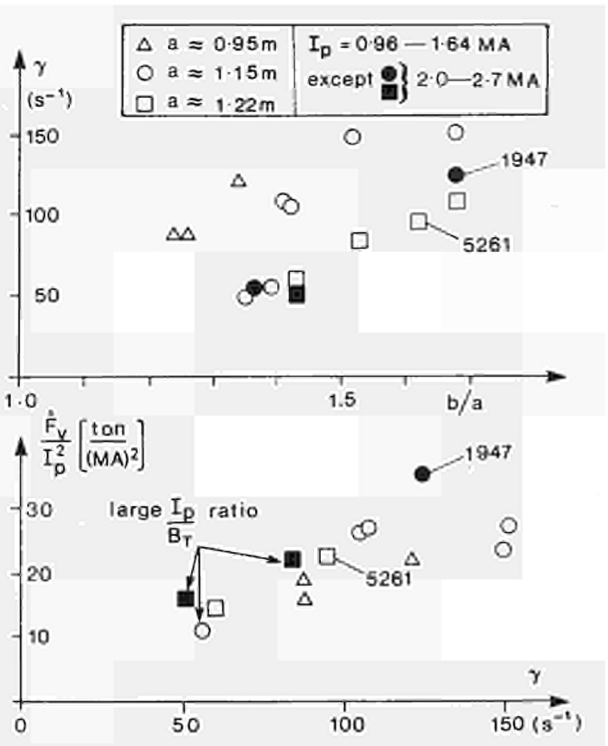

Fig. 6 Growth rate and normalised peak vertical force at the vessel for different plasma parameters

rate γ (fig. 6) increases with increasing elongation ratio b/a and with decreasing radial plasma diameter 2a, as expected from (4) and (5). The peak vertical force at the vessel is of particular interest for JET. In fig. 6 this force is normalised to the square of the plasma current and plotted as function of the growth rate. As suggested from (10) the peak force increases with increasing growth rate and there is no indication of an explicit dependence on the plasma diameter.

Some tests were performed at larger current/toroidal field ratio in order to simulate conditions at extended performance. It had been expected that the current quench would start earlier and that the vertical plasma displacement and the peak vessel force would be smaller than in the majority of test pulses which were performed with a small current/field ratio. This expectation was not supported by the experiments, as indicated in fig. 6. For extrapolation to the potentially dangerous conditions at high current a crude scaling of the peak vessel force

$$\hat{F}_v \propto I_p^2\gamma \propto I_p^2(b/a-1.2) \quad (11)$$

was then chosen on the basis of the tests. This scaling appears to be reasonable for conditions with large plasma diameter 2a = 2.4 to 2.5m as needed to reach high currents.

Vessel displacements and stresses

Originally, the JET vessel was suspended with spring supports at the 8 large horizontal ports and at the octant joints. These supports were not designed to cope with large vertical forces as they arise in a large current vertical instability. In the pulse

1947 the vessel was exposed to a peak vertical force of about 250 tons which caused a rotation of the vessel sectors around an apparent pivot at R = 6.5m. The corresponding vertical deflection of the vessel had an estimated amplitude of - 10mm and the linear range of the spring supports was exceeded.

Firm vertical supports were then added at the ends of the horizontal ports and the radial motion of the 16 large vertical ports at top and bottom was restrained by shock absorbers in order to reduce the vessel displacement. A direct vertical support at the vertical ports could not be applied at this stage. The vertical and radial displacements of the large vertical ports were reduced by more than 50% by this measure. A comparison of tests at different conditions indicates that the ratio of vertical vessel deflection/peak vertical force is independent of the instability growth rate within the error of limits. The average value of this ratio is about 0.018 mm/ton.

An example of deflections measured at one octant is shown in fig. 7. The plasma

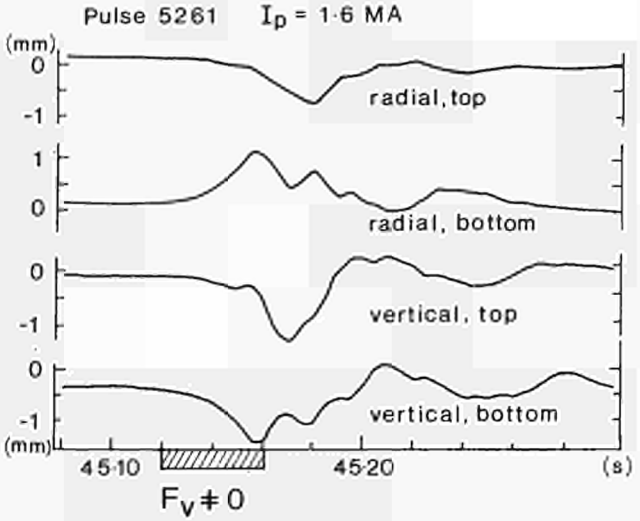

Fig. 7 Radial and vertical displacements of the large top and bottom ports of octant 5 resulting from a vertical instability

moves downwards (fig. 4), the vertical force acts therefore mainly on the lower half of the vessel. This causes a top/bottom asymmetry of the displacements due to bending of the vessel. The same signals obtained at other octants are somewhat different. This may be due to differences of the mechanical properties of supports, such as pre-stresses, and due to different mass loads at the large ports. The vertical force might be non-axisymmetric as well, but there is no evidence from magnetic measurements at different octants. It is therefore reasonable to assume that the reaction forces and stresses of the vessel are not very different among octants.

The deflections and stresses of the vacuum vessel have been studied with a simplified dynamic model and a finite element model [3]. As test case to simulate approximately the instability of pulse No. 1947, a vertical force F = 300 tons was assumed, with sinusoidal time dependence for one half wave of 30 ms duration. Two limiting cases were considered concerning the supports and the actual evolution of deflections and stresses was estimated by interpolation. Results are

- the deflections of ports are in rough agreement with observations, when an appropriate matching of forces is applied
- deflection amplitudes are reduced by about a factor ½ when boundary conditions according to the additional supports are applied
- as expected, the additional supports produce higher local stresses. In the limiting case that the radial motion of the vertical ports is fully restrained a bending stress ~240MPa is found at the narrow end of the vertical ports, the point of highest stress. With shock absorbers the expected stress is reduced.

As a result of the experimental tests and the stress calculations a preliminary limitation of the JET operation has been adopted to avoid overstresses in the event of a vertical instability:

$$I_p^2(b/a-1.2) \leq 5(MA)^2. \qquad (12)$$

This limit corresponds to a vertical force of approximaqtely 350 tons, for plasmas with large radial diameter 2a ≈ 2.4m. In particular, the elongation ratio of 5 MA plasmas must be restricted to b/a ≤ 1.4.

Conclusions and further developments

The dynamics of the vertical instability in JET is not fully understood, there is some uncertainty about the existence of stabilizing poloidal currents in the plasma/vessel system. The magnitude of the vertical force on the vessel, estimated on the basis of experimental tests, is however not affected significantly by this uncertainty.

A preliminary restriction of the JET operation (eq.12) had to be imposed to safeguard the vessel against overstresses in the event of a stabilization failure. Further stress calculations and also some additional experimental tests are foreseen to assess if the operation limit (12) can be relaxed with the present vessel supports.

The requirements for stabilization of elongated plasmas are very stringent : the response time of the feedback circuit including the power amplifier must be smaller than the transverse field penetration time (T_V=3ms) through the vessel. In experiments where the stabilizing coil can be placed directly on the vessel the plasma may be stabilized passively (in the case that $A'^{\frac{1}{2}}_{rp}/A_{rr}$ can be made > A''_{pp}, according to eq.4) on a timescale of the coil time constant. The required response time is then far less critical and the stabilization range can be increased. This concept of

close fitting coils could not be applied in JET which is designed in a modular fashion.

For the next operation period attempts will be made to extend the stabilization range by reducing electronics noise levels which then would permit the reduction of filtering and second order delays (T_u in eq.7). As protection against exceeding the stabilzation range inadvertently the shape feedback control will be supplemented by an automatic limitation of the ratio shaping coil current/plasma current by a preprogrammable function of time.

Further developments comprise:

- Design of additional vertical supports of the vessel for operation at extended performance where vertical forces of order 800 tons are expected in case of a stabilization failure.

- A dual stabilization system aimed at reducing the probability of complete loss of stabilization. This system consists of two separate branches for position measurement, feedback electronics and power amplifiers, connected in series to the stabilizing coil. The functioning of both branches is continuously monitored and protective switching actions are initiated in the case of a failure in one branch. It is intended to investigate and test this scheme during the 1986 operation.

References

[1] P. Noll, M.L. Browne, M. Huart, I. Piacentini, A. Santagiustina, J.R. Watkins, "The JET plasma position and current control system", Proceedings of the 13th Symposium on Fusion Technology, Varese, Italy, 1984, pp. 503-509.

[2] F. Schneider, "Novel method of determining the plasma position and its application to the ASDEX feedback system". Proceedings of the 10th Symposium on Fusion Technology, Padova, Italy 1978, pp. 1013-1018.

[3] L. Sonnerup, "Mechanical design assessment of structural components and auxiliaries of the Joint European Torus", presented at the 8th International Conference on Structural Mechanics in Reactor Technology, Brussels, August 1985. To be published in Nuclear Engineering and Design/Fusion (April 1986).

ENGINEERING DESIGN AND PRELIMINARY PERFORMANCE OF THE JET ICRF SYSTEM

A. Kaye, R. Anderson, J. Arbez, G. Bosia, B. Beaumont*, M. Bureš, J. Jacquinot,
P. Lallia, J. Plancoulaine, F. Sand, M. Schmid, T. Wade, C. Walker
JET Joint Undertaking, Abingdon, Oxon, OX14 3EA, UK
*Attached from Association Euratom-CEA, Fontenay-aux-Roses, France

The JET programme requires the provision of 16 MW of RF heating in the ion cyclotron reign of frequencies. Two prototype systems are now operational and have coupled 4 MW into the plasma for 2 second pulses with localised heating in the plasma centre and with no change in relative impurity levels. Eight cooled antennae and 32 MW of generator capacity will be operational by 1988. The design and manufacture of these systems are described together with a summary of operating results to date.

Introduction

The provision of 15 MW of RF heating was included in the JET programme at an advanced stage in the project following studies carried out in conjunction with EURATOM-CEA Association Fontenay-aux-Roses [1,2]. These investigations concluded that powers large in comparison with the ohmic power (typically 5 MW) could be provided in the ion cyclotron range using established technology for the RF generators and transmission lines and exploiting rapid advances in the design of the launching structure. The studies identified several options for mounting the antennae in the existing vacuum vessel and for providing the necessary access for the transmission lines. Detailed design began in 1982 and two prototype antennae with 6 MW of generator capacity became operational on the torus in early 1985. The full system will be operational in 1988.

Ion cyclotron heating at MW power levels has been exploited on a number of tokamaks [3-7]. These applications followed from breakthroughs in the understanding of ICRF heating mechanisms in the 1970's: development of second harmonic resonance absorption [8], the identification of the role of minority species and recognition of the importance of mode conversion [9-12].

A number of technological problems arose in the design of the launching structure, which must be mounted close to the plasma boundary. In order to maintain the high RF voltages on the antenna, it was necessary to provide an electrostatic screen between the antenna conductor and the plasma, whilst maintaining good RF coupling. Dielectric (ceramic) screens were only partially successful due to high thermal stresses. Subsequently, the all-metal slotted screen was developed [13-15] and became widely adopted. This screen also suppressed excitation of the longitudinally polarised slow magnetosonic surface wave which is thought to lead to production of impurities. Thick screens of sufficient section to accommodate water cooling channels have been shown to give little increase in RF losses or loss of coupling [16]. The technology of coating screen elements with high conductivity metal to reduce losses, followed by a protective coating of titanium carbide has been successfully employed [17]. Open screens which do not limit the line-of-sight are being investigated elsewhere. These screens offer much reduced RF losses and simplification of the mechanical structure.

High levels of metallic impurities were associated with early antenna designs apparently originating from the sides of the antenna and other components on the same magnetic surfaces, rather than the screen. The use of graphite limiters and side protection on the antennae, and carbonisation of the torus have both been effective [6,18] in reducing impurity; the residual influx appears to be partly due to the screen [19]. In addition, the slow wave is driven primarily by the low k component of the excitation. Suppression of this component by appropriate toroidal disposition of the antennae conductors has also been shown to reduce the impurity influx [7]. Impurity production appears to be less severe on large machines when the absorption is well localised near the core of the plasma.

Recent designs of coaxial vacuum windows utilising conical or cylindrical ceramics [20-22] have greatly improved power handling capability and now exceed the requirements of existing ICRF systems.

The development of high power thermionic valves continues. Several suppliers offer 1.5 MW units and a number of higher output units are being developed. Increasingly sophisticated systems for matching the generators to the antennae are being developed [23] to enable the full potential of multiple antenna installations to be exploited in such areas as current drive [24] programmed power deposition profiles and sawtooth stabilisation.

General Description and Present Status of the JET ICRF System

The JET ICRF system is required to operate using various minority species or harmonic heating scenarios [2] over a 25-55 MHz range of frequency. This large bandwith, together with reliance on existing technology for critical components led to the choice of an endstage capable of accepting various tubes, initially the EIMAC 8973, 1.5 MW tetrode. The design studies showed that this power could be transmitted with the anticipated standing wave ratio by a coaxial line through existing 150 mm diameter tubes, mounted in pairs at 16 symmetrical locations around the torus and originally provided to cool the limiters. Thus, a modular system evolved, each module comprising an antenna typically 0.8 x 2 x 0.2 m incorporating two single-turn current loops each connected by a long coaxial transmission line to a 1.5 MW RF amplifier. The two amplifiers for each antenna are mounted in a single modular generator unit. The specification required half of the generator power to be coupled to the plasma as high grade heating. Other major design decisions taken at an early stage include:

- the use of rigid, 30 Ω, ceramic insulated coaxial lines.
- the use of a single stub tuner at the generator or close to the antenna.
- the use of integral antenna/limiter launching structures.

These features are described in detail later.

Table 1

1984/5	2 AØ Antennae + Generators installed 3 MW 2 second pulse heating (6 MJ)
1985	Third AØ Antenna + Generator installed 4.5 MW 2 second pulse heating, (9 MJ)
1987	Eight A1 Antennae + Generators installed 12 MW long pulse heating, (240 MJ)
1988	Generators upgraded to 4 MW 16 MW long pulse heating, (320 MJ)

The JET RF program has been modified to reflect changing requirements and the initial performance of the prototype system, and is presently as given in Table I. The planned complete system now comprises 8 so-called A1 antenna/generator modules rated to give 2 MW each of high grade heating for 20 seconds every 10 minutes. This program is well advanced. The two uncooled prototype A0 antennae and associated equipment have been operational on the torus since early 1985, and the third system has been installed and commissioned. Most of the generators and transmission lines for the complete system are now at JET. The design of the long-pulse A1 antennae is complete and manufacture is well advanced with prototype components being delivered to JET. A contract has been placed for the upgrade of the generators to 4 MW.

The planned location of the 8 antennae in the torus is shown in Fig 1. The four-fold symmetrical disposition facilitates the potential use of the ICRF system for current drive, whilst the adjacent pairs offer a wide range of control of the $k_{\parallel}$ spectrum. The three A0 antennae locations are also shown in Fig 1.

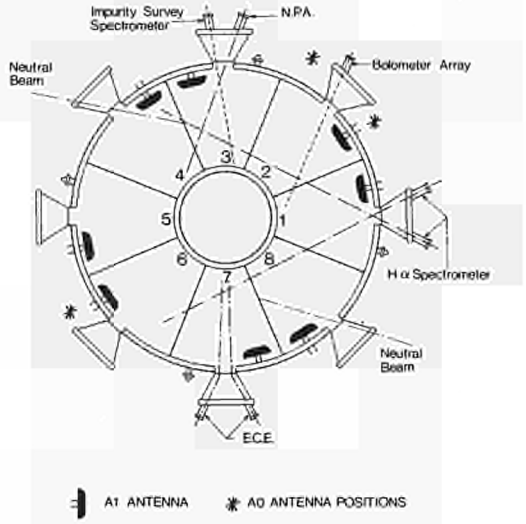

Fig.1 Location of the antennae in the Torus.

The RF Generators

The RF generators have been described in detail previously [25] and only a brief summary is given here. Each 1.5 MW amplifier comprises 600 W transistorized pre-amplifier stages, and three Tetrode amplifiers, a 20 kW pre-driver, 100 kW final driver and a 1.5 MW endstage. The stages are coupled using wide band matching transformers. Tuning over the full frequency range requires some mechanical adjustment of these transformers. The frequency range is thus divided into eight channels each of 4 MHz bandwidth. Channel selection is carried out automatically on demand using pre-programmed motorised mechanical adjustments. The two amplifiers on each module can be locked to a preset, continuously adjustable phase difference and are driven from a single remotely set oscillator. The endstage drives a nominal 120 Ω impedance and is matched to the 30 Ω lines using a special high power, wide bandwidth matching network which also provides filtering of the harmonics from the class B operation. The generators will operate at full power into a maximum VSWR of 1.5.

The DC supplies for the generators [26] are also modular, each 26 kV, 6 MW unit being used to drive 2 generator modules. The DC voltage may be controlled by the RF generators to maintain operation within the limits of the tetrode. The generator tubes are fully protected against excess anode and screen grid dissipation, current and reflected power and will initially limit the output below the requested level, or, if necessary, trip the RF output. Rapid protection against flashover is achieved using ignitrons to remove the anode and screen voltage. To date, only one tube has failed.

The generator output is measured using calibrated wide-band directional couplers. The output may be switched into a soda dummy load for test and calibration purposes. Cooling of the generators is carried out by modular demineralised water circulation systems. These are in turn cooled between pulses by heat-exchangers to the site cooling water.

The generators are designed for local manual control or operation by the central JET computer systems and two units have been routinely operated in this mode since early 1985.

The generators are fully tested to full power levels at the manufacturer's works and require only power supply commissioning after installation at JET. Experience with installation and commissioning of three units has been that operation is achieved after typically 3 weeks work on site.

The Transmission Lines and Matching System

The optimum impedance for the antennae to operate over the wide frequency band is typically 30 Ω. This impedance maximises the power transmission in a coaxial line and has been adopted for the JET system.

The transmission line has to be typically 84 m in length. All lines are designed to be this same length, giving a total installation of 1.3 km incorporating about 300 insulating supports on the central conductors. Each line is many wavelengths long, even at the lowest frequency, and offers the potential of much simplified matching (at discrete frequencies at typically 1.76 MHz intervals) by the use of a single variable stub at the generator end, combined with small frequency changes. As the frequency may be rapidly controlled during a pulse, such a system offers the potential for on-line matching of the antennae to compensate for changes in antenna impedance during the long JET pulse. This system has been adopted at JET. The full line from stub to antenna thus operates at high voltage. Provision has been retained for installation of a matching stub at the antenna if required. A 230 mm line rated at 50 kV peak voltage and 1.6 dB/km was therefore adopted. In addition, in order to maximise the availability of the system, ceramic insulators have been specified. These are found not to be susceptible to the rapid degradation with repeated arcing which is found with plastic insulators. The lines are pressurised with 4 bar absolute air; SF6 may be used to further improve the maximum voltage.

A number of components have been specifically developed for JET including a wideband 60 dB directional coupler, 3 m variable stub, telescopic and articulated elements, trombone phase shifter and a 3 MW, 30 Ω test load. The lines are fabricated from aluminium alloy castings and stock aluminium tube for the outer conductor, and copper tube for the inner conductors. The castings are loaded with epoxy resin for leak tightness and proprietary seals and plug-in connectors are used at all joints to minimise RF leakages and losses.

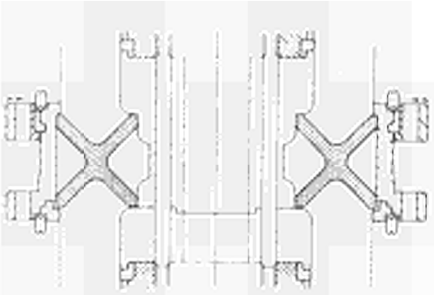

Fig.2 Ceramic support on the main transmission line.

The critical components in the lines are the ceramic supports. Breakdowns in the lines occur predominantly at these ceramics, with the limiting voltage being dependent on the humidity of the air and the general cleanliness of the ceramics. Careful quality control during installation followed by an extended period of drying to a dewpoint typically -50°C are required to meet the specification. Several designs of ceramic and of the detailed profile of the inner conductor at the ceramic have been tested and development work is continuing. The configuration adopted on the present installation is illustrated in Fig 2. The peak voltage is found to increase with pressure up to 3 bar abs; further increase has little effect. Tests with increasing temperature of the line show the peak voltage to be determined by the gas density. Operation in SF6 gives a further increase in voltage but breakdowns produce heavy deposits of powder. All torus operation to date has been with dry air.

The tuning system utilises a motorized variable length (3 m max) short-circuited stub. The stub length ℓ and optimum frequency F are given to a good approximation by

$$\ell = \frac{nc}{2F} \pm \frac{c}{2\pi F} \mathrm{Tan}^{-1}\left[x^{1/2}/(1-x)\right]$$

$$F = \frac{mc}{2L} \pm \frac{c}{4\pi L} \mathrm{Cos}^{-1}\left[(1-x)/(1+x)\right]$$

where R = total losses (line + antenna + coupling)
Z = line characteristic impedance.
L = total electrical length (line + antenna)
x = R/Z and m,n = 0, 1, 2.....

For lines many wavelengths in length, these two parameters are nearly independent. In operation on JET, a single pulse with approximate settings, coupled with a 100 kHz frequency sweep, has been sufficient to match the system with a reflected power less than a few per cent. Whilst this system has been used for most operations, the quadrupole antenna configuration (cf. Section 3) has very low coupling which has required the use of fixed short circuit stubs close to the antenna. The stub length was determined in advance from measured parameters and found to give good matching. This match can only be obtained at discrete widely separated frequencies and severely restricts the versatility of the system.

The quadrupole antenna (cf. Fig. 3) comprises two coupled circuits and requires the two lines to be equal in length with a tolerance of ± 3 cm which was obtained by shimming of the lines. Anticipated use of the ICRF system for current drive will require all the 16 lines to be accurately the same length. A short trombone adjustable line is being developed for this application.

The RF Antennae

General Description of the Prototype Antennae

The 3 prototype antennae presently installed in the torus were designed to be representative of the envisaged A1 antennae except that no active cooling was incorporated. As a result, these antennae are restricted to short pulse operation, typically 1-3 s depending on antenna coupling. These prototype antennae have been described in detail previously [27,28] and the principles of the design tested using a model antenna in TFR [16].

Each antenna comprises single loop Inconel conductors mounted inside an open-fronted shallow Inconel box which prevents flux escaping to the sides of the antenna. The front of the housing is covered by a nickel electrostatic screen fabricated from T-section nickel bars tilted at 15° to the horizontal to be parallel to the magnetic field and mounted alternately so as to prevent line-of-sight access to the housing. The housing is surrounded by graphite tiles originally mounted with the front face 17 mm in front of the screen, but now increased to 25 mm. The housing locates on conical spigots in the limiter guide tubes which also carry the two coaxial transmission lines. These lines are under vacuum for typically 2 m to a double ceramic vacuum window, and each inner conductor is additionally supported by a conical ceramic at the antenna end. As the conductance from the line to the torus is very low, an additional vacuum pumping system giving typically 100 ℓ/s per line is provided.

RF Properties of the Antennae

The antennae are designed to resonate at 33 MHz, chosen to optimise the performance over the wide frequency range. The available line access ports led to the adoption of a modified loop conductor as illustrated in Fig 3b, and installed on the AØ1 antenna in octant 6. The RF characteristics of this antenna have been computed [29] and also measured using a simple model of the antenna. These studies showed that the inductance was dominated by the outer conductor adjacent to the screen and the capacitance by the inner plate.

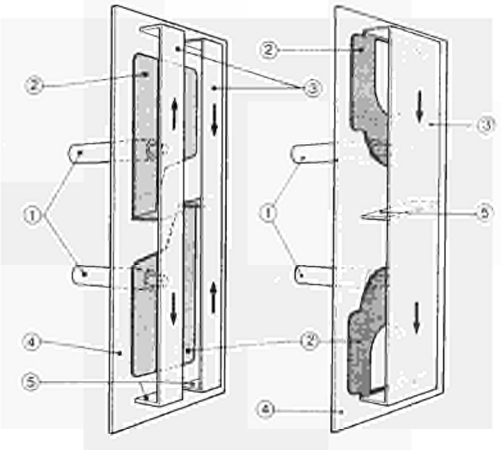

Fig.3 Conductor configuration. Left: Quadrupole/Dipole on AØ2 ; Right: Monopole/Dipole on AØ1. Arrows indicate relative current directions for π phase difference.

The A1 Antennae

The A1 antennae are designed for long pulse operation (20 s) at the maximum JET duty cycle of one pulse every 10 minutes. This requires enhanced cooling of the screen, the inner conductor of the vacuum transmission lines and the side protection tiles. Additional changes to improve coupling of the quadrupole configuration and to facilitate remote handling have also been incorporated.

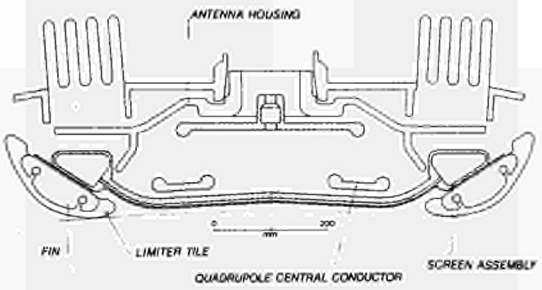

Fig.7 Section through the cooled A1 Antennae.

The A1 antenna is wider and the screen is now curved to follow the magnetic surface (cf Fig 7). The centre of the screen is 32 mm behind the plane of the side protection tiles. The screen elements are water cooled and manufactured by gun drilling a 5 mm hole through 700 mm Nickel bars. The critical feature in fabrication is the element to manifold weld, carried out using pulsed TIG without filler to achieve a penetration equal to the wall thickness. Differential expansion resulting from the alternating orientation of the elements requires good fatigue resistance in this weld.

The side protection of the A1 antennae is of similar construction to the belt limiter, comprising thin tiles mounted between and radiatively cooled by blackened Nickel fins welded to the screen manifold. The tiles are profiled to give uniform power deposition for a 15 mm scrape-off layer, and are mounted with a 23 mm spacing between the limiter and antennae at design elongation of 1.5. The design is compatible with both graphite and beryllium tiles.

The A1 vacuum transmission lines will be cooled by forced convection of gas through the inner conductors as far as the conical support using centrifugal fans in the basement. The connections of the line to the antenna are of bayonet form to facilitate remote installation. The auxiliary vacuum system on the lines utilises non-evaporative getter pumps regenerated into the torus.

Design of the A1 antenna is essentially complete and manufacture well advanced.

Initial ICRF Results

Operation of the JET System

Conditioning of the antenna was carried out using procedures developed on the RF test bed [27] and was completed in typically 1 day for each antenna. During subsequent operations over a period of 6 months the system operated reliably, showed no occurrence of multipactor arcing, and possible arcing in the antenna was observed only with the poloidal limiters retracted to be level with the screen. The system has delivered up to 2.5 MW, 5 MJ per antenna in monopole/dipole configuration; 1.5 MW, 1.5 MJ as a quadrupole; and 4.5 MW, 9 MJ in a single pulse with both antennae.

Subsequent inspection of the antenna revealed a thin (1 micron) surface layer of carbon/nickel mixture on the outer surface of the screen, loosely attached and flaking off in regions of high plasma loading. Inside the housing, the system was very clean with no evidence of breakdowns.

Antenna Plasma Coupling

The effectiveness of the coupling from RF generator to plasma may be expressed in terms of a coupling resistance R defined by [30]

$$R = 2P\, Z_o / V_m^2$$

where P = net generator power, Z_o = characteristic impedance, V_m = peak voltage on the line. This resistance includes contributions from the line, R_L, and the antennae vacuum losses, R_A. The net coupling to the plasma R_p and the fraction η of generator output power delivered to the plasma are

$$R_p = R - R_L - R_A \; ; \qquad \eta = R_p/R$$

R_L has been measured to be ~ 0.35 ohm with the stub at the generator and is negligible with the stub at the antenna. R_A has a measured value ~ 0.25 ohm in a strong magnetic field. At low fields, ferromagnetic effects in the carbonised nickel can strongly increase R_A.

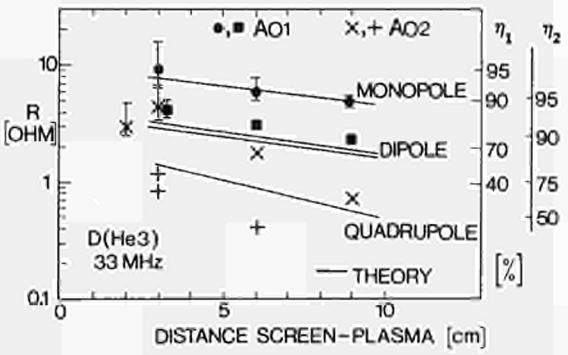

Fig.8 Measured and computed coupling resistances of the prototype antennae. The efficiency of coupling of the generator output to the plasma is also shown for the stub at the generator (η_1) and at the antenna (η_2).

The value of R_p depends on the antenna configuration, the distance from screen to plasma, and on the edge density profile. Measured and computed values [31, 32] are shown in Fig 8. The monopole and dipole have high coupling corresponding to η in the range 60-90%. The quadrupole has much lower coupling giving η of typically 30% unless the fixed stub is used, which increases η to ~ 70%. The voltage on the antenna scales as $1/\sqrt{R_p}$ and the screen losses as $1/R_p$. Thus operation with the quadrupole can increase the screen losses by an order of magnitude compared to the monopole.

A second type of conductor was installed on the AØ2 antennae and also on the new third antenna. This conductor, illustrated on the left in Fig 3 comprises four loops, with each line driving two loops in parallel. The two feeds on either AØ1 or AØ2 antennae have been driven at a relative phase of 0 or π. This enables investigation of the effect of both $k_{//}$ and k_θ on the performance of the system over a range 0-7/m [30]. In future, other phasings will be used to generate a travelling wave of interest for current drive.

Before installation, the RF impedances of the two antennae were measured with one feed open circuited. The results are shown in Fig 4. After installation, the complete systems were tested using time domain reflectometry, which showed the electrical length of the antenna to be close to twice its physical length. The RF losses in the antennae under vacuum with magnetically saturated screen have also been measured; the total losses in the transmission line/antenna are equivalent to 0.6 Ω, of which 0.35 Ω arises in the transmission line.

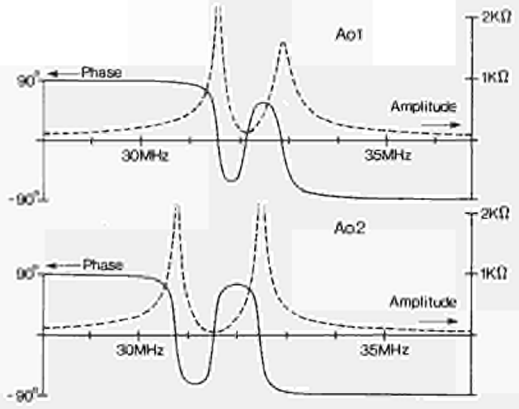

Fig.4 Impedances of the two prototype antennae measured with one line open circuit.

Mechanical Design and Manufacture of the Prototype Antennae

The antennae must withstand the forces on the antennae during disruptions, thermal stresses due both to RF losses and heating by the plasma, and baking to 450°C.

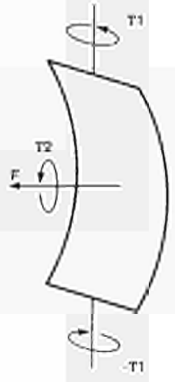

Fig.5 Disruption induced forces on the antennae. For 5MA collapse in 5 ms. F = 8 tonne, T_1 = 10 kNm, T_2 = 24 kNm. Substantial forces also arise on the central conductor

Detailed analysis of the disruption forces has shown the dominant components on the housing and screen to be as indicated in Fig 5, based on a 5 MA disruption in 5 ms. To accommodate these loads, the antenna housing is bolted to the vacuum vessel at each corner, as well as being located on the spigots. In addition, the AØ1 central conductor is attached to the housing by an articulated ceramic support. The forces on the screen can be much reduced by use of a DC break between screen and housing.

The high temperature of operation has required the use of Inconel 600 for the major components, except the screen, which is in pure Nickel. Nickel was chosen because of the thermal and electrical properties combined with moderately good mechanical strength and sputtering resistance. The disadvantages are the low fatigue resistance of Nickel, the relatively high RF losses and minor complication arising from ferromagnetic effects.

Thermal stresses in the graphite, the screen and central conductors have been minimised by use of flexure pivots, disc springs and sliding contacts to allow relative movements.

The vacuum transmission line is designed to sustain high RF voltage, particularly near the conical ceramic support which is close to the first voltage maximum at 33 MHz. The cones are seated on silver helicoflex seals, are silver plated on the contact faces, and coincide with a change in line diameter, which reduces the electric field enhancement. They have been tested to 50 kV peak RF voltage and also maximum current. The inner conductor incorporates a bellows on the current path to accommodate differential expansion. This is fabricated in 0.5 mm Inconel to obtain the necessary fatigue life and silver plated to minimise RF losses. RF heating of this component is nonetheless an important limitation on the duty cycle. Extensive RF tests on the bellows showed no problem with multipactor arcs.

All current carrying surfaces except the screen are silver plated. After plating, these components were baked to 150°C to check the adhesion. All RF contacts are made using silver helicoflex seals; binding is inhibited but not prevented at elevated temperature by rubbing with graphite. Titanium nitride is being tested as an alternative to graphite.

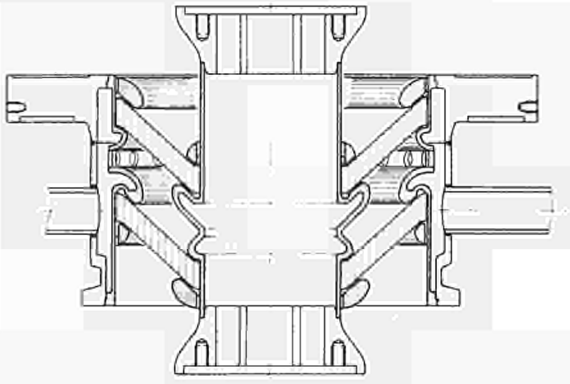

Fig.6 Conical vacuum window for the A1 Antennae.

The vacuum window is fabricated by simultaneously brazing copper inner and outer conductors into two annular 97% alumina ceramics. Corona rings and the outer mechanical support are subsequently electron beam welded in place. RF testing showed the peak voltage on the pressurized side to be sensitively dependent on the location and shape of the corona rings. All units installed on JET have been tested to 30 kV peak RF voltage; as the window is near a voltage minimum at 33 MHz this rating has not been a limitation. A revised conical window has been developed for the A1 antenna as shown in Fig 6. The prototype has been tested to 50 kV peak voltage without any sign of breakdown.

Plasma Heating Results

The results obtained to date have been reviewed in detail previously [3,30]. The conclusion related to the system design are summarised below:

- RF power is well localised at the plasma centre with on-axis resonance.
- the quadrupole produces significantly wider deposition profiles consistent with the high value of k .
- all configurations generate large sawteeth; those excited by the quadrupole are smaller and have shorter period of relaxation.
- the density in the scrape-off layer is doubled by the quadrupole only; the increase in central density is similar for all systems.
- relative impurity levels and Z_{eff} remain constant during RF heating.
- typically 75% of the coupled power can be accounted for by the rate of increase of ion and electron temperature in the centre of the plasma, or independently from magnetic measurements.
- the increase in stored energy in the plasma is nearly independent of the antenna configuration.

References

[1] J. Adam et al, "Physical Aspects and Technical Elements of an ICRF Heating System for JET", EUR-CEA-FC-1065, 1980.

[2] P.P. Lallia & P-H Rebut, "Preliminary Studies of the JET RF Heating System", in Proc. 3rd Varenna-Grenoble Int. Symp. on Heating in Toroidal Plasmas, Grenoble, 1982, pp. 799-811.

[3] J. Jacquinot et al, "ICRF Studies on JET", in Proc 12th European Conference on Controlled Fusion and Plasma Physics, Budapest, Sept. 1985 to be published.

[4] J. Hosea et al, "Heating Confinement and Stability during High Power ICRF Experiment on PLT", ibid.

[5] G. Fussmann et al, "Impurity Behaviour for Various Auxiliary Heating Methods in ASDEX", ibid.

[6] A.M. Messiaen et al, "Ion Cyclotron Resonance Heating in Textor", ibid.

[7] M. Mori et al, "High Power ICRF Heating Experiments in the JFT-2M Tokamak", in Proc. 10th Int. Conf. on Plasma Physics and Controlled Fusion Research, London, Sept. 1984, pp. 433-442.

[8] J. Hosea, "ICRF Heating in Large Tokamaks", in Proc. 3rd Symp. on Heating in Toroidal Devices, Varenna, 1976, pp. 55-62

[9] V.L. Volovin et al, "Wave Generation and Heating of Ions at Ion Cyclotron Frequencies in Tokamak Device TM-I-VCh", in Proc. 3rd Int. Meeting on Heating in Toroidal Plasmas, Grenoble, 1976, pp. 349-357

[10] TFR Group, "Excitation and Damping of the Fast Magnetosonic Wave in TFR Near the Harmonic Cyclotron Frequency", ibid, pp. 87-94.

[11] J. Jacquinot, "ICRF Heating of a Tokamak in a Proton Deuteron Mixture", in Proc. Joint Varenna-Grenoble Int. Symp. on Heating in Toroidal Plasmas, Grenoble, July 1978, pp. 127-132.

[12] F. Perkins, "Heating Tokamaks with the Ion Cyclotron and Ion-Ion Resonances", Nuclear Fusion 17, 1197, 1977.

[13] TFR Group, "ICRF Heating at the Ion-Ion Hybrid Resonance", in Proc. 9th European Conference on Controlled Fusion and Plasma Physics, Oxford, 1979, pp. 355-369

[14] J. Jacquinot, H. Lebot, J. Adam, H. Kuus, "An All-Metal Array of Antennae for RF Heating of Tokamaks in the Ion Cyclotron Range of Frequencies", in Proc. 11th Symp. on Fus. Tech., Oxford, 1980, pp. 1101-1106.

[15] A. Messiaen, "All Metal Limiter Antenna System on Erasmus", in Proc. 4th Topical Conference on RF Plasma Heating, Austin, 1981.

[16] Equipe TFR, "Tests of the JET TRF Antenna". EUR-CEA-FC-1219, March, 1984, paper EIA.

[17] F. Wesner et al, "ICRH Components for ASDEX and WVII", in Proc. 4th Int. Symp. on Heating in Toroidal Plasmas, Rome, 1984, pp. 1109-1116.

[18] Equipe TFR, "ICRF Heating in TFR in Conditions of Low Impurity Radiation", in Proc. 4th Int. Symp. on Heating in Toroidal Plasmas, Rome, 1984, pp. 277-290.

[19] J. Hosea et al, "PLT Ion Cyclotron Range of Frequency Heating Program", ibid. pp. 261-275.

[20] D.Q. Hwang, G. Grotz & J.C. Hosea, "Surface Physics Problems during ICRF Heating of Tokamak Plasmas", J. Vac. Sci. Tech. 20, 1273-1278, 1982.

[21] T.L. Owens, "ICRF Antenna and Feedthrough Development", in Proc. 6th Topical Conference on RF Plasma Heating, Pine Mountain, 1985, to be published.

[22] A. Radiron, "RF Vacuum Feedthroughs", in Proc. 27th APS Plasma Physics Meeting, San Diego, Nov 1985 paper 8P17.

[23] J. Jacquinot, "Heating and Current Drive Scenarios with ICRF", presented Erice Course on Tokamak Start-up, Erice, July 1985, Plenum, to be published.

[24] M. Cox et al, "Fokker Planck Calculations of ICRF Current Drive on JET", in Proc. 12th European Conf. on Controller Fusion and Plasma Physics, Budapest, Sept 1985, to be published.

[25] T. Wade et al, "JET ICRF Power Plant", in Proc. 13th Symp. on Fusion Technology, Varese, 1984, pp. 727-732.

[26] R. Claesen & E. Bertolini, "Additional Heating Power Supplies, Their Design and Behaviour During Operation", in Proc. 11th Symp. on Fusion Engineering, Austin, 1985, paper 1B04.

[27] J. Arbez et al, "The JET ICRF Antennae Systems ; Description and Test Bed Results", in Proc. 13th Symp. on Fusion Technology, Varese, 1984, pp. 669-674.

[28] J. Arbez et al, "RF Tests on JET First Stage Antenna System", ibid, pp. 599-604.

[29] K. Theilhaber & J. Jacquinot, "Variational Theory of the ICRF Antenna", Nuclear Fusion, 24, 5, pp. 541-554, 1984.

[30] J. Jacquinot et al, "Preliminary ICRF Results from JET", in Proc. Inst. of Physics 12th Annual Plasma Physics Conference, Glasgow, 1985 To be published.

[31] A.M.Messiaen et al, "Theoretical Aspects of the Coupling Properties of ICRH Antennae", in Proc. 3rd Joint Varenna-Grenoble Int. Symp., on Heating in Toroidal Plasmas, Grenoble, 1982, pp. 243-257.

[32] M. Bureš et al, "Plasma-Antenna Coupling and Related Scrape-off Layer Studies on JET", in Proc. 12th European Conf. on Controlled Fusion and Plasma Physics, Budapest, 1985, to be published.

ADDITIONAL HEATING POWER SUPPLIES: DESIGN CONCEPT AND FIRST OPERATION

R Claesen, U Baur, J Carwardine, G Celentano,
C Christodoulopoulos, A Dobbing, P L Mondino
(JET Joint Undertaking (OX), U.K.)

ABSTRACT

Two additional heating methods are used in JET, e.g. the Neutral Injection (NI heating) [11] and the Ion Cyclotron Resonance Heating (RF Heating) [7].

In the RF heating, 10 generators each will deliver 3MW to their antenna; for the NI heating 16 ion sources each delivering 4.8MW ion beam will be installed.

In order to minimise the internal dissipation in the generator and hence to obtain the maximum output power of the RF generators under the varying load conditions given by the plasma, the high voltage on the anode of the tetrode is varied. This is one of the main features of the power supply.

The requirements for the NI power supply are different to the ones for the RF power supply. The accelerating grid (G1) power supply has to be very stable and must be able to switch off in 10 microsec in case of a breakdown in the accelerating structure and re-apply within 50 ms. Both these functions, voltage regulation and switching on and off are performed by a high power tetrode (protection system). In addition to the accelerating grid power supply, other power supplies (Aux PS) are necessary. They are the arc power supply, the filament power supply, the suppression grid (G3) power supply, the gradient grid (G2) power supply and the bending magnet power supply.

Because JET will operate with tritium at a later stage, no electronic circuits can be installed in the Torus Hall or in the basement. Therefore, all the power supplies have to be installed outside these areas. A special cable (SF6 Transmission Line) with a length of approximately 100m links each protection system and the associated Aux power supplies for the ion source with this ion source.

These transmission lines are not directly connected to the ion source. They terminate at a pressurized vessel (SF6 Tower) which houses the snubbers (to dissipate the capacitive energy of the transmission lines in case of a breakdown in the ion source) and the high voltage breaks for all services, e.g. the cooling water circuit of the ion source, feeding gas, etc. This SF6 Tower contains passive components only and can therefore be placed close to the injectors in the Torus Hall.

The main characteristics of these power supplies will be discussed, and some voltage response curves given under real load conditions.

1. RECTIFIER REQUIREMENTS

All pulsed power supplies in JET are fed from a 33kV distribution network. This network is fed from the 400kV grid of the Central Electricity Generating Board through three stepdown transformers of 300MW pulsed power each. At maximum pulse power, the voltage dip on the 33kV network is approximately 15%. Because of the response time required in both the NI and the RF power supplies, a transformer with a tapchanger and a simple diode rectifier cannot be used. A thyristor regulated power supply is necessary. For the RF heating power supplies, voltage optimization during the JET pulse was only the next step. Because of the varying voltage, reactive power loading of the 33kV is very high, especially in the case of the RF, where the highest current is obtained with the lowest DC voltage.

The basic rectifier circuit used is a 6-pulse rectifier. The required DC voltage is obtained by connecting two of these 6-pulse rectifier circuits in series to obtain a 12-pulse circuit and hence a lower ripple on the DC side. On the 33kV side the primaries of two of these 12-pulse circuits are phase shifted to obtain a 24-pulse circuit.

The maximum output voltage of the thyristor rectifier for the NI power supply is approximately 110kV and the maximum current is 60A. Each 6-pulse rectifier has therefore a maximum output voltage of 55kV and 60A. For this output voltage, primary regulation is obvious, if it is performed at a suitable voltage and current level so that a single thyristor can be used. The voltage level was chosen to be approx. 1000V.

For the RF power supply, the maximum DC voltage is 30kV and the maximum current 300A and therefore each 6-pulse bridge delivers a maximum of 15kV and 300A. Again primary regulation at a voltage level of 1000V was chosen. In this case two thyristors had to be connected in parallel as the current was too high. Even in this case, this solution was more economical than a straightforward rectifier with the thyristor at the high voltage side.

With the exception of during a load breakdown, the load current, in both the NI and the RF case, remains constant during a pulse. The filter chosen at the DC output was a LCR type filter. The big disadvantage of this type of filter is that during switch on and switch off of the load, severe voltage dips respectively overshoots do occur. This can be avoided by precharging the inductance to the initial required current at switching on of the load and to provide a freewheeling path for the current in the inductor when the load is switched off. Both these requirements are most easily obtained in a special type of primary regulation called the starpoint controller. Table 1 gives the values of the main components of the rectifier circuit.

Table 1: Values of the Main Components in the Thyristor Rectifiers for the Neutral Injection Power Supply (NI) and the Radio Frequency Power Supply (RF).

Component	Unit	N.I.	RF	Remarks
Nom. volts	kV	85	22	(1)
Max. volts	kV	120	30	
Max. current	A	60	300	(4)
Max. power	MW	4.8	6	(4)
Matching transf.1	MVA	4.1	7.0	
2	MVA	4.1	6.1	
Rectifier transf.1	MVA	3.47	5.96	
2	MVA	3.47	5.2	
L	mH	1.6	1	(2)
C	micro F.	9.33	300	(3)
R	Ohm	100	2	(3)

Remarks:
(1) NI has two 42.5kV bridges in series, but no midpoint connection
RF has two 11kV bridges in series with the midpoint used for the driver amplifier;
(2) Inductance in each of the two starpoint bridges
(3) NI: R and C in series over the two bridges;
(4) RF: limited in current or power whatever is reached first.

2. STARPOINT CONTROLLER

The circuit of the starpoint controller is given in Figure 1.

This arrangement has several advantages:

- the required isolation level of the inductor is much smaller than if it was placed in the high voltage side
- the isolation level of the precharging circuit is much smaller than if it had to be placed on the high voltage side
- the freewheeling path can be switched in and out of the circuit when required.
- the equivalent value of the filter inductance is n^2 bigger as the value of L on the primary side of the transformer, where n equals the transformer ratio.

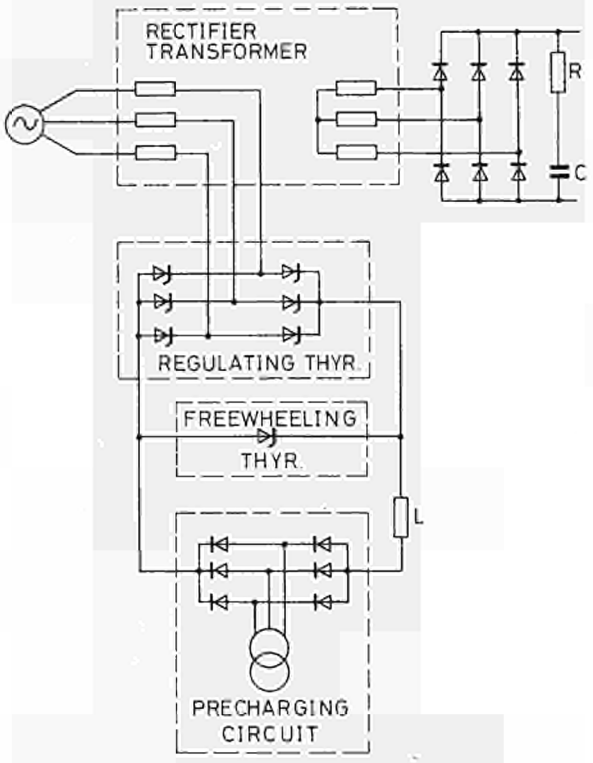

Fig.1. STARPOINT CONTROLLER

Before switching on the load, the inductor is precharged to the required current level by the precharging circuit. During this time, the free-wheeling thyristor is continuously fired by a pulse train of 1kHz. The freewheeling thyristor closes the freewheeling path for the precharging current. By monitoring the current in the filter capacitor or through a separate signal from the load, the switching-on instant of the load is detected. At this instant the firing of the free-wheeling thyristor is stopped. Natural commutation to the rectifier bridge occurs, the moment the voltage across the freewheeling thyristor has the correct polarity. Before the commutation starts and partly during the commutation, the load current is supplied by the filter capacitor. This gives rise to a voltage dip on the output of the power supply.

Once the commutation is complete, the inductor forms part of the filtering circuit. The output diode bridge of the precharging circuit is freewheeling.

When the load is removed, the freewheeling thyristor is fired, providing the freewheeling path for the current in the inductance. Commutation takes place from the main thyristor bridge to the freewheeling thyristor if the polarity across the freewheeling thyristor has the correct polarity. Before commutation takes place and partly during the commutation, part of the energy in the inductor is transferred to the filter capacitor. This gives rise to the voltage overshoot at the end of the pulse.

If the interface signal from the load asks for a re-application of the output voltage, the current in the inductor is kept at the same value it had prior to the load shedding by the precharging circuit, otherwise the remaining energy in the inductance is dissipated in the circuit formed by the inductor, the freewheeling thyristor and the freewheeling diode bridge of the precharging circuit.

3. ION CYCLOTRON RESONANCE HEATING POWER SUPPLY

The characteristics of the RF power supply are given in Table 2.

Table 2: Characteristics of ICRH power supply.

Output voltage end stage	14-26.4kV
Output voltage driver	7-13.2kV
Maximum output current	300A (+45A for driver)
Maximum output power	6MW
Response time: for voltage step	30msec
for current step	30msec
Maximum ripple on DC	±5%
Maximum DC voltage accuracy	±1%
Output power ramp up	≤ 3msec
Mode of operation:	
normal	20s (300A+45A) rep. rate 0.033
conditioning	5-15msec (100A+20A) rep. rate 0.2
Maximum number of breakdowns	400 in 20s pulse
Neutral isolation level	10kV

The power supply for the RF heating is installed at a distance of approximately 100m from the RF generator. The output cables are installed in the same trenches as the 33kV cables. For this reason and also to avoid any RF disturbing the interface signals between the generator and the power supply, it was decided to install a fibre optic link between the generator and the power supply.

All control and operating signals are transmitted over this link, and the power supply can be fully controlled from a local control panel situated near the RF generator or through the JET computer system called CODAS [10].

The two main interface signals between the power supply and the generator are the setpoints for the output voltage and the precharging current of the inductance.

The setpoint of the output voltage forms part of one of the internal control loops of the RF generator. Its value depends on the measurement of the screen grid current of the tetrode in the RF generator.

The setpoint of the precharging current is set manually. It depends on the initial load current for the next pulse. If it is set to a too high value, the output voltage tends to overshoot when switching on, if it is set too low, the output voltage dip might be too high. Experimentally it was found that a difference of 20% keeps the overshoot or the voltage dip within acceptable levels. The correct setting of this value is therefore not too critical.

The circuit diagram of the power supply which feeds one of the RF generators is given in Figure 2.

The 11kV midpoint of the thyristor rectifier is brought out and is used as the High Voltage Supply for the driver circuit. This 11kV voltage is always half the voltage of the 22kV. Both the rectifier bridges therefore always regulate to the same voltage. The voltage regulation is performed by means of the starpoint controller.

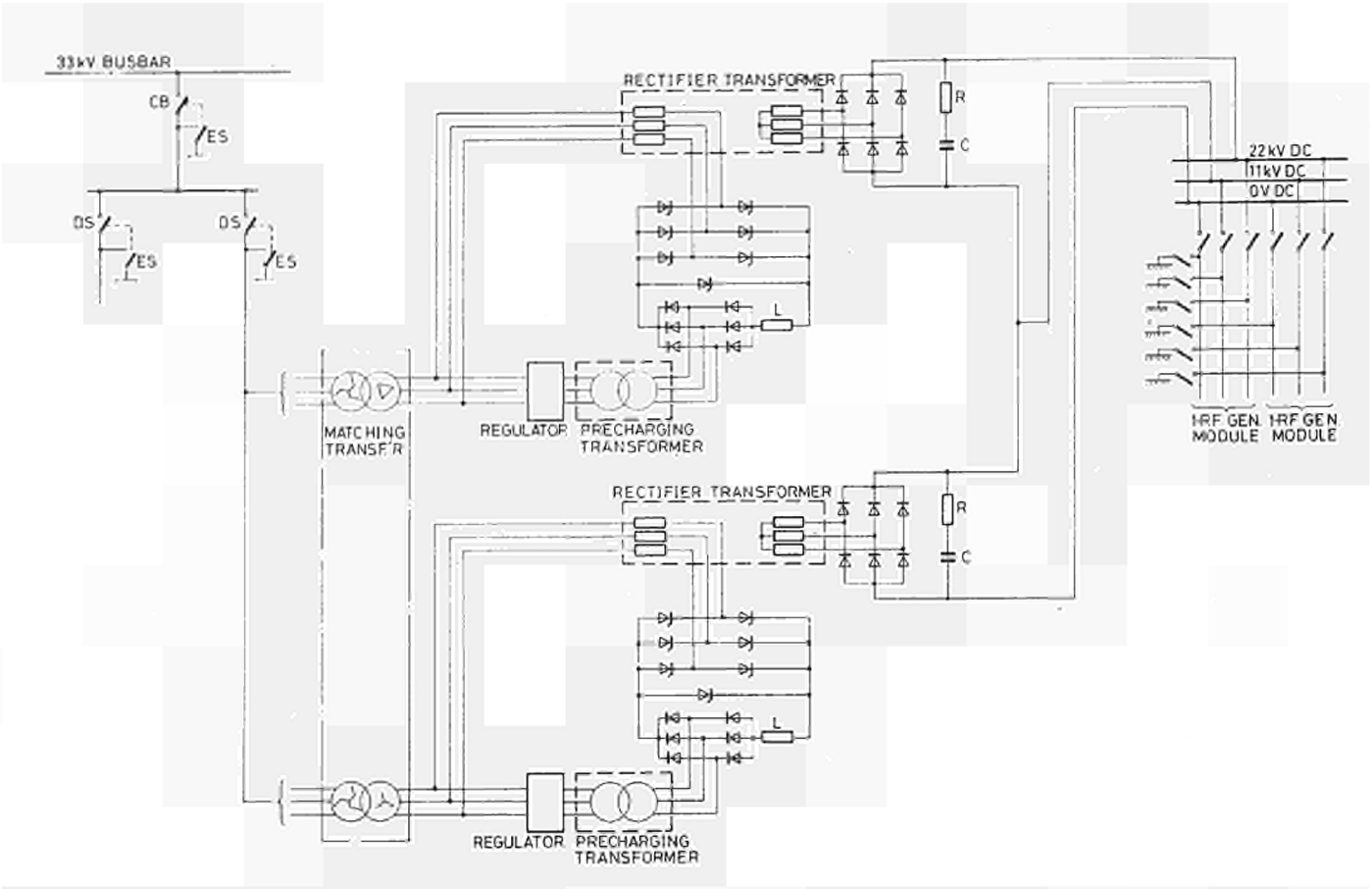

Figure 2: Power Supply for the RF Generator

The precharging circuit of the inductor is fed from the matching transformer, as is the rectifier transformer. In this way phase differences and synchroniaation problems, which give rise to severe current peaks in the precharging circuit, are avoided.

Figure 3a gives the output current and output voltage of the power supply as recorded during a pulse of the RF generator when emitting power in the plasma.

Figure 3b gives the output voltage of Fig 3a on an extended scale to show better the voltage regulation.

The voltage reference is set to 21.25kV prior to the pulse. This value of the voltage prior to the pulse is a value chosen by experience. It depends on the required output power. If the voltage setting is not correct then the voltage control loop between the generator and the power supply automatically adjusts to the correct level to obtain the minimum internal tube dissipation.

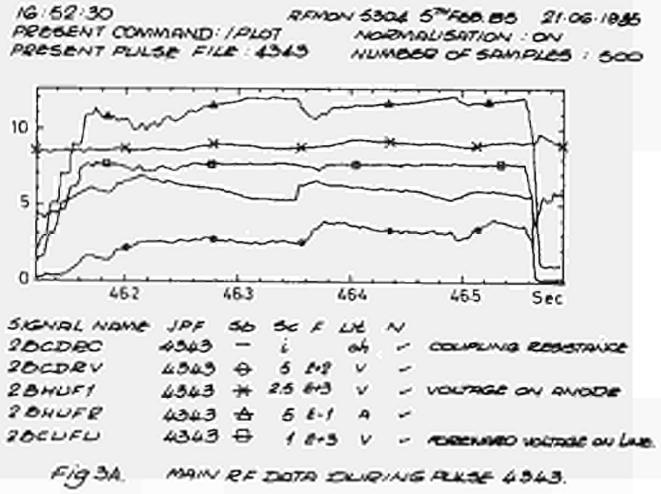

Fig 3A. MAIN RF DATA DURING PULSE 4343.

The coupling resistance in Fig 3a is defined as $R = 2PZ_0^2/V_M^2$ where $P=P_{inc}-P_{refl}$ is the net RF power delivered by the generator, Z_0 the characteristic impedance of the line and V_M the peak voltage along the feeding coaxial line [7].

In Fig 3a at around 46.35s the coupling resistance jumps up. This gives rise to an increase in screen grid current. Instantaneously the output RF power (forward voltage on line) is reduced. The DC voltage is now increased until the required RF power is obtained again. At this point, the control circuit regulates to a constant screen grid current by varying the DC voltage around the optimum value.

Since January 1985 two RF generators, with an RF output power of 3MW each have operated on the JET machine, they have delivered their full output power to the plasma on several occasions. No malfunctioning or faults of the power supplies were observed during this period.

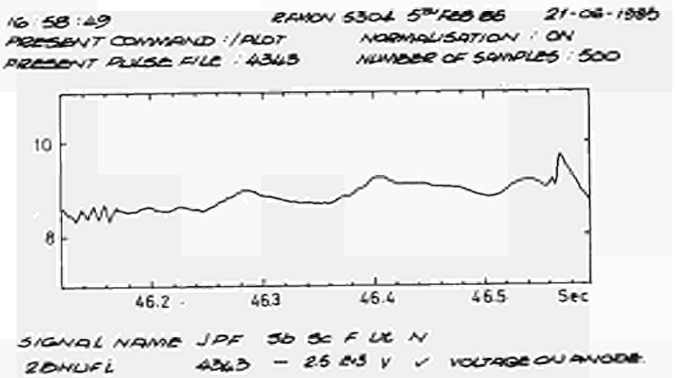

Fig 3B. EXTENDED SCALE OF HV DC.

4. NEUTRAL INJECTION POWER SUPPLIES

The NI power supplies are composed of four major subsystems, e.g. the accelerating grid power supply, the auxiliary power supplies, the transmission lines and the SF6 Tower.

Figure 4 gives the connection diagram of the power supplies. All auxiliary power supplies, with the exception of the grid 3 (suppression grid power supply) and the magnet power supply, are referenced to the grid 1 (accelerating grid) power supply. The JET vessel is earthed in one point only. To avoid any earthloops, any system connected to the vessel must be fully floating from earth. Hence the neutral of the G1 power supply, the outer enclosure of the transmission line and the SF6 Tower are fully isolated up to an isolation level of 10kV.

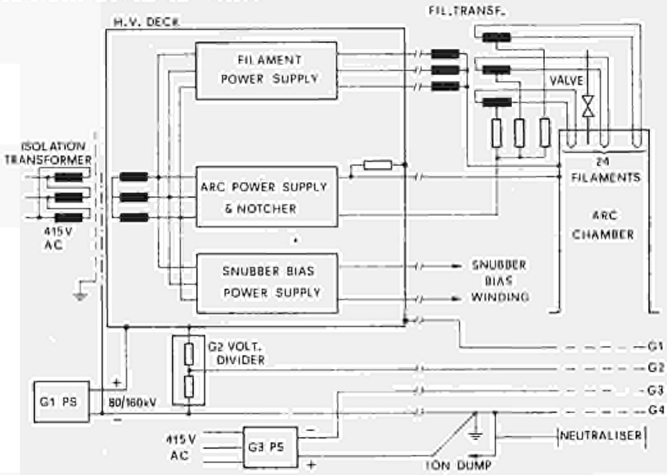

Fig.4 Interconnection Diagram of Neutral Injection Power Supplies.

Table 3 gives the main characteristics of the neutral injection power supplies.

The grid 1 power supply has two parts, the thyristor rectifier and the voltage regulating and switching circuits (protection system).

The thyristor rectifier consists of two starpoint controllers. Before the pulse starts, the required output voltage is set and the thyristors are released. The control loop maintains the voltage constant during the pulse.

The output of the accelerating grid (Grid 1) power supply is a maximum of 80 kV for operation in hydrogen. Two of these power supplies will be connected in series to give 160kV for operation in deuterium. The conversion of one of the power supplies to 160kV is in progress [1].

The main component of the protection system is the tetrode. Its function is to maintain the output voltage to within ±1% and to perform the required fast switching on and off of the output voltage in case of a breakdown in the ion source.

The acceptance test performed reflects these requirements. Deliberate short circuits of the dummy load are made and the response of the entire system is measured [6].

All auxiliary power supplies with the exception the grid 3 and the magnet power supplies are housed inside a fully closed cabinet. This cabinet is mounted on isolators, the whole of this cabinet is connected to the output of the grid 1 power supply. The isolation level of this entire installation was tested up to a voltage of 260kV. With the test voltage of 260kV applied, it was verified that all thyristor controls and the communication links with the computer system were working correctly.

The nominal voltage level for the filament power supply was chosen to be 1kV AC. The main reason for this was to reduce the diameter of the cables as they are installed inside the inner conductor of the transmission line. This voltage is transformed down to 12V nominal at the ion source.

Another feature of the filament power supply is that the arc current is controlled by an automatic control circuit which acts on the filament voltage. In this way the operation of the ion source is much easier because the power supply is more independent from a particular ion source [5].

One complete injection system has been in operation in the test bed since January 1984. During this operation period valuable information was obtained on the operation of the power supplies. Some minor changes had to be done because, as expected, an injector cannot be simulated with a resistive dummy load.

During June and early July 1985, eight power supplies were operated simultaneously at 60kV for approximately 2s together with their ion source. The beam was directed on a specially constructed ion dump which was placed inside the neutral injection box instead of the bending magnets and their associated ion dumps.

During the shutdown from July to October 1985 this ion dump was removed and replaced by the central support column with the bending magnets and the ion dump. Operation with these eight ion sources and injection into the plasma will start in December 1985.

Table 3: Main Data for the Power Supplies of one Injector.

PS	OUTPUT			NORMAL MODE CONDITIONING				Working insulation level (kV)	COMMENTS
	V(kV)	I(A)	AC/DC	Pulse length(s)	Repetition period(s)	Pulse length(s)	Repetition period(s)		
Arc	0.2	1500	DC	30s	600s	0.75	15s	160	
Filament	1	52	AC R.M.S.	30s	600s	7.5	15	160	
Grid 3	-6	7.5	DC	20s	600s	0.5	15	10	Series connection
	-3	15							Parallel connection
Grid 2	67-74	±0.1	DC	20s	600s	0.5	15	160	Passive dividing network fed by G1 P.S.
Grid 1	80	60	DC	20s	600s	0.5	15	160	Outside the scope of this manual
Snubber bias	0.06	150	DC	30s	600s	0.75	15	160	
Bending magnet	0,12	1,000	DC	Continuous				10	One unit for 2 PINIS

Because of the space restrictions imposed, a transmission line with a diameter as small as possible had to be designed. A coaxial construction was preferred as this allowed for the cables for the filament power supply, arc power supply, etc., to be installed inside the inner conductor. Because of the space restrictions, the characteristic impedance of the transmission line was chosen to be around 70 Ohms. This value of characteristic impedance is the optimum value for voltage withstand capability. The actual measured value is 67 Ohms and the capacitance per metre line is 55pF.

The routing of the transmission line is rather complicated and involves several bends. Each of these bends would give rise to a joint if a conventional rigid construction of the transmission line was chosen. It was therefore opted to construct a flexible line. A cross-section of the line is shown in Figure 5.

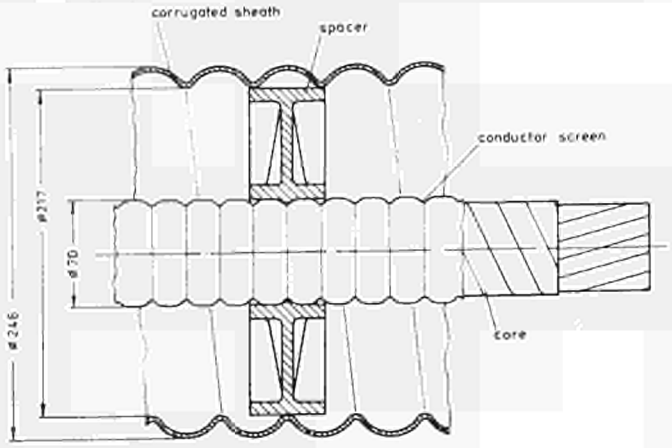

Fig.5 Transmission Line

The outer enclosure is made from 2.5mm aluminium-manganese alloy and a spiral configuration is formed on it to make it more flexible. The outside and inside diameter of the corrugation are 246mm and 217mm respectively.

The circular spacers supporting the central cable bundle is cast from a modified polyphenylen oxide and coated with a varnish which improves their behaviour against surface tracking. The inner coax conductor is made of a corrugated copper tube. The space between the inner and outer conductor is filled with SF6 at an absolute pressure of 3.3 Bar.

In addition to the mechanical tests, several electrical tests were performed successfully. Test voltages of 200kV DC for 15 min and 260kV DC for 1 min were applied. At the transmitting end, the inner conductor of the line is connected to the cabinet which houses the auxiliary power supplies. At the other end the line is connected to the SF6 Tower. This connection comprises a stopjoint so that the SF6 inside the line and inside the tower are contained within separate spaces. This was done, so that in case of leakage, to avoid one system from emptying in the other. Another added advantage is that both systems can be operated at different SF6 pressures.

The outer conductor of the transmission lines is connected to the SF6 Tower.

The SF6 Tower is a a pressurized vessel which contains the snubbers and the high voltage breaks for the cooling water of the ion source. As indicated before, the SF6 Tower is isolated from local earth. The isolation level is 10kV.

Fig 6 gives a view of the SF6 Tower and all its internal components. The transmission lines are terminated at the bottom. The inner conductor is then routed through its correspondent snubber. At the top

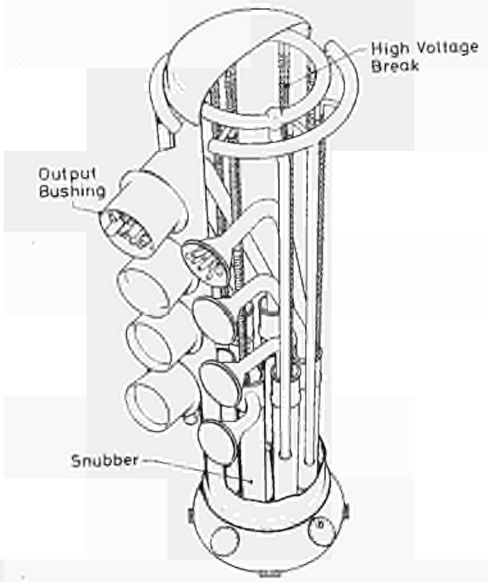

Figure 6: SF6 tower

of the snubber, the cooling water hoses are added. They continue together with the conductors of the auxiliary supplies inside the inner conductor of the coaxial transmission lines. These cooling water hoses are made of a special mixture of EPDM rubber reinforced with kavlar. At the output of the SF6 Tower Ceramic bushings isolate the high voltage from the main frame of the SF6 Tower.

The snubber is premagnetized so that its complete magnetization curve is used in case of a breakdown. This means that less magnetic material has to be used for the same amount of energy dumped which results in a smaller snubber. This is of great importance as it also reduces the actual size of the SF6 Tower. The basic building block of the snubber is the magnetic pancake. It consists of a band of SI-FE steel of 50 micron thickness wound like a coil. These coils are housed inside a plastic container. Around this assembly a coil is wound which provides a high impedance in series with the bias power supply. It prevents any short circuit energy from being dissipated inside the small snubber-bias power supply. Prior to installation in the SF6 Tower the snubbers were tested. A capacitor of 10nF, which simulates a transmission line of 100m, and the other stray capacitance, was discharged through the snubber.

Figure 7 gives a picture of these discharges. Its peak discharging current was measured and found to be 240A which was within the design value of 300A.

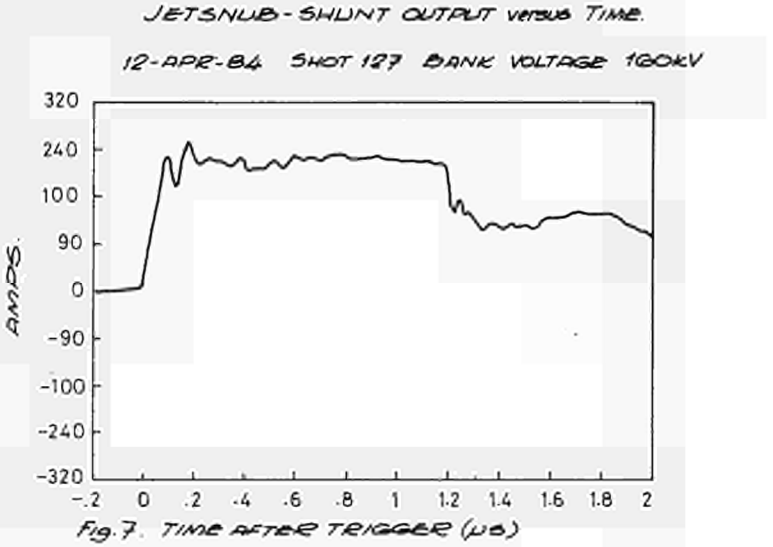

Fig.7. TIME AFTER TRIGGER (μs)

5. CONCLUSIONS

Although all the RF power supplies were commissioned on a dummy load, minor adjustments were necessary when the real load was connected. They are now switched on daily either for commissioning of a RF generator, or for RF operation with plasma. Up to now, no problems have been encountered with any of the power supplies.

The experience of operation of the Complete Neutral Injection Power Supply performed on the Test Bed with the Injectors, allowed to verify that the original design was basically sound and at the same time it was possible to identify and correct minor difficulties. In this respect the first system has been used as a prototype and all the others were a sort of series production.

All Power Supplies for the second Neutral Injection Box will be on site by the end of 1985 and will be fully commissioned on dummy loads by the middle of 1986.

ACKNOWLEDGEMENTS

The authors would like to thank P.H.Rebut for his contribution to the definition of the system and E.Bertolini for his supervision and guidance during the whole project.

TABLES

Table 1: Values of the Main Components in the Thyristor Rectifiers for the Neutral Injection Power Supply (NI) and the Radio Frequency Power Supply (RF).
Table 2: Characteristics of ICRH power supply.
Table 3: Main Data for the Power Supplies of one Injector.

FIGURES

Figure 1: Starpoint Controller
2: Power Supply for the RF Generator
3A: Main RF Data during Pulse 4343.
3B: Extended Scale of HV DC.
4: Interconnection Diagram of Neutral Injection Power Supplies.
5: Transmission Line.
6: SF6 Tower.
7: Time after Trigger (US).

REFERENCES

1. Mondino P.L., Selin K., 7th Symposium on Engineering Problems of Fusion Research, Knoxville Tennesee, 25-28 October 1977.
2. McGregor C.K., Batzer T.H., 8th Symposium on Engineering Problems of Fusion Research, Proceedings pp 1034-1037.
3. Altman H. et al., 12th Symposium on Fusion Technology, Julich, 13-17 September 1982, Proceedings pp 1241-1248.
4. Aslin H. et al., 12th Symposium on Fusion Technology, Julich, 13-17th September 1982, Proceedings pp 391-397.
5. Ciscato D. et al., 13th Symposium on Fusion Technology, Varese, 24-28th September 1984.
6. Dobbing J.A. et al., 13th Symposium on Fusion Technology, Varese, 24-28th September 1984.
7. Jacquinot J. et al., Preliminary ICRF Results from JET; Invited paper at the Institute of Physics Conference, Glasgow, June 1985.
8. Testing of JET Neutral Injector Snubbers: Test Report from Culham Laboratory.
9. Bertolini E: "Basic Design Concepts, Installation, Commissioning and Operation of the JET Integrated Power Supply System"; 10th Symposium on Fusion Engineering, Philadelphia, 1983.
10. Bombi F: "Architecture of the Control and Data Acquisition System of the JET Experiment"; 10th Symposium on Fusion Engineering, Philadelphia, 1983.
11. Duesing G: "JET Neutral Beam Injection System, Construction and Component Tests", 13th Symposium on Fusion Technology, Varese, 1984.

OPERATIONAL TEST OF THE JET NEUTRAL INJECTION SYSTEM IN THE JET TEST BED

H D Falter, R S Hemsworth, G H Deschamps, A P H Goede, T T C Jones, P Massmann, M J Mead

JET Joint Undertaking, Abingdon, Oxon, OX14 3EA, England

A Stäbler (attached from IPP Garching, Germany)

ABSTRACT

One quadrant of the first JET Neutral Beam Injector has been tested extensively in the JET Neutral Beam Test Bed. We find a reduced neutralisation efficiency caused by beam gas interaction. Not yet completely understood effects in the magnet region widen the profile of the full energy ions at higher currents.

1. INTRODUCTION

The JET Neutral Injector [1] consists of 8 beam sources arranged in two vertical banks of 4 sources each. Four deflection magnets and ion dumps are installed on a central column [2] forming four identical quadrants (Fig. 1). Each quadrant handles the beams of two sources rated at 80 kV, 60A for hydrogen and 160 kV, 30 A each for deuterium. The first completely assembled beamline system was installed in the JET Neutral Beam Test Bed for testing one well instrumented quadrant with one beam source (PINI) in either of the two positions for this quadrant. The Test Bed [3], which consists of a standard Neutral Injector Box, a Target Tank and a Beam Dump (Fig. 2) was operating for more than a year prior to this test, so that the tests were carried out using an already operational system. The duct region of the Torus is simulated in the Target Tank by scrapers on either side of the beam. The beam dump behind this duct simulation therefore receives the power that would be transmitted to the plasma except for reionisation losses in the torus duct region.

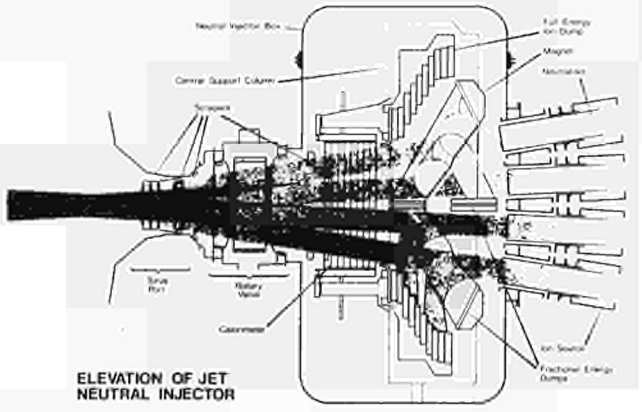

Fig. 1

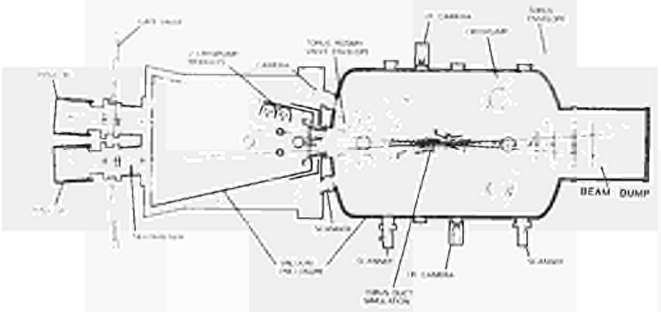

Fig. 2 Plan view of the JET Neutral Beam Test Bed (without beamline system)

Roughly 2000 beam pulses of various energies (40 - 80 kV) and pulse length (up to 10s) have been fired through one quadrant with hydrogen and deuterium beams.

2. BEAM PROPERTIES AND POWER LOADING

Power densities are derived from the initial temperature rise of the thermocouples brazed into the metal 3 mm below the exposed face of the actively cooled components, and from the equilibrium temperature of these thermocouples using a measured conversion factor. The total power is deduced from the water outlet temperature of various components. Water flow rates are measured with either turbine flowmeters (beam source and neutraliser) or with a clamp-on ultrasonic flowmeter where the routing of the pipes does not allow the installations of insertion type flowmeters. Depending on the individual pipe runs these measurements have been corrected by relating them to more accurate ones using energy conservation.

Optical species measurements have been made in the Target Tank. To achieve good signal levels additional gas had to be injected into the tank. For deuterium our measurements agree well with data taken at the Culham Beamline with one of the JET beam sources (Fig. 3). The species mix is 82% D^+, 11% D_2^+ and 7% D_3^+ at an extracted current of 41 A. Only a few measurements have been made in hydrogen, so far with poor signal to noise ratio. Therefore we use in this paper the species ratios measured at the Culham beamline.

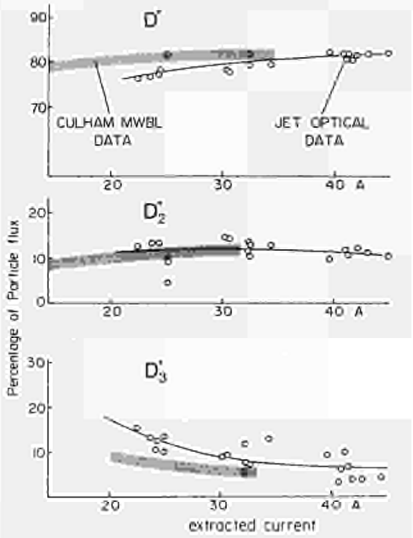

Fig. 3 Species mix for deuterium from Dopppler shift measurements in the Target Tank.

The beam profile measured at the Test Bed Beam Dump is shown in Fig. 4. During the beam on time the beam moves from left to right by approximately 25 mm. There is also a constant deflection of the full beam compared with the neutral beam of between 10 and 20 mm. A

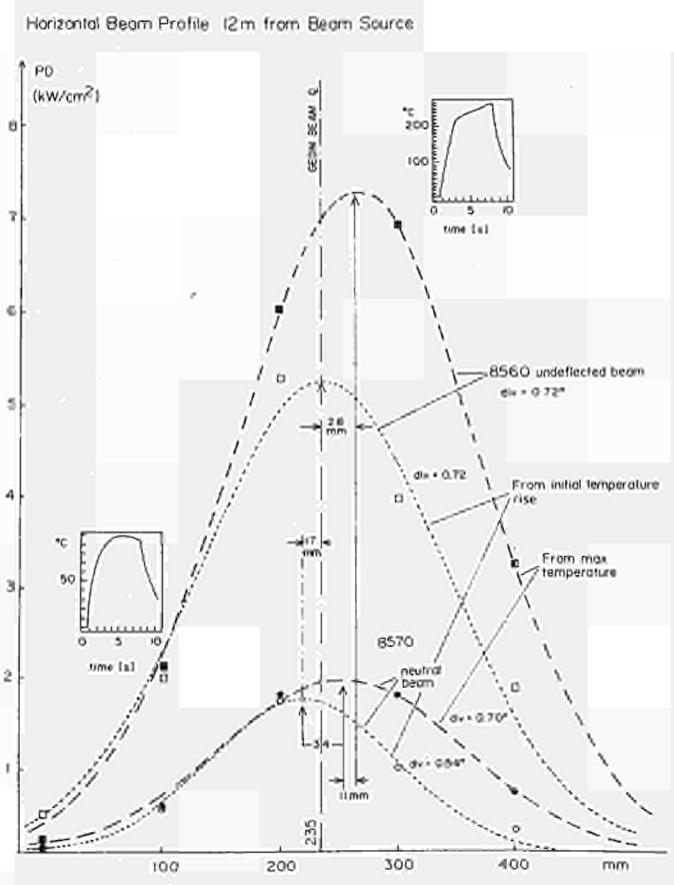

Fig. 4 Horizontal beam profile at the testbed beam dump through the beam centre. Solid symbols: power density derived from the maximum temperatures. Light symbols: power density derived from the initial temperature rise. Top: undeflected beam, bottom: neutral beam only.

deflection of up to 70 mm is expected from the Earth's magnetic field. The beamlet divergence deduced from a fit to either profile is ≈ 0.7°.

The movement of the beam (which is also obvious from the time dependence of the thermocouple traces in Fig. 4) makes the data evaluation more complicated. Profiles derived from the initial temperature rise give the situation during the first few hundred milliseconds after beam initiation while profiles derived from maximum temperatures include the beam movement, but might be distorted by heat conduction along the component. The obvious discrepancy in the power density derived from the two methods is not yet understood and needs further investigations.

Table I gives the power to the components for hydrogen and deuterium as a percentage of the total extracted power. At 80 kV, hydrogen operation roughly 10% is lost in the beam source and neutraliser, 70% goes to the full and fractional energy ion dumps and 17% (minus re-ionisation losses) would go to the plasma. Increasing the line density of the neutraliser by a factor of 1.7 reduces the power to the dumps from 70% to 65%. The actual gain in neutral power is slightly less than 3% of the electrical power while 2% are additionally lost in the beam source. Remarkable is the very small power loading in the duct which is 0.1%, just measurable. As already mentioned this does not include reionisation losses in the duct region as the Torus stray field is not simulated.

TABLE I

POWER LOADING OF VARIOUS ACTIVELY COOLED COMPONENTS AS PERCENTAGE OF THE EXTRACTED POWER FOR DEFLECTED BEAMS

Pulse No.	8570	8600	8684	8693
EXTRACTION VOLTAGE/kV	80	80	80	80
EXTRACTED POWER/MW	4.77	4.82	3.18	3.13
GAS	H_2	H_2	D_2	D_2
NEUTRALISER LINE DENSITY/(10^{19} cm^{-2})	1.2	2	1	2
LOSSES (% of extracted beam power) IN:				
BEAM SOURCE	5.3	7.0	4.9	7.0
NEUTRALISER	3.7	3.7	3.6	4.0
FULL ENERGY ION DUMP	65.9	60.6	36.8	26.8
MAGNET LINERS & FRAC. ION DUMPS	4.2	4.7	4.7	5.7
CALORIMETER (BACK PANEL)	0.9	1.0	1.4	1.4
BOX EXIT SCRAPER	0.7	1.1	1.5	2.7
DUCT SIMULATION	0.1	0.1	0.1	0.1
TB BEAM DUMP	16.9	19.7	44.8	46.6
ACCOUNTABILITY	97.7	97.9	97.8	94.3

3. NEUTRALISATION EFFICIENCY

The JET neutraliser has typical dimensions of 430 x 180 mm² cross section and 1.8 m length. The neutraliser is split into two stages of nearly equal length, gas is introduced into the source and into the neutraliser between the two stages. In the Test Bed a valve separates the two stages with a capacitance manometer [4] at the valve body recording the neutraliser pressure at the mid point.

A nude ion gauge, calibrated against a capacitance manometer, was traced along the beam path through the neutraliser and through the magnet in order to determine the pressure profile with neutraliser flow. Apart from the neutraliser exit, the pressure decreases linearly along the second stage neutraliser. Additionally the pressure drop across the second stage neutraliser is measured as a function of the neutraliser flow Q_n and the source flow Q_s. The source gas flow Q_s is normally set to equal roughly the beam particle flux Q_B. The neutraliser line density is derived by adding the line density measured for the neutraliser flow (Q_n) to that from the surplus source gas ($Q_s - Q_B$) for which we assume a linear pressure drop throughout the neutraliser with measured pressures at the mid point and at the exit of the neutraliser.

The neutralisation efficiency was mainly determined as the power ratio measured in the Target Tank or on the Test Bed Beam Dump for beam pulses with and without ion beam deflection by using otherwise identical beam parameters. In this case the measurements rely only on the integral over the water temperature, not on the flow rate which is kept constant. The result is found to be independent of the beam pulse length for pulses between one and ten seconds long. Alternatively, the power ratio between the full beam (power on ion dumps, liners and calorimeter) and the power on the calorimeter (neutrals) in one single shot was used for a few cases. In this case the results rely on absolute power measurements. Both methods give the same neutralisation efficiency as shown in Fig. 5 where the neutralisation efficiency is plotted versus the measured line density in the neutraliser. The calculated neutralisation efficiencies are based on the measured line density, the species mix as discussed, and published cross sections [5]. The correction for the reionisation losses in the magnet region is calculated using the measured line density. Obviously there is no agreement between the measured and the calculated neutralisation efficiency. Reasonable agreement can be acheived by: using half the measured line density in the neutraliser for the calculation.

Thus it appears as if the actual line density of the neutraliser during beam on time is only half the value measured in the absence of beam. The exact value of this reduction factor depends on the species mix and the reionisation losses used in the calculation. The measured species mix for D_2 shows good agreement with the Culham data (Fig. 3) which supports the value of the species mix used for the calculated neutralisation efficiency. This species mix is also consistent with the power measured on the magnet liner and fractional energy dump. Reionisation and reneutralisation losses will mainly appear as a reduction in the total power accountability as this power is deposited on inertial panels. For D_2 we actually see in Table I a loss in accountability of 2.6% by increasing the line density where 2.3 % is expected [6]. For hydrogen a 1.3% reduction is expected which is within the data scatter. On the inertial plate which collects the devious particles from the magnet we find a power density of 20 W/cm², roughly 80% of the expected value at the standard gas flow (25.5 mbar l/s)[6]. This suggests that the assumed reionisation losses are reasonable. The most likely explanation for the observed reduction in line density is heating of the neutraliser gas by the beam [7]. In our neutraliser, which operates in the transition regime between molecular and viscous flow, an increased gas temperature will show up as increased pressure reading of the neutraliser gauge. Fig. 6 shows the observed pressure rise during hydrogen and deuterium operation.

Increasing the neutraliser flow Q_n helps to increase the neutral power, but also increases the losses in the beam source and the reionisation losses.

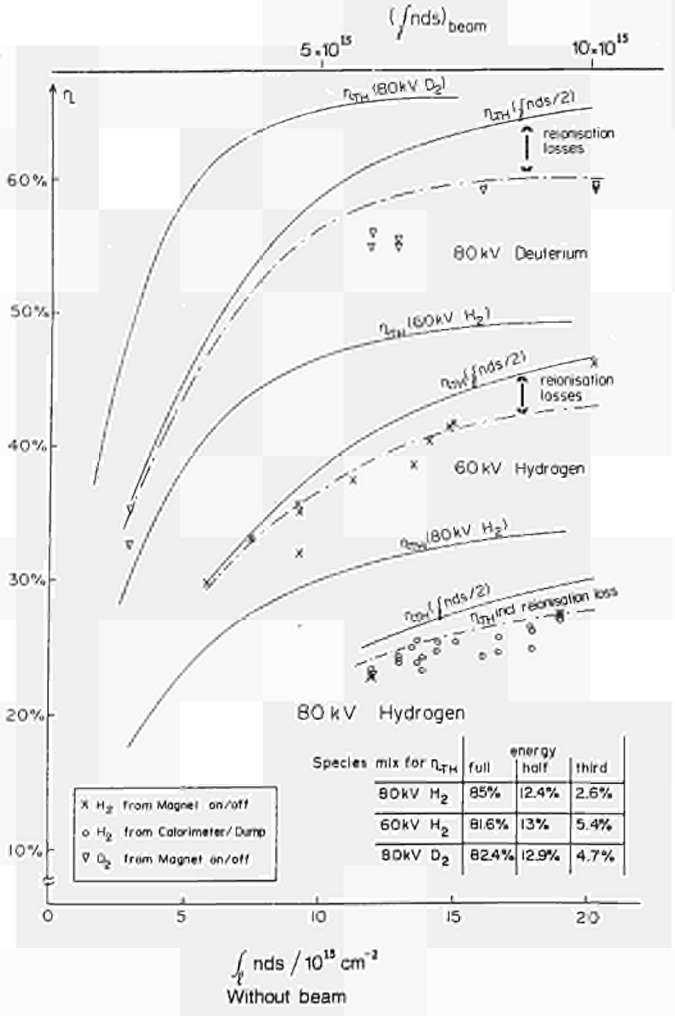

Species mix for η_{TH}	energy full	half	third
80kV H_2	85%	12.4%	2.6%
60kV H_2	81.6%	13%	5.4%
80kV D_2	82.4%	12.9%	4.7%

Fig. 5 Neutralisation efficiency versus measured neutraliser target thickness in the absence of beam (bottom scale) and assumed target thickness with beam (top scale). Upper solid curve: calculated efficiency using measured line density. Lower solid curve: calculated efficiency using half the measured line density. Dashed curve: reionisation losses subtracted.

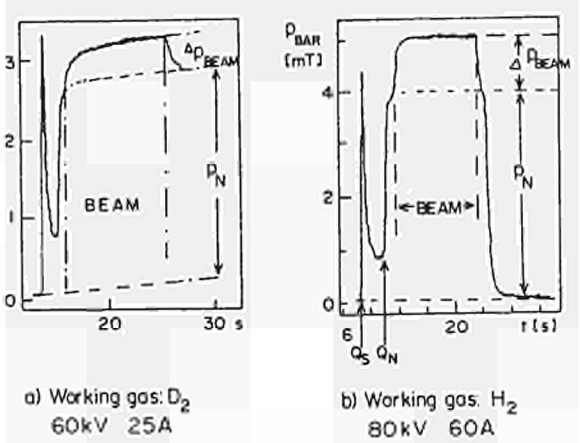

Fig. 6 Pressure versus time at the midpoint of the neutraliser during a beam pulse. The gauge is at room temperature. First the source gas, then (after ≈ 1.5 s) the neutraliser gas, and after another ≈ 1.5 s the beam is turned on. The initial spike is caused by a small volume between the throttle and the absolute valve of the gas introduction system.

4. BEAM PROFILES ON THE FULL ENERGY ION DUMP

The full energy ion dump, described elsewhere [8] is instrumented with 62 thermocouples. Additionally 5 inertial calorimeters have been installed to measure the power loading to the side of element 2, and to measure power densities at the outer part of the profile (Fig. 7). Fig. 8 gives a profile in the non bend plane for

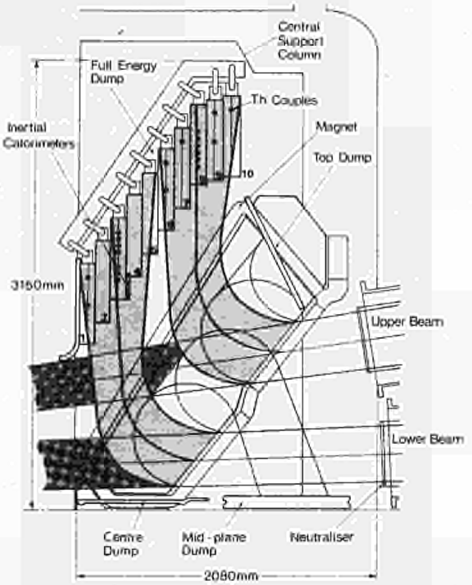

Fig. 7 View on magnet and full energy ion dump showing the thermocouple location of one dump side. The dump elements are staggered. The inertial calorimeters on element No. 3 are mounted at the side of the element flush with its surface. Obviously they are in a different plane compared with the thermocouples in element 3.

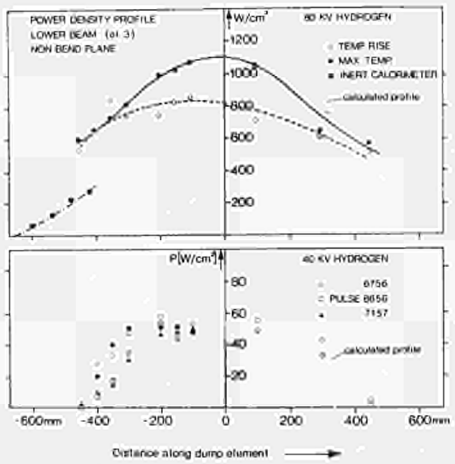

Fig. 8 Power density for the full energy ions at 80 kV hydrogen. Again the points are derived from the maximum temperatures (black symbols) or temperature rise (open symbols). The curves are eye fits. The shading gives the calculated profile.

hydrogen beams at 40 kV and 80 kV. At the lower voltage the measured profile is well described by the calculated profile derived from numerical magnetic field calculations beam emmittance and ray tracing calculations [9]. The 80 kV profile is considerably wider than calculated. The inertial calorimeters mounted at the side of element 3, flush with its surface, show that the power falls off towards the outer edge of the element. As the beam stopping elements are staggered these blocks are "further away" from the magnet than the thermocouples in the centre of the element which explains the discontinuity in Fig. 8. With increasing beam-on time the power gets more concentrated in the centre of the dump. This can be seen from the two profiles derived from the temperature rise (profile shortly after beam initiation) and the maximum temperatures (profile in equilibrium). Adding additional gas through a second neutraliser does not change the profile within the tolerance of the measurement.

The profiles in the bend plane (Fig. 9) are also considerably wider than expected with a long tail along the dump centre line. Again, as in the non bend plane, the profiles become more peaked with increasing beam-on time. The beam broadening results in a peak power density of around 1.2 kW/cm² where the profiles of the upper and lower beam overlap. At present attempts are

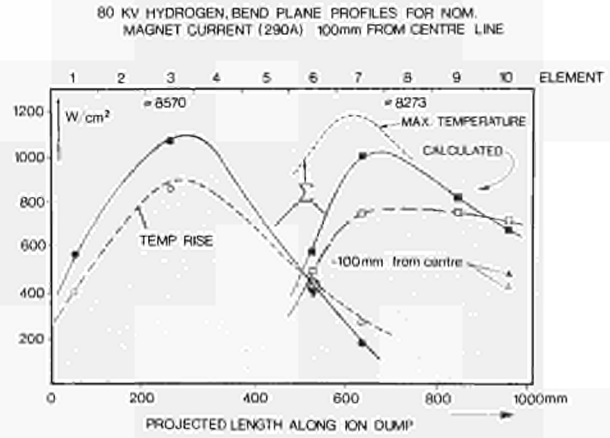

Fig. 9 Beam profiles from two beam pulses in the upper and lower position. Black symbols are derived from the maximum temperature after 6s of beam pulse, open symbols are from the temperature during the first 300 ms. Triangles represent measurements from the opposite dump half.

being made to describe this beam broadening by space charge effects in the magnet. However, beam broadening is not observed for 80 kV deuterium beams as Fig. 10 shows. This is even true for beam pulses with low neutraliser line density where the neutralisation of deuterium is roughly the same as for hydrogen.

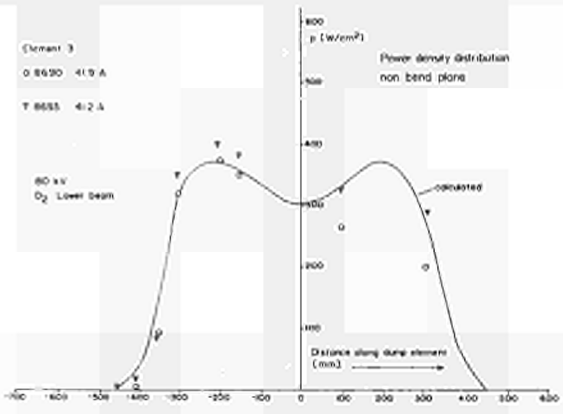

Fig. 10 Power density profile of the full energy deuterium ions in the non bend plane along element No. 3 (lower beam).

The horizontal beamshift as observed on the Test Bed Beam Dump additionally complicates the interpretation of the profiles of the deflected full energy ions.

5. OPERATING EXPERIENCE WITH THE OPEN STRUCTURE CRYOPUMP

The JET cryopumps use a special geometry for the nitrogen shield and helium panel to achieve a very high specific pumping speed of 20 l/s cm^2[10]. The average number of wall collisions with the liquid N_2 temperature shield is lower in this geometry than in a conventional chevron arrangement. Therefore it was important to examine the pump performance in the presence of a beam. In the Test Bed 1/10 (2 modules) of the cryopumping capacity of a JET injector is installed. The two modules are opposite the calorimeter (Fig. 1,2) which acts as a scraper in its non intersecting position. The pumping speed is found not to be influenced during beam on time and the helium consumption only increases by the amount expected from the thermal gas load.

6. CONCLUSION

The system has been operated satisfactorily with the beam at full power (80 kV, 60 A). Further experiments are planned to improve the neutralisation efficiency and to measure the power loading of the full energy ion dump for deuterium beams at up to 160 kV with extended instrumentation on the full energy ion dump. These experiments are required as the observed beam broadening effects do not allow to simply scale the power loading for 160 kV beams from the present measurements.

ACKNOWLEDGEMENT

We would like thank all members of the JET Neutral Beam Heating Division led by G Duesing for their continuous support of the work and many fruitful discussions.

REFERENCES

[1] G Duesing, JET Neutral Beam Injection System, Construction and Component Test, presented at the 13th SOFT Conference in Varese, Italy, (1984), Vol. 1, p. 59.

[2] R Haange, H Altman, S Papastergiou, R B Tivey, M J Watson, JET Neutral Injection Beamline System, Manufacture and Assembly, to be presented at the 11th Symp. on Fusion Engineering, Austin, Texas, Nov. 1985.

[3] H D Falter, G Deschamps, R S Hemsworth, T T C Jones, P Massmann, M J Mead, D Stork, The JET Neutral Beam Test Bed Facility and First Results, presented at the 13th SOFT conference, Varese, Italy, (Sept. 1984), p. 571.

[4] MKS Baratron Head Type 310 CA supplied by MKS Instruments,INC, Burlington, Massachusetts 01803.

[5] J W Stearns, K H Berkner, R V Pyle, Proc. 2nd Topical Meeting on the Techn. of Contr. Nucl. Fusion 1976, p. 1221.

[6] B R Nielsen, A P H Goede, R S Hemsworth, E Thompson Charge Changing Collisions in the JET Neutral Injection Bending Magnets, Vacuum 34, p. 37-40 (1984).

[7] J Paméla, Gas Heating Effects in the Neutralisers of Neutral Beam Injection Lines, Report EUR-CEA-FC 1279 (Sept 1985), CEN Fontenay-aux-Roses, France.

[8] R Haange, Design of Calorimeter and Ion Dump for JET Neutral Injection Beam Line, presented at the Proc. 9th Symp. on Engineering Problems of Fusion Research, Chicago (1981), p. 1352.

[9] A P H Goede, A A Ingersoll, P Kupschus, B R Nielsen, E Thompson, R S Hemsworth, The JET Neutral Injection Deflection Magnet, presented at the 12th SOFT conference, Aachen, (Sept. 1982), p. 1321.

[10] W Obert, G Duesing, E Küssel, P Kupschus, C Mayaux, P H Rebut, H Santos, The JET Cryopump System and its Cryolines for Neutral Injection, presented at the 13th SOFT conference, Varese, Italy, (1984), p. 311.

ASPECTS OF INTERFACING JET DIAGNOSTIC SYSTEMS

P. Millward, C.J. Caldwell-Nichols, A. Ainsworth, M. Barnes, N. Foden,
J. Gowman, C.J. Hancock, R. Lobel, B. Oliver, J. Reid, P.J. Roberts,
A. Tiscornia, J.A. Wilks, C. Wilson,
JET Joint Undertaking, Abingdon, Oxon, OX14 3EA, UK.

Abstract

Of 30 diagnostic systems planned for JET most are now commissioned and the remainder are in an advanced stage of construction. This paper describes the engineering problems encountered of size, radiation, temperature and remote handling that were common to all the diagnostics and the role of the Diagnostic Engineering Group at JET in the successful implementation of these systems.

Introduction

The Scientific Department at JET is responsible for the provision and operation of all the JET diagnostic systems. Some 30 systems are planned and the parameters measured by them are shown in table I. The majority of these systems have been designed and constructed by the Associated Fusion Laboratories in Europe to agreed specifications. Initial discussions with each laboratory established which of the proposed diagnostic systems it would be prepared to design and construct, and after subsequent assessment by JET staged contracts were placed for the detailed design and manufacture of these systems. The precise allocation of responsibilities between the Association and JET were defined in these contracts, as was the necessity for the overall approval of the designs by JET at various stages and the detail approval of all items interfacing to JET and its subsystems, e.g. vacuum components.

The role of the Diagnostic Engineering Group, which is part of the Scientific Department, is one of liaison to ensure that the interfaces between diagnostics and JET are correct, to coordinate the construction and finally to install the diagnostics. Considerable in-house design and construction is undertaken for items where very close liaison with other JET divisions is essential. Items such as ECE internal antennae and external waveguides, internal discrete coils, vacuum beam lines and diagnostic support pillars are some of the items handled by the group.

TABLE I
Diagnostic Measurements

Bolometry	
Magnetic Flux Measurements	
Electron Temperature	- 3 Systems
Density - Interferometers	- 2 Systems
X-Ray Intensity	- 3 Systems
Limiter Temperature	
Neutron Diagnostics	- 6 Systems
Neutral Particle Analysis	
X-Ray Crystal Spectrometer	- 3 Systems
Optical/UV Spectrometer	- 5 Systems
Plasma Boundary Analysis	- 3 Systems
Hydrogen Pellet Injector	

Engineering Problems

The factors that affected the design of diagnostics are the size of the JET machine, requirement for radiation shielding, remote handling of components and the bakeout temperature of the torus.

Size: The linear dimensions of JET are very much larger than the previous generation of machines. Hence the weights of components which were previously a few tens of kilogrammes are now a few tonnes. Thus as well as ensuring their weight is properly supported when in position the fact that nearly all components will have to be handled by crane or other mechanical manipulator has to be considered at the design stage.

The size of the diagnostic equipment also presents a problem in being able to accommodate the planned number at the port space available at the torus. Success has only been achieved by careful allocation of diagnostics to each port and some compromises. Even so shortage of space has complicated designs and installation and access have become more difficult than one would have liked.

Radiation: JET is expected to produce significant quantities of neutrons and associated γ radiation in the active phase. The Torus Hall has walls nearly 3 metres thick for radiation protection. Ultimately electronics will not survive inside the hall so all diagnostics designed for the active phase have detectors, and electronics as well as other components requiring regular maintenance outside the torus hall. Diagnostics whose radiations are capable of being guided use labyrinth paths to connect the torus to the diagnostic hardware. Spectrometer beamlines penetrating the torus hall wall present a secondary shield problem however.

Remote Handling: In common with other components of the JET machine most diagnostics are designed for some remote handling. Non active-phase diagnostics have been designed only to be disconnected from the machine and removed intact, whereas active phase diagnostics need to be capable of complete dismantling and repair by remote handling techniques. Usually Remote Handling needs require the simplest solution rather than a complex one. Further difficulties arise not only due to the space required around a component for manipulator and tools but also the compromise needed between diagnostic and remote handling requirements. For example spectrometers are installed with an all-metal vacuum isolation valve between them and the torus. The valve itself is remotely handleable and the increased length of the valve this demands will result in a loss of viewing angle for the spectrometer.

Temperature: The torus is capable of being baked to 500°C and hence provision has to be made for its expansion of up to 45mm where an unheated diagnostic is attached and where a diagnostic with a heated beam line across the Torus Hall is connected up to 100mm of expansion has to be allowed for. The solution now used wherever possible is to have a stiff bellows at the torus flange and the diagnostic mounted on a slide system. The bellows will take up minor angular misalignments but not axial compression. This method allows the vacuum loads on the torus to remain constant. The alternative method using flexible bellows and a fixed diagnostic results in forces tending to move the torus in its suspension mounting.

Adopted Designs for Diagnostics

Two examples of design solutions to overcome the various problems are those for the Electron Cyclotron Emission systems and the High Resolution X-Ray Crystal Spectrometer.

Electron Cyclotron Emission Diagnostic

The ECE system detectors must be outside the Torus Hall, fortunately their beams can be reflected around labyrinths to ensure adequate radiation protection but the penalty is greatly increased path lengths with corresponding increase in signal loss and complexity. There are 10 waveguides following tortuous paths over 45m long with 15 bends as they also need to avoid other components around the machine. The flange on the torus through which the signal paths pass is also occupied by two other large diagnostics and accommodating them all presented severe restraints.

X-Ray Crystal Spectrometer

The X-Ray Crystal Spectrometer requires direct line-of-sight between the plasma and reflecting crystal, and between the crystal and detectors with only the interposition of a beryllium window close to the torus. The crystal, mounting and detectors had to be outside the Torus Hall, consequently the wall penetration is an escape route for gamma rays and particularly neutrons. Shielding is required not only for line-of-sight radiation but also for the considerable scattered radiation. The beam line outside the Torus Hall is 15m long and required over 500 tonnes of concrete and blockwork to ensure adequate protection. This was constructed above the waveguides, sources and detectors of three existing operating diagnostics.

Cabling

A further consequence of the machine size is that approximately 125 kms of transmission cables have been installed for diagnostics. This was a major installation exercise complicated by being able to work only during shutdowns. Cable requirements had to be defined 6 months before a shutdown to allow for procurement and similarly detailed installation and connection schedules have to be finished two months before a shutdown to allow for contracts to be placed for this cable installation work.

Cable routings generally go through sealed penetrations first from the diagnostic hall into the basement and then through the Torus Hall floor to junction boxes on the transformer limbs. From there jumper cables with remote handling connectors connect to the diagnostics. Indeed all services, water, compressed air, nitrogen etc. follow a similar practice being connected by flexible tubes with remote handling couplings from limb junction boxes. This system allows complete disconnection of all services prior to remotely removing a diagnostic and vice versa.

Vacuum Design

Apart from the neutron diagnostics, all diagnostic systems have a vacuum interface with the JET torus, either through optical windows, whose development is described later, or with a direct connection to the torus vacuum. All diagnostic systems are designed for ultra high vacuum and some also for tritium operation. This has been achieved using metal seals or welded joints, all-metal valves and provision for system baking. The mechanical interfaces to the torus are all-metal pendulum gate valves which had to be tailored to the requirements of individual diagnostics as well as themselves meeting remote handling requirements. Some designs needed to be very complex, particularly when a large viewing angle was required, and great care had to be taken to ensure that the mechanical loadings were within the valve manufacturers' limit. It was a JET responsibility to design and procure these valves, and the flanges on the diagnostic sides became the physical interface between JET and the Association's equipment. Standard components, such as vacuum gauges and their controllers, angle valves and turbomolecular pumps were also designed and procured by JET.

The turbomolecular pumps are all tritium sealed with special features required by JET. However, if suitable non-mechanical pumps become available for the tritium phase, these may replace turbomolecular pumps in the Torus Hall.

Vacuum Windows

The largest and most important development programme undertaken by the Group was to obtain suitable vacuum windows. They were required in crystal quartz, fused silica and sapphire, up to 120mm optical aperture and capable of 400°C operation and some even 500°C. Further they should be remote handleable and in the majority of cases weldable to the torus. After a difficult but eventually highly successful programme undertaken with the Culham Laboratory over 60 windows have been installed. Culham developed a technique using aluminium as the bond material between the window discs and suitable ferrules, and then welding these assemblies into the main tubular bodies of the windows. Two problems exist with these windows, they operate only up to 400°C due to metallurgical reasons and they cannot be immersed in water as the aluminium bond dissolves. Present bakeout temperatures do not exceed 400°C and with human access to the torus windows can be protected before water washes. However for tritium operation 500°C torus bakeout is planned and if beryllium is used inside the torus automatic washing will be undertaken before entry of any personnel to the torus can take place and hence the windows cannot be protected. Gold bonding the windows was always an objective for the few windows for 500°C, however all the windows will need to be replaced in order to resist the water wash. Culham have now developed a gold bonding technique to crystal quartz only and a major new fabrication programme has started to replace all the quartz windows. The problem for the remaining 20 silica and sapphire windows remains, however Culham are hopeful of developing techniques for these materials.

Computer and Electrical Interfaces

The Control and Data Acquisition System (CODAS) interfaces are built around CAMAC systems which are some distance from the subsystem computers and connected to them by fibre optic serial highways. The physical interface between diagnostic, and indeed all JET subsystems, are the terminal blocks on the sides of the (CODAS) cubicles containing the CAMAC hardware. Essentially, each system has to define what is to be inside the cubicle and CODAS has to provide and maintain it. Diagnostic Engineering Group had to liaise between CODAS, which has a set of rigid rules and also large procurement programmes, and the Associations whose requirements were changeable and individualistic, initial proposals rarely met CODAS requirements and considerable adjustment was required. To date, all 30 diagnostics have their CODAS interface cubicles commissioned or almost commissioned with the various compromises incorporated in them.

The two major factors that affect the control and data acquisition for diagnostics are the operation of JET in pulses and the relatively slow fibre optic link to the computer. Control functions requiring quick responses, such as safety systems, must have local controllers operating with firmware to give the

required response. Secondly the CAMAC system must be primed to accept and store data autonomously during a pulse. The amount of data that it is possible to take during a 20 second pulse is enormous. The experimentalists, therefore, have to exercise restraint on the amount of data they take not only because of the problems of data transfer rates possible between JET shots but also to avoid being overwhelmed by the problem of analysing the data afterwards.

Conclusions

JET has now 30 diagnostics operating or nearing completion. Those operating are taking considerable data, which is being transferred through CODAS and archived at Harwell.

After close collaboration with other JET groups there are diagnostics built for active phase operation that are compatible with tritium and are also remotely handleable for maintenance and removal.

Acknowledgements

The authors wish to acknowledge the considerable effort put into the diagnostic systems by their colleagues in the Associated Fusion Laboratories and the help and guidance given by fellow staff members in the Scientific Department and other divisions at JET.

JET NEUTRAL INJECTION BEAMLINE SYSTEM, MANUFACTURE AND ASSEMBLY

R Haange, H Altmann, S Papastergiou, R B Tivey, M J Watson

JET Joint Undertaking, Abingdon, Oxon, UK

Abstract

The first JET neutral injection beamline system has been installed. Many of the components have numerous vacuum brazed, electron-beam welded and friction welded joints including various dissimilar alloy combinations. The large beamline system has been assembled, installed and aligned to tight tolerances. Acceptance leak testing of components has included thermal cycling from ambient temperature to 300 °C followed by pressurisation with helium inside a vacuum furnace. Installation of the large components has required special lifting and alignment equipment.

Introduction

Operation of the first JET neutral injection beamline is now imminent. The system has been installed and many components have been fully commissioned. First injection into the plasma is planned for this year. The design values for the beamline are

80 keV, 60A for hydrogen operation	
160 keV, 30A for deuterium operation	
Pulse length	10 s
Fatigue life	10^5 cycles
Duty ratio	10/600

As described in more detail in [1,2,3,4,5] the beamline is housed in a large vacuum box, as shown schematically in Fig. 1. This box is surrounded by a magnetic shield to minimise the effect of the torus magnetic field on the beamline. Eight beam sources are attached to the back panel of the box. The ports onto which the beam sources are flanged also hold water cooled neutralizers. The neutralizer and plasma source gas is pumped by liquid helium cooled panels which line the two side walls of the box. The eight sources are grouped in four pairs such that, after partial neutralization, each pair of beams passes through one magnet, where the ionic fractions are separated and directed onto full, half and third energy ion dumps. The magnet pole faces are protected by water-cooled copper liners. The neutrals can either be intercepted by a calorimeter or, with the calorimeter moved out of the beams, be injected in the plasma through a duct section containing an absolute rotary high vacuum valve. At the front aperture of the vacuum box the beams are pre-shaped to the race track aperture of the rotary valve by the box scrapers. Furthermore, a fast shutter assembly is mounted here which can close the front aperture rapidly (~0.4 sec) to minimize the ingress of tritium (during later operation) or other contaminants. The fast shutter is water cooled and made of two titamium alloy doors (Ti Grade 5, 6% Al, 4%V) which are actuated pneumatically from outside the box.

The dumps, bending magnets and calorimeter are mounted on a hollow section, stainless steel (SS) structure that also conveys the coolant to and from the

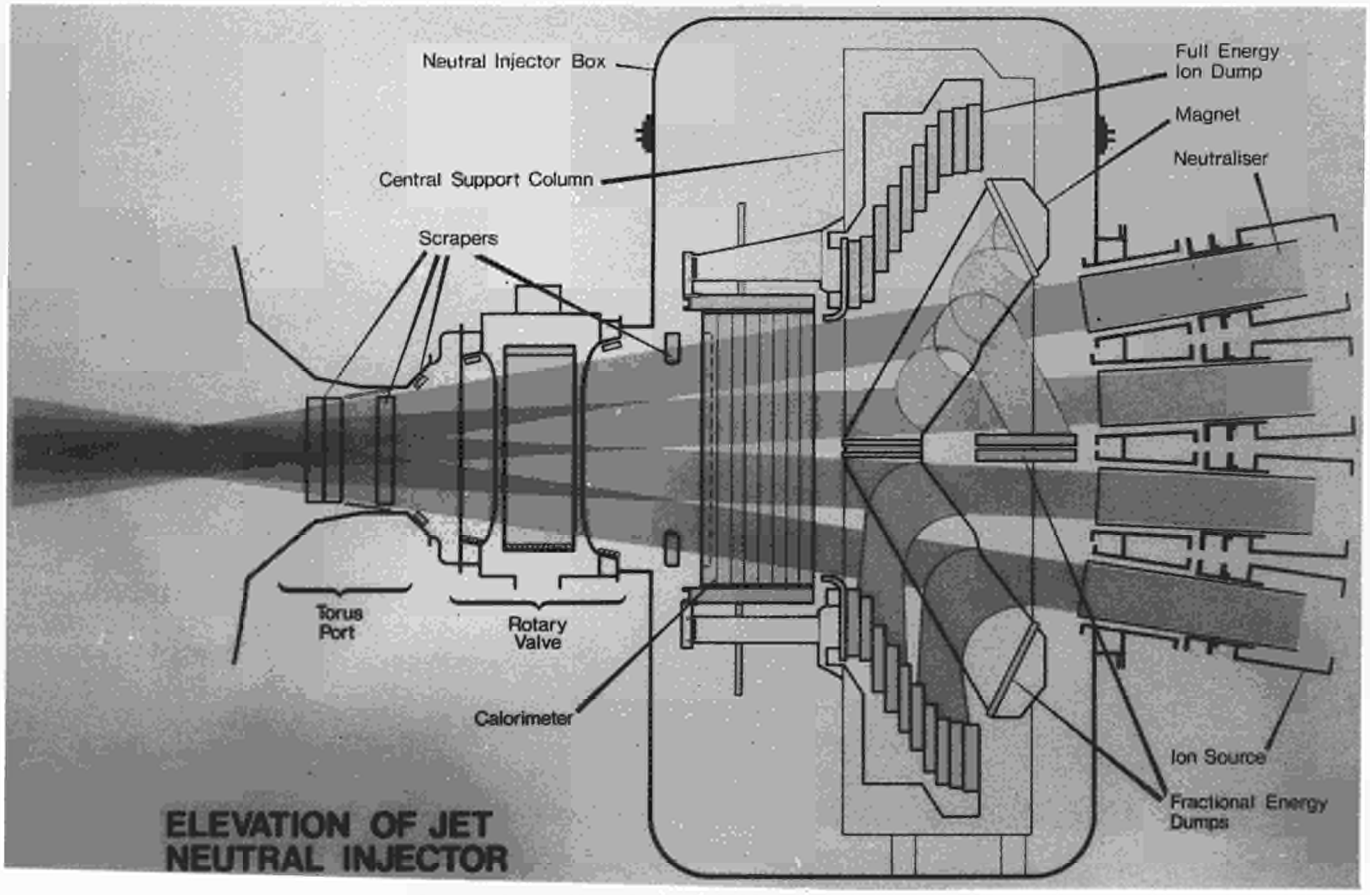

Fig. 1 Schematic view of JET Neutral Injector.

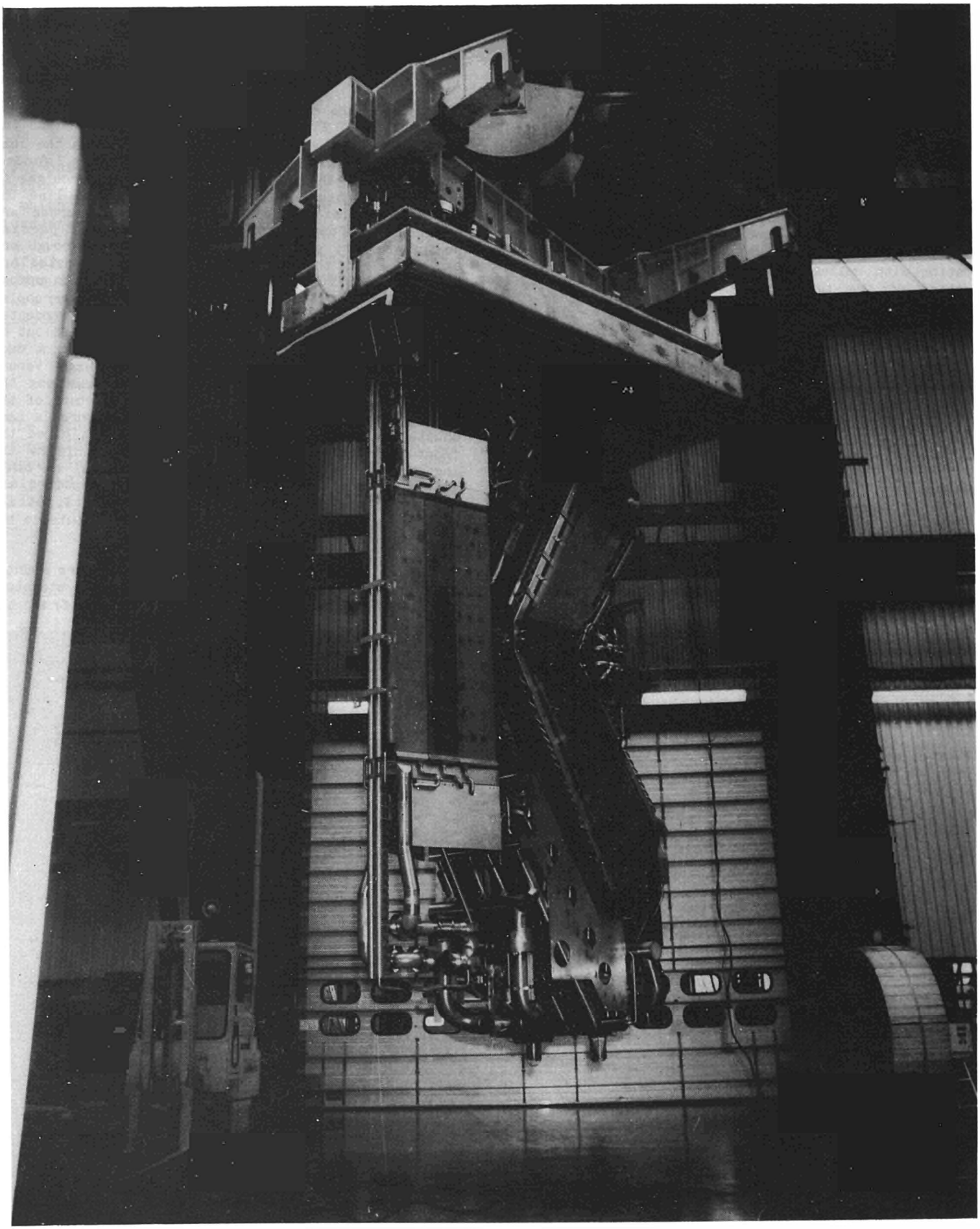

Fig. 2 View of central support column assembly

components. This central support column as shown in Figs. 2, 3 is supported from the lid of the box in such a way that the complete central column assembly can be removed by crane (32 t). This allows relatively simple replacement of a complete central column or maintenance of its components.

Component Manufacture - Some Special Features

Spatial restrictions dictate a rather compact design. This leads to high power densities on beam scraping and stopping elements. The system has been designed such that the maximum nominal power densities are ~ 1kW/cm². By using hypervapatron type elements [4] the coolant pressure drop requirement is very modest. This type of element requires, however, a rather thick copper front plate (6 to 14 mm) giving rise to high thermal stresses during a pulse. In order to satisfy the requirement of a fatigue life of 10^5 full power pulses, a precipitation hardenable copper alloy was selected for these elements (CuCrZr with nominally 1% Cr and 0.07% Zr).

The internally finned shape of the beam stopping element (see Fig 3) is made by machining from forged or extruded bar. Rear and end plates are added by electron-beam (EB) welding. EB-welding is always carried out in the solution heat treated (soft and low conductivity) condition and is followed by precipitation hardening at 470 °C. Depending on the component, SS or Inconel 600 coolant feed/return stubs

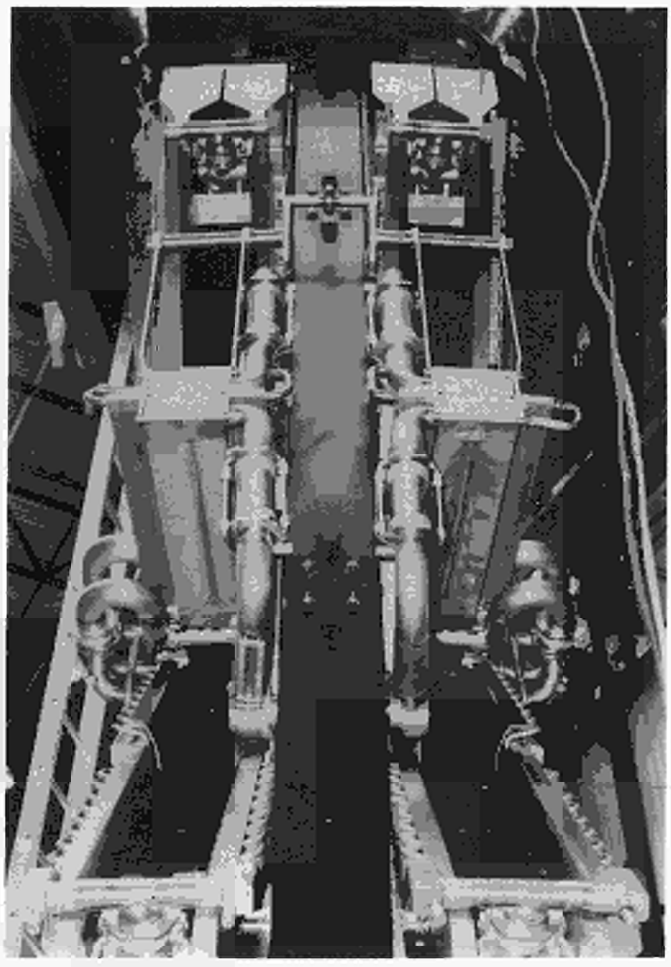

Fig. 3 View of central column assembly in beam downstream direction.

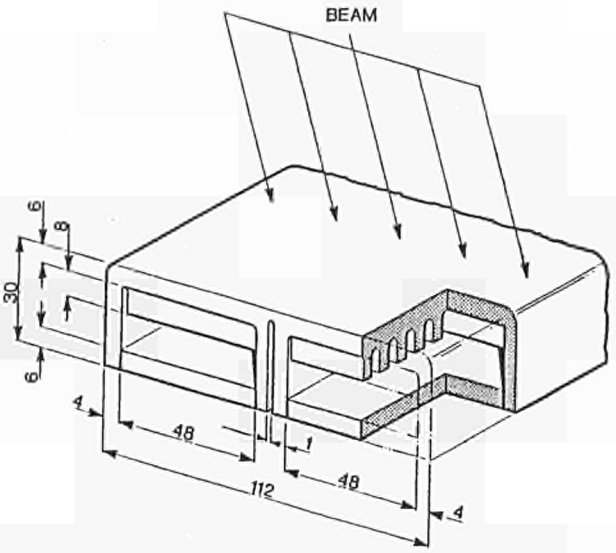

Fig. 4 Cross section through beam stopping element.

are brazed or friction welded to the rear or end plates. These stubs are then welded to SS bellows, which provide the necessary flexibility in the coolant lines during a pulse when the beam stopping elements deflect. In the second beamline, these bellows are changed to Inconel 600 to improve corrosion resistance to demineralised water. As the coolant pressure inside the elements is ~ 5 bar, the stresses generated inside the elements are almost entirely thermal stresses. Fig 4 depicts some results of strain controlled tests on EB-welded samples. The shaded area is the calculated maximum strain range inside the element under steady state conditions (established after ~ 4 s) at 1 kW/cm². As the exact phenomenon of hypervapotron heat transfer is not fully understood, a margin of uncertainty exists with respect to temperature profile calculations and hence with stress and strain distribution. This is reflected in Fig 5. where optimistic and pessimistic assumptions are shown. The weldment samples were tested under conditions to cause failure after 10^4 to 10^5 cycles and the 10^5 values have been calculated using the Coffin formula for strain controlled fatigue [6]. The tests were carried out with 1.5 s rise and

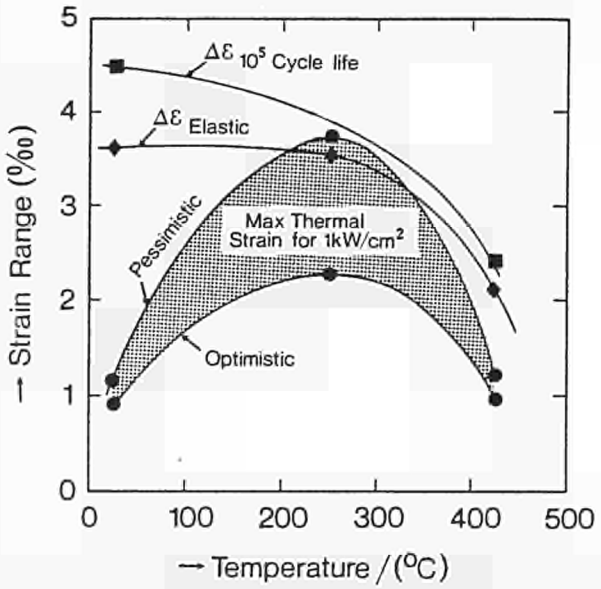

Fig. 5 Strain range vs temperature of CuCrZr alloy (10^5 cycle life derived from electron-beam weldment samples)

TABLE I

JOINTS REQUIRING LEAK TIGHTNESS $\ll 10^{-9}$ mbarl/s

Joint Type	Material Combination	Remarks	Quantity
EB-Weld	CuCrZr/CuCrZr		~ 600
EB-Weld	Ni/CuCrZr		50
Vac-Braze	SS/CuCrZr	Filler NiCrPFe (76/14/10/0.2%)	350
Vac-Braze	SS/CuCrZr	Filler AgCu (28/72%)	4
Friction Weld	SS/Al MgSi (0.5%Mg,0.5%Si)	Cycling cryo temp-RT	
Friction Weld	SS/Al/Ti Grade 5		4
TIG Weld	Ti Grade 5/Ti Grade 5 (6% Ac, 4% V)	Welding is followed by stress relieving treatment at 700 °C	~ 800
Vac-Braze	SS/Cu	Pd-Cu-Ag braze	~ 250
Vac-Braze	SS/SS	Nicrobraze 10	~ 150
Friction Weld	Ni/Cu	Ni in full annealed condition	~ 64
Friction Weld	SS/Inconel 600		~ 750
Friction Weld	SS/Cu		~ 70
Friction Weld	Ni/SS	Ni in full annealed condition	64

ramp-down time and 3 s hold time. As can be seen at 1 kW/cm² the elements can be considered marginally safe or very safe depending on the exact temperature profile. Some tests are underway on an element at JET to measure the temperature profiles during transient and steady state condition.

In addition to some 2500 SS welds which require leak tightness to 10^{-9} mbar l/s, many other leak tight joints are employed in the design of the beamline components. Table 1 lists the main high quality brazed and welded joints. Furthermore, some components have been formed by electro-deposition of copper, which requires to be leak tight in relatively thin (~1 mm) copper layers. In addition, leak tight joints of the interface between deposited copper and copper plate or nickel coated SS stub pipes are required.

The leak tightness of components is tested by thermal cycling between ambient and 300 °C (150 °C for electrodeposited components). Subsequently the component is pressurised with helium and the leak rate into the vacuum furnace is measured.

Acceptance leak rate for most components has been specified to be 10^{-9} mbar l/s or lower in some cases. By this method many small leaks ($< 10^{-7}$ mbar l/s) were discovered that were not found before cycling. In addition small cracks in or near CuCrZr EB-welds were found after thermal cycling [7]. The cracking is now being avoided by additional heat treatment prior to welding and by modifications to the weld design especially by making the weld design more flexible.

Assembly, Installation and Alignment

Assembly of the components to a central support column was carried out by a team of 5 skilled technicians over

Fig. 6 View of magnet assembly prior to installation on central support column.

an average period of 8 months. Strict clean conditions had to be observed to guarantee compatibility of the system with high vacuum conditions. Handling of heavy and large components (~ 32 t, ~ 7 m) under very strict tolerances presented a challenge. Therefore special care had to be taken to ensure that the final position of components with respect to the beamlines was correct within ±2 mm. Weld shrinkage and the resultant induced stresses over ≈ 250 welds had to be accomodated.

The magnets were pre-assembled with all the associated components such as liners, dumps for fractional energy ions and water manifolds in a horizontal position. Thereafter the assemblies were raised to a vertical position, as shown in Fig 6, before being fitted to the support column. Then the dumps for full energy ions and calorimeter were bolted in place, followed by welding of water pipes. These welds were radiographed and leak tested.

In parallel with the central support column assembly, beam protection scrapers have been fitted inside the Torus port. Thereafter the vacuum box with the cryopanels, fast shutter, box scrapers and neutralisers was installed on the support structure which forms the base of the magnetic shielding. Finally the beam sources were fitted and all services, such as water, cryo-fluids, vacuum pumping, and electrical were connected. Electrical connections were also needed for approximately 400 thermocouples that monitor the condition of components.

Special lifting and installation devices have been designed for all major components. These range from a simple counter-balanced beam for installation of neutralizers to purpose-built lifting gear for the erection of the magnet assemblies, beam sources and dumps. Typical installation operations are shown in Figs 7 and 8.

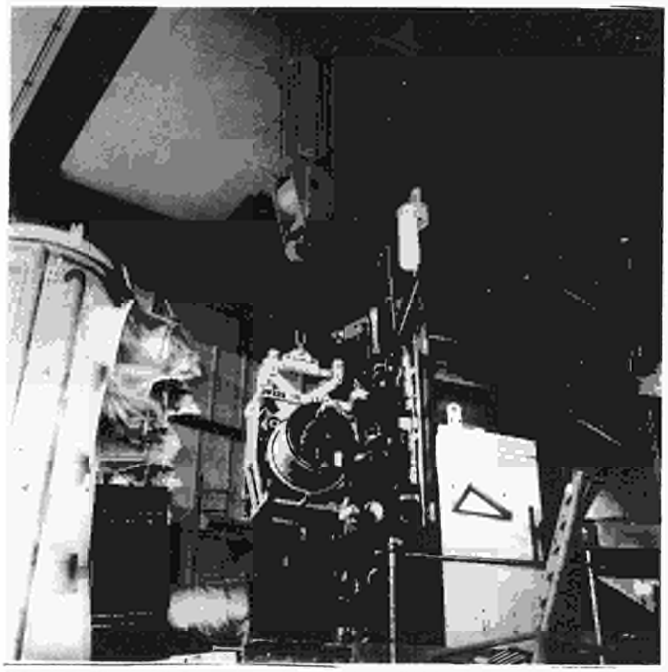

Fig. 7 View of beam source being fitted to vacuum box

It is of great importance that the alignment of all beamline components is within the tolerances specified to ensure correct operation of the beamline and avoid excessive power loading on to the components. The alignment consists of three main parts:

(1) Alignment of the vacuum box, rotary high vacuum valve, and adaptor flange to the Torus with respect to the injection port in the Torus and the nominal beamline centre lines. Using an alignment staff set in the narrowest aperture of the injection port, and accurate survey points in the JET Torus hall, the box and downstream components have been aligned by means of theodolites to within ±1.5 mm of the nominal centre lines.

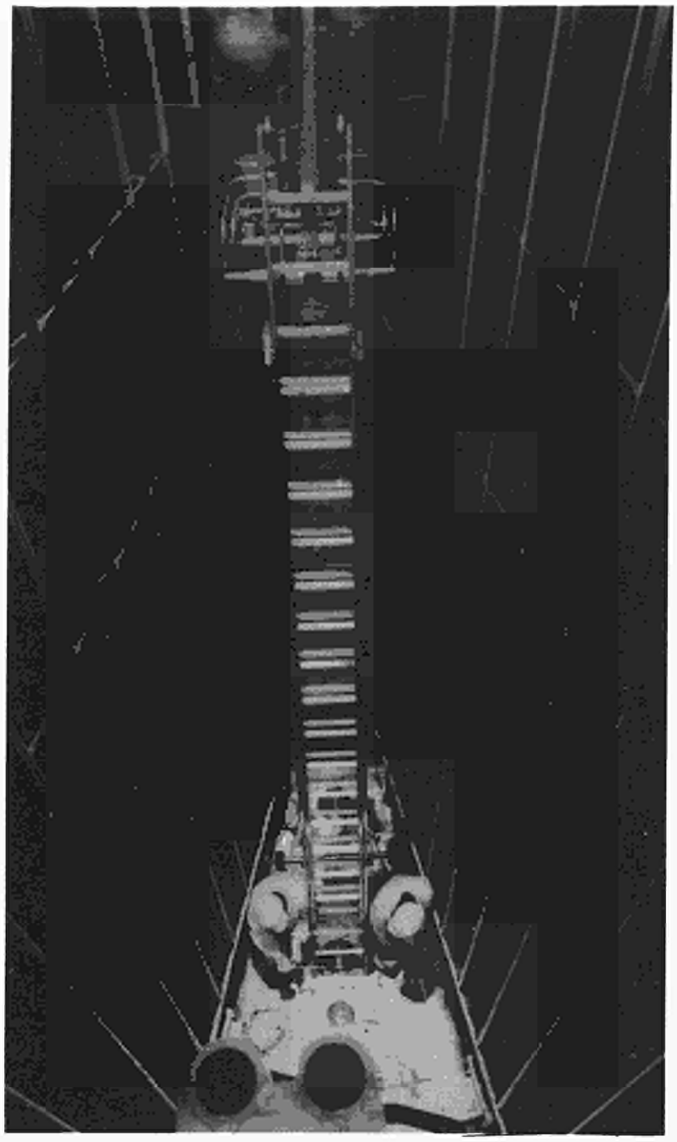

Fig. 8 View inside vacuum box showing cryo-panels and the installation of the box scrapers

(2) Alignment of beam sources.
During conditioning of the beam sources in a testbed, the misalignment between the geometric and beam centre lines of the sources is established using thermal analysis of the beam profiles. The steering flanges of the port on the vacuum box back panel are first adjusted with respect to the nominal geometric beam centre lines using the targets on the alignment staff in the injection port and an alignment telescope mounted on to a special dummy beam source which produces the forces on the source flanges. The alignments thus obtained are then transfered to a secondary target plate outside the vacuum box using lasers mounted onto a lever arm connected to the

steering flanges. This allows subsequent checking of the beam alignment during operation. During mounting, the beam sources are offset laterally to bring the beam centre lines onto the optical centre line and after evacuation (deflection) the steering flanges are adjusted to the correct offset using the external secondary targets. In this way alignment to within ≈ ± 2 mm at the injection port is achieved.

(3) Alignment of other components

Using special alignment targets for each component together with the alignment staff and alignment telescopes or lasers mounted onto adaptor flanges, the misalignment of all other components can be measured. The design allows for positional adjustment during installation with the exception of the central column assembly which can only be adjusted as one unit. The measured alignment of components is generally better than ±2.5 mm which compares favourably with the specified misalignment of ±5 mm.

Figure 9 shows the complete neutral injection beamline installed between the Torus and the high voltage tower which supplies all services to the beam sources.

Following the completion of the central column assembly, the system was installed and operated in a testbed. This successfully submitted one quadrant to the operational conditions [8].

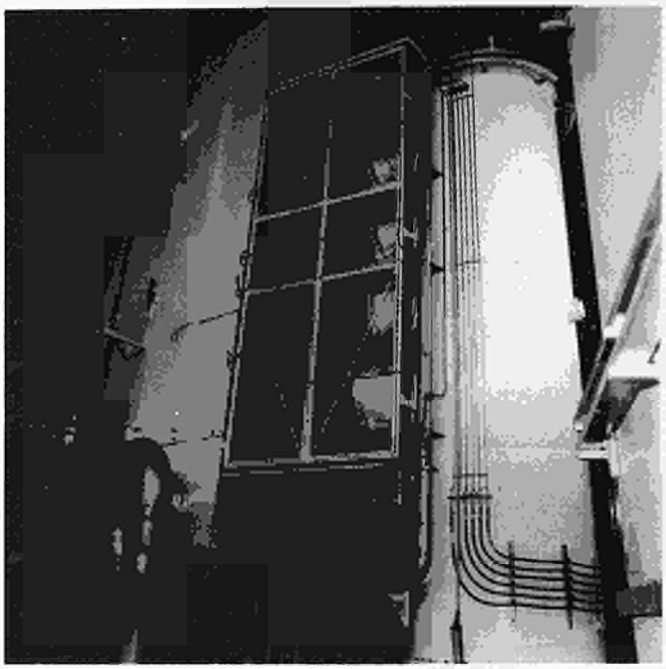

Fig. 9 View of complete neutral injection beamline.

References

(1) G Duesing, "JET Neutral Beam Injection System, Construction and Component Tests", 13th SOFT, Varese (Sept. 1984), p. 59.

(2) A P H Goede, A A Ingersoll, P Kupschus, B R Nielsen, E Thompson, R S Hemsworth, The JET Neutral Injection Deflection Magnet", 12th SOFT Aachen (Sept. 1982), p. 1321.

(3) W Obert, G Duesing, E Küssel, P Kupschus, C Mayaux, P H Rebut, H Santos, "The JET cryopump system and its cryolines for Neutral Injection", 13th SOFT, Varese (Sept. 1984), p. 311.

(4) R Haange, "Design of Calorimeter and Ion Dump for JET Neutral Injection Beamline," 9th Symposium on Engineering Problems of Fusion Research, Chicago (Oct. 1981), p. 1352.

(5) H Altmann, "Manufacture of Beam Sources and Neutralisers for JET Neutral Injection", 13th SOFT, Varese (Sept. 1984), p. 579.

(6) L F Coffin, Product Engineering, 28(6), 175-179, June 1957.

(7) R Haange, "Components for Neutral Injection Beam Lines", to be published soon in Proceedings of Institution of Mechanical Engineers, London

(8) R S Hemsworth, H D Falter, G H Deschamps, A P H Goede, T T C Jones, M J Mead, A Stäbler, "Operational test of the JET Neutral Injection System in the JET Test Bed", 11th Symp. on Fusion Engineering, Austin, Texas, Nov. 1985.

DESIGN AND OPERATION OF THE JET ARTICULATED BOOM

P D F Jones, D Maisonnier, T Raimondi.

JET Joint Undertaking, Abingdon, Oxfordshire, England.

Abstract

After tritium introduction, planned for JET about 1991, remote handling maintenance will be vital to the continued operation of the machine.

An articulated boom has been designed at JET as the sole support device for in-vessel transport of all equipment and servo-manipulators and is part of the JET Remote Handling plan (1), (2), (3). The boom was manufactured by NEI Thompson of Wolverhampton and AET of Coventry, England, delivered to JET in October 1984 and has been commissioned successfully to its full design performance.

The boom has been used during the June 1985 maintenance period as a hands-on lifting device using a hand-held, push-button controller. Dynamic computer modelling of the boom has been carried out to analyse cross-coupling inertial effects arising in the horizontal plane. A ⅕-scale, mechanical model has also been used to control the boom in a master-slave mode.

Introduction

Direct vertical access for lifting of heavy components inside the vacuum vessel is impossible and the only sizeable access ports (940 × 430mm) are on the horizontal equatorial plane. A rail system is not possible as it would be susceptible to damage by plasma and, in any case, the first wall is covered with protective graphite tiles. Various possible methods have been proposed of which the 2 favoured ones are the 'boom' and the 'tracked vehicle' methods.

The problems of inserting a tracked vehicle into the vessel are severe and its use would necessitate the use of troublesome umbilical supplies. Therefore cantilever-type boom lifting arms have been planned for JET as for most conceptual TOKAMAK reactor design (4), and most in-vessel remote handling maintenance operation scenarios include the use of boom-mounted devices (5).

A telescopic boom has 3 main shortcomings: firstly and most importantly, the necessity of reaching both near and far positions within the torus would require an impossible extension ratio; secondly, the problem of cable reeling; and thirdly, the curved geometry of the vessel. Therefore an articulated design was selected for JET.

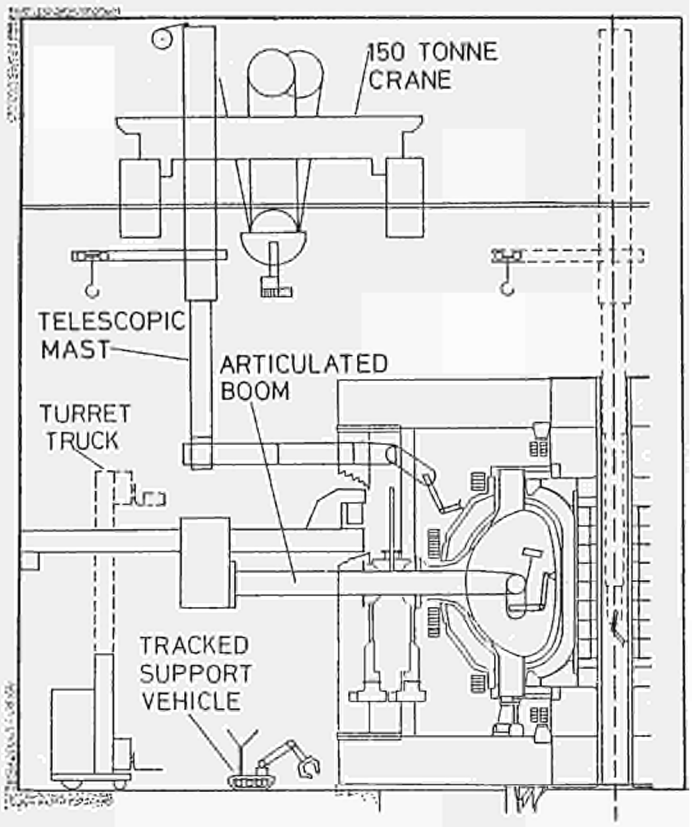

FIG 1 REMOTE HANDLING EQUIPMENT — OVERALL PATTERN

Figure 1 shows the boom in operating position in the JET Torus Hall, together with other proposed transporters, such as the existing 150 tonne crane and the telescopic mast which will be attached to it.

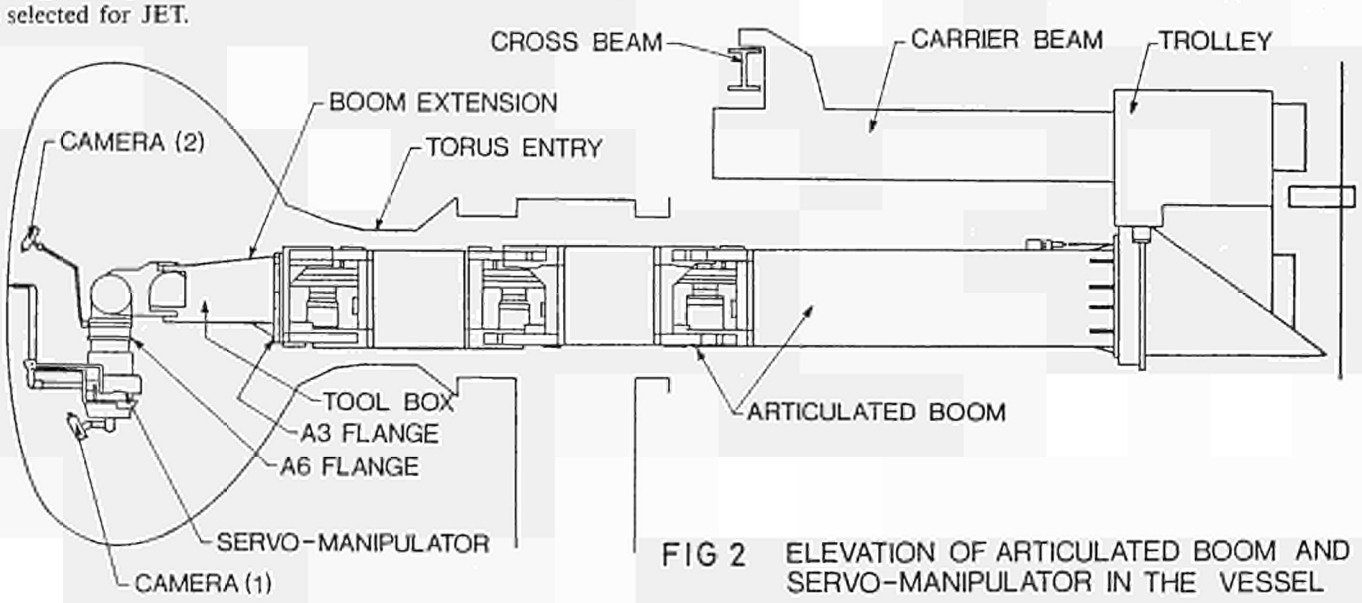

FIG 2 ELEVATION OF ARTICULATED BOOM AND SERVO-MANIPULATOR IN THE VESSEL

Operational Requirements

During the yearly maintenance shutdowns of JET, expendable items are to be replaced or upgraded. Items less than 20kg, such as tiles, are handled by the MASCOT, a feedback servomanipulator, situated at the end of the boom (see Fig 2). The MASCOT will also position special cutting and welding tools and operate wrenches.

Heavier items up to 300kg, such as limiters and RF antennae, are handled by dedicated gripper assemblies which replace the MASCOT at the end of the boom. So far 6 types of end-effectors have been designed and 3 manufactured. These have to be utilised sequentially to perform in-vessel tasks and, so that the minimum of time may be lost, a rapid remote end-effector change system has been designed.

The end-effectors themselves incorporate a special-purpose mechanism for failsafe transferral of antennae and limiters onto the vacuum vessel wall.

A turret truck (later to be radio-controlled) is used to transport equipment and end-effectors from the Assembly Hall into the Torus Hall, which will be active during the D-T phase.

The boom itself carries a maximum of 3 CCTV cameras with fully remote motorised zoom, focus and aperture control. One boom camera is mounted at the rear of the boom directed so as to monitor the critical clearances (order 10mm). The other 2 cameras mounted on special retractable arms near the end-effector are provided for operational viewing.

In addition, the in-vessel inspection system for JET enables 4 equally spaced computer controlled CCTV cameras to view in-vessel boom operations from above.

Boom Description

The limited size access port and the need to reach all points on the inside toroidal surface of the vacuum vessel determined the leading size parameters such as arm length (1.66m), number of arms (4 to reach half the vessel, or 5 to reach the whole vessel), cross-sectional dimensions (880mm × 340mm) and size of motor gearbox unit ($\phi \sim 300$mm and length ~ 400mm).

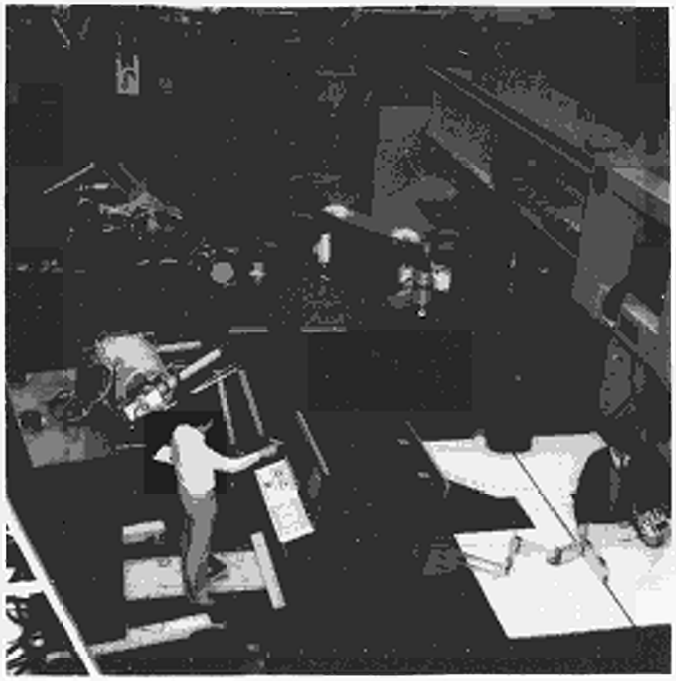

FIG 3 BOOM MASCOT AND MASTER MODEL IN ASSEMBLY HALL.

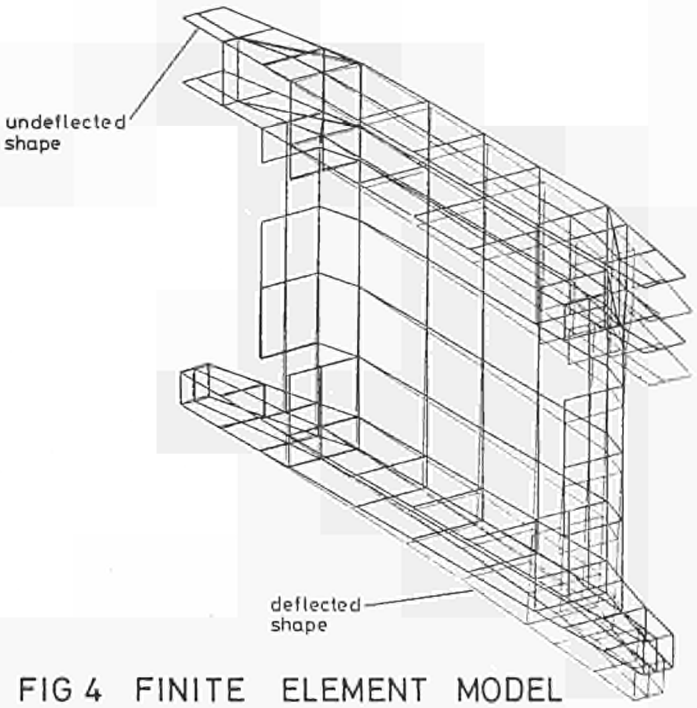

FIG 4 FINITE ELEMENT MODEL

The load capacity is one tonne at 9m from the support in the (horizontal) equatorial plane. An extension to the boom provides 3 additional axes of rotation with a load capacity (out of the equatorial plane) of 350kg at 13.5m from the support (see Figs 2 and 3).

The requirement not to contaminate the vacuum cleanliness of the JET vessel precluded the use of any paint or hydraulic fluid (excepting pure water). Therefore electric motors were selected as prime movers for all the main in-vessel joints. DC torque motors are used to achieve the fine control needed in the simplest way. Harmonic Drive gearboxes with outputs up to 600kgm were chosen to couple the motors to the joints in a modular package as they provide high efficiency, high ratio, high torque, low weight and low volume and may be used with grease fill. Failsafe brakes are arranged to allow the joint to go 'loose' if required.

The trolley with a horizontal travel of 7.4m permits boom entry to the vacuum vessel through the pumping chamber and allows the arms to fold outside the vacuum vessel. The trolley allows for limited slew and tilt ($\pm 3°$) providing vertical motion at the boom tip, compensating for vertical deflection and fine alignment of the arm in the torus access port.

To optimise the strength vs weight the arms near the trolley are of stainless steel (304L) and the arms further away are of aluminium alloy (N8). These are compatible with the clean conditions inside the vessel. Outside the vessel cheaper mild steel was used for the trolley and carrier beam.

The boom extension (see Figs 2 and 3) is open to accommodate a tool box and so could be made simpler as a casting. The HIP (Hot Isostatic Pressing) treatment on these aluminium (LM25) castings improves the yield, tensile toughness and fatigue properties.

A finite element stress and deflection analysis (see Fig 4) was carried out using NASTRAN code for each of the main boom segments and results were verified by strain gauge and brittle lacquer tests during manufacture. Measured vertical deflections at the boom tip were 20mm/tonne straight ahead and 40mm/tonne reaching sideways and putting maximum torque on the first arm.

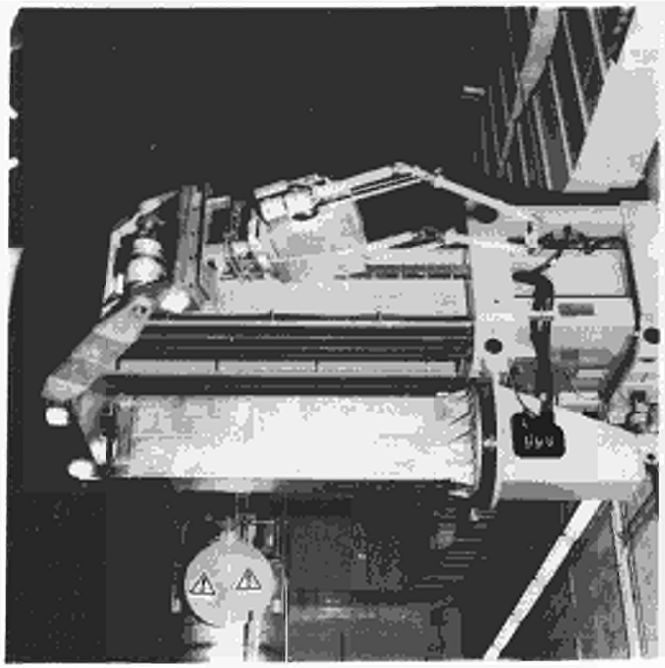

FIG 5 BOOM FOLDED IN TORUS HALL

The electrical and fluid services (MASCOT and boom power and signals, air, cooling water, high pressure water for special tools, gases for welding) are carried inside the arms of the boom for maximum protection and to allow maximum usage of structural material in the given space envelope.

Control and Operation

The boom was procured well in advance of the active phase in order to gain experience in hands-on work and simulated remote conditions. In order to allow for hands-on operation a push-button, portable control box was procured with the initial

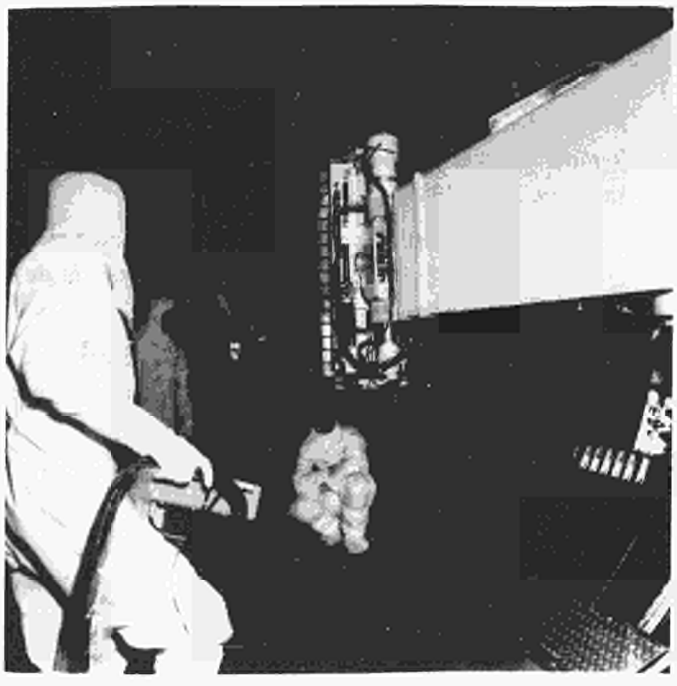

FIG 6 BOOM INSIDE TORUS HOLDING EQUATORIAL LIMITER

delivery of the boom. A separate power supply module allows simultaneous movement in open loop of any combination of any 2 drives in either continuous or inching mode. LED displays indicate required parameters such as joint angle, motor current and speed, output torque and trolley linear position. The boom was manoeuvred without difficulty with this unit and it was used during the summer '85 shutdown to replace 4 equatorial limiters with RF antennae (see Figs 5 and 6).

A simultaneous motion of 4 axes in a master-slave mode has also been implemented using 1/5-scale model as a master (see Fig 3). Obstacle avoidance is achieved by moving the master within simulated equatorial boundaries.

As originally conceived, a fully computerised control system has been defined and will be operational by the end of 1986. This will incorporate a teach and repeat facility for repetitive motions such as vessel insertion and pre-positioning in working areas. It will also compute and execute resolved motion for fine adjustment using a joystick and the system will allow for future implementation of high-level software such as anti-collision algorithms.

For remote operation all identified loads weigh only 30% of the original design capacity. It is now planned to extend the reach of the boom to cover the whole vacuum vessel from one entrance, by adding another vertical axis joint and extending the arms by a total of 2.8m with obvious operational time-saving benefits (see Fig 7). If time were more at a premium, the operation could be speeded up by using 2 booms, entering from opposite sides of the vessel. One would carry the servomanipulator whilst the other would carry the heavy duty end-effector. This would also enable rescue operations to be carried out more easily in the event of a boom motion failure.

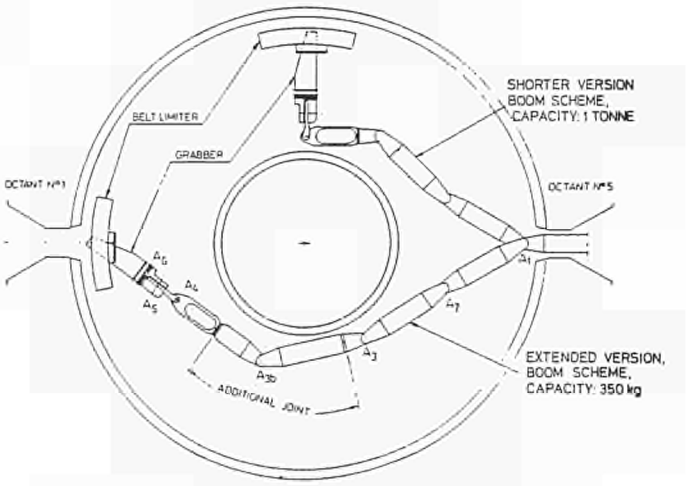

FIG 7 BOOM IN VESSEL, PLAN VIEW

Dynamic Studies

The articulated boom has very low torque to inertia and stiffness to inertia ratios when compared with other robotic arms and those factors increase the problem of inertial cross-coupling between the 4 main vertical axis drives. In order to make the problem amenable to solution the effects of vertical deflection, which would not in any case have affected the fundamental behaviour, were neglected. Also the cross-coupling effect of the linear travel was not included as this motion is slow and contains a high mechanical damping.

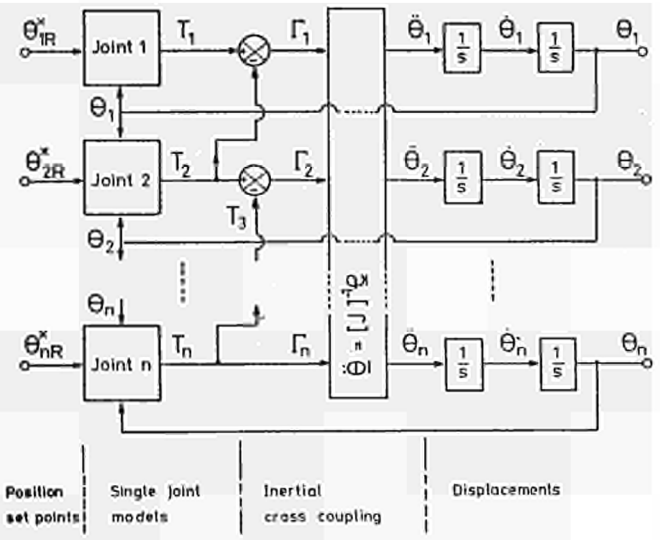

FIG 8 BLOCK DIAGRAM OF A TWO DIMENSIONAL ARTICULATED TRANSPORTER

The equations of the dynamic cross-coupling between arms, obtained by the Lagrange equation, can be summarised by the following matrix equation:

$$\underline{\Gamma} = [J(\theta)]\,\underline{\ddot{\theta}} + [C(\theta)]\,\underline{\dot{\theta}}^2$$

where

$$\underline{\Gamma} = (\Gamma_1, \Gamma_2, \Gamma_3, \Gamma_4)$$

$$\underline{\ddot{\theta}} = (\ddot{\theta}_1, \ddot{\theta}_2, \ddot{\theta}_3, \ddot{\theta}_4)$$

$$\underline{\dot{\theta}}^2 = (\dot{\theta}_1^2, \dot{\theta}_2^2, \dot{\theta}_3^2, \dot{\theta}_4^2)$$

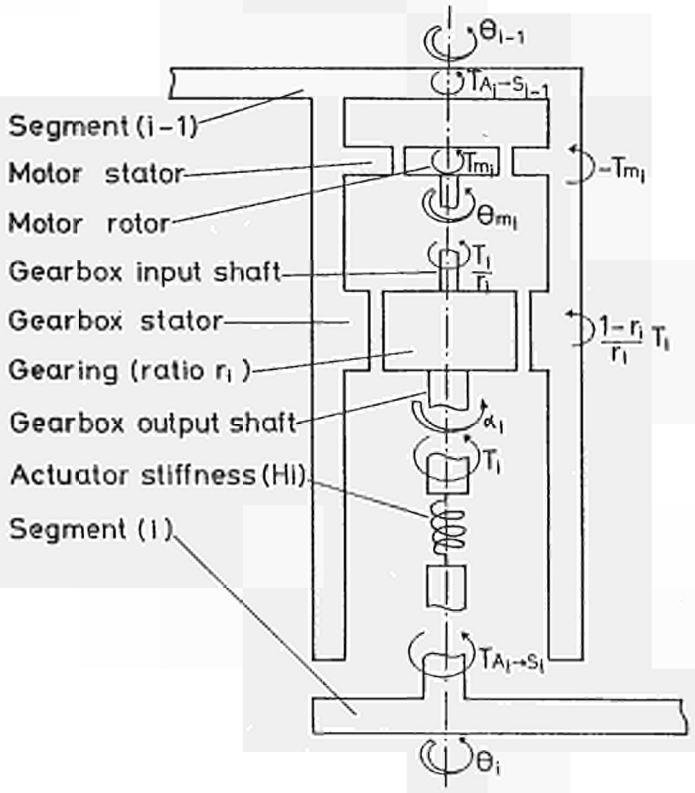

FIG 9 EXPLODED VIEW OF THE I^{TH} JOINT (A_i)

Γ_i is the torque applied by the actuators to the arm A_iA_{i+1}, θ_i its absolute angular position, $\dot{\theta}_i$ and $\ddot{\theta}_i$ its speed and acceleration.

$[J(\theta)]$ represents the inertia tensor of the arm referred to the output shafts of the actuator.

$[J(\theta)]\ \underline{\ddot{\theta}}$ is the inertia torque vector and $[C(\theta)]\underline{\dot{\theta}}^2$ the centrifugal and Coriolis torque vector.

$[J(\theta)]$ and $[C(\theta)]$ depend on the boom geometrical configuration.

Vector $\underline{\Gamma}$ is obtained by modelling the joint actuators and servosystems in a conventional way, simulating the non-linearities (such as backlash and amplifier saturation) and torsional flexibility of the joints.

A computer simulation (using the CSMP-III code from IBM) was carried out using the above model (see Figs 8 and 9), and the results compared well with the real measured responses (see Fig 10).

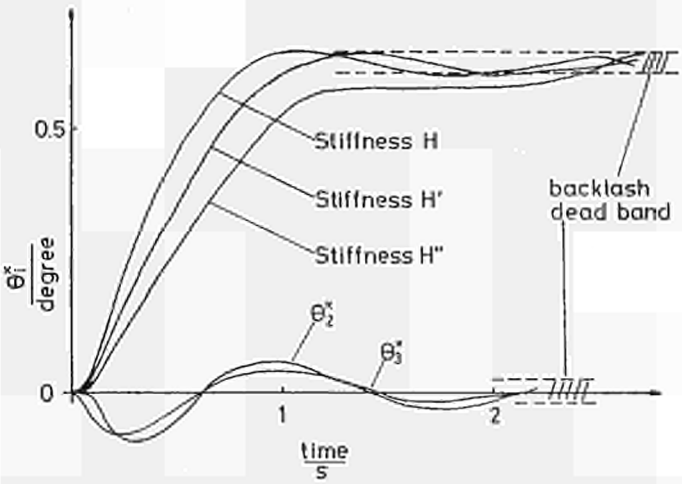

FIG 10 STEP INPUT RESPONSE, WITHOUT OVERSHOOT, OF JOINT A_1 FOR DIFFERENT VALUES OF STIFFNESS

References

(1) J Dean 'Remote Maintenance of the JET Tokamak'; Proceedings of the ANS Executive Conference on Remote Operations and Robotics in the Nuclear Industry, April 1985.

(2) J Dean, T Raimondi 'Concepts and Status of Remote Handling in JET'; Proceedings of 10th Symposium on Fusion Engineering, 1983.

(3) T Raimondi 'Remote Operations in JET: Problems and Solutions'; Proceedings of First European Symposium on Fusion Devices, 1982.

(4) J Guthrie, P Budjen 'Assessment of European Remote Systems Technology Relevant to Fusion Reactor Maintenance Requirements'; Proceedings of 32nd Conference on Remote Systems Technology, 1984.

(5) P Spampinato 'In-Vessel Maintenance Operations'; FED-Engineering Study Report ORNL/FEDC-82/2 Published April 1983.

CD-NA-10-616-EN-C